NOVA SCHOOL OF SCIENCE & TECHNOLOGY

DEPARTAMENT OF MATERIALS SCIENCE

# NANOTECHNOLOGY FOR ENERGY HARVESTING: FROM FUNDAMENTAL TRIBOELECTRIFICATION TO SELF-POWERED SMART APPLICATIONS VIA TRIBOELECTRIC AND PIEZOELECTRIC NANOGENERATORS

RAFAEL RESENDE ASSIS SILVA

Master in Food Science and Technology

DOCTORATE IN NANOTECHNOLOGIES AND NANOSCIENCES

NOVA University Lisbon

December, 2025

NOVA SCHOOL OF
SCIENCE & TECHNOLOGY

DEPARTAMENT OF MATERIALS SCIENCE

# NANOTECHNOLOGY FOR ENERGY HARVESTING: FROM FUNDAMENTAL TRIBOELECTRIFICATION TO SELF-POWERED SMART APPLICATIONS VIA TRIBOELECTRIC AND PIEZOELECTRIC NANOGENERATORS

**RAFAEL RESENDE ASSIS SILVA**

Master in Food Science and Technology

**Adviser:** Rodrigo Ferrão de Paiva Martins
*Full Professor, NOVA University Lisbon*

**Co-adviser:** Luiz Henrique Capparelli Mattoso
*Senior Researcher, Embrapa Instrumentação*

**Examination Committee:**

**Chair:** Caio Gomide Otoni,
Assistant Professor, Institute of Chemistry, State University of Campinas

**Rapporteurs:** Elvira Maria Correia Fortunato,
Full Professor, NOVA School of Science and Technology, NOVA University of Lisbon

Carmen Luiza Feitosa de Lima Gomes,
Associate Professor, Department of Mechanical Engineering, Iowa State University

**Members:** Pedro Miguel Cândido Barquinha,
Associate Professor, NOVA School of Science and Technology, NOVA University of Lisbon

João Carlos Mesquita Coelho,
Researcher, Sevilla University Faculty of Physics

Carlos Henrique Scuracchio,
Assistant Professor, Federal University of São Carlos

DOCTORATE IN NANOTECHNOLOGIES AND NANOSCIENCES
NOVA University Lisbon
December, 2025

**Nanotechnology for Energy Harvesting: From Fundamental Triboelectrification to Self-Powered Smart Applications via Triboelectric and Piezoelectric Nanogenerators**

Copyright © Rafael Resende Assis Silva, NOVA School of Science and Technology, NOVA University Lisbon.

The NOVA School of Science and Technology and the NOVA University Lisbon have the right, perpetual and without geographical boundaries, to file and publish this dissertation through printed copies reproduced on paper or on digital form, or by any other means known or that may be invented, and to disseminate through scientific repositories and admit its copying and distribution for non-commercial, educational or research purposes, as long as credit is given to the author and editor.

# ACKNOWLEDGMENTS

Nenhum avanço científico floresce sozinho, é o resultado da soma de apoio, paciência e inspiração compartilhada. Toda conquista é um mosaico de pequenas contribuições, e cada peça deste trabalho carrega um pouco das pessoas que cruzaram meu caminho. Expresso minha gratidão:

À pessoa que tornou tudo isso possível, minha inspiração e mãe de coração, Sandra Rezende, que me criou, incentivou, orientou e sempre foi um exemplo de profissional e de ser humano. Você nunca mediu esforços para me ajudar, sempre acreditou em mim e me motivou a seguir os estudos. Se cheguei até aqui, tenho certeza que é por sua causa. Saiba que sempre poderá contar comigo e que sempre fará parte de mim. Muito obrigado. Te amo!

Ao professor Dr. Rodrigo Martins, referência mundial na ciência e nanotecnologia, e um erdadeiro exemplo de líder e professor. Sem você, esta tese, e o nível que ela atingiu, não seriam possíveis. Muito obrigado pelas condições excepcionais de pesquisa oferecidas no CENIMAT&CEMOP e por inspirar a busca constante pela excelência científica. Admiro profundamente seu trabalho e espero poder trabalhar novamente com você em Portugal.

À professora Dr. Elvira Fortunato, exemplo na ciência e na inovação, pela liderança inspiradora e pela oportunidade de aprendizado. Sua visão e dedicação ao avanço da ciência me motivaram em cada etapa deste trabalho.

Ao meu orientador Dr. Caio Otoni, que, além de ensinar e orientar, é uma inspiração profissional. Foi visionário ao sugerir esse tema de pesquisa emergente para o meu doutorado. Sou grato por ter acreditado neste projeto desde o início e por me motivar a persistir mesmo diante das dificuldades dessa jornada. Muito obrigado!

Ao professor Dr. Luiz Mattoso, que, além de orientador e conselheiro, foi um verdadeiro apoio humano durante toda esta jornada, um exemplo de gentileza e sabedoria. Muito obrigado por acreditar em mim e tornar possível a realização deste sonho.

Meu agradecimento especial às pessoas essenciais na minha vida:

À minha irmã Janaína Resende, ao meu padrinho Marcos Carvalho, às minhas sobrinhas Priscila Resende e Ana Laura Resende, e ao meu pai Gilberto Resende, por todo amor, carinho e compreensão nos momentos de ausência.

À minha avó Maria Rezende (in memoriam) e à minha mãe Teresinha Rezende (in memoriam), que continuam presentes em mim em cada conquista.

À Bianca Martins, que há tão pouco tempo entrou na minha vida, mas já parece fazer parte dela há anos, tornando tudo mais leve e prazeroso. Obrigado por estar ao meu lado nos momentos de estresse, por já fazer parte dos melhores momentos da minha vida e por me lembrar que a vida não é só trabalho. Vejo em você um exemplo de ser humano e espero ser o melhor para você. A sorte da minha vida foi te encontrar. Te amo!

A toda minha família Res(z)ende, pela união, pelas raízes e pelo amor que me sustentam, mesmo à distância.

Aos meus amigos de Portugal, Mariana Cortinhal (Mari) my bestfriend, Guilherme Ferreira, Cátia Figuereido, Henrique Almeida, Guilherme Henrique, Emanuel Carlos (Manu), Francisca Paraíso, David Bento, Zulema Ixchel, Sara Silvestre, Tomás Pinheiro, João Coelho (Lapin), Luna Lochmatter, Marta Luis, Maria Morais, Alexandra Gonçalves, Rui André, Raquel Martins, e Carlos Silva, sinto imensas saudades de vocês! Espero revê-los em breve, pá, pá!

Aos amigos brasileiros em Portugal, Maíza Ozório, Douglas Vieira, Maykel Klem, Tati Oliveira, Rodolfo Pinto (Romeu) e Livia Coutinho, pela amizade, pelos cafés no LIDL e por cada momento compartilhado, espero revê-los logo!

To my forensic science colleagues, Andrea Spanou, Jahid Islam, Anitta Mathew, and Giulio Fatti, for all the support, partnership, and the opportunity to collaborate and learn through your respective works.

Aos meus ex-orientadores ao longo de toda a minha trajetória acadêmica, Nilda Soares, Paulo Stringheta, Eric Garcia, Amauri Souza e Júlio Onésio, registro minha gratidão por cada orientação, cada ensinamento e cada oportunidade de aprendizado, fundamentais para minha evolução científica e pessoal.

Aos amigos da UFSCar, Erick Gabriel, Thiago Wisley, Marcos Nicolino, Eduardo Backes, Bárbara Guimarães, Rafael Shimoda, Ana Soares, Anderson Zhong, Laís Possari, e Ewerton Teotonio, pela parceria, apoio e força nesta caminhada de doutorado.

Aos meus amigos próximos, Caio Melo, Clara Suprani, Tarsila Arruda e Érica Cardoso, por serem meu ponto de apoio emocional e me ajudarem a superar tantos desafios. Vocês são amigos para a vida toda. Contem sempre comigo!

A todos os membros dos grupos Matreerials, CENIMAT, CEMOP e Embrapa, pela colaboração e apoio constante.

Aos colegas Ana Santa, Jenny Boane, Andrea Spanou, Carlos Ureña, e Giulio Fatti pelas colaborações, treinamentos e ensinamentos práticos, sem vocês, a pesquisa não teria alcançado este nível.

Aos colegas João Silva e Frederico Barbosa, do Instituto Superior Técnico (i4HB), pelo excelente suporte e contribuições nas caracterizações biológicas do capítulo III. Sem vocês, não teríamos alcançado um trabalho e artigo de grande relevância e impacto!

Agradeço a todos que contribuíram, direta ou indiretamente, para o meu crescimento pessoal e profissional ao longo desses quase cinco anos. Este trabalho, certamente, não foi feito a duas mãos.

Muito obrigado a todos vocês!

À Universidade Federal de São Carlos (UFSCar) e a todos os seus funcionários, pela oportunidade e pelo suporte durante o doutorado em Ciência e Engenharia de Materiais.

This study also acknowledges the Department of Materials Science (DCM) at NOVA University Lisbon, as well as CENIMAT|i3N and CEMOP/UNINOVA, for their continuous structural support and collaboration.

This study acknowledges the Federal University of São Carlos (UFSCar), Graduate Program in Materials Science and Engineering (PPGCEM).

This study was financed in part by the Coordenação de Aperfeiçoamento de Pessoal de Nível Superior - Brasil (CAPES) - Finance Code 001.

This study was financed by CAPES – grant: 88887.625336/2021-00.

This study was financed, in part, by CNPq SWE – Conselho Nacional de Desenvolvimento Científico e Tecnológico – Brasil, grant: 200337/2022-0.

"If you want to go fast, go alone. If you want to go far, go together."

(African proverb).

# ABSTRACT

The urgent global demand for sustainable, decentralized, and reliable energy solutions has fuelled research into nanotechnology-based energy harvesting. This thesis advances both the fundamental understanding of triboelectrification and the development of multifunctional nanogenerators - triboelectric (TENGs) and piezoelectric (PENGs) - with the objective of enabling next-generation self-powered smart applications. To establish the foundation, a comprehensive analysis of the triboelectric effect - particularly under dirt-prone environments - was conducted alongside the role of functional materials for environmental energy harvesting and smart sensing. Charge-transport mechanisms, device architectures, and stimuli-responsive systems were examined, highlighting durability, contamination, and variability challenges, and providing the conceptual framework for smart TENGs applications developed in this thesis. Systematic investigations of liquid-solid triboelectrification revealed how flow dynamics, device structure, and ionic content govern electrical output. To translate TENGs into self-powered pressure sensors, a hierarchical surface-engineering strategy enhanced output and introduced self-cleaning capability for durable e-skin. Dual-scale micro/nanostructuring with chemical modification produced hydrophobic surfaces, achieving superior energy harvesting (~270 $mW \cdot m^{-2}$), high-pressure sensitivity, and 94% contaminant removal. Toward sustainable electronics, laser-induced graphene (LIG) electrodes were developed for food-quality monitoring and integrated with self-powered barcodes via TENGs. Anthocyanin incorporation catalyzed graphene synthesis ($I_D/I_G = 0.87$) and conferred $NH_3$ responsiveness, enabling tri-modal detection-colorimetric, electrochemical, and RFID-with a 110 ppm detection limit and 1.2 $\Omega \cdot m^3 \cdot mg^{-1}$ sensitivity, thereby allowing real-time, wireless, and reagent-free freshness monitoring. In the biomedical domain, PENGs and mechanically triggered electric fields developed stimuli-responsive gyroid scaffolds with $NaNbO_3$ nanostructures for bone regeneration. Com-

bining hierarchical porosity with ultrasound stimulation, these scaffolds enhanced cell proliferation, alignment, and mineralization, achieving >1200 % calcium deposition and establishing bioelectric scaffolds as transformative for regenerative therapies. Collectively, this thesis demonstrates how multifunctional nanogenerators, grounded in fundamental mechanisms, can be engineered as a sustainable and versatile nexus for self-powered sensors in healthcare, agriculture, smart packaging, and pressure-sensing applications.

**Keywords**: Nanotechnology; Triboelectric nanogenerators; Piezoelectric nanogenerators, Energy harvesting; Polymers; Self-powered sensors; Laser-induced graphene; Surface engineering.

# RESUMO

A crescente demanda global por soluções energéticas sustentáveis, descentralizadas e confiáveis tem impulsionado pesquisas em colheita de energia baseada em nanotecnologia. Esta tese aprofunda a compreensão da triboeletrificação e o desenvolvimento de nanogeradores multifuncionais, triboelétricos (TENGs) e piezoelétricos (PENGs), voltados a aplicações inteligentes e autônomas. Foi realizada uma análise abrangente do efeito triboelétrico, especialmente em ambientes sujeitos à contaminação, juntamente com o papel de materiais funcionais na colheita de energia ambiental e em sistemas de detecção inteligente. Mecanismos de transporte de carga, arquiteturas de dispositivos e sistemas responsivos a estímulos foram investigados, destacando desafios e estabelecendo o arcabouço conceitual das aplicações desenvolvidas. Estudos da triboeletrificação líquido-sólido revelaram como a dinâmica do fluxo, a estrutura e o conteúdo iônico governam a geração elétrica. Para converter TENGs em sensores de pressão autônomos, uma estratégia hierárquica de engenharia de superfície aumentou o desempenho e introduziu autolimpeza em *e-skins* duráveis. A micro/nanoestruturação e modificação química produziram superfícies hidrofóbicas, alcançando alta colheita de energia (~270 $mW \cdot m^{-2}$), sensibilidade e de remoção de contaminantes (94 %). Eletrodos de grafeno induzido a laser (LIG) foram desenvolvidos para monitoramento da qualidade de alimentos e integrados a códigos de barras autoalimentados. A incorporação de antocianinas catalisou a síntese do grafeno ($I_D/I_G$: 0,87) e conferiu responsividade a $NH_3$, permitindo detecção trimodal, colorimétrica, eletroquímica e RFID, com limite de 110 ppm e sensibilidade de 1,2 $\Omega \cdot m^3 \cdot mg^{-1}$, possibilitando monitoramento sem fio e em tempo real. No campo biomédico, PENGs e campos elétricos induzidos mecanicamente geraram scaffolds giroides com nanostruturas de $NaNbO_3$ para regeneração óssea. A combinação de porosidade hierárquica e estimulação ultrassônica aprimorou proliferação, alinhamento e mineralização celular, atingindo aumento >1200 % na deposição

de cálcio. Assim, esta tese demonstra como nanogeradores multifuncionais, fundamentados em princípios básicos, podem formar um elo sustentável-versátil para sensores autoalimentados em saúde, agricultura, embalagens inteligentes e interfaces robóticas.

**Palavras-chave:** Nanotecnologia, Nanogeradores triboelétricos (TENGs), Geração de energia, Sensores inteligentes, Polímeros, Sensores autoalimentados, Grafeno induzido a laser, Engenharia de superfície.

# CONTENTS

**1 INTRODUCTION ..... 1**

1.1 Motivation ..... 1

1.2 Objectives ..... 5

1.3 Thesis outline ..... 7

1.4 Research impact ..... 10

1.4.1 List of scientific publications ..... 10

1.4.2 List of presentations in conferences ..... 12

1.4.3 List of patent ..... 13

**2 FUNCTIONAL MATERIALS FOR ENVIRONMENTAL ENERGY HARVESTINGIN SMART AGRICULTURE VIA TRIBOELECTRIC NANOGENERATORS ..... 15**

2.1 Introduction ..... 15

2.1.1 Scope of this review ..... 21

2.2 Theory ..... 23

2.2.1 A brief history of triboelectrification ..... 24

2.2.2 Triboelectric effect ..... 27

2.2.3 Operational mechanism ..... 28

2.2.4 TENG working modes ..... 31

2.2.5 Figure of merit and key electrical measurements ..... 36

2.3 Transport mechanisms of electric charges ..... 41

2.3.1 Electron transfer ..... 43
2.3.2 Ion transfer ..... 47
2.3.3 Transfer of (nano)materials ..... 48
2.3.4 Mechano-responsive charge transfer mechanism ..... 49
2.3.5 Humidity, pollutants, and environmental effects ..... 50
2.3.6 Prevalence of charge transfer mechanisms under environmental factors ..... 52
2.3.7 Dirt interaction length scale and effects on the potential well model ..... 53
2.3.8 Distance-dependent electric charge transfer ..... 57
2.4 Requirements for the application of energy harvesting devices in agriculture ..... 62
2.4.1 Mechanical properties ..... 63
2.4.2 Structural attributes ..... 72
2.4.3 Biological characteristics ..... 77
2.4.4 Device stability ..... 78
2.4.5 Sustainability ..... 103
2.5 Challenges of nanogenerators performance in agriculture environments ..... 110
2.5.1 Relative humidity ..... 110
2.5.2 Temperature ..... 111
2.5.3 Air composition ..... 116
2.5.4 Contaminants ..... 119
2.5.5 Contact force ..... 122
2.5.6 Frequency & amplitude ..... 123
2.5.7 Impact of co-occurring bio-chemical contaminants on charge transfer efficiency 125
2.5.8 Issues raised ..... 127
2.6 Applications in Agricultural Environments ..... 128
2.6.1 Conventional applications ..... 128
2.6.2 Smart and self-powered applications ..... 142

2.7 Conclusion and outlook ..... 156
2.7.1 Outlook ..... 156
2.7.2 Conclusions ..... 161
**3 STIMULI-RESPONSIVE GYROID SCAFFOLDS: HIERARCHICAL ARCHITECTURE AND ELECTRIC STIMULATION PROMOTE BONE REGENERATION 167**
3.1 Introduction ..... 167
3.2 Experimental Section ..... 169
3.2.1 Materials ..... 169
3.2.2 Synthesis of $NaNbO_3$ nanocubes ..... 170
3.2.3 3D printing of sacrificial ABS templates ..... 170
3.2.4 Development of gyroid-structure scaffolds ..... 170
3.2.5 Electrical polarization by corona discharge ..... 171
3.2.6 Chemical, morphological, and compositional characterizations ..... 171
3.2.7 Mechanical properties ..... 172
3.2.8 Mechano-electrical output ..... 173
3.2.9 Finite elemental analysis ..... 174
3.2.10 Biological characterization ..... 174
3.2.11 Statistical analyses ..... 178
3.3 Results and Discussion ..... 179
3.3.1 Fabrication and biological assessment of gyroidal bioactive scaffolds ..... 179
3.3.2 Chemical and morphological characterization of gyroidal scaffolds ..... 181
3.3.3 Structural features and stability work regimes ..... 186
3.3.4 Mechano-electrical performance of scaffolds ..... 191
3.3.5 Ultrasonic stimuli-responsive effects on scaffold bioactivity ..... 198
3.4 Conclusion ..... 211

**4 FLEXIBLE SMART LASER-INDUCED GRAPHENE SENSOR FOR VOLATILE AMMONIA DETECTION VIA COLORIMETRIC ELECTROCHEMICAL AND RFID SIGNALS FOR INTELLIGENT PACKAGING APPLICATIONS ..... 213**

4.1 Introduction ..... 213

4.2 Experimental section ..... 215

4.2.1 Materials ..... 215

4.2.2 Extraction of anthocyanins from red cabbage ..... 216

4.2.3 UV-Vis absorption and colorimetric stability of RCE ..... 216

4.2.4 Fabrication and optimization of smart LIG electrodes ..... 217

4.2.5 Fabrication of RFID antennas, barcodes, and TENGs ..... 218

4.2.6 LIG electrode characterization ..... 218

4.2.7 Water absorption of sensors ..... 219

4.2.8 Colorimetric response to $NH_3$ detection ..... 219

4.2.9 Electrochemical $NH_3$ monitoring ..... 219

4.2.10 Scan rate study ..... 220

4.2.11 Current-scan rate analysis of capacitive response ..... 220

4.2.12 $NH_3$ quantification ..... 221

4.2.13 Irreversibility analysis ..... 221

4.2.14 UV-Vis absorption and colorimetric stability of RCE ..... 221

4.2.15 Arrhenius plot and temperature effect ..... 221

4.2.16 TENG and self-powered barcode characterization ..... 222

4.2.17 RFID tag measurement ..... 222

4.2.18 Multivariate regression modeling via machine learning ..... 223

4.2.19 Statistical analyses ..... 223

4.3 Results and Discussion ..... 224

4.3.1 Fabrication of $NH_3$-responsive smart LIG sensors ..... 224

4.3.2 Fabrication and optimization of smart LIG electrodes ..... 227

4.3.3 Structural and chemical characterization of $NH_3$-responsive smart LIG sensors 230
4.3.4 Ionic Strength-Tunable Colorimetric Sensing for $NH_3$ Detection ..... 240
4.3.5 Electrochemical and impedance response of $NH_3$-responsive LIG sensors ..... 249
4.3.6 RFID-based wireless $NH_3$ sensing and self-powered bar code ..... 255
4.4 Conclusion ..... 261
**5 HIERARCHICALLY STRUCTURED TRANSPARENT ELECTRONIC SKIN FOR SELF-CLEANING AND SELF-POWERED PRESSURE SENSING VIA TRIBOELECTRIC NANOGENERATORS FOR SOFT ROBOTICS ..... 263**
5.1 Introduction ..... 263
5.2 Experimental section ..... 266
5.2.1 Materials ..... 266
5.2.2 Fabrication of PDMS-Based Electronic Skin ..... 266
5.2.3 Deposition of polystyrene (PS) particles ..... 267
5.2.4 Hierarchical micro/nanostructures engineering of PDMS surfaces ..... 267
5.2.5 Surface characterization ..... 268
5.2.6 Chemical characterization ..... 269
5.2.7 Wetting characterization and functional stability ..... 269
5.2.8 Surface energy ..... 270
5.2.9 Electrical characterization of TENG-based electronic skin ..... 270
5.2.10 Smart TENG-based electronic skin applications ..... 271
5.2.11 Evaluation of water- and air-assisted self-cleaning performance ..... 272
5.2.12 Quantification of self-cleaning efficiency via UV-Vis spectroscopy ..... 273
5.2.13 Fine elemental analysis ..... 273
5.2.14 Statistical analyses ..... 273
5.3 Results and discussion ..... 274
5.3.1 Designing hierarchical PDMS surfaces via colloidal lithography ..... 274
5.3.2 Mechanistic insight into $O_2/SF_6$ plasma-driven PDMS surface modification ..... 277

5.3.3 Micro/nanostructures-chemical interplay for hydrophobic surface optimization 281

5.3.4 Self-cleaning mechanisms of hierarchical $O_2/SF_6$-engineered PDMS surfaces .... 288

5.3.5 Enhanced energy harvesting and stability via hierarchical surface design ..... 293

5.3.6 Smart applications of hierarchical micro/nanostructured (HMN-TENG) ..... 298

5.4 Conclusion ..... 306

**6 LIQUID FLOW ENERGY HARVESTING: A COMPREHENSIVE INSIGHTS ON THE ROLE OF LIQUID DYNAMICS FROM A WATER DROPLET TO A STREAMLINES ..... 307**

6.1 Introduction ..... 307

6.2 Experimental section ..... 309

6.2.1 Materials ..... 309

6.2.2 Fabrication of L-S TENG Devices ..... 310

6.2.3 Wettability characterization ..... 310

6.2.4 Surface morphology and structural characterization ..... 310

6.2.5 Electrical characterization of liquid-solid electrification ..... 311

6.2.6 Probing Liquid-Solid Electrification ..... 311

6.2.7 Decoupling Flow-Induced and Impact-Induced Electrification ..... 311

6.2.8 Influence of sliding distance on L-S electrification ..... 312

6.2.9 Device geometry parameters ..... 312

6.2.10 Device materials parameters ..... 312

6.2.11 Temperature dependence ..... 312

6.2.12 Influence of liquid dynamics ..... 312

6.2.13 Electrolyte influence on L-S electrification ..... 313

6.2.14 Decoupling ionic and electronic effects in EDL-mediated L-S electrification ... 313

6.2.15 Enhancing L-S electrification via surface and dielectric engineering ..... 314

6.2.16 Statistical analysis ..... 315

6.3 Results and Discussion ..... 315

6.3.1 From droplet impact to steady-state liquid–solid electrification ..... 315
6.3.2 Hydrodynamic and device geometry influence on electrical output ..... 319
6.3.3 Dielectric shielding and grounding effects on electrostatic induction ..... 322
6.3.4 Mechanistic model of liquid–solid charge transfer ..... 325
6.3.5 Physicochemical modulation: role of liquid type and temperature ..... 328
6.3.6 Electrolyte effects on EDL structure on electrical output ..... 330
6.3.7 Engineering dielectric and surface properties for enhanced energy harvesting . 335
6.3.8 Engineering dielectric and surface properties for enhanced energy harvesting . 337
6.3.9 Mechanisms governing electrostatic induction in falling electrolyte droplets .... 341
6.4 Conclusion ..... 346
**7 FINAL CONCLUSIONS ..... 349**
7.1 Conclusions ..... 349
7.1 Outlook and future directions ..... 354
**A AN APPENDIX ..... 379**

# LIST OF FIGURES

**Figure 1.1.** Summary of the main contributions of each chapter and their alignment with United Nations Sustainable Development Goals (SDGs). ..... 4
**Figure 2.1.** Nanogenerators characteristics and publication trends. ..... 19
**Figure 2.2.** Schematic organization of the review on energy harvesting for smart agriculture. ..... 22
**Figure 2.3.** Timeline of breakthroughs and literature advances on triboelectricity and triboelectric nanogenerators ..... 25
**Figure 2.4.** Operating stages of triboelectric nanogenerators through four sequential stages: before contact (initial state), in contact (equilibrium), in separation (disequilibrium), and after contact (complete separation). ..... 29
**Figure 2.5.** TENG operational modes, their agricultural challenges, and the pros and cons of each. ..... 32
**Figure 2.6.** Stages of TENG operating mechanisms in single-electrode configuration. ..... 35
**Figure 2.7.** Charge transport mechanisms. ..... 43
**Figure 2.8.** Schematic illustration of the main mechanisms of charge transfer at triboelectric interfaces. ..... 46
**Figure 2.9.** Dirt effects on the potential well model for electron charge transfer. ..... 56
**Figure 2.10.** Distance dependence of electric charge transfer efficiency across three surface charge transfer mechanisms (electron, ion, and nanomaterials) on four common agricultural surface conditions: clean and uncharged, clean and charged, stiff dirty, and soft dirty surfaces. ..... 60
**Figure 2.11.** Effect of stiffness compatibility on effective contact area and electrical output stability, and extending physical integrity of nanogenerators ..... 68

**Figure 2.12.** Statistical analysis of key parameters in energy harvesting devices, based on published literature on agricultural applications. ..... 75
**Figure 2.13.** Strategies to tailor surface properties for active functions in triboelectric nanogenerators to enable functionalities beyond energy harvesting ..... 90
**Figure 2.14.** Comprehensive overview of the challenges and issues faced by nanogenerators in agricultural applications, which compromise the reliability and efficiency of electrical output ..... 115
**Figure 2.15.** Schematic illustration of nanogenerators applied as energy harvesters in environmental agriculture. ..... 130
**Figure 2.16.** Comparison of traditional sensors with nanogenerator-based systems. ..... 143
**Figure 2.17.** Smart agricultural applications of nanogenerators. ..... 147
**Figure 2.18.** Outlook roadmap for advancing TENG-enabled smart agriculture. ..... 157
**Figure 3.1.** Schematic illustration of the development of gyroid-based $NaNbO_3$@PDMS scaffolds with tunable porosity and their biological assessment for bone tissue regeneration. ..... 180
**Figure 3.2.** Characterization of synthesized materials and gelatin-PDMS@$NaNbO_3$ scaffolds. ..... 183
**Figure 3.3.** Structural features of 18% and 63% porosity scaffolds. ..... 186
**Figure 3.4.** Influence of scaffold porosity on structural organization, microarchitecture, mechanical behavior, and functional performance. ..... 187
**Figure 3.5.** Pore-size and surface-area characterization of gyroid scaffolds. ..... 190
**Figure 3.6.** Relationship between porosity levels and mechanical force triggers on the performance of mechano-electrical output and functional stability of electrically charged scaffolds. ..... 192
**Figure 3.7.** Cyclic mechanical and viscoelastic characterization of scaffolds. ..... 195
**Figure 3.8.** Constructs' biocompatibility and mineralization analyzed via confocal microscopy and EDS-SEM. ..... 199
**Figure 3.9.** Impact of ultrasound stimulation (US) and scaffold porosity on cell activity, calcium deposition, gene expression, and cell morphology. ..... 200
**Figure 3.10.** SEM and EDS of constructs after 14 d of bone cell growth. ..... 201
**Figure 3.11.** Raman spectroscopy and mapping of constructs after 14 d of cell culture. ..... 202
**Figure 3.12.** Absolute expression levels of gene markers of constructs. ..... 203

**Figure 3.13.** Osteopontin and F-actin confocal images of constructs after 14 d of cell growth. ..... 206
**Figure 3.14.** DAPI/collagen-I confocal images of constructs after 14D. ..... 207
**Figure 3.15.** Influence of ultrasound stimulation (US) and construct porosity on cellular alignment and actin filament organization. ..... 208
**Figure 3.16.** Distribution of cell alignment as a function of degree range accumulation ..... 209
**Figure 4.1** Schematic illustration of the extraction protocol, pH-dependent optical response, and speciation of red cabbage extract (RCE). ..... 226
**Figure 4.2.** Fabrication and characterization of sensors and laser-induced graphene (LIG) interdigitated electrodes. ..... 228
**Figure 4.3.** Structural, chemical, and morphological characterization of sensors with varying RCE contents and ionic strengths ..... 231
**Figure 4.4** Raman spectra and effect of $Ca^{2+}$-mediated hydration on LIG graphitization. .... 233
**Figure 4.5.** Mechanistic role of anthocyanins in energy-saving for LIG synthesis and $NH_3$ sensing ..... 235
**Figure 4.6.** Proposed mechanism of anthocyanin-chitosan interactions in the absence and presence of $CaCl_2$. ..... 240
**Figure 4.7.** Illustration of smart LIG sensors for $NH_3$ detection applied to food quality monitoring. ..... 241
**Figure 4.8.** Mechanistic role of anthocyanins copigmentation in $NH_3$ colorimetric sensing. 243
**Figure 4.9.** Colorimetric response and irreversibility of the smart LIG sensor under varying ionic strengths (IS) during $NH_3$ exposure and its integration with machine learning for concentration prediction ..... 245
**Figure 4.10.** Statistic evaluation and predictor analysis of the machine learning–assisted multivariate regression model for $NH_3$ prediction ..... 248
**Figure 4.11.** Electrochemical and impedance characterization of sensors with laser-induced graphene (LIG) interdigitated electrodes (IDEs) under $NH_3$ exposure. ..... 251
**Figure 4.12.** Charge transfer in $NH_3$-responsive LIG sensors (a) without and (b) with anthocyanins. Incorporation of anthocyanins leads to a 22,000% enhancement in transferred charge, attributed to electroactive chalcone species (cis- and trans-isomers). ..... 253
**Figure 4.13.** Wireless RFID sensor response to $NH_3$ and self-powered barcode TENG characterization ..... 256

**Figure 4.14.** Working mechanism and mechano-electrical performance of a self-powered smart LIG-based triboelectric nanogenerator (TENG). 259
**Figure 5.1.** Surface engineering of hierarchical micro/nanostructures PDMS for self-cleaning and triboelectric energy harvesting. 275
**Figure 5.2.** Stepwise $O_2/SF_6$ plasma processing for hierarchical micro/nanostructuring of PDMS. 278
**Figure 5.3.** Hierarchical micro/nanostructuring surface-chemistry optimization of PDMS via $O_2/SF_6$ plasma treatment. 287
**Figure 5.4.** Surface modification and optimization of PDMS via $O_2/SF_6$ plasma treatment for self-cleaning. 291
**Figure 5.5.** Hierarchical surface engineering of PDMS for self-cleaning and triboelectric energy harvesting. 295
**Figure 5.6.** Smart applications of hierarchical micro/nanostructured triboelectric nanogenerators (HMN-TENGs). 304
**Figure 6.1.** Influence of liquid release height and sliding distance on electrical output of L-S TENGs. 317
**Figure 6.2.** Influence of liquid dynamics and device geometry on electrical output of L-S TENGs. 320
**Figure 6.3.** Effect of dielectric shielding and water grounding on the open-circuit voltage ($V_{oc}$) of L-S TENGs. 323
**Figure 6.4.** Liquid-solid electrification mechanism in a water sliding on TENG. 326
**Figure 6.5.** Effect of liquid type, contact sequence, and temperature on electrical output of L-S TENG. 329
**Figure 6.6.** Influence of electrolytes on $V_{oc}$ output in L-S electrification. 332
**Figure 6.7.** Influence of electrolyte concentration and pH on liquid-solid electrification under streamline flow (75°). 334
**Figure 6.8.** Engineering dielectric and interfacial properties to enhance energy-harvesting efficiency and demonstrate the L-S TENG as a self-powered electrochromic window. 336
**Figure 6.9.** Wireless energy harvesting via non-contact L-S TENGs, generating open-circuit voltage ($V_{oc}$) induced by flow-mediated electric fields through streaming potential. 339
**Figure 6.10.** Mechanisms governing electrolyte-dependent electrostatic induction from falling water 343

# LIST OF TABLES

**Table 2.1.** Stimuli-responsive functional materials for agricultural TENG systems: stimulus, functional material, response mechanism, and applications. ..... 95
**Table 2.2.** Overview of triboelectric nanogenerators harvesting energy from gas, liquid, solid, and hybrid sources applied in agricultural environments: energy sources and counterpart materials, working modes, device materials, fabrication and assembly processes, electrical outputs, agricultural challenges, and applications. ..... 134
**Table 2.3.** Current status, challenges, and recommended strategies for triboelectric nanogenerators in agricultural and environmentally challenging settings. ..... 162
**Table 3.1.** Parameters used in COMSOL® simulation for electric field intensity and distribution analysis of scaffolds. ..... 174
**Table 3.2.** Primer sequences used in the RT-qPCR analysis. ..... 177
**Table 3.3.** Structural features and mechanical properties of gelatin-$NaNbO_3$@PDMS scaffolds with 0%, 18%, and 63% porosities. ..... 189
**Table 3.4.** Average electric field intensity for 18% and 63% porosity scaffolds in air and aqueous media with $\varepsilon_r = 4$. ..... 196
**Table 3.5.** Cell alignment (%) within accumulated degree ranges (1, 3, 5, 7, and 10°) for constructs with 0%, 18%, and 63% porosity under ultrasound stimulation of 0, 50, and 250 $mW \cdot cm^{-2}$. ..... 210
**Table 4.1.** Ionic strength and red cabbage extract content in chitosan dispersions with corresponding optimal sheet resistance. ..... 216
**Table 4.2.** Raman graphene index parameters and corresponding optimal sheet resistances. ..... 236
**Table 4.3.** Machine learning–assisted multivariate regression model for $NH_3$ quantification using colorimetric parameters of the optimized sensor (11% RCE – 500 mM IS). ..... 247

**Table 5.3.** Experimental conditions for hierarchical micro/nanostructure optimization on PDMS surfaces via reactive ion etching (RIE) following the 1st-step $SF_6$ physical modification. ..... 268
**Table 5.4.** Figures of merit for structure-dependent PDMS-based TENG pressure sensors. 298
**Table 5.5.** Figures of merit comparison table for PDMS-based TENGs pressure sensors with diverse micro/nanostructured architectures..... 300
**Table 6.1.** Spin-coating parameters for precise PDMS film thickness control..... 310
**Table 6.2.** Physical, chemical, and physicochemical parameters explored in liquid-solid electrification..... 313

# ACRONYMS

**2D -** Two-Dimensional

**3D -** Three-Dimensional

**ABS -** Acrylonitrile Butadiene Styrene

**AFM -** Atomic Force Microscopy

**AI -** Artificial Intelligence

**BLE -** Bluetooth Low Energy

**BTO -** Barium Titanate

**CAPES -** Coordenação de Aperfeiçoamento de Pessoal de Nível Superior

**CENIMAT -** Centro de Investigação de Materiais

**CNT -** Carbon Nanotube

**COMSOL® -** COMSOL Multiphysics (Simulation Software)

**DoE -** Design of Experiments

**EDL -** Electric Double Layer

**EDX -** Energy-Dispersive X-ray Spectroscopy

**EIS -** Electrochemical Impedance Spectroscopy

**EMG -** Electromagnetic Generator

**E-skin -** Electronic Skin

**ES -** Emeraldine Salt

**FFM -** Fusing Filament Fabrication

**FOM -** Figure of Merit

**FOMp -** Performance Figure of Merit

**FOMs -** Structural Figure of Merit

**FT -** Freestanding Triboelectric Layer

**hBM-MSCs -** Human Bone Marrow-Derived Mesenchymal Stem Cells

**HMN-TENG -** Hierarchical Micro/Nanostructured Triboelectric Nanogenerator

**HOMO -** Highest Occupied Molecular Orbital

**IDE -** Interdigitated Electrode

**IoT -** Internet of Things

**ISO -** International Organization for Standardization

**ITO -** Indium Tin Oxide

**KPFM -** Kelvin Probe Force Microscopy

**LCA -** Life Cycle Assessment

**LIG -** Laser-Induced Graphene

**LOQ -** Limit of Quantification

**LOD -** Limit of Detection

**L-S -** Liquid–Solid

**L-S TENG –** Liquid-Solid Triboelectric Nanogenerator

**LUMO -** Lowest Unoccupied Molecular Orbital

**MB -** Methylene Blue

**$NH_3$ -** Ammonia Gas

**$Nb_2O_5$ -** Niobium(V) Oxide

**PCA -** Principal Component Analysis

**PENG -**Piezoelectric Nanogenerator

**PET -** Poly(ethylene terephthalate)

**PDMS -** Poly(dimethylsiloxane)

**P(VDF-TrFE) -** Poly(vinylidene fluoride-co-trifluoroethylene)

**PI -** Polyimide

**PTFE -** Poly(tetrafluoroethylene)

**R2R -** Roll-to-Roll

**RCE -** Red Cabbage Extract

**RFID -** Radio-Frequency Identification

**RIE -** Reactive Ion Etching

**RMS -** Root-Mean-Square

**RL -** Return Loss

**RT-qPCR -** Reverse Transcription Quantitative Polymerase Chain Reaction

**SD -** Standard Deviation

**SDG -** Sustainable Development Goals

**SE-TENG -** Single-Electrode Triboelectric Nanogenerator

**SEM -** Scanning Electron Microscopy

**$T_c$ -** Curie Temperature

**TENG -** Triboelectric Nanogenerator

**$TiO_2$ -** Titanium Dioxide

**UFSCar -** Universidade Federal de São Carlos

**UNICAMP -** Universidade Estadual de Campinas

**US -** Ultrasound Stimulation

**VCS -** Vertical Contact-Separation

**$WO_3$ -** Tungsten Trioxide

**XPS -** X-ray Photoelectron Spectroscopy

**XRD -** X-ray Diffraction

**X-ray μCT -** X-ray Micro-Computed Tomography

# SYMBOLS

| | |
|---|---|
| $A$ | Area |
| $Å$ | Angstrom |
| $C$ | Concentration |
| $C_s$ | Separation Distance |
| $\Delta E^*$ | Colorimetric Parameter (Total Color Difference) |
| $\Delta V$ | Activation Volume |
| $\Delta Y$ | Thickness Deformation Percentage after 100 Cycles |
| $\Delta Z$ | Change in Impedance Magnitude |
| $E_a$ | Activation Energy |
| $E_{a0}$ | Stress-Free Energy Barrier |
| $E_{max}$ | Maximum Energy Conversion Efficiency |
| $E_v$ | Vacuum Energy Level |
| $E_{VAC}$ | Vacuum Energy |
| $E_{VBM}$ | Valence Band Maximum Energy |
| $E/I$ | Electron-to-Ion Transfer Ratio |
| $\varepsilon$ | Dielectric Permittivity |
| $\varepsilon_m$ | Maximum Dielectric Permittivity |
| $\eta$ | Healing Efficiency |
| $\phi$ | Work Function |
| $\gamma$ | Degree of Diffuseness |
| $h^*$ | Colorimetric Hue Angle |
| $i$ | Electrical Current |
| $IS$ | Ionic Strength |
| $I_D$ | Raman D-Peak Intensity |

$I_D/I_G$ Intensity Ratio of D and G Bands (Raman)

$I_G$ Raman G-Peak Intensity

$I_2D$ Raman 2D-Peak Intensity

$I_{sc}$ Short-Circuit Current

$L^*$ Colorimetric Lightness Parameter

$L_a$ Crystallite Size in the a-Plane

$|Z|$ Impedance Magnitude

$q$ Elementary Charge

$Q$ Transferred Charge

$R$ Universal Gas Constant

$R^2$ Coefficient of Determination

$R_{CT}$ Charge-Transfer Resistance

$RH$ Relative Humidity

$R_{MS}$ Root-Mean-Square

$R_S$ Solution Resistance

$Re$ Real Part of Complex Reflection Coefficient

$Rq$ Root-Mean-Square Roughness

$Im$ Imaginary Part of Complex Reflection Coefficient

$rpm$ Rotation per Minute

$S$ Sensor Sensitivity or Seebeck Coefficient (context-dependent)

$\sigma$ Charge Density

$\psi$ Relative Damping

$T$ Absolute Temperature

$t$ Time

$V_{oc}$ Open-Circuit Voltage

$V_{pp}$ Peak-to-Peak Potential

$V_C$ Contact Potential Difference

$Z$ Complex Impedance

$Z_{eff}$ Effective Nuclear Charge

$Z_{max}$ Maximum Surface Separation

$\lambda$ Wavelength

$\lambda_{max}$ Wavelength of Maximum Absorbance

$\nu$ Frequency or Scan Rate

# 1

# INTRODUCTION

## 1.1 Motivation

The escalating global demand for sustainable and renewable energy has become one of the most pressing challenges of the 21st century. As the number of smart electronics and Internet of Things (IoT) devices continues to increase, there is a growing requirement for distributed energy systems that can operate efficiently and over extended periods. Although batteries currently underpin most portable and decentralized electronics, they present substantial drawbacks, including limited operational lifetimes, frequent replacement needs, and dependence on materials associated with high environmental costs. Their widespread use contributes to the escalating generation of electronic waste (e-waste), introducing toxic constituents that threaten human health, ecosystems, and biodiversity. In addition, high collection costs and inefficient recycling infrastructure further exacerbate the environmental burden. As battery-powered technologies continue to expand globally, these challenges intensify, underscoring the urgent need for more sustainable energy alternatives.

At the same time, environmental degradation and the depletion of fossil fuels have intensified the global urgency to transition to green, autonomous energy systems that cause minimal ecological impact. Despite increasing awareness of sustainability challenges, a broad range of modern technologies, *e.g.*, healthcare devices, precision agriculture systems, sensors, and communication systems, still depend primarily on batteries or fossil-fuel-based electricity. This dependence not only perpetuates greenhouse gas emissions and accelerates resource depletion but also introduces critical limitations related to finite raw materials such as lithium, cobalt, and rare earth elements. Furthermore, centralized power infrastructure remains vul-

nerable to grid instabilities, limited access in remote areas, and substantial energy losses during transmission. As the demand for distributed, low-power electronics grows, reliance on conventional energy storage and fossil-derived power exposes escalating risks in environmental sustainability, resource security, and long-term scalability.

This challenge extends across multiple scientific and societal domains. For instance, in biomedical and wearable electronics, dependence on wired power or finite-lifetime batteries limits continuous physiological monitoring and personalized healthcare. In environmental sensing and smart agriculture, power scarcity in remote areas restricts real-time data collection essential for applications, *e.g.*, automatic irrigation control, soil analysis, and livestock monitoring, as well as for smart systems in crop management and climate-adaptive farming. In the food-quality sector, energy-autonomous sensors enable real-time monitoring of freshness and contamination, thereby reducing waste and protecting consumers. In recent advanced robotics applications, self-powered tactile and pressure sensors can improve precision and electrical stability for robot-assisted surgery and dexterous manipulation. Collectively, these features highlight the urgent need for sustainable, autonomous energy solutions that enhance human capability and quality of life.

In this context, the development of self-powered technologies based on energy-harvesting principles offers a compelling, sustainable strategy to mitigate reliance on conventional energy sources, minimize environmental impact, and enable the next generation of intelligent, interconnected systems. Among the various transduction mechanisms explored, triboelectric and piezoelectric effects have gained considerable attention, particularly following the advent of triboelectric nanogenerators (TENGs) in 2012, which enable simultaneous mechanical energy harvesting and environmental sensing within a single multifunctional platform. TENGs can harvest ubiquitous low-grade mechanical energy from raindrops, human motion, structural vibrations, and airflow, offering versatile power solutions for low-power electronics. Furthermore, TENGs can be fabricated from environmentally benign materials and exhibit advantageous characteristics, *e.g.*, lightweight construction, mechanical flexibility, optical transparency, and low-cost manufacturing, that make them well-suited for emerging sustainable electronics. Consequently, leveraging advances in materials science and applied nanotechnology, TENG-based devices can enable decentralized power solutions, improving energy accessibility and reducing dependence on conventional battery technologies.

Beyond the pursuit of new energy-harvesting mechanisms, nanogenerators exhibit exceptional stimuli-responsive behavior, whereby the high mechanical sensitivity of TENGs

yields quantifiable electrical signals, *e.g.*, voltage, current, and electric fields, in response to mechanical stimuli. This dual functionality allows a single device to operate as both a power source and a sensor, providing electrical energy and environmental information from the same physical interaction. This capability becomes even more advantageous when the active layers of TENGs are engineered with functional materials that predictably alter specific properties, such as dielectric permittivity or electrical conductivity, in response to environmental cues, including pH, humidity, temperature, or targeted chemical species. As a result, nanogenerators can be tailored for diverse application scenarios that address real human needs, ranging from self-powered sensors for food spoilage detection to high-sensitivity pressure sensors for robot-assisted surgery, and even electrical-stimulation scaffolds for accelerated tissue repair and rehabilitation.

Inspired by this emerging field, this thesis identifies a unique opportunity to leverage stimuli-responsive energy-harvesting technologies via TENGs and piezoelectric nanogenerators (PENGs) to address global sustainability challenges and support several United Nations Sustainable Development Goals (SDGs). When intelligently engineered, nanogenerator-based devices can:

- Advance SDG 3 – Good Health and Well-Being through applications in biomedical and rehabilitative technologies;
- Support SDG 4 – Quality Education by promoting research, innovation, and knowledge transfer in materials science and nanotechnology;
- Promote SDG 7 – Affordable and Clean Energy via renewable micro-energy harvesting for self-powered electronics;
- Strengthen SDG 9 – Industry, Innovation and Infrastructure through the development of autonomous, smart sensors and devices;
- Contribute to SDG 12 – Responsible Consumption and Production by reducing battery dependence and e-waste generation; and
- Advance SDG 13 – Climate Action by lowering reliance on fossil-derived energy across distributed and embedded electronic systems.

These collective scientific and societal motivations form the foundation of this doctoral research, which unites materials science and nanotechnology to engineer TENGs PENGs capable of addressing these challenges through the development of self-powered smart devices. Figure 1.1 provides an overview of how each chapter of this thesis addresses the scientific,

technological, and societal challenges outlined above, highlighting their alignment with key SDGs.

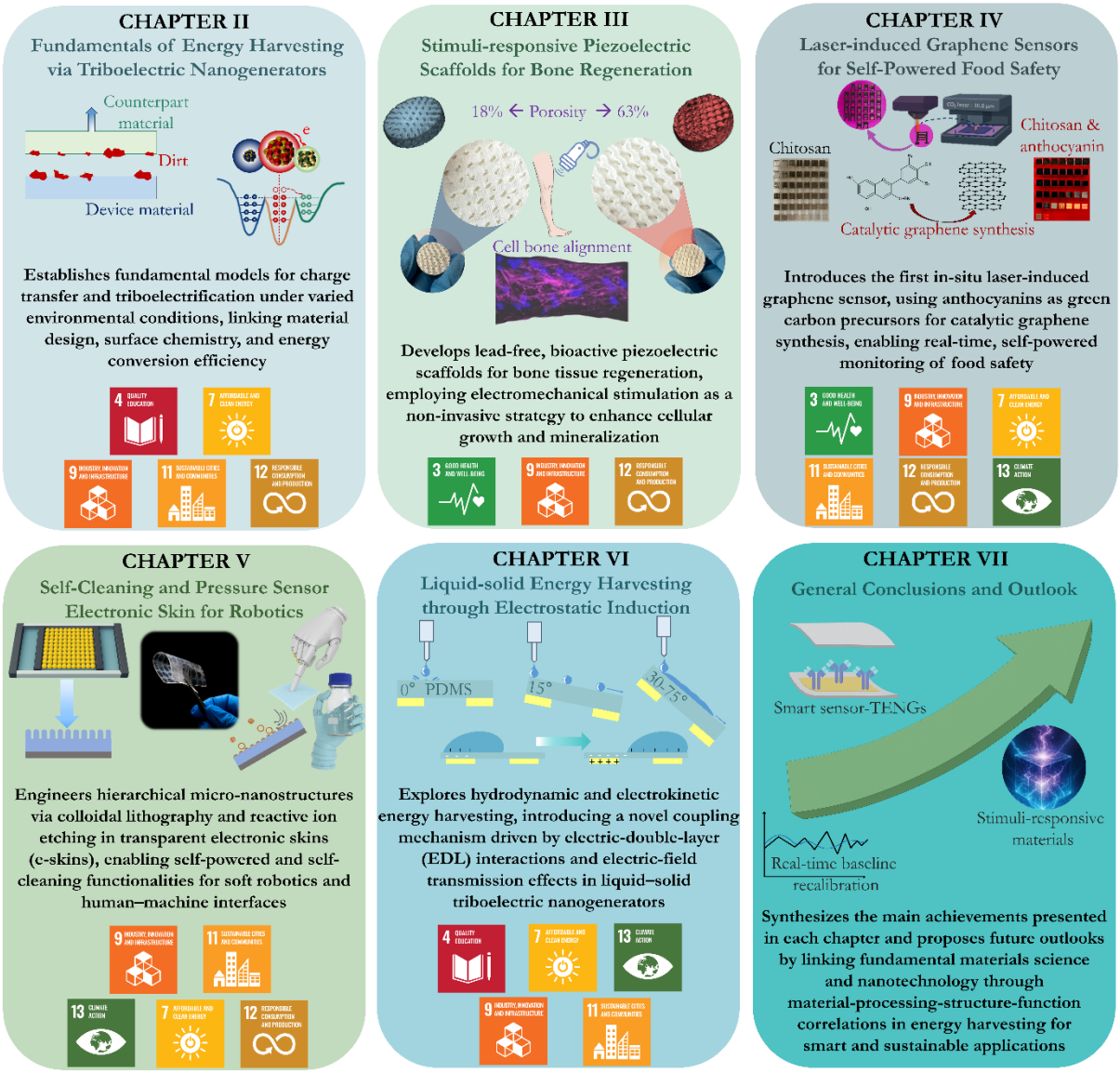


**Figure 1.1.** Summary of the main contributions of each chapter and their alignment with United Nations Sustainable Development Goals (SDGs). Chapter II - Fundamentals of Triboelectric Energy Harvesting: Provides the conceptual and mechanistic basis of triboelectrification, establishing principles that govern interfacial charge generation and transfer. Chapter III - Piezoelectric Scaffolds for Bone Regeneration: Introduces architected piezoelectric scaffolds capable of generating bioelectrical cues under mechanical stimulation. Chapter IV - Laser-Induced Graphene for Food Safety: Presents an eco-engineered strategy for producing laser-induced graphene for self-powered ammonia sensing, using naturally derived molecular precursors. Chapter V - Transparent Self-Powered Electronic Skin: Develops hierarchical micro/nanostructured e-skin devices for self-powered pressure sensing and self-cleaning functionalities. Chapter VI – Liquid-Solid Energy Conversion Mechanisms: Uncovers the coupled triboelectric, electrostatic induction, and electrokinetic phenomena that govern charge generation at liquid-solid interfaces, revealing new pathways for contact and wireless fluidic energy harvesting. Chapter VII - Integrated Conclusions and

Outlook: Consolidates the materials, mechanisms, and device concepts developed across the thesis, highlighting future opportunities for next-generation self-powered technologies.

## 1.2 **Objectives**

Motivated by the aforementioned challenges and opportunities, this doctoral thesis aims to bridge fundamental materials science and applied nanotechnology to advance the frontiers of energy-harvesting science, transforming fundamental principles into sustainable, self-powered, and intelligent technologies for the next generation of autonomous systems. By focusing on triboelectric and piezoelectric nanogenerators (TENGs and PENGs), this work seeks to support progress toward key SDGs through the intelligent design of multifunctional nanogenerators that foster technological innovation and environmental sustainability. Accordingly, the core direction of this research is articulated through two overarching objectives:

❖ To establish the fundamental principles governing triboelectric charge generation and conversion, emphasizing charge transfer and electrification at solid–solid and liquid–solid interfaces to advance self-powered smart sensor technologies.

❖ To develop multifunctional smart nanogenerators capable of autonomously powering self-sustained devices, functioning as self-powered platforms for sensing, communication, and actuation without dependence on external energy sources.

To comprehensively address the objectives of this research, each chapter was designed to explore a distinct aspect of energy harvesting through triboelectric and piezoelectric nanogenerators. The most significant specific objectives corresponding to each chapter are outlined below.

- *Chapter II – Fundamentals of Energy Harvesting via Triboelectric Nanogenerators*

To establish the conceptual and theoretical foundations of triboelectric nanogenerators (TENGs) for environmental energy harvesting, elucidating the influence of surface contamination, mechanical compatibility, and materials selection on charge transfer efficiency for functional and smart TENG applications.

- *Chapter III – Piezoelectric Scaffolds for Bone Regeneration*

To design a stimuli-responsive piezoelectric scaffold that enhances bone tissue regeneration through electromechanical stimulation, accelerating healing and reducing the healthcare burden associated with prolonged recovery times.

- *Chapter IV – Laser-Induced Graphene Sensors for Self-Powered Food Safety*

To develop a multifunctional, laser-induced graphene (LIG) sensor for real-time food-quality monitoring, integrating colorimetric, electrochemical, and RFID-based detection into a self-powered and sustainable platform for food safety and supply-chain monitoring.

- *Chapter V – Self-Cleaning and Pressure Sensor Electronic Skin for Robotics*

To fabricate a transparent, self-powered, and self-cleaning electronic skin (e-skin) based on plasma-engineered hierarchical PDMS structures and TENGs, capable of pressure sensing and contamination resistance for soft robotics and human–machine interfaces.

- *Chapter VI – Liquid-Solid Energy Harvesting through Electrostatic Induction*

To elucidate the fundamental mechanisms of liquid–solid energy harvesting in TENGs through the study of dynamic electric double-layer (EDL) formation across diverse electrolyte environments, with the goal of enhancing energy-conversion efficiency and guiding the design of next-generation EDL-governed systems for energy harvesting.

To achieve these objectives, this thesis was conducted within the framework of a joint doctoral program between the Graduate Program in Materials Science and Engineering (PPGCEM) at the Federal University of São Carlos (UFSCar, Brazil) and the Materials Research Center (CENIMAT|i3N) at NOVA University Lisbon (Portugal). The research represents four years of collaborative work between these two leading institutions in the fields of materials science and nanotechnology. This joint program reflects strategic priorities in fostering innovation, international collaboration, and scientific excellence by integrating expertise in materials science, nanotechnology, electronics, and device physics, enabling the exploration of energy harvesting from the nanoscale to real-world applications.

## 1.3 Thesis outline

This thesis is organized into five main research chapters, each contributing to progress toward relevant SDGs through the development of nanogenerator concepts and the intelligent design of self-powered smart platforms. The final chapter (Chapter 7) provides a comprehensive conclusion, integrating the key insights and scientific contributions spanning materials science, nanotechnology, and energy harvesting using TENGs and PENGs. The overall objectives and principal achievements of each chapter are outlined below.

**Chapter II** establishes the conceptual and theoretical foundation for energy harvesting in this thesis. It provides an extensive review of functional materials and TENGs for environmental energy harvesting, highlighting their potential for a wide range of smart applications. The chapter discusses how ambient mechanical energy, originating from wind, raindrops, and vibrations, can be effectively converted into electrical energy via triboelectrification and how these energy inputs can be used to self-power environmental monitoring systems. For the first time, this study elucidates how contamination effects and stiffness compatibility influence the potential-well model and, consequently, the charge-transfer efficiency in TENGs.

Furthermore, it proposes strategies to mitigate contamination-induced charge loss through several forms of active surface functionalization, including hierarchical micro/nanostructuring, chemical modification, and biological immobilization. In addition to these theoretical developments and advanced insights, this review offers a forward-looking perspective on TENGs as a key enabling technology for self-powered agricultural systems, of significant relevance to researchers in materials science, energy systems, environmental technology, and agricultural innovation.

**Chapter III** focuses on energy harvesting via PENGs and demonstrates how stimuli-responsive gyroid scaffolds redefine bone regeneration strategies, offering transformative insights for the development of advanced biomaterials in implants and physiotherapy. Complex hierarchical gyroid scaffolds with tunable porosity and high $NaNbO_3$ piezoelectric content (30 wt%) were fabricated using a sacrificial template-assisted methodology. Combined with corona poling, this strategy yields electrically active architectures that mimic the anisotropy and porosity of cancellous bone, enhancing piezoelectric response under mechanical stimulation. The study analyzes how porosity, zero-curvature geometry, and corona-discharge poling influence the mechanical strength, damping capacity, and electric-field distribution of the scaf-

folds. Under ultrasound stimulation, the scaffolds show remarkable improvements in cell proliferation, alignment, and mineralization, with calcium deposition increases exceeding 1200% compared to controls.

For the first time, this work reveals that electric field alignment directs bone cell organization within zero-curvature 3D scaffolds, in contrast to conventional sharp-pore designs. These findings establish electrically active gyroid scaffolds as a new class of bioelectric materials that bridge materials science and biomedical engineering, serving as a blueprint for advanced 3D scaffold fabrication and dynamic regenerative therapies. This work represents a significant advancement for public health, offering potential to reduce healthcare burdens associated with prolonged healing times and escalating treatment costs.

**Chapter IV** focuses on elucidating how graphene-like structures can be *in-situ* functionalized via direct laser writing for use as self-powered sensors in food-quality monitoring. This work pioneers the development of the first *in-situ* smart laser-induced graphene (LIG) sensor for volatile ammonia ($NH_3$) detection, serving as a real-time indicator of food freshness in intelligent packaging systems. By exploiting the electromagnetic response of RFID antennas and a functional electrode barcode, this work also demonstrates the energy-harvesting capability of the device for continuous, non-invasive food-quality monitoring and identification. The flexible LIG sensors are fabricated via direct laser writing of chitosan films doped with naturally derived anthocyanins, which serve as both carbon precursors and redox-active sensing agents. High flexibility and $NH_3$ sensitivity arise from an optimized composition containing $Ca^{2+}$ ions, which mediate crosslinking between chitosan and anthocyanins, forming metallo-anthocyanin complexes that stabilize the conductive network during laser-induced graphitization. This process yields a porous, conductive graphene-like network with tunable sensitivity and mechanical compliance.

At the core of this study is the discovery that anthocyanins play a dual role during laser scribing: (i) as graphitization promoters, reducing the activation barrier for carbon rearrangement and producing high-quality graphene ($I_D/I_G$ = 0.87; sheet resistance = 48 $\Omega \cdot sq^{-1}$); and (ii) as redox-active centers enabling $NH_3$ transduction. The resulting sensor achieves a detection limit of 110 ppm and sensitivity of 1.2 $\Omega \cdot m^3 \cdot mg^{-1}$, supported by AI-based signal processing for enhanced accuracy. These discoveries demonstrate the use of electroactive molecular precursors to achieve *in-situ* LIG functionalization, transforming laser-induced graphene from a passive conductor into a chemically encoded, energy-harvesting platform with wireless data

transmission capability for self-powered smart sensors in food-safety and environmental monitoring. Overall, this chapter has high technological, health, and societal relevance, enabling real-time food-quality monitoring, waste reduction, and supply-chain safety through scalable, sustainable sensor technologies.

**Chapter V** targets the fabrication of transparent, self-cleaning, and self-powered electronic skin (e-skin) for soft robotics and human–machine interfaces. Using colloidal lithography and reactive-ion etching, hierarchical micro/nanostructured TENGs (HMN-TENGs) with fluorinated surface chemistry were developed on PDMS to achieve durable hydrophobicity, efficient contaminant removal, and enhanced triboelectric energy harvesting. A sequential $O_2/SF_6$ plasma process precisely balanced oxidation and fluorination, forming stable Si–F and C–F bonds that impart hydrophobicity (~152° contact angle) and high contamination resistance (~91% removal efficiency).

The optimized HMN-TENG delivers a 650 % increase in power density (≈270 mW·m-2) and maintains over 80% performance after 10,000 cycles, demonstrating excellent durability. Beyond energy harvesting, it functions as a self-powered pressure-sensitive tactile sensor, enabling smart-lock control and autonomous robotic operation. For the first time, this work shows that the open-circuit voltage ($V_{oc}$) of TENGs can be exploited for real-time superficial-area estimation, extending the multifunctionality of TENG-based e-skins. This represents a significant step toward durable, adaptive, and transparent self-powered e-skins for next-generation soft robotics and human–machine interfaces. Collectively, the study establishes a materials–process–function correlation, integrating surface physics, plasma chemistry, and triboelectric engineering into a single tunable architecture with high technological relevance for advanced robotic systems.

**Chapter VI** investigates liquid-solid (L-S) electrification, proposing a unified framework for L–S charge generation and dynamic EDL formation during liquid flow, thereby advancing the understanding of interfacial charge transfer under diverse electrolytic conditions. It isolates key factors often overlooked in L–S electrification, such as liquid impact, flow regime, dielectric shielding, and flow-induced potentials linked to ionic strength and electrolyte composition. By studying L–S electrification across 18 different electrolytes and isolating the influence of physicochemical device parameters, we decouple the respective roles of EDL dynamics and ionic effects in governing the electrical output of L–S TENGs.

A key contribution of this work is the introduction of wireless energy harvesting via streaming-potential effects and the evaluation of the roles of water composition, temperature,

device configuration, and angular orientation. The results show that the device behaves as an antenna-like TENG, enabling non-contact energy harvesting for smart applications, such as non-invasive pH sensing and potentiometric ion detection. Finally, we illustrate their potential in smart applications by activating electrochromic transitions in windows through L-S electrification, simulating raindrop-driven energy for autonomous color modulation in automotive systems. These findings advance the fundamental understanding of L-S electrification and dynamic EDL formation, fostering the development of EDL-governed technologies, *e.g.*, supercapacitors, electrocatalysis, electrochemical sensing, and energy harvesting, and opening new avenues toward self-powered, multifunctional, and intelligent applications.

**Chapter VII** synthesizes the key findings and overarching contributions from all preceding chapters, underscoring how fundamental materials science and nanotechnology principles can drive real-world implementation of smart self-powered technologies. It highlights the interrelationships among material selection, processing, chemical functionalization, and property optimization that collectively enhance the performance and functionality of self-powered devices for advanced smart applications, while also outlining future research directions toward next-generation nanotechnology-enabled energy systems.

## 1.4 Research impact

The main research outcomes and collaborations established throughout this PhD, in the fields of polymer science and nanotechnology applied to energy harvesting, triboelectric and piezoelectric nanogenerators, and smart sensing devices, have been published in several high-impact, peer-reviewed journals. These contributions collectively amount to a cumulative impact factor of 86.3, include one patent filed, and have been presented at six international symposia and conferences, as listed below.

### 1.4.1 List of scientific publications

- SILVA, R.R.A.; FATTI, G.; CARLOS, E.; FERREIRA, G.; GOSWAMI, S.; NANDY, S.; MATTOSO, L.H.C.; FORTUNATO, E.; OTONI, C.G.; MARTINS, R. Functional Materials for Environmental Energy Harvesting in Smart Agriculture via Triboelectric Nanogenerators. **Advanced Functional Materials**, v. 1, p. 1, 2025.

- SILVA, R.R.A.; BARBOSA, F.; FERREIRA, G.; UREÑA, C.; BACKES, E.H.; INÁCIO, J.M.; BELO, J.A.; IGREJA, R.; SILVA, J.C.; MATTOSO, L.H.C.; FORTUNATO, E.; ALMEIDA,

H.M.V.; MARTINS, R.; OTONI, C.G. Stimuli-responsive gyroid Scaffolds: hierarchical architecture and electric stimulation promote bone regeneration. **Materials Today**, v. 88, p. 1, 2025.

- ISLAM, J.; SILVA, R.R.A.; IMBROGNO, A.; OTONI, C.G.; MARTINS, R.; MATTOSO, L.H.C; QUINN, A.J.; IACOPINO, D. Eco-Friendly Energy Storage and Energy Harvesting Devices Fabricated by Direct Laser Writing of Chitosan-Lignin-Boric Acid Substrates. **ACS Applied Electronic Materials**. 2025, 7, 11, 4801–4813.

- FERREIRA, G.; DAS, S.; COELHO, G.; SILVA, R.R.A.; GOSWAMI, S.; PEREIRA, R.N.; PEREIRA, L.; FORTUNATO, E.; MARTINS, R.; NANDY, S. Energy harvesting and movement tracking by polypyrrole functionalized textile for wearable IoT applications. **Journal of Energy Chemistry**, v. 1, p. 1, 2024.

- FERREIRA, G.; DAS, S.; REGO, A.; SILVA, R.R.A.; GASPAR, D.; GOSWAMI, S.; PEREIRA, R.N.; FORTUNATO, E.; PEREIRA, L.; MARTINS, R.; NANDY, S. Eco-designed recycled newspaper for energy harvesting and pressure sensor applications. **Chemical Engineering Journal**, v. 480, p. 147995, 2024.

- SPANOU, A.; SILVA, R.R.A; SHTENDER, V.; ALMEIDA, H.V.DE; MARTINS, R.; PERSSON, C.; JOHANSSON, S. "3D - Printed Piezoelectric Devices for Sustainable Energy Harvesting and Health Monitoring using PVDF-TrFE/rGO Electrodes", in preparation, 2025.

- SILVESTRE, S. L.; MORAIS, M., SILVA, R.R.A.; SERRANO, Z.; MARTINS, R.; FORTUNATO, E.; PEREIRA, L.; COELHO, J. "Laser-Induced ZnO-LIG Hybrid Structures on Cork as a Versatile Platform for Piezoresistive sensing with energy harvesting potential", in preparation, 2025.

- MATHEW, A.; FERREIRA, G.; SILVA, R.R.A.; GOSWAMI, S.; PEREIRA, L.; FORTUNATO, E.; MARTINS, R.; NANDY, S. "Mechano-electric CNF based cellulose foam with intercalated Layer-by-Layer conductive MXene for pressure sensing", in preparation, 2025.

- SILVA, R.R.A.; IGREJA, R.; MATTOSO, L.H.C.; FORTUNATO, E.; MARTINS, R.; OTONI, C.G. "How do polarization parameters and polymer composites influence the electrical performance of piezoelectric triboelectric nanogenerators?", in preparation, 2025.

- SILVA, R.R.A.; FERREIRA, G.; CLARO, P.I.C.; DEUERMEIER, J.; NANDY, S.; BARQUINHA, P.; MATTOSO, L.H.C.; FORTUNATO, E.; MARTINS, R.; OTONI, C.G. "Hierarchical Micro/Nanostructured Electronic Skin for Self-Cleaning and Self-Powered Pressure Sensing via Triboelectric Nanogenerators for Soft Robotics", in preparation, 2025.

- SILVA, R.R.A.; ISLAM, J.; PINHEIRO, P.; FERREIRA, F.; ALMEIDA, H.; IACOPINO, D.; MATTOSO, L.H.C.; FORTUNATO, E.; MARTINS, R.; OTONI, C.G. "Flexible Smart Laser-Induced Graphene Sensor for Volatile Ammonia Detection via Colorimetric Electrochemical and RFID Signals for Intelligent Packaging Applications", submitted, 2025.

- SILVA, R.R.A; FERREIRA, G.; LOCHMATTER, L.; CORTINHAL, M.; MATTOSO, L.H.C.; NANDY, S.; FORTUNATO, E.; MARTINS, R.; OTONI, C.G. "Liquid Flow Energy Harvesting: A Comprehensive Insights on the Role of Liquid Dynamics from a water droplet to a streamlines for Smart Self-Powered Applications", in preparation, 2025.

### 1.4.2 List of presentations in conferences

- SILVA, R.R.A.; ISLAM, J.; PINHEIRO, T.; FERREIRA, G.; ALMEIDA, H.V.; MATTOSO, L.H.C.; IACOPINO, D.; FORTUNATO, E.; MARTINS, R.; OTONI, C. G. "Sustainable Colorimetric-electrochemical Ammonia Sensor with RFID Integration for Next-generation Smart Food Packaging". Brazilian Materials Research Society (XXIII B-MRS Meeting). 2025. Salvador, Brazil **This work won Bernhard Gross Award for the Best Oral Presentation**.

- SILVA, R.R.A.; SANTOS. F.G.; FORTUNATO, E.; OTONI, C.G.; GOSWAMI, S.; BACKES, E. H.; MATTOSO, L.H.C.; INACIO, J.M.C.; MARTINS, R.; NANDY, S.; IGREJA, R.N.; ALMEIDA, H.V. "Sacrificially templated 3D printed piezoelectric scaffolds with tunable porosity for enhanced cellular regeneration". Materials Science and Engineering (MSE), 2024, Darmstadt, Germany.

- SILVA, R.R.A.; PINHEIRO, T.; ISLAM, J.; FERREIRA, G.; ALMEIDA, H.V.; MATTOSO, L.H.C.; IACOPINO, D.; FORTUNATO, E.; MARTINS, R.; OTONI, C. G. "Polyelectrolyte-Based Colorimetric and Electrochemical RFID Sensor for Ammonia Gas Monitoring for Smart Packaging Applications". 14$^{th}$ International Symposium on Polyelectrolytes (ISP). 2025. Campinas, Brazil.

- SILVA, R.R.A.; FERREIRA, G.; NANDY, S.; FORTUNATO, E.; MATTOSO, L.H.C.; OTONI, C.G.; MARTINS, R. "Energy harvesting for diverse applications including bio-medical, liquid sensing, and self-cleaning pressure sensors". IX Annual Meeting i3N. 2024. Leiria, Portugal.

- SILVA, R.R.A.; FERREIRA, G.; MARTINS, F.; MATHEW, A.; HASSAN, T.; PEREIRA, C.; IGREJA, R.; MATTOSO, L.H.C.; MARTINS, R.; OTONI, C.G.; NANDY, S. "Mechanical-Electrical Property Interrelationship in Electrically Charged Porous Nanogenerators for Energy Harvesting Applications". European Academy of Sciences (EurASc). 2024. Lisboa, Portugal.

- MATHEW, A; FERREIRA, G.; SILVA, R.RA.; MARTINS, F.; HASSAN, T.; PEREIRA, C.; ELVIRA, F.; MARTINS, R.; NANDY, S. "Cellulose: The Smart Materials for Green Electronics". European Academy of Sciences (EurASc). 2024. Lisboa, Portugal.

- FERREIRA, G.; SILVA, R.R.A.; MARTINS, F.; PEREIRA, C.; MATHEW, A.; HASSAN, T.; DAS, S.; GOSWAMI, S.; PEREIRA, L.; MARTINS, R.; NANDY, S. "Advanced conformable textiles with PPy for Wearable IoT Applications". European Academy of Sciences (EurASc). 2024. Lisboa, Portugal.

### 1.4.3 List of patent

- SILVA, R.R.A.; OTONI, C.G.; MARTINS, R.; FORTUNATO, E. Sensores colorimétricos e eletroquímicos de substâncias alcalinas voláteis com integração RFID, processo de obtenção dos eletrodos via grafeno induzido por laser e seus usos. **Patente: Privilégio de Inovação**. Instituição de registro: INPI - Instituto Nacional da Propriedade Industrial, 05/09/2025. Depósito: Número do registro: BR1020250189720.

# 2

# FUNCTIONAL MATERIALS FOR ENVIRONMENTAL ENERGY HARVESTINGIN SMART AGRICULTURE VIA TRIBOELECTRIC NANOGENERATORS

## 2.1 **Introduction**

In recent years, there has been an increasing emphasis on adopting sustainable practices in smart agriculture, focusing on utilizing renewable energy sources.[1–4] With the world's population growing and climate change causing resource scarcity, agriculture faces the challenge of producing more food while causing less environmental harm. Consequently, the demand for environmentally sustainable energy solutions, while being accessible and cost-effective, has grown. One promising approach involves converting abundant and underutilized energy into electrical energy, e.g., using Triboelectric Nanogenerators (TENGs).[5] TENGs function as mechanical energy harvesting systems, utilizing the combined effects of contact electrification (triboelectrification) and electrostatic induction.[6]

Unlike conventional energy sources, which often contribute to environmental degradation and carbon emissions, nanogenerators operate cleanly without depleting finite resources or emitting significant pollutants. Nanogenerators support sustainable agricultural practices by reducing the carbon footprint and the environmental impact associated with electrical energy consumption. As demonstrated by Xu et al., a life cycle assessment (LCA) of $CO_2$-filled TENGs showed that their clean energy output can result in net-negative carbon emissions (up to −43,400 kg $CO_2.m^{-3}$ over a 10-year lifespan) due to minimal material-related emissions and high energy conversion efficiency.[7] This makes TENGs not only operationally clean but also

environmentally advantageous across their entire lifecycle, supporting their use in sustainable, off-grid agricultural applications. Furthermore, nanogenerators are scalable and adaptable, making them suitable for integration into agricultural infrastructure, open farming fields, marine environments, and remote areas.[8,9] Their high voltage output and environmental responsiveness, when combined with smart data processing through artificial intelligence,[10] can enable the development of self-powered sensors and other smart applications that extend well beyond power generation. For instance, smart nanogenerators can stimulate seed growth,[11–13] manage pesticide release,[14,15] sterilize food,[16,17] monitor food quality,[18,19] and purify water and air.[20,21]

Notwithstanding, several challenges must be addressed to maximize nanogenerator effectiveness and minimize environmental footprint, particularly their reliability and durability in the field, standing at typical adverse and dynamic conditions. For example, the intermittent nature of wind and water as energy sources challenges consistent energy production. Mitigating this challenge may involve integrating TENGs with other energy generators – e.g., piezoelectric,[22] thermal,[23] solar,[24] electromagnetic,[25] and chemical[26] – and implementing energy storage and management systems to stabilize fluctuations and ensure a reliable energy supply. Additionally, exposure to dust, debris, moisture, and temperature fluctuations can degrade nanogenerators' performance over time, reducing efficiency and reliability. This degradation is significant in smart applications where consistent performance is crucial. Therefore, to ensure the sustained operational reliability of nanogenerators in agriculture, it is essential to conduct further research aimed at understanding and enhancing their mechanical performance, chemical stability, structural properties, and electrical consistency.

Addressing concerns related to environmental sustainability and impacts on ecosystems is of utmost importance. While nanogenerators offer a clean and renewable energy solution,[8,27–29] the manufacturing processes and materials used may have critical environmental footprints, which should be minimized. Furthermore, deploying nanogenerators in natural ecosystems must be conducted to minimize disruption to wildlife habitats and ecological processes. To achieve this, assessing the biodegradability and sustainability of nanogenerators must consider the entire devices and the interactions between their components instead of solely focusing on individual parts, as is often the case. This is crucial because interactions can trigger catalysed degradation,[30,31] chemical reactions,[32] and the release of toxic compounds,[33] altering the nanogenerator's sustainability. Therefore, employing methodologies such as LCA to evaluate the environmental impact of the device, rather than just its components, is essential

for accurately assessing its ecological footprint and carbon emissions. Moreover, this concern is heightened when materials harmful to human health (e.g., some nanomaterials, copper, or toxic plasticizers) are used in nanogenerators in the proximity of food.

The high adaptability and multitasking features of TENGs, combined with their sustainable energy source, highlight their use for numerous applications. **Figure 2.1a** illustrates this with a literature survey chart showing the evolution of the number of publications and their primary application areas from 2012 to 2024. Despite being a recent and embryonic area worldwide, the data reveals a substantial increase in research output over this period, indicating a growing interest and significant advancements in TENG technology. Additionally, publications related to sensors have seen significant growth, underscoring the importance of TENGs in sensing applications. Although the growth in publications related to agriculture is still on the rise, it has been steadily increasing, highlighting the importance on the applications of TENGs in agricultural fields. Overall, the chart underscores the dynamic and rapidly evolving nature of TENG research, with significant diversification into various application areas. Therefore, the steady increase in publications across multiple fields suggests that TENGs are becoming an outstanding technology for advancing smart applications.

Among the types of nanogenerators, TENGs exhibit the greatest potential to rapidly advance the frontiers of smart agriculture. They contribute to producing clean energy sustainably and have applications in enhancing food productivity, plant growth, food security, precise sensing, and waste treatment.[2,34,35] The effectiveness of energy harvesting by nanogenerators is primarily determined by their specific operational mechanisms and modes. Each type of nanogenerator has distinct advantages and limitations, and understanding these characteristics is essential for developing advanced, efficient, and sustainable energy harvesting technologies for smart agriculture. This is illustrated in **Figure 2.1b**, which compares various nanogenerator technologies and their key characteristics, emphasizing the higher potential use of TENGs.

The spider chart comparing energy harvesting by nanogenerators utilizing triboelectric, piezoelectric, electromagnetic, thermoelectric, and biochemical effects provides insights into their respective characteristics. TENGs achieve the highest energy conversion efficiency, reaching up to 85%,[36,37] with some studies reporting efficiencies as high as 98%.[38] This is followed by electromagnetic nanogenerators, ca. 66%;[38] piezoelectric nanogenerators, ca. 62%;[39] biochemical nanogenerators, up to 60%;[40] and thermoelectric nanogenerators, ca. 17%.[41] Regarding manufacturing and process costs, TENGs generally exhibit lower costs due to simpler

materials (e.g., paper and aluminium) and production processes (hand-made). In contrast, biochemical nanogenerators tend to be more expensive due to the use of complex biological materials, the need for qualified labour, and sophisticated processes. Maintenance is lower for triboelectric and thermoelectric nanogenerators, as they have fewer moving parts. It is moderate for piezoelectric nanogenerators, which lose polarization efficiency over time, while electromagnetic nanogenerators require more upkeep due to the mechanical wear of components, e.g., magnets, springs and coils, which are necessary to induce electrical currents. Biochemical nanogenerators also necessitate fine-tuning of specific environmental conditions and frequent replacement of dead cells and cleaning to prevent performance degradation.

Although biochemical and thermoelectric systems may not intuitively seem to fit within the "nanogenerator" category, the term is applied when the energy conversion mechanisms involve nanoscale materials, interfaces, or effects. In biochemical nanogenerators, for instance, enzymes often function at the nanoscale, enabling energy harvesting from biochemical reactions. Similarly, thermoelectric nanogenerators utilize nanostructured materials (e.g., nanowires, thin films, or quantum dots) to enhance the Seebeck effect and reduce thermal conductivity. The "nano-" designation thus refers not to the overall device size, but to the scale of the materials or fundamental mechanisms enabling energy harvesting, in alignment with current usage in triboelectric and piezoelectric nanogenerator research.[42,43] This categorization is widely accepted in the literature, particularly in the context of self-powered nanosystems and next-generation energy harvesting technologies.[44–48]

The environmental impact is low for TENGs, as these can incorporate biodegradable (e.g., vegetal-based such as cellulose nanofibers, starch; animal-based such as chitin, chitosan, gelatin) and recyclable materials (e.g., PET, polypropylene, aluminum foil), along with materials that have a low ecological footprint and utilize eco-friendly manufacturing processes (e.g., inkjet printing, screen printing, roll-to-roll processing). It is moderate for thermoelectric and biochemical nanogenerators due to concerns about the end-of-life disposal of materials and byproducts and the frequent need for human intervention. Electromagnetic and piezoelectric nanogenerators generally exhibit a higher environmental impact, mainly due to the magnetic and lead-based piezoelectric materials, and energy-intensive manufacturing processes (e.g., high electrical voltage to polarize the piezoelectrics). In addition, heavy-metal components, hazardous emissions during ceramic processing, and challenges in recycling contribute to their overall environmental burden.

However, it is important to note that several lead-free and biodegradable piezoelectric materials, e.g., barium titanate (d33 ~350-500 pC.N-1)[49] and cellulose-based crystals (d33 up to ~60 pC.N-1)[50], are under active development, and their adoption could significantly reduce environmental impact in future implementations. Nevertheless, the most widely commercialized and practically applied piezoelectric material remains PZT (d33 up to ~1000 pC.N-1)[50], or advanced PZT-based compounds such as Sm-doped PMN-PT (d33 up to ~4100 pC.N-1)[51], whose superior performance, despite environmental drawbacks, continues to drive their use.[50,52,53]

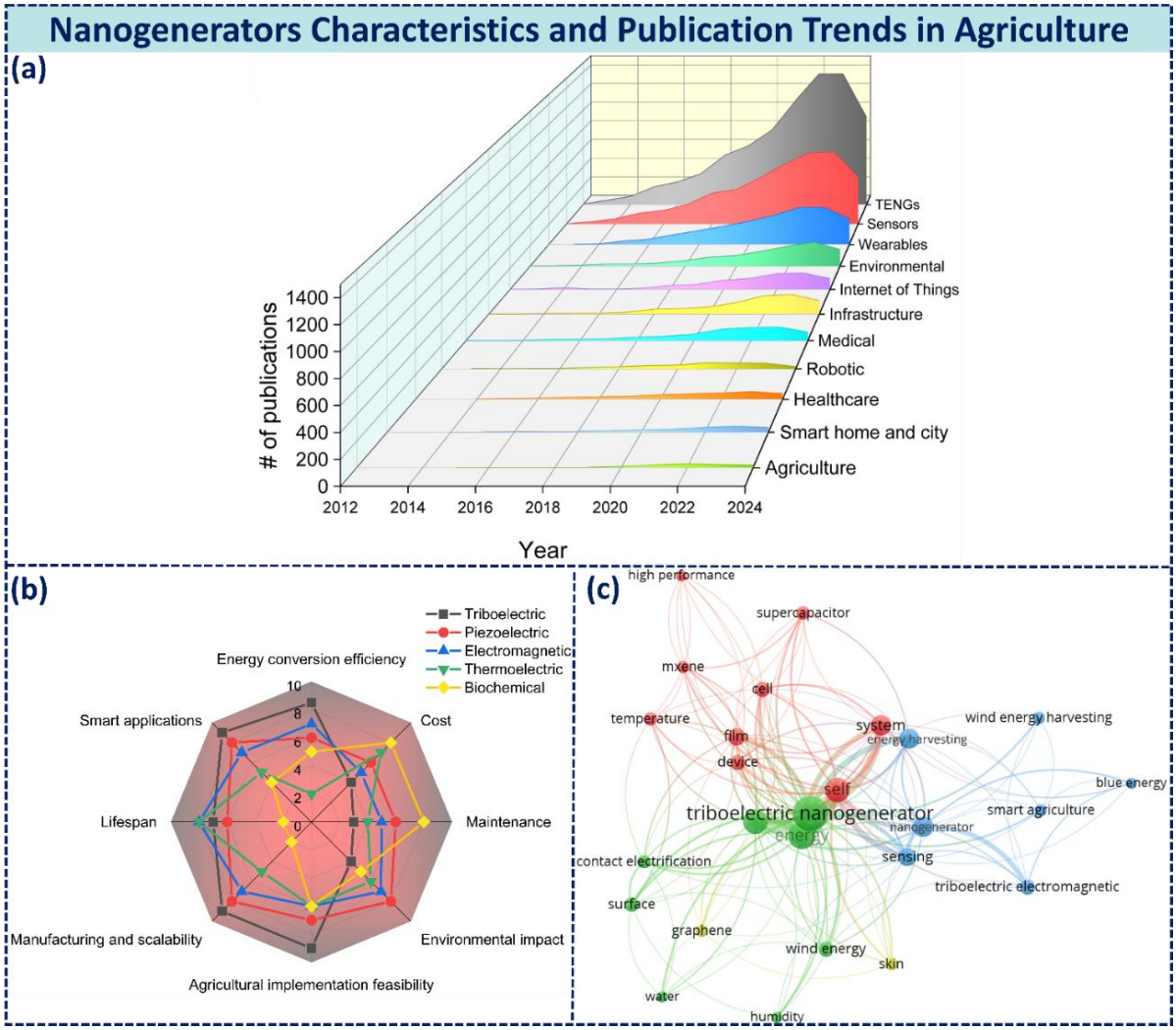


**Figure 2.1.** Nanogenerators characteristics and publication trends. (a) Web of Science core collection literature survey portraying the evolution of the number of publications on triboelectric nanogenerators and their main application areas per year from 2012 to 2024. (b) Spider chart comparing energy harvesting by nanogenerators using triboelectric, piezoelectric, electromagnetic, thermoelectric, and biochemical effects in relation to energy conversion efficiency, cost, maintenance, environmental impact, feasibility of agricultural implementation, manufacturing and scalability, lifespan, and smart applications. (c) Network map visualization of the bibliometric analysis based on keyword co-occurrences related to triboelectric nanogenerators in the agricultural environment, generated using

the VOSviewer software. Note: the thickness of the lines indicates the strength of the correlation, with thicker lines representing stronger correlations. The colour of the lines matches the colour of the keywords, where each colour represents a distinct cluster of closely related keywords. Keywords within the same cluster are more closely connected to each other than to those in other clusters.

TENGs have the highest feasibility for agricultural implementation as they can harness free and all-in-one mechanical energy from agricultural activities.[2,54,55] Piezoelectric nanogenerators, which also have a triboelectric component, can harvest different sources of energy (e.g., solid, liquid, gas triggers). Biochemical nanogenerators can utilize agricultural bio-waste, while thermoelectric nanogenerators require a significant temperature difference, which leads to efficiency and reliability fluctuations throughout the day and across seasons. Electromagnetic nanogenerators need a specific directional trigger, limiting their ability to utilize all underutilized energy sources.

Manufacturing and scalability are high for TENGs, i.e., easily fabricated due to simple production processes involving the straightforward assembly of dielectric and conductive materials. Piezoelectric nanogenerators follow, requiring a large electric field setup for polarization.[56,57] Electromagnetic nanogenerators face challenges in scaling due to complex designs and the need for high-quality magnets.[58,59] Biochemical nanogenerators present the greatest scalability challenges due to the need for complex materials, e.g., glucose oxidase, enzymes, and their complex immobilization processes on conductive substrates.[60–62]

Electromagnetic nanogenerators exhibit good stability over time due to lower friction and mechanical triggers than triboelectric and piezoelectric nanogenerators, which suffer from intrinsic mechanical wear. Despite the intrinsic thermal expansion of materials in thermoelectric nanogenerators, this technology is also considerably more stable due to the absence of mechanical triggers, ensuring a longer lifespan. Conversely, biochemical nanogenerators have a shorter lifespan due to the use of biological materials, which have a shorter life expectancy and are more unstable to environmental changes.[63,64]

Nanogenerators can advance smart agriculture not only as power sources but also as active sensors for detecting, transducing, and emitting signals. TENGs are particularly well-suited for this role due to their ease of integration into agricultural environments, flexibility, sensitivity, and high voltage output, enabling diverse applications. In contrast, piezoelectric and electromagnetic nanogenerators face design rigidity, while thermoelectric and biochemical nanogenerators generate low voltage and exhibit limited responsiveness to external factors, restricting their use in environmental monitoring. These features underscore the potential of

TENGs to drive advancements in smart agriculture, which can be further optimized by tailoring materials and manufacturing processes for specific applications.

To better understand research trends and gaps in TENG-based energy harvesting for agriculture, a bibliometric study was conducted, analyzing keyword co-occurrences in articles related to triboelectric nanogenerators in agricultural contexts **(Figure 2.1c)**. The network visualization highlights three key research areas linked to the central node, "triboelectric nanogenerator." The green cluster, encompassing terms like "wind energy," "humidity," "water," and "surface," emphasizes environmental factors. The red cluster, including "supercapacitor," "film," "MXene," and "high performance," focuses on materials and device performance. In particular, MXenes, with their high conductivity and tunable surface functionalities, have been shown to significantly boost the electrical output of TENGs by enhancing charge transfer efficiency and improving charge retention when used as charge-trapping layer.[65–68] Notably, high-performance TENGs are not yet utilized in agricultural applications. The blue cluster, featuring "smart agriculture," "blue energy," and "sensing," highlights specific agricultural and energy-harvesting applications. The interconnected nature of the graph underscores the interdisciplinary integration of material performance, environmental factors, and applications, showcasing the potential of TENGs to advance smart agricultural technologies through energy harvesting and sensing.

### 2.1.1 Scope of this review

This review explores advancements in smart and sustainable agriculture through energy harvesting and self-powered sensor technologies to improve food quality and production **(Figure 2.2, Section 1)**. We first discuss the theories of nanogenerators concerning electrical charge generation, essential for understanding their application in agricultural contexts **(Figure 2.2, Section 2)**. This section elaborates on the fundamental principles governing the generation of electrical charges at the nanoscale. The physical and chemical processes underlying electrical charge generation in nanogenerators are then detailed **(Figure 2.2, Section 3)**. We outline the requirements for employing energy nanogenerators in agriculture **(Figure 2.2, Section 4)**, emphasizing mechanical and device stability, structural attributes, sustainability, and biological compatibility while integrating them with existing agricultural infrastructure.

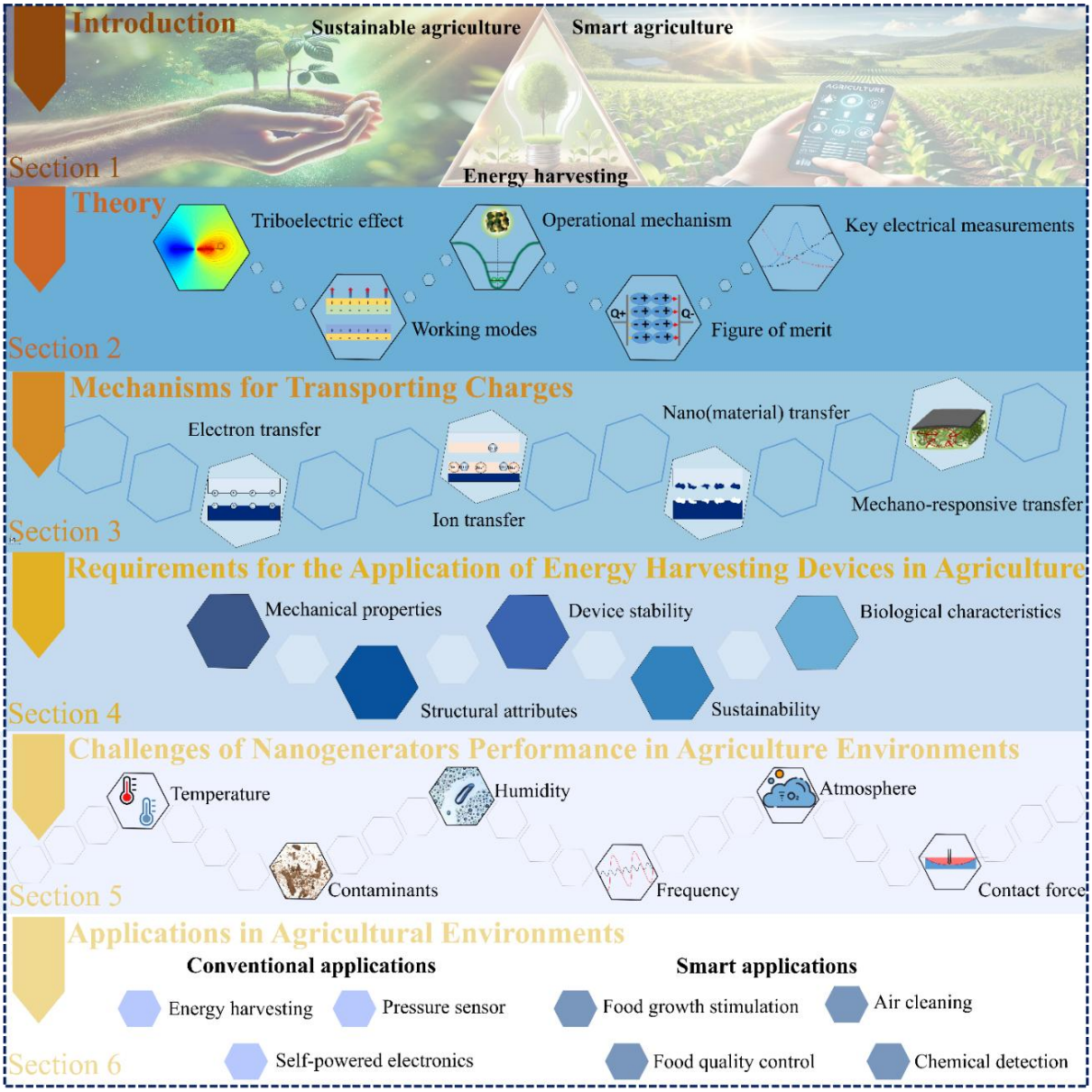


**Figure 2.2.** Schematic organization of the review on energy harvesting for smart agriculture. Schematic illustration of the organization of this review includes a brief introduction (Section 1), theories of nanogenerators focusing on the triboelectric effect, working modes, operational mechanisms, Figure of merit, and key electrical measurements (Section 2), as well as their charge transport mechanisms (Section 3). Requirements for applying energy harvesting devices in agriculture aim to achieve long-lasting and stable electrical output (Section 4) and address challenges encountered in agricultural environments (Section 5). The primary and cutting-edge applications of nanogenerators in agricultural settings are highlighted (Section 6).

Furthermore, we highlight primary challenges during the *in-situ* deployment of nanogenerators in agriculture, proposing solutions to enhance their electrical output reliability, du-

rability, and stability in smart applications **(Figure 2.2, Section 6)**. This section explores technical hurdles, e.g., environmental variability and mechanical reliability in agricultural environments. We close this review by presenting diverse applications of nanogenerators in agriculture, encompassing both traditional energy harvesting applications and advanced smart agricultural applications, highlighting their perspectives and outlines. The overarching goal of this review is to inspire and accelerate theoretical and technological research on energy nanogenerators applied in agriculture food production, contributing to the evolution of modern agriculture characterized by intelligent, sustainable, reliable, health-safe, and enduring monitoring practices.

## 2.2 Theory

Understanding triboelectrification and its evolution is essential for appreciating how TENGs have emerged as viable energy harvesters in real-world applications such as agriculture. In the following subsections, we trace the development of this phenomenon from its earliest recorded observations to the sophisticated devices in use today, highlighting key scientific milestones, technological breakthroughs, and shifts in theoretical understanding. We outline how the basic concept of contact electrification evolved into the broader framework of triboelectrification, encompassing both pure contact and frictional charge generation, and how these principles were harnessed in progressively more advanced electrostatic devices. Particular attention is given to how modern TENG architectures and operational modes respond to environmental challenges, e.g., particulate contamination, moisture, and airflow, that are especially relevant to agricultural settings.

By integrating the realities of particle–surface interactions into the theoretical framework, this section provides the foundation for designing TENGs that maintain stable performance in the inherently variable and contaminant-rich environments of agriculture. This theoretical perspective also sets the stage for the subsequent discussion of the Figure of Merit and key electrical measurements, which are essential

for quantitatively evaluating device performance in both controlled and agricultural environments.

### 2.2.1 A brief history of triboelectrification

**Figure 2.3** presents a timeline highlighting important breakthroughs and representative literature advances in triboelectricity. Triboelectricity, a phenomenon recognized for over 2400 years, traces its origins back to the discovery of contact electrification (CE) by the Greek philosopher Thales of Miletus. Notably, Thales observed the attraction of small pieces of straw, threads, and hair when amber was rubbed with hair.[69,70] The term 'triboelectric' finds its roots in the Greek words τριβ (tribe) and ἤλεκτρον (electron), signifying rub and amber, respectively.[71] In 1600, William Gilbert made significant contributions by coining the term "*electricus*" and documenting the triboelectric charge of various materials in his book "*de Magnete*", establishing a foundational basis for the study of electricity and magnetism.[72] In the 1700s, Stephen Gray and Charles du Fay discovered that bodies could be electrified not only by friction but also by contact, leading to the classification of materials as conductors or insulators.[72] In 1759, Johan Carl Wilcke developed the first triboelectric series, listing materials based on their tendency to gain or lose electric charge.[73] His sequence consisted of ten common materials: smooth glass, wool, quills, wood, paper, sealing wax, white wax, rough glass, lead, sulphur, and metals, listed in order of polarity.[73] Besides theoretical research, there have been longstanding efforts to apply triboelectric charges. The first attempt was made by Otto von Guericke around 1663 when he invented the first friction machine.[74] This machine utilized triboelectrification between hands and a ball of sulphur, later replaced with a glass globe as suggested by Isaac Newton and implemented by Francis Hauksbee.[75,76] Further advancements in electrostatic machines were achieved through the utilization

of glass disks and Leyden jars to store substantial amounts of charge.[70] Following their contributions, Alessandro Volta and Abraham Bennet pioneered the development of electrostatic induction machines.[77] However, it was Robert Jemison Van de Graaff who significantly advanced this field with his development of the Van de Graaff generator in 1937, which has been used as a particle accelerator in recent times.[70,77] The period from 1800 to 1937 also marked the development of electrostatic machines, e.g., the Kelvin water dropper, the Holtz machine and the Wimshurst machine, harnessing the triboelectric effect to generate high voltages and further advancing the applications of electrostatics.[70,78]

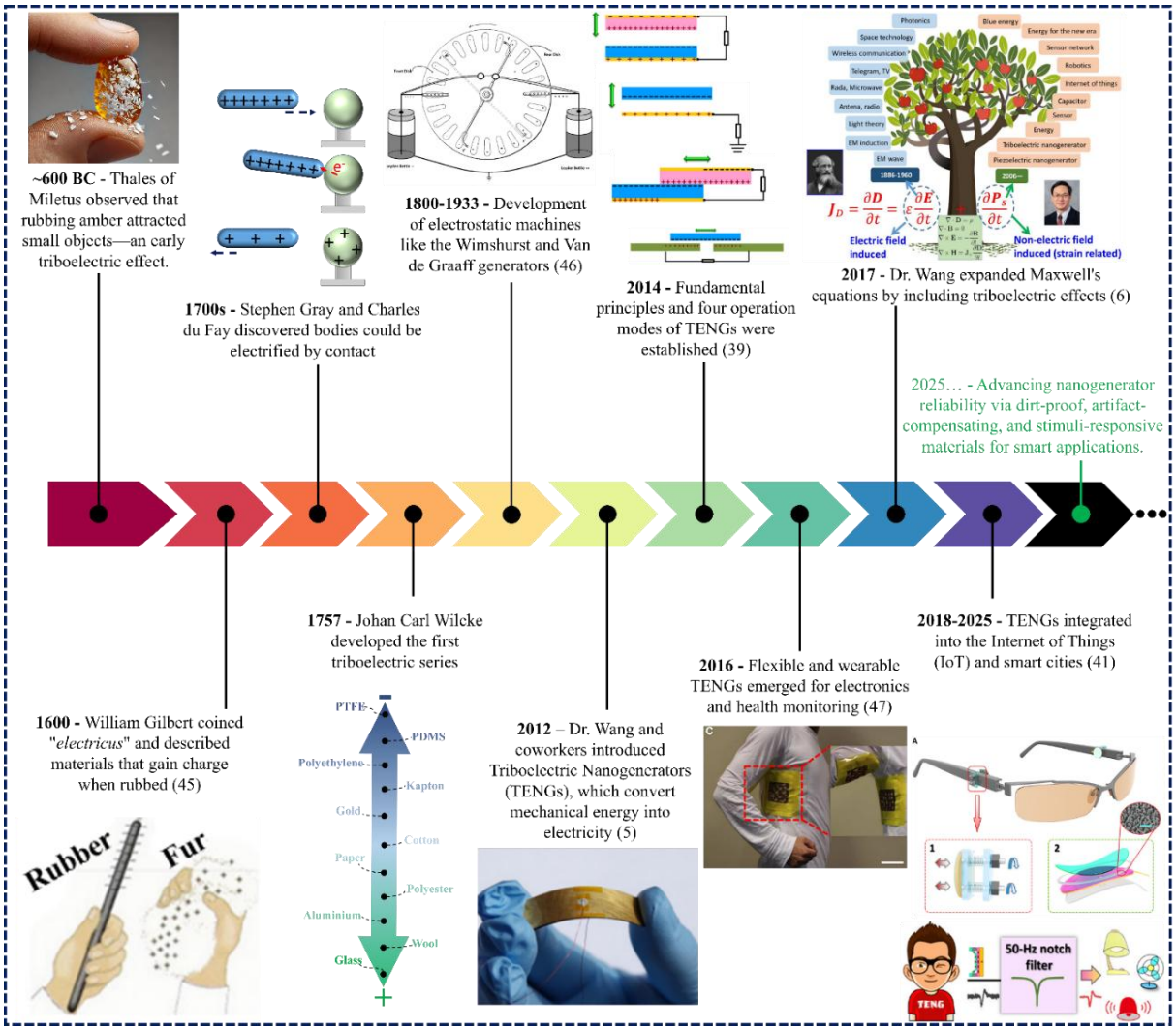


**Figure 2.3.** Timeline of breakthroughs and literature advances on triboelectricity and triboelectric nanogenerators. Illustration of the triboelectric effect observed when rubbing rubber and fur, reprinted with permission from ref.[43]

Image of the classic Wimshurst machine, reprinted with permission from ref.[79] Image of the first triboelectric nanogenerator developed, reprinted with permission from ref.[5] Illustration of the four working modes of triboelectric nanogenerator, reprinted with permission from ref.[80] Image for the first flexible and wearable triboelectric nanogenerator sensor developed, reprinted with permission from ref.[81] Image of the proposed expansion of Maxwell's equations to incorporate triboelectric effects, reprinted with permission from ref.[6] Image of the triboelectric nanogenerator integrated into smart applications such as IoT, reference reprinted with permission from ref.[82]

Groundbreaking progress in the field of triboelectricity occurred in 2012 when Dr. Zhong Lin Wang and his team introduced the first TENG, a device that converts mechanical energy into electricity by leveraging the triboelectric effect and electrostatic induction.[5] By 2014, the fundamental operational principles of TENG were elucidated, including a detailed explanation of their four fundamental modes of operation: contact-separation, lateral sliding, single-electrode, and freestanding triboelectric-layer modes.[80] Underpinned by these developments over the decades, the recent creation of wearable and flexible TENGs in 2016 expanded their applications to include wearable electronics, health monitoring, and self-powered sensors. Further advancements were achieved by developing the first hybrid nanogenerators that integrate triboelectric, piezoelectric, and pyroelectric mechanisms, thereby expanding the potential for harnessing wasted energy.[83] In early 2017, Dr. Wang extended Maxwell's equations to incorporate triboelectric effects and non-electric field-induced polarization resulting from mechanical triggering.[6] From 2018 to 2025, TENGs have been increasingly integrated into the Internet of Things (IoT) and smart cities, enhancing their viability for large-scale production and diverse smart applications.[82]

Looking toward 2025 and beyond, and from an agricultural perspective, TENGs are expected to envolve into smart, stimuli-responsive devices that integrate energy harvesting, selective sensing and wireless communication within a single, unified platform, regardless of mechanical drive artifacts. Future milestones will likely include the commercialization of smart sensor–TENG applications for large-area greenhouse

and open-field deployment, enabling energy generation alongside AI-assisted data analytics for real-time agronomic decision-making. A key enabler for this transition will be the incorporation of stimuli-responsive materials, functional layers whose triboelectric or sensing properties change predictably in response to environmental cues (e.g., pH, humidity, temperature, or specific agrochemicals). Such materials can allow TENGs to serve not only as power sources and highly selective detectors but also as active agricultural tools, enabling functions such as humidity-triggered irrigation or seed release, dynamic shading control, antimicrobial and anti-biofouling protection, and pH-sensitive biodegradable coatings for reduced environmental impact.

Emerging directions also encompass bio-inspired structural designs, e.g., leaf-mimicking morphologies that enhance wind-energy capture and self-cleaning efficiency, alongside self-healing composites to extend device lifetime in abrasive, particle-rich environments. The integration of stimuli-responsive surfaces with adaptive mechanical architectures could enable autonomous recalibration of sensor thresholds, self-regulation of contact interfaces, and selective activation under target conditions, thereby increasing both sensing specificity and operational reliability. By integrating these advanced TENGs directly into agricultural infrastructure, e.g., irrigation systems, crop covers, and smart sensing, future systems could deliver continuous energy and high-fidelity environmental data, supporting climate-resilient, low-carbon farming practices. This convergence of energy harvesting, selective sensing, and adaptive responsiveness marks a decisive shift from niche experimentation toward scalable, farm-ready solutions capable of transforming smart agriculture.

### 2.2.2 **Triboelectric effect**

The triboelectric effect, or contact electrification, occurs when two distinct materials come into contact or rub against each other, subsequently parting ways and generating electrostatic charges of opposite signs on each surface. Consequently,

triboelectrification is an inherent process occurring not only at the solid-solid interface but also at interfaces involving solids, liquids, and gases, encompassing solid-liquid, solid-gas, gas-gas, liquid-gas, and liquid-liquid interfaces.[84]

Until 2012, triboelectrification was predominantly viewed as a potential hazard or an undesired phenomenon rather than a valuable technique. For instance, clothing rubbing during physical activity attracts particles and dirt, and the accumulation of electrical charges generates noise and distorts signals produced by equipment. Generating high-voltage electrostatic discharges presents a risk to electronic circuits, potentially causing unintended fires. While in agriculture, static charges accumulating in grain storage silos elevate the risk of ignition. Notably, volcanic plumes demonstrate this phenomenon, with ash particles colliding and generating electrical charges followed by volcanic sparks.[85] Interestingly, there is speculation that this phenomenon could have played a role in the origin of life, as volcanic rays might have triggered the synthesis of amino acids from the atmospheric gas mixture. Besides the adverse effects, in 2012, Wang et al. revealed that triboelectrification and electrostatic induction can be harnessed to harvest energy from mechanical movements, giving rise to the term TENG.[5]

### 2.2.3 **Operational mechanism**

The operational mechanism of TENGs involves the combination of contact electrification (CE) and electrostatic induction, facilitating the conversion of mechanical energy into electrical energy. Xu et al. proposed a model based on the atomic-scale electron cloud potential to elucidate the CE process **(Figure 2.4a)**.[86] Initially, when the atoms of two dielectric materials are distantly positioned, their electron clouds remain non-overlapping, resulting in a high energy barrier for charge transfer **(Figure 2.4a,i)**. Under external mechanical drive, the atoms approach each other until reaching a re-

pulsive region where their electron clouds overlap, substantially reducing the interatomic potential barrier. Consequently, electrons in the highest occupied molecular orbital (HOMO) of material 1 can overcome the diminished potential barrier and transfer to the lowest unoccupied molecular orbital (LUMO) of material 2, thus lowering the potential energy **(Figure 2.4a,ii)**. Following separation, the transferred charges remain as static charges on the surfaces of materials 1 and 2 **(Figure 2.4a,iii)**.[86]

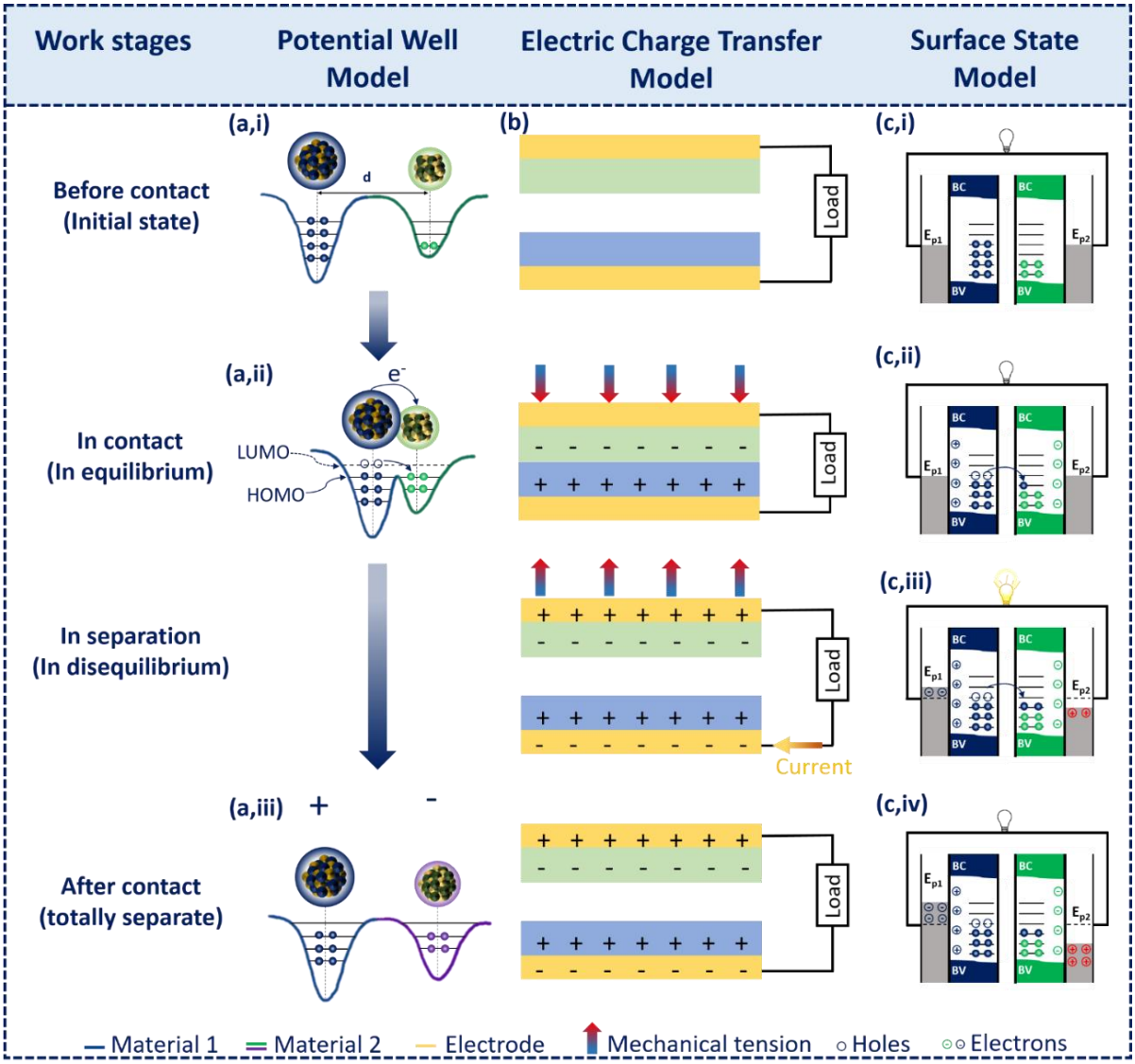


**Figure 2.4.** Operating stages of triboelectric nanogenerators through four sequential stages: before contact (initial state), in contact (equilibrium), in separation (disequilibrium), and after contact (complete separation). (a) Electron cloud–potential well model explaining contact electrification (CE) and charge transfer between two atoms: in (a,i), the two materials are initially separated with distinct potential wells; in (a,ii), upon contact, electrons transfer from one material to another as their molecular orbital - specifically the lowest unoccupied molecular orbital (LUMO)

and the highest occupied molecular orbital (HOMO) - interact and reach equilibrium; in (a,iii), after separation, the materials retain opposite charges. Adapted with permission from ref.[87]. (b) Electric charge transfer in triboelectric nanogenerators, representing the evolution of charge distribution across the materials, where separation induces a potential difference that drives current through an external load. (c) Surface state model explaining charge transfer between electrodes via the Fermi level, with corresponding band diagrams at each stage: (c,i) initial alignment, (c,ii) contact-induced band bending, (c,iii) separation with potential difference and current generation, and (c,iv) stabilized charged surfaces after full separation. In the schematic, Material 1 is represented in blue and Material 2 in green, with electrodes shown in yellow. Mechanical tension applied during separation is denoted by red arrows, while charge carriers are indicated as open circles for holes and filled circles for electrons. Adapted with permission from ref.[88]

The charge transfer process between the triboelectric surfaces in **Figure 2.4b** aligns well with the electron cloud-potential well model. The generation of alternating electric current is elucidated through the surface state model. Before surface contact, the Fermi levels are at the same energy level **(Figure 2.4c,i)**. Upon contact, despite charge transfer between the dielectrics, the transferred charges remain trapped on the surfaces and mutually compensate **(Figure 2.4c,ii)**, resulting in no current flow in the external circuit. Upon separation, the transferred charges change the Fermi level of the corresponding electrodes **(Figure 2.4c, iii)**, creating an electrical potential difference between the electrodes through electrostatic induction.[88] This induces current flow through the external circuit. When the dielectrics are fully separated, the Fermi level difference reaches equilibrium due to transported electrons and no current flows **(Figure 2.4c,iv)**. As the two dielectrics approach each other again, the Fermi level difference decreases, generating an electric current in the opposite direction until the dielectric materials return to a charge balance state during contact between the triboelectric layers.[88] This final stage completes the operating cycle of the TENGs, resulting in alternating current generation.

### 2.2.4 TENG working modes

Four fundamental working modes of a TENG were proposed in 2014, depending on the direction of polarization change and electrode configuration.[80] These modes, illustrated in **Figure 2.5**, include the vertical contact-separation mode, lateral sliding mode, single electrode mode, and freestanding triboelectric layer mode.[80]

#### 2.2.4.1 Vertical contact-separation mode

The vertical contact-separation (VCS) mode was first developed.[5] In this mode, two dielectric materials with friction layers facing each other, and electrodes are deposited on the opposite surfaces of both friction materials, connected to an external circuit **(Figure 2.5a)**. These electrodes serve as a source of free electrons in the TENG's general working mechanism.

When the surfaces of the dielectric materials approach and physically contact each other, charges of opposite polarity are transferred through various phenomena. Upon separating the two triboelectric layers, the transferred charges remain on the surface, creating an electric field between the friction layers. This induces a potential difference across the electrodes, generating an electric current in the external circuit to balance the altered electrical potential. When the two friction layers are forced closer until they reach contact, the positive and negative charges cancel each other out, the potential difference disappears, and the electrons return to the electrode in the opposite direction, producing alternating current.

#### 2.2.4.2 Lateral sliding mode

The lateral sliding (LS) mode utilizes polarization in the lateral direction due to relative displacement parallel to the interface between two dielectrics **(Figure 2.5b**).[86] Initially, the triboelectric layers overlap entirely, resulting in no drop in potential. However, as lateral separation occurs due to external force, the charges and surfaces become separated by the difference in electrostatic potential. This creates polarization

and a potential difference along the direction of displacement, leading to a flow of electrons between the electrodes. Sliding backward generates an electric current in the opposite direction, completing the operational cycle.

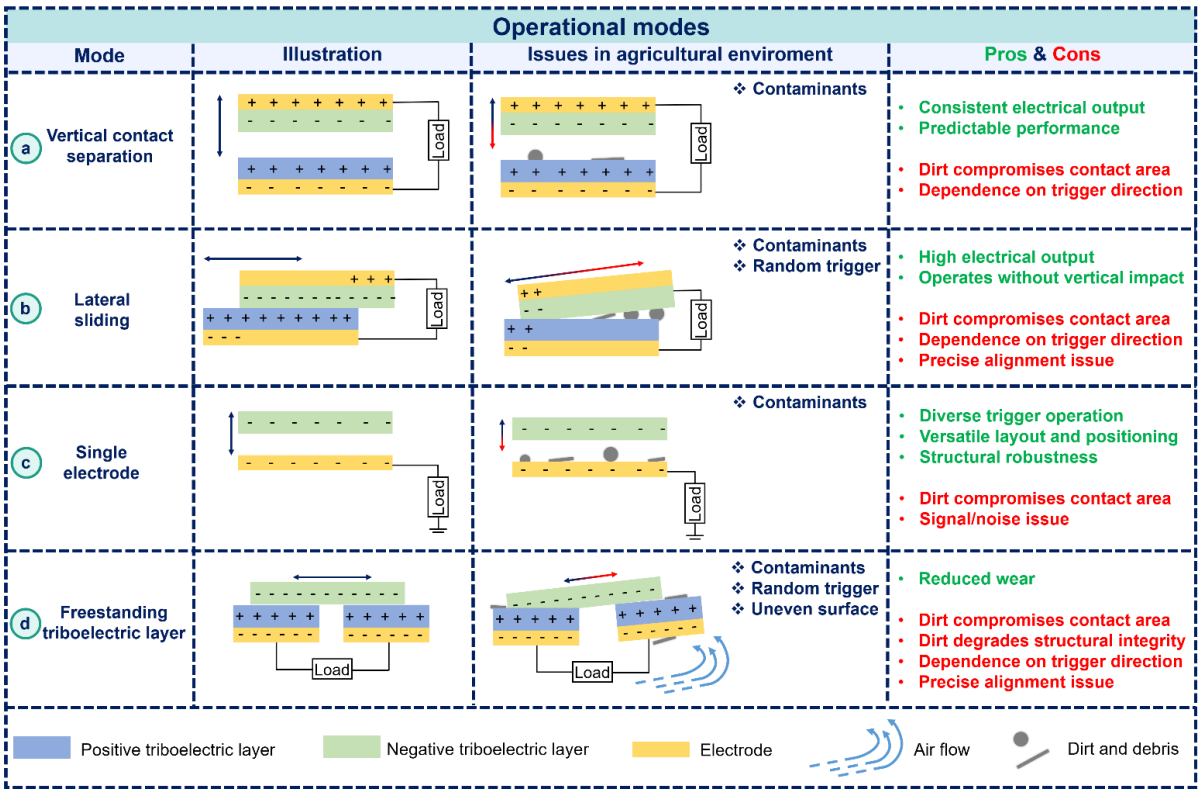


**Figure 2.5.** TENG operational modes, their agricultural challenges, and the pros and cons of each. (a) Vertical contact-separation mode. (b) Lateral sliding mode. (c) Single electrode mode. (d) Freestanding triboelectric layer mode. For each mode, the schematic illustrates the working principle, typical issues in agricultural environments (e.g., contaminants, random triggering, uneven surfaces), and the main advantages and disadvantages. Positive and negative triboelectric layers are shown in blue and green, respectively, with electrodes in yellow. Mechanical motion and airflow are indicated by red and blue arrows, while dirt and debris are represented by grey particles. Key trade-offs include consistent output and predictability versus sensitivity to contamination and structural challenges. This comparison highlights considerations for deploying TENGs in practical, contamination-prone settings.

In agricultural deployments, LS-mode TENGs offer the advantage of high electrical output and the ability to operate without direct vertical impact, making them suitable for harvesting energy from steady mechanical motions such as conveyor belts, sliding panels, or crop-sorting mechanisms. However, as illustrated in **Figure 2.5b**, their performance is highly sensitive to precise alignment between layers and sliding

direction consistency, both of which can be difficult to maintain in outdoor farm environments exposed to wind-induced vibrations, irregular trigger motions, or shifting structural supports.

Moreover, contaminants such as dust, soil particles, and plant debris can embed at the interface, reducing effective contact area and increasing frictional resistance. This not only diminishes charge generation efficiency but also accelerates mechanical wear of the triboelectric layers, shortening device lifespan. In addition, random triggering events, common in agricultural machinery and natural stimuli, can lead to unstable output waveforms, complicating direct use in sensing applications unless coupled with advanced signal processing or power conditioning. These limitations underscore the need for robust device packaging and, more importantly, the integration of active functional surfaces based on materials with self-cleaning, dirt-degrading, or air-cleansing capabilities (as discussed in *Section 2.4.4.3*), thereby enabling LS-mode TENGs to operate reliably over extended periods in agricultural environments.

#### 2.2.4.3 **Single electrode mode**

The single electrode (SE) mode was introduced to harvest energy from a freely moving object without connecting both active layers with springers or spacers, using only the ground as the reference electrode **(Figure 2.5c)**. Nevertheless, the SE mode yields merely half the output compared to the other two modes, attributable to the electrostatic shielding effect.[89] Initially, two unpolarized surfaces, polytetrafluoroethylene (PTFE) and polydimethylsiloxane (PDMS) film, contain electrodes on the back **(Figure 2.6a,i)**. Upon contact with the PDMS film, the electrostatic balance is disrupted, leading to the attraction of negative triboelectric charges to PTFE – due to its superior charge-capturing capability – resulting in a positive charge accumulation on the PDMS surface **(Figure 2.6a, ii)**. This initiates an instantaneous flow of electrons from the ground to the electrode through the external charge, driven by the electrostatic induction effect **(Figure 2.6a, iii)**. The electron flow continues until electrostatic equilibrium

is achieved. Upon approach, electrons are repelled from the electrode to the ground, causing charges to move in the opposite direction, producing alternating current **(Figure 2.6a, iv)**. Notably, the dielectric constant of the active layer profoundly influences the duration of charge retention on the surface. Materials with higher electrical insulation retain charges for longer periods.

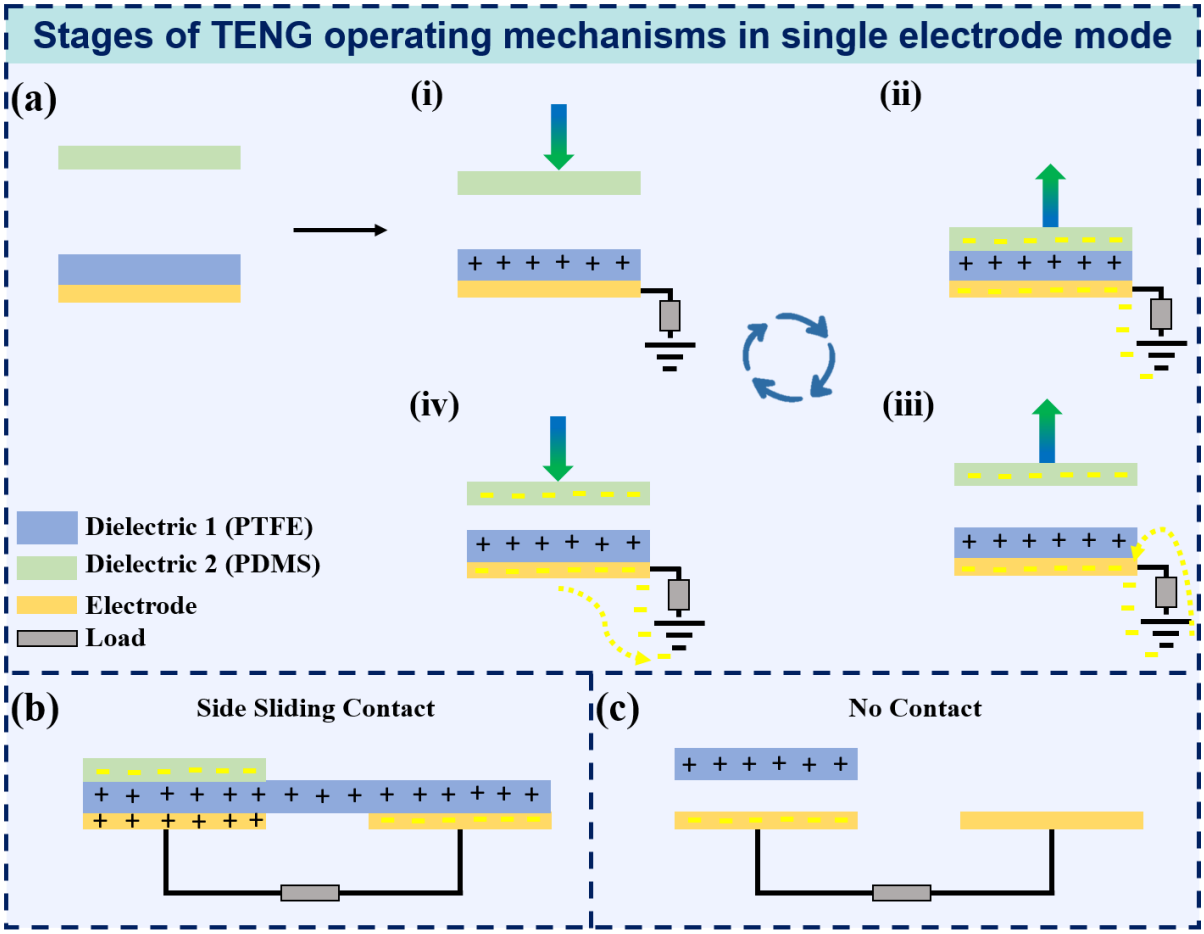


**Figure 2.6.** Stages of TENG operating mechanisms in single-electrode configuration. (a) Stages of TENG operating mechanisms in single electrode mode. (b) Schematic representation of a dielectric-to-dielectric contact-independent triboelectric layer. (c) Schematic representation of a freestanding triboelectric layer with no contact between a conductor and a dielectric. Adapted with permission from ref.[90]

#### 2.2.4.4 **Freestanding triboelectric layer mode**

The freestanding triboelectric layer (FT) mode is centered on lateral movement between the outer triboelectric layer (independent counterpart) and the TENG's triboelectric layer **(Figure 2.5d)**. Two operational scenarios exist for this mode: lateral sliding contact and the no-contact mode.[90] In the first scenario, assuming the dielectric and electrodes are initially discharged, static charges are generated by triboelectrification upon physical contact. Once generated, the negative charges on the dielectric surface equate to the positive charges on the electrodes. When the dielectric fully overlaps with the first electrode **(Figure 2.6b)**, positive charges migrate to the left electrode to

balance the electrical potential.[90] As the dielectric layer slides toward the right electrode, positive charges flow from the left to the right electrode through the external load.[90] Subsequently, a slide of the dielectric to the initial position induces the flow of positive charges in the same direction, producing alternating current.

In the second scenario, illustrated in **Figure 2.6c**, the TENG necessitates two regions with conductive materials connected by an external load. The dielectric (independent counterpart) must be initially charged, and the vertical separation of the counterpart must be much smaller than the relative displacement of the two electrodes. Under these conditions, the relative sliding of the layers containing immobile charges induces electron flow between the electrodes. Electricity generation follows the same mechanism as in the previous scenario, considering the oscillation of the dielectric between the two electrodes without direct contact.[90] This is feasible because triboelectric charges can be preserved on the insulator surfaces for extended periods. Unlike the first scenario, where direct contact occurs, the absence of such contact significantly reduces wear on the TENG's surface. Despite the lower electrical voltage, this extends the usage life, especially in agricultural environments.

### 2.2.5 **Figure of merit and key electrical measurements**

Figure of merit (FOM) is used to quantitatively evaluate the performance of TENGs from both structural and material perspectives. The performance figure of merit ($FOM_p$) for TENGs consists of the structural figure of merit (FOMs), related to TENG design, and the material figure of merit (FOM), related to surface charge density ($\sigma$). For a dimensionless FOM, i.e., independent of the TENGs mode and size, Zi et al. demonstrated that the efficiency of TENGs depends only on the maximum distance between the surfaces ($Z_{max}$) and the maximum energy conversion efficiency ($E_{max}$).[91] To exclude the effects of TENG dimensions, the area (A) and the charge density ($\sigma$)

were placed in the denominator of the term referring to the structure ($FOM_s$). Therefore, $FOM_s$ are defined by Equation 2.1.

$$FOM_s = \frac{2\varepsilon_0}{\sigma^2 A}\frac{E_{max}}{Z_{max}} \quad (2.1)$$

Where σ is the only component related to material properties ($FOM_m$). Thus, the $FOM_p$ of the TENGs is defined in Equation 2.2.

$$FOM_p = FOM_s \times \sigma^2 \quad (2.2)$$

The performance of TENG will be significantly increased when σ is optimized due to its quadratic dependence. There are two typical approaches to optimizing $FOM_p$. For $FOM_s$, this can be achieved by increasing the effective contact area, e.g., by developing micro, nano, or hierarchical patterns on surfaces, which increases roughness and ensures higher charge accumulation for transfer. The second approach is to choose materials with a strong tendency to gain or lose electrons and are highly polarizable (through electronic, orbital, ionic polarization, etc.), thereby increasing σ. Furthermore, the potential difference between the active layers also contributes to improving the performance of TENGs. For instance, if two contacting materials are positioned further apart in the triboelectric series, a greater charge will be transferred between them. Therefore, ideally, the two triboelectric surfaces should be made of materials located at the two ends of the triboelectric series.

Considering aspects beyond electrical performance, such as durability, sustainability, and reproducibility in agricultural environments, several other properties must be considered when selecting materials. These include flexibility, chemical stability, permeability, elasticity, scalability, cost, weight, and manufacturing complexity (which is covered in *Section 2.4*). Furthermore, to better understand the functioning and efficiency of each nanogenerator, it is essential to know the primary electrical characterizations and the key information that can be extracted from them to enable fair comparisons with other developed devices. These aspects are covered in the following subsections.

#### 2.2.5.1 **Open circuit voltage**

The open circuit voltage ($V_{oc}$) in nanogenerators results from the triboelectric effect and contact electrification. During mechanical contact and separation between materials with different electron affinities, charge transfer occurs due to the redistribution of electrons. $V_{oc}$ is a manifestation of the potential difference created by the separated charges. A detailed understanding involves exploring the triboelectric series, which ranks materials based on their electron affinity, work function differences, and the spatial distribution of charges at the material interface. The CE of a material is utilized to categorize materials within the triboelectric series. Despite not being random, the assigned values lack reproducibility.[92] Such inconsistencies are inevitable due to complexities and uncontrollable factors inherent in material development, where factors like molecular interactions at interfaces, specific chemical compositions, surface functional groups, and crystalline structures introduce complexities that hinder the accurate classification of electron affinity.

Advancing the understanding of $V_{oc}$ involves the utilization of state-of-the-art characterizations, e.g., Kelvin probe force microscopy (KPFM) and X-ray photoelectron spectroscopy (XPS), facilitating a detailed investigation into charge distribution and fluctuations in work function at the material interface. This knowledge enables optimizing nanogenerator electrical performance, e.g., enhancing surface charge accumulation capacity through chemical and physical modifications.

#### 2.2.5.2 **Short circuit current**

The short circuit current is an output in nanogenerators, reflecting the maximum current flow when the electrodes are directly connected with the lowest possible electrical resistance. The science behind $I_{sc}$ investigates the kinetics of charge transfer during the contact and separation processes of nanogenerator operation. The contact area between triboelectric materials influences the $I_{sc}$ intensity, as a larger contact area allows for more effective charge transfer, leading to higher $I_{sc}$. The speed of mechanical

motion also affects $I_{sc}$, since the kinetics of charge transfer are closely tied to the velocity of the contact and separation processes. Faster motion can enhance the charge transfer rate, resulting in a higher short circuit current. While nanogenerators present promising mechanical energy harvesting, the main drawback lies in the low $I_{sc}$, around microamperes (μA). Consequently, optimizing $I_{sc}$ is essential, requiring optimizing its output by external loads. Furthermore, caution should be exercised when comparing currents across different working modes of TENGs. For instance, despite the freestanding triboelectric-layer mode typically exhibiting a lower short-circuit current peak than the contact-separation mode, its output power can be similar or even greater, largely due to its higher internal impedance.[43]

#### 2.2.5.3 **Surface charge density & transfer**

Surface charge density is crucial for determining output power, as it is directly related to the square of the surface charge density. When different materials with different triboelectric polarities come into contact, charge transfer occurs due to CE. Each material has a maximum capacity for holding charges, dictated by its susceptibility to discharging in air. Typically, surface charge density is restricted by the breakdown voltage of a surface, usually ~250 $\mu C.m^{-2}$.[43] There have been efforts to boost surface charge density by adding micro/nanostructures to surfaces, injecting external charges, modifying functional groups, and enhancing electronegativity differences between the active layers. Moreover, reducing gas pressure will improve surface charges, strengthening resilience to air degradation and facilitating electron transfer within friction layers. It is important to note that triboelectric charges are not confined solely to surface layers but can permeate within friction layers, especially in porous devices. Conversely, the short-circuit charges transfer ($\Delta Qsc$) refers to the maximum transferred charges within a single cycle. Upon rectification, this value nearly doubles in a single cycle as charges move unidirectionally without flowing back.

Cui et al. demonstrated that aligning the charge rise characteristic time with the charge decay characteristic time is crucial for maintaining ultra-high surface charge density in triboelectric materials.[93] According to the dynamic charge transfer model, adjusting the decay coefficient and initial surface charge density through material selection can enhance the charge transfer efficiency of TENGs. For instance, materials with poor long-term charge stability can significantly increase their surface charge density through optimized dynamic charge transfer during triboelectric and de-electrification processes. By screening or synthesizing high-performance triboelectric materials, the dynamic charge transfer process can be fine-tuned, improving both the charge trapping capability (charge rise characteristic time) and the charge release capability (charge decay characteristic time). However, it is essential to consider the stability of charge rise and decay in agricultural environments. For instance, exposure to variations in temperature and humidity can significantly alter the dielectric constant, surface states, and defects, impacting surface charge density accumulation. These fluctuations can cause variations in electrical output, thereby affecting the reliability of TENGs in sensing applications.

#### 2.2.5.4 **Power density & efficiency**

Power density and efficiency are key metrics for assessing energy harvesting technologies. Efficiency represents the proportion of harvested energy relative to the total energy input, expressed as a percentage. In contrast, power density provides a more consistent measure by standardizing the electrical power output per unit area of the device. At its core, power density is the product of the $V_{oc}$ and the $I_{sc}$, divided by the area of the device. In TENG devices, peak power typically surpasses average power by several or even dozens of times, varying depending on the TENG mode.[43] Hence, optimizing power density and power management is crucial to advance efficient energy harvesting in diverse applications. According to Wang, based on theoret-

ical and in-lab studies, TENGs exhibit notable power densities (up to $kW.m^{-3}$) alongside impressive energy conversion efficiencies (~80%).[43] Hence, to boost the power density involves a comprehensive exploration of the underlying mechanisms governing the energy conversion processes within the device.

## 2.3 Transport mechanisms of electric charges

Traditional descriptions of TENGs focus on their operation in idealized laboratory conditions, where clean, smooth surfaces and controlled environments allow charge generation and transfer to be studied under optimal circumstances. However, the realities of environmental deployment are far from pristine. Dust, soil particles, pollen, and other environmental contaminants constantly interact with device surfaces, altering interfacial contact, surface potential, charge trapping, and electron transfer pathways. These particulate interactions (often overlooked in conventional TENG theory) can significantly influence triboelectric output, efficiency, and long-term stability, demanding a deeper and more application-specific understanding of the underlying mechanisms. In this section, we move beyond the conventional framework to address questions critical for real-world environmental applications:

How does particle adhesion, with different size distributions and mineral or organic compositions, affect the potential well model and the energy barrier for electron transfer?

How do surface contaminants modify the effective contact area, and what is the minimum gap or contact distance needed to maintain efficient charge transfer?

How do roughness, stiffness mismatches, and dirt layers influence the electrical output performance of TENGs under field conditions?

To address these questions, it is essential first to revisit the fundamental principles of contact electrification and electrostatic induction, including material

dependence, interfacial phenomena, and charge transfer mechanisms - and to recognize that in real environments, these mechanisms rarely occur in isolation. This is because, in practical applications, mechanical interactions often involve both normal contact and lateral motion, thereby introducing frictional effects into the charge generation process. Thus, in most instances, the generation of triboelectric charges doesn't solely arise from pure contact electrification (CE), involving vertical physical contact between two materials but can also occur through friction, i.e., sliding and rubbing motion between the materials in contact.[94] In this case, the term triboelectrification is more appropriate, although the two terms are often used interchangeably in the literature. This is to take into account that, in practice, it is complicated to separate proper contact electrification from tribological effects due to the overlap between purely contact-separation and frictional effects at the microscale.[84]

According to Wang, CE is a physical effect involving the mechanical contact or sliding of two materials, while triboelectrification is an engineering consequence capable of generating friction and/or debris.[84] Despite the extensive history of empirical observations, the theoretical foundation for triboelectric charge generation is still evolving. Describing all the relevant mechanisms is challenging, as experiments have progressively added new elements disproving previously accepted theories, making it difficult to elaborate. This has made it difficult to elaborate a comprehensive theory of triboelectrification. Thereby, up to now, four primary mechanisms are proposed for transporting triboelectric charges: electron transfer, ion transfer, (nano)material transfer, and mechano-responsive charge transfer, as illustrated in **Figure 2.7**.

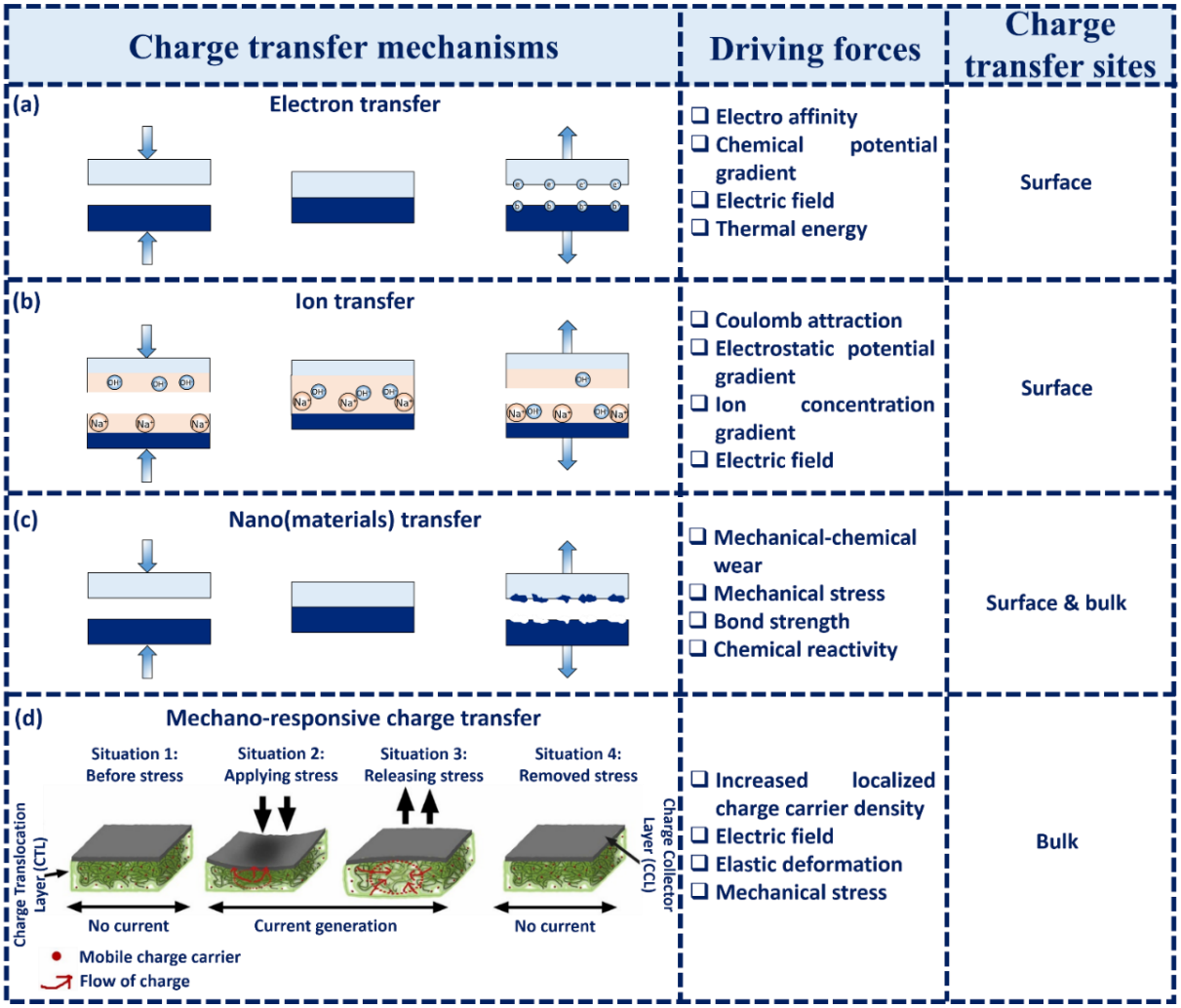


**Figure 2.7.** Charge transport mechanisms. (a) Electron transfer, (b) Ion transfer, (c) Transfer of (nano)materials, (d) Charge transfer mechanism. The image of the mechano-responsive charge transfer was reprinted with permission from ref.[95]

### 2.3.1 **Electron transfer**

The first and most-studied source of charge transfer is electron transfer, as depicted in **Figure 2.7a**. Although the general conditions for electron transfer have not been entirely clarified, it is consensus that it is the dominant triboelectric mechanism in metal-metal contact.[94] In metals, the electronic properties are governed by the work function ($\phi$), defined as the minimum thermodynamic work necessary to remove an electron from the metal surface to the vacuum next to the surface: $\phi = E_V - E_F$, where $E_v$ is the vacuum energy level and $E_F$ the Fermi level, the level of maximum energy for

electrons in metals. In the case of conducting materials, thus, the exchange of electrons arises from the difference in the $\phi$. When two metals are put into contact, they establish the following contact potential difference ($V_c$), where $e$ is the elementary charge (Equation 2.3).[43]

$$V_C = \frac{\phi_2 - \phi_1}{e} \tag{2.3}$$

The material with the higher work function $\phi_2$ receives electrons from the material with the lower work function $\phi_1$ until their Fermi levels align, balancing the potential difference. Then, during separation, the transferred charges flow back through tunnelling to restore equilibrium. Real contact, however, is a non-equilibrium process, and tunnelling becomes impossible beyond a critical separation distance,[96] leaving residual charges on the surfaces.[97] To determine the total charge transferred ($Q$), the parallel plate capacitor approach is employed, where the total charge transferred is determined by the product of $V_c$ and capacitance based on the metal-to-metal separation distance ($C_s$) (Equation 2.4).

$$Q = C_s \times V_c \tag{2.4}$$

However, the triboelectrification model for metals has a critical limitation: most metals naturally develop insulating oxide layers, particularly in agricultural environments where moisture, soil, fertilizers, and wear drive their growth. When at least one dielectric is involved, the mechanism is not as straightforward as it is for metals, due to the significant gap between the valence and conduction bands, as shown in the general model in **Figure 2.4**. To overcome this gap, other forces need to intervene and make electron transfer possible, such as, stress and temperature. When an external force pushes the two dielectrics close enough, at a distance below d ~ 0.2 nm, their surface electronic clouds overlap, according to the electron cloud-potential well model developed by Wang.

The primary mechanisms of charge transfer are schematically illustrated in **Figure 2.8**. For instance, pressure influences charge transfers via deformation. At the microscale, nominally flat surfaces are in fact formed by several nano-asperities, that can undergo pressures $10^5$ stronger than the nominal macroscopic pressure, reaching several GPa.[98] These extreme pressures induce non-uniform deformations at contact points, shifting electronic band energy levels, a phenomenon known as the flexoelectric effect **(Figure 2.8a$_1$)**. The flexoelectric change in the energy of the band of two materials A and B in contact is given by the Equation 2.5.

$$\Delta(E_{VBM}^{A} - E_{vac}^{A}) = \Delta(E_{VBM}^{B} - E_{vac}^{B}) + \Delta\phi \quad (2.5)$$

where $E_{VBM}$ is the valence band energy, $E_{VAC}$ is the vacuum energy, and $\Delta\phi$ represents the work function difference between materials A and B.

Electron transfer occurs when the valence band of material A overcomes the conduction band of material B, or vice versa.[99] In this context, Young's modulus and roughness emerge as critical parameters to determine charge transfer, which are further affected by dirt. Temperature *(*T*)* is also a driver of triboelectric charge transfer. Two materials in contact have different temperatures on their surface, because, due to different thermal properties, they dissipate energy and diffuse heat differently **(Figure 2.8a$_2$)**. This establishes an abrupt temperature gradient at the interface, which forms a thermoelectric potential difference, known as the *Seebeck* effect (Equation 2.6).

$$\Delta V = -ST \quad (2.6)$$

where *S* is the *Seebeck* coefficient.

The key parameters influencing temperature-driven triboelectrification are thus material density, specific heat, thermal conductivity and the *Seebeck* coefficient.[100] Temperature plays a crucial role in triboelectrification through thermionic emission as well. It has been shown that charge dissipation after dielectric-metal contact is much faster when the temperature is increased.[101] Moreover, the range of temperatures of

the observed thermionic emission unequivocally identifies electrons as charge carriers, also for systems, e.g., liquid-solid, liquid-polymer, and gas-solid interactions.[84]

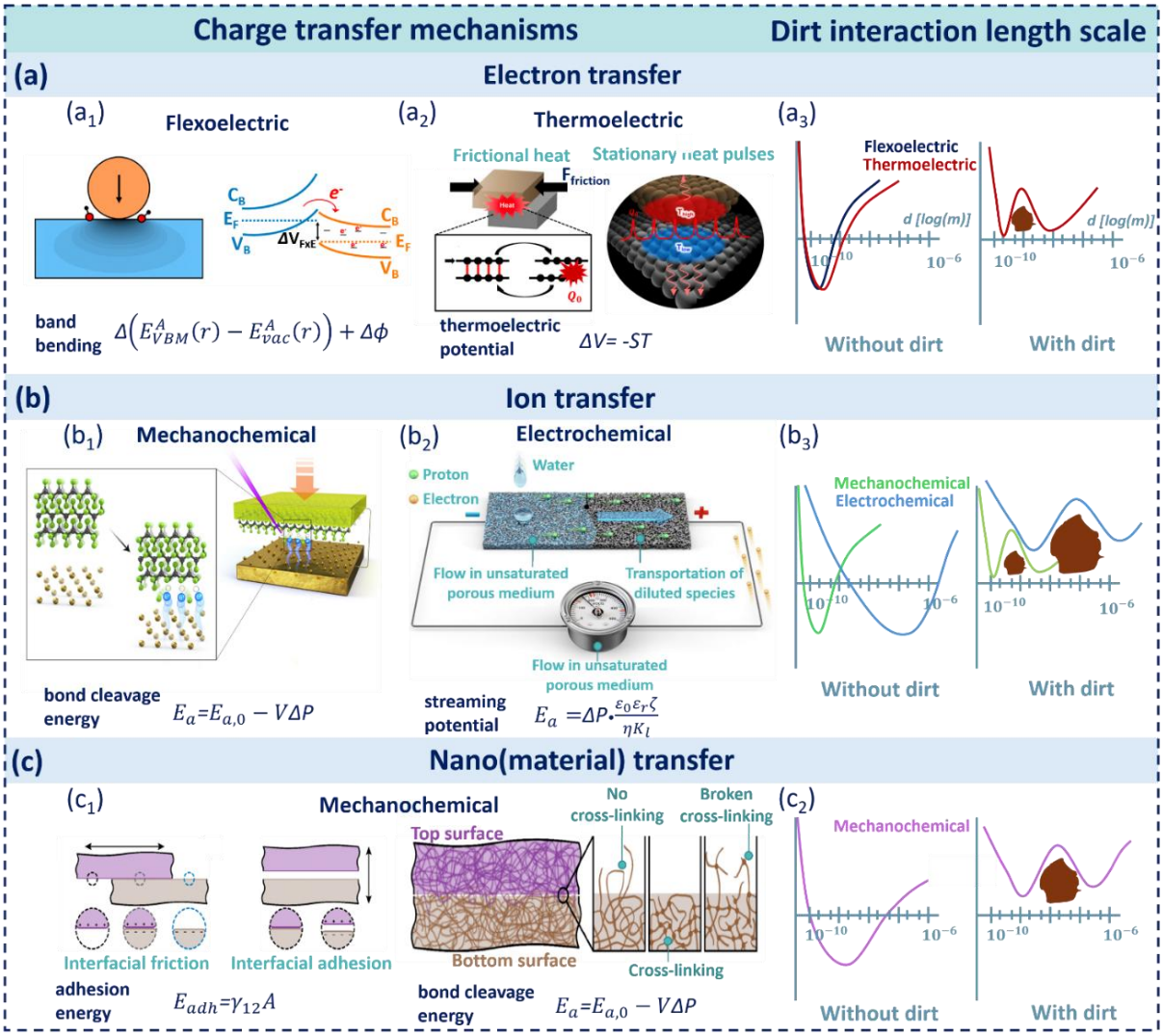


**Figure 2.8.** Schematic illustration of the main mechanisms of charge transfer at triboelectric interfaces. (a) Electron transfer occurs via ($a_1$) thermoelectricity and ($a_2$) flexoelectricity, adapted with permission from ref. [99,100]. (b) Ion transfer occurs via ($b_1$) electrochemical and ($b_2$) mechanochemical processes, adapted with permission from ref.[102,103] (c) Nano(material) transfer also occurs via ($c_1$) mechanochemical processes but through a distinct mechanism, often related to stronger adhesion in polymers, adapted with permission from ref.[104] The diagrams on the right illustrate the interaction length scales for charge transfer, both in the absence and presence of dirt. Dirt particles significantly hinder charge transfer for ($a_3$) electron, ($b_3$) ion, and ($c_3$) nano(material) mechanisms. The X-axis shown in Figure $a_3$ applies to all length scale graphs.

### 2.3.2 **Ion transfer**

The transfer of ions occurs differently depending if the triboelectric contact is between solids or between a solid and a liquid. In solid-solid interactions, ion transfer is influenced by external mechanical forces and the stability of ions within the crystal lattice, i.e., by mechanochemical mechanism **(Figure 2.8b$_1$)**. Since ions are tightly bound to the lattice, significant forces are required to disrupt these bonds. Such forces often originate from the extreme pressure exerted on nanoasperities at the contact interface, where mechanical stress reduces the energy barrier for bond cleavage or ion transfer ($E_a$), as described by Equation 2.7.

$$E_a = E_{a,0} - \Delta V P \tag{2.7}$$

where $E_{a,0}$ represents the stress-free energy barrier, P is the applied stress, and $\Delta V$ is the activation volume, i.e., the region affected by interfacial stress.[105]

When mechanical stresses are sufficiently large, $E_a$ approaches zero, leading to bond cleavage and the transfer of a charged ion to the opposing surface. Similar to electron transfer, this process occurs at sub-nanometer scales, requiring direct atomic-scale contact for ion transfer.[106,107]

Ion transfer in liquid-solid contacts, particularly relevant in moisture-rich environments like soil, occurs through distinct mechanisms. Two key electrostatic effects are the electric double layer (EDL) and Wang's hybrid layer.[108] The EDL forms when a solid surface contacts an aqueous solution, creating two layers: a compact layer of tightly bound ions and a diffuse layer with ion concentration decreasing with distance. This ion deposition facilitates charge transfer from the liquid to the solid by forming a charged-ion layer that generates an electric field. This field attracts a second, diffuse layer of opposite polarity, with ion concentration decreasing as the distance from the surface increases.

Electrochemical mechanism also contributes to charge transport **(Figure 2.8b$_2$)**.[109] Lin et al. showed that the electron-to-ion transfer ratio (E/I) varies with solid material,

with electrons comprising over 88% of transferred charges in some cases, altering the EDL into a hybrid layer.[110] This hybrid layer arises when surface sites gain charge through electron transfer, strengthening the electrostatic attraction of positive ions or, less frequently, adsorbing anions via van der Waals forces. As a result, anions accumulate in the diffuse layer, complicating the EDL structure.[111] Both ion transfer mechanisms (EDL and the hybrid layer) can extend up to tens of nanometers. For agricultural applications involving a porous medium, such as soil, flowing water shifts the dominant charge generation mechanism from electrostatics to the streaming potential. The movement of water under pressure drives ion transport within the EDL or hybrid layer via electrostatics, fluid convection, and concentration gradients, creating an ion gradient that generates current and enables energy generation in these environments.[102]

### 2.3.3 **Transfer of (nano)materials**

(Nano)material transfer, primarily occurring at the sub-micrometer scale, involves the exchange of nanomaterials during rubbing. As shown in **Figure 2.8c**$_1$, this mechanochemical charge transfer mechanism is particularly evident in polymer-polymer contacts, where charges originate from broken bonds or surface contaminants. Polymers like polyethylene (PE), polypropylene (PP), PTFE, and polyethylene terephthalate (PET) can transfer charges due to impurities or environmental contamination during triboelectrification. Mechanical stress triggers material transfer, breaking bonds and generating ions and radicals through heterolytic or homolytic bond dissociation.[112,113] This effect is especially relevant for polymer-polymer contact and establishes a correlation between the amount of (nano)material transferred and CE intensity.[114] This mode of transfer explains why materials of the same origin can be charged by CE, as well as why material surfaces do not charge uniformly but with a “mosaic”

pattern of positive and negative charges.[115] When polymers are rubbed together, material exchange occurs, roughly proportional to their cohesion, adhesion forces, and the difference in their hardness.[116] However, adhesion, crosslinks at the interface, molecular organization, contamination, and local composition differences cause material transfer and charging even if the polymers are identical.[117] Additionally, environmental conditions like temperature significantly alter surface stability and energy,[118] weakening cohesion, especially in biopolymers and other non-chemically inert materials.

### 2.3.4 **Mechano-responsive charge transfer mechanism**

The concept of mechano-responsive charge transfer mechanism (MRCTM) describes the dynamic process by which charges move between semiconducting polymers, e.g., conjugated polymers, and conductive materials, as shown in **Figure 2.7d**. This phenomenon is extensively studied across fields such as energy harvesting, pressure sensing,[119] self-powered sensors,[95] and other smart applications.[120] The ability of conjugated polymers to harvest energy relies on the transfer of energy through $\pi$-$\pi^*$ interactions within their molecular structure when subjected to localized pressure.[95]

Under mechanical stress and release conditions, these polymers facilitate the movement of charges across the interface layer between the electrode and polymer, leading to the generation of electrical energy. Application of localized mechanical stimuli to the polymer surface results in an increase in localized charge density within the deformed polymer network, causing Fermi level pinning and subsequent transmutation of charge carriers between the polymer and electrode layers.[95] Therefore, this phenomenon arises due to the conductive character exhibited by the conjugated polymer and the accumulation of mobile ions in the stressed area.[120]

Consequently, the localized mechanical stress induces a small non-uniform energy state, initiating a transfer of charges between the Charge Collector Electrode (CCL) and the Charge Translocation Layer (CTL). It is advantageous for mobile charges within the conjugated polymer system to transition to the nearest available energy level, which is typically within the charge collector electrode, rather than the distant back electrode.[120] Upon stress release, the compressed polymeric chain returns to its original state, leading to localized Fermi level depinning and a relative scarcity of charge carriers compared to the surrounding regions, resulting in a localized nonuniform electrostatic field.[120] The scarcity of charge carriers in the stressed region is compensated by energy transfer from neighboring polymeric chains through a hopping conduction mechanism, enabling a new cycle of MRCTM.[95]

### 2.3.5 **Humidity, pollutants, and environmental effects**

Other environmental effects affect the charge transfer mechanism, among which humidity is the most relevant in agricultural environments. Several studies have attempted to assess the impact of humidity on triboelectric charge generation in solid-solid contact, with significant progress made in the last 20 years. McCarty and Whitesides initially proposed water molecules as the key driver for triboelectrification. They found evidence that surfaces can charge via ion transfer in air and proposed that contact electrification between insulators results from the exchange of $H_3O^+$ and $OH^-$ ions coming from adsorbed water.[121] Later, Baytekin et al. proved that, during contact between polymers, water is not necessary to generate triboelectric charges, but it has a stabilizing effect on the charges, reducing charge dissipation and extending the duration of charge retention.[122] In a different study, Waitukaitis' group showed that humidity permanently shifts the quantity of transferred charges. Most importantly, the direction of the shift is random and related to different patterns of water adsorption

during the sample's history.[123] This highlights the material-dependent nature of humidity effects. Waitukaitis' results were, in fact, obtained using silica ($SiO_2$) samples, whose surface is highly sensitive to water. The use of fluoropolymers and nonpolar polymers should thus help reduce humidity-induced randomness and obtain a steadier and more consistent triboelectric output in agricultural environments.

Pollutants, such as ammonia and phosphates, can also affect the behavior of TENGs in agricultural settings, as the TENG electric signal is sensitive to the adsorption of charge-transfer-altering molecules. Recent studies have shown that TENGs' signal is indeed modified by the presence of ammonia in the atmosphere.[124] Likewise, doping PVDF with phytates has been shown to flip its polarity from tribonegative to tribopositive.[125] However, like with water, the charge-transfer regime is material-dependent and governed by the specific pollutant-surface interaction. Referring to the two mentioned cases, the change in triboelectric response to ammonia was due to a change in electric conductivity caused by ammonia deposition. On the other hand, the tribopositive behavior of phytate-doped PVDF is caused by the formation of hydrogen bonds that can trap both holes and protons, i.e. by a complex change in the surface chemical properties that both shifts its LUMO level, making it trap holes more easily, and alters its ion adsorption properties. Thus, TENGs' sensitivity to pollutants shows that they can be used both for the removal and sensing of such contaminants. We envisage this as an underexplored frontier that requires systematic investigation, particularly under field-relevant conditions where multiple pollutants coexist. Progress in this direction could not only deepen the fundamental understanding of charge-transfer processes but also guide the rational design of pollutant-tolerant or pollutant-responsive TENGs for agricultural and broader environmental applications.

### 2.3.6 Prevalence of charge transfer mechanisms under environmental factors

Determining which charge transfer mode takes precedence under agricultural conditions is far from straightforward, yet it is fundamental to optimizing TENG electrical output and enabling reliable smart applications. While multiple mechanisms may operate concurrently at an interface, their relative contributions are shaped by material properties, surface states, and environmental parameters, e.g., humidity, temperature, pH, and contamination. Correlating these factors with known mechanistic pathways is complex, but can be approached by evaluating the driving forces in conjunction with environmental influences to anticipate charge transfer behavior and mitigate spurious electrical output in smart applications.

The four main mechanisms (electron transfer, ion transfer, nano(material) transfer, and mechano-responsive charge transfer) can all occur at triboelectric interfaces, with their relative contribution depending strongly on the nature of the contacting materials, the interfacial environment, and the operating conditions. For instance, electron transfer is typically predominant in metal–metal and metal–dielectric contacts under low humidity, where clean, oxide-free surfaces allow direct electron exchange driven by work function differences or localized deformation (flexoelectric effect).[99,126,127] Ion transfer is likely more significant in liquid–solid interfaces,[109,128,129] particularly in moisture-rich agricultural environments such as soil, where electric double layer formation, streaming potentials, and electrochemical effects enhance this charge transfer. However, in some cases, the total charge transferred via electron transfer can surpass that from ion transfer in liquid–solid CE, indicating that the two processes are not strictly coupled but instead occur independently, depending on the intrinsic characteristics of the solid surface.[84] For example, we suggest that ion transfer is likely to dominate in solid–liquid interfaces when the solid material exhibits a high degree of dissociation (high dissociation constant) or low ionization energy, thereby

surpassing the electron transfer mechanism. Nano(material) transfer is most prevalent in polymer–polymer contacts, owing to lower adhesion energy, especially under high friction, and is exacerbated by surface contamination.[114,126] While, mechano-responsive charge transfer is a more specialized mechanism that dominates in conjugated polymer–electrode systems, where localized mechanical stress directly modulates charge carrier density.[95]

In agricultural applications, where surfaces are often exposed to variable humidity, temperature, particulate contamination, and biofilms, hybrid charge generation is likely: ion transfer often prevailing under wet or soil-contact conditions, nano(material) transfer during persistent friction or abrasion, and electron transfer during dry, clean contacts or in well-packaged devices. However, the precise interplay and quantitative contribution of each mechanism in such complex field conditions remains largely unexplored, warranting in-depth experimental and modeling studies to unravel these effects. Advancing this understanding will directly inform material selection, device encapsulation strategies, and operational mode design to mitigate environmental artifacts and maximize charge transfer, enabling reliable and stable electrical output, particularly for active TENG-based sensors. However, the precise mechanistic links between interfacial chemistry, HOMO–LUMO alignment, and charge-transfer pathways remain poorly understood.

### 2.3.7 **Dirt interaction length scale and effects on the potential well model**

In agricultural environments, the presence of dirt and various contaminants is inevitable, necessitating a thorough understanding of their interactions with nanogenerator surfaces. The primary impact of dirt on charge transfer mechanisms is steric hindrance, which physically obstructs the effective contact area between the counterpart material and the active layer. Beyond steric effects, dirt also alters the local energy

landscape in the electron transfer mechanism **(Figure 2.8a$_3$)**, making it dependent on the interaction characteristics of the impurity. This alteration can shift the minimal point upward, introducing an additional energy barrier and reducing charge transfer efficiency.

Within the potential well model, the disruption caused by dirt depends on its specific characteristics and manifests in three distinct scenarios: (i) an increase, (ii) a decrease, or (iii) a negligible change in the outermost electron cloud and the corresponding minimal activation energy for electron transfer, compared to the pristine active layer **(Figure 2.9a)**. For instance, when the dirt possesses a higher HOMO than the LUMO of the counterpart material, electron transfer can occur with minimal impact on charge transfer efficiency **(Figure 2.9a$_1$)**. Conversely, when the dirt shares the same potential well characteristics as the active layer and also has a higher HOMO than the LUMO of the counterpart material, electron transfer is possible only if the counterpart material exhibits a higher effective nuclear charge ($Z_{eff}$), allowing it to attract electrons when the electron clouds overlap **(Figure 2.9a$_2$)**. However, if the potential well characteristics are identical and the $Z_{eff}$ of the counterpart material is lower than that of the dirt and active layer, electron transfer is effectively inhibited.

When the dirt exhibits a LUMO energy level equivalent to that of the counterpart material but lower than the HOMO of the device material, electron transfer efficiency is significantly reduced **(Figure 2.9a$_3$)**. This occurs because electrons are transferred from the HOMO of the device material to the LUMO of the dirt particle, where they remain trapped and are prevented from transferring to the active materials. As the counterpart material separates, electrons are retained on the dirt coating the device, resulting in minimal charge transfer. Therefore, impurities with similar chemical features to the counterpart material, with the same potential well characteristics, limit the overall charge transfer by preventing effective electron exchange. However, some

charge transfer may still occur through alternative mechanisms, such as nanomaterial transfer, depending on the conditions.

The dirt-coating of the active layer and counterpart material has thus a significant impact on the charge transfer efficiency of nanogenerators exposed for prolonged periods to agricultural environments **(Figure 2.9b)**. Since electron transfer is the primary mechanism for charge transfer, surface contamination obstructs this process, as shown through the potential well model theory, especially with materials of similar potential well features (e.g., sand), significantly cosmpromising the electrical output. This issue is particularly critical for soft-feature dirt (e.g., manure and food waste), which spreads more easily under compressive stress, forming a coating on both the active and counterpart materials.

While, during intermediate stages of environmental exposure - when surfaces transition from clean to fully dirt-coated - the potential well between the dirt and the counterpart material is established. At this stage, distortions in the potential surfaces can temporarily enhance or reduce electron transfer. However, once both surfaces are fully coated with dirt possessing a HOMO comparable to the LUMO of the counterpart material, electron transfer is effectively inhibited. These effects, alongside factors such as roughness, micropatterning, and applied pressure, are further discussed in the stiffness-compatibility section (*Section 2.4.1.1*).

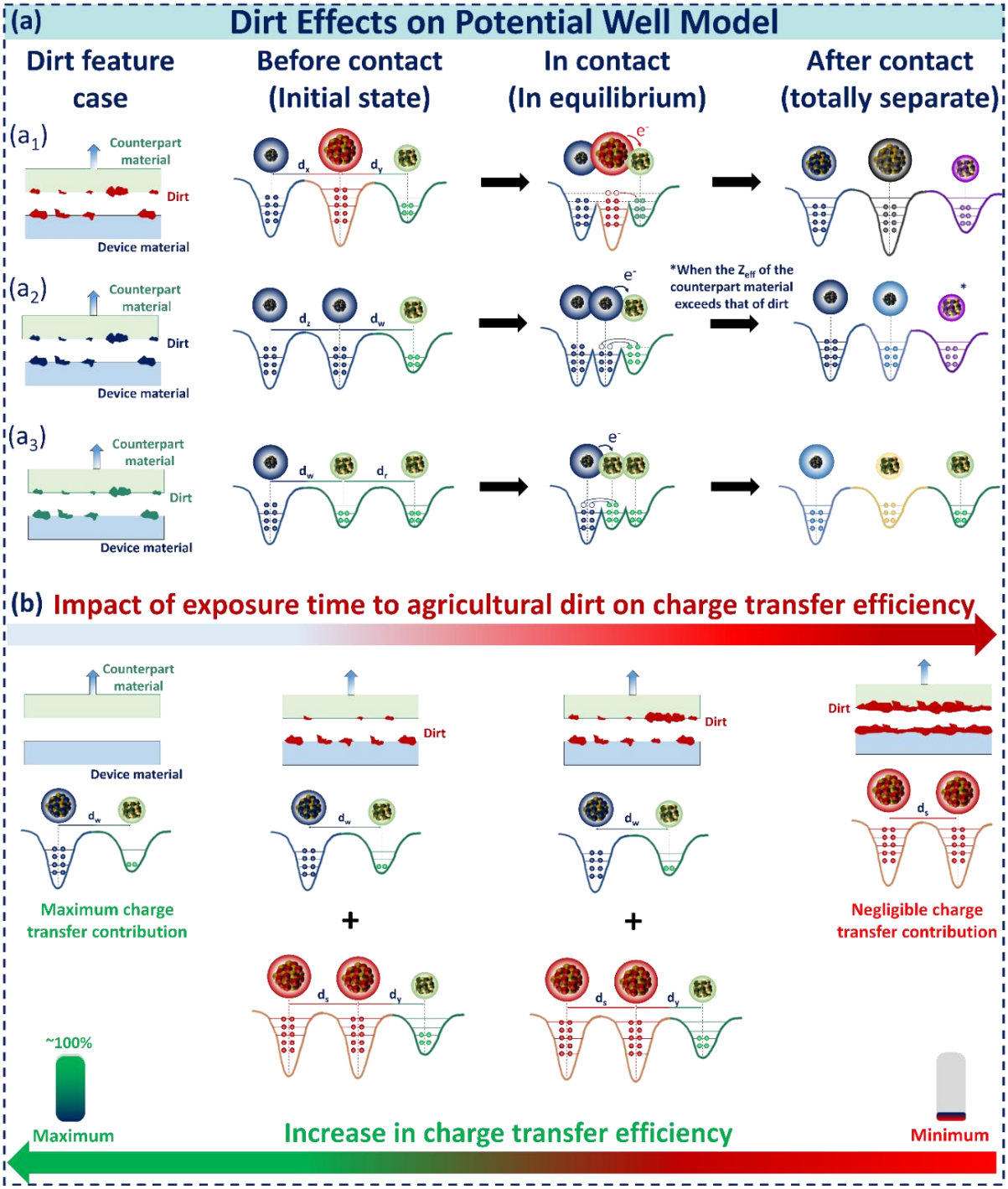


**Figure 2.9.** Dirt effects on the potential well model for electron charge transfer. The impact of dirt with three distinct feature-compositions on charge transfer dynamics: ($a_1$) Dirt with a higher HOMO energy level compared to the LUMO of the device material and a lower LUMO than the counterpart material. ($a_2$) Dirt with a HOMO energy level equivalent to the device material but higher than the LUMO of the counterpart material; and ($a_3$) dirt with a LUMO energy level equivalent to the counterpart material but lower than the HUMO of the device material. Mind the different effective nuclear charge ($Z_{eff}$) represented by the color of the potential well and electron cloud with red for highest $Z_{eff}$, green for intermediate, and blue for lowest. (b) Illustrates the effect of prolonged exposure to

an agricultural environment on the charge transfer efficiency of nanogenerator devices. Over time, the active layer transitions from a clean surface in its initial state to a dirt-covered surface, eventually forming a dirt-coating on both surfaces. This gradual contamination reduces charge transfer efficiency, as the alignment of potential wells diminishes the contribution of charge transfer across the surfaces.

Also, in the ion transfer mechanism **(Figure 2.8b$_3$)** dirt obstructs ionic motion both by clogging pores and altering the electrochemical gradients and intercepting the transported charges. This increases activation energy, shifting the minimal point into the positive range. For nanomaterial transfer **(Figure 2.8c$_2$)**, contamination disrupts processes by altering interfacial friction, reducing cross-linking efficiency, and introducing foreign particles that dampen stress distribution. Consequently, additional energy is required to overcome dirt-induced barriers, further underscoring the detrimental impact of contamination on nanomaterial transfer efficiency. Moreover, when dirt particles cover the contact surfaces, CE charges start to be transferred to the dirt particle rather than the relevant surface, preventing the very charge generation mechanism that allows the device to function.

### 2.3.8 **Distance-dependent electric charge transfer**

Once charge transfer mechanisms, as well as dirt and environmental effects have been described, it is crucial to understand one of the main factors affecting its efficiency: the distance range at which electric charges can be transferred. In other words, it is important to determine the maximum distance between two surfaces at which the cohesive forces between charges are overcome by external triggers, allowing charge transfer. This is crucial to establish at what scale dirt can prevent TENGs from working efficiently, obstructing the contact between the triboelectric layers and preventing specific charge transfer mechanisms.

**Figure 2.10** illustrates the relationship between charge transfer efficiency and distance, comparing three primary mechanisms - electron transfer, ion transfer, and material-based charge exchange - on both clean and contaminated surfaces. As previously discussed, the efficiency of electron transfer depends on the interatomic distance between atoms on opposing surfaces. Xu et al. and Fatti et al. proposed that electron transfer begins when the electron clouds between two atoms start to overlap, transferring the electron from the HUMO to the LUMO.[86,130] To make the clouds overlap, the two atoms need to be closer than their equilibrium distance, therefore, the effective distance where electron transfer can occur is usually on the scale of a few Ångstroms. Thus, it is possible to categorize the maximum distance at which electron transfer occurs based on the atoms van der Waals radius, e.g., for C, Ca, and Cs, it is 1.7, 2.4, and 3.0 Å, respectively.[131] At these scales, even a single molecular layer of contaminants is sufficient to block charge transfer. It needs to be considered that electrons can also easily dissipate due to temperature increases. Thermionic experiments have shown that electrons can escape a surface where they are transferred more easily if the temperature is increased, constituting another important efficiency-limiting factor.[101]

The intensity of charge transfer also varies by mechanism. Electron transfer is typically more intense due to the spatial distribution of electrons across surfaces, making them more readily available for transfer compared to ions or discrete material regions. However, electrons are less stable as charge carriers, as they are more easily dissipated by temperature fluctuations. In contrast, ions are more stable carriers, as their transfer depends on electrostatic and chemical forces rather than electron cloud overlap, and they are emitted thermally only at significantly high temperatures. Electrostatic interactions, in particular, are much longer-range interactions, extending over several micrometers in some cases. Moreover, both the streaming potential and electrostatic interactions can act through porous media, like most dirt particles are, making them harder to disrupt. However, if the transported charged ions are deposited on a

dirt particle instead of the device material, this prevents the basic charging mechanism from occurring, severely affecting the device's efficiency. Moreover, non-porous microscale dirt particles can further suppress charge generation by disrupting these interactions, even in humid conditions.

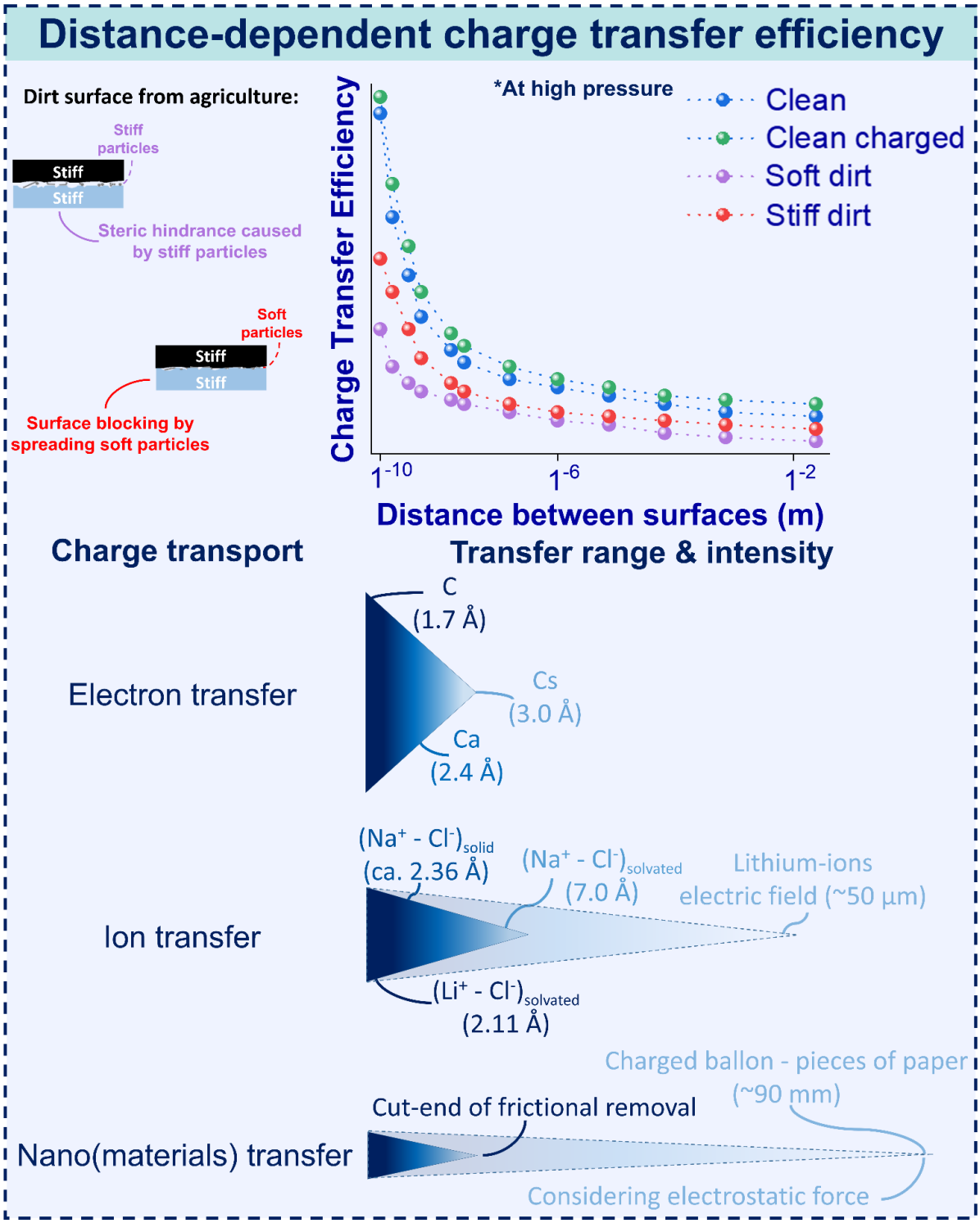

**Figure 2.10.** Distance dependence of electric charge transfer efficiency across three surface charge transfer mechanisms (electron, ion, and nanomaterials) on four common agricultural surface conditions: clean and uncharged, clean and charged, stiff dirty, and soft dirty surfaces. Electron transfer, determined by the van der Waals radius of individual atoms, demonstrates the shortest transfer range but the highest intensity, as modeled using Wang's well potential. Ion transfer exhibits a moderate range, driven by Coulombic attraction specific to ionic bonds, with external factors such as Brownian motion and electric fields further enhancing transfer efficiency. Nanomaterial transfer, while contributing lower intensity, operates over the largest range, initiated by close-atom interactions due to wear and abrasion. This mechanism is further influenced by strong external electrostatic forces, such as dipole-dipole polarization induced by friction (e.g., balloon-paper interactions).

Ion transfer efficiency and the maximum transfer distance are also influenced by the medium's physical state. For example, in solid NaCl, ionic bonds have a bond length of ca. 2.36 Å,[132] with Coulombic attraction remaining strongest near this equilibrium distance. When ions are solvated, however, the range of Coulombic interactions increases due to external forces, e.g., Brownian motion, enabling charge transfer over distances of up to 7 Å.[133] Conversely, the attraction between solvated $Li^+$ and $Cl^-$ is ca. 2.11 Å,[134] confirming that reducing the ionic radius diminishes Coulombic attraction. Since VCS-TENG devices can generate electric fields as high as 7 $kV.cm^{-1}$,[13,135] various ion types can be readily attracted by this mechanism, further enhancing charge transfer efficiency.

In the transfer of nanomaterials, depending on the materials, the maximum cut-off distance can be very short (~Å scale for metals or ceramics) due to the need for strong physical contact to induce bond cleavage. In polymers, crosslinking, higher adhesion, and lower hardness allow for significantly longer distances. During contact between two materials, polymer chains up to tens of nanometers in length can be cleaved and transferred as charged fragments to the counterpart surface.[136] However, dirt particles can compromise direct contact between polymeric surfaces, hindering crosslinking and severely reducing charge generation efficiency.

Electrostatic forces, commonly observed in nature, extend charge transfer beyond ca. $10^{-6}$ m. For instance, a charged balloon attracts pieces of paper through Coulomb forces. For example, a charged balloon can attract pieces of paper due to Coulomb forces. The balloon's electric field polarizes the paper, repelling electrons and attracting positive charges, resulting in a stronger attractive force than repulsive forces like gravity. This phenomenon highlights the role of electrostatic attraction in charge transfer over larger distances.

In agricultural environments, where dirt and debris are prevalent, understanding charge transfer efficiency in relation to surface conditions is crucial for maintaining high performance and preventing malfunctions in nanogenerators, especially for smart applications where signal reliability is crucial. Charge transfer efficiency declines sharply as the distance between surfaces increases, with electron transfer - effective only over a few Ångstroms - becoming negligible. For this reason, pre-charged surfaces exhibit slightly higher efficiency across all distances compared to clean surfaces, due to the continued contribution of electrostatic attraction. Beyond ca. $10^{-6}$ m, all charge transport mechanisms cease, with only external effects like electric fields and Brownian motion facilitating minimal transfer.

Dirt significantly accelerates the decline in charge transfer efficiency by disrupting mechanisms of charge transfer, altering surface potential, and reducing the effective interaction length scale. For instance, soft dirt under high pressure can spread across surfaces, forming a coating that amplifies steric hindrance and distorts the potential well. This underscores the urgent need for strategies to mitigate dirt-related effects. In the following sections, we outline the challenges and requirements to guide efforts and foster innovations in nanogenerator development for agricultural applications, enabling durable devices with consistent output performance for smart and sustainable solutions.

## 2.4 Requirements for the application of energy harvesting devices in agriculture

Enabling energy-autonomous smart agriculture begins with adapting energy harvesting devices to survive and perform under the inherently unstable and harsh conditions of real-world farming systems. Unlike controlled laboratory settings, agricultural environments are characterized by continuous exposure to fluctuating factors such as temperature shifts, moisture, wind, ultraviolet radiation, dust, and chemical or biological contaminants. Ensuring reliable performance under these conditions requires careful alignment of material properties, device architecture, and functional integration within energy harvesting devices.

This section outlines the essential requirements for the practical application of TENGs in agricultural settings, with a focus on achieving long-term operational stability, mechanical robustness, and environmentally responsive functionality for smart applications. It begins by examining environmental stressors that influence device performance and durability, followed by design strategies that promote resilience, e.g., self-healing materials, encapsulation techniques, substrate flexibility, and surface functionalization. The section also highlights the importance of material compatibility, particularly in achieving stiffness matching between triboelectric layers to enhance energy conversion efficiency and contact reliability. Finally, it considers the integration of functional materials capable of dual roles - energy generation and stimulus responsiveness - which further contribute to overcoming current limitations and advancing the development of smart TENG-based agricultural technologies. Through this comprehensive evaluation, the section provides a roadmap for transitioning TENGs from proof-of-concept devices to reliable components in real-world agricultural applications.

### 2.4.1 **Mechanical properties**

The performance of nanogenerators is significantly affected by the mechanical properties of materials, attributed to their intrinsic mechanical contact used for energy harvesting. Young's modulus (stiffness) stands out among these properties as it directly influences the device's electrical efficiency and stability. Additionally, characteristics such as elasticity, tensile strength, and compressive strength have a significant impact. For instance, in agricultural environments prone to strong climatic variations and extreme weather events like storms and hurricanes, mechanical triggering with irregular frequency and force can considerably affect performance and stability. Therefore, materials with low flexibility, elasticity, and tensile strength/compression are often brittle and prone to structural failure. In this context, it is imperative to assess the mechanical properties of the entire device, diverging from the prevailing emphasis solely on the mechanical performance of the active layer in existing literature. This is especially pertinent for devices exhibiting high stiffness incompatibility between the electrode and the active layer. A significant discrepancy in these properties can lead to excessive wear at the interface over prolonged usage, thereby diminishing the nanogenerator's lifespan. Furthermore, instances of incompatibility between the elasticity of the active layer and the electrode are frequently observed, particularly due to the low elasticity of commonly used conductive materials such as copper and aluminium. This mismatch inhibits any potential high elasticity benefits offered by the active layer. In the subsequent sections, we discuss key concerns and solutions to enhance the performance and longevity of nanogenerators, focusing on improving the mechanical performance for use in agriculture harvesting.

#### 2.4.1.1 **Stiffness-compatibility**

Stiffness compatibility is a fundamental property for optimizing the performance of nanogenerators. When the active layer and the electrode exhibit similar stiffness levels, mechanical activation results in uniform interfacial deformation, enhancing real

contact area without compromising the integrity of the conductive network. This, in turn, promotes more efficient electrostatic induction, leading to enhanced electrical output. In contrast, stiffness mismatch induces asymmetric deformation: softer electrode may undergo plastic strain, while active layer resist compression. This imbalance can trigger microcracking or delamination, ultimately degrading the electrode's conductive network and reducing device performance and operational stability.[137–140]

Conversely, when a softer active layer deforms against a stiffer electrode, the resulting plastic deformation may increase surface area but also reduces dielectric thickness, impacting capacitance and altering triboelectric output.[141–143] Such variations are particularly undesirable in TENG smart applications that require stable electrical output, e.g., agricultural sensing. Moreover, under conditions of low-pressure activation scenarios, excessive stiffness in the mismatched active layer further restricts conformal contact area **(Figure 2.11a,i)**, thereby diminishing energy conversion efficiency. We therefore emphasize that stiffness-matched architectures between the active layer and electrode are ideal for minimizing damage to the conductive electrode network and ensuring stable electrical performance. This design strategy enhances both mechanical durability and functional reliability, particularly relevant for real-world agricultural applications that demand long-term resilience, resilience, and precision.

Given the challenge of achieving two perfectly flat surfaces, a complete match in total surface contact may be considered hypothetical, especially if these materials are stiff. Consequently, real-world active layer surfaces often exhibit roughness, unevenness, contaminants, and macro-to-nanopatterns, each exercising a distinct influence on electrical output by affecting the effective contact area. For instance, materials with high stiffness struggle to deform under low pressure (< 1 kPa), as the applied force may not overcome strong intermolecular forces, impeding deformation and reducing contact area efficiency. Stiff materials, characterized by strong forces of attraction as

hydrogen bonds, may need higher pressures (e.g., 10 GPa) to deform. Conversely, employing at least one soft active layer ensures a highly effective contact area due to its superior deformation capacity, guaranteeing high $V_{oc}$ in nanogenerators. In this case, the applied pressure has a low impact on contact effectiveness, as the soft active layer easily fills gaps due to its deformability, enhancing efficiency for highly rough active surfaces.[144]

Given the high probability of surfaces getting dirty in agricultural environments, selecting materials and surface patterns becomes even more critical. Dirt particles, commonly originating from agricultural activities, obstruct the effective contact area between active layers, compromising sensing applications as well. Stiff particles on surfaces likely reduce the effective contact area between active layers, even under high-pressure conditions, due to their limited deformation capacity caused by steric effects, which maintain gaps between the layers. On the other hand, soft particles primarily affect contact by spreading their material across the surface. This reveals a blocking contact dependence on the pressure applied. When the pressure significantly exceeds the yield stress, the particles undergo plastic deformation, covering the pristine surface with dirt-like features.

Recent studies have explored macro- to nano-patterns with shape memory structures in active layers to increase contact area, optimize energy harvesting performance, conferring active functions, e.g., reversible wettability, controlled droplet transport, tunable adhesion, and sensing capabilities.[145,146] However, achieving a truly high effective contact area requires considering the Young's modulus (E), also known as Elastic Modulus, of each active surface. We further demonstrate how tailoring material stiffness and surface patterns can maximize the contact area and output of TENGs, ensuring reliable operation across a range of farm scenarios (from soft plant materials to hard equipment surfaces). Young's modulus can be directly obtained from the slope

in the linear viscoelastic region of the stress-strain curve, given by the angular coefficient of linearly fitted data points **(Figure 2.11b,ii)**.

If both active layers are stiff and one is macro-patterned, despite the increased surface area, the electrical output may be negligible or reduced due to the low deformation capacity of both materials, thus limiting the effective contact area. In contrast, when a soft macro-patterned surface (i.e., with low elastic modulus) is used, the initial low-pressure application may result in air gaps between the patterns, reducing the effective contact area. However, as mechanical pressure increases, the soft layer deforms, thereby improving the contact area.[147] Additionally, optimizing the pattern spacing (pitch) is critical. For instance, insufficient spacing can cause the patterns to deform and merge, reducing the effective surface area.

In the case of a stiff micropatterned surface, applying low mechanical pressure can allow partial penetration of the stiff pattern into the soft layer due to the weaker intermolecular interactions of the soft layer, resulting in moderate surface contact.[148] Increasing pressure deforms the soft layer, occupying the entire surface area of the stiff material. However, the reverse scenario does not follow the same logic. For example, when a high-stiffness flat surface comes into contact with a patterned surface of lower stiffness, the patterned surface will deform. This deformation tends to smooth out the pattern, resulting in a flatter surface, a reduction in the initial high surface area, and, consequently, a decrease in the $V_{oc}$. Therefore, optimal efficiency in the effective contact area is achieved when both surfaces are soft and have compatible stiffness (i.e., have low and similar Young's moduli), ensuring large surface contact area regardless of the applied pressure.

Thus, stiffness compatibility and surface complexities (Young's modulus, dirt, patterns, mechanical pressure) are crucial factors for attaining high and stable electrical output in nanogenerators, often overlooked. Furthermore, in agricultural applications due to various atmospheric particles hindering efficient energy harvesting and

its smart applications. Barri et al. demonstrated that active layers with lower stiffness undergo larger displacements under identical loading scenarios compared to those with higher stiffness, resulting in enhanced electrical output for TENGs.[149]

The interface contact between the active layer and electrode and the effects of stiffness, which are highly dependent on intimate contact, were not illustrated but are equally important. For instance, a physical connection between these interfaces, as opposed to a chemical one, can retain air bubbles, water droplets and debris, reducing the effective contact area and thus mitigating the induction effect. For example, when low-pressure triggering occurs in the active layer, such as with water flow, the applied is so negligible that it fails to remove air bubbles or debris, leading to a loss of the effective induction effect.

For the ideal long-term use of nanogenerators, a comprehensive cyclic mechanical assessment can be conducted to determine the range of mechanical stress that ensures device longevity and stable electrical output within the elastic regime **(Figure 2.11b,i)**. Mechanical stress beyond the elastic region leads to permanent deformation, which adversely affects both the physical integrity and electrical performance of the device. This occurs because the elastic regime - characterized by reversible deformation and energy storage - is surpassed at the yield point, transitioning into the plastic regime, where permanent deformation and energy dissipation occur.

Knowing that several nanogenerators are activated for long cycles and, most of the time, in the plastic region, identifying the onset of the plastic region is essential to avoid degradation of the shape and integrity of the conductive material (which is responsible for the induction effect). This loss in the integrity of the conductive network normally occurs due to the longitudinal expansion of the material when subjected to strong compressive stresses, reducing the efficiency in energy conversion **(Figure 2.11b, iii)**. Therefore, recognizing the elastic region of the active layer in these devices

is imperative to maintain a long lifetime, high electrical output stability, low maintenance, and effective use in smart applications.

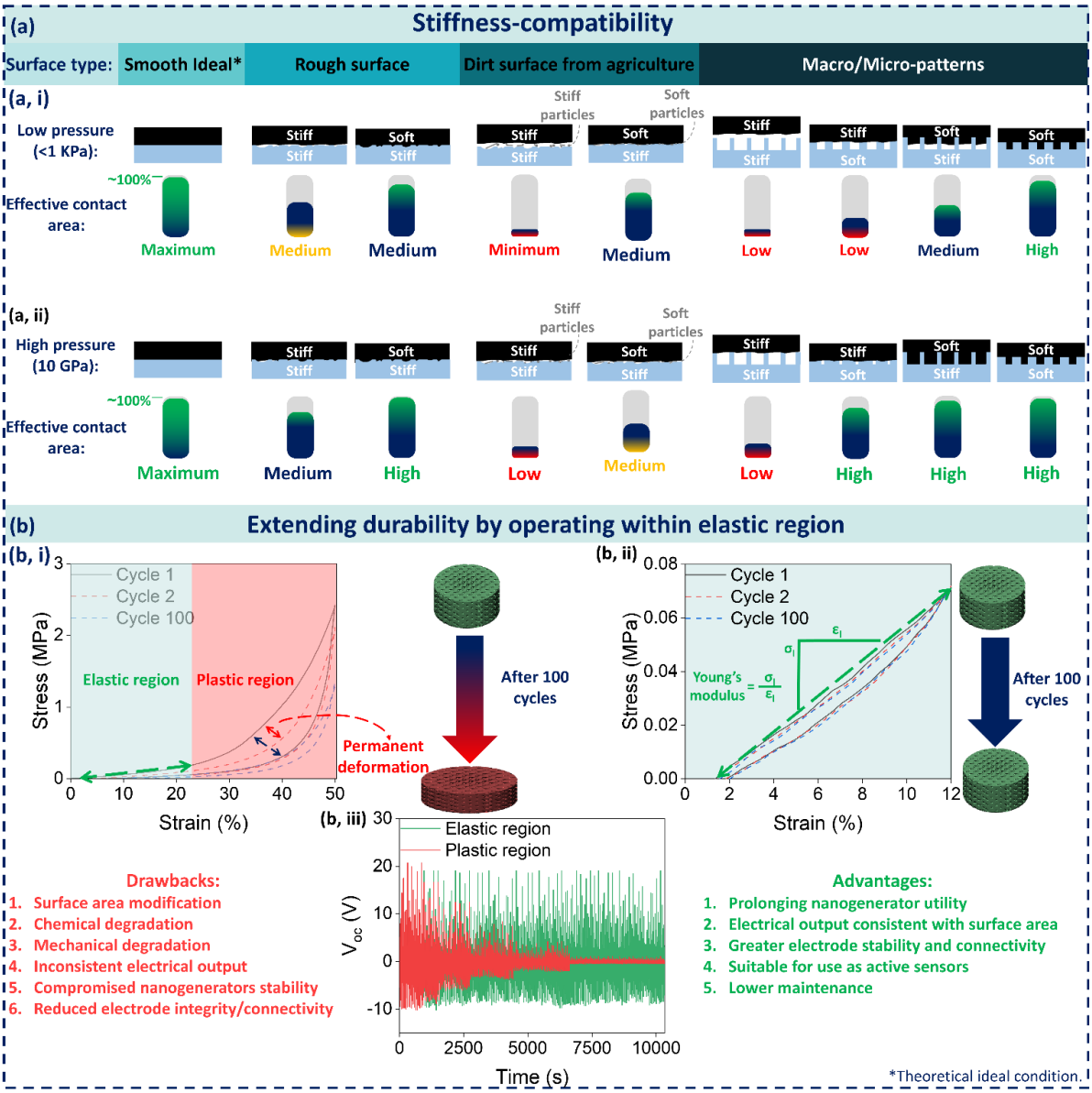


**Figure 2.11.** Effect of stiffness compatibility on effective contact area and electrical output stability, and extending physical integrity of nanogenerators. Illustration of how stiffness compatibility affects the effective contact area with dependence on surface type and (a,i) low and (a, ii) high mechanical pressure. Impact of the mechanical drive of nanogenerators in the (b, i) elastic-plastic and (b, ii) elastic region (resilience area) on their structural stability and (b, iii) electrical output for prolonged use.

The threshold between the elastic and plastic regions can be easily identified using two approaches: (i) respecting the linear correlation of Young's Modulus and (ii)

conducting mechanical cyclic tests at different strain compressions. The first approach is a mechanical property reflecting a material's ability to undergo reversible changes without permanent deformation when subjected to longitudinal tension or compression. Any additional force applied beyond the elastic limit is designed to permanently degrade the material, at least dimensionally. Consequently, the stress-strain curve representation will deviate from linear regression, confirming the offset of elastic behaviour.

Alternatively, using the second approach, it is possible to determine the elastic region by overlapping stress-strain curves in compression cycle tests, indicating minimal mechanical hysteresis loss. To determine this mechanical stress value accurately, compression tests with a gradual increase in deformation, e.g., in 5% increments, must be conducted until incompatibility in the overlap of the curves between the first cycle and subsequent ones is observed.

Unlike monotonic compression tests (1$^{st}$ approach), this cyclic compression method provides additional information, e.g., mechanical hysteresis, toughness, damping capacity, and fatigue. Mechanical hysteresis indicates the ability to disperse energy after load and unload cycles, suggesting that materials with large hysteresis are more suitable for absorbing vibrations or sound. Conversely, toughness refers to their ability to absorb energy and deform before fracturing. For instance, materials with high toughness are necessary for stretchable materials, dissipating much energy to resist crack extension.[150]

Additionally, damping capacity refers to a material's ability to dissipate elastic energy and dampen vibrations. Materials with high damping capacity are valuable for suppressing vibration in noisy output, ensuring the stability of sensitive systems.[151] Furthermore, fatigue indicates the structural damage occurring when a material undergoes cyclic loading over time. Materials with good fatigue resistance can withstand repeated loads over time without premature failure, ensuring a long-lasting life.[152]

#### 2.4.1.2 **Long-term stability**

Over time, nanogenerators experience wear and degradation due to mechanical stress, friction, and environmental factors. The wear and tear of triboelectric layers, electrodes, and structural components impact the electrical output, particularly when the connectivity between the dielectric and the conductor is compromised. In order to sustain consistent electrical output over prolonged testing and ensure their viability, it is imperative to comprehend the mechanical effects on the long-lasting performance of nanogenerators.

Nanogenerators naturally induce surface friction, abrasion, and heat during operation. Understanding the mechanical properties of wear materials, such as stiffness, mechanical strength, resilience, ductility, and fatigue resistance, is crucial in improving durability and minimizing the maintenance of nanogenerators. Mechanical strength reflects a material's ability to withstand forces without failure, while resilience allows a material to store and release energy without permanent deformation, essential for preventing damage from impact or cyclic loading **(Figure 2.11b)**. For instance, high-resilience 3D materials are less likely to flatten over time compared with low-resilience materials. Ductility describes a material's capacity for deformation before fracturing, while fatigue resistance is the ability to withstand repeated loading cycles without failure, which is crucial for long-term stability.

Moreover, to minimize wear and physical friction, lubrication at the interfaces of the active layer presents an alternative for enhancing durability and signal output. Li et al. developed the noncontact modes of electricity generation, offering the potential for a "zero-wear" nanogenerator, maintaining 95% of maximum output after 120,000 cycles, compared to 60% for conventional contact-based.[153] Furthermore, advancements in technologies, e.g., self-cleaning and self-healing materials, can be utilized to address mechanical damage and contamination that can degrade the surfaces of nanogenerators.

#### 2.4.1.3 **Extending mechanical performance by self-healing**

Indeed, energy nanogenerators convert mechanical energy into electrical energy; however, their operational mechanism renders them susceptible to malfunction, diminished performance, and unpredictable damage, thereby limiting their operational lifespan, stability, and scope of applications. To address these challenges effectively, the development of self-repairing materials is essential.

Numerous approaches have been proposed for the development of self-healing materials, categorized into three types: (I) repair through (a) intrinsic mechanisms, wherein polymers autonomously heal molecular and macroscopic damage, and (b) extrinsic approaches, involving the incorporation of pre-cured healing agents into the polymeric matrix.[154] Another classification is based on (II) the repair mode, distinguishing between (a) autonomous repair triggered by damage itself and (b) non-autonomous repair induced by external stimuli, e.g., pH, temperature, pressure, radiation, etc.

Furthermore, self-healing materials can be classified based on the (III) nature of interaction, differentiating between (a) physical interactions and (b) chemical interactions. Physical interactions leverage supramolecular chemistry to (re)establish networks through attractive non-covalent interactions, encompassing hydrogen bonds, hydrophobic interactions, guest-host interactions, crystallization, multiple intermolecular interactions (e.g., $\pi$-$\pi$ interactions), etc.[155] Conversely, chemical interactions involve the (re)establishment of bonds through dynamic covalent bonds, such as sulphur-sulphur (disulfide) bonds, electrophilic carbon-nitrogen (Schiff base, imine) interactions, boron-oxygen (phenylboronate ester complexation), and cyclohexenes (reversible cycloaddition Diels–Alder).[155]

The effectiveness of self-healing materials is commonly assessed through the "healing efficiency, η," a metric that measures the restoration and recovery of a compromised property or performance metric. This efficiency is determined by the ratio of alterations in material properties, as described in Equation 2.8.

$$\eta = \frac{P_{healed} - P_{damaged}}{P_{pristine} - P_{damaged}} \quad (2.8)$$

where *P* is the material property of interest, e.g., mechanical, electrical, optical.[156]

Incorporating self-healing materials into mechanically activated TENGs improves functional stability and durability by mitigating fatigue and accidental damage.[157,158] However, in agricultural conditions, the self-healing capacity of nanogenerators may face challenges from dirt or pollutants in the atmosphere and environment. These external elements can adversely affect the intrinsic properties of the original surface and even impact bulk properties through dirt absorption, thereby affecting the self-healing capability and performance of nanogenerators. Consequently, there is a need to develop advanced self-healing and self-cleaning materials for integration into nanogenerators, ensuring sustained functionality in diverse environmental conditions. However, developing materials featuring integrated self-cleaning and self-healing capabilities presents scientific challenges owing to their inherently contradictory properties. For instance, self-healing materials necessitate a high surface energy to facilitate the reestablishment of chemical bonds or physical interactions. Conversely, self-cleaning materials demand the lowest achievable surface energy to minimize physical interactions and facilitate the removal of environmental contaminants. Consequently, developing such dual-action materials necessitates identifying an optimal balance point in the trade-off, ensuring the minimum required properties in each scenario.

### 2.4.2 **Structural attributes**

Concerns are also raised regarding the macrostructure and design of nanogenerators, particularly with respect to the integration of novel materials into agricultural

environments. Furthermore, in addition to accommodating regional variations in fauna and flora, materials must be developed with considerations for ease of handling, transportability, and adaptability across diverse regions of application.

For instance, when nanogenerators are deployed in agricultural fields, prolonged usage can alter environmental conditions by redirecting rainfall to modifying soil pH levels and altering sunlight exposure. Moreover, deploying nanogenerators, cables, and other energy storage components should be planned to minimize disruption to agricultural operations. Thus, flexibility (low E) and elasticity (high elongation before rupture) become fundamental characteristics, especially in applications where the surface topology is diverse and subject to strong mechanical forces, e.g., wind, rain, and snow. Another crucial aspect is to minimize coupling with other energy storage devices and structures. For example, implementing wireless power transfer mechanisms and communications, like Bluetooth Low Energy (BLE), not only mitigates the environmental impact of cables but also reduces economic costs by minimizing raw material usage and maintenance requirements.

A significant challenge for TENG deployment in agricultural environments is maintaining a stable contact interface, particularly when devices are integrated with dynamic, growing, and physiologically active substrates such as living plant tissue or shifting soil. Over seasonal timescales, growth-induced strain, tissue expansion, and substrate instability can disrupt proper layer contact, reducing TENG electrical output performance. Several mechanical and structural strategies can help address this, including the use of flexible and stretchable functional layers (e.g., elastomers, hydrogels, fabric) that accommodate strain while preserving intimate contact;[158–161] self-shaping materials that permit repositioning with substrate growth;[162–164] and stimuli-responsive materials (e.g., shape-memory polymers) that adapt surface roughness in response to environmental changes, e.g., humidity, pH, and temperature,[145,165,166] sustaining charge generation efficiency over extended periods.

A more pragmatic and field-ready approach involves non-invasive coupling strategies, where TENGs are anchored to stable, fixed structural supports (e.g., trellises or auxiliary frames) rather than directly adhered to sensitive plant tissues. This reduces mechanical stress and physiological interference, while also limiting biofouling, particulate contamination, and surface degradation inherent to direct biological contact. Emerging advances also include wireless TENG systems that transmit pulsed voltage output directly from the TENG,[136,167] enabling non-contact operation and collection. Such configurations have achieved energy delivery distances of up to 18 cm, making them particularly suited to applications where physical contact with unstable soil and dynamic plant growth is undesirable.[136] While these systems currently rely on unmodulated signal transmission through a wire antenna, with output diminishing rapidly as antenna separation increases, they offer a promising direction for mitigating contact instability in agricultural deployments. To clarify predominant structural configurations, associated challenges, and materials used, and guide future development of TENGs in agricultural applications, we conducted a systematic statistical analysis of published research within agricultural contexts **(Figure 2.12)**.

The working modes are largely dominated by VCS and FT configurations, each comprising 27% of the reported systems. This prevalence is attributed to their mechanical simplicity and effectiveness in harvesting irregular, low-frequency mechanical stimuli commonly present in agricultural environments, e.g., wind, raindrops, and animal motion. However, the relatively low representation of lateral sliding modes suggests that this configuration may be less suitable for agricultural applications, likely due to the high negative impact of dirt on electrical output consistency and efficiency. Conversely, the low adoption of hybrid configurations may be attributed to the complexity of fabrication and assembly processes; nonetheless, it presents an underexplored potential for multi-modal designs that could enhance energy harvesting efficiency and robustness in the field.

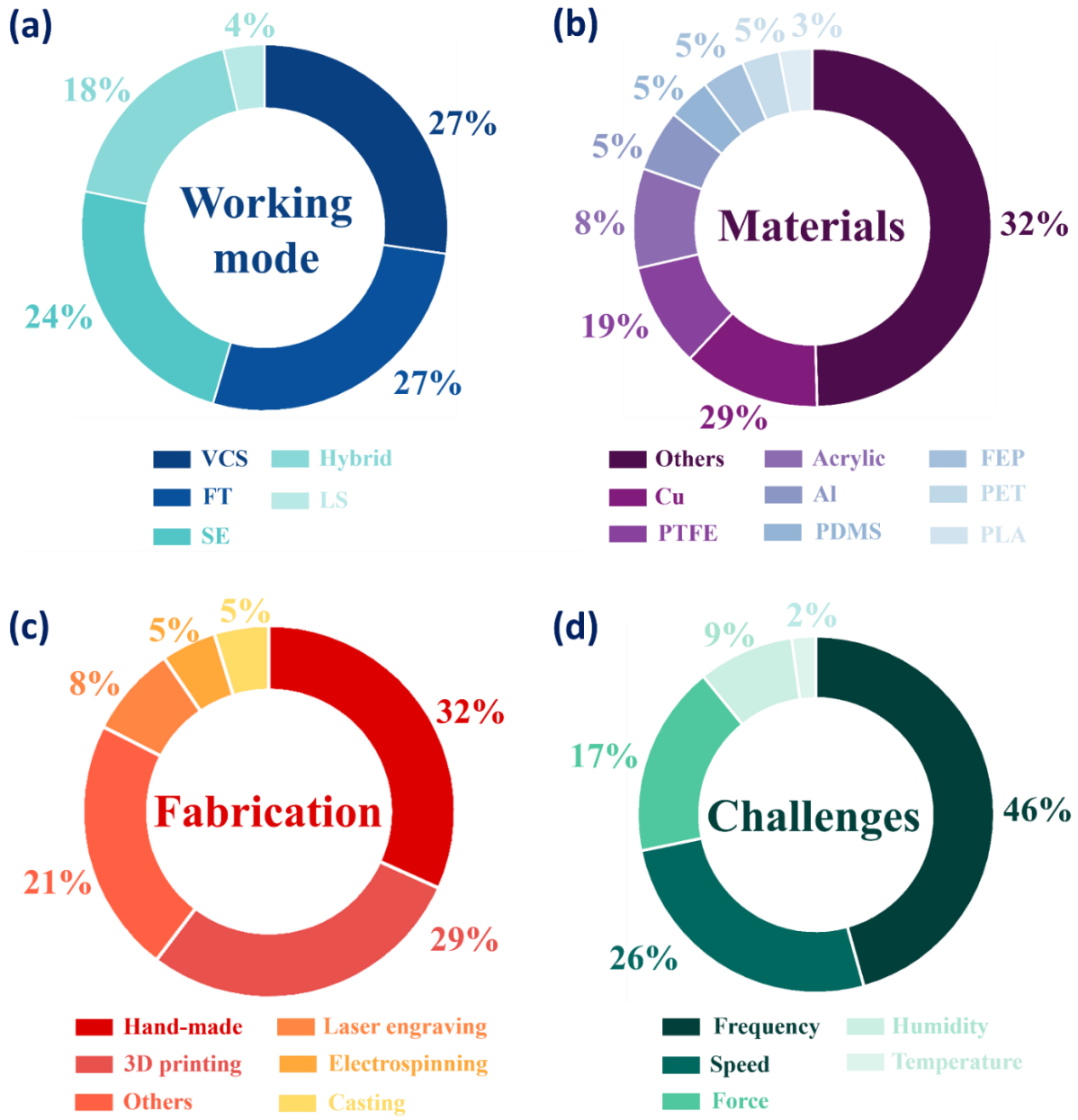


**Figure 2.12.** Statistical analysis of key parameters in energy harvesting devices, based on published literature on agricultural applications. The statistical percentages represent: (a) the working modes employed, i.e., VCS (Vertical Contact-Separation), FT (Freestanding Triboelectric), SE (Single Electrode), hybrid (e.g., VCS + FT), and LS (Lateral Sliding); (b) the prevalence of primary materials utilized in device fabrication, highlighting Cu, PTFE, Acrylic, Al, FEP, PET, PDMS, PLA, and others; (c) the fabrication processes adopted for TENGs, including hand-made, 3D Printing, laser engraving, electrospinning, casting, and others; and (d) the main agricultural challenges addressed by TENG-based systems, involving frequency, speed, force, humidity, and temperature.

Material selection shows a heavy reliance on conventional synthetic dielectric materials, e.g., PTFE, acrylic, and PDMS, while metallic electrodes like Cu and Al are widely used despite their susceptibility to oxidation, which can compromise long-term electrical output. Although these materials offer excellent triboelectric performance and mechanical stability, their widespread use raises concerns about environmental sustainability. Notably, biodegradable or eco-friendly materials are almost absent from current research, highlighting a significant gap and opportunity for developing green TENGs tailored for agricultural applications. For example, eco-friendly electrodes such as laser-induced graphene (LIG) and biopolymers like chitosan and lignin have already been explored in TENGs and supercapacitors, contributing to reduced carbon footprints.[168]

Furthermore, the predominance of hand-made (32%) and 3D-printed (29%) fabrication methods underscores the field's current orientation toward prototyping and small-scale applications. Scaling up to industrial deployment will require more standardized and scalable fabrication approaches, such as Roll-to-Roll (R2R) processing and screen printing. Finally, the analysis of agricultural challenges shows a disproportionate focus on dynamic parameters such as frequency (46%), speed (26%), and force (17%), while environmental factors like humidity (9%) and temperature (2%) are comparatively underrepresented. This imbalance suggests the need for broader investigations into how environmental variability affects TENG performance in real-world agricultural settings. Importantly, we emphasize that these challenges are seldom investigated collectively, even though they occur and interact simultaneously in agricultural environments. This fragmented perspective remains a significant barrier to the practical implementation of TENG-based active sensing technologies.

### 2.4.3 **Biological characteristics**

Biological growth on the surface of polymer-based nanogenerators can harm its output and performance by altering surface properties, releasing organic matter and other byproducts, degrading the integrity of the active layer, modifying morphology, and reducing the lifespan. Besides the reduction of energy harvesting efficiency, bacterial growth within devices represents biological risks to crops, reducing yield, efficiency, and safety.

In general, biopolymers are more susceptible to biological growth than polymers such as PDMS, PTFE, and PMMA. This leads to biofouling, the accumulation of biological organisms on surfaces, leading to performance degradation over time. Biofouling can increase surface roughness, promote corrosion, and reduce electrical conductivity, thereby decreasing the output and reliability of nanogenerators. Some key factors that contribute to the susceptibility of materials to biofouling include hygroscopicity, surface hydrophilicity, roughness, porosity, and chemical composition. Hygroscopic materials tend to adsorb water from the environment, promoting the formation of a hydrated layer that facilitates microbial attachment.[169,170] In contrast, hydrophobic surfaces repel water and are less conducive to biofouling. Porous and rough materials provide additional surface area for microbial attachment and colonization, increasing the likelihood of biofouling. Some chemical compositions can offer binding sites for attachment when their chemical groups undergo lysis, catalysing biofouling by supplying nutrients for microbial growth. For instance, organic-rich materials containing N-functional groups (e.g., amine and amide) are prone to biofouling due to carbon's energy role in protein synthesis.[171] These characteristics, combined with environmental factors, can further accelerate degradation processes and compromise the long-term performance of nanogenerators.

Polymers such as cellulose, chitin, chitosan, alginate, polyhydroxyalkanoates, collagen, and gelatin can be used as the active layer in nanogenerators. However, these

materials are inherently prone to biofouling because of their chemical structures rich in hydroxyls and long glycol groups that provide attachment sites for microorganisms.[172] In addition, the films can also be developed as hydrocolloid films, i.e., containing incorporated water content, facilitating microorganism adhesion.[173] Therefore, effective strategies for preventing or mitigating biological growth, e.g., surface coatings,[174] antibacterial agent incorporation,[175] or regular cleaning protocols, are essential to maintaining the efficiency and reliability of nanogenerators in agricultural environments, particularly with minimal impact on food safety. Despite eco-friendly and sustainable reasons, using biodegradable polymers can also harm food crops by releasing toxic byproducts, plasticizers, and, foremost, contributing to the development of bacterial populations. Therefore, polymers such as PDMS and PTFE emerge as the leading candidates for nanogenerator coatings applied in agricultural environments because of their chemical stability, low moisture uptake and surface energy, and long-lasting durability. Furthermore, they can be effectively cleaned using chemical agents or even self-cleaning processes.[176–178]

### 2.4.4 Device stability

#### 2.4.4.1 Electrical stability

A critical feature of nanogenerators is their ability to deliver stable electrical output under varying environmental conditions. Ensuring efficient and reliable performance at high yield rates requires advancements in materials compatibility between the electrode and active layer to address issues such as low effective contact area caused by air bubbles. Uneven contact between the electrode and active layer hinders charge transfer and creates non-uniform potential distribution due to surface heterogeneity, reducing effective charge density.[179] For example, ductile materials with limited elastic deformation, like aluminum (Al) foil electrodes, cannot fully recover their shape after deformation or compression beyond their yield point. This results in

suboptimal contact uniformity, especially under low input forces, severely impacting the electrical output of nanogenerators. Despite these limitations, Al is widely used in nanogenerators due to its work function (~4.1 eV), which is lower than that of many other materials (e.g., Cu, Au, Ti, Fe, Ag), and its environmental stability.

One of the primary challenges that nanogenerators used in agriculture will encounter is the electrical contact between material interfaces, especially between the conductor responsible for the induction effect and the wires (e.g., copper tape). The presence of ohmic contact, as opposed to resistive contact, will also convey a signal that aligns more closely with reality. Ohmic contact denotes a scenario where there is minimal resistance at the interface between two materials, ensuring a smooth flow of electrical current without significant loss. Conversely, resistive contacts may result in energy dissipation and decreased power output due to contamination or inadequate contact area, compromising the stability and reliability of the device.

Effective Ohmic contact in nanogenerators facilitates linear, low-resistance charge transport, maximizing power output. Unlike Schottky contacts, which impose rectifying barriers due to SBH, Ohmic contacts enable efficient energy harvesting by minimizing interfacial impedance.[180,181] Conversely, nanogenerators with resistive contacts are more prone to environmental influences and wear over time, exhibiting reduced efficiency and power output. To tackle this electrical issue, various strategies can be devised to ensure optimal efficiency. These include selecting materials with high charge mobility and similar work functions to establish robust electrical interfaces, facilitating efficient charge transfer. Additionally, to maximize electrical efficiency generation, ensuring enhanced adhesion and the effective contact area between conductive layers should be guaranteed rather than solely relying on physical contact. For instance, chemically depositing material onto the conductive layer can enhance interfacial contact by minimizing air gaps and reducing interfacial mismatch, thereby ensuring a highly effective and uniform contact area.

Moreover, the materials and devices connected to nanogenerators should exhibit excellent electrical insulation properties, e.g., capacitive devices, in order to minimize leakage current and maintain high voltage. In this regard, emerging technologies, such as artificial intelligence, can assist in designing high-performance materials and structures for efficient nanogenerator operation, particularly when considering the adverse conditions encountered in agricultural environments.

#### 2.4.4.2 **Chemical stability**

Beyond considerations of biodegradability, certain materials demonstrate enduring chemical stability but are markedly influenced by external conditions. A prime example is polyaniline (PANi), a conductive polymer known for its transition from high electrical conductivity (10–100 $S.cm^{-1}$ in the emeraldine form) to dielectric state (~10 $S.cm^{-1}$) under basic pH, transforming into the pernigraniline form.[182,183] This transformation is attributed to the susceptibility of PANi to pH variations, resulting in significant alterations in its molecular structure.[184]

PANi's conductivity relies on the presence and mobility of positive polarons formed during oxidation. In a basic environment, PANi is deprotonated, leading to polymer coiling and molecular rearrangement, favouring the fully reduced leucoemeraldine form.[185] Upon lowering the pH to ≅ 7, the species converts to the emeraldine form, characterized by partial protonation of amine groups and formation of the polyanilinium cation.[183] This form exhibits enhanced electrical conductivity owing to increased electronic conjugation along the polymer chain, facilitating better charge transport. Conversely, in an acidic environment, PANi becomes protonated (resulting in the fully oxidized pernigraniline form),[186] leading to polymer blob expansion and disorder in molecular structure, thereby reducing electronic conjugation and electrical conductivity.

The use of PANi in nanogenerators holds significant potential for self-powered pH monitoring, exploring the modulation of electrical properties via polymer protonation/deprotonation. For instance, in regions with industrial activities emitting gases like sulphur dioxide ($SO_2$) and nitrogen dioxide ($NO_2$), acid rain is common, posing challenges. In such scenarios, the interaction of acidic water with PANi's active layer triggers doping and conversion to the conductive emeraldine salt (ES) species, altering the electrical charge generation mechanism (as discussed in *Section 2.3.4*). This alteration will likely affect the electrical output, useful for pH monitoring via a PANi nanogenerator-based smart sensor.

Moreover, chemical stressors such as acid rain and intensive pesticide exposure extend far beyond standard laboratory conditions and can severely compromise the integrity of triboelectric active layers and electrodes. For example, acid rain (pH values below 5.6)[187] can accelerate hydrolytic degradation of ester, amide, and carbonate linkages in polymeric tribolayers,[188–190] while promoting oxidative pitting or disrupting passivation layers in metallic electrodes.[191–194] Likewise, concentrated pesticides are commonly mixed with solvents that, on contact with polymers, may cause swelling and induce plasticization, thereby altering mechanical properties (e.g., Young's modulus and elongation at break).[195,196] Over time, by altering surface chemistry and bulk properties, these stressors change the capacity to retain triboelectric charge, resulting in unstable electrical output. The combined effects of acidic deposition and pesticide residues can exacerbate these pathways, likely amplifying charge dissipation, mechanical wear, and long-term performance instability. Thus, ensuring durability under such conditions depends on combining intrinsic material resilience with protective measures such as inert fluoropolymer encapsulation, corrosion-resistant coatings or chemically inert electrodes (e.g., Au, Pd, Ti), and self-cleaning or pH-responsive barrier layers.

Oxygen is another critical factor influencing the chemical stability of materials, particularly metals prone to oxidation e.g., aluminium, copper, and iron, which are commonly used as electrodes. Oxidation compromises the integrity of the interfacial connection with the active layer, reducing the effective contact area and thereby reducing energy conversion efficiency. The combination of oxygen and moisture further accelerates device malfunction, particularly in materials with poor chemical stability, highlighting the significance of material selection and encapsulation to mitigate these effects. For instance, hygroscopic materials utilized as active layers will absorb moisture from the environment.[197] This can lead to the accumulation of water molecules at the electrode-active layer interface, resulting in a notable reduction in effective contact and the electrostatic induction effect.

Hygroscopicity refers to the capacity of certain materials, e.g., cellulose, and nylon, to attract and retain water molecules from their surroundings. Hygroscopic polymers undergo physical changes, including alterations in free volume, viscosity, and dielectric constant, upon water absorption. Therefore, the equilibrium moisture content, influenced by temperature and relative humidity, will significantly influence the dielectric properties. Hence, solutions to these challenges involve selecting more stable materials or nanogenerators' encapsulation to prevent contact with detrimental elements, e.g., oxygen, moisture, and dust.

Therefore, the limited stability of hygroscopic materials, such as cellulosic-based polymers, in nanogenerators poses challenges for sensing in environments with significant climatic variations, primarily due to fluctuations in their dielectric constant. Moreover, the elevated water content in the polymer matrix can accelerate chain-breaking reactions, boosting biodegradation through hydrolysis reactions.[189] This not only impacts energy generation efficiency and sensing capabilities but also has the potential to release harmful substances into the environment.

#### 2.4.4.3 **Active sensing via functional materials**

The environmental conditions, which are continuously exposed to a wide array of substances and contaminants, can significantly alter the surface properties of nanogenerators. Particles and debris that accumulate on the surface can modify the triboelectric series mismatch of the materials involved, leading to inconsistencies in electrical measurements. This disturbance not only impacts the efficiency of energy generation but also compromises the reproducibility and consistency of advanced applications such as sensing. Therefore, an effective strategy to address this issue involves developing multifunctional surfaces capable of self-cleaning, primarily achieved by reducing the surface energy of the layer exposed to the environment. These surfaces can also support a range of smart applications through physical, chemical, or biological modifications, enabling functionalities such as antibacterial activity, self-cleaning, and biosensing.[175,178,198,199]

For instance, engineering surfaces with chemical modifications, such as coating them with low surface energy materials, e.g., functionalized PMMA or thiolated Au, reduces intermolecular interactions and decreases the adsorption of dust and bacteria. PMMA can be chemically modified by introducing reactive functional groups, such as silanes or fluorinated compounds,[200] to reduce surface energy and enhance hydrophobicity. Similarly, gold surfaces can be functionalized through thiolation reactions, where thiol (-SH) groups form strong covalent bonds with the gold surface, creating self-assembled monolayers (SAMs).[201] These chemical modifications not only lower surface energy but also enable further functionalization for specific applications, such as antifouling coatings or tailored surface interactions **(Figure 2.13)**.

One of the main factors affecting the TENG signal output is the change in surface composition caused by wear. Wang et al. developed a solid-liquid TENG for wear sensing by utilizing anti-corrosion coatings (lacquer paint) to protect metal substrates.[202] The TENG signal output decreased from 3.2 to 2.2 V, and the coating

thickness was reduced by 1.7 μm after 10 min of wear on the lacquer paint. This confirms that TENG generates electric signals corresponding to different wear states, facilitating easy monitoring of the coating's wear conditions. The coating-liquid contact-separation motion generated real-time output signals that directly reflect the coating wear states without the need for additional equipment.

Chung et al. developed a TENG submerged in a liquid lubricant to enhance its electrical and mechanical properties compared to conventional designs.[203] The surface charge of the PTFE is increased through the suppression of air breakdown by the liquid, while the friction wear during operation is significantly reduced, thereby improving the mechanical stability of the TENG. Furthermore, the electric current is amplified through direct electron flow that occurs when the rolling and plate electrodes make contact. However, despite these improvements, retaining the liquid lubricant remains challenging, limiting the applicability in diverse scenarios.

Through covalent bond functionalization, nanogenerators can achieve enhanced electrical output while also serving as effective tools for molecular and ion sensing.[204–206] For instance, Cui et al. developed a flexible, self-powered nanosensor for ammonia ($NH_3$) by growing polyaniline nanofibers (PANi NFs) on a Kapton substrate.[207] This layer was utilized as the active component of the TENG, which generates response signals for $NH_3$ detection and provides energy to power small electronics. The high specific surface area of PANi NFs facilitates efficient adsorption and desorption of $NH_3$ molecules, enabling a detection limit of ~500 ppm and thereby confirming the material's sensitivity.[207] Despite the complex fabrication, this work shows that effective chemical covalent modification can be used to detect chemicals with high sensitivity and selectivity. Therefore, identifying substances with high sensitivity to analytes and functionalizing them on surfaces is a promising strategy to achieve high performance in self-powered chemical sensing TENGs. However, wear stability over

time due to natural mechanical triggers and environmental dirt accumulation remains a significant limitation.

Physical modifications, which do not involve changes in chemical composition, can significantly enhance sensitivity in pressure sensor applications by developing patterned surfaces. Wang et al. developed a flexible, transparent TENGs incorporating three types of regular and uniform PDMS patterned arrays (cubic, linear, pyramid).[208] These patterns were designed to enhance frictional effects, significantly boosting the nanogenerator's output efficiency by increasing the effective contact area. They achieved a low-end detection limit of approximately 13 mPa. The sensors featuring linear and cubic patterns exhibited sensitivities ~five and ten times greater, respectively, compared to those of unstructured films. At the same time, the pyramid-patterned device demonstrated the highest sensitivity due to a consistent increase in effective contact area with increasing pressure. However, a major drawback lies in the stiffness-compatibility (as discussed in *Section 2.4.1.1*) and the low structural stability of micro-patterns over extended periods, which hinders reliability and long-term applications.

Creating hierarchical structures – such as integrating nanopatterns into micropatterns – can enhance the effective contact area to achieve high sensitivity in pressure sensors.[209,210] In that regard, Jang et al. developed a hierarchical surface using hexagonally packed colloidal arrays in the active layer for a self-powered pressure sensor based on TENGs.[211] The dual embossed surface, which mimics micro/nanostructured dimension, ensured a superhydrophobic surface (>150°) that repels water effectively by minimizing physical contact. The self-powered sensor exhibited excellent stability and maintained electrical output even amidst fluctuations in relative humidity from 20 to 80%. This effect could also enable the surfaces to achieve self-cleaning capabilities, e.g., low surface energy and/or repulsive forces against dust.[208] Similarly, Chen et al. designed a flexible hierarchical elastomer-tuned

self-powered pressure sensor capable of achieving both high sensitivity (7.9 $V.kPa^{-1}$) and a wide pressure range (0.1-60 kPa) simultaneously.[212] The sensor demonstrated a fast response time (40 ms), high signal-to-noise ratio (38 dB), and good stability. This smart device sensitively monitors pulse, arterial conditions, heart rate, and blood pressure. Consequently, owing to its high sensitivity, this device could serve as a presence sensor, detecting organisms, insects, and pests, showcasing the potential of hierarchical surface structures in enhancing pressure sensor performance for agricultural environments.

Physical adsorption is a strategy that can enhance triboelectrification by donating or withdrawing electrons, and it can also adsorb specific analytes. This occurs because the chosen molecules adsorbed onto the TENG surface can interact favourably with the functional groups of analytes, promoting their attachment to the TENG surface. For example, Cheng et al. modified the surface structure using a single-step fluorocarbon plasma treatment, creating a wrinkled structure on PDMS surfaces **(Figure 2.13b,iii)**.[198] This significantly enhanced the TENG's performance and increased the surface area for potential adsorption. XPS confirmed the physical attachment induced by the fluorocarbon plasma treatment, improving the surface charge density by up to 810%.

In turn, Liu et al. developed an electrostatic adsorption face mask using a poly(vinylidene fluoride) electrospun nanofiber film respiration-driven TENG.[213] Physical adsorption on the triboelectric layer is generated from the mechanical energy of breathing, increasing the adsorption of ultrafine particles on the mask through electrostatic adsorption. The mask demonstrated a removal efficiency of over 99.2% for coarse and fine particulates. It maintained an efficiency of 86.9% for ultrafine particulates after continuous use for 240 min and even after a 30-d interval. Compared to commercial face masks, the developed mask showed superior performance,

particularly in filtering ultrafine particulates due to the coupling of physical filtration and adsorption.

Another engineering approach that tailors active functionality is charge accumulation, which can subsequently be utilized as electrostatic discharge (ESD) energy in food sterilization. The mechanism behind this sterilization process relies on the ability of TENG surfaces to accumulate electric charges through CE, creating an electric field between dielectric layers. When the electric field strength exceeds the dielectric strength of the surrounding medium (e.g., air), the medium becomes conductive. For air, this dielectric breakdown occurs at a field strength of ~3 $kV.mm^{-1}$, releasing the accumulated charge and enabling ESD sterilization.[214–216]

Taking advantage of this effect, Heo et al. designed a TENG to achieve ultrahigh current output performance aimed at producing high electrostatic discharge.[217] The TENG leverages a synergistic effect between unidirectional charge accumulation and direct electron flow, resulting in significant improvements in electrical output. The nanogenerator produced ~2 kV and ~7 A, under normal conditions, potentially useful for food sterilization. Furthermore, the self-powered system produced significant amounts of hydrogen and oxygen (370 and 230 μL, respectively) over 12 h, demonstrating its potential for practical water treatment and purification.

Conversely, Luo et al. developed a rotating-disk freestanding mode TENG for water sterilization using its high charge density capacity.[216] At 300 rpm, the TENG reached approximately 9 kV, enabling a water droplet (62.5 μL) to be charged to 6.3 μC at a flow rate of 0.31 $mL.min^{-1}$. The charged water droplets killed bacteria, e.g., *E. coli* and *S. aureus*, through an electroporation mechanism. The sterilization efficiency for *E. coli* and *S. aureus* was approximately 98.3 and 97.9%, respectively, ensuring effective water sterilization based on TENG technology.

The electric field generated by a TENG can be used to create self-cleaning surfaces through electrostatic repulsion or electrowetting. For example, TENG-

induced charges on dust particles can repel similarly charged particles, preventing them from settling on the surface. Conversely, the electric field can control liquid droplets on the surface through electrowetting by altering their surface tension, enabling the TENG to move, merge, or spread the droplets to remove contaminants and debris from the surface.

For instance, Heo et al. developed a wind-driven rotating TENG to work as an electrodynamic screen (EDS) system for autonomous dust removal to enhance solar panel efficiency **(Figure 2.13b,v)**.[218] The self-cleaning principle is based on applying the high-voltage output from the TENG to the EDS surface. This creates a non-uniform electric field between the interdigitated electrodes of the EDS plate. As a result, electrophoretic and dielectrophoretic forces repel dust from the solar panel's surface, causing it to fall due to gravity. It was shown that the rotational speed of the nanogenerator increased with wind speed, enhancing dust removal efficiency and achieving over 90% recovery of original solar panel efficiency after EDS operation. Furthermore, the effect of different dielectric materials (perfluoro alkoxy, polyimide, PET, and Nylon™) on self-cleaning efficiency was studied. The polyamide film exhibited the highest dust removal efficiency by weight (~52%), followed by PET (~41%), PI (~26%), and PFA (~24%), in agreement with the relative permittivity of the dielectric films. This correlation indicates that a higher relative permittivity in a dielectric material leads to a stronger surface electric field intensity, resulting in a higher self-cleaning capability.

In addition to their role as pressure sensors, hierarchical surfaces in the devices can also be engineered for self-cleaning capabilities, thereby prolonging their operational lifespan and minimizing the need for human intervention.[219] This efficiency could be further amplified through physicochemical modification, where established physical patterns are combined with surface chemical treatments to achieve low surface energy. This modification reduces secondary interactions between

contaminants and the active surface, typically resulting in superhydrophobicity. Methods for achieving this include coating,[220] chemical vapor deposition,[221] plasma treatment,[222] and reactive ion etching.[223]

Besides using physicochemical modification to achieve efficient self-cleaning capability, physicochemical modification can also be utilized for antibacterial applications in nanogenerators.[175,224,225] For instance, Peng et al. developed a micro-to-nano hierarchical porous structure, providing a high specific surface area for contact electrification and numerous capillary channels for thermal-moisture transfer, ensuring a breathable and self-powered e-skin sensor **(Figure 2.13c,i)**.[175] Furthermore, the device is fabricated from poly(lactic-*co*-glycolic acid) (PLGA) and poly(vinyl alcohol) (PVA), enabling the e-skin to degrade over time, thereby reducing electronic waste. Additionally, incorporating silver nanowires (Ag NW) provided antibacterial activity against *S. aureus*, effectively inhibiting bacterial growth and preventing infections. The diameters of the zones of inhibition against *E. coli* and *S. aureus* for the PLGA/Ag NWs/PVA nanofiber film were 10 and 12 mm, respectively, whereas the pure PVA and PLGA nanofiber, each with an initial diameter of 8 mm, showed no antibacterial properties against either bacterium.

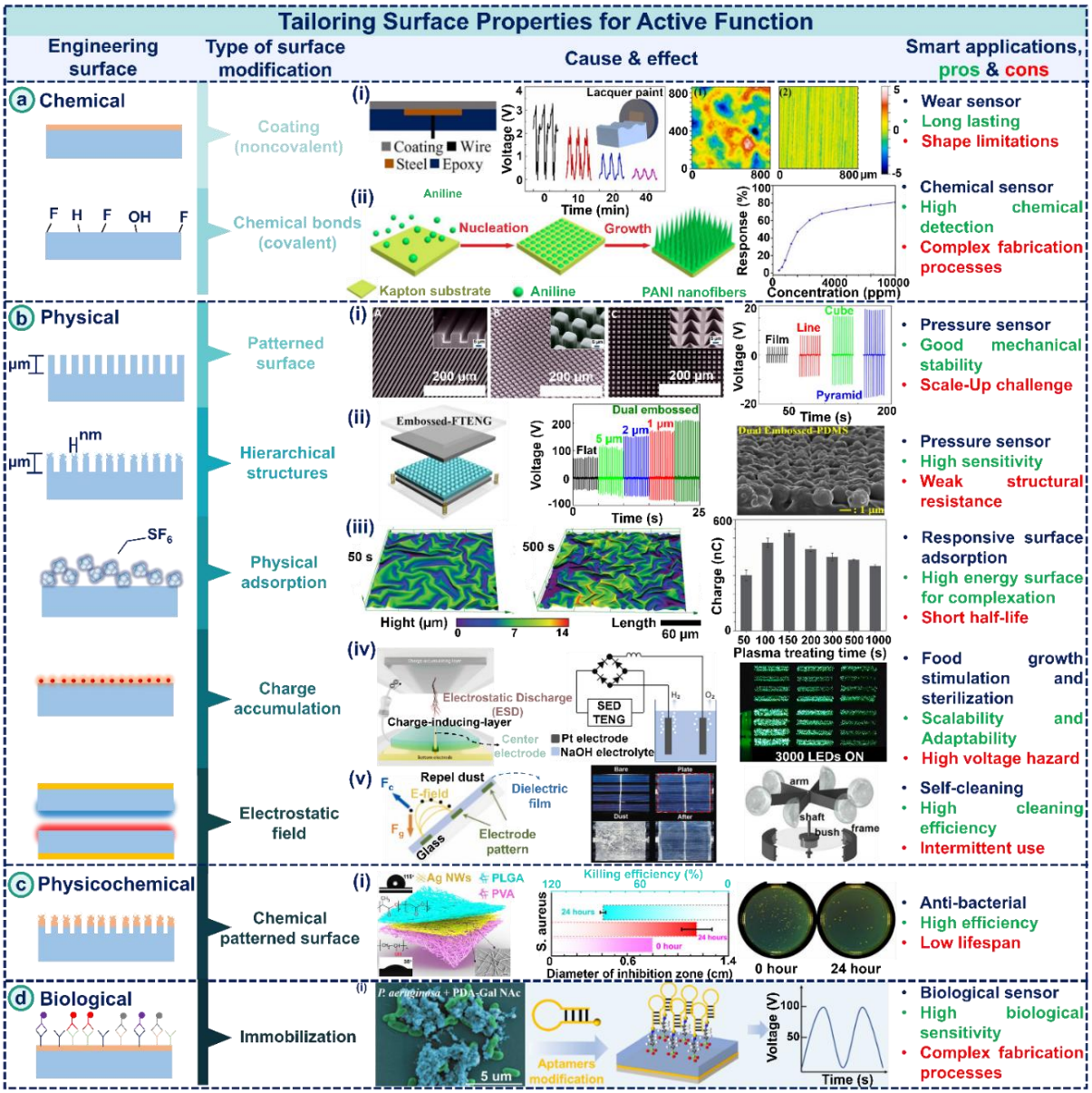


**Figure 2.13.** Strategies to tailor surface properties for active functions in triboelectric nanogenerators to enable functionalities beyond energy harvesting: Chemical modification: (a,i) by coating deposition is employed for wear sensor development; reprinted with permission from ref.[226]; (a,ii) via covalent bonds is utilized to develop chemical sensors; reprinted with permission from ref.[207] Physical modification: (b,i) through patterned surface development is applied for pressure sensor applications; reprinted with permission from ref.[208]; (b,ii) via hierarchical structures is employed for high sensitivity in pressure sensor applications; reprinted with permission from ref.[211]; (b,iii) by physical adsorption is used for responsive surface adsorption and complexation applications; reprinted with permission from ref.[198]; (b,iv) involving charge accumulation is applied for food growth stimulation and sterilization; reprinted with permission from ref.[217]; (b,v) utilizing electrostatic fields is applied for self-cleaning surface applications; reprinted with permission from ref.[218] (c,i) Physicochemical modification through patterned surface or bulk development is utilized for antibacterial application; reprinted with permission from ref.[175] (d,i) Biological

modification via enzyme immobilization serves as a biological self-powered sensor; reprinted with permission from ref.[199]

Accumulated electrostatic charges enable self-cleaning characteristics by repelling dust, dirt, and other particles from surfaces. Applying a high voltage to a material with a high dielectric constant can induce electrostatic charges on the surface. These charges create an electrostatic field that repels dirt particles, preventing them from adhering to the surface.[227] When the surface is exposed to wind or rain, the loosely bound particles are easily washed away, resulting in a self-cleaning effect. Additionally, these charges create an electrostatic field that repels water molecules, inhibiting the formation of ice crystals, thus serving as an anti-icing surface.[227] Even if ice does form, the electrostatic forces weaken the bond between the ice and the surface, making it easier to remove mechanically or by natural forces such as wind or vibration. In both cases, manipulating electrostatic charges offers a passive and environmentally friendly approach to achieving self-cleaning and anti-icing properties on surfaces without additional chemicals or mechanical interventions.

One overlooked surface engineering aspect, especially for TENGs, is biological modification. Biological structures such as enzymes, antibodies, and tissues can be immobilized on surfaces through physical adsorption, crosslinking, covalent binding, or entrapment. These modifications can make the material more biocompatible, e.g., by using nanogenerators as scaffolds to provide electrical stimuli for cell body growth. This approach reduces the need for medical intervention and increases the efficiency of injury recovery. Furthermore, biological functionalization of surfaces can act as a biosensor, enabling the detection of specific biological analytes and enhancing specificity and sensitivity. This occurs because surfaces functionalized with antibodies can selectively bind to specific antigens, allowing for the detection of pathogens, toxins, and biomarkers.

For instance, Lu et al. developed a self-powered biosensor based on a TENG for dual-specificity bacterial detection, aiming for highly specific, sensitive, and on-site detection of *Pseudomonas aeruginosa*.[199] The electrode surface was for bacterial recognition using specific aptamers for primary binding and polydopamine-N-acetyl-D-galactosamine (PDA-GalNAc) nanoparticles for secondary recognition. The aptamers capture *P. aeruginosa*, while the PDA-Gal NAc amplifies the detection signal by altering the TENG's output voltage. The TENG demonstrated a linear relationship between the output voltage and *P. aeruginosa* concentration ($10^7$ – $10^3$ CFU.mL$^{-1}$) and maintained its output voltage over several days. Furthermore, the biosensor based on TENG exhibited high specificity for *P. aeruginosa* with a detection limit of ~8.7 × $10^3$ CFU.mL$^{-1}$, which relies on the specific interactions between Gal NAc and PA-IL lectin in *P. aeruginosa*.

However, other significant factors were not analysed, such as environmental effects (e.g., temperature, humidity, unpredictable trigger frequency, and force) and especially the accumulation of dirt and debris on the surface contact, which strongly affects the ability to gain or lose electrons and the effective contact area. Therefore, this self-powered sensor based on TENG faces similar challenges to those documented in existing literature, specifically a low signal-to-noise ratio primarily caused by uncontrollable trigger actions.

Although not a fundamental requirement for the functionality of nanogenerators, the development of a functional active layer not only improves the reproducible and long-lasting performance of the device but also can enable smart applications. By adopting "self-functional" approaches, nanogenerators can be utilized in diverse and hostile environments, minimizing the need for human intervention. However, identifying new routes to ensure high specificity for sensing applications is a milestone for the upcoming implementation of self-powered sensors based on nanogenerators.

Achieving this will elevate the technology from simple screening sensors to highly reliable, (semi)quantitative, and self-powered sensors.

#### 2.4.4.4 **Functional material strategies for stimuli-responsive TENGs**

The integration of stimuli-responsive materials into TENG architectures has established a new paradigm in energy-harvesting systems, particularly suited for smart agricultural applications. These materials confer environmental reactivity to TENGs, enabling self-regulating behavior via physicochemical transformations triggered by external stimuli, e.g., light, temperature, pH, humidity, and chemical exposure. As summarized in **Table 2.1**, each stimulus induces distinct molecular or interfacial mechanisms, ranging from phase transitions and protonation to host–guest interactions and ionic swelling, that modulate triboelectric output and smart functionality.

We envision that elucidating the role of functional materials and their stimuli-responsive mechanisms will provide a materials-centric framework for designing TENGs tailored to agricultural environments. This materials-driven approach merges autonomous energy harvesting with stimulus-responsive actuation, aligning with the principles of Agriculture 4.0 by enabling real-time environmental sensing, facilitating data-driven decision-making, targeted agrochemical release, climate-adaptive control, and reduced labor input across crop and livestock systems.[228,229]

Light-responsive materials enable tunable photophysical behavior in TENGs by dynamically modulating surface charge and carrier mobility under solar exposure, enabling photonic sensing and light-adaptive smart responses. In agricultural environments, this renewable and information-rich stimulus is advantageous for solar-triggered actuation and crop light-management systems. For instance, semiconducting oxides such as $TiO_2$ and ZnO exploit photogenerated electron–hole pairs to modulate surface potential,[230–232] while $MoS_2$, with its strong photogating effect, enhances charge carrier transport. [233,234] These properties can be harnessed in

sunlight-triggered shading systems, UV-decontaminating surfaces, and photo-modulated growth monitoring platforms, allowing autonomous optimization of photosynthetic conditions and reduction of pathogen load on agricultural surfaces.

Additional candidates for light-responsive behavior can be found among semiconducting oxides, 2D materials, photoconductive polymers, and perovskites, as these classes commonly exhibit light-induced changes in electronic structure, surface potential, or carrier dynamics. For example, graphitic carbon nitride (g-$C_3N_4$) offers visible-light photoactivity and chemical stability for photocatalytic sensing layers;[235,236] $Cu_2O$, a p-type oxide, provides high photoconductivity for solar-modulated interfaces;[237,238] and perovskites materials provide tunable bandgaps and photovoltage generation for wavelength-selective charge modulation.[239,240] These light-active materials broaden the functional landscape of agricultural TENGs by integrating photonic sensing with autonomous actuation, enabling self-powered and adaptively intelligent interfaces.

**Table 2.1.** Stimuli-responsive functional materials for agricultural TENG systems: stimulus, functional material, response mechanism, and applications.

| Stimulus | Functional material | Response mechanism | Potential smart agricultural applications |
|---|---|---|---|
| Light | $TiO_2$, $SiO_2$ | UV-induced photocatalysis modulates surface hydrophilicity [230–232] | Self-cleaning, antimicrobial TENGs for dusty/biofouling conditions |
| | ZnO | UV excitation alters surface conductivity via electron activation [241] | Light-TENGs for photoperiod monitoring |
| | $MoS_2$ | Photogating modulates charge carrier density and mobility [233,234] | Light-responsive TENGs for shading control |
| pH | PANI | Protonation alters conductivity and color [207] | Soil acidity sensors via TENGs |
| | PMAH, gelatin | pH-dependent swelling modifies solubility and chain conformation [242,243] | Biodegradable coatings TENGs for soil health |
| | HEMA, APBA | Acidic microenvironments trigger antibiotic-releasing reactions [244] | Anti-fouling TENGs for livestock/aquaculture |
| Temperature | $VO_2$ | Reversible metal-insulator phase transition alters electrical conductivity [245] | Temperature-sensitive TENGs for crop stress or cold/heat event detection |
| | IPU | Heat-triggered hydrogen bond reformation enables self-healing of fractured interfaces [246] | Self-healing TENGs for long-term field use |
| | UPy | Thermal activation of UPy bonds restores original geometry [165] | TENGs with shape-memory for structural integrity in the field |
| Humidity | Zeolite | Water vapor adsorption changes dielectric constant/capacitance [247] | Humidity-triggered TENGs for precision irrigation |
| | Hygroscopic salts | Moisture absorption plasticizes matrix, enhancing mechanical and conductivity [248,249] | Flexible and resilient TENG structures for harsh environments |
| | Nafion | Ionic polymer swells with water uptake, inducing shape change via electrostatic interactions [250] | Moisture-driven actuators for seed release |
| Chemicals | PDA | Analyte-induced backbone distortion shifts conjugation and color 187,188 | TENGs for detecting pesticides/heavy metals |
| | Cyclodextrins | Host–guest interactions modify dielectric | Selective active TENG sensors |

| | | |
|---|---|---|
| | and energy transfer properties [253–255] | via molecular recognition |
| PANI, PPY | Redox reactions modulate material conductivity [207,256,257] | TENG alerts for chemical spills |

Footnote: Titanium dioxide ($TiO_2$), Silicon dioxide ($SiO_2$), Zinc oxide (ZnO), Molybdenum disulfide ($MoS_2$), Polyaniline (PANI), Poly(methacrylic acid) (PMAH), Poly(2-hydroxyethyl methacrylate) (HEMA), 3-Acrylamidophenylboronic acid (APBA), Vanadium dioxide ($VO_2$), Ionic polyurethane (IPU), Ureido-pyrimidinone-functionalized polymer (UPy), Hygroscopic salts (e.g., calcium chloride, lithium chloride, and magnesium chloride), Perfluorosulfonic acid ionomer (Nafion), Polydiacetylene (PDA), Polypyrrole (PPY).

Agricultural systems frequently experience pH fluctuations due to soil composition, fermentation byproducts, and metabolic activity in livestock environments. Stimuli-responsive materials with protonation-dependent conductivity or swelling behaviors offer direct transduction of these biochemical cues into TENG performance modulation. For example, PANI exhibits reversible shifts in both electrical conductivity and optical absorbance upon protonation, making it ideal for real-time soil pH monitoring.[207] Similarly, poly(methacrylic acid) (PMAA) and boronic acid-functionalized hydrogels undergo pH-induced ionization and crosslinking, supporting controlled release systems for antibiotics or fertilizers.[242–244] Given the importance of pH monitoring in agricultural systems, these pH-responsive mechanisms equip TENGs for autonomous agrochemical release, pathogen-triggered therapeutic deployment, and real-time biochemical sensing, advancing toward fully self-regulating and intelligent agricultural technologies.

Materials exhibiting pH sensitivity are typically categorized into ionizable materials (or proton-sensitive systems) and dynamic covalent networks, where pH modulates charge distribution, bonding, or material morphology.[258,259] For instance, poly(2-vinylpyridine) (P2VP) acts as a proton-responsive polybase, exhibiting reversible ionization-driven changes in charge and hydrophilicity for pH-sensitive sensing and gating;[260,261] poly(β-amino esters) undergo hydrolysis in acidic environments for triggered degradation;[262,263] and chitosan-based systems swell and protonate under mild acidity, enhancing ionic conductivity.[264,265] Building on these capabilities, ionizable materials and pH-sensitive architectures hold strong potential for integration into TENGs as biosensing modules, controlled-release interfaces, and pH-regulated actuators tailored for agricultural applications.

Temperature variations in agricultural environments, ranging from diurnal fluctuations to heat stress events, necessitate thermally stable energy-harvesting platforms capable of exploiting ambient stimuli to induce mechanical, electrical, or

structural transformations. This thermal input can be harnessed through thermoresponsive materials, enabling TENGs to autonomously self-repair, reconfigure, or regain shape in response to environmental heat. For example, vanadium dioxide ($VO_2$) undergoes a semiconductor-to-metal transition near 68 °C, enabling reversible modulation of conductivity and dielectric behavior.[245] Ureido-pyrimidinone (UPy) and ionic polyurethanes (IPU) exhibit thermally induced shape-memory and self-healing capabilities, restoring device integrity following mechanical disruption.[165,246] These features support resilient TENG sensor networks, autonomous structural recovery, and self-sustaining interfaces designed for extended operational lifetimes.

To expand the scope of thermally responsive TENGs, materials such as shape-memory polymers, phase-change materials, and thermoresponsive polymers offer reversible modulation of mechanical (e.g., self-healing) and dielectric properties under thermal stimuli.[166,266–268] For instance, poly(N-isopropylacrylamide) (PNIPAM) undergoes a sharp volume transition near physiological temperatures, facilitating actuation;[269,270] paraffin–elastomer composites provide latent heat buffering with thermally controlled reshaping;[271,272] and supramolecular imine–PDMS networks enable self-healing through reversible imine bonding.[273,274] These materials offer a promising pathway for constructing environmentally adaptive and damage-resilient TENGs capable of withstanding thermal stress and environmental variability.

Fluctuating humidity levels shape the microenvironment of agricultural systems, affecting nutrient uptake, water balance, and plant development.[275] Materials responsive to atmospheric moisture - via swelling, dielectric modulation, or water-induced softening – can enable passive environmental sensing and adaptive mechanical behavior in TENG devices. Zeolites, for example, exhibit humidity-dependent dielectric shifts via water adsorption, modulating triboelectric output accordingly.[247] Hygroscopic salts, e.g., $CaCl_2$ and $MgCl_2$ act as polymer plasticizers,

enhancing flexibility and mechanical resilience under wet conditions.[248,249] Nafion undergoes significant swelling with water uptake, enabling soft actuator systems for seed dispersion and stomatal mimicry.[250] Collectively, these mechanisms allow TENGs to integrate humidity-triggered responses while improving durability against field-induced mechanical stress.

Additional materials demonstrating humidity-responsive behavior are closely bonded to water hygroscopic materials. PVA, for instance, swells under high relative humidity, facilitating actuation and conductivity modulation;[276,277] cellulose nanofibrils alter surface charge characteristics through moisture uptake,[278,279] potentially tuning TENG output. These systems support applications in hydration mapping, moisture-responsive release systems, and adaptable interfaces in rain-exposed or irrigation-managed agricultural environments.

The agricultural environment comprises a diverse array of volatile compounds, pesticides, and chemical contaminants that can be selectively monitored via chemically responsive functional materials. These systems transduce molecular binding events and redox activity into triboelectric signal variations, enabling TENGs to function as self-powered chemical sensors. For example, polydiacetylene (PDA) exhibits chromatic and dielectric changes upon analyte interaction, cyclodextrins (CDs) facilitate specific molecular recognition through host–guest complexation,[253–255] and redox-active polymers such as polypyrrole (PPY) and PANI undergo conductivity modulation through electron transfer, making them suitable for detecting pesticides, ammonia vapors, and $NO_2$.[207,256,257] These mechanisms support *in-situ* monitoring of environmental pollutants, gas leakage, and adaptive agrochemical control via TENGs.

We identify additional opportunities in expanding the chemical responsiveness of TENGs through classes of redox-active materials, host–guest assemblies, and gas-sensitive frameworks, which undergo reversible structural or electronic changes upon analyte exposure. For instance, natural pigments such as anthocyanins exhibit redox-

based responses to alkaline volatiles (e.g., $NH_3$, triethylamine, and hydrazine);[248,280] molecularly imprinted polymers (MIPs) enable tailored detection through analyte-specific surface potential modulation;[281,282] and metal–organic frameworks (e.g., ZIF-8) detect volatile organic compounds (VOCs) by generating electrochemical signals.[283,284] We foresee these materials will enable the next generation of TENG sensors for continuous, real-time, and non-invasive detection of agrochemical hazards, ensuring safer crop production and environmental stewardship.

#### 2.4.4.5 **Signal stability**

Ensuring signal stability is a critical challenge for smart agricultural TENG applications, given the ubiquitous mechanical triggers and baseline fluctuations driven by environmental variability. Seasonal cycles expose devices to fluctuating humidity, temperature extremes, particulate contamination, and chemical stressors, all of which can induce signal drift, baseline offsets, and spurious event generation. Baseline shifts reduce measurement accuracy by altering the reference level, leading to false positives or missed detections, while random peaks and poorly tuned triggers introduce noise-related errors that lower sensing reliability.

A prominent example of a bio(chemical) stressor is persistent biofouling from agricultural pests, which can alter triboelectric performance by modifying surface morphology, chemistry, and contact mechanics. Organic residues (e.g., secretions, frass, cuticular wax) can locally change surface energy, increase ionic conductivity, and accelerate charge leakage. Repeated contact or abrasion can shift the triboelectric operating point and induce micro-scratching, reducing contact uniformity. Such cumulative effects compromise electrical output and hinder the long-term stability of TENG-based smart sensors in agricultural settings. Addressing these issues requires a combined strategy that leverages both advanced functional materials for environmental resilience and machine learning–assisted signal processing for real-time correction and noise suppression.

From a hardware perspective, anti-fouling or antimicrobial surface treatments,[175,285] encapsulation,[286] and protective coatings (e.g., inert fluoropolymers or superhydrophobic films)[176,287] can act as physical and chemical barriers to moisture ingress, particulate fouling, and ionic contamination. Fluoropolymers like PTFE provide extremely low surface energy and high dielectric strength, minimizing water adsorption and preventing charge leakage through thin moisture films.[288,289] Micro/nanotextured engineered surfaces can further reduce water–surface contact and limit adhesion of dust and organic debris.[209,211] When properly engineered, these protective layers slow surface oxidation and wear, extending operational lifetimes and maintaining stable baseline outputs under seasonal exposure cycles.

Beyond material protection, stability can be actively maintained through machine learning–assisted signal processing, enabling adaptive baseline recalibration and intelligent noise rejection in real-time. State-of-the-art models can learn the characteristic time–frequency signatures of genuine agronomic events (e.g., pest movement, irrigation flow) and distinguish them from environmental artifacts such as wind-induced vibrations, raindrop impacts, or particulate collisions.[10,290–292] Continuous or periodic retraining with in-field data allows adaptation to gradual drift, electrode degradation, and contamination effects. In distributed TENG sensor networks, consensus-based validation across multiple nodes can further suppress spurious readings, enhancing robustness, specificity, and delivering high-confidence outputs for precision agriculture.

To translate these concepts into practice, we propose a signal-processing pipeline that integrates primary signal conditioning, baseline stabilization, event discrimination, and edge inference to enable reliable long-term operation of TENG-based sensors under variable conditions. Specifically: (i) primary signal conditioning through normalization and noise-aware filtering of raw TENG outputs to reduce variability from environmental perturbations;[10,293] (ii) baseline stabilization with

Kalman filtering to correct drift from humidity or temperature;[294–296] (iii) signal characterization and discrimination, combining feature extraction (e.g., wavelet analysis for impulsive, variable-frequency signals) with artifact rejection via multi-sensor consensus to suppress spurious events from wind, rain, and particulates; and (iv) lightweight machine-learning models (e.g., ML-scale or neighborhood linear discriminants) updated through continual learning to adapt to seasonal drift and electrode degradation.[297,298]

Signal separation can be strengthened by exploiting meso-scale patterns that define genuine agronomic events (e.g., pest motion detection) in contrast to the broadband, quasi-random signatures of wind and rain. Conventional approaches such as recurrence quantification and cyclostationary analysis remain useful for feature extraction,[299–301] but their specificity is markedly enhanced when coupled with machine learning classifiers.[302] For instance, support vector machines (SVMs) have shown strong performance in distinguishing subtle, overlapping signal classes under noisy conditions.[10,303] In combination with wavelet-based decomposition, SVMs can identify nonlinear decision boundaries that separate agronomic signals from environmental artifacts with high accuracy.[304,305] Semi- and self-supervised pretraining on unlabeled TENG data can stabilize classifiers trained on limited labeled sets,[10,302] while periodic self-calibration during low-activity periods allows models to refresh priors without manual intervention. Implemented on low-power edge processors, these strategies enable real-time operation, transforming smart TENG sensors from passive harvesters into adaptive, self-correcting systems capable of stable performance under fluctuating conditions.

Ultimately, ensuring long-term reliability of TENG-based agricultural sensors requires an integrated approach that balances device engineering with intelligent data management. Advances in functional materials can delay physical and chemical degradation, while adaptive data analytics can compensate for residual drift and

environmental interference. By distinguishing genuine events from artifacts, machine learning improves both sensitivity and specificity. Together, functional materials and intelligent signal processing allow TENG sensors to sustain accuracy and reliability across multi-season deployments, reinforcing their role as key components of precision agriculture.

### 2.4.5 **Sustainability**

Given environmental pollution and climate change concerns, developing eco-friendly, biodegradable nanogenerators will further contribute to green energy technologies. Therefore, concerns regarding biodegradability, LCA, and toxicity of these devices must be discussed to promote their sustainable implementation in agricultural environments. This review aligns the United Nations' 17 Sustainable Development Goals, with a particular focus on:

- Goal 2 – Zero Hunger: by enabling precision agriculture and real-time monitoring, TENGs support improved food production and sustainable farming practices;
- Goal 6 – Clean Water and Sanitation: TENGs facilitate autonomous water quality monitoring and promote efficient resource management in agricultural systems;
- Goal 7 – Affordable and Clean Energy: by harvesting ambient mechanical energy, TENGs offer low-cost, renewable power solutions for agricultural technologies;
- Goal 11 – Sustainable Cities and Communities: TENGs contribute to smart rural infrastructure through self-powered sensors and sustainable energy systems;
- Goal 12 – Responsible Consumption and Production: the use of biodegradable and recyclable materials in TENGs supports waste reduction and circular economy strategies;
- Goal 15 – Life on Land: TENG-based sensors enable environmental monitoring that aids in conserving terrestrial ecosystems and promoting sustainable land management.

#### 2.4.5.1 **Biodegradability**

The key challenge is to manage the degradation of nanogenerators. The operational lifespan may fall short of meeting application requirements if degradation is too swift. Conversely, excessively slow degradation may result in substantial environmental impacts. For instance, if a nanogenerator is intended to cover a specific area within a food production field, it is essential to acknowledge that the prolonged use of the device and its biodegradation could alter environmental conditions. For example, when PLA is employed as the active layer in nanogenerators and undergoes composting, it produces lactic acid, carbon dioxide, and water.[306,307] Consequently, its use can alter the pH and potentially affect the soil, either causing harm or promoting the growth of plants or bacteria.

Controlled degradation, even if sustained, risks releasing toxic substances such as bisphenol-A (BPA) and other metals (Pb, Cu, Cd), contaminating groundwater and adversely affecting water quality. [308–310] Addressing these concerns requires careful planning during the nanogenerator design, considering potential adversities and interferences throughout its intended lifespan. Predicting long-term climatic conditions is challenging, but estimates can be made by primarily focusing on the mechanical drive of the device to modulate degradation and recognize the loss of electrical efficiency, predicting its operational lifespan. To mitigate these potential environmental hazards, pH-responsive functional materials can be employed in the development of self-immolative polymers, degradable macromolecules capable of translating a single bond-cleavage event at the polymer terminus or within the backbone into a cascade of depolymerization reactions.[311] By carefully tailoring the trigger conditions, such materials can enable TENGs to maintain long-term electrical and functional performance during their service life, yet undergo controlled breakdown at end-of-life into benign,

environmentally assimilable byproducts. This approach not only aligns with eco-design principles but also offers a means to reconcile operational durability with post-use environmental compatibility.

Furthermore, despite the world's current transition to eco-friendly materials, there has been an increase in the number of companies adopting green marketing strategies and labeling products with more environmental benefits than they actually have, a marketing process called "Greenwashing".[189] Greenwashing involves misleading consumers about a company's environmental practices or the environmental benefits of its products or services, e.g., claiming material biodegradability without verifying it. For a material to truly be considered biodegradable, e.g. in soil, the following four stages must be observed: (i) (bio)deterioration, (ii) (bio)fragmentation, (iii) assimilation, and (iv) mineralization.[189] Therefore, only after the mineralization stage, which is recommended to be measured by the evolution of $CO_2$ and/or $CH_4$ gases through standardized respirometry (ISO 14852), can the material be properly considered biodegradable. Thus, the biodegradation process can stop at any stage. Therefore, a strict biodegradation monitoring process must be carried out by government agencies and entities, aiming not only to combat greenwashing but also to guarantee the use of more environmentally friendly materials.

In that regard, using stable materials like PDMS as the active layer and stainless steel as the electrode remains a viable solution. Despite initial material costs, these choices offer high stability and minimal environmental impact over the device's lifespan, offsetting the initial investment. In the context of environmental impact, an often-overlooked aspect is the LCA of the entire device. Conducting a comprehensive assessment of the device's LCA aids in understanding its environmental implications and supports informed decisions regarding the sustainability of nanogenerators.

#### 2.4.5.2 **Life cycle assessment (LCA)**

LCA is a comprehensive method to compare the environmental effects of goods and services by quantifying all inputs and outputs of elementary flows, assessing how these flows may impact the environment.[312] It is commonly known as "cradle to grave," involving collecting data at all stages of a product's life cycle, comprising four key steps: definition of objective and scope, inventory analysis, assessment of environmental impacts, and interpretation.

In the initial step, the product under evaluation is defined along with its function for comparison with other products, specifying the required level of detail.[313] The second step involves collecting data on materials, energy consumption, and emissions throughout the product's life cycle. In the third step, impacts are assessed, with the defined inventory flows transformed into environmental impacts using equivalence factors, such as kg of $CO_2$ equivalent for the global warming category.

The final step involves evaluating the results of the inventory analysis to identify significant issues, aiding in the selection of the preferred product, process, or service. This assessment also checks the integrity, sensitivity, and consistency of the results, considering a clear understanding of the uncertainties and assumptions used in result generation.[313]

The ISO 14040 series of standards governs the structure, principles, requirements, and guidelines for LCA studies. This series emphasizes the high degree of interaction among its four steps, outlined in:

- ISO 14040 – General principles (1997)
- ISO 14041 – Definition of objective, scope, and Inventory of Consumables and Outputs (ICV) (1998)
- ISO 14042 – Life Cycle Impact Assessment (LCIA) (2000)
- ISO 14043 – Interpretation (2000)
- ISO 14040 – General principles (2006)

- ISO 14044 – Requirements and guidelines (2006)

It is crucial to note that LCA is a decision-making tool that should complement other criteria, such as cost and performance, to facilitate a balanced decision-making process.

#### 2.4.5.3 **Toxicity**

Toxic substances, such as heavy metals, are naturally occurring elements vital for survival in the environment. However, their accumulation in organisms can pose significant dangers. Humans can be exposed to toxic substances through various routes, including ingestion, inhalation, and dermal contact. Elevated levels of essential or non-essential trace elements may result in physiological abnormalities, morphological changes, or genetic mutations, leading to growth retardation or mutagenesis. Therefore, using heavy metals as a component in nanogenerators must be avoided or their release into the environment must be completely inhibited, e.g., by encapsulating with stable thermosetting polymers.

As shown in **Figure 2.12**, PTFE, acrylic, and PDMS are widely employed as polymeric dielectrics in TENGs for agricultural applications due to their excellent flexibility, chemical stability, ease of processing, and favorable triboelectric properties that enable efficient energy harvesting from mechanical stimuli in outdoor environments. However, these materials pose significant environmental concerns: they are non-biodegradable, persist in ecosystems as microplastics or stable polymers, and their production often involves toxic precursors or byproducts, such as perfluorinated compounds in PTFE. Additionally, the precursors of PDMS, such as uncured siloxane oligomers and chlorosilanes, are toxic to humans, posing risks of skin irritation, respiratory harm, and environmental contamination prior to full curing into its inert elastomeric form.[314,315] The accumulation of these synthetic polymers in agricultural soils

can disrupt microbial communities, affect soil health, and contribute to long-term pollution, emphasizing the need for the development of biodegradable alternatives and more sustainable fabrication methods for TENG deployment in agriculture.

Therefore, the exploration and development of more sustainable and biodegradable alternatives, even if currently less efficient, is essential to mitigate the overall toxicological footprint of nanogenerators deployed in agricultural and environmental applications. For example, cellulose-based materials,[316] chitosan,[168] silk fibroin, and poly(lactic acid) (PLA)[317] have been explored as eco-friendly dielectrics for TENGs, offering reduced environmental persistence. Likewise, natural rubber and bio-based polyesters are being explored as flexible triboelectric layers.[318] In terms of electrodes, carbon-based materials such as graphene, carbon nanotubes, or conductive inks derived from biomass (e.g., carbonized lignin)[168] are gaining attention as low-toxicity alternatives to conventional metal electrodes. Additionally, the use of naturally derived additives, e.g., plant-based plasticizers or green cross-linkers, such as tannic acid and citric acid,[318,319] can further reduce the reliance on synthetic and potentially hazardous compounds in TENG fabrication.

Mercury, cadmium, arsenic, chromium, nickel, copper, and lead are among the most common heavy metals contaminating the environment.[320] Copper, particularly, is widely used in nanogenerators as an inductive component or for data transmission wires. The bioaccumulation of heavy metals in agricultural settings poses risks to human health by potentially transferring pollution from soil and water into the food chain. Moreover, industrial chemicals, organic solvents, plasticizers, nanomaterials, and other toxic substances should be avoided as components in nanogenerators whenever possible. Volatile Organic Compounds (VOCs), such as benzene, formaldehyde, and toluene, are notable examples due to their propensity to evaporate into the atmosphere, contributing to air pollution and posing direct health risks to agricultural workers through inhalation.[321–323] Plasticizers can also leach into the environment through

exudation, contaminating air, water, and soil.[324,325] Their unbound nature allows for leaching, especially under heat, humidity, or mechanical stress, which are often encountered in mechanical nanogenerators used in agricultural applications.

With the rapid development of nanotechnology, vigilance is required to monitor nanomaterials indiscriminate use. Nanomaterials exhibit unique properties due to their nanoscale dimensions, which can lead to concerns regarding their potential toxicity to living organisms and the environment. Materials such as gold nanoparticles, carbon nanotubes, and titanium dioxide nanoparticles exhibit unique toxicological properties owing to their small size, high surface area, and ability to interact with biological systems.[326,327] Despite the enhancement of nanogenerator output through the use of $TiO_2$ nanoparticles with increased dielectric constants in active layers, their entry and accumulation within cellular structures pose health risks.[328]

Given the significance of food crops in human nutrition, the use of devices containing highly toxic materials in agriculture should be regulated or prohibited. It is imperative to explore less toxic alternatives that are equally effective for energy harvesting applications in agriculture. Additionally, concerted efforts by governmental bodies and regulatory agencies, such as Food and Agriculture Organization (FAO), World Health Organization (WHO), and the European Chemicals Agency (ECHA), are necessary to establish protocols for monitoring the release of toxic compounds from exposed devices, particularly nanogenerators, into the environment. Such measures are crucial for combating the indiscriminate and hazardous use of materials that jeopardize both quality of life and human health.

## 2.5 Challenges of nanogenerators performance in agriculture environments

An investigation into nanogenerators reveals a network of operational, structural, and environmental factors that affect their electrical output efficiency and structural stability. The challenges intensify when nanogenerators are deployed in uncontrolled environmental conditions, such as those encountered in agricultural environments. In pursuit of meeting standards for energy harvesting or sensor monitoring, we outline key factors shaping nanogenerators performance. This offers insights to optimize or sustain overall efficiency, particularly in challenging environmental conditions.

### 2.5.1 Relative humidity

Humidity levels significantly influence the performance of nanogenerators by affecting their charging and discharging behaviour. This occurs by forming water films on plastic surfaces, disrupting surface polarization between active layers and reducing surface charge density **(Figure 2.14a)**. For example, high atmospheric water content can also discharge charged layers by adsorption or surface layer formation.[329] Furthermore, the loss tangent (tan δ) is known to be very sensitive to humidity, which affects the efficiency of the dielectric material in storing electrical energy.[330] A higher value of tan δ indicates more excellent energy dissipation, while a lower value indicates that the material is more efficient in storing energy with less loss.

Nanogenerator performance is further impacted when active layers are made with hygroscopic materials like PET, ABS, or cellulose derivatives containing free hydroxyl groups. Incorporating hygroscopic salts such as $CaCl_2$, $MgCl_2$, or NaCl into devices is critical, as they facilitate the formation of water layers. Mule et al. demonstrated that enclosing TENG devices in pouch-type polyethylene bags preserves stable

output voltage even with rising humidity levels, underscoring the importance of environmental moisture management.[331] For instance, the pouch-type nanogenerators maintained a consistent output $V_{OC}$ value of ~400 V despite a rise in humidity from 35 to 81%. Conversely, the nonpouch-type device experienced a reduced $V_{OC}$ value from 400 to 105 V under similar conditions.

### 2.5.2 **Temperature**

The effect of temperature on energy harvesting is significant, elevated temperatures typically lead to decreased output performance in nanogenerators due to three critical properties in materials that directly correlate with capacitance and electrical output in nanogenerators: (i) phase transitions, (ii) thermal expansion, and (iii) dielectric constant.

Nowadays, recent efforts to increase the electrical output in nanogenerators have focused on hybridizing with piezoelectric materials to enhance capacitance. However, temperature changes primarily influence these materials' polarization, which is crucial for their piezoelectric properties. For instance, many piezoelectric materials undergo phase transitions at specific temperatures, e.g., the Curie temperature ($T_c$), above which they lose their piezoelectric characteristics. This transition generally involves a shift from a ferroelectric phase, with spontaneous polarization, to a paraelectric phase, where such polarization is absent. Consequently, the piezoelectric properties are only useful below their $T_c$. The temperature dependence of polarization in ferroelectric and piezoelectric materials can be better understood through the modified Curie-Weiss law (Equation 2.9).[332]

$$\frac{1}{\varepsilon_r} = \frac{1}{\varepsilon_m} + C(T - T_C)^{\gamma} \tag{2.9}$$

where $\varepsilon_r$ is the relative permittivity, $\varepsilon_m$ is the maximum dielectric permittivity at transition temperature $T_c$, $T_c$ is the Curie temperature, $T$ is absolute temperature, and $\gamma$ is a measure for the degree of diffuseness ranging from 1 to 2, obeying the equation to

Curie–Weiss law which is the character for the case of normal ferroelectric and for an ideal relaxor ferroelectric.[332,333]

Thermal expansion also affects the lattice parameters and symmetry, influencing the electric dipole moments within the material.[334,335] For example, a transition to a more ordered phase can improve charge transfer efficiency due to enhanced electron mobility, smoother surfaces, better-defined interfaces, and reduced defect sites. While disordered phase can reduce efficiency due to increased charge trapping.[336] Therefore, minimizing thermal expansion is essential to reduce fluctuations in electric output and maintain material integrity and stable interfaces between electrodes and dielectrics. To understand thermal expansion's effect on the dielectric constant, Ren et al. developed a model linking the dielectric constant to the thermal expansion coefficient of PDMS over a specified temperature range (0 to 50 °C).[337] This model can be employed to normalize electrical outputs, thereby reducing fluctuations and noises, enhancing its utility in smart agricultural applications.

Regarding the dielectric constant of materials, it varies with temperature due to changes in the material's capacitance and its ability to store electric charge. Polarization in these materials primarily arises from the alignment of molecular dipoles and the displacement of bound charges under an electric field. Increasing temperature enhances the thermal motion of molecules, which can disrupt dipole alignment, thereby decreasing net polarization.[338–340]

Relaxation times are also temperature-dependent, increasing with decreasing temperature as molecular mobility decreases. At higher temperatures, relaxation times decrease, allowing dipoles to reorient more freely and respond to higher frequencies.[341] However, the increased thermal agitation at higher temperatures tends to randomize dipole orientations, reducing net alignment and overall polarization.[342] Additionally, higher temperatures lead to greater dielectric losses, where energy is dissi-

pated as heat, reducing the energy stored as polarization. Therefore, despite the reduction in relaxation time at higher temperatures, the dominant effect of increased thermal agitation and dielectric losses disrupts dipole alignment and leads to a net decrease in the dielectric constant.

Beside those effects, the high temperature can cause the dissipation of charges through thermionic emission. Cheng et al. investigated the thermal difference between the hotter and cooler active layers, revealing that as temperatures rise from 0 to 219 K, the electrical output performance of the nanogenerator exhibited an initial increase followed by a subsequent decrease, with the optimal $\Delta T$ output occurring at approximately 145 K.[343] This pattern arises from a trade-off between electron transfer from hotter to cooler friction layers and thermionic emission-induced electron discharge from the cooler layer. Lu et al. contributed additional evidence supporting the optimal electrical output trend across temperature variations by maintaining consistent temperatures between the active layers and the environment.[344] They also observed a reduction in $V_{oc}$, $I_{sc}$, and $\Delta Q_{sc}$ as temperatures elevated from -20 to 20 °C. This behaviour can be attributed to variations in the relative permittivity of the active layer with temperature, impacting charge storage capacity.

Moreover, material properties undergo changes with temperature fluctuations. As temperature increases, materials become more ductile and less stiff, potentially improving contact area effectiveness. For instance, when using amorphous polymers as active layers, this behaviour occurs as temperatures exceed their glass transition temperatures ($T_g$), shifting from a glassy state to a rubbery flow. Additionally, the loss of plasticizers (e.g., bisphenol type A, and Dioctyl Phthalate) and other additives from plastics at $T > T_g$ alters the material's dielectric constant, consequently affecting electrical output.

Given that the charge accumulation capacity is directly proportional to the dielectric constant, devices experiencing significant variations in dielectric constant with

temperature will witness pronounced alterations in efficiency, particularly in outdoor environments such as agriculture. For example, temperature-sensitive materials such as water exhibit a significant dielectric constant drop, decreasing from ca. 80 to 58 as the temperature increases from 20 to 90 °C **(Figure 2.14b)**, resulting in a considerable decline in energy conversion efficiency.[345,346] On the other hand, PDMS exhibits only ca. 6% variation in its dielectric constant across the same temperature range, underscoring its high potential for use in environments with significant temperature fluctuations.[340] However, considering the sensitivity of materials to temperature fluctuations, careful placement of nanogenerators and the selection of temperature-resistant materials must be taken into account, particularly in agricultural and sensing applications.

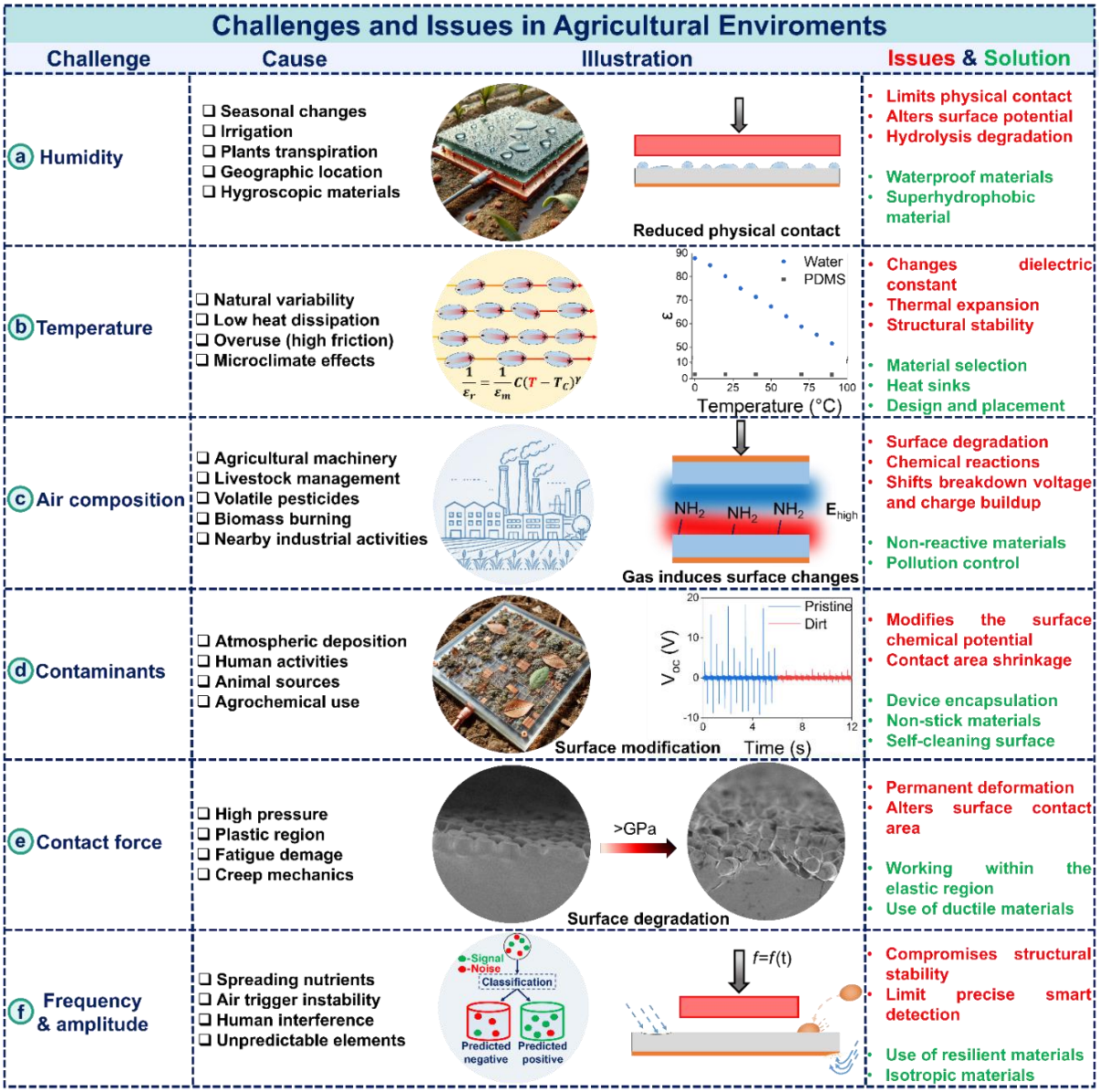


**Figure 2.14.** Comprehensive overview of the challenges and issues faced by nanogenerators in agricultural applications, which compromise the reliability and efficiency of electrical output**.** (a) Humidity effects are shown by the formation of a water layer on the surface. (b) Temperature effects are depicted by the reduction in dielectric constant due to the thermal motion of molecules, disrupting dipole alignment. (c) Changes in air composition catalyses chemical modifications on the nanogenerators' surface. (d) Contaminants are illustrated by natural dirt accumulation, reducing the effective contact area. (e) Contact force demonstrates the permanent degradation of a patterned surface under high pressure. (f) Frequency and amplitude of triggers affected by unpredictable elements and interferences increase the noise signal.

### 2.5.3 **Air composition**

Chemical modifications and catalysed aging are expected to occur on the surface of nanogenerators over time. Since reactive gases such as ammonia, volatile organic compounds, methane, and sulphur dioxide are commonly found in agricultural environments, chemical reactions on the surfaces of nanogenerators can be catalysed, especially given the high electric field and occasional electrical discharges generated by the nanogenerator's operation **(Figure 2.14c)**. These changes alter surface properties, primarily impairing smart applications.

Considering the generation of ultra-high voltage by nanogenerators, comprehending air breakdown and composition's impact on performance is crucial to avoid efficiency losses.[202] Notably, air breakdown leads to the premature release of triboelectric charges before they can be fully induced in the external circuit, resulting in induced charges that are typically smaller than produced. It is noteworthy that triboelectric charges may also induce sparking discharge and ionization of the atmosphere, attracting opposite charges in the atmosphere at trace levels, altering the surface composition.[347]

Paschen's Law curves can be used to accurately assess the impact of ambient conditions on nanogenerator performance. It provides insights into the breakdown voltage of a gas between two electrodes under different pressures and electrode distances, offering predictions for the behaviour of electrical discharges in gases.[348] Zi et al., observed that increasing air pressure elevates the threshold breakdown voltage due to the reduced mean free path and kinetic energy of electrons.[348] Conversely, at pressures around $10^{-6}$ atm, air breakdown requires electrode distances of approximately 3 m due to the ultralow density of air molecules, indicating negligible air breakdown effects for typical nanogenerators with small sizes and limited displacements in ultralow-pressure environments.[348] Concerning gas atmospheres, $SF_6$ exhibits consistently higher

breakdown voltages compared to air due to its higher molecular weight, which makes it more resistant to electron ionization.[349]

Zheng et al. demonstrated that gas concentration and pressure directly influence the ionization process, which involves the breakdown of gas molecules into ions and electrons.[350] Therefore, to accurately assess the impact of $CO_2$ concentration on the electrical output of TENGs, ionization voltage values were used instead of open-circuit voltage (Voc). Their findings revealed that increasing the atmospheric $CO_2$ concentration from 10% to 90% raised the ionization voltage from 700 to 1500 V. This occurs due to the ionization characteristics of $CO_2$ gas, which allow it to ionize more readily under a high electric field. As the concentration of $CO_2$ increases, more molecules are available for ionization, leading to a higher rate of ionization events. $CO_2$'s lower electron affinity compared to other gases facilitates electron capture, resulting in more negative ions. This enhances the ionization efficiency as more $CO_2$ molecules collide with accelerated electrons, creating a chain reaction or avalanche effect that amplifies the ionization process. Consequently, the increased density of ionized $CO_2$ particles boosts the charge density and strengthens the local electric field, leading to a higher voltage output.

Furthermore, Ghosh et al. demonstrated that the hydrophobicity of PDMS is compromised due to various aging processes, including electrical discharge, UV radiation, thermal aging, and exposure to high-intensity rain during its service life.[351] The extent of degradation is significantly greater when the sample was subjected to intense UV radiation for a short duration compared to natural aging under typical sunlight conditions experienced by actual insulators in service. Two primary mechanisms are associated with surface modification in PDMS: chain scission and cross-linking of fragmented chains under adverse environmental conditions, e.g., UV radiation. The natural aging process in service is a complex series of reactions that can lead to not only

chemical degradation of PDMS' surface but also physical damage to the bulk, including cracking and erosion caused by environmental factors like sandstorms, acid rain, and electrical discharge.

Gorin et al. demonstrated that the static electric field influences the potential energy surface of the reaction and catalyses epoxide rearrangement by altering the activation barriers.[352] This, in turn, affects the reaction rates and leads to the formation of electrochemical double layers at the $Al_2O_3$-solution interface. Additionally, electrical discharge, such as corona discharge, impacts surface properties by transforming the hydrophobic surface of PDMS into a hydrophilic one.[353] Therefore, caution in the arrangement of nanogenerators is crucial. Although the effect of atmospheric composition and pressure might initially appear negligible, the accumulation of gases in microenvironments, especially near factories and livestock areas (which release significant amounts of $CH_4$ and $CO_2$ during enteric digestion and fermentation), can alter the surface charge density capacity of nanogenerators.[347,354,355] This can also compromise smart applications where discharges, such as ionization, are used for food sterilization and water treatment. Thus, understanding the environmental variations where the nanogenerators will be deployed is essential to ensure not only high efficiency but also reliability and stability in their electrical output for smart applications.

Therefore, in the context of smart applications where surface properties should be altered solely through analyte interaction, the reliance of nanogenerator performance on air decomposition and environmental conditions becomes a significant concern. Given that dirty air compositions with high particle density tend to accumulate on material surfaces, implementing strategies to protect these surfaces is essential. This can be achieved, e.g., through device encapsulation, atmospheric composition control, and the development of self-cleaning surfaces. Furthermore, such understanding contributes to nanogenerators not only offering high performance but also remaining suitable for smart applications.

### 2.5.4 **Contaminants**

Surface contamination in nanogenerators can be considered one of the main challenges impacting their performance within agriculture. This is because contamination reduces the effective contact area between the surfaces of the nanogenerators (which have optimal charge transfer efficiency at distances <10 Å). Additionally, contamination can modify the surface potential and surface charge density by spreading across it and creating a dirt-based coating **(Figure 2.14d)**.

While protective packaging can mitigate certain contamination challenges, it often introduces trade-offs that compromise the core functionalities of TENGs. Encapsulation may hinder the surface accessibility required for sensing, obstruct stimulus exposure critical for photonic or chemical monitoring, and restrict the mechanical motion necessary for TENG-based actuation systems. For instance, active TENG sensors must remain exposed to detect environmental cues – e.g., organic compound and pesticides,[356,357] gases,[207] and heavy metals[206] - an interaction precluded by traditional packaging. These limitations are particularly detrimental in agricultural and environmental contexts, where dynamic, unfiltered interaction with ambient stimuli is essential for optimal performance of smart systems.

Although packaging may temporarily reduce dust and dirt deposition, it also inhibits the removal of nanomaterial residues and particulates that accumulate over extended operation. This buildup can reduce the effective contact area and degrade charge transfer efficiency, both of which are critical for sustained TENG performance. Therefore, rather than proposing packaging as a universal solution, we emphasize a materials-informed design strategy that prioritizes self-cleaning mechanisms, dirt-degrading surfaces, and air-cleansing functionalities. Such approaches preserve functional exposure while enhancing environmental resilience, enabling TENGs to operate reliably in unstructured, real-world agricultural settings, especially for smart applications.

Contaminants can be both abiotic and biotic, with the latter often forming biofilms. A biofilm is a sessile microbial community with cells irreversibly attached to a surface or each other, embedded in a self-produced matrix of extracellular polymeric substances and exhibiting altered growth and gene transcription.[358,359] This is particularly common in dielectrics made from polysaccharides (e.g., cellulose derivatives and chitosan), proteins (e.g., gelatin and casein), and polyphenols (e.g., lignin, tannic).[360,361] Biofilm formation on these surfaces alters the surface properties of the nanogenerators, impacting charge accumulation density and the reliability of electrical output, and it also degrades the physical integrity of the dielectric over time.

Biopolymers are more susceptible to microbial growth compared to conventional polymers like PET, PE, and PP. This is because many biopolymers have hydrated surfaces that create an ideal environment for microbial proliferation. The presence of functional groups such as hydroxyl, carboxyl, and sulphate facilitates attachment through chemical interactions, such as hydrogen bonding, enhancing bioaffinity and colonization.[360,361] When ionized or dissociated, these groups also promote physical interactions, like electrostatic adhesion, with cell surfaces.[362] Furthermore, microorganisms can utilize these polymers as sources of carbon and energy by releasing enzymes such as amylases, cellulases, and chitinases that break down polysaccharides into simpler sugars that are readily metabolized [359,360]. Therefore, the development of nanogenerators using biopolymers must account for biological interactions, ensuring that changes in device performance are anticipated, particularly in agricultural environments.

Considering abiotic contamination, countless types of particles, dirt, debris, and chemicals, notably fertilizers and pesticides, can contaminate the surface of nanogenerators in agricultural settings. Two main properties help to understand the impact of each type of contamination on the surface of nanogenerators affecting their electrical charge transfer and, in turn, the energy conversion efficiency of nanogenerators: (i) Young's modulus and (ii) ductility.

Ductility measures a material's ability to undergo significant plastic deformation before rupture or failure. Given that different levels of mechanical stress can be applied to nanogenerators, surface contamination with materials that have high ductility and low resistance to deformation presents the greatest risk of reducing charge transfer. These materials deform under low mechanical stress, significantly increasing their area and physically blocking the initial surface area of the nanogenerator, thus reducing load transfer and electrical output.

On the other hand, materials with low ductility (brittle materials) are less capable of plastic deformation. When subjected to low mechanical stresses, they rupture catastrophically, i.e., suddenly and with minimal deformation. Therefore, materials with low ductility will be impacted mainly due to their initially occupied area, presenting a smaller impact on the electrical output than contamination from highly ductile materials.

Conversely, materials with a high Young's modulus, i.e., rigid materials, act as a steric hindrance, reducing the effective contact area between the two surfaces depending on the applied force and surface rigidity. *Section 2.4.1.1* of this article further details the impact of this material property on changes in the effective contact area during the operation of nanogenerators.

Surface chemistry significantly impacts the level of surface soiling, which can be understood through the adhesion properties of both the nanogenerator's material and the contaminants. Strong attractive forces between these materials can keep the surface dirty, even when external forces like wind, rain, and the nanogenerator's operating mechanism could otherwise remove them. Therefore, it is essential to study the chemical surface properties of the materials to reduce attractive forces. This can be achieved by lowering high surface energy or conferring self-cleaning characteristics, ensuring consistent electrical output and long lifespan for the device.

An important consideration is that, despite the qualitative description of the effects of dirt based on their physical and chemical properties, precisely classifying or quantifying the impact of this dirt is challenging. This difficulty arises because, during the operation of nanogenerators, fragile materials with low deformation (i.e., low ductility) can fragment numerous times, significantly increasing their effective area covered on the surface of the nanogenerator. Depending on the adhesion forces, new and light fragments can be easily removed, reducing the initial impact of the dirt, or they can remain on the surface, increasing the steric effect. Therefore, precisely classifying the level of impact of each type of dirt, considering the numerous factors inherent to the environment and the functioning of the nanogenerator, is difficult. However, this challenge also presents opportunities for research aimed at understanding how contamination interacts with the surface and how stable and impactful it is for the performance of nanogenerators.

### 2.5.5 **Contact force**

The contact force represents the mechanical tension applied during the contact between triboelectric layers. Greater tension normally (depends also on stiffness-compatibility) increases the contact surface area, boosting charge transfer and enhancing charge density and potential difference between electrodes. Balancing contact force is crucial to ensure efficient charge transfer without causing excessive deformation or damage to materials. In this context, studying the device's mechanics becomes imperative to identify the elastic region of the nanogenerator's constituent elements, thereby extending its operational lifespan.

For instance, when the elastic region is exceeded, the applied mechanical force can permanently deform the surface material. This issue is more critical when the material is patterned, as illustrated in **Figure 2.14e**. Such permanent deformation alters

the effective surface contact area, modifies charge accumulation on the surface, and hinders stable electrical output, thereby reducing reliability for smart applications.

A significant challenge hindering precise sensing in agriculture is the inconsistent drive force. This issue arises due to the sporadic activation of nanogenerators throughout the day and seasons, even with the integration of energy storage systems like capacitors. Such irregularities threaten the reliable energy supply required for continuous monitoring. To address this, it may be necessary to incorporate supplementary electrical supply sources to ensure uninterrupted monitoring during periods unsuitable for nanogenerator utilization. Notably, for active sensors directly connected to nanogenerators, the absence of external stimulation results in an immediate cessation of monitoring.

### 2.5.6 **Frequency & amplitude**

Drive speed or frequency, referring to the relative velocity of movement between active layers, significantly impacts how quickly charges transfer and the resulting electrical current. Higher speeds lead to faster charge transfer and increased current.[43] As a result, TENG voltage remains invariant regardless of high-frequency fluctuations, while current exhibits a direct proportionality to changes in frequency. Nevertheless, there exists an asymptotic behaviour in the enhancement of electrical output, where a plateau is reached at approximately 5 Hz.[363] Considering the depletion of surface charges due to prevalent leakage currents in dielectric films and the breakdown effect in air,[93,364] adjusting the triggering frequency optimizes electrical output (e.g., power density) by mitigating these losses.

The activation frequency of nanogenerators is significantly influenced in agricultural contexts due to the continuous and unpredictable distribution of nutrients, pesticides, and various triggers throughout the day **(Figure 2.14f)**. For example, variations in airflows and their random impacts on the nanogenerator surface, combined with

the biotic activities of small animals such as ants and insects, introduce substantial noise into the electrical output. For smart applications, the signal-to-noise ratio should be as high as possible; however, classifying false signals as noise in an uncontrolled environment is challenging. This is particularly critical when some nanogenerators have a cut-in speed for $V_{oc}$ generation as low as 1 $m.s^{-1}$,[365] emphasizing the need to functionalize or produce materials only responsive to the desired counterpart material. Furthermore, random impacts can compromise the device's integrity, particularly due to the divergence in mechanical properties between the electrodes and dielectric material, which can introduce wear at the interface due to incompatibility.

The amplitude-motion also strongly affects the consistency of the output signal, as the separation distance between the device and the surface of the counterpart material alters not only the electric field produced but also the rate of electric charge transfer.[366,367] For example, Zhao et al. demonstrated that the movement amplitude changed the $V_{oc}$ from 11 to 16 V by increasing the separation distance between the two surfaces by only 1 mm, while the EMG remained more stable within the same range.[366] However, when comparing energy conversion efficiency at low frequencies (≤5 Hz), triboelectric and piezoelectric nanogenerators outperform EMG. Moreover, it is important to note that piezoelectric nanogenerators benefit greatly from applied force, while the output voltage of TENGs depends more on triboelectric surface charge density and surface area. This means that TENGs can be used for a wider range of motions where the cut-in force applied is minimal, such as sliding and friction, making them useful for movement monitoring.

As highlighted by Cao et al., given the high variability of trigger events during TENG operation, paired power management is essential because the energy harvested from ambient mechanical sources is inherently time-dependent, unstable, and susceptible to environmental changes.[291] This instability, particularly relevant in agricultural

deployments where frequency and amplitude vary unpredictably, necessitates advanced power-conditioning strategies to maintain reliable sensor operation. In line with this, Cao et al. proposed that machine learning algorithms, together with AI technologies, can be leveraged to classify and process large volumes of sensing data.[291]

The need for such tools is underscored by the vast quantity and high randomness of TENG-generated data, often complicated by noise, low signal clarity, or ambiguous outputs in complex environmental conditions, place exceptional demands on accuracy in smart applications.[10] Zhang demonstrated that advanced processing techniques, e.g., principal component analysis (PCA) and convolutional neural networks (CNNs), can learn the characteristic time–frequency signatures of genuine mechanical stimuli, effectively filtering out environmental noise (e.g., wind-induced vibrations, raindrop impacts) and improving detection specificity.[302] Similarly, Wen et al. reported a KNN-based TENG monitoring system achieving >97% classification accuracy for complex motion detection when combined with machine learning.[290] Therefore, in agricultural settings, the integration of IoT platforms with machine learning could enable discrimination between true agronomic triggers and random mechanical artifacts, enhancing sensor sensitivity and reliability even under fluctuating frequency and amplitude conditions.

### 2.5.7 **Impact of co-occurring bio-chemical contaminants on charge transfer efficiency**

In agricultural environments, triboelectric interfaces are rarely subjected to a single stressor; instead, biofilms, mineral scaling, and colloidal suspensions frequently act simultaneously, creating complex and interdependent interactions between TENG surfaces and their surroundings. Biofilms can increase surface hydrophilicity through hygroscopicity,[368–371] elevate ionic conductivity,[372] and introduce viscoelastic damping,[373,374] thereby accelerating charge leakage and reducing effective contact stress.

These effects likely shift charge generation toward ion-dominated mechanisms due to the formation of interfacial water layers. Mineral scaling (e.g., calcium and magnesium salts, sulfates, phosphates from hard water or agricultural additives) can initially enhance triboelectric output by increasing local asperity-induced electric field concentration; however, over time, scaling deposits fill surface microstructures, reducing true contact area and suppressing electron transfer efficiency (as discussed in *Section 2.3.7* and shown in **Figure 2.10**). Colloidal suspensions, e.g., organic debris and fine dust, act as a mobile third-body layer, introducing abrasive wear that promotes (nano)material transfer while simultaneously modifying surface potentials through electric double-layer formation.[375–377]

When these stressors co-occur, they can progressively reduce charge-retention times, degrade signal-to-noise ratios, and alter the prevailing charge-transfer pathway, likely from electron transfer toward ion or (nano)material transfer, especially under high-moisture, particle-rich conditions. Thus, advances in functional and stimuli-responsive materials offer opportunities to mitigate these effects, e.g., through anti-fouling and antibacterial coatings, dirt-degrading or self-cleaning surfaces, encapsulation, sacrificial overlays, and *in-situ* performance monitoring to detect and compensate for electrical output drift during TENG operation. Although systematic studies quantifying the combined impacts of these stressors on charge-transfer efficiency and TENG performance are currently lacking, this remains a promising research direction with the potential to significantly advance mechanistic understanding and enhance device resilience in agricultural applications.

### 2.5.8 **Issues raised**

Nowadays, contact force and frequency are the main challenges thoroughly explored for long-life nanogenerator applications, typically described as long-cycle characterization. However, other significant challenges are often overlooked, for example:

What are the primary contaminants and debris attracted to the surface?

What is the chemical compatibility that attracts these materials to a surface?

How stable is the attachment of these contaminants?

These questions remain unanswered, and similar investigations could be expanded to address other challenges, for instance:

Can variations in humidity or gas composition over prolonged use chemically modify the surface?

How does this behaviour occur and affect the electrical output?

Seasonal temperature changes, especially during summer when thermal expansion is at its peak, can compromise the structural integrity, e.g., reducing contact between the dielectric material and the electrode. How does this affect the calibration for smart sensing applications?

The scenario becomes even more critical when these challenges occur simultaneously in real-world conditions, making accurate calibration and analytical sensing in the agricultural field a significant challenge. Therefore, substantial advancements are needed to address these scientific and technological issues and accelerate the implementation of energy-harvesting technology for smart and precise agriculture. To overcome these challenges, researchers should not only focus on developing nanogenerators with materials not used before but also thoroughly investigate the problems, effects and causes of common issues encountered in agriculture. This comprehensive approach will be essential for advancing energy harvesting technology for smart and precise agriculture applications.

## 2.6 Applications in Agricultural Environments

Since the onset of the Industrial Revolution, marked by the advent of mechanization, the synergy between humans and machines has driven agricultural productivity to meet the demands of a growing population. However, facing imminent population growth requires heightened efforts not only to enhance productivity but also to ensure food safety and sustainable practices. In this regard, technological advancements, particularly TENGs, have emerged as promising solutions to address this challenge, offering both green energy generation and multifunctional applications. In agriculture, TENGs present an opportunity to harvest low-frequency, irregular, and underutilized mechanical energy from the environment, including wind, rain, and water impact and flow. Furthermore, nanogenerators can serve as active sensors, enabling self-powered real-time agricultural monitoring and adaptive production strategies, thereby facilitating the transition from traditional to smart agriculture. To fully leverage the potential of nanogenerators and propel the transition towards Agriculture 4.0, it is essential to explore their applications comprehensively. This section delineates the specific roles of nanogenerators in agriculture, categorized into conventional (power and portable energy harvesting) and smart (food growth stimulation, food quality, air cleaning, and chemical detection) modes.

### 2.6.1 Conventional applications

The most explored form of energy harvesting in nanogenerators is derived from ambient sources, including mechanical vibrations, environmental noises, wind, and liquids. These sources typically exhibit a wide range of frequencies (from a few to hundreds of Hz), which are prevalent in agricultural environments.

#### 2.6.1.1 **Gas energy**

Gas energy, such as wind and breeze air, is renowned for its abundance and environmental sustainability and holds paramount significance in electricity generation. Traditional methods of wind energy extraction, such as electromagnetic induction and turbines, fall short in effectively harnessing random, low-frequency, and low-velocity winds prevalent in agricultural settings due to their inherent limitations, including large physical footprint, high initial wind speed requirements, complex structural designs, and costly manufacturing processes. Hence, nanogenerators emerge as a promising solution for efficiently capturing wind energy in agricultural landscapes, as elucidated through the forthcoming examples.

To advance self-powered crop production, Li et al. developed an all-weather nanogenerator that efficiently harvests wind and raindrop energy for agricultural sensing **(Figure 2.15a,i)**.[12] The device achieved ~20 nC of transferred charge from raindrops at frequencies ≥1 Hz, with stable output across pH levels of 4 to 6, demonstrating adaptability to natural rainfall. Its instantaneous power density reached ~1 $W.m^{-2}$, significantly surpassing conventional single-electrode TENGs. The nanogenerator charged a 1 mF capacitor to 3 V in 100 s. To enhance performance, it was integrated with a raindrop-driven nanogenerator, boosting output power and reducing capacitor charging time for sensors. The system successfully powered a thermohygrometer, pH sensor, and total dissolved solids sensor solely using environmental energy **(Figure 2.15a,ii)**, confirming its feasibility for self-powered agricultural sensing.

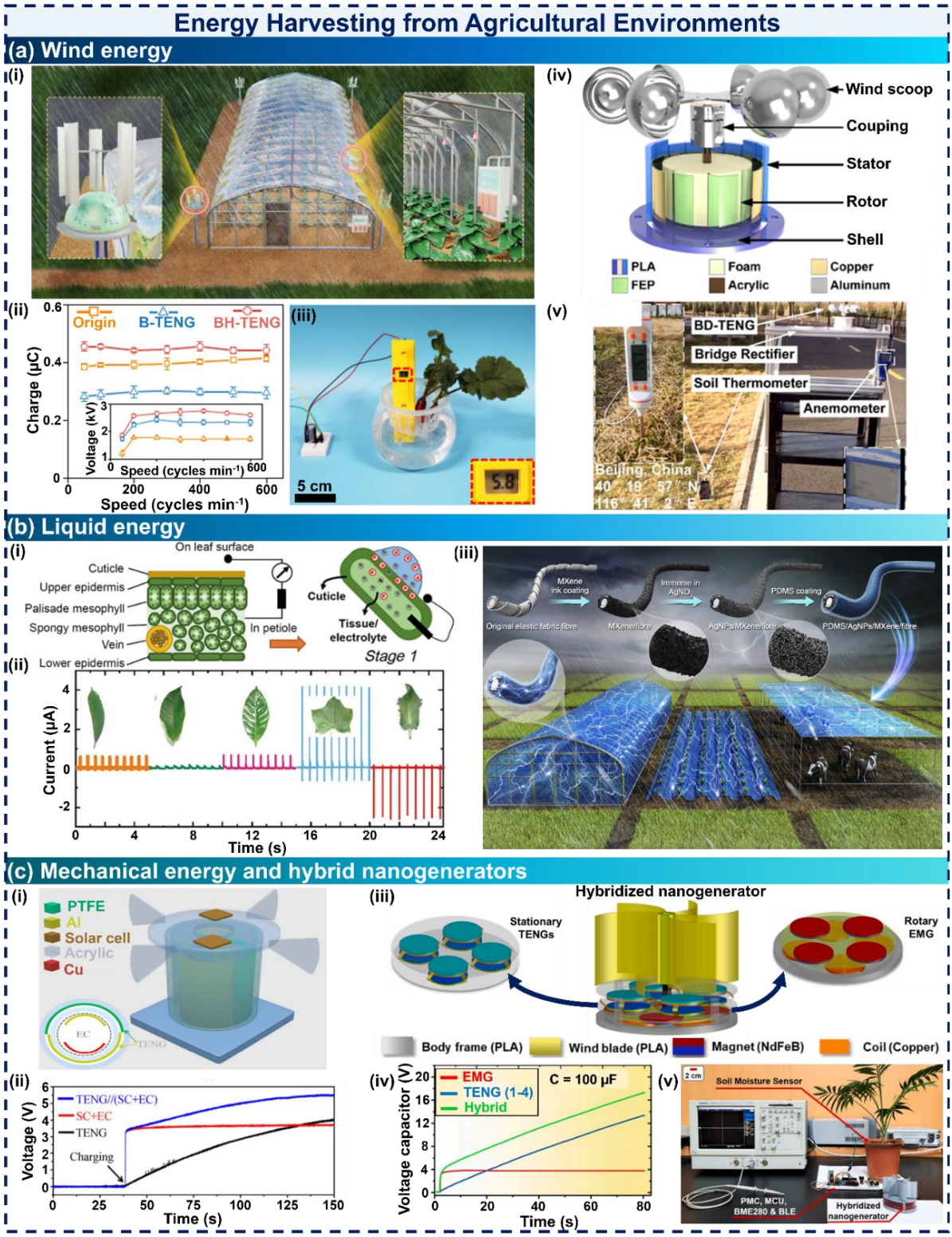


**Figure 2.15.** Schematic illustration of nanogenerators applied as energy harvesters in environmental agriculture. (a,i) Schematic diagrams of the all-weather triboelectric nanogenerator and the self-powered electric field array. (a,ii) maximum charge transferred from three different nanogenerators at various rotational speeds, with the inset showing the output voltage for each nanogenerator under different speeds; and (a,iii) a digital photograph of total

dissolved solids being powered; reprinted with permission from ref.[12] (a,iv) Illustration of the breeze-driven triboelectric structure. (a,v) Digital photograph showing a nanogenerator harvesting natural breeze energy to power a soil thermometer; reprinted with permission from ref.[378] (b,i) Schematic illustration of a leaf cross-section and its external circuit connection. (b,ii) Short-circuit current generated by droplet impacts on leaves from various plant types, reprinted with permission from ref.[28] (b,iii) Schematic illustration of a fabric fiber-based TENG used to construct an intelligent agricultural greenhouse net. (c,i) Schematic diagram of a fabricated hybrid energy cell, with an inset showing the cross-sectional view of the device. (c,ii) Measured voltage of a 10 μF capacitor charged by a TENG, solar cell (SC), electrochemical cell (EC), and the hybrid energy cell (SC+EC+TENG), reprinted with permission from ref.[26] (c,iii) Schematic illustration of a hybridized nanogenerator based on contactless mode triggering, consisting of contact-separation mode triboelectric nanogenerators and a rotating electromagnetic generator. (c,iv) Charging curves of a 100 μF capacitor at 500 rpm. (c,v) Digital photograph of the experimental setup used to power a fabricated soil moisture sensor, reprinted with permission from ref.[379]

Considering the low efficiency of nanogenerators in converting wind energy, especially at low wind speeds, Li et al. increased the energy conversion efficiency up to 12.06%.[378] This enhancement was achieved by selecting low-density materials for the rotor, thereby reducing kinetic energy and friction losses. The wind scoop collects natural wind, propelling the FEP film to create sliding friction against the copper electrode **(Figure 2.15a,iii)**. As a result, the BD-TENG can effectively operate in low wind speed environments, efficiently harnessing breeze energy. The BD-TENG demonstrates an output performance of 330 V, 7 μA, and 137 nC, with a peak power of 2.81 mW at a wind speed of 4 $m.s^{-1}$. In natural environments, it can utilize natural breeze energy to power 300 LEDs connected in series, supplementing plant lighting during the night. It also powers the soil thermometer by collecting energy from the breeze **Figure 2.15a,iv**. Consequently, this nanogenerator holds promise for applications in smart agriculture, where it can collect and utilize low-speed natural wind energy to power soil thermometers, thereby fostering the sustainable development of smart agriculture.

#### 2.6.1.2 **Liquid energy**

Liquid-solid interface for energy harvesting stands as one of the most prevalent energy sources within agricultural environments, encompassing raindrop energy and water flow energy. Rainwater, upon impact with highly sensitive nanogenerators, holds the potential to yield substantial energy output, albeit low-frequency and discrete droplet energies. Conversely, water flow originating from river springs or dew condensation exhibits a more consistent and distributed energy source within agricultural contexts. Harnessing water energy from such sources presents an enticing avenue for supplying distributed energy needs in smart agriculture, thus underlining its considerable promise for future applications.

Wu et al. developed a fully biodegradable TENG composed entirely of natural substances, eliminating the use of plastic materials.[28] The ion-conductive tissue was used as bottom electrode (working as ionic conduction), while the dielectric capacitor and tribo-material were derived from the leaf cuticle. In the external circuit configuration, one end was inserted into the petiole, contacting the conducting liquid within the leaf, while the other end comprised a conductive wire positioned on the leaf blade's surface **(Figure 2.15b, i)**. To assess the broad applicability of the proposed fully biodegradable TENG, various types of leaves were evaluated for their electrical output efficiency through liquid-solid electrification **(Figure 2.15b, ii)**. The electricity generation varied depending on the leaf species, with high and sharp current peaks achievable only with leaves presenting hydrophobic surfaces. Through water impact harvesting, voltage and current outputs exceeding 1 V and 4 μA, respectively, were attained using a *Mytilaria laosensis* leaf. However, leaves with relatively hydrophilic surfaces, e.g., *Michelia champaca* Linn., exhibited broader and lower $I_{sc}$. This phenomenon arises because water residues on the hydrophilic surface maintain a connection between the leaf capacitor and the external circuit, thus keeping the switch in the equivalent circuit

closed. Therefore, the intensity of $I_{sc}$ depends not only on the vibration of the liquid/leaf interface but also on surface wettability. Given the abundance of plant leaves, widespread static charges, and water droplets in nature, the proposed nature-driven nanogenerator could integrate with urban greening initiatives for energy harvesting and sensing and extend its application to other natural materials being a sustainable approach.

Jiang et al. developed a fabric fibber-based nanogenerator for constructing an intelligent agricultural greenhouse net **(Figure 2.15b,iii)**.[380] To enhance electrostatic adsorption and decrease highly reactive particles in the elastic fabric fibre, it was functionalized with MXenes and anchored with Ag nanoparticles. Energy harvesting from water impact yielded an approximate output of 8 V, regardless of whether it was rainwater, distilled water, or tap water. Moreover, considering the harvesting of water flow energy, the output voltage signal becomes denser (after 2.5 $mL.s^{-1}$) as the speed of water flow increases, showing the potential to provide basic information on weather conditions in real natural environments. As a result, the fibrous nanogenerator demonstrates potential for autonomous dynamic force sensing, eliminating the need for external power sources. Moreover, this nanogenerator yarn can serve as rainproof, anti-icing, and sunshade fabric, safeguarding crops and livestock in natural conditions and thereby enhancing agricultural product quality and yield. Therefore, integrating this nanogenerator yarn into fabric enables self-powered monitoring of dynamic forces, presenting a novel approach to smart agriculture.

To draw comparisons between TENGs harvesting energy from gas, liquid, solid, and hybrid sources in agricultural applications, **Table 2.2** outlines their working modes, materials, fabrication processes, electrical outputs ($V_{oc}$ and power density), and specific agricultural challenges (e.g., temperature, humidity, dirt, frequency). These challenges warrant further investigation in future studies.

**Table 2.2.** Overview of triboelectric nanogenerators harvesting energy from gas, liquid, solid, and hybrid sources applied in agricultural environments: energy sources and counterpart materials, working modes, device materials, fabrication and assembly processes, electrical outputs, agricultural challenges, and applications.

| Energy source & counterpart material | Working mode | Device materials | Fabrication and assembly process | $V_{oc}$ peak and power (density) | Agricultural challenge explored | Applications | Ref. |
|---|---|---|---|---|---|---|---|
| **Gas** | | | | | | | |
| Wind (air, FEP) | Hybrid (FT-TENG + EMG) | Acrylic, Cu, FEP, magnets, NdFeB | Hand-made | ~38 V, 118 mW | Speed (2.6-6 $m.s^{-1}$) | Power temperature, and humidity sensors, and fan status | [1] |
| Wind (air, cotton) | FT | Cotton, Cu, PTFE | 3D printing | 2500 V, (2200 $mW.m^{-2}$) | Force (1- 16 N)<br>Frequency (0.5-5 Hz) | Power pH, temperature, and humidty sensors | [4] |
| Wind (air, Cu) | VCS | Acrylic, Cu, magnets, PTFE | 3D printing, laser cutting | 179 V, 0.68 mW | Frequency (1-5 Hz)<br>Humidity (30-90%)<br>Speed (1-5 $m.s^{-1}$) | Power temperature, humidity and light intensity sensors | [365] |
| Wind (air, FEP) | FT | Acrylic, Al, FEP, nylon, PLA, PTFE | 3D Printing | 330 V, 15 mW | Frequency (100-900 rpm) | Power temperature and soil thermometer sensors | [378] |
| Wind (air, PTFE) | VCS | Acrylic, Al, PTFE, nylon, PLA | 3D Printing | 360 V, (35 $mW.m^{-2}$) | Speed (1.5 $m.s^{-1}$)<br>Humidity (30-90%)<br>Temperature (15-45°C) | Power temperature and hygrometer sensors | [381] |
| Wind (air, PTFE) | VCS, FT | Corn husk, Cu, epoxy, glass, PTFE | 3D Printing, casting | 3200 V, ~5000 W | Frequency (30-300 rpm) | Power temperature, humidity, light intensity, and soil moisture sensors | [382] |
| Wind (air, PTFE) | FT | PET, PTFE, PU, Steel | Hand-made | 6 kV, 178 mW | Frequency (60-180 rpm)<br>Humidity (30-90%) | Power hygrothermograph and soil thermometer sensors | [383] |

| | | | | | | | |
|---|---|---|---|---|---|---|---|
| Wind (air, PDMS) | SE, VCS | Al, cotton, leaves, PDMS, silk, SUR-MOFs | Hand-made | 14 V, (450 $mW.m^{-2}$) | Speed (1-5 $m.s^{-1}$) Humidity (0-80%) | Wind speed sensor | [384] |
| Wind (air, HEC) | VCS | Acrylic, HEC, ITO, PDMS | Hand-made | 600 V, 3.2 mW | Frequency (1-4 Hz) Speed (0.5-10 $m.s^{-1}$) Temperature (10-40°C) Humidity (40-80%) | Wind vector sensor | [385] |
| Wind (air, ecoflex) | Hybrid (VCS-TENG + EMG) | Ecoflex (00-30), Cu, magnets (NdFeB-N35), PTFE, steel | 3D Printing | 220 V, 68 W | Speed (3.6-9.6 $m.s^{-1}$) | Power small electronics, temperature, humidity, and light intensity sensors. | [386] |
| Wind (air, Cu) | Hybrid (VCS-TENG + EMG) | Cu, FEP, magnets | 3D Printing | 92 V, 212 W | Speed (1-10 $m.s^{-1}$) | Power micrometeorological monitoring system | [387] |
| Wind (air, Al) | VCS | Acrylic, Al, EPE, kapton | Hand-made | 62 V, (11.7 $mW.m^{-2}$) | Frequency (1-5 Hz) | Power hygrothermograph sensor, and wind vector sensor | [388] |
| Wind (air, PLA) | FT | Cu, FEP, PLA, steel | 3D Printing | ~1400 V | Speed (3-7.6 $m.s^{-1}$) | $NH_3$ production | [389] |
| Wind (air, Cu) | LS | Acrylic, Al, Cu, magnets, PTFE | Hand-made | 13 V, 32 mW | Speed (3-15 $m.s^{-1}$) Frequency (50-500 rpm) | Wind sensor | [390] |
| Wind (air, PTFE) | Hybrid (FT-TENG + EMG) | Al, Cu, magnets, PLA, PTFE | Hand-made | 187 V, 0.8 mW | Frequency (50-300 rpm) Humidity (30-90%) | Power crop light supplementation, rain, temperature and humidity sensors | [391] |
| Wind (air, PLA) | Hybrid (FT-TENG + EMG) | Acrylic, Cu, FEP, magnets, PLA, steel | 3D Printing | 750 V, 29 mW | Speed (4.5-13 $m.s^{-1}$) | Wind sensor, and power light intensity and temperature sensors | [392] |

| | | | | | | | |
|---|---|---|---|---|---|---|---|
| Wind (air, PTFE) | Hybrid (VCS-TENG + EMG) | Acrylic, Cu, magnets, PET, PTFE | Laser cutting, 3D printing | 680 V, 19 mW | Frequency (10-200 Hz)<br>Speed (2.2-10 $m.s^{-1}$) | Power temperature and humidity sensors | [393] |
| **Liquid** | | | | | | | |
| Flow (water) | SE | Acrylic, Cu, PDMS | Hand-made | 16 V, (13 $W.m^{-3}$) | - | Regulation of pH, urea concentration and pH sensor | [3] |
| Impact (water wave, PTFE) | VCS | Acrylic, Al, paper, PTFE | Hand-made | 240 V, 12 W | Frequency (0.1-1.25 Hz)<br>Speed (7-17 $m.s^{-1}$) | Controllable pesticide release | [15] |
| Flow (water) | FT | Agricultural debris, plant fibers, PVC | 3D printing | 2600 V, (1240 $mW.m^{-2}$) | Frequency (30-300 rpm) | Automatic irrigation, and power sensors | [394] |
| Flow (water) | Hybrid (TENG + EMG) | Cu, Kapton™, FEP, magnets, PVC | 3D printing | 3200 V, 8 mW | Frequency (30-180 rpm)<br>Speed (0.21-0.61 $m.s^{-1}$) | Power for supplemental plant growth lighting and water quality monitoring. | [395] |
| Impact (Raindrop and water) | VCS | Cu, PE, PEDOT, PSS | ICP etching, spin coating | 72 V, (38 $mW.m^{-2}$) | Frequency (0.5-6 Hz) | Power temperature and humidity sensors | [396] |
| Impact (rainwater) | SE, FT | Acrylic, Al, Cu, PMMA, stainless steel, FEP, PTFE | Injection molding, 3D printing | 45 V, (0.09 $mW.m^{-2}$) | Humidity (30-70%) | Rainfall intensity sensing | [397] |
| Flow (water) | SE | Cu, glass, LIG, PI, PDMS | Laser cutting | 8.9 V, 21.6 μW | - | Harvest rain droplet energy | [398] |
| **Solid** | | | | | | | |
| Vibration exciter (PDMS) | VCS | Al, PDMS, PEDOT:PSS, PLA, protein-based materials | Casting | 90 V, 15 W | Frequency (1-25 Hz) | Growth promoting system | [11] |
| Stepper motor (Nylon, PTFE) | FT | Acrylic, Cu, nylon, polyester fur, PTFE | Laser cutting | 10 kV, 201 mW | Frequency (150-900 rpm) | Seeds germination | [13] |

| | | | | | | | |
|---|---|---|---|---|---|---|---|
| Motor (PTFE) | FT | Cu, PTFE | Hand-made | 1800 V | Air pressure (-10;-20;-60 kPa) [$CO_2$] (10-90%) Humidity (0-97%) | $CO_2$ gas detection | [350] |
| Human walking (PU) | VCS | Ebonite sheet, Ni, PC, PU | Hand-made | (430 $mW.m^{-2}$) | Force (70 N) Frequency (7 Hz) | Nitrogen fixation system; bean germination and growth | [399] |
| Human walking (nylon) | Hybrid (VCS-TENG + EMG) | Cu, MXene, nylon, PANI, PTFE | *In-situ* polymerization, Etching, sandpaper treatment | 500 V, (415 $W.kg^{-1}$) | Temperature (17-25°C) Humidity (0-97%) Frequency (2-10 Hz) | $NH_3$ gas detection, power sensors and small devices | [400] |
| Tractor operation (PZT) | SE | PZT, stainless steel | Hand-made | 180 V, (12 $\mu W.mm^{-3}{\cdot}g^{-2}$) | Frequency (0-1 kHz) | Power air pressure sensors | [401] |
| Vibration exciter (Paper) | SE | LIG, MXene, PI, PDMS, paper | Spin-coating, laser engraving | 119 V, (609 $mW.m^{-2}$) | Force (1-20 N) Frequency (1-15 Hz) | Handwriting recognition and harvest leaf swing energy | [402] |
| Motor (Cu) | VCS | Acrylic, β-$Ni(OH)_2$@PVDF, Cu, MXene | Hand-made | 427 V, (482 $mW.m^{-2}$) | - | Power thermo-hygrometer, gas and ethanol sensors, and body movement recognition | [403] |
| Motor (Nylon) | Hybrid (LS-TENG + EMG) | Cu, Fe, magnets, nylon, PMMA | Hand-made | 109 V, (41 $mW.m^{-2}$) | Speed (5-8 $m.s^{-1}$) Frequency (100-1000 Hz) | Power temperature, humidity GPS and barometer-noise sensor | [404] |
| Rotational motor (PTFE) | FT | Acrylic, Cu, polyester fur, PTFE | Hand-made | 9.7 kV, 70 W | Frequency (200-800 rpm) | Agricultural product preservation, and power sensors for storage environment tracking | [405] |

| | | | | | | | |
|---|---|---|---|---|---|---|---|
| | | | | | | and transport information | |
| Honeybee touch (PTFE) | SE | Acrylic, Al, PAA, PTFE | Hand-made | 0.6 V | - | Flytrap sensor | [406] |
| Motor (EVA) | VCS | Al, CFRP, EVA, PU | 3D printing | 4.5 V | Humidity (20-80%) Pressure (0-13 kPa) | Pressure and weighing sensor, crop harvesting and packaging | [407] |
| Finger (Cu) | VCS | Cu, nylon, PC, $TiO_2$ | Electrospinning, spray coating | 330 V, (5000 $mW.m^{-2}$) | Humidity (10-90%) | Humidity sensor and self-cleaning surface | [408] |
| **Hybrid source** | | | | | | | |
| Gas, liquid, solid (air, water impact, plant leaves) | SE | GO, plant leaves, PVA, VTMOS | Casting | 153 V, (90 $mW.m^{-2}$) | Frequency (1-5 kHz) Humidity (20-75%) | Wind alarm system, power temperature and humidity sensors | [2] |
| Gas, and liquid (air, raindrop, PTFE) | FT | Acrylic, Cu, PTFE, rabbit hair, zirconia | Hand-made | 3 kV, (1000 $mW.m^{-2}$) | Frequency (0.5-10 Hz) Speed (0.5-6 $m.s^{-1}$) | Crop growth stimulation, power temperature, humidity, rainfall and soil pH sensors | [12] |
| Gas, and solid (paper, water flow) | SE | AgNPs, MXene, paper, PDMS | Hand-made | 7.7 V | Force (0.5-9.5 N) Frequency (0.5-9.5 Hz) | Raining and dynamic force sensing | [380] |
| Gas, and solid (air, PI) | FT | PAA, PANI, PI, rGO | Freeze-drying, hydrothermal reactor, ultrasonic homogenizer | 21 V, (424 $mW.m^{-2}$) | Pressure (85 KPa) Frequency (4; 1000 Hz) | LED power, plant growth sensor, ammonia sensor | [409] |
| Gas, and liquid (air, water flow) | FT | Acrylic, fur, PTFE | Laser cutting | 3750 V, (5000 $mW.m^{-2}$) | Humidity (40-90%) Torque (0.01–1 N.m) | Automatic irrigation, weather monitoring and water level warning | [410] |
| Gas, and solid (air, PET) | VCS | Cu, ITO, Nylon, PE, PET, PTFE | 3D printing | 250 V, (3 $mW.m^{-2}$) | Frequency (0.5-5 Hz) Amplitude (10-25 mm) | Power temperature and humidity sensors, lights, and irrigation system | [411] |

| | | | | | | | |
|---|---|---|---|---|---|---|---|
| Gas, and solar (air, PTFE) | Hybrid (VCS-TENG + SC + EMG) | Acrylic, Cu, Ni magnets, PMMA, PLA, PTFE | 3D printing, laser engraving | 570 V, 8 mW | Wind speed (7 $m.s^{-1}$) | Power sensors and remote monitoring | [412] |
| Liquid (water, solar) | SE | Ag, AgNWs, FEP, glass, ITO, $MoO_3$, PET, Pt, PEDOT:PSS | 3D printing | 100 V, (101000 $mW.m^{-2}$) | Frequency (0.5-7.5 Hz) | Self-powered sensor for adjusting temperature and light for plant growth | [413] |
| Liquid, solid (water impact, nylon) | FT | Acrylic, Cu, magnets, nylon, PPCF, PVDF, PDMS | 3D printing | 795 V, (20 $W.m^{-3}$) | Force (0.25-2.5 N) Frequency (0.1-1.6 Hz) | Power TDS, pH, temperature, and humidity sensors | [414] |
| Gas, liquid, solid (water flow and impact, air, leaf) | SE | LIG, PDMS, PI, silver ink | Laser engraving | 170 V, (80 $mW.m^{-2}$) | Force (0.5-13.3 N) Frequency (1-30 Hz) | Self-cleaning ability, temperature and humidity sensors | [54] |
| Gas, solid (air, FEP) | SE | Acrylic, Cu, FEP, wheat, PET | Hand-made | 250 V, (404 $mW.m^{-2}$) | Speed (2.9-9.1 $m.s^{-1}$) Frequency (0.5-4 Hz) Humidity (15-64%) | Power watch, and hygrometer sensor, and wind speed sensor | [55] |
| Gas, and solid (air, PSP) | LS | Al, Kapton™, PET, PTFE, PSP | Hand-made | 248 V, (365 $mW.m^{-2}$) | Speed (3.9-9.8 $m.s^{-1}$) Frequency (1-5 Hz) | Power anti-corrosion system, hygrometer, electronic watch, and calculator | [415] |
| Gas, liquid, and solid (air, water, Al) | VCS | Al, F-CNT, PET, PVDF-HFP | Electrospinning | ~450 V, (3306000 $mW.m^{-2}$) | Frequency (1-5 Hz) Force (1-30 N) | Power soil moisture and fertility, light intensity, and temperature sensors | [416] |
| Gas, liquid (air, rainwater) | SE, FT | Cu, Cu/Ni-based fabric tape, Nylon™, PVC, TPFE | Electrospinning | 252 V, (11000 $mW.m^{-2}$) | - | Smart lighting | [417] |
| Gas, liquid (wind, water) | FT | Ag, Al, FEP, ITO, PE, silver fabric | 3D printing | 228 V (7.35 $W.m^{-2}$) | Frequency (1-2 Hz) | Power automatic irrigation and soil moisture sensor | [418] |

Footnote: Polymer (CFRP), Ethylene-vinyl acetate (EVA). Polycarbonates (PC Carbon Fiber Reinforced Polymer (CFRP), Coconut Husk (CH), Ethylene-Vinyl Acetate (EVA), Expandable Polyethylene (EPE), Fluorinated Carbon Nanotubes (F-CNT), Fluorinated Ethylene Propylene (FEP), Fluorinated Ethylene Propylene (FEP), Freestanding Triboelectric-Layer Mode (FT), Hydroxyethyl Cellulose (HEC), Indium Tin Oxide (ITO), Laser Induced Graphene (LIG), Lateral Sliding Mode (LS), Lead zirconate titanate (PZT), Metal-organic Frameworks (SUR-MOFs), Multilayer Graphene Oxide (GO), N-Methyl-2-Pyrrolidone (NMP), Peanut Shell Powder (PSP), Polyaniline (PANi), Poly(Vinylidene Fluoride-co-Hexafluoropropylene) (PVDF-HFP), Polyacrylic acid (PAA), Polyacrylic Acid (PAA), Polycarbonates (PC), Polyimide (PI), Polyurethane (PU), Polyvinyl alcohol (PVA), Reduced Graphene Oxide (rGO), Single-Electrode Mode (SE), Solar Cell (SC), Total Dissolved Solids (TDS), Vertical Contact-Separation Mode (VCS), Vinylrimethoxysilane (VTMOS).

#### 2.6.1.3 **Solid energy and hybrid**

Despite the efficacy of TENGs in harvesting irregular and low-frequency mechanical energy within agricultural environments, their limited power output often constrains certain applications, e.g., active sensors and continuous power provision for coupled sensor systems. Consequently, the integration of hybrid nanogenerators employing different energy harvesting strategies presents a viable solution. For instance, electromagnetic generators (EMGs) are renowned for their capacity to yield higher output currents, whereas TENGs demonstrate proficiency in generating elevated output voltages for equivalent mechanical stimuli. Integrating both technologies synergistically enhances overall energy conversion efficiency by leveraging their complementary attributes within a unified system.

Rahman et al. developed a rotary hybrid nanogenerator combining an electromagnetic generator with soft magnets and a non-contact TENG **(Figure 2.15c,iii)**.[379] The EMG, designed in axial flow orientation, used a rotor with four cylindrical magnets on a disc connected to an intermediate shaft, with four coils placed beneath the magnets. The TENG, positioned above the EMG, consisted of two circular triboelectric layers supported by Kapton spring-like structures for enhanced durability, with a soft rubber magnet fixed to the upper substrate. The hybrid achieved a maximum power density of 1568 $mW.kg^{-1}$ and an average of 386 $mW.kg^{-1}$, with durability confirmed over 8.5 hours (~2,000,000 cycles) at 1000 rpm. Compared to standalone nanogenerators, hybridization significantly improved performance, charging a 100 μF capacitor to 17.2 V in 80 s **(Figure 2.15c,iv)**, versus 3.9 V (EMG) or 13.3 V (TENG). As a proof of concept, it powered a soil moisture sensor, demonstrating its potential for sustainable agricultural monitoring **(Figure 2.15c,v)**.

TENGs can also be integrated with chemical energy generators, such as electrochemical cells (ECs), to enhance efficient and stable electrical energy production. ECs

generate electricity through spontaneous oxidation-reduction reactions at metal electrodes in an electrolyte solution. Wu et al. developed a hybrid energy cell combining a TENG, an EC, and a solar cell (SC) to harvest wind, solar, and chemical energies simultaneously or individually for agricultural applications.[26] The device includes a silicon-based EC at the top to capture solar energy **(Figure 2.15c,i)**. The TENG, consisting of a PTFE film and aluminium foil on transparent acrylic tubes, leverages wind-induced rotation for periodic contact and separation, facilitating electron transfer between the aluminium foil and the soil. The EC in NaCl solution (3 wt.%) generates 6.5 mA and 0.5 V, while the TENG produces 0.5 $mA \cdot m^{-2}$ and 90 V. The hybrid system (TENG//SC+EC) achieves the highest charging voltage (~5.5 V) within the same duration, outperforming standalone TENG (~4 V) and SC+EC (~3.5 V) units **(Figure 2.15c,ii)**. By charging a commercial Li-ion battery, the device powers a wind speed sensor and a temperature sensor, showcasing its utility for agricultural monitoring.

Therefore, considering the wide range of sustainable energy generation devices with complementary performances, the rapid implementation of these nanogenerators for self-powering electrical devices and sensors in smart agriculture is expected to bring significant advances in continuous and real-time food monitoring, thereby enhancing food productivity and security. Moreover, even more substantial progress is foreseen as nanogenerators are increasingly employed as smart devices, a key focus of our forthcoming discussion.

### 2.6.2 **Smart and self-powered applications**

Nanogenerators employed in smart applications can be categorized based on their active role either as portable power sources or as self-powered active sensors.[96] Traditional sensor systems rely on chemical or biological detection achieved through interactions between the analyte and receptor molecules, yielding highly specific and selective detection outcomes **(Figure 2.16a)**. This specificity is attributed to the targeted

interaction between the analyte and recognition elements, e.g., aptamers and antibodies, along with the preservation of functionalized surfaces in conventional sensor operations.[96,419] However, the reliance on external power sources limits the portability of these devices and makes it more expensive. This limitation can be addressed by employing nanogenerators as portable energy sources, generating high voltage and alternating current signals that require prior processing through an energy management system, comprising rectifiers and energy storage components **(Figure 2.16b)**.[96] In such configurations, any operational instabilities occurring in the nanogenerator would primarily affect the charging efficiency of the energy storage unit and would not compromise the sensor's detection performance. In addition, Cao et al. proposed coupling self-powered sensing architectures and power management strategies with machine-learning-assisted signal processing to significantly enhance stability and accuracy in variable agricultural environments.[291] This approach can improve data reliability by learning the statistical characteristics of environmental signals, enabling discrimination between genuine agronomic events and background noise.

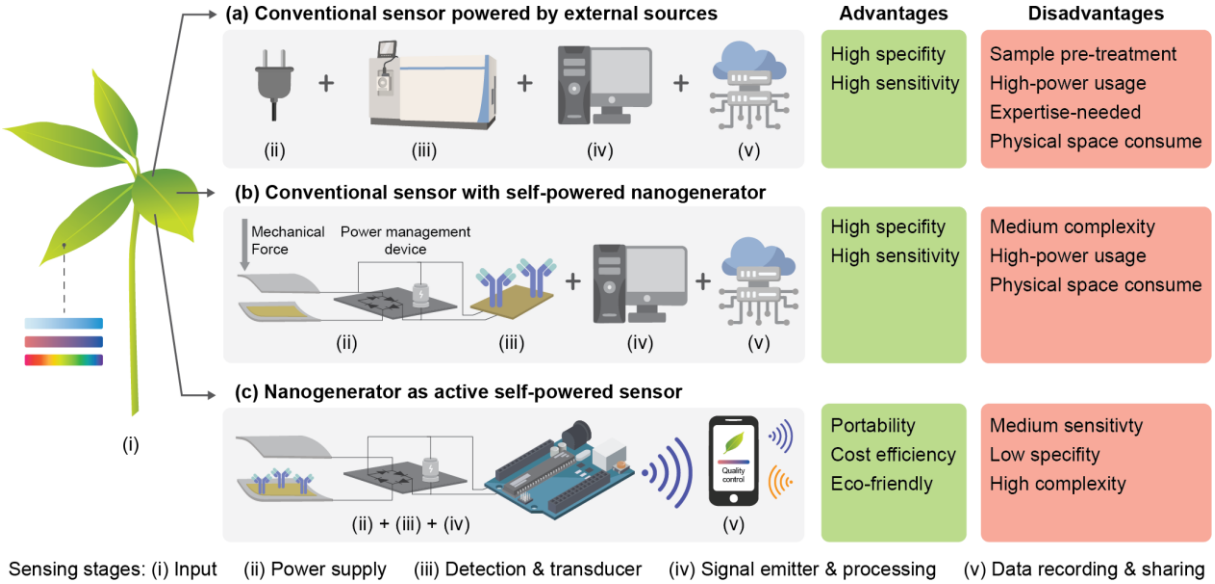


**Figure 2.16.** Comparison of traditional sensors with nanogenerator-based systems. (a) Conventional sensor powered by external sources. (b) Conventional sensor integrated with a nanogenerator for portable power generation. (c) Self-powered active sensor, wherein the nanogenerator serves as the power supply, detection and transduction system, as well as the signal processor and emitter when coupled with microcontroller board.

Self-powered active sensors operate by directly recognizing substances that interact or adsorb onto the active surface of the nanogenerator, i.e., the (i) input, inducing disturbances in the triboelectric properties of the active layer. This disruption serves as the detection signal, leading to a simplified sensor structure **(Figure 2.16c)**. Therefore, utilizing a nanogenerator as a self-powered active sensor condenses all the essential elements necessary to function as conventional biosensors, including the (ii) power supply, (iii) detection layer, (iv) transducer, and (v) signal emitter and prosing, offering several advantages. Notably, it enhances portability by reducing cables and significantly shrinking device size. Nanogenerators are also more cost-effective to produce compared to other robust systems. Their intrinsic self-powering capability adds an environmentally friendly dimension. Nevertheless, there are drawbacks to consider. Specificity and sensitivity are compromised due to the impact of natural mechanical triggers (unpredictable elements) and uncontrollable environmental factors on electrical output, unlike controlled and standardized equipment and protocols used in traditional sensors. Furthermore, degradation of the active functionalized layer due to mechanical actuators makes it difficult to achieve high sensitivity. Addressing this challenge involves selecting friction materials with substantially different triboelectric properties from the target analyte. However, concerns regarding the anchoring and stability of recognition elements within the friction layer persist. Consequently, most sensors powered by nanogenerators primarily function as physical sensors.[420–424]

Moreover, constructing and calibrating the nanogenerator's self-powered sensor system presents significant challenges, particularly amidst the array of interferences encountered in the agricultural field. Thus, forthcoming research efforts should focus on two critical aspects: effectively discerning electrical outputs amidst environmental fluctuations and maximizing the disturbance of electrical output upon analyte detection. This might involve changing the charge accumulation capacity to a conductive

property, triggering chemical reactions, degradation of the active layer, etc. Despite these sensing limitations, nanogenerators remain positioned for widespread adoption globally, fostering digital connectivity and leveraging ecological sources for its functionality.

#### 2.6.2.1 **Food growth stimuli**

As the world's population grows, there is an urgent need to enhance food production efficiency and advance agricultural development. Emerging technologies like nanogenerators offer promising solutions to improve agricultural productivity and crop quality. Additionally, considering the high energy consumption and environmental impacts associated with fertilizer production and usage, nanogenerators have the potential to address these challenges while also promoting plant growth through electrical stimulation. By incorporating eco-friendly materials with low toxicity and self-powered capabilities, nanogenerators can play a crucial role in modern agriculture, prioritizing sustainability. The following examples highlight research endeavours exploring smart application of nanogenerators in cultivating food crops.

Integrating bio-based films into nanogenerators offers an eco-friendly solution to soil pollution caused by residual plastics. Smart utilization of bio-nanogenerators marks a significant advancement in smart agriculture, harnessing nanogenerator technology to enhance crop growth by tapping into environmental mechanical energy. Jiang et al. developed eco-friendly devices using biodegradable mulch films, fostering growth-promoting systems.[11] By energy harnessing using bio-nanogenerators, the system was designed to display an electric field directed into bean seed germination **(Figure 2.17a,i)**. Mechanical excitation during testing simulated crop growth, resulting in ~180 V at 15 Hz for 1 h at 12-hour intervals. Employing bio-nanogenerators as mulch films enhanced bok choi growth, particularly for plants closer to the electric field. These devices can potentially address electronic waste, residual plastic, and plant pro-

tein waste, supporting sustainable agriculture. However, optimizing plant growth requires comprehensive understanding and control of electrical parameters, including stimulation duration, electric field intensity, and frequency. Further research should explore effects across various growth stages, including reproductive and senescence phases, where unexplored effects persist.

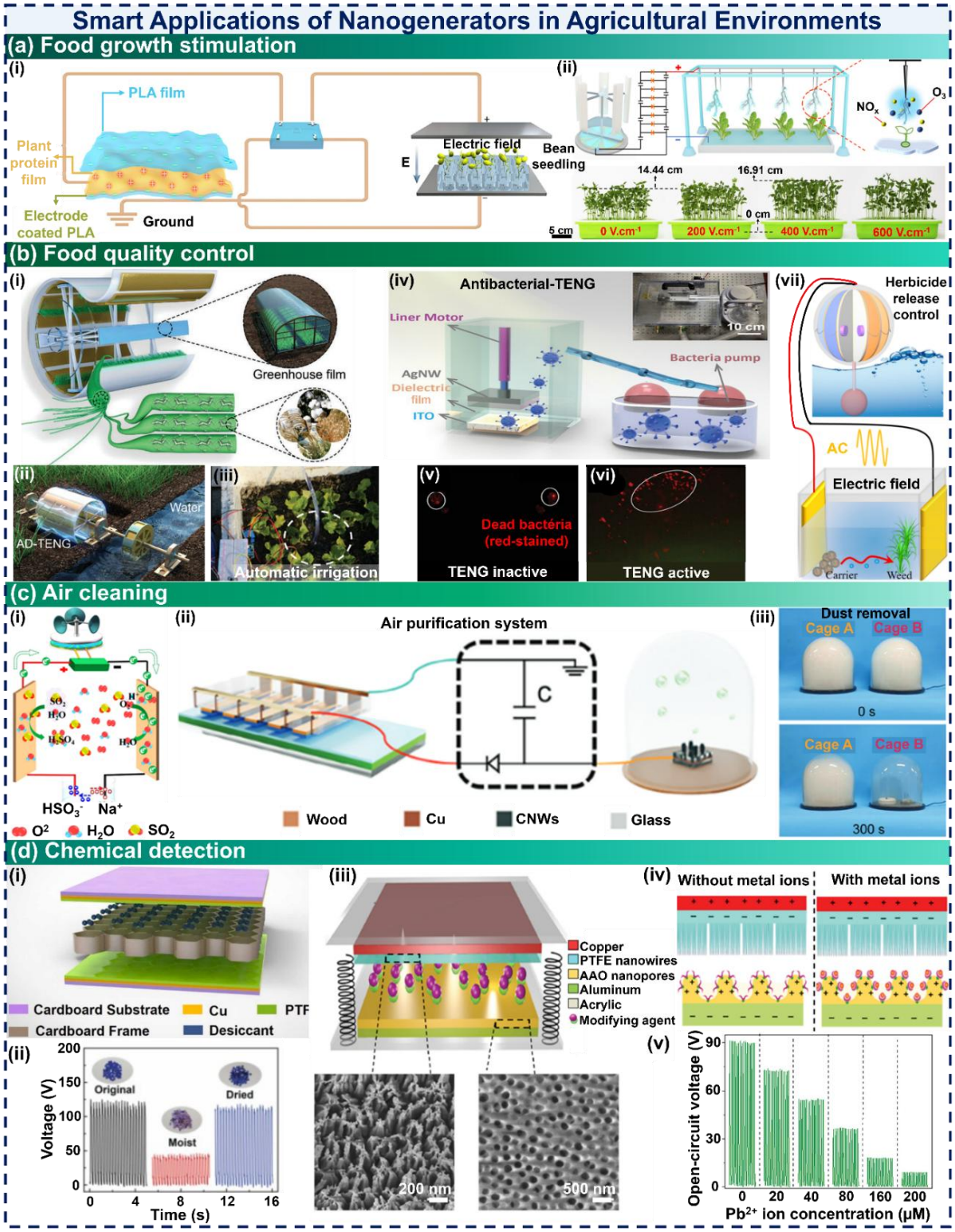


**Figure 2.17.** Smart agricultural applications of nanogenerators. (a,i) Biodegradable nanogenerator promoting tomato seed growth via electric fields, reprinted with permission from ref.[11] (a,ii) Schematic illustrations of a self-powered electric field system for pea seedling treatment, alongside digital photographs showing the growth of pea seedlings exposed to different electric field strengths (0 to 600 V.cm$^{-1}$) over 5 days, reprinted with permission from ref.[12] (b,i) Schematic of a TENG-based greenhouse film for real-time monitoring, reprinted with permission from

ref.[394] (b,ii) AD-TENG device harvesting hydrodynamic energy, reprinted with permission from ref.[394] (b,iii) Automatic irrigation system powered by AD-TENG-based energy harvesting for precision water delivery to crops, reprinted with permission from ref.[394] (b,iv) Antibacterial TENG device driven by a liner motor to generate bactericidal effects; inset: experimental setup, reprinted with permission from ref.[215] (b,v) Fluorescence images showing bacterial viability under TENG operation: TENG inactive, high bacterial survival (red-stained cells), (vi) TENG active, reduced bacterial count, reprinted with permission from ref.[215] (b,vii) Schematic diagram illustrating the controlled release of herbicides using an electric field generated by a nanogenerator, reprinted with permission from ref.[15] (c,i) Schematic illustration of $SO_2$ removal based on electrostatic principles, reprinted with permission from ref.[425] (c,ii) Schematic diagram of an air purification system, and (c,iii) a digital photograph showing dust removal in action, reprinted with permission from ref.[426] (d,i) Design of a desiccant-based triboelectric nanogenerator, with (d,ii) its energy harvesting performance as a function of moisture, reprinted with permission from ref.[427] (d,iii) Structure design and working principle of a tribo-nanosensor for heavy metal ion detection, including an SEM image of the PTFE nanowires and anodic aluminum oxide nanopores. (d,iv) Schematic illustration of the tribo-nanosensor's mechanism for detecting heavy metal ions via triboelectrification and complexation reactions. (d,v) Open-circuit voltage of the tribo-nanosensor as a function of $Pb^{+2}$ concentration, reprinted with permission from ref.[206]

Li et al. developed a high-voltage pulsed electric field (HVPEF) generator using a TENG to polarize tomato seeds.[13] The rotary ternary dielectric triboelectrification in non-contact mode provided high stability, durability (100k cycles), and high outputs (15 kV DC, 10 kV AC, 201 mW). The HVPEF effectively enhanced seed germination, achieving comparable results to conventional HV sources. Treated seeds exhibited improved germination rates, longer roots (52.9 vs. 5.11 mm in controls), and increased vigor indices (351% higher than untreated seeds). Despite the high voltage, the microampere-level current ensured operator safety and avoided overstimulation of seeds. Additionally, the electric field can be precisely adjusted by varying the distance between parallel plate electrodes in the homemade polarization device, enabling its use in sensitive electric-field crop seeds. This smart device demonstrates potential as a viable tool for high-tech agricultural applications. However, optimizing voltage and treatment time through comprehensive studies is essential to effectively integrate

smart nanogenerators into Agriculture 4.0, enhancing seed germination, vitality, and growth.

Li et al. developed a wind- and rain-driven electrical stimulation system to enhance crop production via triboelectrification **(Figure 2.17a,ii)**.[12] The system incorporates a bearing-and-hair structured nanogenerator with a rotating-disk design, capable of harnessing all-weather energy to generate a stable and durable electric field with minimal starting torque. The system's effectiveness was validated through growth experiments with pea seedlings under electric fields of varying intensities. After 7 d, seedlings exposed to the electric field showed a 17% increase in height and a 20% increase in weight compared to controls. The authors suggest that the significant positive effect of the self-powered electric field on the growth of pea seedlings may arise from its continuous influence on photosynthesis. Overall, the developed system exhibited notable enhancements in germination speed and pea yield, validating the electric field-induced enhancement of physiological activity and representing a breakthrough in the development of eco-friendly smart nanogenerators to address diverse challenges in agricultural production.

To achieve a thorough understanding of the application of smart nanogenerators in crop growth, it is essential to investigate several key parameters in depth. For instance, (i) the biological growth behaviour of crops in response to electrical fields is likely to impact productivity, stress tolerance, plant physiology, growth, and development. Conversely, (ii) intrinsic factors related to electrical output, such as electric field strength, duration of exposure, frequency, waveform (sinusoidal, square, pulsed), spatial distribution (including uniformity and directionality), and even electric field gradient, should also be considered. Systematically analysing these electrical parameters alongside plant growth behaviour responses will contribute to understanding the stimulation of specific biochemical pathways in plants, enhancing nutrient uptake, and improving growth outcomes. This approach will advance the understanding of the

relationship between electrical signals and crop seed responses, pushing the boundaries of knowledge in smart self-powered agriculture.

#### 2.6.2.2 **Food quality control**

In an effort to regulate pesticide dosages in agricultural environments, Zhang et al. engineered an inverted pendulum-type multilayer triboelectric nanogenerator (IPM-TENG) to manage pesticide doses in farming settings.[15] This device efficiently converts water wave energy, achieving a conversion efficiency of 14.5%. Additionally, the optimized IPM-TENG serves as a control system for the targeted release of pesticides, promoting the development of self-sustaining smart agricultural practices. Glyphosate is a weak acid mixture that ionizes in water, producing hydronium ions and the conjugate base of the acid. Driven by electrostatic forces, the acid's conjugate base moves towards the electrode, effectively targeting and eliminating weeds **(Figure 2.17b,i)**. In both DC and AC conditions, glyphosate concentration consistently rises with distance, indicating controllable release capabilities. Consequently, this system facilitates the gradual release of glyphosate to specific locations, preventing rapid environmental dispersion and ensuring effective, on-demand pesticide control through a self-powered smart agricultural system.

As consumer preferences lean towards reduced chemical intervention in food production, especially concerning pesticides and preservatives, physical sterilization methods emerge as a promising means to ensure food safety. Nanogenerators present an innovative solution by utilizing mechanical energy to induce electric fields or discharges for self-powered food sterilization. Food sterilization aims to eradicate or suppress microorganisms physically or chemically, thereby delaying food spoilage and extending shelf life.

Chen et al. developed a self-powered bacterial sterilization system based on a nanogenerator incorporating g-$C_3N_4$/MXene-Au composites.[215] They proposed a method to enhance TENG output performance by utilizing charge traps generated

through the mutual coupling of photogenerated carriers and surface plasmons in a vertical contact-separation mode comprising two layers **(Figure 2.17b,ii)**. Experimental findings showcased optimal system performance under visible light irradiation, achieving a maximum open circuit voltage of 510 V and an output power of 20 mW. The exposure of photogenerated hole-electrons to the surrounding air, along with the generation of photogenerated holes and reactive oxygen species such as ·OH, $O^{2-}$, $HO_2$, and $H_2O_2$, facilitates direct interaction with cellular components, leading to bacterial inactivation. The observed reduction in bacterial populations primarily results from the oxidizability conferred by $C_3N_4$/MXene-Au composites. This study demonstrates the successful application of a portable, self-powered, and effective method for salmonellosis sterilization using a TENG, with potential implications for enhancing food quality in environmental agriculture.

#### 2.6.2.3 **Air cleaning**

The air purification capability of nanogenerators plays a significant role in sustainably improving the quality of the agricultural environment, thereby avoiding the risks of food contamination, reducing crop yields, and preventing soil degradation, while also contributing to human health. For instance, fine particulate matter, including soot, ash, and other combustion byproducts with a diameter of 2.5 μm ($PM_{2.5}$) or smaller, can settle on crops and impede photosynthesis.[428] Additionally, particulate matter can lead to respiratory issues upon inhalation and may carry harmful chemicals, pesticides, and pathogens that can harm crops and soil.

For example, acid rain, resulting from the deposition of sulphur dioxide and nitrogen oxides into the soil, leads to soil acidification and nutrient depletion. These pollutants can disrupt photosynthesis, nutrient uptake, and overall plant growth, decreasing productivity. Therefore, reducing emissions of these pollutants through enhanced air quality regulations and sustainable agricultural practices is crucial for safeguarding crop production and ensuring food security. Furthermore, monitoring air quality and

implementing mitigation measures can help minimize the impact of atmospheric pollutants on agriculture.

The conventional approach to air pollution purification involves large and costly system projects that also demand significant energy consumption. Hence, nanogenerators, serving as high-voltage sources, have been demonstrated to purify atmospheric and indoor air through electrostatic adsorption and electrochemical reactions while also serving as self-powered devices aimed at transitioning from fossil energy to green energy.

For instance, Chen et al. developed a simple and practical self-powered cleaning system based on a rotating TENG to address toxic materials and particles such as sulphur dioxide ($SO_2$) in the air.[425] $SO_2$ in the air can be effectively removed through self-powered oxidation and electrostatic interaction. The alternating current electricity produced by the TENG is converted into direct current electricity through a rectifying bridge to continuously oxidize $SO_2$. The self-powered cleaning system operates effectively at different wind speeds and significantly enhances the efficiency of $SO_2$ removal with increasing wind speed, thereby confirming a more effective cleaning effect. The electrochemical reaction of $SO_2$ involves the loss of two electrons at the cathode material, transforming it into sulfuric acid in water and purifying the air **(Figure 2.17c,i)**.

Additionally, the device is capable of electrostatically precipitating airborne dust particles. When generated from a solid aerosol generator, dust aerosols become positively or negatively charged due to the triboelectric effect between the particles and the air. Using compressed air, the charged aerosols are pumped into a chamber through an inlet by an air pump. Under the Coulombic force of attraction and repulsion, charged dust particles are attracted to two electrodes. The key distinction between $SO_2$ removal and dust precipitation principles lies in the fact that dust precipitation relies on electric field density, whereas $SO_2$ removal requires a closed circuit.

Shi et al. optimized nanogenerator's structural design to attain a $V_{oc}$ exceeding 3 kV, alongside a high charge density of 320 $\mu C.m^{-2}$.[426] Despite its small size (2.25 $cm^3$), the nanogenerators effectively produce negative ions, promoting dust settlement within 300 s. This occurs because when high voltage is generated via the triboelectric effect, it is directed to the carbon nanowires, inducing corona discharge between the nanowire tip and the air **(Figure 2.17c,ii)**. This discharge leads to air ionization, resulting in the generation of negative air ions. Upon contact with smog particles, these negative air ions attract the particles, including $PM_{2.5}$, forming aggregates. These aggregated particles settle due to gravity until 300 s **(Figure 2.17c,iii)**. Thus, this high-voltage nanogenerator offers a promising sustainable solution for effectively combating dust, thus contributing to cleaner environments.

Li et al. developed a triboelectric air filtration system based on TENGs to actively remove outdoor $PM_{2.5}$ and harmful bacteria.[18] The system comprises a layer of synthetic fibre filter cotton and PTFE membrane. Friction charging during nanogenerator operation significantly enhances the particle filtration efficiency of the filter material. Simultaneously, the positive charge of fibre filter cotton demonstrates high filtration efficiency against Staphylococcus aureus. The mechanism underlying bacterial filtration is elucidated alongside the operating principle of TENG. Since bacterial cell walls and membranes consist of a phospholipid bilayer and exhibit electronegativity, activation of the filter cotton/sponge generates a positive frictional charge, attracting bacteria. This restricts bacterial movement, inhibits respiratory function, and induces complete deformation and rupture of cell walls and membranes, impeding reproduction and survival. Furthermore, the particle filtration efficiency of filter cotton (F6-type) increased from 36.7% to 74.6 % after charging the sponge, which is justified due to the greater adsorption force of electrostatic adsorption on small particles. Therefore,

this real-time self-powered particulate filter device holds significant potential for application in agriculture, aiming to ensure food safety by eliminating both particles and pathogenic bacteria.[18]

#### 2.6.2.4 **Chemical detection**

Gao et al. developed a self-powered active biochemical sensor with high sensitivity for urea detection.[3] The sensor utilizes urease-catalysed hydrolysis of urea to regulate the pH value, enhancing the sensitivity and specificity of detection based on the pH-sensitive TENG. This occurs because urea is hydrolysed into ammonium and hydroxyl ions ($OH^-$) through the urease-catalysed reaction, increasing the output performance in liquid-solid interface. As the reaction proceeds, the solution has increasing hydroxide ions. The generated hydroxide ions will react with the PDMS surface, producing more negatively charged functional groups and a more negative zeta potential ($\zeta$), increasing the $V_{oc}$. The device's capacity to monitor urea content in plant culture medium is also demonstrated, as the urea concentration measured by HPLC and the voltage variations recorded by the self-powered biochemical sensor exhibit a similar trend with increased incubation time. However, despite the potential incorporation of this smart nanogenerator into agricultural IoTs and precise fertilization guidance, the comparison with other common ions and salts in water was not evaluated. The reliability of this urea sensor is reduced when several other parameters (temperature, liquid flow, ion composition, and other environmental factors) remain uncontrollable, hindering accurate urea detection and compromising selectivity. Therefore, a more selective sensor, e.g., developing an active surface containing amidohydrolase (for enzymatic methods) or copper (II) (chemical method), which specifically interacts with urea, is imperative, ensuring the $V_{oc}$ output is directly affected by this chemical recognition.

Testing the freshness of collected fruits during storage is vital for reducing fruit waste and the risk of food-borne contamination. To ensure sustainable power for long-

term monitoring, Pang et al. developed a smart packaging nanogenerator system to monitor fruit quality and enhance supply chain efficiency during distribution and transportation.[427] The nanogenerator consists of a cardboard honeycomb frame, a PTFE/Cu triboelectric layer, and desiccant filling the honeycomb holes **(Figure 2.17d,i)**. While the desiccant protects the packaged foods by absorbing moisture, this moisture absorption can impact the nanogenerator's output due to its hygroscopic nature. **Figure 2.17d,ii** shows the nanogenerator's $V_{oc}$ signals before and after moisture absorption, showing a decrease from 125 to 48 V. This decline occurs because water absorbed on the surfaces dissipates the generated triboelectric charge, resulting in reduced voltage. In addition to functioning as an active sensor, the system activates a digital thermometer and hygrometer to monitor the package's temperature and humidity. Multiple nanogenerators can be employed in a single package based on its size, volume, and the energy requirements of electronic sensors. Thus, the smart packaging offers a practical strategy for continuous monitoring of the status and quality of packaged foods throughout the supply chain, reducing food waste.

Li et al. developed a self-powered heavy metal ion treatment system enabled by triboelectrification, using a water-driven TENG.[206] The system includes a multilayered tribo-nanosensor consisting of acrylic and PTFE layers adhered to back-coated copper electrodes. PTFE nanowire arrays were created on the PTFE surface via reactive ion etching. The lower substrate features an Al foil layer with anodic aluminium oxide nanopores. The nanogenerator-based sensor bearing chemically modified nanopores with ligand molecules to enhance chelating properties for different metal ions **(Figure 2.17d,iii)**. These ligands selectively adsorb heavy metal ions, and the differences in complexation constants between heavy metal ions and ligand molecules determine their affinity to metal ions **(Figure 2.17d,iv)**. The adsorbed metal ions on the modified surface significantly influence the $V_{oc}$ of tribo-nanosensor. For instance, in the $Pb^{2+}$ concentration region of 0 to 200 μM, the $V_{oc}$ monotonically decreases from approximately

90 to 10 V **(Figure 2.17d,v)**. The excellent selectivity of the tribo-nanosensor for $Pb^{2+}$ detection is observed by the highest and significant $Pb^{2+}$ absorption compared with other heavy metal ions. Therefore, chemically modifying the tribo-nanosensor represents an efficient approach to developing an environmentally friendly, cost-effective, and self-powered chemical sensor based on a TENG, with significant potential for applications in agriculture monitoring.

## 2.7 Conclusion and outlook

### 2.7.1 Outlook

The agricultural sector represents one of the most challenging yet impactful frontiers for TENGs. Field deployment requires not only the capability to harvest distributed, low-frequency, and irregular mechanical energy, but also the resilience to operate continuously under fluctuating and often harsh environmental conditions. While proof-of-concept studies have demonstrated the feasibility of TENGs in certain agricultural contexts, transitioning toward large-scale, field-ready systems demands overcoming a set of interconnected challenges involving functional materials, device and mechanical design, software and data integration, and field validation and scalability **(Figure 2.18)**. We envision these four areas as the next critical steps toward establishing smart TENG-based sensors suitable not only for agriculture, but for a broad range of open-field applications.

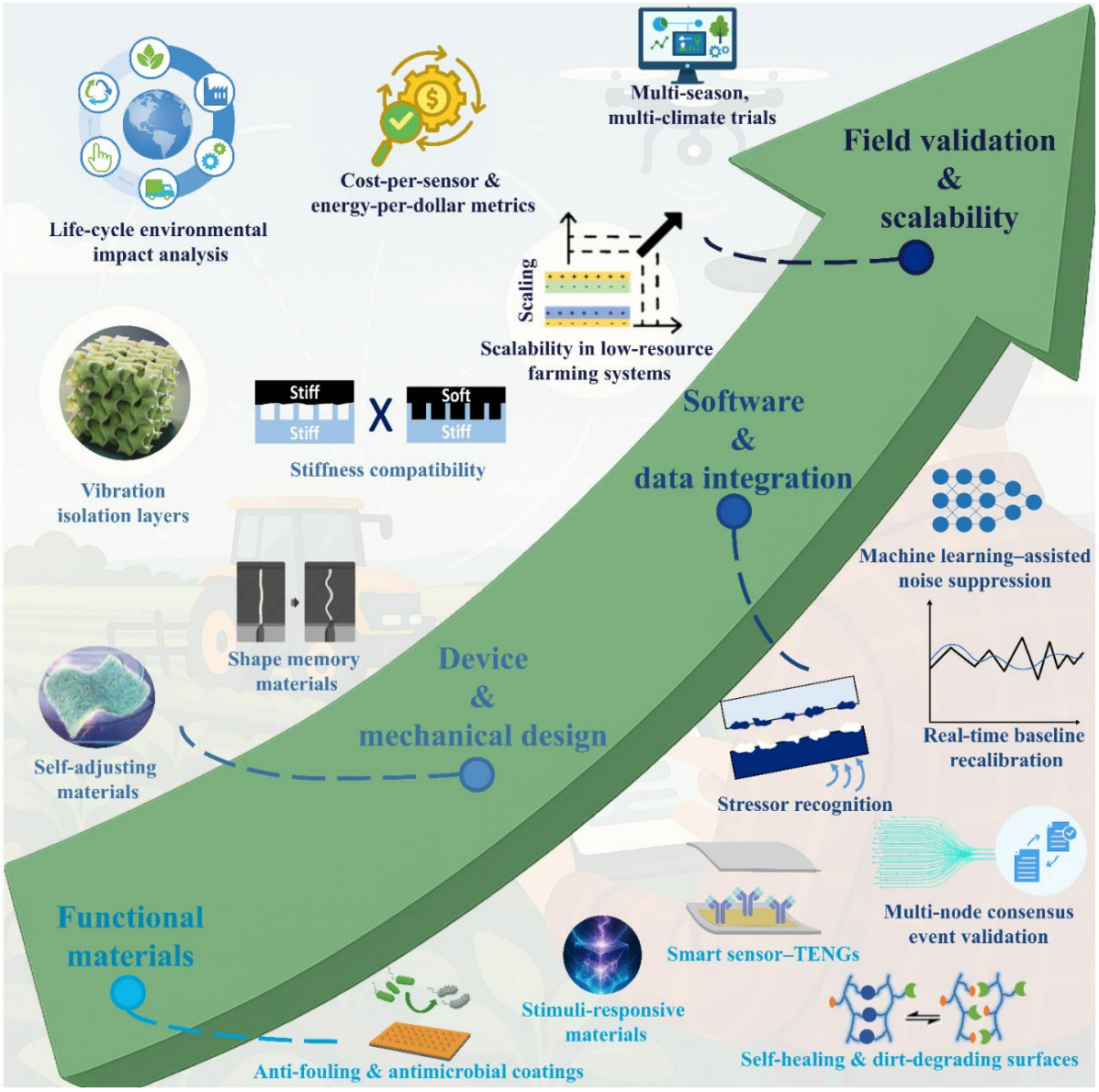


**Figure 2.18.** Outlook roadmap for advancing TENG-enabled smart agriculture. The roadmap highlights four key directions: (i) functional materials (anti-fouling and antimicrobial coatings, self-healing and dirt-degrading surfaces, stimuli-responsive, smart sensor-TENGs), (ii) device and mechanical design (self-adjusting architectures, shape-memory, stiffness compatibility, vibration isolation), (iii) software and data integration (multi-node validation, stressor recognition, baseline recalibration, machine learning–assisted noise suppression), and (iv) field validation and scalability (scalability in low-resource systems, life-cycle impact, cost metrics, multi-season trials).

The next stage of TENG development for environmental applications will largely depend on functional materials that unite long-term stability with active, responsive behaviors. Future agricultural TENGs should employ functional materials that combine high mechanical stability with environmental responsiveness. For example,

(i) anti-fouling and antimicrobial layers could serve a dual role, providing pest control while preventing degradation of the triboelectric layers, thereby extending operational efficiency. After service life, self-immolative polymers could be used to break down macromolecules into environmentally assimilable byproducts, minimizing environmental impact. (ii) Active functional surfaces, e.g., self-cleaning and self-healing coatings (highlighted in **Figure 2.13** and **Table 2.1**), can further stabilize performance in abrasive, particle-rich environments. (iii) Stimuli-responsive materials also offer opportunities to develop smart TENG sensors: light-sensitive semiconductors (e.g., $MoS_2$, ZnO, $TiO_2$) could provide self-cleaning, shading control, and photoperiod monitoring, while chemically responsive materials, e.g., PDA, PANI, and PPy, could enable detection of chemical spills or sensing of pesticides. Beyond stability, functional materials can transform TENGs from simple harvesters into (iv) smart sensors, where the active surface itself functions simultaneously as the power source, detection layer, transducer, and communication interface within agricultural and other environmental applications. However, a broad spectrum of functional materials remains unexplored, presenting clear opportunities to impart advanced sensing and adaptive capabilities to next-generation agricultural TENGs.

Device and mechanical design must move beyond rigid, laboratory-optimized formats toward mechanically adaptive systems that integrate seamlessly with the dynamic and irregular surfaces found in farms. (i) Self-adjusting and stretchable TENG layers could be designed to conform to plant stems or irregular environmental substrates without losing contact intimacy. Similarly, modular geometries that expand or contract in response to plant growth, wind, or soil shifts can help preserve triboelectric interface integrity. Thus, (ii) structural designs incorporating shape-memory materials could improve durability, reduce mechanical fatigue, and maintain a high signal-to-noise ratio. (iii) Matching the mechanical stiffness of triboelectric interfaces to optimize contact area can enhance energy conversion efficiency. (iv)

Incorporating vibration isolation layers or directional coupling mechanisms could improve mechanical-to-electrical conversion efficiency while filtering non-relevant noise. Thus, we envisage that integrating adaptive mechanical principles with vibration isolation layers could improve mechanical-to-electrical conversion efficiency while simultaneously filtering out non-relevant noise.

Software and data integration for decision-making will ultimately determine the impact of TENG-enabled agriculture. (i) Multi-node validation across distributed sensors can first suppress spurious readings by cross-checking events detected at different nodes, improving robustness against local noise. At the signal level, (ii) stressor recognition systems could identify the specific environmental triggers (e.g., wind, rainfall, or pest activity) that influence triboelectric outputs. (iii) Real-time baseline recalibration then compensates for gradual drift caused by environmental variability, mechanical wear, or electrode degradation, maintaining accuracy over long deployments. Finally, (iv) machine learning–assisted noise suppression further refines detection by learning the characteristic time–frequency patterns of genuine agronomic events, thereby filtering out random vibrations or transient disturbances. For instance, recent advances in AI-assisted signal processing using models such as PCA-based feature extraction, convolutional neural networks, and k-nearest neighbor classifiers have shown the ability to distinguish valid mechanical stimuli,[290] suppress environmental noise, and enhance detection specificity. Coupling these strategies with ultra-low-power edge-computing nodes allows *in-situ* data cleaning, compression, and decision-making, reducing transmission demands and latency in distributed IoT networks.[10,290–292] Over the long term, the convergence of functional materials, intelligent data analytics, and TENG technology could produce adaptive sensing platforms capable not only of detecting but also predicting critical agricultural events, thereby enabling proactive and resource-efficient farm management.

Finally, our last outlook highlights field validation and scalability as key to accelerating commercialization, since TENGs are not yet widely adopted. We envision four main steps toward this transition: (i) life-cycle impact, (ii) multi-season trials, (iii) reliability and cost metrics, and (iv) scalability in low-resource systems. First, standardized LCA frameworks tailored for nanogenerators should be developed, covering raw material extraction, scalable fabrication, operational lifespan, and end-of-life disposal or recycling. Such assessments would allow comparison of biodegradable or self-immolative polymers with conventional fluoropolymers in terms of carbon footprint and persistence. Second, long-term multi-season trials across diverse climates and crop systems are required to test durability, stability, and environmental resilience under real agricultural conditions. Complementary accelerated aging protocols (mechanical wear cycles, UV exposure, chemical spraying) can further help estimate mean time to failure. Third, techno-economic models quantifying cost-per-sensor and energy-per-dollar generated are needed to provide realistic adoption metrics. Predictive maintenance algorithms trained on output patterns could also support reliability and reduce downtime. Finally, scalability in low-resource farming systems will depend on low-cost, modular, and repairable designs that can be integrated into existing practices without specialized tools. This ensures that TENG deployment is not restricted to high-tech farms but also benefits smallholders and low-income communities.

In conclusion, the path forward for TENGs in agriculture lies at the intersection of four directions: advanced functional materials, device architecture and design, software advancement, and validation and scalability. By integrating energy harvesting directly into agricultural infrastructure, TENGs could evolve from niche research devices into core enablers of resilient, sustainable, and intelligent farming practices, pushing the boundaries of both nanogenerator technology and precision agriculture.

### 2.7.2 **Conclusions**

Translating energy harvesting technologies from the lab bench to the farm field introduces a host of environmental variables that challenge both device stability and sensing precision. In response to the rising demand for sustainable and innovative agricultural practices, integrating TENGs into agricultural systems offers a transformative opportunity to advance Agriculture 4.0 through smart applications. By incorporating TENGs, agriculture can transition toward cleaner energy, sustainable resource use, and intelligent, technology-driven practices. In this article, we highlight the primary challenges encountered during the *in-situ* application of TENGs in agriculture, focusing on electrical output consistency, improving durability and device stability, and optimizing their utilization for smart systems. **Table 2.3** summarizes the current status, key challenges, and recommended strategies for implementing TENGs in agricultural and environmentally demanding settings, offering a comprehensive overview of potential pathways for overcoming these barriers.

**Table 2.3.** Current status, challenges, and recommended strategies for triboelectric nanogenerators in agricultural and environmentally challenging settings.

| Aspect | Current Status | Challenges | Recommendations |
|---|---|---|---|
| Device design | Four working modes (VCS, LS, SE, FT), SE most common, limited adaptability | Mechanical mismatch, wear, and wiring limit real-world adaptability | Tailor design to field conditions; adopt hybrid designs for multi-axis energy harvesting |
| Material selection | Common use of dielectrics: PDMS, PET, PTFE; Electrodes: Cu, Al | Poor durability; interfacial failure; environmental risks | Use biodegradable, robust, and hydrophobic materials; assess LCA |
| Charge transfer efficiency | Highly affected by contamination and stiffness mismatch | Inconsistent output; no predictive control | Optimize surface design and stiffness match, add self-cleaning and data-driven control |
| Power output | High $V_{oc}$ (~10 kV), low $I_{sc}$ (μA range) | Pulsed and irregular electrical output undermines sensor reliability | Integrate storage, hybrid harvesters, and regulation circuits |
| Environmental durability | Degrades with UV, moisture, temperature, and dust | Unreliable performance in open-field; and insufficient protection and material fatigue | Encapsulation; use of thermally stable and hydrophobic materials, and UV/moisture resistance |
| Integration with sensors | Proven effective in agricultural proof-of-concepts | Electrical and protocol mismatch with commercial sensors; integration issues | Design modular; plug-and-play systems with flexible electronics; self-healing devices |
| Scalability | Lab-scale, early prototypes | Performance variability and lack of batch-to-batch uniformity; limited repeatability | Use low-cost printing techniques and scalable designs |
| Lifecycle and sustainability | Few comprehensive LCA or biodegradability studies at the device level | E-waste risks; and environmental footprint | Design for disassembly; perform full-device LCA, and prioritize biodegradable and recyclable materials |
| Eco-friendly devices | Dielectrics: polysaccharide, animal-derived, synthetic biopolymers; Electrodes: LIG, carbon-based | Low durability under humidity, heat, UV, and microbial exposure; unresolved functionality–biodegradability trade-off | Use GRAS-certified, bioinert, and field-tested materials and eco-friendly electrodes (e.g., LIG-based electrodes) |

Footnote: Vertical contact-separation (VCS), Lateral sliding (LS), Single-electrode (SE), and Freestanding triboelectric-layer (FT) modes, Polydimethylsiloxane (PDMS), Polyethylene terephthalate (PET), Polytetrafluoroethylene (PTFE), Copper (Cu), Aluminum (Al), Laser induced graphene (LIG), Generally Recognized as Safe (GRAS), Bioinert: Chemically stable and biologically non-reactive materials suitable for environmental and agricultural applications.

We have discussed the substantial influence of contaminants on nanogenerator surfaces, offering valuable insights into charge transfer mechanisms, their efficiency, and the interplay with several active surface conditions. Our review is the first to advance the understanding of electron transfer mechanisms between dirt and active materials, elucidating potential well changes caused by contaminants of different sizes and compositions. To address these challenges, strategies for tailoring surface properties have been explored, unlocking functionalities that extend beyond energy harvesting to advanced sensing and resource monitoring, e.g., developing antibacterial activity and food sterilization. As a result, we explore applications that range from conventional energy harvesting to smart systems designed to enhance chemical sensing, food production, security, and environmental oversight. Despite extensive research and promising smart applications, several challenges must be addressed before TENGs can be widely commercialized in agricultural settings, such as:

(i) Structural (expanding the mechanical elastic range) and functional (smart applications) resilience of nanogenerators under adverse environmental conditions.

(ii) Advancements in integration and ease of plug-in-off in smart applications.

(iii) Use on non-toxic and abundant materials in the device production.

(iv) Assessment of the environmental footprint across the device's entire lifecycle and its potential independent interactions.

(v) Discriminative analyte recognition and elimination of environmental interferences, e.g., dirt and biotic mechanical triggers, during operation and in smart applications.

(vi) Reversibility of detection for sustained utilization in smart systems, ensuring long service life.

(vii) Increasing signal selectivity by reducing the energy harvesting from environmental artifacts stimuli.

(viii) Integration with other generators to yield adequate electrical currents, reducing reliance on fossil fuels and grid electricity.

Looking forward, the practical deployment of high-specificity, self-powered TENG-based sensors will require overcoming the complex and varaible environmental adversities encountered in the field, e.g., temperature fluctuations, humidity, wind, radiation, and chemical or biological contamination. Ensuring accurate, stable and specific detection under such conditions remains the central challenge for self-powered sensing in smart agriculture. For this, we have advanced the understanding of electron transfer mechanism between dirt and active materials by elucidating well potential changes caused by contaminants of varying sizes and compositions. However, further research is required to understand and mitigate interactions between environmental phenomena and nanogenerator surfaces to reduce noise and artifacts from ubiquitous triggers.

Equally important will be the advancement of surface engineering technologies to maximize signal-to-noise ratios and ensure device performance across seasons and climates. While reports often overestimate the readiness of TENG-based self-powered sensors, these devices are currently best suited as initial screening tools, reducing sample volumes and associated costs while complementing analytical evaluations in controlled environments. Although significant efforts are still required for the effective deployment of TENGs in smart agriculture, the abundant availability of natural triggers offers a trade-off: they provide clean energy sources but also introduce unpredictable noise signals, hindering advancements in smart applications. Therefore, harnessing these energy reservoirs, while regulating environmental variables and enhancing the efficiency and reliability of TENGs, represents a critical step toward their successful integration into agricultural systems.

Finally, adoption of TENG-based technologies can be accelerated through policies mechanisms such as tax incentives or subsidies tied for sharing agricultural sensing data (e.g., pesticide levels and chemical residues) with regulatory agencies. Such initiatives can aid in pollution control, ensure food safety, and foster a cleaner, smarter agricultural future.

# 3

# STIMULI-RESPONSIVE GYROID SCAFFOLDS: HIERARCHICAL ARCHITECTURE AND ELECTRIC STIMULATION PROMOTE BONE REGENERATION

## 3.1 **Introduction**

Stimuli-responsive materials exhibit the remarkable ability to adapt and respond to external stimuli in a tunable manner, representing a significant advancement over non-responsive materials. To enhance and modulate scaffold responsiveness, bioactive scaffolds can be developed by electrically charging their surfaces, harnessing bioelectricity to accelerate bone repair. This promising yet underexplored approach in tissue engineering holds particular potential for treating non-union fractures that fail to heal spontaneously. These scaffolds accelerate bone regeneration and clinical outcomes by leveraging bioelectric mechanisms central to bone homeostasis, e.g., cell proliferation, extracellular matrix secretion, and remodeling.[429–431] Bone cells respond to mechanical and electrical stimuli via pathways involving calcium signaling, growth factor release, and remodeling, while electric fields facilitate ion movement across cell membranes to support bone formation.[429–433] While weak electric currents have been studied extensively in enhancing calcium entry and mineralization,[432,434–436] the use of electric fields in stimuli-responsive scaffolds with hierarchical porosity, e.g., produced by ultrasound stimulation (US), remains largely untapped.

US offers a novel, non-invasive method to enhance bone regeneration through electrically charged scaffolds that promote tissue repair, cell growth, and wound healing. To achieve

the desired bioactivity, scaffolds must replicate bone tissue by incorporating hierarchical pores with precisely controlled sizes and bioactive inorganic particles.[437] However, creating such complex pore structures is challenging, particularly when incorporating high inorganic content. Fused filament fabrication (FFF) often struggles with poor particle distribution and nozzle clogging, compromising scaffold quality. A sacrificial template approach in FFF addresses these limitations, enabling the fabrication of complex scaffolds, e.g., gyroid structures with interconnected pores. These gyroids, mimicking cancellous bone, exhibit hierarchical macro-to-micro pores and a high surface area-to-volume ratio, promoting cell attachment, proliferation, and nutrient transport.[438–440] Additionally, their triply periodic minimal surface (TPMS) structure provides smoothly curved surfaces resembling trabecular bone, with isotropic mechanical properties ensuring uniform responses to mechanical stimuli, such as US.[441,442]

The design structure and porosity level play a crucial role not only in influencing the mechanical performance but also in promoting bone cell ingrowth, e.g., by facilitating cellular attachment, neovascularization, and nutrient transport. While, recent studies have advanced our understanding of how porosity and surface charge influence mineralization under dynamic mechanical conditions,[443] their impact on electric field distribution and intensity within scaffold structures, particularly those with hierarchical interconnected sinuous pores, remains largely unexplored. Therefore, the key focus is on designing gyroid scaffolds with hierarchical pore structures at two extreme porosity levels – low (18%) and high (63%) – to evaluate the impact of electric field intensity on biological features, e.g., stem cell growth and differentiation. Additionally, considering the membrane that covers the outer surface of all bones, i.e., the periosteum, composed of collagen, a gelatin coating on the scaffold surface is also essential to mimic the membrane and closely replicate real-world conditions.[444–447]

Furthermore, because bone exhibits piezoelectric properties, strongly affecting the biological tissue's state, there has been growing interest in utilizing piezoelectric materials for bone tissue engineering lately.[432] However, commonly used piezoelectric materials like lead zirconate titanate (PZT) and lead titanate ($PbTiO_3$) present toxicity concerns, limiting their biomedical applications.[448,449] To address this, sodium niobate ($NaNbO_3$) demonstrates potential as a piezoelectric material and modulator of the dielectric constant, offering a lead-free, cost-effective, and non-toxic alternative. $NaNbO_3$ enhances surface charge retention in scaffolds, enabling fine control over electric field intensity and interactions within the pores, while its mechanical strength reinforces structural integrity and its antibacterial properties lower infection risk, making it a promising material for stimuli-responsive bioactive scaffolds.[450,451]

Although piezoelectric scaffolds polarized by conventional methods achieve higher degrees of polarization and electrical output, corona discharge polarization offers a more versatile approach by electrically charging the surface regardless of scaffold geometry. Unlike DC polarization, limited to micrometer-scale thickness, corona discharge enables the injection of electrical charges into scaffolds with geometry-independent dimensions. Corona discharge also eliminates the challenging deposition of electrodes in porous scaffolds. Moreover, it enhances biocompatibility by eliminating the need for dielectric media, e.g., oils and fluorocarbon fluids, thus preventing the introduction of potentially harmful and persistent substances used in conventional techniques. This is essential for bioactive scaffold implants, as they can absorb dielectric media, leading to contamination, altered surface properties, and compromised functionality, potentially triggering inflammatory responses or other adverse effects *in vivo*.

In this study, we address three key issues, namely: (i) designing stimuli-responsive scaffolds containing at least 30 wt% inorganic particles with high structural complexity to replicate cancellous bone characteristics; (ii) elucidating the interrelationship among mechanical, structural, electrical, and bioactive responses, focusing on how US intensity and hierarchical pore levels synergistically enhance biological outcomes; and (iii) demonstrating, for the first time, the influence of electric field alignment on bone cell organization within 3D bioactive scaffolds with zero-curvature surfaces, in contrast to traditional sharp-pore designs. Using a sacrificial template method, we fabricated high-quality $NaNbO_3$@PDMS scaffolds with tunable porosity, providing novel insights into the synergy between scaffold architecture, electrical stimulation, and mechanical performance in promoting bone cell regeneration. This work offers promising directions for next-generation bioactive scaffolds and innovative physiotherapy approaches in bone regenerative medicine.

## 3.2 Experimental Section

### 3.2.1 Materials

Sylgard® 184 was purchased from Dow Corning® (Midland, MI, USA). Niobium (V) oxide ($Nb_2O_5$, 99.9%) was acquired from Thermo Fisher Scientific® (Loughborough, UK). ABS light natural filament (1.75mm) purchased from F3D (Novo Hamburgo, RS, Brazil). Sodium hydroxide (NaOH) pellets and type-A gelatin from porcine skin were purchased from Sigma-Aldrich Co. (St. Louis, MO, USA).

### 3.2.2 Synthesis of $NaNbO_3$ nanocubes

$NaNbO_3$ nanocubes were synthesized using a hydrothermal reactor with precise temperature control. The synthesis followed a modified procedure described by Jung et al. (**Figure 3.1a)**.[452] To produce $NaNbO_3$ nanocubes, a 15-M aqueous NaOH solution was prepared by dissolving 12 g of NaOH in 20 mL of deionized (Milli-Q™) water, followed by magnetic stirring for 10 min. Then, 1 g of $Nb_2O_5$ was added to the solution, and the mixture was stirred for additional 10 min. The mixture was transferred to a PTFE container, sealed with PTFE tape to minimize mass exchange, and placed inside a hydrothermal reactor. The temperature was ramped at 10 °C·min$^{-1}$ to 150 °C, which was maintained for 10 h to promote isotropic growth and nanocube formation. The reactor was then rapidly cooled by immersion in cold water.

The precipitate, identified as $6NaNbO_3{\cdot}2H_2O$, was washed with 1 L of deionized water to remove residual sodium hydroxide and filtered under vacuum to isolate the $NaNbO_3$ nanoparticles.[453] Due to the existence of multiple polymorphs of $NaNbO_3$ (e.g., orthorhombic, cubic, tetragonal), annealing was necessary to achieve phase purity and crystallinity. The nanoparticles were then placed in an alumina crucible and annealed at 600 °C for 12 h to promote the formation of perovskite $NaNbO_3$ nanocubes.

### 3.2.3 3D printing of sacrificial ABS templates

A temperature calibration tower was used to improve printability and shape consistency, resulting in 3D scaffolds with enhanced reproducibility. Sacrificial ABS templates were printed using a Sethi S3 FFF 3D printer (Campinas, Brazil) at 200-205 °C and a printing speed of 20 mm·s$^{-1}$. Three cylindrical templates, each 100 mm in diameter and height, were printed: one without internal patterns (quasi-0% porosity) and two with gyroid-based structures exhibiting 35% and 80% porosity, respectively.

### 3.2.4 Development of gyroid-structure scaffolds

PDMS was prepared by mixing silicone elastomer and curing agent at a 10:1 weight ratio. $NaNbO_3$ (30 wt%) was incorporated, and the mixture was stirred for 20 min to ensure uniform dispersion. The resulting composite was poured into sacrificial ABS templates, vacuum-degassed for 1 h, and cured at 110 °C for 1 h. After curing, the ABS templates were dissolved in chloroform under magnetic stirring (450 rpm) overnight. The chloroform was replaced, and the process was repeated four times to ensure complete removal of the sacrificial

templates. The $NaNbO_3$@PDMS scaffold was then washed three times with 70% ethanol and ultrapure water to remove chloroform residues and dried at 70 °C for 6 h. The dried scaffolds were resized to 2.5 mm thickness and 8 mm diameter using a manual hollow punch. Finally, the scaffolds were coated with a 5 wt% gelatin solution (4 g of gelatin in 80 mL of deionized water) for 30 min and air-dried at room temperature.[454]

### 3.2.5 Electrical polarization by corona discharge

Following the fabrication of the gelatin- $NaNbO_3$@PDMS scaffolds, the top and bottom surfaces were coated with gold/palladium (Au/Pd) via sputtering. While sputtering can theoretically coat all surfaces, the porous and sinuous geometry of the gyroid structure creates a "shadowing" effect, leaving internal surfaces largely uncoated and disrupting the formation of a continuous conductive path. Consequently, electrical connectivity is confined to the exposed external surfaces due to the line-of-sight nature of the sputtering process, effectively preventing short-circuiting and ensuring proper charge separation for measurable $V_{oc}$. The scaffolds were electrically polarized using corona discharge (custom-made machine), with electric fields of 2, 3, and 4 $kV \cdot cm^{-1}$ applied at a current of ~3.7 μA for 40 min. Scaffolds without polarization (0 $kV \cdot cm^{-1}$) served as controls to evaluate the efficiency of charge injection. A custom-built system was employed for the polarization process, utilizing a potential difference between a needle and a grounded grid positioned above the scaffold.

### 3.2.6 Chemical, morphological, and compositional characterizations

Various characterization techniques were employed throughout the scaffold manufacturing process to evaluate morphology, chemical properties, and composition. X-ray diffraction (XRD; Rigaku Ultima IV) was used to confirm the synthesis of sodium niobate from the $Nb_2O_5$ precursor, identify the crystalline structure, and verify its transformation into the piezoelectric perovskite phase. The material was analyzed in powder form using CuK$\alpha$ radiation ($\lambda$ = 1.5405 Å), with Bragg angles (2$\theta$) ranging from 20° to 80° at a scanning speed of $1° \cdot min^{-1}$. The volume fraction of the perovskite phase was calculated based on the intensity ratio of the primary XRD peaks corresponding to the perovskite phase ($NaNbO_3$) and $Nb_2O_5$,[455] using Equation 3.1.

$$Wt\%\ perovskite\ = \frac{I_{perov}}{I_{perov}+I_{Nb_2O_5}} \times 100 \quad (3.1)$$

where $I_{perov}$ and $I_{Nb2O5}$ represent the intensities of the strongest reflection peaks for the perovskite phase (110) and $Nb_2O_5$ (180), respectively.

Morphological analysis of the scaffolds was performed using a magnifying lens (Leica, DM2700 M) and field emission scanning electron microscopy (FESEM; Hitachi TM3030 Plus). Elemental composition was analyzed via energy-dispersive X-ray spectroscopy (EDX; Oxford INCA Energy 350). Fourier-transform infrared (FTIR) spectroscopy was carried out on a Nicolet 6700 spectrometer (Thermo Nicolet 6700) with an ATR accessory featuring a diamond crystal. The scan range was 4000–500 $cm^{-1}$ with 64 scans and a spectral resolution of 4 $cm^{-1}$.

2D and 3D projections of the scaffolds were obtained using X-ray micro-computed tomography (X-ray μCT; SkyScan 1272, Belgium), with quantitative analysis and volume/surface rendering performed using the CT-Analyser software. Static water contact angles (CA) were measured with a DataPhysics OCA 15 Plus using the sessile drop method and 1 μL ultrapure water droplets. The CA was recorded over 60 s with one data point per second, analyzed using the SCA 20 software and the Laplace-Young approximation model, with at least three measurements per sample.

### 3.2.7 **Mechanical properties**

Cyclic mechanical tests were performed on the scaffolds using a universal testing machine (Instron, model 5569) with a 5-kN load cell and a crosshead speed of 60 $mm \cdot min^{-1}$. The mechanical compression cycle methodology, with a strain range of 12.5% to 50%, is shown in **Figure 3.7a**. Compressive behavior was studied at 12.5, 25, 37.5, and 50% strains over 100 cycles using scaffolds with a uniform diameter and thickness of 100 mm. At each strain level, the maximum compressive stress, energy absorption capacity, and elastic modulus were determined. Young's modulus was calculated using linear regression in the linear viscoelastic region, following Hooke's law, with data fitted using the least squares method in OriginPro 8.5.

To assess damping capacity, the ratio of energy loss to total strain energy was determined every 10 cycles. The relative damping (ψ) value was calculated using Equation 3.2.

$$\psi = \frac{Energy\ loss}{Strain\ energy} \times 100 \tag{3.2}$$

where energy loss (corresponding to dissipation of energy, e.g., heat release) was obtained by integrating the area enclosed by the hysteresis loop, while strain energy was determined by integrating the area under the loading curve.

Densification strain was determined from stress-strain curves by identifying the point at which the slope increased significantly - by at least 50% - following the elastic region. This point was further refined using the second derivative of the curve to accurately pinpoint the onset of pore collapse. Structural stability was assessed by monitoring Y-axis deformation (i.e., thickness-deformation) over 100 cycles under non-monotonic loading conditions, replicating the mechanical forces experienced by bones during real-world human activities. Thickness deformation was calculated using Equation 3.3.

$$\Delta Y = \frac{Y_f - Y_i}{Y_i} \times 100 \tag{3.3}$$

where $\Delta Y$ represents the percentage of thickness deformation after 100 cycles, $Y_i$ is the initial thickness, and $Y_f$ is the thickness after 100 cycles of compressive stress at 25% or 50% strain.

The Young's modulus in the compression test was determined using the linear regression method applied to the linear viscoelastic region, based on Hooke's law, which describes the proportional relationship between stress and strain in this region. The slope of the fitted line was determined using the least squares method via Origin V8.1 software. Data points corresponding to the linear region were selected, while those outside the elastic regime or exhibiting non-linear behavior, such as the onset of plastic deformation, were excluded. The regression was performed until an $R^2$ value greater than 0.98 was obtained. Young's modulus was then calculated directly from the slope of the fitted line.

### 3.2.8 **Mechano-electrical output**

Open circuit electrical voltage ($V_{oc}$) was measured on cylindrical scaffolds (8 mm in diameter and 2.5 mm in thickness) by applying mechanical tensions of 20, 40, 60, and 80 N at 2 Hz, using a custom-built device. The $V_{oc}$ was also characterized from US at 50 and 250 $mW \cdot cm^{-2}$ under the bone cell growth conditions used in biological characterization. Carbon tape was used to connect the positive and ground electrodes, and measurements were recorded with a Tektronix TBS1000C oscilloscope with data collected at 625 samples per second (20k points over a 30-s range). To evaluate structural stability, the $V_{oc}$ was monitored during prolonged mechanical cycling (up to 20,000 cycles) in the plastic region (80 N at 2 Hz), focusing on the most unstable scaffold (63% porosity).

### 3.2.9 Finite elemental analysis

COMSOL® Multiphysics simulations were performed to examine the impact of varying porosity levels (0%, 18%, and 63%) and structural design on the intensity and distribution of the electric field within the scaffold pores. 2D images obtained from X-ray μCT were used to accurately design the scaffold structures and pores. Additional simulations considered different media (air or aqueous) and dielectric constants ($\epsilon_r$ = 4, 8, and 25). The modeling parameters are detailed in **Table 3.1**.

**Table 3.1.** Parameters used in COMSOL® simulation for electric field intensity and distribution analysis of scaffolds.

| Parameters | Value |
|---|---|
| Thickness of the dielectric (mm) | 10 |
| Relative permittivity of gelatin-30%-$NaNbO_3$@PDMS | 4 |
| Relative permittivity of gelatin-40%-$NaNbO_3$@PDMS | 8 |
| Relative permittivity of air | 1 |
| Relative permittivity of aqueous medium | 70 |
| Electrode (Au/Pd) thickness (mm) | 0.01 |
| Scaffold width (mm) | 20 |
| Scaffold length (mm) | 20 |
| Surface charge density of scaffold with $\varepsilon_r$ = 4 ($C \cdot m^{-2}$) | $1x10^{-5}$ |
| Surface charge density of scaffold with $\varepsilon_r$ = 8 ($C \cdot m^{-2}$) | $2x10^{-5}$ |
| Surface charge density of scaffold with $\varepsilon_r$ = 24 ($C \cdot m^{-2}$) | $4x10^{-5}$ |

### 3.2.10 Biological characterization

All biological characterizations were conducted using cylindrical scaffolds (8 mm in diameter, 2.5 mm in thickness) treated with 4 $kV \cdot cm^{-1}$ corona discharge for 40 min.

#### 3.2.10.1 Cell culture

The human bone marrow-derived mesenchymal stem cells (hBM-MSCs) used in the following study were isolated from bone marrow aspirates (Male, 24) (obtained from Centro Clínico da GNR, Portugal) according to protocols established at Stem Cell Engineering Research Group, Institute for Bioengineering and Biosciences (iBB) at Instituto Superior Técnico

(IST).[456] The cells were preserved in liquid/vapor nitrogen tanks as part of the cell bank available at iBB-IST. All human samples were obtained from healthy donors after written informed consent according to Directive 2004/23/EC of the European Parliament and of the Council of 31 March 2004 on setting standards of quality and safety for the donation, procurement, testing, processing, preservation, storage, and distribution of human tissues and cells (Portuguese Law 22/2007, June 29), with the approval of the Ethics Committee of the respective clinical institution. Before conducting the cell culture assays, the isolated hBM-MSCs were expanded on tissue culture flasks (T-75 $cm^2$) using low-glucose Dulbecco's Modified Eagle Medium (DMEM) (ThermoFisher, Waltham, MA, USA) supplemented with 10 vol% fetal bovine serum (Gibco FBS) (ThermoFisher, Waltham, MA, USA) and 1 vol% antibiotic-antimycotic (ThermoFisher, Waltham, MA, USA). The cell culture media was replaced every 3-4 d. The cells were kept in an incubator at 37 °C and 5% $CO_2$ in a humidified atmosphere. All the experiments were conducted using cells between passages P5 and P6.

#### 3.2.10.2 **Scaffold preparation and sterilization**

The scaffolds were then sterilized by UV light exposure overnight. Afterward, the gelatin-$NaNbO_3$@PDMS with different porosities were transferred to ultra-low cell attachment 6- and 24-well plates (Corning, Somerville, MA, USA), with the former being used for scaffolds under US and the latter being used for the respective static conditions. The scaffolds were then washed twice with a 70 vol% ethanol solution and three times with a 1 vol% anti-anti solution (prepared in PBS). Before cell seeding, the scaffolds were incubated in cell culture media for 1 h at 37 °C.

#### 3.2.10.3 **Cell seeding, culture, and osteogenic differentiation**

Previously expanded hBM-MSCs were seeded in the gelatin-$NaNbO_3$@PDMS scaffolds at a density of 120.000 cells per construct. The cell-seeded scaffolds were incubated without cell culture media at 37 °C and 5% $CO_2$ in a humidified atmosphere for 2 h to promote initial cell adhesion. Osteogenic media comprised of DMEM supplemented with 10 vol% FBS (MSC qualified), 10 mM of β-glycerolphosphate (Sigma-Aldrich, St. Louis, MI, USA), 10 nM of dexamethasone (Sigma-Aldrich), 50 μg·mL-1 of ascorbic acid (Sigma-Aldrich) and 1 vol% anti-anti was added to the cell-seeded scaffolds. Media were renewed every 3-4 d. Cells was cultured for 14 d at 37 °C and 5% $CO_2$ in a humidified atmosphere.

#### 3.2.10.4 **hBM-MSC metabolic activity assay**

The metabolic activity of human bone marrow-derived mesenchymal stem cells (hBM-MSCs) cultured on the scaffolds was assessed using an AlamarBlue™ assay (AlamarBlue™ Cell Viability Reagent; ThermoFisher) according to the manufacturer's guidelines. This non-destructive assay was performed under both static and mechanically stimulated experimental conditions on days 1, 7, and 14 of culture to evaluate cellular responses over time. A 10 vol% AlamarBlue™ solution prepared in cell culture media was added to the scaffolds, which were incubated at 37 °C in a humidified atmosphere with 5% $CO_2$, protected from light, for 3 h. Fluorescence intensity was measured using a microplate reader (Infinite 200 Pro; Tecan, Zurich, Switzerland) at an excitation/emission wavelength of 560/590 nm. For each experimental group, measurements were obtained from three independent scaffolds (n = 3), with fluorescence intensity recorded in triplicates per sample. Acellular scaffolds served as blank controls.

#### 3.2.10.5 **Calcium content and mineralization**

Calcium deposition after 14 d of osteogenic differentiation was evaluated using a calcium colorimetric assay. Absorbance was measured following reaction with a chromogenic reagent and buffer, normalized to cell numbers. Mineralization on the gelatin-$NaNbO_3$@PDMS scaffolds was assessed using Raman spectroscopy after 14 d of cell culture. Spectral analysis focused on the 400–1200 $cm^{-1}$ range to detect calcium phosphate production, with Raman mapping at 600, 970, and 1045 $cm^{-1}$ conducted using an inVia™ Qontor confocal Raman microscope. A 532 nm laser at 50% power, 1800 lines·$mm^{-1}$ grating, and a 50x objective lens were used for the measurements.

#### 3.2.10.6 **Immunofluorescence of ECM proteins**

The production of type I collagen and osteopontin, key bone ECM proteins, by differentiated MSCs on the constructs, was assessed after 14 d using immunofluorescence imaging. Constructs fixed with PFA were washed with PBS and then treated with a 1% BSA solution in PBS. Subsequently, cell-seeded gelatin-$NaNbO_3$@PDMS constructs were immersed in a permeabilization/blocking solution (1% BSA, 10% FBS, and 0.3% Triton X-100) for 45 min at room temperature. Samples were then incubated overnight at 4 °C with primary antibodies for type I collagen (MA1-26771; ThermoFisher) and osteopontin (ab8448; Abcam) at a 1:250 dilutions in the blocking solution. The next day, constructs were treated with secondary antibodies (1:250 in 1% BSA) for 1 h at room temperature in the dark: AlexaFluorTM 448 (ThermoFisher) for osteopontin and AlexaFluorTM 546 (ThermoFisher) for type I collagen. After two PBS

washes, constructs were counterstained with DAPI (1.5 μg·mL$^{-1}$ in PBS) for 10 min, rinsed with PBS, and visualized under a 20x lens on a Zeiss Axio Imager Z2m confocal microscope.

#### 3.2.10.7 **RNA isolation and qRT-PCR analysis**

Total RNA extraction was performed using the RNeasy Mini Kit (Qiagen, Hilden, Germany) on MSC-seeded gelatin-$NaNbO_3$@PDMS scaffolds after 14 d of osteogenic differentiation. Briefly, lysis buffer (RLT buffer) was added to each scaffold sample and agitated for 1 h. Total RNA was then isolated and purified according to the manufacturer's instructions. RNA concentration was measured using a NanoVue Plus spectrophotometer (GE Healthcare, Chicago, IL, USA). Complementary DNA (cDNA) was synthesized from the purified RNA using the High-Capacity cDNA Reverse Transcription Kit (Applied Biosystems, Waltham, MA, USA), following the manufacturer's protocol. Reaction mixtures were incubated in a T100™ thermal cycler (Bio-Rad, Hercules, CA, USA) at 25 °C for 10 min, 37 °C for 120 min, and 85 °C for 5 min, before being held at 4 °C until further use. Primer sequences for the qRT-PCR analysis are listed in **Table 3.2**. Relative gene expression was calculated using the $2^{-\Delta\Delta Ct}$ method (n =3).

**Table 3.2.** Primer sequences used in the RT-qPCR analysis.

| Gene | Forward primer sequence | Reverse primer sequence |
|---|---|---|
| ***GAPDH*** | 5′-GGTCACCAGGGCTGCTTTTA-3′ | 5′-CCTGGAAGATGGTGATGGGA -3′ |
| ***ALP*** | 5′-ACCATTCCCACGTCTTCACATTT-3′ | 5′-AGACATTCTCTCGTTCACCGCC-3′ |
| ***Runx2*** | 5′-AGATGATGACACTGCCACCTCTG-3′ | 5′-GGGATGAAATGCTTGGGAACT-3′ |
| ***COL I*** | 5′-CATCTCCCCTTCGTTTTTGA-3′ | 5′-CCAAATCCGATGTTTCTGCT-3′ |
| ***OC*** | 5′-TGTGAGCTCAATCCGGCATGT-3′ | 5′-CCGATAGGCCTCCTGAAGC-3′ |
| ***OPN*** | 5′-CAGGTCTGCGAAACTTCTTAG-3′ | 5′-CTCCATTGACTCGAACGACTC-3′ |
| ***PIEZO1*** | 5′-CAGGCCTATGAGGAGCTGTC-3′ | 5′-TTGTAGAGCTCCCGCTTCAT-3′ |
| ***PIEZO2*** | 5′-GCCCAACAAAGCCAGTTGAA-3′ | 5′-GGGCTGATGGTCCACAAAGA-3′ |
| ***TRPV4*** | 5′-GACGGGGACCTATAGCATCA-3′ | 5′-AACAGGTCCAGGAGGAAGGT-3′ |
| ***CACNA1C*** | 5′-GTACAAAGACGGGGAGGTTGAC-3′ | 5′-GTAGTTGTAGATGGGGCCCTTG-3′ |
| ***ERK1*** | 5′-ACCTGCGACCTTAAGATTTGTGA-3′ | 5′-AGCCACATACTCCGTCAGGAA-3′ |
| ***SOST*** | 5′- ACTCGGACACGTCTTTGGTG-3′ | 5′-GTACATGCAGCCTTCGTTGC-3′ |

A heatmap was generated to visualize gene expression changes under varying US intensities and scaffold porosities. To quantify the effect of US, the percentage change in gene expression between 250 and 50 mW·cm$^{-2}$ was calculated for each porosity condition (0%, 18%, and 63%), normalized to the expression at 250 mW·cm$^{-2}$. For porosity comparisons, the percentage change in gene expression between 18% and 63% porosity was calculated for each US intensity (50 and 250 mW·cm$^{-2}$), relative to the expression at 18% porosity. These percentage differences were then used to construct a standardized heatmap on a 200% scale, featuring 10 major and 20 minor gradient levels for detailed visualization.

#### 3.2.10.8 **Cell morphology via SEM and confocal microscopy**

SEM imaging (FESEM, Hitachi TM3030 Plus) was used to analyze cell morphology after 14 d of culture, while the elemental composition was examined using energy-dispersive X-ray spectroscopy (EDX; Oxford INCA Energy 350). Samples were fixed, dehydrated, air-dried, and coated with gold/palladium before imaging. Additionally, DAPI and Phalloidin staining were used to visualize the nuclei and cytoskeleton of MSCs using confocal microscopy.

#### 3.2.10.9 **Ultrasound stimulation (US)**

US was applied using a SP300 ultrasound generator (Sonidel, Dublin, Ireland) with a 7 cm$^2$ ultrasonic probe in pulsed mode. Two stimulation regimens were tested: US intensities of 50 and 250 mW·cm$^{-2}$, at a frequency of 1 MHz, pulse repetition frequency (PRF) of 1 kHz, and a 20% duty cycle. These were compared to a non-stimulated control. Constructs were stimulated for 3 min every two days over a 14-d culture period. **Figure 3.1b,c** illustrates the US methodology for scaffolds with porosities of 0%, 18%, and 63% at 0, 50, and 250 mW·cm$^{-2}$ intensities, as well as the experimental timeline from scaffold seeding on day 0.

### 3.2.11 **Statistical analyses**

Data are presented as mean values with the standard error of independent measurements or assays ($n \geq 3$). Statistical analysis was performed using the OriginPro 8.5 and Minitab 17 softwares. Quantitative data were subjected to analysis of variance (ANOVA), followed by Tukey's mean comparison test. P-values of $< 0.05$ were considered significant for all statistical tests, where applicable.

## 3.3 Results and Discussion

### 3.3.1 Fabrication and biological assessment of gyroidal bioactive scaffolds

Developing composite scaffolds with high and uniformly distributed inorganic content within complex 3D geometries remains a critical challenge in tissue engineering. To address this, a gyroid-based sacrificial template was fabricated via 3D FFF printing using the acrylonitrile-butadiene-styrene (ABS) terpolymer, producing porosities of ca. 35%, 80%, and 100% **(Figure 3.1a$_1$)**. The gyroid architecture was strategically selected to mimic trabecular bone microarchitecture while ensuring isotropic mechanical behavior and uniform transmission of mechanical and electrical stimuli, particularly during ultrasound stimulation. Its continuous, zero-mean curvature pore network minimizes stress concentrations, promotes uniform acoustic wave propagation, and enhances mechano-electrical coupling throughout the 3D scaffold, supporting efficient and homogeneous cellular stimulation. In addition, to enhance dielectric properties and piezoelectric performance, 30 wt% $NaNbO_3$ was incorporated into the PDMS matrix, cast into the templates, thermally cured **(Figure 3.1a$_2$)**, and immersed in

chloroform to dissolve the ABS templates **(Figure 3.1a$_3$)**, yielding porous scaffolds with confirmed porosities of ~0%, 18%, and 63% as analyzed by X-ray μCT **(Figure 3.1a$_4$)**.

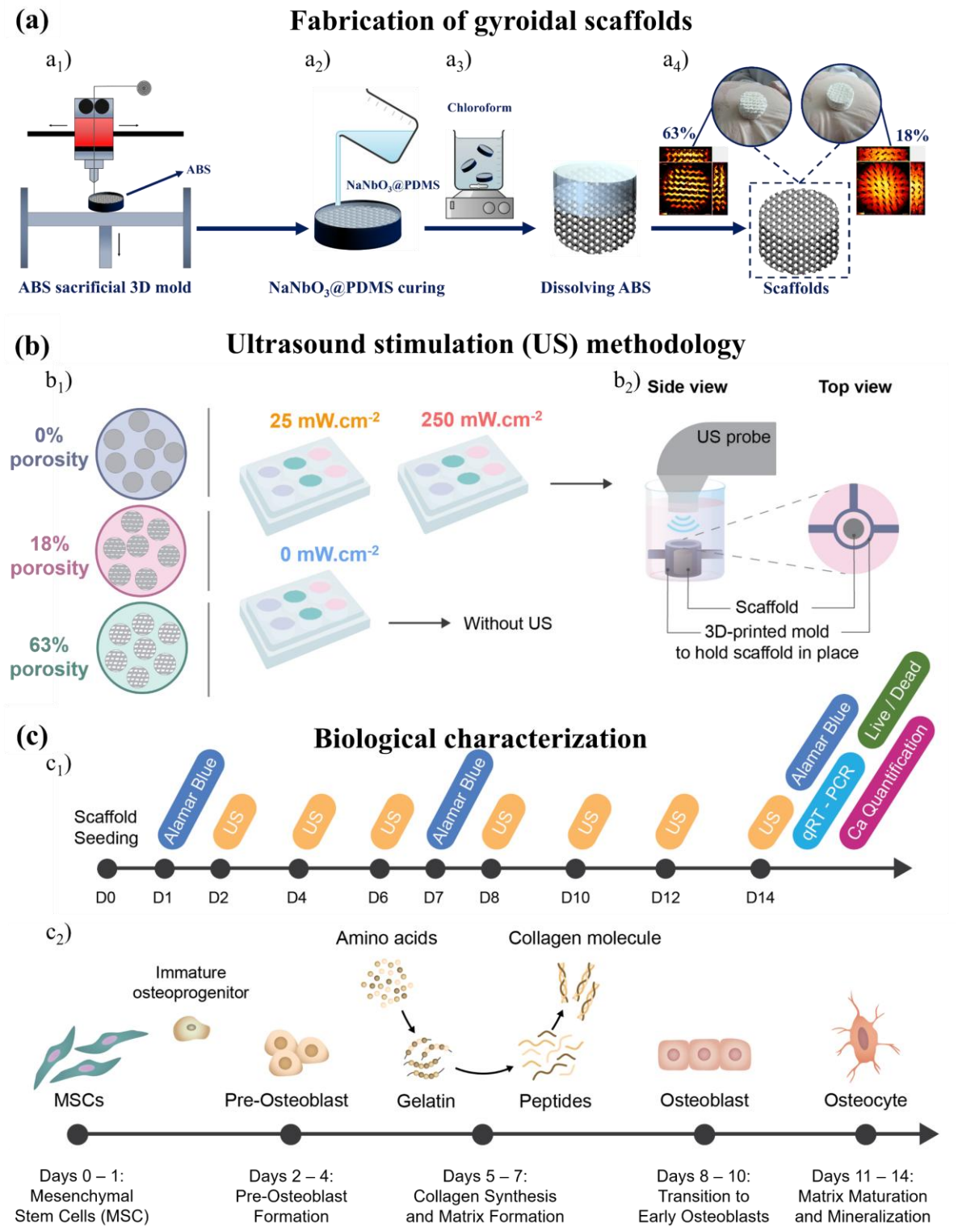


**Figure 3.1.** Schematic illustration of the development of gyroid-based NaNbO$_3$@PDMS scaffolds with tunable porosity and their biological assessment for bone tissue regeneration. (a) Fabrication process: a$_1$) Sacrificial templates are created using a 3D fused filament fabrication (FFF) printer. a$_2$) NaNbO$_3$@PDMS composite is poured into the

template and cured to form the scaffold structure. $a_3$) ABS sacrificial template is dissolved in chloroform. $a_4$) Final scaffolds with porosities of 0%, 18%, and 63% are obtained, as quantified by X-ray microcomputed tomography. (b) Schematic representation of the ultrasound stimulation (US) methodology: $b_1$) Scaffolds with 0%, 18%, and 63% porosities underwent US at intensities of 0, 50, and 250 mW·cm$^{-2}$ in 9-well plates. $b_2$) Scaffolds were held in position using a custom 3D-printed model within a cell culture plate. Each well corresponded to a specific US condition, with the control condition representing non-stimulated samples. (c) Biological characterization timeline: $c_1$) Experimental timeline outlines scaffold seeding on 0 d, followed by 3-min US treatments every 2 d with bone cell growth monitored over 14 d. Alamar Blue assays were performed on days 1, 7, and 14, while qRT-PCR and calcium quantification assays were conducted on day 14 to assess cellular activity and mineralization. $c_2$) Stages of cellular growth and differentiation during osteogenesis: MSCs (Days 0 - 1) differentiate into pre-osteoblasts (Days 2 - 4). Collagen synthesis and matrix formation occur (Days 5 - 7), followed by transition to osteoblasts (Days 8 - 10). The matrix matures and mineralizes into osteocytes (Days 11 - 14).

**Figure 3.1b** illustrates the protocol used to evaluate the bioactivity of the scaffolds, focusing on bioelectricity mechanisms stimulated by physiotherapy-like procedures, *i.e.*, US. Two distinct US regimens were tested: low-US (50 mW·cm$^{-2}$) and high-US (250 mW·cm$^{-2}$), along with a non-stimulated control condition (0 mW·cm$^{-2}$) **(Figure 3.1b$_1$)**. Scaffolds were positioned using a custom-designed 3D-printed holder within a cell culture plate and subjected to stimulation for 3 min every other day over a 14-d culture period **(Figure 3.1b$_2$)**.

**Figure 3.1c** presents the experimental timeline for biological characterization, designed to assess the bioactivity of scaffolds in response to US. Scaffold seeding occurred on day 0, followed by 3-min US treatments every other day, with Alamar Blue assays measuring cell viability and metabolic activity on days 1, 7, and 14, and qRT-PCR and calcium quantification assessing gene expression and mineralization, respectively, on day 14 **(Figure 3.1c$_1$)**. A framework for understanding the temporal effects of US on each stage of bone tissue formation is presented, aiding in the interpretation of experimental outcomes **(Figure 3.1c$_2$)**. It illustrates the progression of cellular growth and differentiation during osteogenesis, beginning with mesenchymal stem cells (MSCs) on days 0 - 1, and transitioning to pre-osteoblasts by days 2 - 4. Collagen synthesis and matrix formation occur from days 5 to 7, followed by osteoblast development on days 8 - 10. By days 11 - 14, the matrix matures and mineralizes into osteocytes.

### 3.3.2 Chemical and morphological characterization of gyroidal scaffolds

$NaNbO_3$ nanocubes were synthesized via a hydrothermal process with precise temperature control **(Figure 3.2a)**. 15 M NaOH solution was mixed with 1 g of $Nb_2O_5$ for 10 min, then transferred to a PTFE container, sealed with PTFE tape, and placed in a hydrothermal reactor.

The temperature was raised at 10 °C·min$^{-1}$ to 150 °C and held for 10 h to enable nanocube formation. After rapid cooling in cold water, the precipitate ($6NaNbO_3 \cdot 2H_2O$) was washed with Milli-Q water to remove residual NaOH and vacuum-filtered to isolate $NaNbO_3$ nanoparticles. Since $NaNbO_3$ can form various polymorphs (e.g., orthorhombic, cubic, tetragonal), annealing at 600 °C for 12 h was performed to improve crystallinity and ensure phase purity, yielding perovskite $NaNbO_3$ nanocubes consistent with previous studies.[455,457]

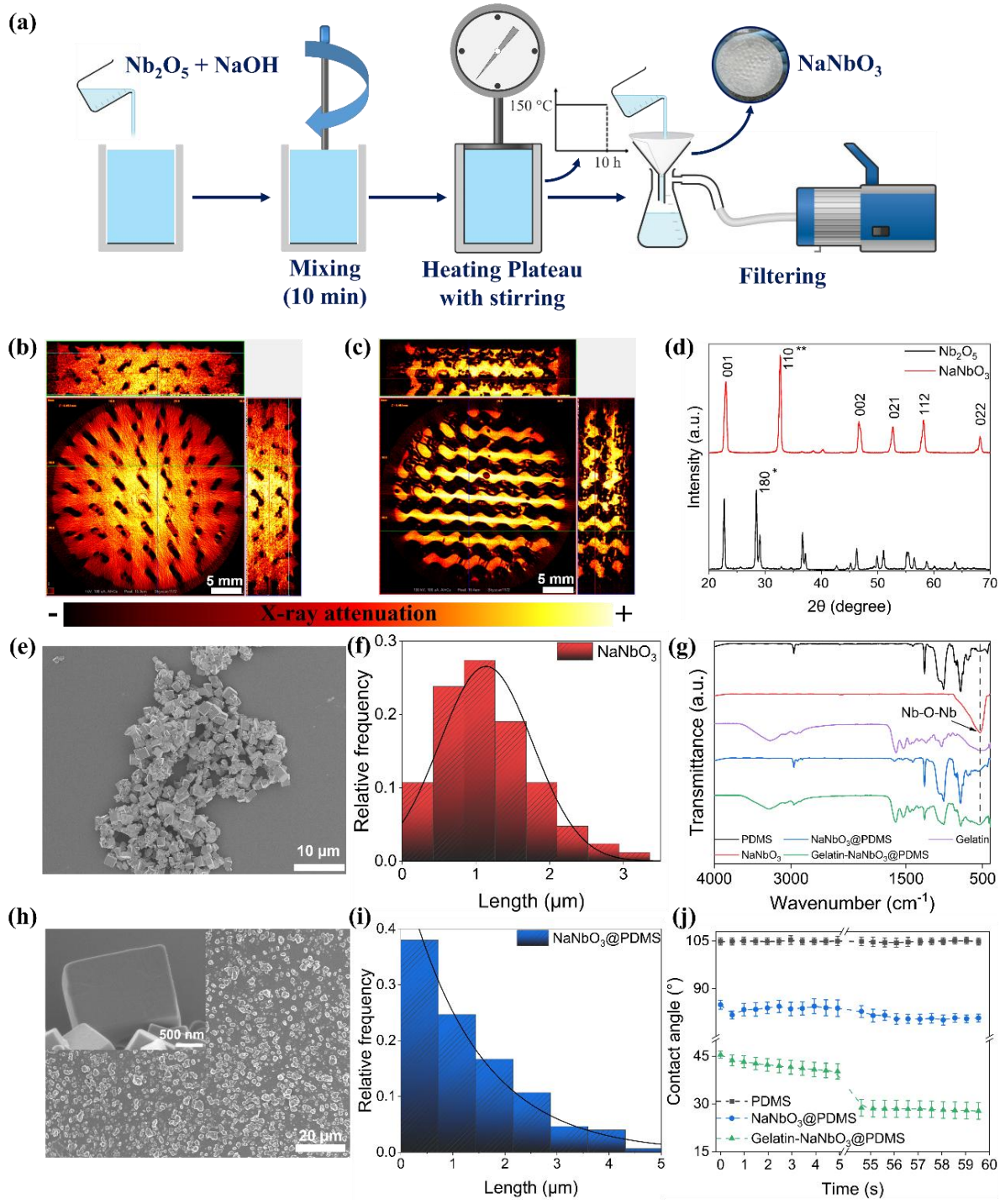

**Figure 3.2.** Characterization of synthesized materials and gelatin-PDMS@$NaNbO_3$ scaffolds. (a) Schematic illustration of the hydrothermal synthesis approach for cubic $NaNbO_3$ particles, employing the reaction of $Nb_2O_5$ with NaOH (15 M) at 150 °C for 10 h, followed by filtration and drying to yield perovskite-phase $NaNbO_3$. X-ray micro-computed tomography reconstructions (top, frontal, and side views) of scaffolds with (b) 18% and (c) 63% porosity (scale bar = 5 mm). Lighter areas indicate higher X-ray attenuation. (d) XRD patterns of annealed $NaNbO_3$ nanoparticles: * marks the strongest $Nb_2O_5$ peak, and ** indicates the $NaNbO_3$ perovskite phase. (e) SEM images of $NaNbO_3$ at (f) 2k magnification (scale bar = 10 μm) and (h, inset) 40k magnification (scale bar = 500 nm), and (h) $NaNbO_3$@PDMS surface at 950x magnification (scale bar = 20 μm). Particle size distribution of synthesized (f) $NaNbO_3$ and (i) 30 wt% $NaNbO_3$ particles incorporated on the PDMS. (g) ATR-FTIR spectra of PDMS (black), $NaNbO_3$ (red), $NaNbO_3$@PDMS (blue), and gelatin-$NaNbO_3$@PDMS (green). (j) Contact angle measurements of PDMS (black), $NaNbO_3$@PDMS (red), and gelatin-$NaNbO_3$@PDMS (blue) over 60 s.

The $Nb_2O_5$ precursor exhibited an XRD peak at 28.5° **(Figure 3.2d)**, corresponding to pseudohexagonal $Nb_2O_5$ (JCPDS: 28-317).[458,459] Additionally, six prominent peaks at 22.9, 32.5, 46.6, 52.5, 58.1, and 68.13° were identified, corresponding to the (001), (110), (002), (021), (112), and (022) planes of the orthorhombic $NaNbO_3$ phase.[460–462] The FTIR spectrum of the $NaNbO_3$@PDMS composite further confirmed the synthesis and crystalline structure of $NaNbO_3$, indicated by the band cantered at 536 $cm^{-1}$ for M–O stretching, M–O–M bending (M = Nb, Na), and lattice vibrations typical of the perovskite phase **(Figure 3.2g)**.[461,463,464] This broad absorption band, along with the absence of the 1640 $cm^{-1}$ water-stretching signal, confirms the loss of hydrated water upon annealing of $NaNbO_3 \cdot 2H_2O$, while the absence of additional bands further validates the $NaNbO_3$ perovskite phase, consistent with XRD results. Furthermore, the coating of $NaNbO_3$@PDMS with gelatin confirmed the presence of O-H stretching at 3600 $cm^{-1}$, C=O stretching at 1637 $cm^{-1}$ (amide I), and N-H deformation between 1500 and 1550 $cm^{-1}$ (amide II).[465] These bands contribute to surface hydrophilization of scaffolds and also serve as non-specific binding sites for cells.

X-ray μCT confirmed scaffold porosities of 18% and 63% after dissolving the ABS template **(Figure 3.2b-c, respectively)**. The slight difference in porosity (2% less porous) between the experimentally determined porosity by X-ray μCT and the designed 3D model is attributed to thermal warping of ABS during 3D printing. A 60% porosity level has been shown to facilitate neovascularization and bone ingrowth, facilitating oxygen and nutrient transport, essential for tissue regeneration.[466–468]

The $NaNbO_3$ particles had a predominantly cubic morphology, as revealed by SEM **(Figure 3.2e, and 3.2h inset)**. Using Scott's rule to determine the optimal bin width, a Gaussian curve was fitted to the relative frequency distribution of $NaNbO_3$ particle lengths, revealing a peak content (25%) at 1 μm **(Figure 3.2f)**. Furthermore, after incorporating 30 wt% $NaNbO_3$ into PDMS, uniform distribution and dispersion of the particles were observed **(Figure 3.2h)**, with an exponential curve indicating a peak content (37%) at the nanoscale, i.e., < 1 μm **(Figure**

**3.2i)**. Following the development of $NaNbO_3$@PDMS scaffolds, the gelatin coating was applied, resulting in a submicron-scale surface roughness that can promote enhanced cell attachment **(Figure 3.3c)**.

Gyroidal scaffolds displayed hierarchical pores with internal diameters varying across micro-to-macro scales, replicating the interconnected architecture of native bone tissue [438,469]. This structural biomimicry is critical for developing scaffolds that emulate natural cancellous bone, thereby improving their utility in bone tissue engineering. Further features of interconnected pores in 18% and 63% porosity scaffolds are shown in **Figure 3.3**.

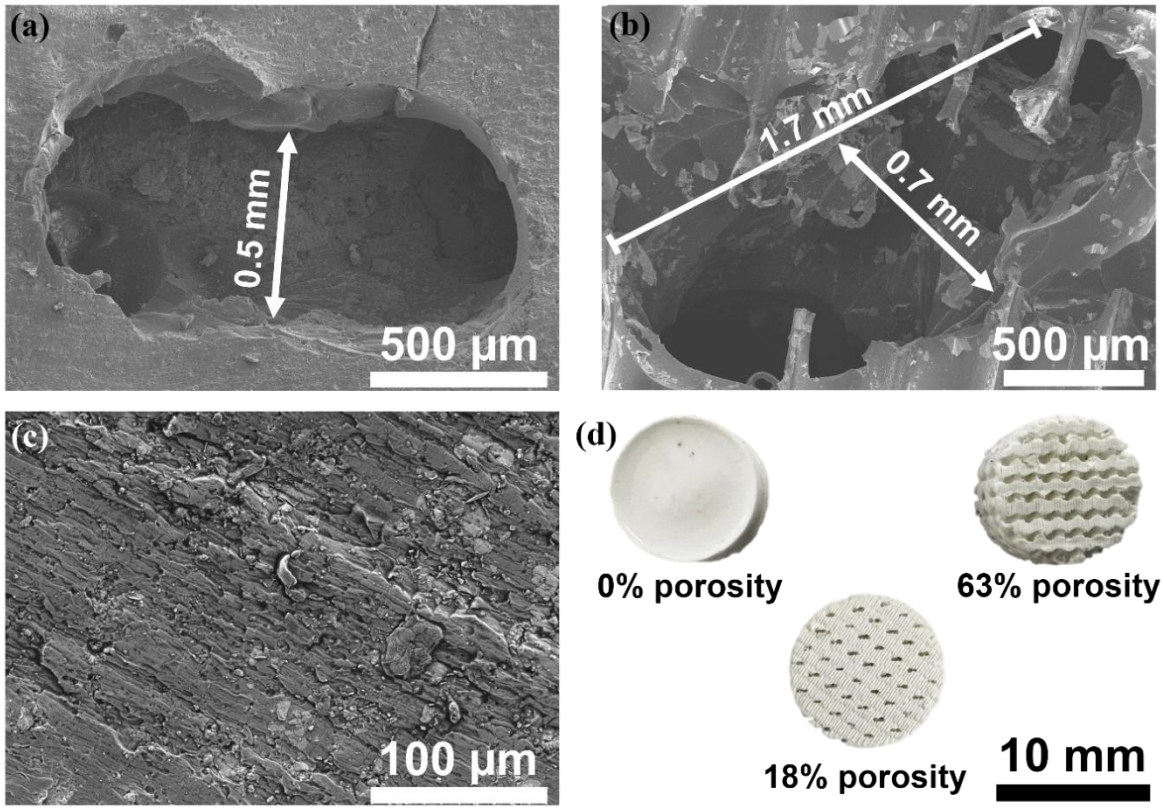
(a)
0.5 mm
500 µm
(b)
1.7 mm
0.7 mm
500 µm
(c)
100 µm
(d)
0% porosity
63% porosity
18% porosity
10 mm
(e)
2 mm
(f)
200 µm
(g)
2 mm
(h)
500 µm

**Figure 3.3.** Structural features of 18% and 63% porosity scaffolds. SEM images of (a) 18% and (b) 63% porosity scaffolds focusing on the porous regions of each scaffold (scale bar = 500 μm). (c) SEM image of the PDMS surface coated with gelatin (scale bar = 100 μm). (d) Digital images of the original scaffolds with 0%, 18%, and 63% porosity (scale bar = 10 mm). Stereo microscope views of (e) 18% resized scaffolds (scale bar = 2 mm) and focusing its the (f) porous regions (scale bar = 100 μm) and (g) 63% resized scaffolds (scale bar = 2 mm) and its focusing the (h) porous regions (scale bar = 250 μm).

Contact angle measurements confirmed the hydrophobic nature of the PDMS scaffold (105°) **(Figure 3.2j)**. After incorporating $NaNbO_3$, the contact angle significantly decreased to 86°, indicating a shift towards a hydrophilic surface (< 90°), attributed to the presence of hydrophilic groups (e.g., M-O). The gelatin coating further enhanced the wettability by water, with an initial contact angle of 45°, which steadily decreased to 26° within 60 s. This surface modification is crucial not only for promoting protein adsorption and cell adhesion through functional groups (e.g., amides) but also for forming a hydration layer that better mimics the aqueous conditions of the human body, thereby minimizing immunogenic reactions.[169,470] Furthermore, because gelatin is derived from collagen, the primary component of the extracellular matrix (ECM) in tissues, it helps to create a scaffold that closely resembles the natural bone microenvironment. This resemblance facilitates enhanced cell adhesion, cell-cell and cell-ECM interactions, and supports cellular growth and differentiation, thereby promoting tissue regeneration. This biomimetic scaffold allows for a more effective investigation of the interrelationship between porosity, US, and electric field intensity in gyroid-structured scaffolds.

### 3.3.3 Structural features and stability work regimes

The structural features of the bioactive scaffolds were characterized to confirm the quality of their hierarchical porous structures, focusing on porosity level, pore dimensions, and distribution of pores **(Figure 3.4)**. The sacrificial template 3D digital models for scaffolds, where the porous regions transform into solid sections following the incorporation of $NaNbO_3$@PDMS for 18 and 63% porosity, are shown in **Figure 3.4a-b**, respectively. High-resolution 3D X-ray μCT reconstructions validate the quality and integrity of the gyroid-structured scaffolds for both porosity levels, showcasing well-defined pores. Further corroboration is provided through digital images of scaffolds in their original dimensions, along with magnified views showing the scaffolds after resizing their diameters from 100 to 8 mm.

SEM reveals peripheral pore dimensions of 1.3 × 0.5 and 4.2 × 0.7 $mm^2$ for scaffolds with 18 and 63% porosity, respectively. These results indicate that both scaffolds possess macro-

scale peripheral pores, with major diameters of 1.3 and 4.2 mm, respectively. These features are conducive to fluid and nutrient exchange, while their minor diameters (ca. 500 μm) align with optimal pore sizes for supporting cell growth. Previous studies have shown that larger pore sizes, e.g., 800 μm, significantly enhance bone regeneration by providing sufficient space for cell ingrowth.[471,472] For instance, Montazerian et al. reported that magnesium scaffolds with larger pore sizes promote mature bone formation by promoting vascularization.[473]

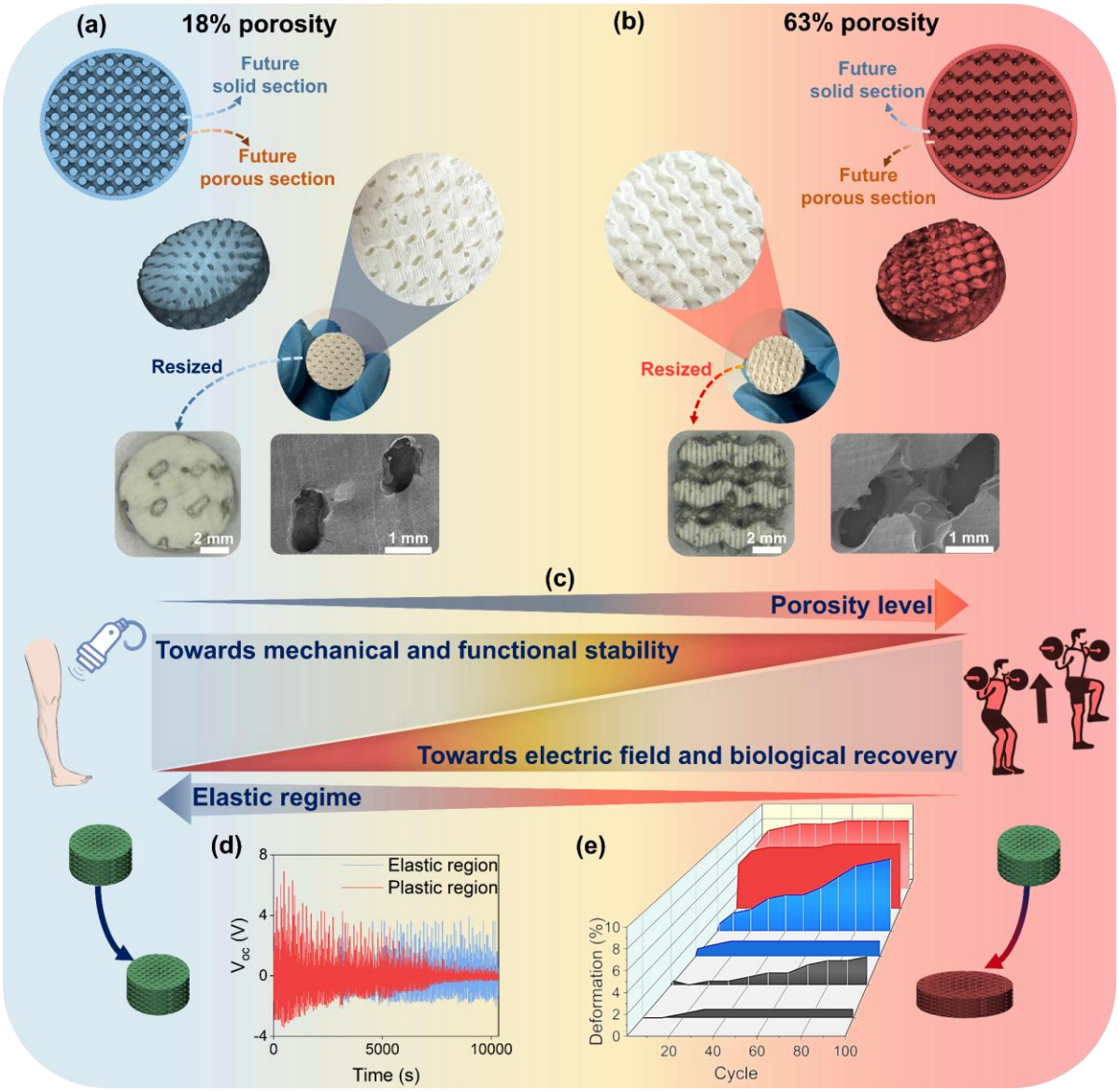


**Figure 3.4.** Influence of scaffold porosity on structural organization, microarchitecture, mechanical behavior, and functional performance. Comparison of gyroid-based scaffolds with (a) low porosity (18%) and (b) high porosity (63%), highlighting differences in structural organization and pore distribution. The comparative analyses include 3D X-ray microcomputed tomography reconstructions, digital photographs of scaffolds (100 mm in thickness and 100 mm in diameter), stereo microscope views of resized scaffolds (scale bar = 2 mm), and SEM images of porous regions at 35x magnification (scale bar = 1 mm). (c) Trade-off diagram illustrating the interplay between porosity levels and mechanical stress regimes on mechanical stability and biological/electrical performance. (d) Open-circuit

voltage ($V_{oc}$) signal fluctuations of 63% porosity scaffold under elastic (0.2 MPa) and plastic (3 MPa) regimes across 10,000 cycles. (e) Progressive deformation (densification) of scaffold thickness under 12.5% (darker curves) and 50% strain (lighter curves, hatched with vertical lines) over 100 cycles for scaffolds with 0% (black), 18% (blue), and 63% (red) porosity. Green scaffolds indicate pristine structural integrity, whereas red highlights thickness-compression deformation under mechanical stress in the plastic regime.

The trade-off between scaffold porosity and mechanical, functional, and biological properties is illustrated in **Figure 3.4c**. Increasing porosity in scaffolds reduces material density, weakening mechanical stability but enhancing electric field intensity and biological recovery by facilitating electric field propagation through the pores. Lower porosity enhances mechanical stability by resisting deformation but diminishes electrical functionality and biological performance due to reduced dielectric shielding and smaller pore size. Mechanical stress further affects functionality, as low stress within the elastic regime preserves structural integrity but reduces stimuli-responsive effects for biological outcomes.

Preserving pore structural integrity is crucial for evaluating stimuli-responsive biological outcomes in scaffolds, ensuring bone cells are not stressed by pore wall compression under plastic deformation. The functional stability of the 63% porosity scaffold, evaluated via $V_{oc}$ signal fluctuations under elastic (0.2 MPa) and plastic (3 MPa) stress conditions, showed a steady decline over 10,000 cycles **(Figure 3.4d)**. This decline likely reflects degradation of the top and bottom electrodes, disrupting the conductivity network and reducing electrical output. The degradation results from mismatched plastic deformation between scaffold materials, with yield stress points of ca. 2 MPa for PDMS and 200 MPa for the Au/Pd electrodes, leading to inevitable surface cracking and compromised electrical connectivity over prolonged cycles.

Assessing thickness deformation is vital for evaluating scaffold stability over extended cycles and identifying stress-strain ranges that mechanically activate scaffolds without overstressing cells and compromising structural integrity. Thickness deformation correlates positively with porosity and strain; as both increase, so does the deformation **(Fig 4e)**. Scaffolds with 63% porosity exhibit significant degradation after the second cycle, with ~8% thickness deformation, regardless of applied strain, indicating lower structural stability and higher densification rates. In contrast, 0 and 18% porosity scaffolds show minimal densification (~1.5%) at 12.5% strain but experience progressive deformation at 50% strain. Therefore, higher mechanical stress (e.g., 3 MPa in the plastic regime) further affects scaffold functional stability via thickness deformation. These findings highlight the need for lower-stress stimuli, such as US, to preserve pore structure and scaffold integrity while reducing stress on bone cells.

Densification strain increases with porosity, reaching ca. 40%, 45%, and 49% as porosity increases from 0% to 18% and 63%, respectively **(Table 3.3)**. This underscores the importance of limiting applied stress, with mechanical compression stress on gelatin-$NaNbO_3$@PDMS constructs should remain below ca. 2.5 MPa to prevent scaffold densification, plastic deformation, and adverse effects on cell viability.

**Table 3.3.** Structural features and mechanical properties of gelatin-$NaNbO_3$@PDMS scaffolds with 0%, 18%, and 63% porosities.

| **Property** | **Output** | | |
|---|---|---|---|
| Porosity (vol%) | 0 | 18 | 63 |
| Major pore diameter (mm) | - | 0.5 | 0.8 |
| Minor pore diameter (mm) | - | 0.3 | 0.5 |
| Aspect ratio | - | 3 | 3.5 |
| Density* ($kg \cdot m^{-3}$) | 1264 | 1036 | 468 |
| Densification strain (%) | 40 | 45 | 49 |
| Maximum stress (MPa) | 16.9 | 3.9 | 3.1 |
| Young's modulus (kPa) | 37.0 | 16.2 | 7.1 |
| Energy loss ($kJ \cdot m^{-3}$) | 7.8 | 3.5 | 2.1 |
| Damping capacity (%) | 51.8 | 45.3 | 56.4 |

*Density was theoretically calculated using the rule of mixtures. Aspect ratio was calculated as the ratio of the smallest pore's diameter to its length. All mechanical properties were measured at 50% strain during the 1st cycle. Major and minor pore diameters represent the maximum and minimum pore sizes within the dominant frequency range (>80%) identified in the pore size histograms.

**Figure 3.5a-b** shows that the gyroid architecture inherently leads to a hierarchical network of interconnected pores, ranging from macro- to micro-scale features, which is a fundamental property of the minimal surface geometry rather than a fabrication artifact. Specifically, **Figure 3.5a** demonstrates that in the 18% porosity scaffold, more than 85% of the pores are concentrated between 0.3 and 0.5 mm, whereas **Figure 3.5b** shows that for the 63% porosity scaffold, over 80% of the pores are distributed between 0.5 and 0.8 mm.

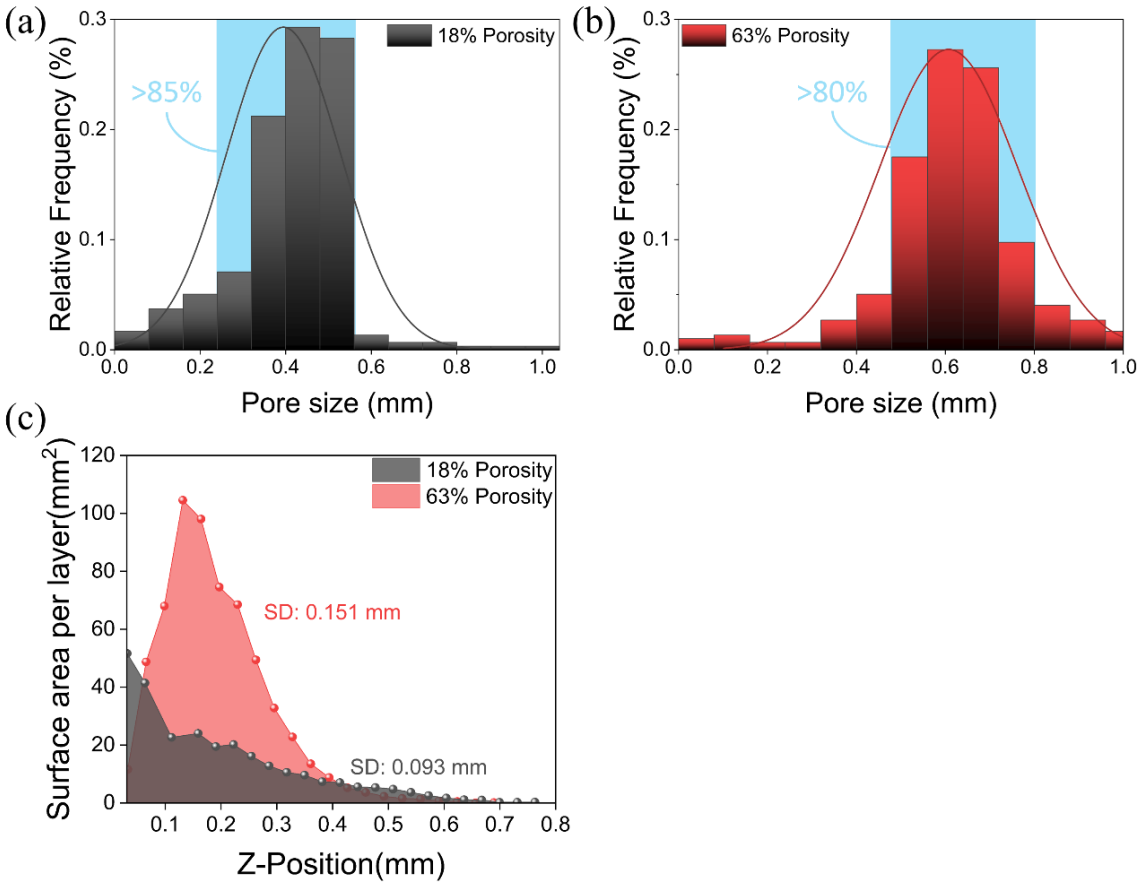


**Figure 3.5.** Pore-size and surface-area characterization of gyroid scaffolds. Pore size distributions for (a) 18% porosity showing >85% of pores between 0.3–0.5 mm, and (b) 63% porosity scaffolds with >80% of pores concentrated between 0.5–0.8 mm, respectively. (c) Surface area per layer as a function of Z-position, in the 63% porosity scaffold (SD = 0.151 mm²) compared to the 18% porosity scaffold (SD = 0.093 mm²).

Furthermore, the layer-by-layer surface area analysis reveals that the 18% porosity scaffold exhibits relatively low and stable surface areas across its height, with a maximum value below 50 mm² **(Figure 3.5c)**. In contrast, the 63% porosity scaffold displays significantly higher surface areas, peaking around 100 mm² at shallow depths (0.1–0.2 mm) and maintaining elevated values throughout the scaffold height. The higher standard deviation of surface area in the 63% porosity scaffold (0.151 mm²) compared to the 18% porosity scaffold (0.093 mm²) further reflects the intended hierarchical complexity of the structure, confirming that the observed variations are a direct consequence of the gyroidal geometry rather than fabrication inconsistencies.

### 3.3.4 **Mechano-electrical performance of scaffolds**

Determining the viscoelastic properties of scaffolds is crucial for mechanical compatibility with human tissues and predicting behavior under cyclic loading. During the first cycle, scaffolds with 18% and 63% porosity exhibit Young's moduli of 7–16 kPa **(Figure 3.6a)**, closely matching that of bone marrow in cancellous femoral bone (0.25–25 kPa) [474–476] and minimizing stress shielding. This alignment facilitates healthy bone remodeling under physiological loads and reduces the activation of osteoclast-mediated bone resorption, a common issue with overly rigid implants. Thus, it preserves bone density and maintains the long-term stability of the prosthetic interface, ensuring effective load distribution and minimizing the risk of stress shielding as per Wolff's Law.

This viscoelastic behavior is further clarified by examining the damping capacity **(Figure 3.6b)**. In the first cycle, the 63% porosity scaffold dissipates the most energy - likely via heating - followed by the 0% and 18% porosity scaffolds. Despite initially dissipating more energy, the 63% porosity scaffold shows lower stress resistance, indicating that it undergoes early permanent deformation, which reduces damping capacity and a diminished ability to recover its original form. This suggests that the 63% porosity scaffold behaves more plastically at early cycles, quickly losing its energy dissipation capability due to permanent deformation. After the 20$^{th}$ cycle, the 63% porosity scaffold behaves more elastically, with stable damping capacity until the 100$^{th}$ cycle.

Scaffolds with 0% and 18% porosities exhibited superior elastic behaviors, providing long-term durability and resistance to permanent deformation across multiple cycles. 0% porosity scaffold demonstrates enhanced energy dissipation through absorption and conversion to heat or other non-recoverable forms, a critical property for bone scaffolds subjected to dynamic loads (e.g., walking, running, jumping), reducing implant damage and stress transfer to surrounding bone. However, because the 0% porosity scaffold lacks macro-to-micro porosities, it limits cell adhesion and tissue integration. In contrast, the 18% porosity scaffold combines significant damping capacity with elastic behavior, making it an effective choice for scaffolds designed to provide holistic mechanical and biological functionality.

The ability to dissipate energy as heat during cyclic loading reflects a balance between viscous (energy loss) and elastic (energy storage and recovery) properties. Energy dissipation stability inversely correlates with porosity: as porosity increases, both dissipation and stability decrease **(Figure 3.6c)**. For instance, increasing porosity from 0% to 18% and 63% reduces energy storage from 7.8 to 3.7 and 2.1 kJ, respectively, with dissipation capacity declining by 6%,

13%, and 56% between the first and second cycles. These findings underscore the advantage of low porosity for energy absorption, making denser scaffolds better suited for load-bearing applications requiring effective cushioning and shock absorption.

Highly porous scaffolds (e.g., 63%) exhibited reduced structural stability, increasing the risk of pore collapse and bone cell stress. To address this, mechanical stimulation was applied within the elastic region (<3 MPa) using US, thereby mitigating permanent deformation and minimizing artifacts that could compromise the interpretation of biological effects. This approach preserves scaffold integrity during stimulation and enables a more accurate evaluation of the scaffolds' stimuli-responsive behavior under US.

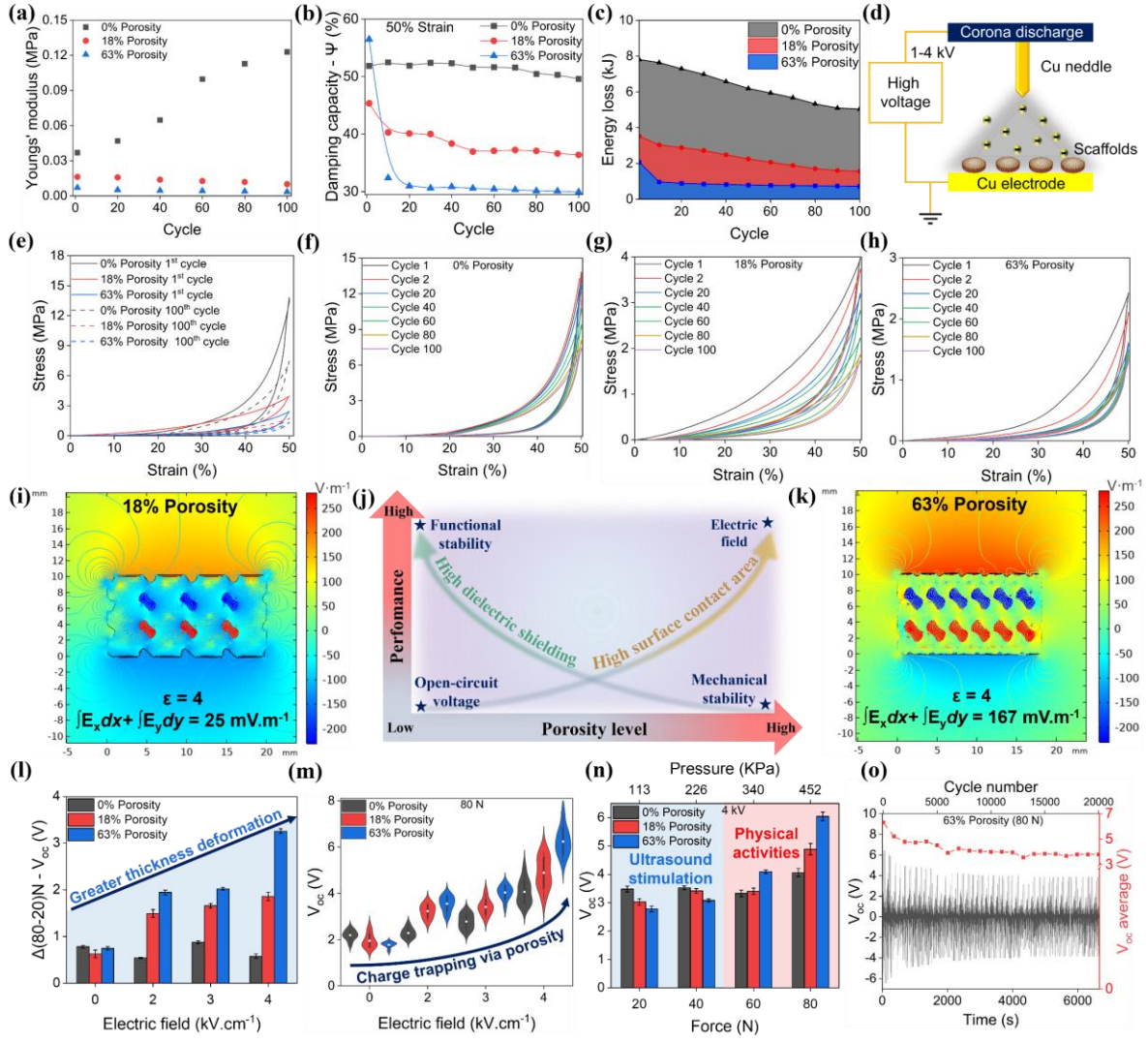


**Figure 3.6.** Relationship between porosity levels and mechanical force triggers on the performance of mechano-electrical output and functional stability of electrically charged scaffolds. Cyclic mechanical tests on scaffolds with 0%, 18%, and 63% porosity scaffolds over 100 cycles at strain 50% yielding (a) Young's modulus, (b) damping capacity, and (c) energy loss. (d) A schematic illustration of corona discharge for electrically charged scaffolds, with an applied voltage difference between a needle and grid ranging from 1 to 4 kV. (e) Cyclic stress-strain curves at 1st

and 100th cycles for scaffolds with 0%, 18%, and 63% porosity scaffolds at 50% strain. Sequential stress-strain curves in increments of 10 cycles over 100 cycles at 50% strain for (f) 0%, (g) 18%, and (h) 63% porosity scaffolds. Mind that Y-axes vary among the e-h charts, so please use care when comparing the profiles. COMSOL® simulations display electric field intensity and distribution for scaffolds with (i) 18% and (k) 63% porosity with a dielectric constant of 4 in aqueous media. The distribution of the electric potential along the X-axis within the scaffold and surrounding environment is displayed for each condition, while the integral of the electric field intensity along the X- and Y-axes ($\int E_x\,dx + \int E_y\,dy$) within all scaffold pores is described. (j) Conceptual diagram highlights the trade-off between porosity levels and scaffold performance, highlighting how effective contact surface area and dielectric shielding influence mechanical, electrical, and functional stabilities during stress. (l) Open-circuit voltage ($V_{oc}$) differences between 80 and 20 N force triggers across 1-4 $kV \cdot cm^{-1}$ electric fields for scaffolds with 0, 18, and 63% porosity, indicating a thickness-dependent output. (m) $V_{oc}$ output under an 80 N driving force across electric field polarization of 0, 2, 3, and 4 $kV \cdot cm^{-1}$, indicating increased charge trapping capacity with higher pore levels in the scaffold. (n) $V_{oc}$ output under low- (≤300 kPa, e.g., US) and high-pressure triggers (>300 kPa, e.g., physical human activities) for scaffolds with 0%, 18%, and 63% porosity polarized at 4 $kV \cdot cm^{-1}$. (o) Long-term $V_{oc}$ functional stability of 63% porosity scaffolds over 20,000 cycles under 80 N load.

Cyclic mechanical testing across increasing strain (%) revealed the elastic regime and material densification associated with pore collapse, which could induce stress on bone cells. Densification occurred at ~40% strain for the 0% porosity scaffold, identified by a steep increase in stress slope, whereas gyroid scaffolds with 18% and 63% porosity exhibited delayed densification at ca. 45% and ~49% strain, respectively **(Figure 3.6e)**.

Under high strain levels, scaffold performance is increasingly influenced by structural design, porosity level, and densification processes. For instance, in gyroidal scaffolds, covalent bond suppression at 50% strain led to a significant stiffness reduction after 100 cycles, compared to the 100th cycle at 12.5% strain, where bond breakage was less pronounced **(Figure 3.7g-h)**. Conversely, in low-stress applications, stiffness is primarily governed by the material's intrinsic properties, such as the depth and steepness of the potential energy curve of atomic bonding. Under high-stress conditions (e.g., plastic deformation), macroscopic stiffness changes between cycles are influenced by both intrinsic material properties and evolving microstructural alterations, emphasizing the importance of scaffold design for long-term load-bearing applications.

Given that scaffolds experience mechanical loading over extended periods, monitoring changes in macroscopic stiffness is crucial for ensuring mechanical compatibility and preventing stress shielding throughout their lifespan. The non-macro-porous scaffolds (0% porosity) exhibited a Young's modulus of 37 kPa during the first cycle, while over 100 cycles at 50%

strain, stiffness progressively increased, reaching 123 kPa (a 332% increase) **(Figure 3.7f)**. Despite this significant increase, the stiffness remains within the range of human cancellous bone, such as in the acetabulum.[477–480] This increase in macroscopic stiffness during cycling can be attributed to nano-densification, where the structure becomes more compact as the material deforms, filling submicron pores and increasing resistance to compression. This occurs because high strain induces local collapse in porous regions, triggering a high nano-densification stage in which van der Waals interactions become more pronounced.

Moreover, 0% porosity scaffolds subjected to 12.5% strain exhibited a slight increase in Young's modulus over cycles, though at a slower rate than at 50% strain. This further suggests that van der Waals interactions steadily increase with strain as atoms move closer and nanoscale pores become filled **(Figure 3.7f)**. Therefore, nano-densification enhances cohesive strength, similar to crystalline polymers where strong hydrogen bonding yields a higher Young's modulus than amorphous polymers with weaker interactions. This strengthening of intermolecular forces enhances the compression resistance in highly solid-densified scaffolds (e.g., ~0% porosity), further increasing the macroscopic Young's modulus during prolonged densification cycles.

On the other hand, gyroid scaffolds with 18% and 63% porosity exhibited stiffness reductions of 6% and 18%, respectively, after 100 cycles at 50% strain **(Figure 3.7g-h)**. This inverse behavior - decreasing stiffness in gyroid scaffolds under prolonged high-strain cycles - is attributed to covalent bond rupture. In this case, nano-densification is compromised due to residual macro-to-micro voids, which impede the contribution of van der Waals interactions by preventing sufficient nanoscale proximity between atoms. Contrastingly, high plastic deformation (e.g., 50% strain) further exacerbates covalent bond breakage, weakening the material's resistance to compressive forces in the elastic region and lowering stiffness over extended cycles. This is further supported by the negligible changes in Young's modulus observed in 18% and 63% porosity scaffolds at 12.5% strain (near the elastic region), where plastic deformation and nano-densification effect are minimal **(Figure 3.7g-h)**.

Long-term stability testing showed that increasing porosity from 0% to 18% and 63% significantly reduced maximum stress after the first cycle at 50% strain, dropping from 17 to 4 and 3 MPa, respectively **(Figure 3.7b)**. Over 100 cycles, higher-porosity scaffolds exhibited greater compressive stress reduction (56%) compared to 0% porosity scaffolds (8.6%), highlighting their shorter functional lifespan due to plastic collapse and diminished strength.

Increasing strain (%) in cyclic mechanical testing reveals both the elastic regime and material densification, indicating pore collapse that may induce bone cell stress. In the 0% porosity scaffold, densification occurs at ~40% strain, marked by a steep rise in the maximum stress slope **(Figure 3.7c)**. Gyroid scaffolds, with retained porosity, show delayed densification at ~45% and ~49% strain for the 18% and 63% porosity scaffolds, respectively **(Figure 3.7d-e)**.

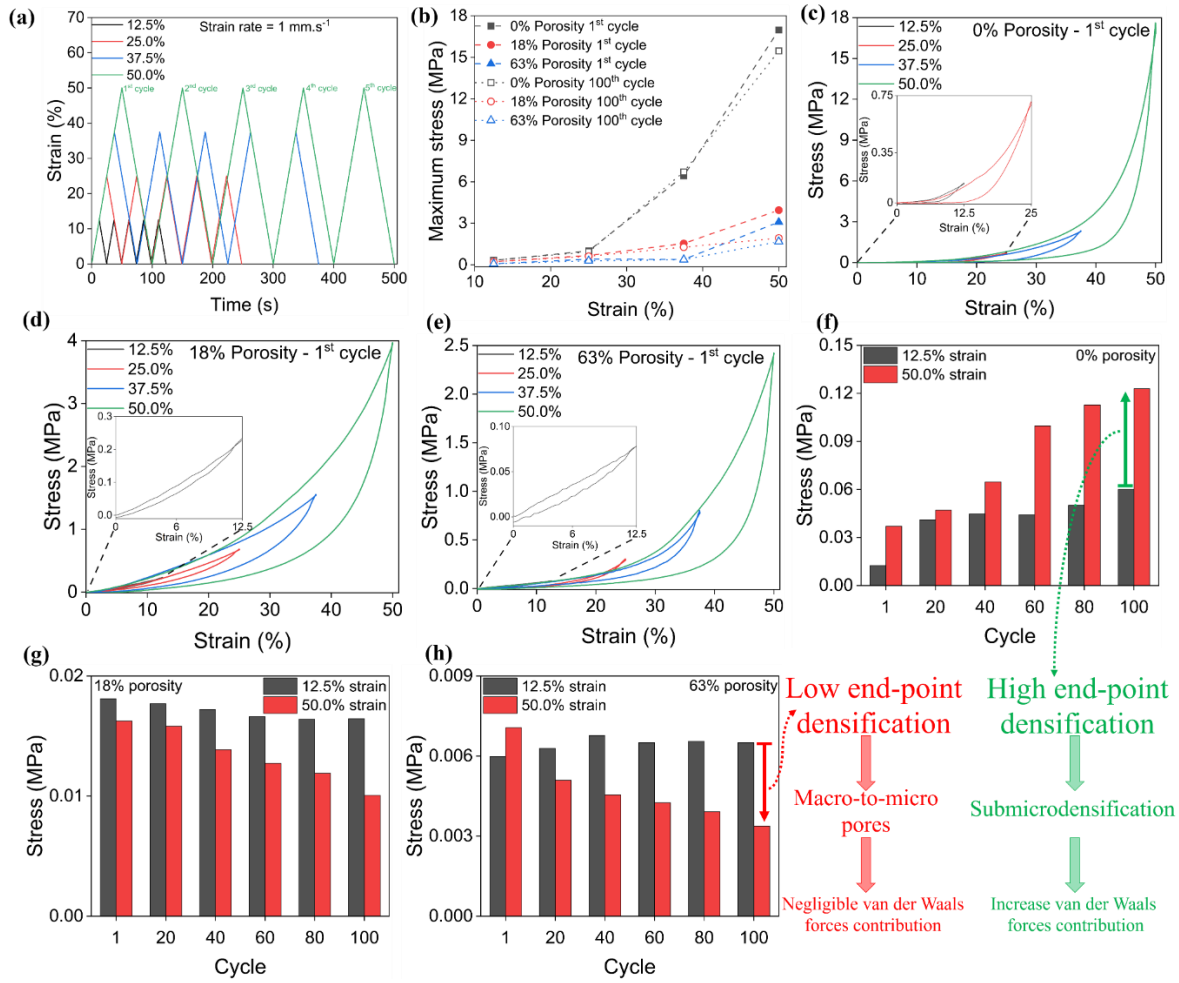


**Figure 3.7.** Cyclic mechanical and viscoelastic characterization of scaffolds. (a) Mechanical compression cycle methodology demonstrating 12.5, 25, 37.5, and 50% strain at a strain rate of 1 mm·s$^{-1}$. (b) Maximum stress for scaffolds with 0%, 18%, and 63% porosity at the 1$^{st}$ and 100$^{th}$ cycles for 12.5, 25, 37.5, and 50% strain. Cyclic stress-strain curves of scaffolds with (c) 0%, (d) 18%, and (e) 63% porosity over 100 cycles, with strain increasing from 12.5% to 50%. Young's modulus, calculated from the slope of a linear regression in the elastic regime (strain ≤ 5%), at 12.5% and 50% strain for (f) 0%, (g) 18%, and (h) 63% porosity scaffolds over 100 cycles. The adjusted linear equation and slope were obtained with a minimal quality value of $R^2 \geq 0.96$.

Compressive stress curves from the 1$^{st}$ and 100$^{th}$ cycles reveal energy loss, absorption, and permanent plastic deformation, indicated by non-overlapping curves **(Figure 3.6f-h)**. At

50% strain, the 0% porosity scaffold exhibits minimal curve decay, demonstrating high structural stability under cyclic loading **(Figure 3.6f)**. Stability decreases with porosity, as shown by moderate decay in the 18% porosity scaffold **(Figure 3.6g)** and significant non-overlapping curves in the 63% porosity scaffold **(Figure 3.6h)**. These findings highlight a plastic-like response and greater structural collapse with increasing porosity.

To comprehend the electric field distribution and intensity within porous scaffolds, we conducted COMSOL® simulations using the same physical and chemical parameters as the biological assessments **(Figure 3.6i-k)**. From a biological perspective, the integrated electric field intensity across all pores is a more relevant measure than the average value, as biological outcomes depend on the entire scaffold volume. The total integrated electric field in the 63% porous scaffold was approximately 6.7 times higher than in the 18% porous scaffold under identical conditions, while the average electric field was about 350% greater **(Table 3.4)**. Thus, we further demonstrate that lower dielectric content (i.e., higher porosity) could be used to reduce the dielectric shielding effect, thereby enhancing electric field intensity within the pores.

**Table 3.4.** Average electric field intensity for 18% and 63% porosity scaffolds in air and aqueous media with $\varepsilon_r = 4$.

| Porosity | Environment | Electric field in X ($V \cdot m^{-1}$) | Electric field in Y ($V \cdot m^{-1}$) | $\langle Ex \rangle + \langle Ey \rangle$ ($V \cdot m^{-1}$) |
|---|---|---|---|---|
| 18% | Aqueous | -59 | 1459 | 1400 |
| | Air | -75529 | -452779 | -528310 |
| 63% | Aqueous | -279 | 5287 | 5008 |
| | Air | 2569 | -20566 | -17998 |

$\langle Ex \rangle + \langle Ey \rangle$ = The sum of the average electric fields in the X- and Y-directions.

To enhance responsiveness to stimuli and biological performance, electrically charged scaffolds were fabricated using corona discharge **(Figure 3.6d)**, leveraging $NaNbO_3$ for its piezoelectric functionality. To better understand the range of scaffold applications in human implants, the pressure exerted on scaffolds during various human activities was categorized based on the electro-mechanical-structural relationship. Low-pressure conditions (≤300 kPa)

correspond to activities with minimal mechanical impact, e.g., physiotherapy, US, and resting while lying down. In contrast, normal to high-pressure levels (>300 kPa) are associated with walking, standing, swimming, and sports, which induce greater mechanical stresses on scaffolds.

Two key dependencies of $V_{oc}$ behavior on mechanical tension regimes emerge, defined by a threshold pressure of approximately 300 kPa **(Figure 3.6n)**. In the low-pressure regime (≤226 kPa), $V_{oc}$ decreases with increasing scaffold porosity, attributed to a reduced effective contact area that limits charge generation. Conversely, in the high-pressure regime (≥340 kPa), significant structural deformation enhances $V_{oc}$, driven by an increase in the effective contact surface area, especially in higher-porosity scaffolds that reduce compression resistance and facilitate X-deformation.

Given that the 63% porosity scaffold represents the most mechanically unstable design, we evaluated its stimuli-responsive $V_{oc}$ stability over extended cycles under an 80-N (~452 kPa) load, representative of typical human mechanical triggers **(Figure 3.6o)**. During the initial cycles (<1,000), $V_{oc}$ decreased significantly due to plastic deformation and electrode degradation, dropping from 6.3 to 3.8 V after 20,000 cycles before stabilizing with further cycling. These findings highlight the necessity of cyclic mechanical evaluations in scaffolds to identify stress-strain ranges that preserve pore integrity under mechanical stimuli. Our results confirm that ultrasound is the most effective mechanical stimulus for assessing scaffold bioactivity.

These findings highlight the trade-off between porosity levels and scaffold performance in terms of mechanical, electrical, and functional stability, with surface area contact and dielectric shielding significantly influencing outcomes **(Figure 3.6j)**. Higher porosity increases the integrated electric field intensity by reducing dielectric shielding, potentially boosting biological outcomes and recovery in functional activities. Additionally, the superior charge-trapping capability of the 63% porous scaffold suggests that the actual electric field likely exceeds the theoretical values predicted by COMSOL®. Conversely, reducing porosity enhances mechanical properties and functional stability by increasing material resistance and structural integrity. We established this trade-off to guide the design of advanced stimuli-responsive scaffolds, enabling fine-tuned structural optimization for specific mechanical, electrical, and biological outcomes.

The $V_{oc}$ differences observed between scaffolds at 80 and 20 N under 4 $kV \cdot cm^{-1}$ **(Figure 3.6l)** highlight the structural impact of a 60-N load increase, particularly in higher-porosity

scaffolds, which exhibit lower mechanical resistance and greater deformability. At low tension, the reduced $V_{oc}$ output in 63% porosity scaffolds is attributed to their limited contact surface area compared to 0% and 18% porosity scaffolds, diminishing charge transfer efficiency. The increased charge capacity of higher-porosity scaffolds is demonstrated by the $V_{oc}$ improvement relative to non-polarized scaffolds (0 $kV \cdot cm^{-1}$), reaching 86%, 150%, and 240% for porosities of 0%, 18%, and 63% at 80 N, respectively **(Figure 3.6m)**. This suggests that higher porosity creates additional charge traps within the scaffold, amplifying the electric field confined within the pores and potentially enhancing cell growth.

### 3.3.5 Ultrasonic stimuli-responsive effects on scaffold bioactivity

Assessing biocompatibility is crucial before conducting biological tests to ensure materials do not harm cell viability or function. Our results confirmed the biocompatibility of $NaNbO_3$, showing that its incorporation into PDMS did not adversely affect cell viability, as indicated by live/dead staining **(Figure 3.8a-b)**. Metabolic activity significantly increased from days 7 to 14 across all porosities and US conditions, demonstrating that the construct supports cell proliferation **(Figure 3.9a)**. US further enhanced metabolic activity, with more significant effects observed on day 14. The highest metabolic activity occurred in the 63% porosity construct stimulated with 50 $mW \cdot cm^{-2}$ at D14, suggesting this condition optimally promotes cellular activity. These findings indicate that cellular growth and proliferation are positively regulated by the electric field, supported by the highest electric field intensity (0.215 $V \cdot m^{-1}$) observed in 63% porosity scaffolds.

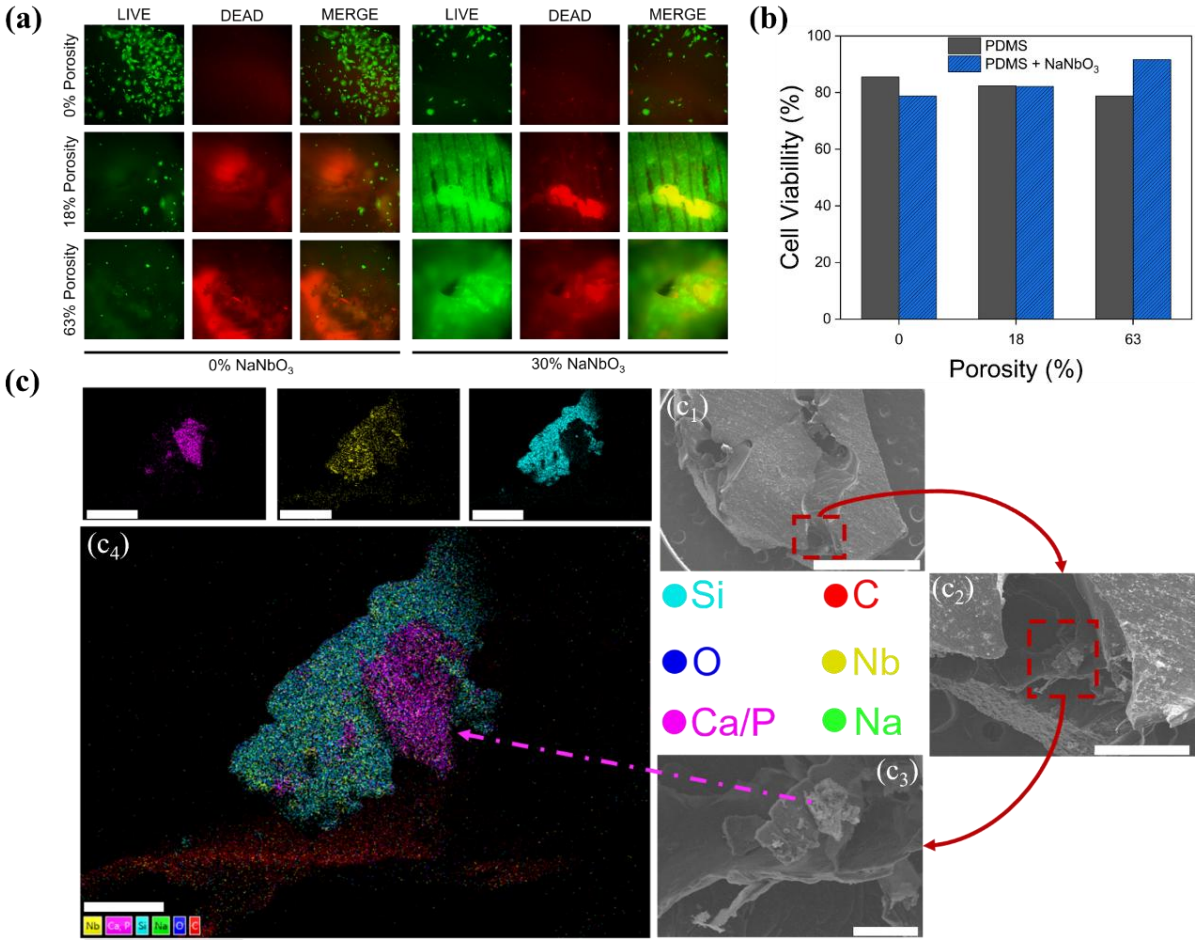


**Figure 3.8.** Constructs' biocompatibility and mineralization analyzed via confocal microscopy and EDS-SEM. Confocal images of (a) PDMS scaffolds and gelatin@$NaNbO_3$-PDMS scaffolds with 0%, 18%, and 63% porosity, along with (b) cell viability analysis using the live/dead cell counting method. (c) SEM image of the 18% porosity scaffold at $c_1$) x25 magnification (scale bar = 2 mm), $c_1$) x90 magnification (scale bar = 500 μm), $c_3$) x300 magnification (scale bar = 300 μm), and corresponding $c_4$) chemical composition determined by energy-dispersive X-ray spectroscopy (EDS), highlighting calcium and phosphorus distribution at x800 magnification (scale bar = 50 μm).

US upregulated calcium content compared to non-stimulated constructs, indicating that the mechano-electrical stimuli generated by US and electric field within the construct architecture promote osteogenic differentiation and mineralization, supporting bone tissue regeneration processes **(Figure 3.9b)**. This effect is associated with enhanced expression of osteogenic markers (*RUNX2*, *OSX*) under mild stimulation conditions, with the most significant improvements observed at 50 $mW \cdot cm^{-2}$ US for the 63% porosity scaffold and 250 $mW \cdot cm^{-2}$ US for the 18% porosity scaffold **(Figure 3.9a-b)**. These findings suggest the presence of an optimal US and electric field intensity, as higher US levels (250 $mW \cdot cm^{-2}$) in 63% porosity scaffolds may lead to overstimulation. Notably, the significant increase in calcium content - up to 1200%

compared to unstimulated controls - observed in the 63% porosity scaffold at 50 mW·cm$^{-2}$ US aligns with the upregulation of osteogenic markers such as *OSX*, which are directly associated with bone matrix formation and mineralization. This demonstrates the role of these conditions in enhancing calcium deposition, a key marker of bone tissue formation.

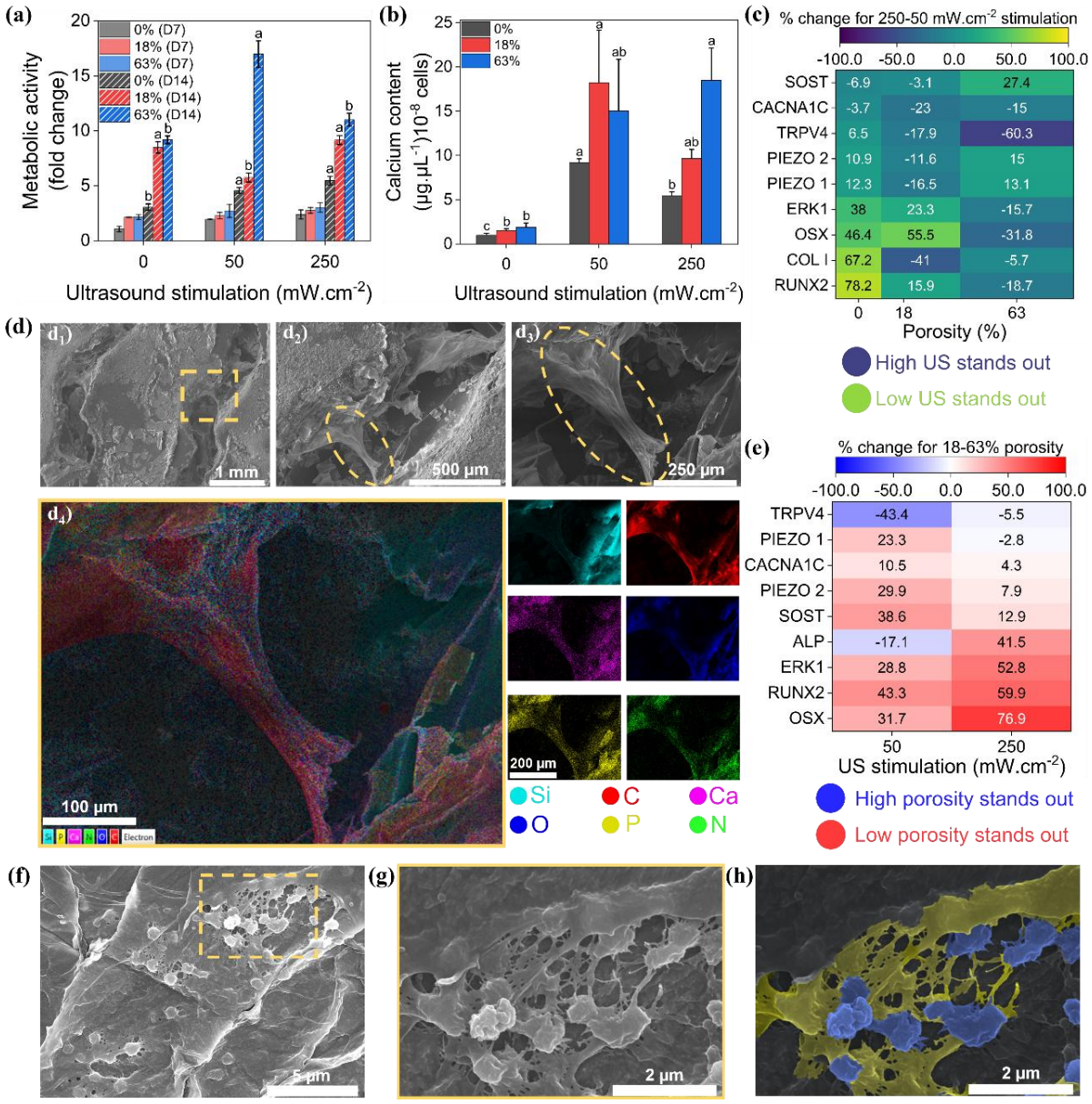


**Figure 3.9.** Impact of ultrasound stimulation (US) and scaffold porosity on cell activity, calcium deposition, gene expression, and cell morphology. (a) Metabolic activity (fold change) and (b) calcium content in constructs with varying porosities (0%, 18%, and 63%) under different US intensities (0, 50, and 250 mW·cm$^{-2}$) at 7 (D7) and 14 d (D14). Data are reported as mean values with errors (n = 4). Mean values followed by different superscript letters differ significantly (*p < 0.05) with comparisons of the same porosity levels and between US treatment groups at D14. (c) Heatmap showing the percentage change in gene expression markers (%) resulting from the difference between 250-50 mW·cm$^{-2}$ US for constructs with varying porosity (0%, 18%, and 63%). (d) SEM images of 18% porosity construct with 50 mW·cm$^{-2}$ US after 14 d, showing zoomed-in sections detailing cell growth through the

pores at $d_1$) 30x (scale bar = 1 mm), $d_2$) x100 (scale bar = 500 µm), and $d_3$) 250x magnification (scale bar = 200 µm), and $d_4$) chemical composition determined by energy-dispersive X-ray spectroscopy (scale bar = 100 µm). (e) Heatmap displaying the percentage change in gene expression markers (%) comparing 18 and 63% porosity of construct under different US (50 and 250 mW·cm$^{-2}$). SEM images of 0% porosity of construct without US after 14 d at (f) 7k magnification (scale bar = 5 µm), (g) zoomed-in section highlighting cell nuclei at 20k magnification (scale bar = 2 µm) and (h) corresponding digitally colored image showing the cytoskeleton (yellow) and nuclei (blue) of cells at 20k magnification (scale bar = 2 µm).

**Figure 3.9d** shows cell morphology on the 18% porosity construct at 50 mW·cm$^{-2}$, where cells align along bridge-like structures spanning the pores. EDS analysis of these structures confirmed the presence of calcium and phosphorus, indicating calcium phosphate deposition associated with cell-driven mineralization. Additional SEM images demonstrate cell growth and spreading on 18% and 63% porosity constructs under 0, 50, and 250 mW·cm$^{-2}$ US **(Figure 3.10a-f)**.

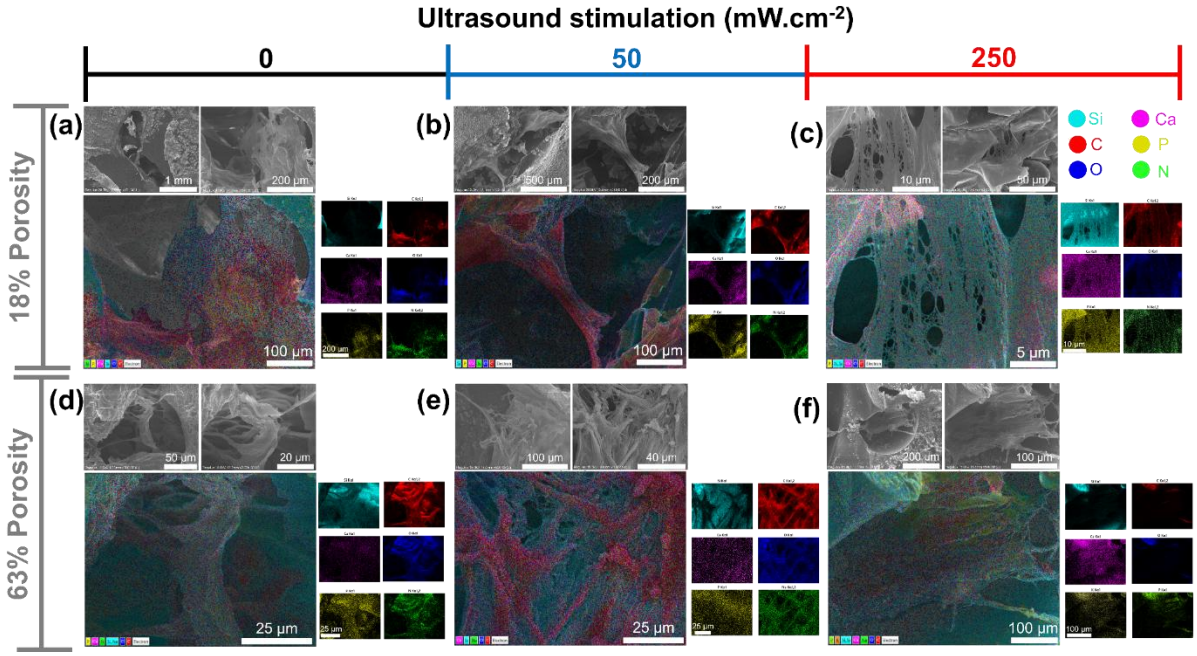


**Figure 3.10.** SEM and EDS of constructs after 14 d of bone cell growth. SEM and EDS analysis of 18% porosity scaffolds after US at 0 (a), 50 (b), and 250 mW·cm$^{-2}$ (c), and 63% porosity scaffolds under the same conditions (d, e, and f, respectively) after 14 d. Zoomed-in SEM images (top) reveal cell growth and interaction with scaffold pores. EDS mapping (bottom right) highlights the elemental distribution, including calcium and phosphorus, across the scaffold surface.

Raman mapping further verified the presence of calcium phosphate, with characteristic peaks at ca. 600 cm$^{-1}$ (P-O-P bending), ca. 970 cm$^{-1}$ (phosphate ($PO_4^{3-}$) symmetric stretching), and 1045 cm$^{-1}$ (P-O asymmetric stretching) **(Figure 3.11a-d)**.[481] In contrast, the 0% porosity

construct exhibited reduced cell spreading, with prominent nuclei suggesting limited attachment due to the absence of pores and decreased surface area **(Figure 3.9f-h)**. These findings highlight the role of porosity in enhancing cell spreading and stretching, as observed in SEM images of porous constructs, through increased cell-surface interactions under both low and high US conditions.

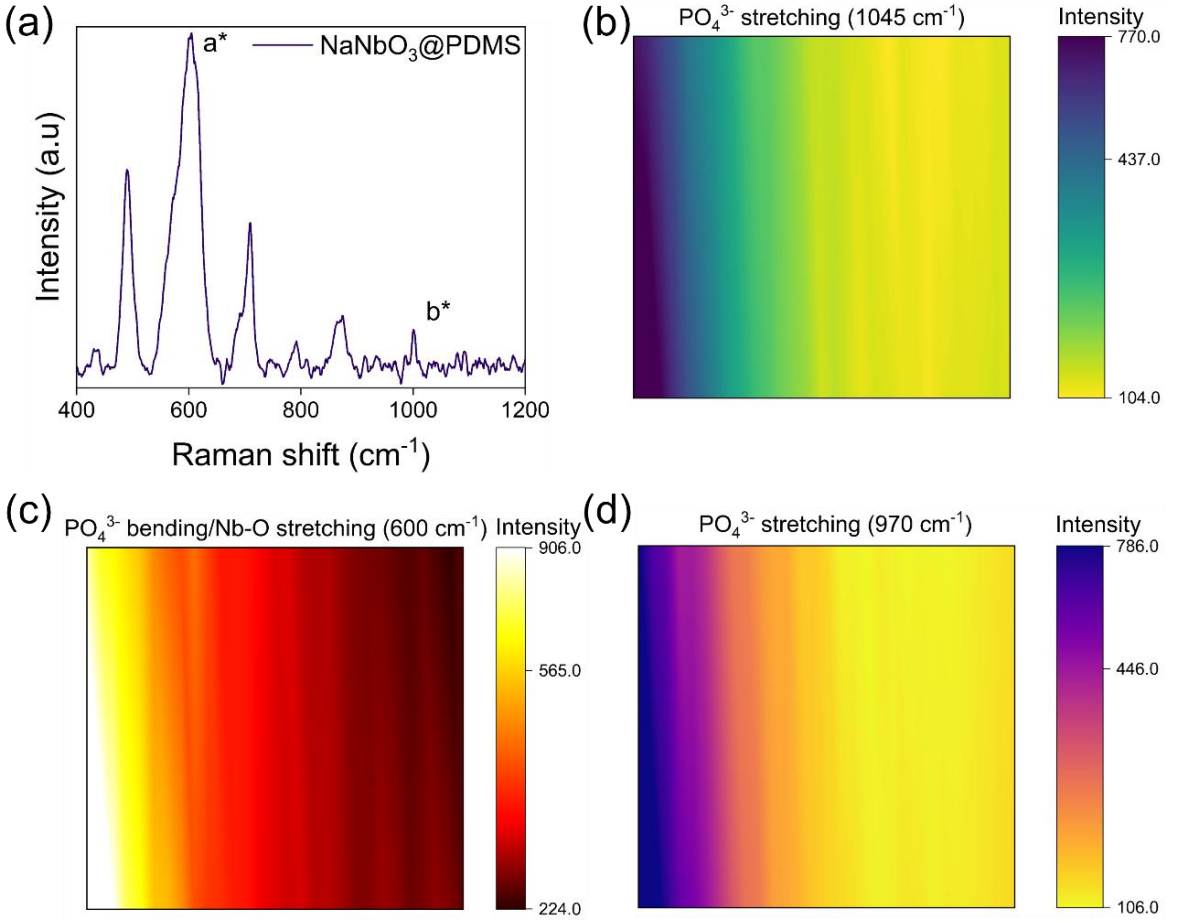


**Figure 3.11.** Raman spectroscopy and mapping of constructs after 14 d of cell culture. Raman spectral analysis and intensity mapping of gelatin-$NaNbO_3$@PDMS constructs after 14 d of cell culture. Raman spectrum with peaks at 600 $cm^{-1}$ (a*) corresponding to $PO_4^{3-}$ bending and Nb-O stretching and 1045 $cm^{-1}$ (b*) attributed to $PO_4^{3-}$ stretching (a). 2D Raman intensity map for the $PO_4^{3-}$ asymmetric stretching mode at 1045 $cm^{-1}$ (b), for $PO_4^{3-}$ bending and Nb-O stretching modes at 600 $cm^{-1}$ (c), and for $PO_4^{3-}$ symmetric stretching at 970 $cm^{-1}$ (d). Color gradients represent intensity variations.

Our findings show that 0% porosity constructs exhibit higher gene expression for all markers at higher US (250 $mW \cdot cm^{-2}$) compared to lower intensity (50 $mW \cdot cm^{-2}$), except for the *ALP* marker and negligible difference in *CACNA1C* expression **(Figure 3.12a-h)**. This high-

lights that increasing US effectively activates mechanosensitive pathways in non-porous constructs, leading to the upregulation of osteogenesis-related genes. The elevated *RUNX2* activity at 250 mW·cm$^{-2}$ further supports this, likely due to stronger activation of mechanosensitive pathways that enhance osteogenic signaling.

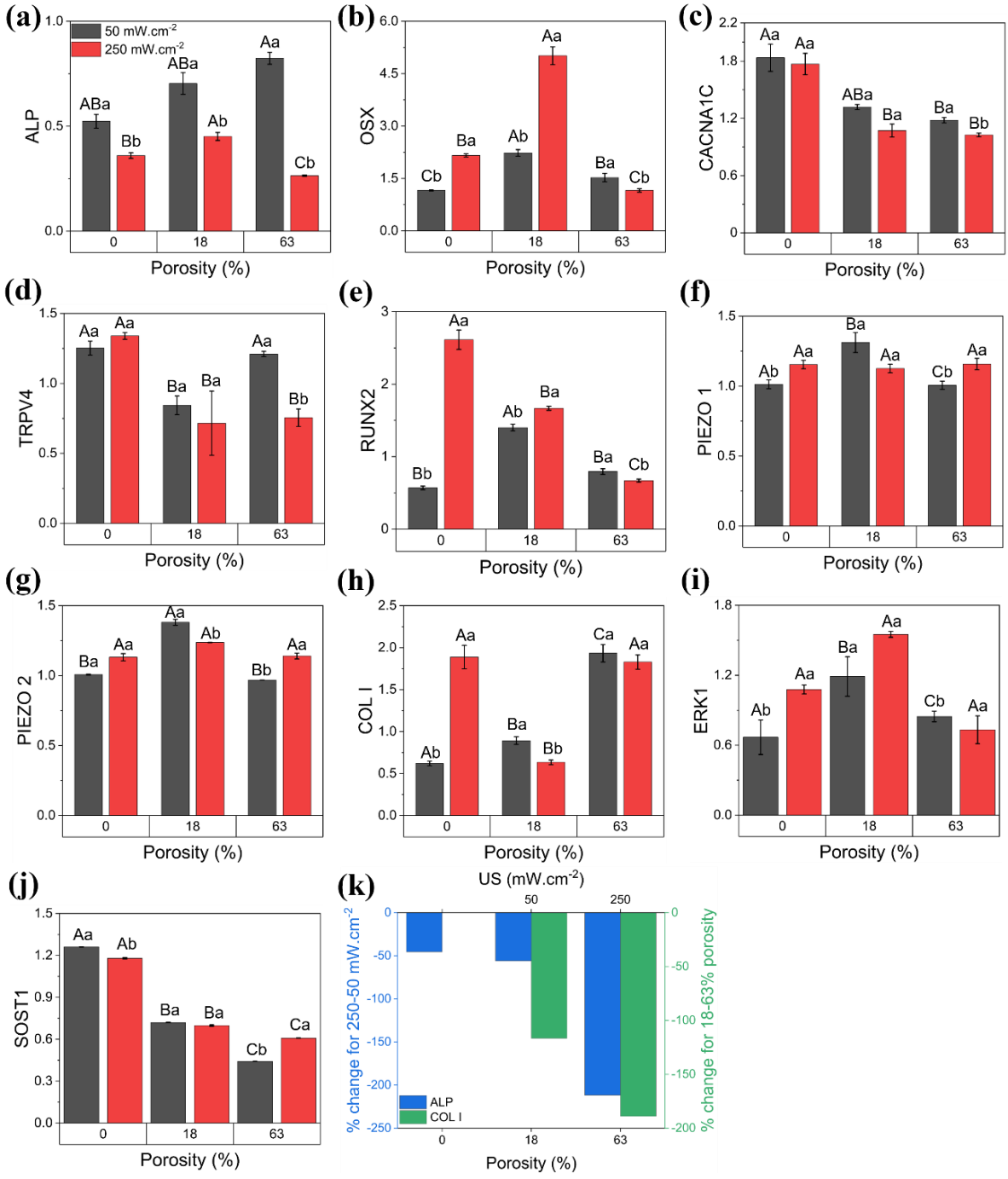


**Figure 3.12.** Absolute expression levels of gene markers of constructs. Absolute expression levels of gene markers, calculated using the $2^{-\Delta\Delta Ct}$ method, for (a) *ALP*, (b) *OSX*, (c) *CACNA1C*, (d) *TRPV4*, (e) *RUNX2*, (f) *PIEZO1*, (g) *PIEZO2*, (h) *COL I*, *(i) ERK1*, *(j) SOST1*. Percentage change in *ALP* and *COL I* expression due to the difference between 250 (red bars) and 50 mW·cm$^{-2}$ (black bars) US exposure for constructs with varying porosity (0%, 18%,

and 63%) (k). For each experimental group, measurements were obtained from three independent scaffolds (n = 3). Mind that the Y-axes differ from (a) to (h). The color coding in Figure 12a applies to all graphs.

The focus of our stimuli-responsive scaffolds was to evaluate the effects of low (50 $mW \cdot cm^{-2}$) and high (250 $mW \cdot cm^{-2}$) US intensities, as well as low (18%) and high (63%) porosity in constructs, on gene expression markers. To ensure a fair comparison, we calculated the percentage change in gene expression by subtracting values for 50 from 250 $mW \cdot cm^{-2}$ US for each porosity construct (0%, 18%, and 63%) and normalized them to 250 $mW \cdot cm^{-2}$ US at the corresponding porosity. To examine the impact of porosity, we subtracted values for 18 from 63% porosity under the same US intensity (50 or 250 $mW \cdot cm^{-2}$) and normalized them to 50 $mW \cdot cm^{-2}$ US for the respective porosity. This data processing method highlights the percentage differences in gene expression, allowing a clear comparison of treatment conditions. Additionally, absolute values without normalization or comparisons are provided in **Figure 3.12a-h**. Heatmaps in **Figure 3.9c** depict percentage changes in gene expression based on differences between 250 and 50 $mW \cdot cm^{-2}$ US across porosity constructs, while **Figure 3.9e** presents heatmaps comparing percentage changes between 18% and 63% porosity constructs under 50 and 250 $mW \cdot cm^{-2}$ US.

The higher metabolic activity of the 63% porosity construct compared to the 18% construct at 50 $mW \cdot cm^{-2}$ is further supported by ion channel activation mechanisms (*TRPV4* marker), showing a 60% improvement over the 18% porosity construct **(Figure 3.9c)**. This suggests that increased porosity and higher US intensity reduce the activity of voltage-gated calcium channels, which, due to overstimulation, may impair cellular processes involved in early osteogenesis and mechanotransduction. Furthermore, at high US intensity, *RUNX2* expression decreases with increasing porosity, indicating reduced early osteogenic differentiation **(Figure 3.12e)**.

These results are likely explained by excessive US, which amplifies the electric field intensity within the pores as porosity increases, leading to cellular overstimulation. This effect also accounts for the reduced metabolic activity of the 63% porosity construct when US is increased from 50 to 250 $mW \cdot cm^{-2}$. Conversely, at 18% porosity, increasing US from 50 to 250 $mW \cdot cm^{-2}$ significantly upregulates the osteogenic transcription factor *OSX*, with a 55.5% increase, indicating enhanced osteogenic differentiation likely driven by mechanotransduction pathways. An optimal electric field strength appears to be achieved within an intermediate US intensity range of 50 to 250 $mW \cdot cm^{-2}$, depending on scaffold porosity. This is supported by the

upregulation of gene expression at 250 mW·cm$^{-2}$ in low-porosity constructs, whereas higher porosity constructs favor upregulation at 50 mW·cm$^{-2}$ **(Figure 3.9e)**.

The most significant changes in gene expression induced by US and porosity are observed in *ALP* and *COL I* **(Figure 3.12i)**. *ALP* expression consistently increases with pore level at 50 mW·cm$^{-2}$, peaking at intermediate electric field intensity. However, in the 63% porosity construct at 250 mW·cm$^{-2}$, *ALP* expression decreases, likely due to electrical overstimulation, suggesting that higher US intensity shifts cells toward later differentiation stages. Similarly, *COL I* expression is highest in the 63% porosity construct at 50 mW·cm$^{-2}$, with a steady decrease as pore level increases under higher US, further confirming the optimal range for electric stimulation.

To investigate the molecular mechanisms underlying osteogenic differentiation induced by zero-curvature geometries and ultrasound-triggered electromechanical stimulation, we analyzed key signaling markers associated with mechanotransduction and bone formation. Specifically, we quantified the gene expression levels of ERK1, a central mediator in the MAPK pathway,[482,483] and SOST, a negative regulator of Wnt/β-catenin and YAP/TAZ signaling.[484–488] RT-qPCR analysis revealed that ERK1 expression was significantly upregulated in 18% porous scaffolds under higher ultrasound intensity (250 mW·cm$^{-2}$), while decreased in 63% porous scaffolds under the same conditions **(Figures 3.9c,e and 3.12i)**. This trend was consistent with the upregulation of downstream osteogenic transcription factors RUNX2 and OSX, suggesting that optimal ERK1 activation occurs at intermediate porosity and US conditions.[489,490] In parallel, SOST expression was reduced in both 18% and 63% porous scaffolds compared to the non-porous group, with the lowest levels observed in the 63% porosity condition under low-intensity US **(Figures 3.9c,e and 3.12j)**. These findings support a model in which scaffold architecture and US-driven piezoelectric activation synergistically modulate electromechanical signaling, enhancing osteogenic pathways through ERK1 activation and SOST suppression. Together, this mechanistic insight complements our biological assessments and underscores the importance of scaffold design and dynamic stimulation in promoting bone regeneration.

**Figure 3.13a-i** shows that US enhances osteopontin deposition and cytoskeletal organization across all porosities, with the most pronounced effect at 250 mW·cm$^{-2}$ in the 18% porosity construct. In contrast, non-stimulated constructs exhibit minimal osteopontin deposition, regardless of porosity, reinforcing that US promotes deposition through enhanced electric field interactions. Improved F-actin organization under 250 mW·cm$^{-2}$, particularly in the 18%

porosity construct, further highlights the role of US in enhancing both osteopontin deposition and cell alignment. Consistent with DAPI/Actin staining, ultrasound-stimulated constructs display more organized cytoskeletal structures, likely supporting effective matrix deposition and mineralization. Moreover, 250 mW·cm$^{-2}$ US appears to facilitate advanced stages of bone formation, as osteopontin is closely associated with bone remodeling and repair rather than early osteogenesis.

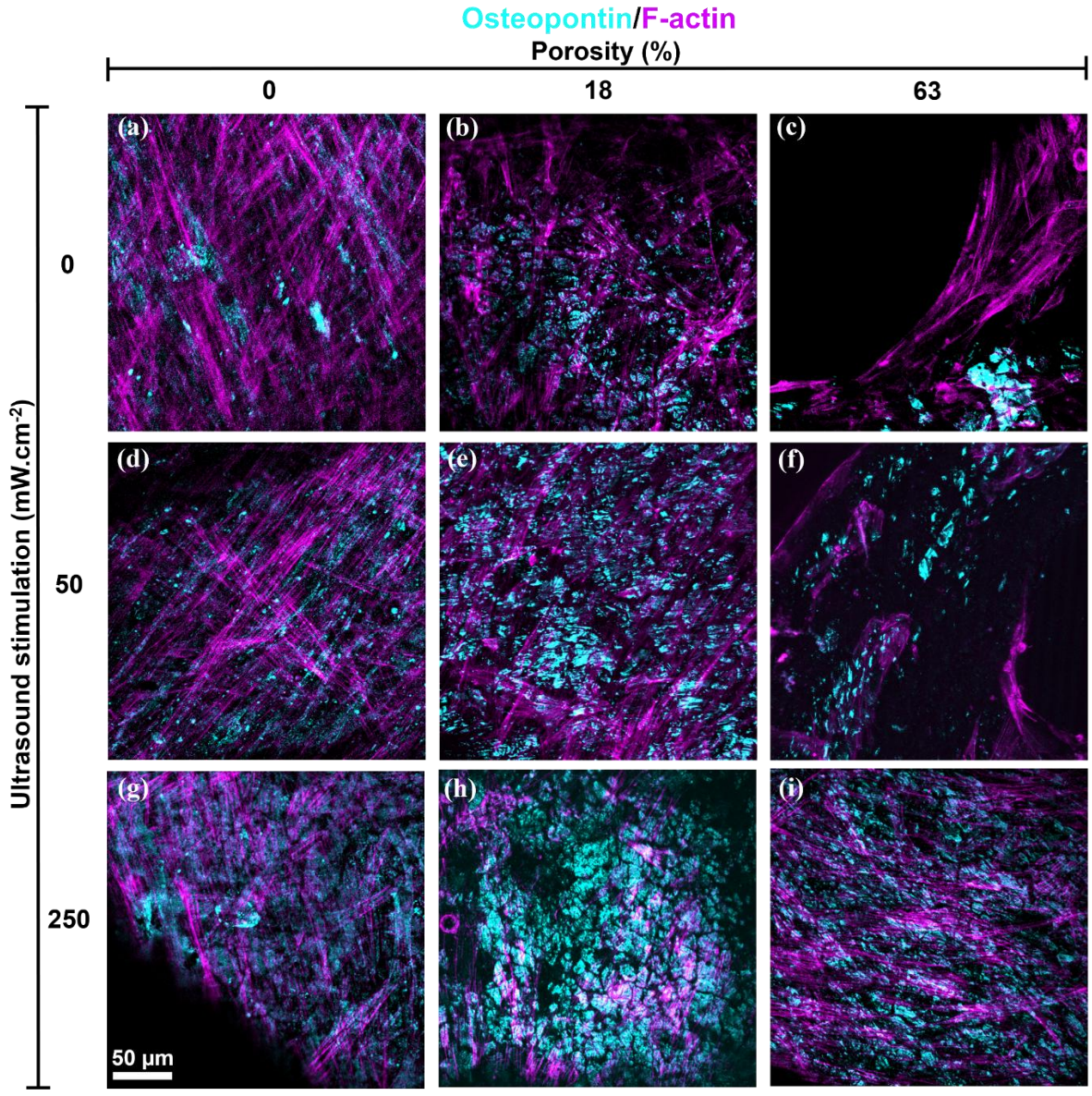


**Figure 3.13.** Osteopontin and F-actin confocal images of constructs after 14 d of cell growth. Osteopontin/F-actin confocal images of constructs at 0 mW·cm$^{-2}$ for 0% (a), 18% (b), and 63% porosity (c); at 50 mW·cm$^{-2}$ for 0% (d), 18% (e), and 63% porosity (f); and at 250 mW·cm$^{-2}$ for 0% (g), 18% (h), and 63% porosity (i). Osteopontin deposition (cyan) and cytoskeletal organization (F-actin, magenta). The scale bar in (g) applies to all images.

Meanwhile, Collagen-I production and distribution remain unaffected by US treatment, indicating a negligible impact on Collagen-I synthesis **(Figure 3.14a-i)**.

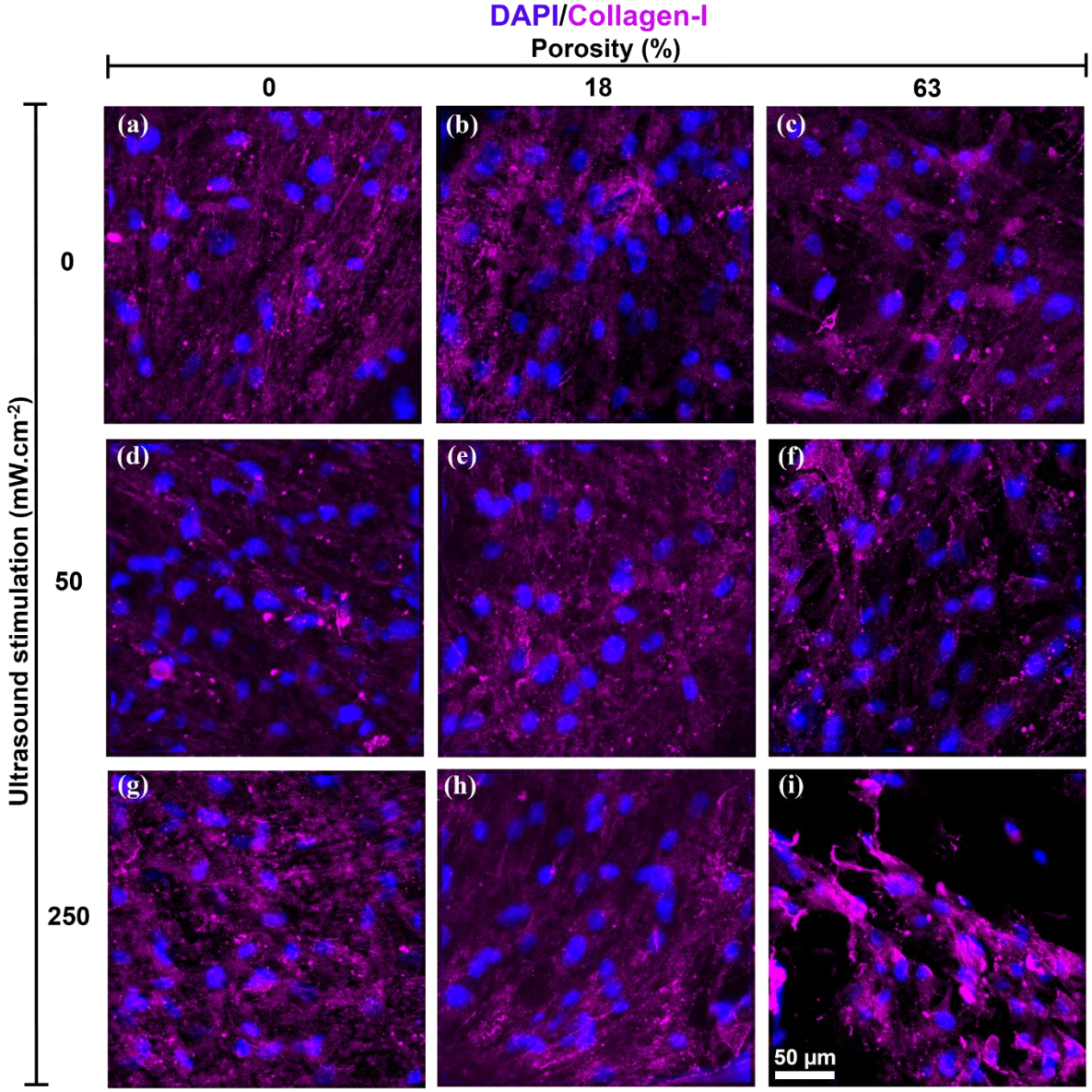


**Figure 3.14.** DAPI/collagen-I confocal images of constructs after 14D. DAPI/collagen-I confocal images of constructs under US at 0 mW·cm$^{-2}$ for 0% (a), 18% (b), and 63% porosity (c); at 50 mW·cm$^{-2}$ for 0% (d), 18% (e), and 63% porosity (f); and at 250 mW·cm$^{-2}$ for 0% (g), 18% (h), and 63% porosity (i). Collagen-I (magenta) and nuclei (DAPI, blue) staining. The scale bar in (i) applies to all images.

Furthermore, we confirmed the positive influence of the electric field and US on cell alignment through qualitative DAPI/F-actin confocal imaging **(Figure 3.15a–i)** and quantitative degree-based cell counting **(Figure 3.15j–l)**.

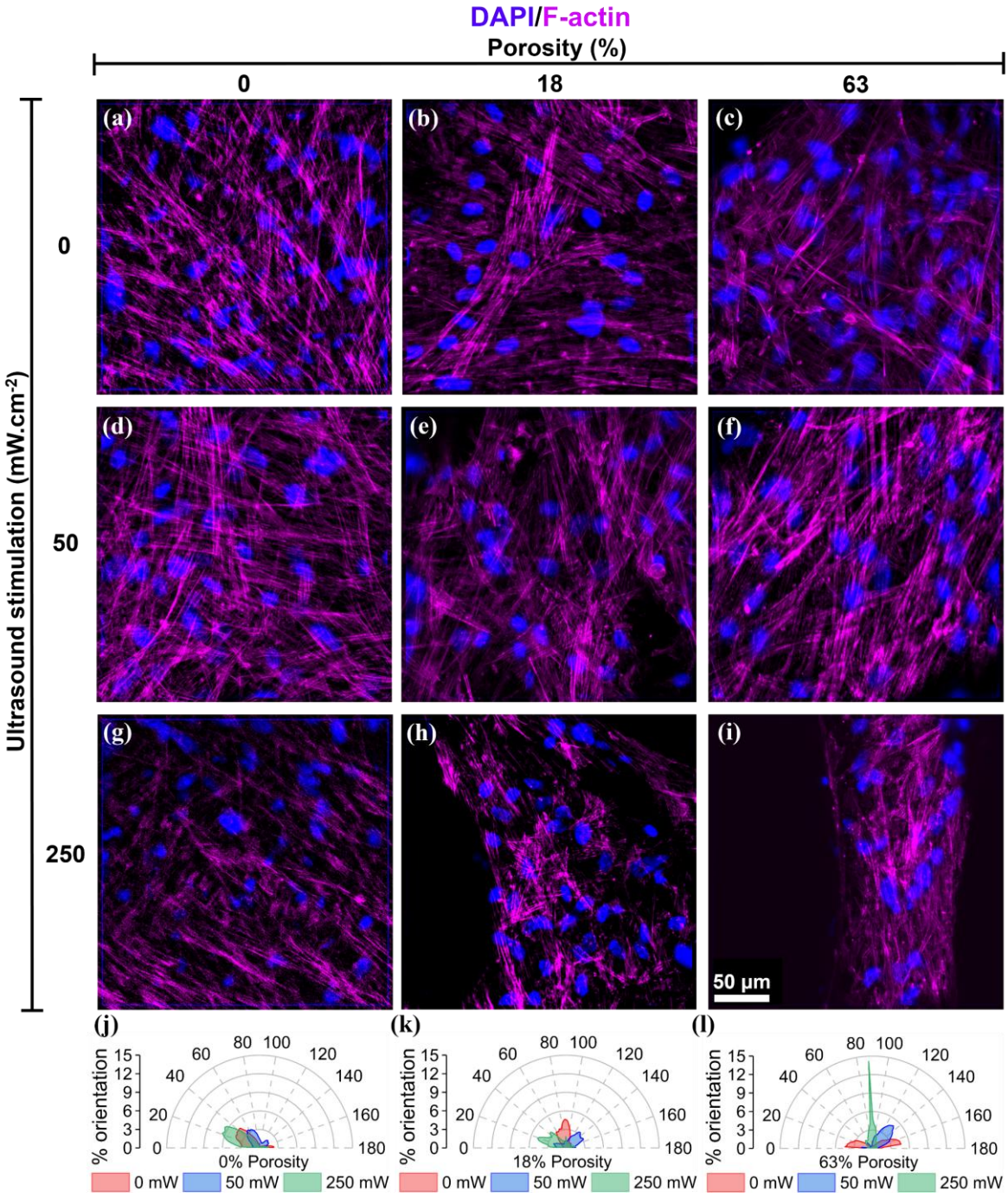


**Figure 3.15.** Influence of ultrasound stimulation (US) and construct porosity on cellular alignment and actin filament organization. DAPI/F-actin confocal images of constructs under US at 0 mW·cm$^{-2}$ for (a) 0%, (b) 18%, (c) 63% porosity; at 50 mW·cm$^{-2}$ for (d) 0%, (e) 18%, (f) 63% porosity; and at 250 mW·cm$^{-2}$ for (g) 0% (h), 18% (i), 63% porosity. Scale bar = 50 µm (applies to all images). Polar plots quantify cell alignment for (j) 0%, (k) 18%, and (l) 63% porosity using three-degree accumulation range under each US condition (0, 50, and 250 mW·cm$^{-2}$). Cytoskeleton (F-actin, magenta) and nuclei (DAPI, blue) staining.

To investigate this effect in detail, we analyzed the distribution and intensity of cell alignment based on cytoskeleton orientation, including accumulated cell counts within degree ranges of 1, 3, 5, 7, and 10° across 0-180° **(Figure 3.16a–l)**.

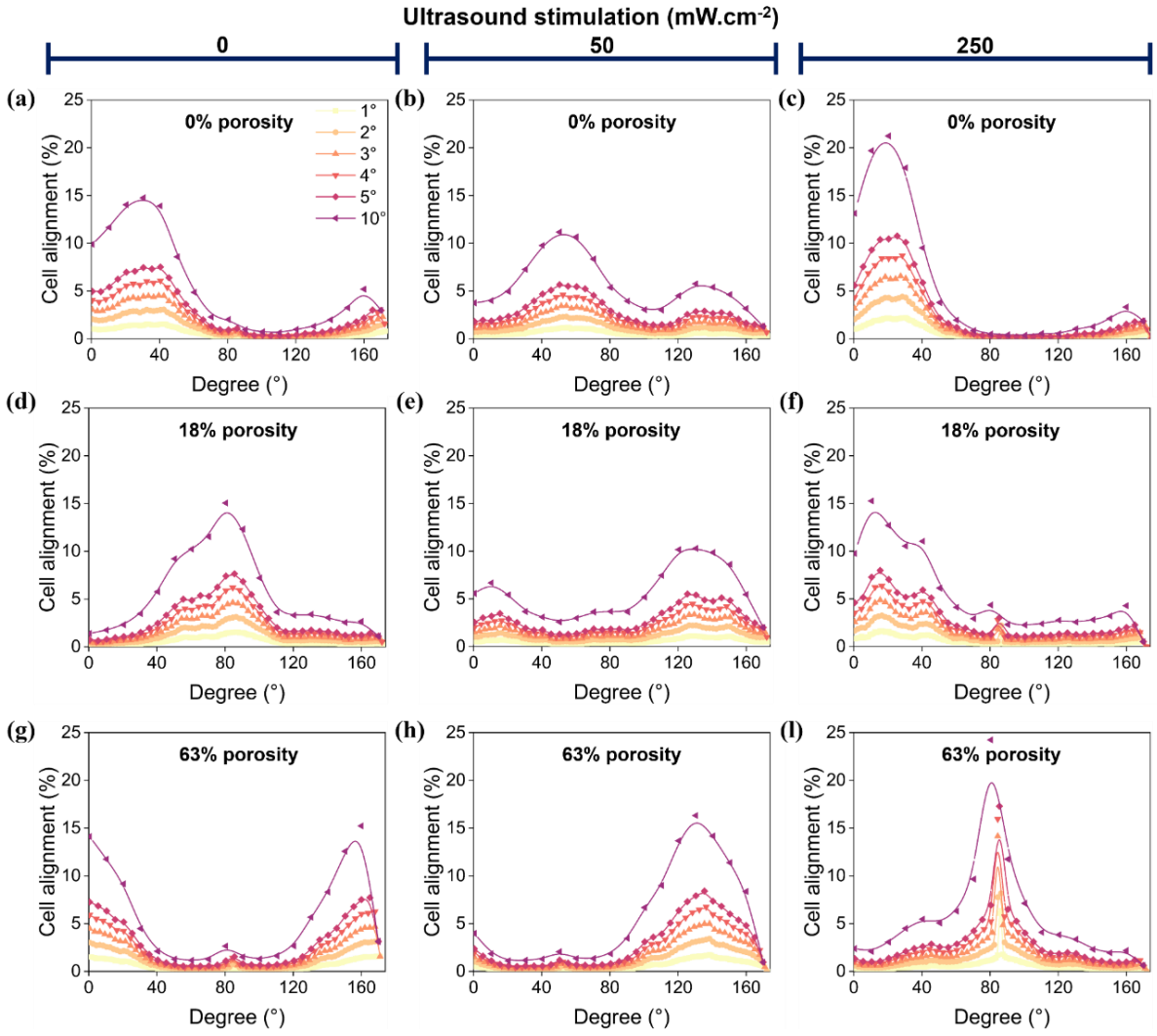


**Figure 3.16.** Distribution of cell alignment (%) as a function of degree range accumulation. Cell alignment distribution obtained by cytoskeleton orientation from 0° to 180°, considering ultrasound stimulation intensities of 0, 50, and 250 mW·cm$^{-2}$ applied to 0% (a, b, and c, respectively), 18% (d, e, and f, respectively), and 63% (g, h, and l, respectively) porosity scaffolds. Accumulated cell was counted using degree ranges of 1, 3, 5, 7, and 10°. The color coding in Figure 16a applies to all graphs.

**Table 3.5** further highlights cell alignment peaks (%) within these ranges, showing a consistent increase in cell accumulation at 63% porosity under 250 mW·cm$^{-2}$ US. To avoid overestimation and maintain accuracy, we used a three-degree range for constructing polar plots for each condition **(Figure 3.15j–l)**. Compared to unstimulated controls, US improved cell

alignment by ca. 10% with just 3 min of exposure every other day over a 14-d period, underscoring its significant potential as a physiotherapeutic strategy to enhance bone anisotropy and accelerate biological recovery.

**Table 3.5.** Cell alignment (%) within accumulated degree ranges (1, 3, 5, 7, and 10°) for constructs with 0%, 18%, and 63% porosity under ultrasound stimulation of 0, 50, and 250 mW·cm$^{-2}$.

| **Construct porosity (%)** | **US (mW·cm$^{-2}$)** | **% Cell alignment by accumulated degree range** | | | | |
|---|---|---|---|---|---|---|
| | | 1° | 3° | 5° | 7° | 10° |
| 0 | 0 | 1.5 | 4.5 | 7.5 | 10.3 | 14.8 |
| 0 | 50 | 1.2 | 3.4 | 5.7 | 7.9 | 11.2 |
| 0 | 250 | 2.2 | 6.6 | 10.8 | 14.7 | 21.2 |
| 18 | 0 | 1.6 | 4.6 | 7.6 | 10.7 | 15.1 |
| 18 | 50 | 1.1 | 3.4 | 5.5 | 7.8 | 10.3 |
| 18 | 250 | 1.7 | 4.9 | 8.0 | 11.1 | 15.3 |
| 63 | 0 | 1.6 | 4.7 | 7.7 | 10.6 | 15.2 |
| 63 | 50 | 3.4 | 4.9 | 6.7 | 8.4 | 16.3 |
| 63 | 250 | 6.4 | 14.2 | 17.3 | 20.4 | 24.2 |

Higher US (250 mW·cm$^{-2}$) markedly enhanced cell alignment across all porosities, with the strongest effect observed in the 63% porosity construct, achieving approximately 14.2% alignment. In contrast, at the non-stimulated condition, cells exhibited reduced alignment (4.7%) with dispersed nuclei and disorganized cytoskeletal structures. This suggests that the electric field intensity, modulated by US within the construct pores, promotes cytoskeletal alignment and contributes to bone anisotropy, which in turn supports daily mechanical loads while reducing the risk of injury. These findings underscore the synergistic effects of US and electric field intensity on cellular organization, offering insights into bone cell growth and advancing our understanding of tissue regeneration processes.

Although the gyroid structure was intentionally chosen to mimic trabecular bone microarchitecture rather than to impose strong directional steric guidance, the results suggest that further optimization of ultrasound parameters, e.g., intensity, duration,

and frequency, could amplify alignment effects and potentially drive higher levels of anisotropy. In addition to mechanical modulation, future strategies could also explore surface functionalization with aligned biochemical cues or controlled electrochemical stimulation to further guide cellular orientation within 3D scaffolds. Together, these approaches highlight a promising avenue for future research using the precisely engineered scaffolds structures developed in this study, which can serve as a blueprint for advancing 3D scaffold fabrication and dynamic regenerative therapies.

## 3.4 **Conclusion**

In this study, we synthesized a biocompatible piezoelectric compound ($NaNbO_3$), fabricated hierarchical porous scaffolds using sacrificial templating, and conducted mechano-electro characterization to advance stimuli-responsive biomaterials. We explored the effects of ultrasound stimulation on the biological performance of electrically charged scaffolds, focusing on the interplay between porosity, mechanical properties, and electric field intensity in promoting *in vitro* bone tissue formation. Corona discharge poling created electrically charged scaffolds, enhancing electric field intensity via charge trapping. Cyclic mechanical compression tests indicate the stress-strain range required to ensure the functional stability of scaffolds, demonstrating that ultrasonic stimulation effectively preserves pore integrity while delivering mechanical stimuli.

High-porosity scaffolds (63%) showed increased electric field intensity due to the reduced dielectric shielding effect, significantly enhancing bioactivity. In contrast, low-porosity scaffolds (18%) exhibited superior viscoelastic properties, ideal for load-bearing applications. The 63% porous scaffolds synergized with US to enhance metabolic activity, mineralization, and gene expression, resulting in a 1200% increase in calcium deposition. US also improved bone cell alignment by ~10% with just 3 min exposures every other day over 14 d, demonstrating its potential to enhance bone anisotropy and biological recovery.

These findings advance the understanding of ultrasound stimuli in scaffolds mimicking cancellous bone architecture and highlight the potential of 3D sacrificial template methodologies for designing stimuli-responsive scaffolds. Our outcomes are expected to inspire future

research to refine bone cell regeneration strategies by optimizing mechanical stimulation parameters, e.g., duration, power, and frequency, unlocking the full potential of ultrasound stimuli in advanced bioactive scaffolds for bone tissue engineering.

# 4

# FLEXIBLE SMART LASER-INDUCED GRAPHENE SENSOR FOR VOLATILE AMMONIA DETECTION VIA COLORIMETRIC ELECTROCHEMICAL AND RFID SIGNALS FOR INTELLIGENT PACKAGING APPLICATIONS

## 4.1 **Introduction**

Food spoilage and waste pose escalating global challenges, threatening environmental sustainability, food safety and security, and supply chain integrity. According to the UNEP Food Waste Index Report 2024, 1.05 billion tonnes of food were wasted in 2022;[491] combined with a further 13% loss before retail, this exceeds one-third of global output and drives major economic losses, resource depletion, and greenhouse gas emissions.[492] From a public health perspective, microbial spoilage of protein-dense foods also remains a critical concern as it contributes significantly to an estimated 600 million annual cases of foodborne diseases worldwide.[493] A hallmark of protein-rich food spoilage is the emission of ammonia gas ($NH_3$), produced via microbial deamination, which is especially pronounced in meat and seafood matrices.[494–496] Together, these challenges underscore the urgent need for robust, real-time $NH_3$ sensing technologies to enable effective food quality monitoring and support the development of next-generation smart packaging solutions.

Despite the urgency of $NH_3$ detection for food quality monitoring, existing sensing technologies fall short in meeting the demands of commercial packaging applications. A plethora of $NH_3$ sensors have been reported,[280,497–500] yet challenges in achieving high sensitivity with compact form factors, non-invasive operation, mechanical flexibility, biocompatibility, and continuous wireless monitoring continue to hinder their real-world implementation. Current methods range from colorimetric strips - often imprecise, non-quantitative, and prone to false positives -[248,500,501] to invasive, laboratory-based techniques (e.g., gas chromatography), which are costly, require trained personnel, and are incompatible with real-time or distributed use.[502,503] Even electrochemical sensors, while more accurate, often depend on rigid, costly, and non-biocompatible substrates, external power sources, hardwired architectures, and demanding storage conditions, all of which limit their scalability and integration into smart packaging.[499,504] These limitations have collectively prevented the commercial deployment of $NH_3$ sensors for *in-situ* freshness monitoring, highlighting the pressing need for eco-friendly, low-cost sensing platforms that integrate food-safe materials and wireless functionality to bridge the gap between functional materials and practical food safety technologies.

Among emerging materials poised to meet these demands, laser-induced graphene (LIG) has attracted increasing attention as a versatile and scalable platform, owing to its direct-write fabrication, carbon-rich architecture, and low cost, carbon footprint, and toxicity, positioning it as a strong candidate for next-generation sensing technologies.[505,506] Since its introduction in 2014,[507] LIG has been applied across a wide range of sensing applications spanning chemical, biological, and environmental domains.[505,508] This versatility arises from a unique combination of mechanical flexibility, thermal stability, biocompatibility, and porous morphology, which enhance surface area and analyte accessibility, both critical for high-performance signal transduction.[506,508] In addition, LIG can be fabricated via a solvent-free, maskless laser writing process, offering a more environmentally benign alternative to conventional synthesis routes.[168,509] This direct patterning yields graphene-like structures with tunable morphology, excellent electrochemical properties, positioning LIG as a leading candidate for flexible, on-site sensing in intelligent packaging.

However, *in-situ* functionalization of LIG during direct laser writing remains largely underexplored, particularly strategies that enable molecular selectivity without compromising biocompatibility or food-contact safety. Conventional approaches often rely on synthetic polymers or metal nanoparticles (e.g., Ag, Au, or Pd), raising concerns over cytotoxicity, environmental persistence, and regulatory approval for food-related applications.[510–513] To address

this, we leveraged the aromatic rings and conjugated π-systems of anthocyanins, natural flavonoid pigments,[514] to catalyze graphene-like domain formation during laser-induced graphitization. In parallel, their pH-dependent structural transitions, redox activity, and reversible coloration make them intrinsically responsive to $NH_3$.[248,280,500] This dual role - serving as both redox-active $NH_3$ transducers and laser-assisted graphene precursors - provides a sustainable route to engineer smart $NH_3$-sensitive LIG electrodes. Bridging this gap enables the fabrication of highly sensitive, food-compatible sensors for non-invasive, real-time, and continuous monitoring in packaging. Moreover, the resulting $NH_3$-responsive LIG electrodes can be integrated into triboelectric nanogenerators (TENGs) for self-powered sensing and barcoded signal outputs, advancing intelligent packaging applications.

In this study, we report on the pioneer fabrication of eco-friendly, flexible $NH_3$-responsive LIG sensors via anthocyanin-$Ca^{2+}$ crosslinking, assisted by laser-induced graphitization. This approach enables synergistic colorimetric, electrochemical, and passive RFID-based responses to $NH_3$. By harnessing the intrinsic redox activity of anthocyanins and the conductivity of patterned LIG, the hybrid sensors deliver quantifiable shifts in color, impedance, and resonant frequency under ambient $NH_3$ exposure. The platform addresses key limitations of current sensing technologies by offering multimodal, label-free readouts - optical (colorimetric), electrical (electrochemical), and wireless (RFID) - without external power sources or reagents. This advancement pushes the functional boundaries of LIG-based electrodes beyond conventional lab-based approaches, toward real-time, low-cost, and non-invasive monitoring tailored for next-generation smart packaging and intelligent sensing.

## 4.2 Experimental section

### 4.2.1 Materials

Sodium hydroxide pellets (>97.0%), chitosan (190,000-375,000 Da, 75-85% deacetylated, >200 cP, 1 wt% solution in 1% acetic acid at 20 °C), glycerol, boric acid, acetic acid (>99%), ammonia solution (25%), and hydrochloric acid (37%) were purchased from Sigma-Aldrich Co. (St. Louis, MO, USA). Calcium chloride (>97.0%) was acquired from honeywell Fluka (Seelze, Germany). Ethanol (96%) was obtained from LabChem (Zelienople, PA, USA). Red cabbage (*Brassica oleracea* L. var. *capitata* 'Red Acre') was purchased from a local supermarket in Caparica, Almada, Portugal.

### 4.2.2 Extraction of anthocyanins from red cabbage

Red cabbage extract (RCE) was prepared following Freitas et al.,[515] with modifications. Initially, 200 g of red cabbage was crushed and mixed with 100 mL of 70% (w·v-1) ethanol. The pH of the dispersion was adjusted to 2.0 using 1 M HCl and stored at 4 ± 2 °C for 24 h. The mixture was then filtered and centrifuged at (Remi Healthcare, Centrifuge Neya 16) 5,000 rpm for 15 min. The supernatant was passed through a quantitative filter paper (Whatman No. 1), neutralized to pH 7.0 ± 0.3 using 3 M NaOH, and stored in the dark at −20 ± 2 °C until use.

### 4.2.3 UV-Vis absorption and colorimetric stability of RCE

The procedure for fabricating the $NH_3$-responsive electroactive substrates is illustrated in **Figure 4.2a**. Boric acid (30 wt% relative to chitosan) and 1 mL of acetic acid (99% aqueous solution) were dissolved in 100 mL of deionized (Milli-Q) water and stirred at 800 rpm, 25 °C for 30 min. Chitosan (2 g) and glycerol (1 mL) were then added and stirred at 1,500 rpm, 45 °C for 2 d. To form graphene-like structures during laser scribing and introduce a $NH_3$-responsive behavior, RCE was added at 0-40 vol% relative to the chitosan dispersion **(Table 4.1)**. $CaCl_2$ (0-500 mM) was simultaneously added to enhance $NH_3$ sensitivity by shifting the chemical equilibrium, according to Le Chatelier's principle, toward irreversible anthocyanin-derived species (e.g., chalcone), as shown in our previous work.[248] IS values refer only to $CaCl_2$ contributions in Milli-Q water, excluding ionization from chitosan, and were calculated as described in Equation 4.1.

$$IS = \frac{\sum_{i=1}^{n} Z_i^2 * C_i}{2} \quad (4.1)$$

where $IS$ is ionic strength (mol·L$^{-1}$), $C_i$ is the concentration of the ion $i$ (mol·L$^{-1}$), and $Z_i$ is the number of the electrical charge of the ion $i$.

**Table 4.1.** Ionic strength and red cabbage extract content in chitosan dispersions with corresponding optimal sheet resistance.

| Treatment | Ionic strength (mM) | RCE (% mL·mL$^{-1}$) | Optimal sheet resistance (Ω·sq$^{-1}$) |
|---|---|---|---|
| T1 | 0 | 11 | 303 |
| T2 | 100 | 11 | 520 |
| T3 | 200 | 11 | 880 |

| | | | |
|---|---|---|---|
| T4 | 300 | 11 | 1140 |
| T5 | 400 | 11 | 2480 |
| T6 | 500 | 11 | 3000 |
| T7 | 0 | 5.5 | 363 |
| T8 | 0 | 22 | 243 |
| T9 | 500 | 0 | 921 |
| T10 | 0 | 44 | 48 |
| T11 | 0 | 0 | - |
| T12 | 0 | 2.75 | 663 |

The final mixture was homogenized by stirring at 3000 rpm and 60 °C for 2 h, then cast into petri dishes (90 mm diameter × 15 mm height; 40 mL volume). Films were dried sequentially at 55 °C and 50% RH for 12 h, followed by 35 °C and 65% RH for 48 h, and finally preconditioned at 25 °C and 65% RH for 24 h before laser scribing and characterization.

### 4.2.4 Fabrication and optimization of smart LIG electrodes

$NH_3$-responsive electroactive substrates were converted into laser-induced graphene (LIG) electrodes using a $CO_2$ laser system (VLS 3.50, Universal Laser Systems). A 6 × 7 matrix was used to optimize laser parameters for low sheet resistance, varying power (5-10%, i.e., 2.5-5 W), scan speed (4-10%, i.e., 50.8-127 $cm \cdot s^{-1}$), and focal height (−1.2 to +1.2 mm). Squares (0.5 × 0.5 $cm^2$) were scribed under nitrogen using a 10.6 μm $CO_2$ laser (0.127 mm beam diameter, 2.0 lens, 1000 $pulses \cdot inch^{-1}$).

Following optimization, IDE patterns, with dimensions and design shown in **Figure 4.11**, were scribed under fixed conditions (2.5 W, 63.5 $cm \cdot s^{-1}$, 0.2 mm defocus) to ensure consistency. Silver ink was applied to define electrical contacts for electrochemical measurements. The resulting $NH_3$-responsive graphene electrodes were stored under vacuum at 20 °C (±5 °C) and 55% RH (±5%) until characterization. Treatment T11 showed uneven morphology and brittleness, due to the absence of additives ($CaCl_2$ and anthocyanins) that act as plasticizers,[197] hindering LIG formation and comparability; hence, it was excluded from further study.

### 4.2.5 Fabrication of RFID antennas, barcodes, and TENGs

To fabricate RFID antennas and barcodes, larger $NH_3$-responsive electroactive substrates (100 × 100 $mm^2$) were prepared using the T6 formulation, keeping the same thickness (~220 μm) as in smaller-scale samples. Two RFID antenna designs and one barcode electrode design were tested; dimensions are provided in **Figure 4.13b**. Laser scribing was performed using optimized parameters (2.5 W power, 63.5 $cm \cdot s^{-1}$, 0.2 mm defocus) for all barcode and antenna patterns.

For the single-electrode triboelectric nanogenerator (SE-TENG), square LIG electrodes (225 $cm^2$) were fabricated using the same optimized laser conditions. A poly(vinyl chloride) (PVC) film (~50 μm thick) was applied to the electrode surface as a triboelectric layer, simulating conditions relevant to food packaging. Copper tape was affixed to the LIG surface to facilitate electrical connections during performance testing.

### 4.2.6 LIG electrode characterization

Sheet resistance measurements were performed at the corners of the square-patterned electrodes using a UNI-T Industrial Digital Multimeter (UT171A). The morphology of the LIG composites was examined by field-emission scanning electron microscopy (FE-SEM) using a Hitachi Regulus 8220 operated at 5 kV with a secondary electron detector. For chemical characterization, Raman spectroscopy was carried out using a Renishaw® inVia™ Qontor® confocal Raman microscope (Gloucestershire, UK) equipped with a Renishaw Centrus 2957T3 detector. Spectra were acquired in extended mode over a range of 500-3000 $cm^{-1}$ using a 532 nm laser (1800 $l \cdot mm^{-1}$ grating) at 5% laser power, with a 10 s exposure time, three accumulations, and one acquisition per point. Data represent the average of at least three repeated measurements. Raman spectra were then used to calculate the crystalline size of LIG along the a-axis ($L_a$) from the intensity ratio of the G peak ($I_G$) to the D peak ($I_D$) according to Equation 4.2.

$$L_a = (2.4 \times 10^{-10}) \times \lambda_I^4 \frac{I_G}{I_D} \quad (4.2)$$

where $\lambda_I$ denotes the Raman excitation wavelength (532 nm).

X-ray photoelectron spectroscopy (XPS) was conducted using a Kratos Axis Supra system (Thermo Scientific, UK) with monochromated Al K$\alpha$ radiation (1486.6 eV) to analyze the surface elemental composition and chemical states of the LIG materials. Peak deconvolution and fitting were performed using CasaXPS software.

### 4.2.7 Water absorption of sensors

To evaluate the water absorption capacity, each sensor film (~2.0 ± 0.1 g) was placed in a sealed desiccator maintained at 84% RH using a saturated potassium bromide (KBr) solution at 25 °C. After 48 h of equilibration, the films were removed and weighed. The films were then dried at 50 °C, with periodic weighing until a constant mass was obtained (mass variation < 0.005 g). Water absorption (*WA*) was calculated using Equation 4.3.

$$WA(\%) = \frac{W_{wet} - W_{dry}}{Wet} x100 \quad (4.3)$$

where $W_{wet}$ is the mass of the film after equilibration, and $W_{dry}$ is the constant mass after drying. All measurements were performed in triplicate for each treatment.

### 4.2.8 Colorimetric response to $NH_3$ detection

The sensors' response to $NH_3$ was evaluated following the methodology proposed by Silva et al.[248] To simulate consumer perception of food quality, colorimetric changes were recorded using digital imaging. Sensors (4 $cm^2$) were placed in sealed desiccators at 25 ± 3 °C and 75% RH, maintained using a saturated NaCl solution. Color changes in the alkaline environment were monitored, and color coordinates L*, a*, and b* were recorded at 0, 10, 30, 60, 120, 180, 240, and 300 min using the ColorMeter RGB Colorimeter® software. The camera was positioned at a fixed distance of 150 mm and a 90° angle relative to the sensor surface. Total color difference (ΔE*), Chroma (C*), and hue angle (h°) were calculated according to Equations 4.4, 4.5, and 4.6, respectively. All measurements were performed in triplicate.

$$\Delta E^* = \sqrt{\left[\left(\Delta L^*\right)^2 + (\Delta a^*)^2 + \left(\Delta b^*\right)^2\right]} \quad (4.4)$$

$$C^* = \sqrt{[(a^*)^2 + (b^*)^2]} \quad (4.5)$$

$$h^* = tan^{-1}\left(\frac{b^*}{a^*}\right) \quad (4.6)$$

where $\Delta L^* = (L^* - L_0^*)$; $\Delta a^* = (a^* - a_0^*)$; $\Delta b^* = (b^* - b_0^*)$; and $L_0^*$, $a_0^*$ *e* $b_0^*$ are color coordinates of the sensor before the test.

### 4.2.9 Electrochemical $NH_3$ monitoring

The sensors underwent electrochemical characterization to assess their responsiveness to $NH_3$ and facilitate a comparative analysis of different electrode designs and compositions. Sensors were exposed to volatilized $NH_3$ (~1500 ppm) in a sealed desiccator over a 300 min at 20 °C (±5 °C) and 75% RH, using 50 mL of saturated NaCl solution to maintain RH inside the

chamber. Prior to $NH_3$ exposure, sensors were equilibrated at 75% RH for at least 1 h to ensure a stable baseline. All electrochemical measurements were conducted using a PalmSens 4.0 potentiostat (PalmSens, Compact Electrochemical Interfaces). Electrochemical measurements, i.e., CV and electrochemical impedance spectroscopy (EIS), were recorded at 0, 60, 120, 180, 240, and 300 min. CV was performed within a potential window of -1.3 to +1.3 V at a scan rate of 0.5 $V \cdot s^{-1}$, with three consecutive scans per measurement. EIS was carried out using a sinusoidal potential input with an amplitude of 25 mV, acquiring 61 data points across a frequency range from 1 Hz to 1 MHz. A 10-s stabilization period was allowed prior to each EIS measurement to ensure system equilibrium.

### 4.2.10 **Scan rate study**

To investigate the charge storage mechanism and evaluate whether the sensor response is capacitive, a scan rate study was performed during $NH_3$ detection. This analysis also provides insights into the kinetics of $NH_3$ adsorption, particularly the speed of interaction at different scan rates. At higher scan rates, reduced interaction time helps assess the response speed and robustness of the sensor. To distinguish between surface-controlled and diffusion-controlled processes, log(current) was plotted against log(scan rate). A slope near 1 indicates a surface-controlled (capacitive) mechanism. For this study, the most sensitive sensor configuration (S-IDE T6) was exposed to volatilized $NH_3$ (~1500 ppm) for 30 min. CV measurements were then conducted over a scan rate range of 50-900 $mV \cdot s^{-1}$ within a potential window of -1.3 to +1.3 V.

### 4.2.11 **Current-scan rate analysis of capacitive response**

The capacitive response of the electrode was evaluated from CV profiles collected between -1.5 and 1.5 V at scan rates of 50-900 $mV \cdot s^{-1}$. For an ideal capacitive process, the current is expected to scale linearly with the scan rate ($i=Cv$), whereas diffusion-limited redox processes deviate from this behavior. To test this relationship, the current values at a fixed potential (0 V) were extracted from each CV curve and averaged between anodic and cathodic directions. The resulting current-scan rate dependence exhibited a linear trend, confirming a predominantly capacitive charge-storage mechanism.

Further validation was obtained from a power-law analysis of the form ($i=av^b$), where $a$ and $b$ are adjustable parameters. A slope of $b$~1 confirms capacitive control, whereas $b$~0.5

indicates diffusion-limited redox processes. Intermediate values ($0.5 < b$) reflect mixed behavior.

### 4.2.12 $NH_3$ quantification

Sensors were exposed to volatilized $NH_3$ in the range of 12 to 2600 ppm for 15 min in a sealed desiccator at 20 (±5) °C and 75% RH. Prior to $NH_3$ exposure, sensors were equilibrated at 75% RH in an $NH_3$-free environment for at least 1 h to ensure baseline stability. $NH_3$ solution was then introduced into the desiccator, and electrochemical measurements (CV and EIS) were recorded after 15 min. The LOD and LOQ were calculated using the standard signal-to-noise approach, where LOD = 3.3 $\sigma \cdot S^{-1}$ and LOQ = 10 $\sigma \cdot S^{-1}$, with $\sigma$ representing the standard deviation of the blank signal and S the slope of the calibration curve.

### 4.2.13 Irreversibility analysis

To evaluate the irreversibility of the sensor response after $NH_3$ exposure, sensors were exposed to volatilized $NH_3$ (~1500 ppm) in a sealed desiccator for 30 or 300 min at 20 °C and 75% RH. After exposure, the sensors were stored in fresh air under the same conditions (20 °C, 75% RH) for 7 d. Colorimetric parameters, digital photographs, and electrochemical measurements (CV and EIS) were recorded immediately after exposure (day 0) and again after 7 d.

### 4.2.14 UV-Vis absorption and colorimetric stability of RCE

UV-Vis absorption spectra of RCE (0.01 vol% in Milli-Q water) were recorded over pH 1-14 (in increments of 1 pH unit) on days 0, 3, and 7 using a Lambda 950 UV-Vis spectrophotometer (PerkinElmer, Waltham, MA, USA) over 350-750 nm.

### 4.2.15 Arrhenius plot and temperature effect

The influence of temperature on $NH_3$ detection was investigated over a range of 20 to 70 °C, in 10 °C increments, to understand the temperature-dependent behavior. Sensors were exposed to volatilized $NH_3$ (~1500 ppm) for 300 min at each temperature point, and EIS measurements were recorded at the end of each exposure period. The activation energy for the sensing process was determined using the Arrhenius Equation 4.7.

$$\ln(Z) = \ln(A) + \frac{E_a}{RT} \tag{4.7}$$

where Z is the measured sensor response, i.e., the impedance. $A$ is a pre-exponential factor related to the frequency of molecular interactions at the sensor surface. $E_a$ is the activation energy ($J \cdot mol^{-1}$), representing the energy barrier for $NH_3$ adsorption or charge transfer. $T$ is the absolute temperature in kelvin, and $R$ is the universal gas constant (8.314 $J \cdot mol^{-1} \cdot K^{-1}$).

By plotting $\ln(Z)$ against $1 \cdot T^{-1}$, the activation energy is obtained from the slope of the linear plot, helping to explain how temperature affects the sensor's response mechanism.

### 4.2.16 **TENG and self-powered barcode characterization**

Open-circuit voltage ($V_{oc}$) and short-circuit current ($I_{sc}$) outputs were evaluated using Thevenin and Norton equivalent circuit models, respectively.[516] Electrical outputs from the SE-TENG device were measured under varying mechanical forces (20-100 N) at 2 Hz, using wood as the counterpart material at a custom-built mechanical drive. The TENGs were connected to an external circuit, and signals were recorded using an oscilloscope (Tektronix TBS1000C). Electrical stability was assessed by monitoring $V_{oc}$ over 10,000 cycles under 80 N and 2 Hz. Instantaneous power output was calculated using the relation $P = V^2R^{-1}$, based on voltage measurements across a range of external load resistances (0.1-200 MΩ) at 50 N and 2 Hz. To simulate real-world consumer interaction, the barcode electrodes were activated by sliding a finger across all barcode regions.

### 4.2.17 **RFID tag measurement**

The RFID sensor system employed a passive RFID antenna (tag), wirelessly excited and interrogated through magnetic coupling by an external copper coil linked to a vector network analyzer (VNA), following principles of passive RFID inductive coupling described by Chen and Thomas **(Figure 4.13a)**.[517] Two RFID sensor designs were tested with different electrode configurations: a thin tag (D = 1 mm) and a thicker tag (D = 2 mm) **(Figure 4.13b)**.

Sensors were exposed to volatilized $NH_3$ (~1500 ppm) in a sealed desiccator for 300 min. After each exposure, RFID measurements were performed in ambient air to assess the lasting impact of $NH_3$ adsorption on the sensor's electromagnetic response. All measurements were conducted under controlled conditions: 20 (±5) °C, 45% (±5%) RH, and a fixed 2-cm separation between the tag and the excitation/receiving coil. Raw VNA data - real and imaginary components of the RL - were used to calculate the magnitude of the reflection coefficient, which was then expressed as return loss (RL, dB) using the Equation 4.8.

$$RL = -20 \times \log_{10}\left(\sqrt{Re^2 + Im^2}\right) \quad (4.8)$$

where *Re* is the real part and *Im* is the imaginary part of the complex reflection coefficient (Γ).

This return loss (RL, dB) served as the primary indicator of sensor performance, i.e., changes in RL (dB) can track resonance shifts and impedance variations induced by $NH_3$ uptake. We highlight serves as a proof of concept, demonstrating the potential of the smart responsive sensor for RFID-based chemical sensing. Further investigations are required to systematically assess the influence of environmental conditions, $NH_3$ release kinetics, sensor geometry, and material properties on sensing performance.

### 4.2.18 **Multivariate regression modeling via machine learning**

Multivariate regression analyses were conducted using Minitab 17 software. Colorimetric descriptors (ΔE*, L*, a*, b*, C*, and h°) were introduced as independent variables, and $NH_3$ concentration was defined as the response variable. To construct the predictive model, a forward stepwise selection procedure was applied with a significance threshold of $p < 0.05$. This approach systematically evaluated all variables, retaining only those with statistically significant contributions while eliminating redundant or collinear descriptors. The regression coefficients, model statistics ($R^2$, $R^2_{adj}$, and $R^2_{pred}$), and residual diagnostics (normal probability plots, residuals versus order, and variable correlation analyses) were automatically generated by the software.

### 4.2.19 **Statistical analyses**

Data are presented as mean values with the standard error of independent measurements or assays ($n \geq 3$). Statistical analysis was performed using the OriginPro 8.5 and Minitab 17 softwares. Quantitative data were subjected to analysis of variance (ANOVA), followed by Tukey's mean comparison test. P-values of $< 0.05$ were considered significant for all statistical tests, where applicable.

## 4.3 Results and Discussion

### 4.3.1 Fabrication of $NH_3$-responsive smart LIG sensors

Developing a dual-emission $NH_3$-responsive smart LIG sensor remains a significant challenge and, to the best of our knowledge, has not yet been reported. This approach is particularly impactful because it overcomes the limitations of relying solely on colorimetric changes, enabling the integration of electrical outputs that can be continuously monitored in a non-invasive manner. Such functionality is particularly relevant for intelligent packaging, where electrical signals can be coupled with RFID or wireless moduli to enable real-time food quality tracking and digital data logging throughout cold-chain transport, thereby mitigating food losses and foodborne risks.

To achieve multimodal sensing, an electroactive substrate must be engineered to provide reliable signal transduction upon $NH_3$ exposure. To this end, we incorporated anthocyanin into the sensing matrix, exploiting its multifunctionality beyond conventional colorimetry. Here, anthocyanin plays two synergistic roles: (i) as a graphitization promoter during laser scribing, where its $\pi$-conjugated aromatic structure promotes the formation of conductive $sp^2$-rich carbon frameworks; and (ii) as a redox-active molecular transducer that undergoes structural transformation (e.g., flavylium to chalcone) under alkaline conditions, modulating the electronic properties of the LIG network through proton-coupled electron transfer. This dual functionality enables the *in-situ* fabrication of $NH_3$-responsive smart LIG sensors with simultaneous colorimetric and electrochemical readouts, representing the first demonstration of a dual-mode LIG platform for $NH_3$ detection.

To meet food-contact safety requirements, we isolated red cabbage extract (RCE), a natural anthocyanin source, through a green, optimized route tailored for stability and high recovery efficiency **(Figure 4.1a)**. Fresh red cabbage (*Brassica oleracea* L. var. *capitata*) was shredded and homogenized in 70% ethanol (2:1 $w \cdot v^{-1}$), acidified to pH 2 with 2 M HCl to stabilize anthocyanins, and then subjected to ultrasonic-assisted extraction (1 h). The mixture was held at 4 °C for 24 h to promote further extraction. Solid residues were removed via vacuum filtration, and the extract was centrifuged (5,000 rpm, 15 min) and filtered again to ensure clarity. Subsequently, the pH was adjusted to 7.0 ± 0.2 with 3 M NaOH to convert anthocyanins into their quinoidal base form, which is more stable under ambient conditions. The final extract

was cryopreserved at -20 °C in the dark until use. This route yielded a halochromic, anthocyanin-rich extract exhibiting pH responsiveness and long-term stability, ideal for incorporation into stimuli-responsive sensing systems.

UV-Vis spectroscopy revealed the distinctive multichromic behavior of RCE **(Figure 4.1b)**, with well-defined spectral features from pH 1 to 14. At acidic conditions (pH 1-3), a strong absorption band centered at ca. 530 nm corresponds to the flavylium cation ($AH^+$). As pH increased to mildly acidic and neutral values (pH 4-7), a bathochromic shift and intensity changes were observed, consistent with the formation of neutral (A) and anionic quinonoid ($A^-$) species. Under alkaline conditions (pH ≥ 8), spectral profiles broadened and flattened, indicating transformation into chalcone forms. To assess colorimetric stability, time-lapse photographs of RCE across the pH range **(Figure 4.1c)** demonstrated consistent and distinguishable chromatic transitions up to 7 d, with only minor degradation at basic pH. In particular, red-to-pink transitions under acidic pH remained visually stable, while blue, green, and yellow shades progressively faded under alkaline exposure, corroborated by the time-dependent decrease in absorbance at $\lambda_{max}$ **(Figure 4.1d)**.

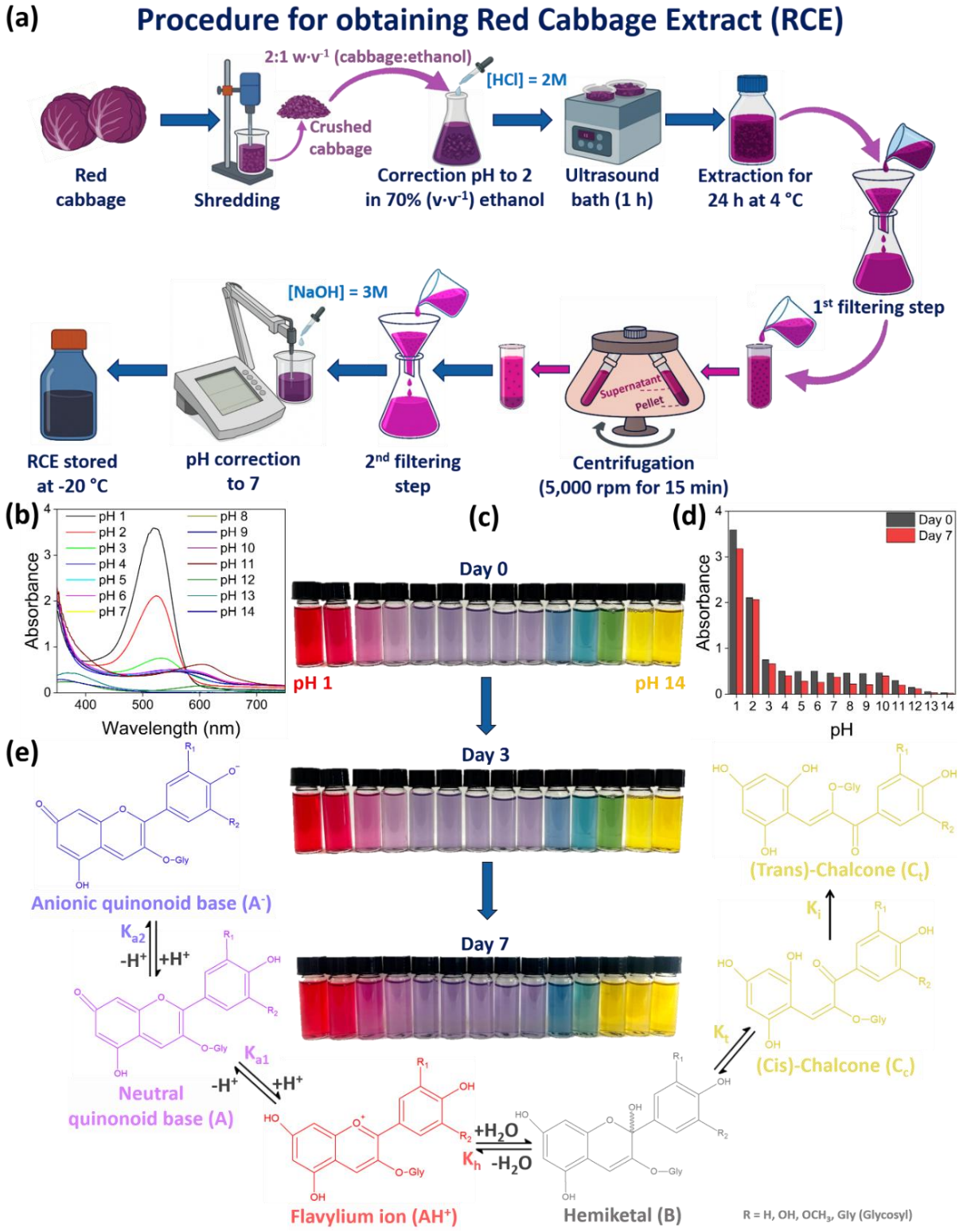


**Figure 4.1** Schematic illustration of the extraction protocol, pH-dependent optical response, and speciation of red cabbage extract (RCE). (a) Schematic illustration of RCE preparation involving ethanol extraction, acid stabilization, neutralization, and storage at −20 °C. (b) UV-Vis absorption spectra of RCE from pH 1 to 14, with distinct spectral features at each pH. (c) Digital photographs of RCE solutions at pH 1-14 at days 0, 3, and 7, highlighting color

stability and pH-responsiveness. (d) Corresponding absorbance at $\lambda_{max}$ for each pH at days 0 and 7. (e) pH-dependent speciation of anthocyanins in RCE: flavylium ion ($AH^+$, pH ~1-3), neutral quinonoid base (A, pH ~4-6), anionic quinonoid base ($A^-$, pH ~6-8), hemiketal (B, pH ~5-7), and cis-/trans-chalcone forms ($C_c$ and $C_t$, pH ≥ 8).

The pH-responsive color arises from the well-known multi-equilibria system of anthocyanins **(Figure 4.1e)**.[514,518,519] In highly acidic media (pH ≤ 2), the thermodynamically favored flavylium ion ($AH^+$) dominates. With increasing pH, $AH^+$ undergoes hydration and tautomerization to yield the hemiketal (B), which further interconverts into cis- and trans-chalcone species ($C_c$/$C_t$).[518,519] Concurrently, deprotonation forms neutral and anionic quinonoid bases (A and $A^-$), which contribute to purple and blue hues. These reversible transitions underpin the chromogenic tunability of RCE, establishing it as both a halochromic indicator and a pH-responsive redox-active probe for smart sensing applications.

### 4.3.2 **Fabrication and optimization of smart LIG electrodes**

$NH_3$-responsive smart LIG sensors were prepared by incorporating anthocyanin-rich RCE into chitosan matrices **(Table 4.2)**, following the protocol shown in **Figure 4.2a** and detailed in the *Experimental Section*. To optimize LIG formation for low sheet resistance and assess the catalytic role of anthocyanin in graphene-like structure development, a matrix of laser power (2.5-5 W) and scan speed (50.8-127 $cm \cdot s^{-1}$) was applied **(Figure 4.2b,d)**. Distinct visual contrasts emerged across these conditions, corresponding to different laser-induced regimes based on measured sheet resistance: ranging from unmodified areas and heat-affected zones (HAZ) at low-power/high-speed settings, to partially graphitized regions, well-defined LIG zones, and ablation at high-power/low-speed combinations.

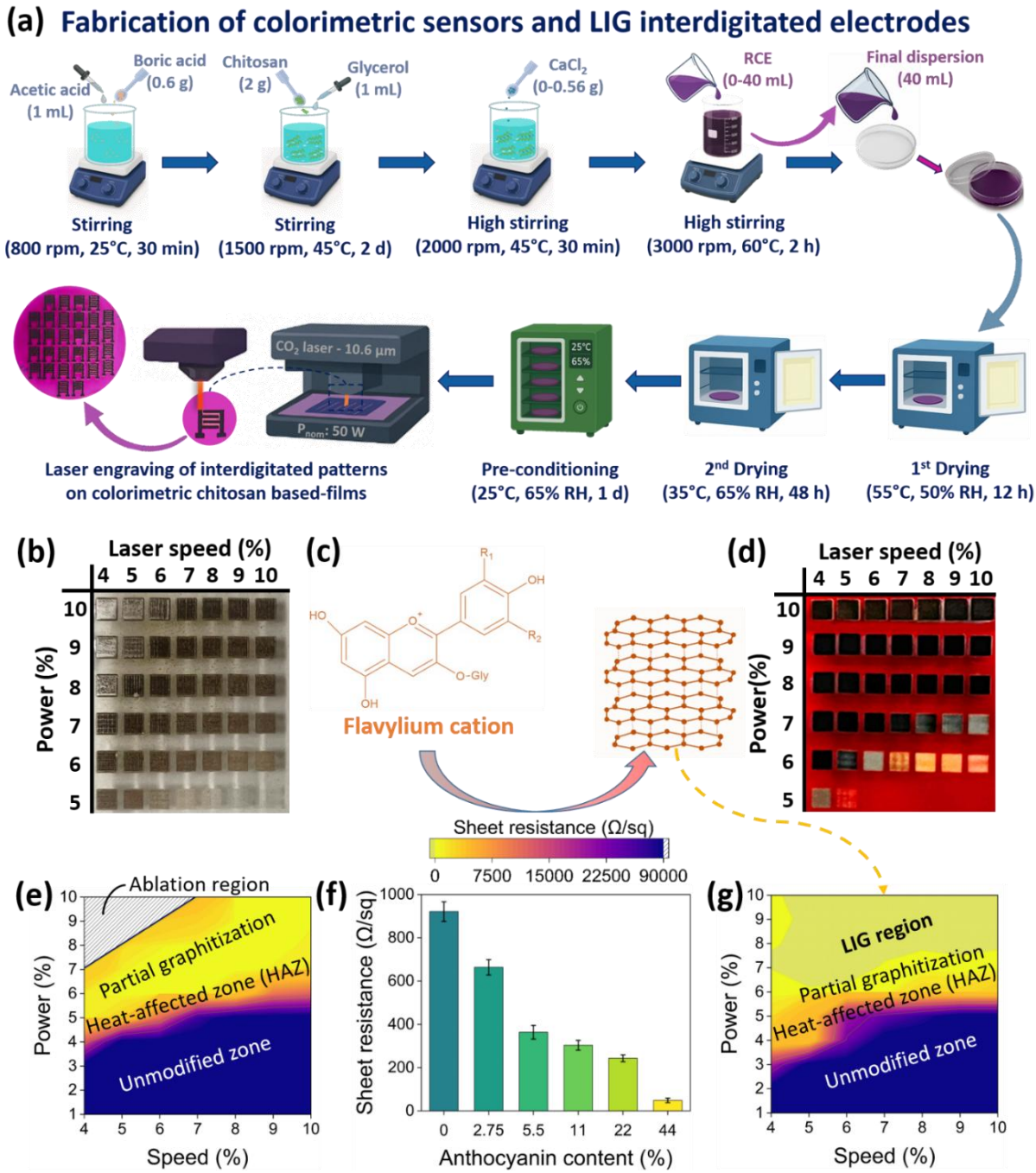


**Figure 4.2.** Fabrication and characterization of sensors and laser-induced graphene (LIG) interdigitated electrodes. (a) Schematic illustration of the fabrication process: chitosan-based films were prepared by sequential mixing of acetic acid, boric acid, chitosan, glycerol, and $CaCl_2$, followed by addition of red cabbage extract (RCE, 040 mL). The final dispersion was cast into films and subjected to sequential drying (55 °C, 12 h; 35 °C, 48 h) and pre-conditioning (25 °C, 24 h). Laser engraving is performed using a $CO_2$ laser (10.6 µm, 50 W) to produce interdigitated electrode (IDE) patterns on the colorimetric chitosan-based films. (b) Digital photographs of laser-induced patterns on chitosan-based films with 0% RCE-0 mM ionic strength (IS), produced at varying laser power (5-10%) and speed combinations (4-10%). (c) Schematic illustration showing the flavylium cation structure catalyzing graphene formation with increasing anthocyanin concentration. (d) Digital photographs of laser-induced patterns on chitosan-based films with 44% RCE and 0 mM IS at varying laser power (5-10%) and speed (4-10%). (e) Heat map of sheet

resistance ($\Omega \cdot sq^{-1}$) for 0% RCE-0 mM IS, delineating distinct laser processing regimes as a function of laser power and speed: unmodified zone, heat-affected zone (HAZ), partial graphitization, and ablation region. (f) Sheet resistance ($\Omega \cdot sq^{-1}$) as a function of anthocyanin content, showing progressive reduction with increasing anthocyanin concentration. (g) Heat map of sheet resistance ($\Omega \cdot sq^{-1}$) for 44% RCE-0 mM IS, delineating distinct laser processing regimes as a function of laser power and speed: unmodified zone, heat-affected zone (HAZ), partial graphitization, and the LIG region.

Anthocyanins, incorporated via RCE, strongly influenced the laser-material interaction, promoting efficient graphitization while suppressing ablation. As shown in **Figure 4.2d**, films with 44% RCE yielded darker, more uniform LIG patterns without detectable ablation, indicating enhanced photothermal conversion efficiency and graphitization. This behavior supports the hypothesis that anthocyanins, owing to their π-conjugated aromatic structures and thermal stability, enhance localized graphitization during laser irradiation, presenting the same role as other aromatic substances such as lignin and tannins.[520–522] This effect was quantitatively confirmed by sheet resistance mapping across the matrix array **(Figure 4.2g)**, where anthocyanin-containing films consistently exhibited lower resistance.

Furthermore, under identical laser parameters, conductive LIG regions - defined by a sharp drop in sheet resistance and high $I_d/I_g$ ratio - only formed in RCE-containing films. At 44% RCE, sheet resistance reached as low as ~48 $\Omega \cdot sq^{-1}$, whereas RCE-free films remained poorly conductive (~921 $\Omega \cdot sq^{-1}$), highlighting the critical role of anthocyanins in enabling effective $sp^2$-carbon domain formation. This concentration-dependent effect **(Figure 4.2f)** supports the hypothesis that anthocyanins, owing to their π-conjugated aromatic structure, catalyze carbon rearrangement during photothermal graphitization via energy-saving localized photothermal conversion **(Figure 4.2c)**, a mechanism we further elucidate through Raman spectroscopy in *Section 4.3.3*. Additionally, the absence of ablation under high-energy settings in anthocyanin-rich films suggests improved thermal tolerance and broader processability. Together, these findings provide the first demonstration that anthocyanins not only promote high-quality graphene-like synthesis but also broaden the laser processing window, offering a scalable route to fabricate highly sensitive $NH_3$-responsive LIG sensors on biodegradable substrates.

### 4.3.3 Structural and chemical characterization of $NH_3$-responsive smart LIG sensors

To investigate the influence of anthocyanins and ionic strength (IS) on LIG formation, four representative sensor formulations were selected for detailed analysis: (i) a control sample lacking anthocyanins but with high IS (0% RCE, 500 mM IS), (ii) an anthocyanin-loaded formulation (11% RCE, 0 mM IS), (iii) a combined anthocyanin-IS hybrid system (11% RCE, 500 mM IS), and (iv) an anthocyanin-rich condition (44% RCE, 0 mM IS). These compositions were chosen to decouple and evaluate the individual and synergistic effects of anthocyanin loading and $Ca^{2+}$-mediated ionic interactions on carbon ordering, graphitization efficiency, and film microstructure.

In Raman spectroscopy, the D band reflects structural disorder in defective $sp^2$ domains, the G band corresponds to the in-plane stretching of graphitic carbon, and the 2D band serves as a fingerprint of graphene ordering.[523] Raman spectra **(Figure 4.3a)** revealed pronounced differences in carbon structure across treatments. To isolate the effect of moisture, arising from the hygroscopic nature of $Ca^{2+}$, on LIG formation, we compared laser scribing on both dried and hydrated control films (0% RCE, 500 mM IS). In the hydrated state, the Raman spectrum exhibited merged D and G peaks with the absence of a 2D band **(Figure 4.4)**, indicative of suppressed graphitization and predominantly amorphous carbon.

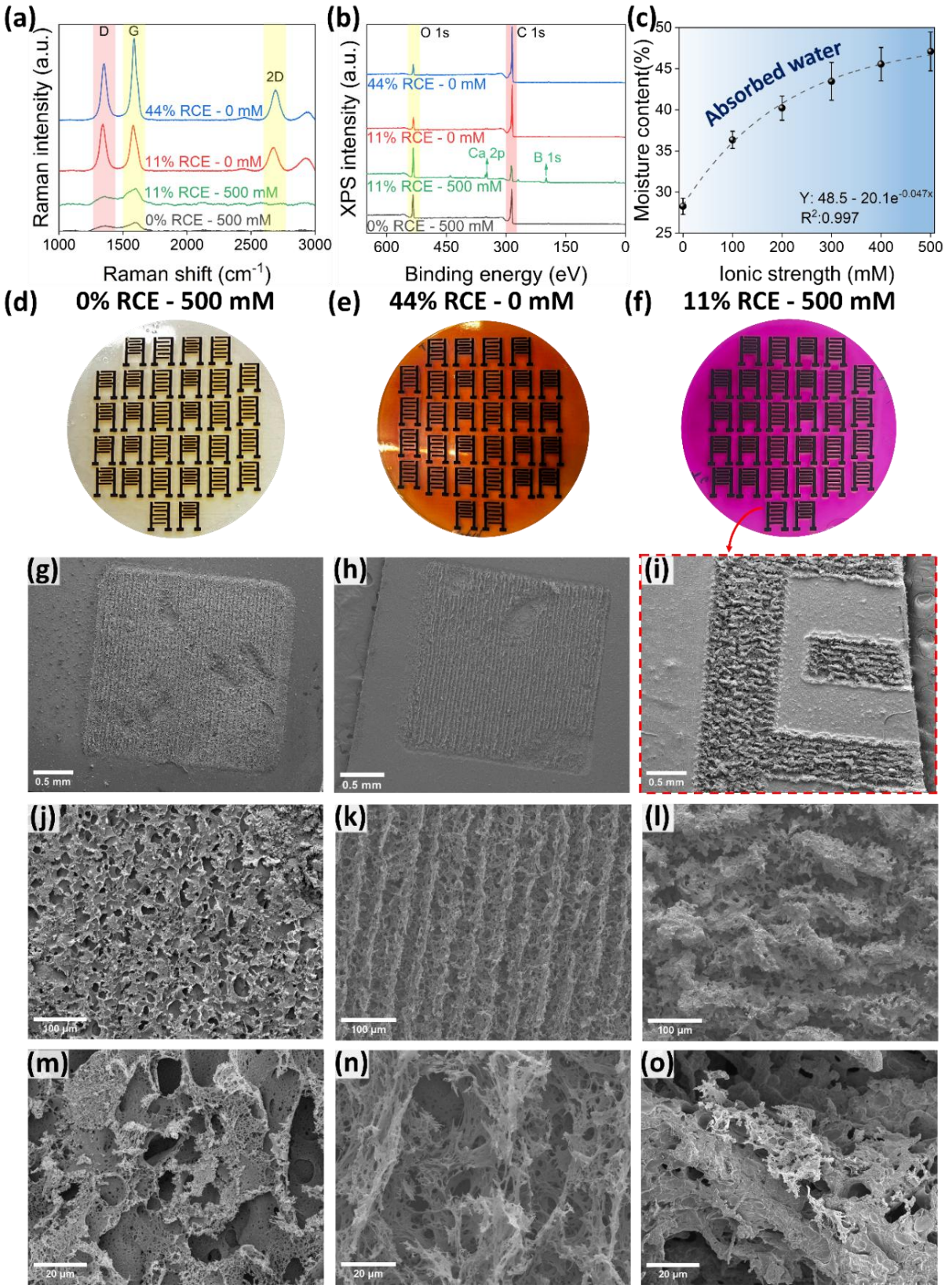


**Figure 4.3.** Structural, chemical, and morphological characterization of sensors with varying RCE contents and ionic strengths. (a) Raman spectra and (b) XPS profiles of chitosan-based films with 0% RCE at 500 mM IS (black line), 11% RCE at 500 mM IS (green line), 11% RCE at 0 mM IS (red line), and 44% RCE at 0 mM IS (blue line). (c)

Moisture content of sensors with 11% RCE as a function of IS. Digital photographs of sensors showing interdigitated electrode (IDE) configurations with short gap and longer gap between fingers: (d) 0% RCE at 500 mM IS, (e) 44% RCE at 0 mM IS, and (f) 11% RCE at 500 mM IS. SEM images of sensors at magnifications of ×30, ×200, and ×1000 (scale bars: 500, 100, and 20 μm, respectively) with: (g, j, m) 0% RCE at 500 mM IS; (h, k, n) 44% RCE at 0 mM IS; and (i, l, o) 11% RCE at 500 mM IS, respectively.

In contrast, laser scribing on dried films produced an improved $I_D/I_G$ ratio of 1.01, though the 2D band remained weak, confirming that water evaporation during scribing disrupts structural continuity and limits $sp^2$ domain formation. When RCE was introduced (11% RCE, 500 mM IS), the G-band intensity increased, although it remained merged with the D-band, and no 2D band emerged, again suggesting incomplete graphitization. These results support our hypothesis that $Ca^{2+}$-induced moisture retention interferes with carbon rearrangement during photothermal processing, yielding disordered, low-conductivity carbon networks.

The mechanistic origin of this contrast is illustrated in **Figure 4.4**. In the hydrated state, the strong hygroscopicity of $Ca^{2+}$ leads to the formation of extensive hydration shells (~6 $H_2O$ molecules), which generate localized vapor microbursts under $CO_2$ laser irradiation. These transient pressure spikes disrupt the evolving carbon lattice, introducing structural disorder and defects. Conversely, in the dried state, the absence of excess hydration suppresses vapor microbursts, allowing more controlled thermal rearrangement and facilitating the nucleation and growth of extended $sp^2$-hybridized domains. Thus, minimizing hydration is essential strategy to achieve high-quality LIG with improved carbon ordering, complementing the role of molecular sensitizers such as anthocyanins in driving efficient energy-saving graphitization.

$Ca^{2+}$-mediated hydration on LIG graphitization effect is further corroborated by the positive correlation between IS and moisture content **(Figure 4.3c)**, confirming that increased $Ca^{2+}$ loading enhances water uptake within the chitosan matrix. The resulting elevated moisture likely acts as a thermal sink and generates localized vapor microbursts during laser scribing, both of which disrupt $sp^2$ domain formation. These disruptions explain the diminished graphitization quality, increased sheet resistance, and greater structural disorder observed in $Ca^{2+}$-rich formulations. Nevertheless, the hygroscopic nature of $Ca^{2+}$ also plasticizes the chitosan matrix, conferring flexibility to the sensor, making the trade-off worthwhile and justifying its inclusion, as discussed in later sections.

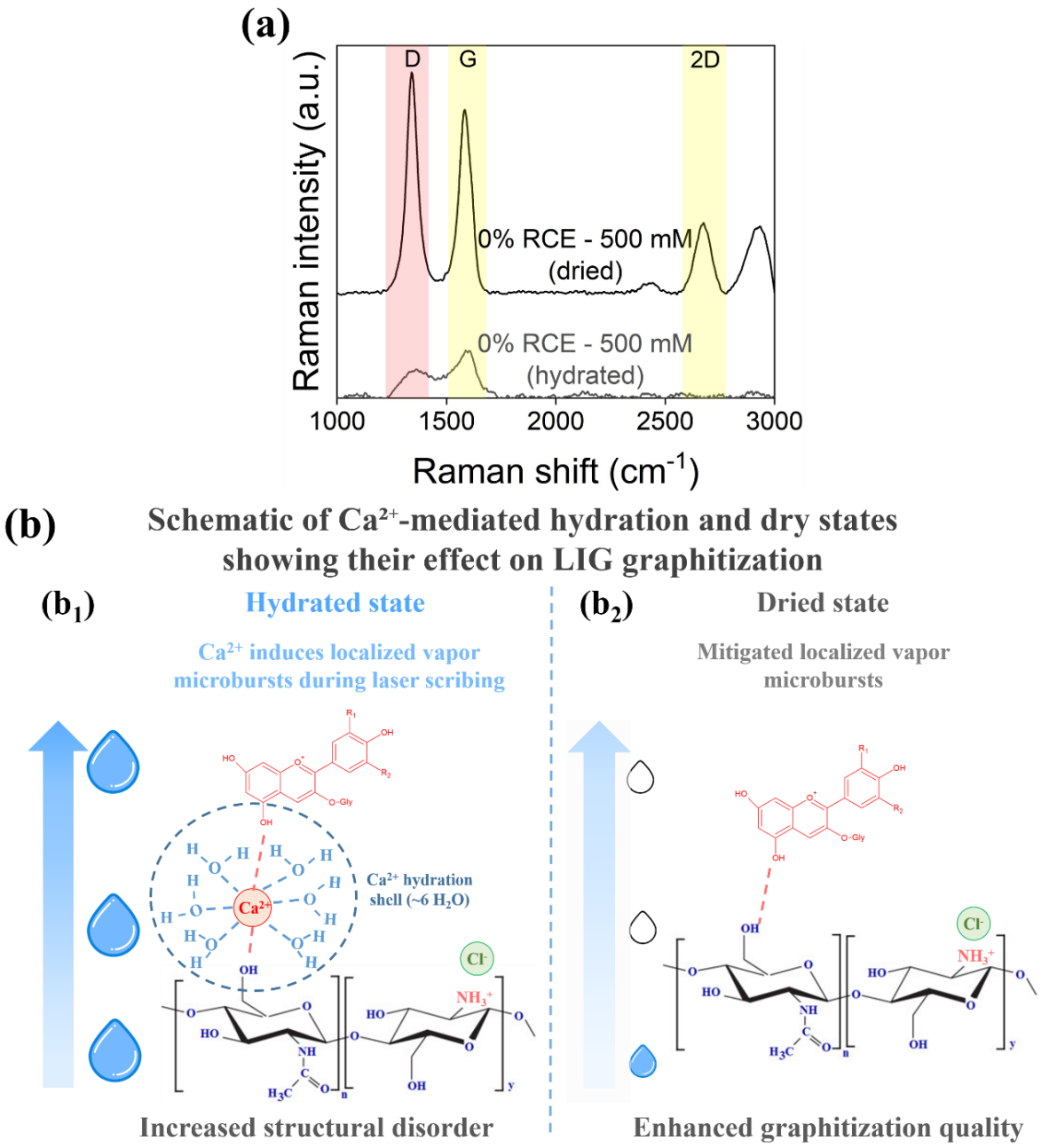


**Figure 4.4** Raman spectra and effect of $Ca^{2+}$-mediated hydration on LIG graphitization. (a) Raman spectra of chitosan films (0% RCE, 500 mM IS) under hydrated and dried conditions, highlighting differences in D, G, and 2D bands. (b) Schematic illustration of $Ca^{2+}$-mediated hydration versus dry states. ($b_1$) In the hydrated state, $Ca^{2+}$ hygroscopicity induces localized vapor microbursts during laser scribing, leading to increased structural disorder. ($b_2$) In the dried state, reduced hydration mitigates vapor microbursts, resulting in enhanced graphitization quality.

In contrast, in the absence of added salt, the 11% RCE-0 mM IS formulation exhibited sharper D and G peaks along with an emerging 2D band, indicative of partial graphitization and improved carbon ordering. Notably, the anthocyanin-rich formulation (44% RCE, 0 mM

IS) yielded the highest graphitization quality, which exhibited the lowest $I_D/I_G$ ratio (0.87), a pronounced 2D band ($I_{2D}/I_G$: 0.35), and the lowest sheet resistance (48 $\Omega \cdot sq^{-1}$). These improvements are corroborated by crystallite domain sizes ($L_a$), which increased from 16.9 (5.5% RCE) to 22.1 nm (44% RCE), evidencing reduced disorder and expansion of $sp^2$ domains.

The enhanced graphitization of anthocyanin-rich films can be attributed to their aromatic and π-conjugated structures, which undergo distinct chemical transformations under $CO_2$ laser irradiation. As with lignin and other aromatic precursors, localized photothermal excitation cleaves labile O-H, C-O, and C-H bonds, releasing volatile products ($H_2O$, CO, $CO_2$) and leaving radical sites that reorganize into extended $sp^2$ domains. The unsaturated C=C bonds of anthocyanins act as energy-absorbing sites, delocalizing incoming laser energy and lowering the barrier for carbon reorganization **(Figure 4.5)**. We propose that the π-conjugated anthocyanin rings act as molecular scaffolds, directing carbon rearrangement and stabilizing graphene-like nuclei, thereby accelerating $sp^2$-carbon network formation through energy-saving localized photothermal conversion.

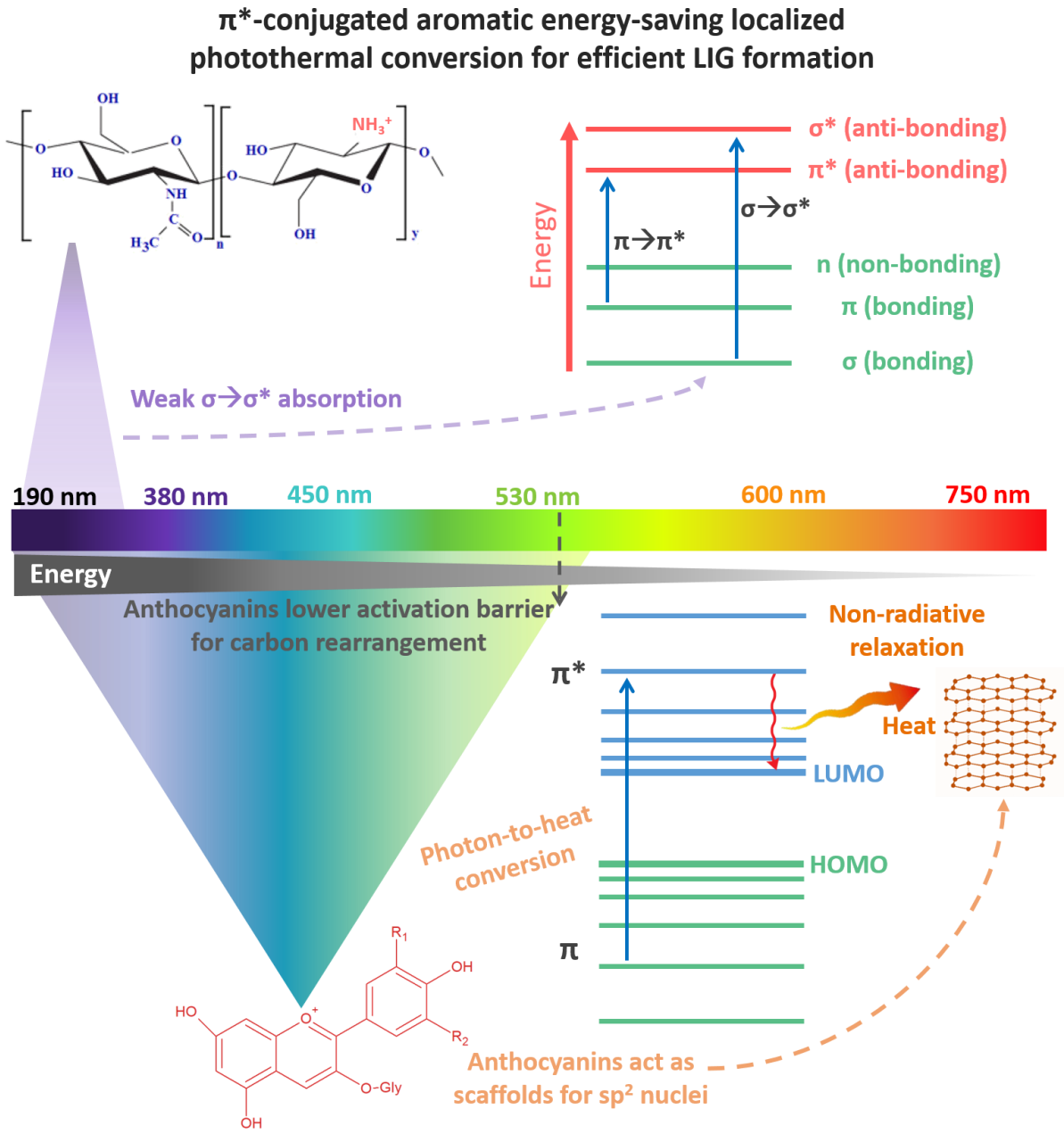


**Figure 4.5.** Mechanistic role of anthocyanins in energy-saving for LIG synthesis and $NH_3$ sensing. (a) π-Conjugated anthocyanins act as photothermal sensitizers during laser scribing: efficient π→π* absorption and non-radiative relaxation concentrate photon energy into localized hotspots, lowering the activation barrier for carbon rearrangement. This energy-saving localized photothermal conversion promotes volatile release (e.g., $H_2O$, CO, $CO_2$), $sp^2$ nucleation, and the stabilization of graphene-like domains, thereby enabling high-quality, functional LIG formation.

This mechanism aligns with the observed Raman signatures, i.e., progressive decreases in $I_D/I_G$ ratio, expansion of crystallite sizes ($L_a$), and the emergence of a pronounced 2D band,

all of which indicate reduced disorder and improved carbon ordering **(Table 4.2)**. By leveraging the π-conjugated rings of anthocyanins, we show that anthocyanins promote efficient graphitization while preserving redox-active centers within the carbon lattice, delivering a rare combination of conductivity and chemical responsiveness.

Equally important, the flavylium ⇄ quinonoid ⇄ chalcone interconversions preserve redox-active moieties even after partial graphitization, endowing the resulting smart LIG with both enhanced conductivity and intrinsic electrochemical responsiveness. Thus, anthocyanins fulfill a dual mechanistic role: (i) structural amplification, by lowering the energetic cost of graphitization via localized photothermal conversion; and (ii) chemical encoding, by retaining reactive π-conjugated centers that enable $NH_3$ redox transduction within the LIG lattice.

**Table 4.2.** Raman graphene index parameters and corresponding optimal sheet resistances.

| **Treatment (IS mM, RCE %)** | **$I_D/I_G$** | **$I_{2D}/I_G$** | **$L_a$ (nm)** | **Optimal sheet resistance ($\Omega \cdot sq^{-1}$)** |
|---|---|---|---|---|
| T1 (0, 11) | 1.04 (0.04) | 0.45 (0.02) | 18.5 (0.9) | 303 (36) |
| T6 (500, 11) | Amorphous carbon | | | 3000 (120) |
| T7 (0, 5.5) | 1.14 (0.05) | 0.49 (0.09) | 16.9 (0.6) | 363 (42) |
| T8 (0, 22) | 0.98 (0.01) | 0.39 (0.13) | 19.6 (0.2) | 243 (34) |
| T9 (500, 0) | Amorphous carbon | | | 921 (70) |
| T10 (0, 44) | 0.87 (0.02) | 0.35 (0.04) | 22.1 (0.5) | 48 (12) |

Data are reported as mean values with errors in parentheses (n = 3).

X-ray photoelectron spectroscopy **(Figure 4.3b)** provided complementary insights into surface chemistry and carbonization efficiency. The control sample lacking RCE but rich in $Ca^{2+}$ (0% RCE, 500 mM IS) showed weak C 1s and the strongest O 1s signals, indicating poor graphitization and an oxygen-dominated surface, likely arising from moisture-assisted oxidation. In contrast, LIG derived from the anthocyanin-rich formulation (44% RCE, 0 mM IS) showed the highest C 1s signal and a markedly reduced O 1s contribution, indicating more extensive graphitization and fewer oxygenated surface species. The intermediate formulation (11% RCE, 500 mM IS) presented a broadened O 1s peak and reduced C 1s intensity relative to the RCE-only sample, suggesting suppressed $sp^2$-domain development and increased dis-

order. These findings are consistent with the Raman results and further underscore the detrimental role of $Ca^{2+}$, as water retention during evaporation perturbs localized thermal gradients and compromises graphitic network formation.

Importantly, the detection of Ca 2p and B 1s peaks in the 11% RCE-500 mM IS sample confirms their incorporation into the LIG matrix, consistent with the formation of metalloanthocyanin-chitosan coordination complexes. This is further supported by a chemical shift in the C 1s core-level spectrum, from ~284.6 to ~287.0 eV (relative to the 11% RCE-0 mM IS sample), indicative of electron-withdrawing environments such as carbonyl or coordinated carboxyl groups.[524] The observed ~2.4 eV shift likely reflects $Ca^{2+}$ complexation with oxygen-containing sites in both anthocyanins and chitosan, lowering local electron density and increasing binding energy. While this crosslinking suppresses graphitization, it introduces pH-responsive chemical functionality within the LIG matrix, demonstrating a sensitivity-enhancing strategy for *in-situ* molecular tailoring of $NH_3$-selective electrodes.

Digital photographs revealed uniform and well-defined interdigitated electrode (IDE) structures, with sharp edges and darker scribed regions indicative of high graphitization, especially in films with higher anthocyanin content **(Figure 4.3d-f)**. SEM images further elucidated the structural effects of $Ca^{2+}$ and anthocyanins on LIG morphology **(Figure 4.3g-o)**. Films with high $Ca^{2+}$ loading (e.g., 0% RCE-500 mM IS) exhibited highly porous, cracked, and disordered surfaces, hallmarks of structural instability likely driven by moisture retention and vapor expansion during laser scribing **(Figure 4.3g, j, m, i, l, o)**. These morphological features support our hypothesis that $Ca^{2+}$-induced water retention impairs graphitization by destabilizing the matrix through water evaporation under thermal stress.

Conversely, the anthocyanin-rich film without $Ca^{2+}$ (44% RCE-0 mM IS) produced continuous LIG microstructures with well-aligned edges and enhanced interconnectivity between carbon domains **(Figure 4.3h, k, n)**. This morphology highlights the catalytic role of anthocyanins, via their $\pi$-conjugated aromatic structures, in promoting efficient graphitization, consistent with the lowest measured sheet resistance. By contrast, at 11% RCE with elevated $Ca^{2+}$ loading **(Figure 4.3o)**, the resulting LIG microstructure exhibited enhanced cohesion and a more integrated carbon-polymer interface. This is attributed to $Ca^{2+}$-mediated crosslinking between chitosan and anthocyanins, forming metalloanthocyanin complexes (copigmentation interactions) that stabilize the conductive network via coordination bonding **(Figure 4.6)**.[197,248]

$Ca^{2+}$ coordination establishes dynamic bridges between anthocyanins and chitosan, extending the color spectra while hydrated shells further enhance $NH_3$ sensitivity and sensor

flexibility. In the absence of $Ca^{2+}$, interactions are mainly restricted to hydrogen bonding, and without hydration layers, the matrix becomes rigid, leading to reduced sensitivity. These results highlight the crucial role of calcium ions as crosslinkers in governing the functional performance of smart LIG sensors. Crucially, this coordination network also introduces pH-responsive functionality to the LIG electrodes after laser scribing, enabling, to the best of our knowledge, the first demonstration of *in-situ* functionalization of LIG electrodes for selective tri-modal $NH_3$ sensing.

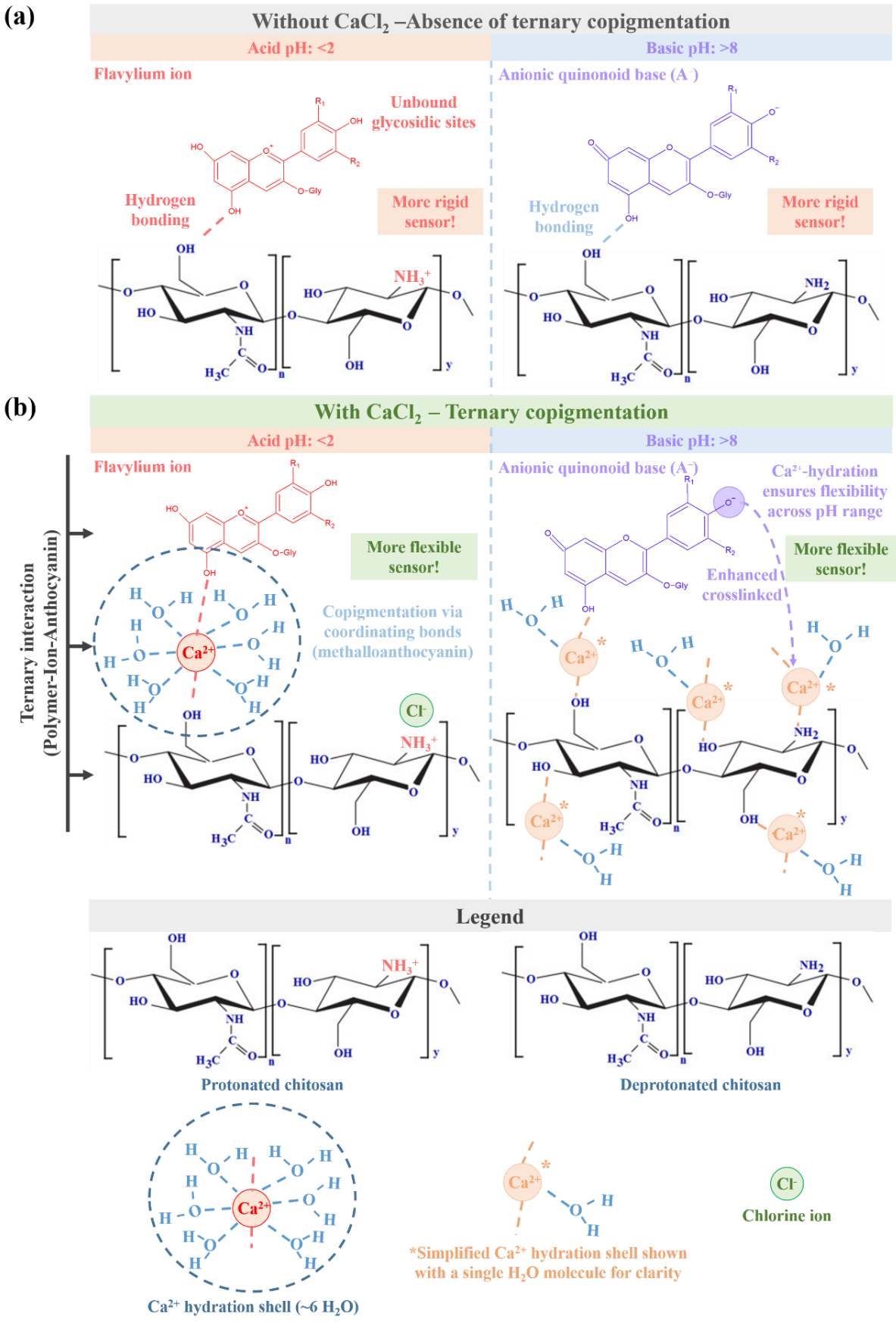
(a)
Without CaCl2 –Absence of ternary copigmentation
Acid pH: <2
Basic pH: >8
Flavylium ion
Anionic quinonoid base (A⁻)
Unbound glycosidic sites
Hydrogen bonding
More rigid sensor!
Hydrogen bonding
More rigid sensor!
(b)
With CaCl2 – Ternary copigmentation
Acid pH: <2
Basic pH: >8
Ternary interaction (Polymer-Ion-Anthocyanin)
Flavylium ion
Anionic quinonoid base (A⁻)
Ca²⁺-hydration ensures flexibility across pH range
More flexible sensor!
Copigmentation via coordinating bonds (methalloanthocyanin)
Enhanced crosslinked
More flexible sensor!
Legend
Protonated chitosan
Deprotonated chitosan
Ca²⁺ hydration shell (~6 H2O)
*Simplified Ca²⁺ hydration shell shown with a single H2O molecule for clarity
Chlorine ion

**Figure 4.6.** Proposed mechanism of anthocyanin-chitosan interactions in the absence and presence of $CaCl_2$. (a) Without $CaCl_2$: Under acidic conditions (pH < 2), flavylium cations interact only via hydrogen bonding with chitosan, leaving glycosidic sites unbound and yielding a rigid, unstable network. At basic pH (> 8), quinonoid bases exhibit minimal interaction with chitosan, further preventing network stabilization. Overall, ternary copigmentation is absent. (b) With $CaCl_2$: $Ca^{2+}$ mediate ternary copigmentation by bridging anthocyanins and chitosan, assisted by hydrated shells (~6 $H_2O$ molecules). At low pH, flavylium cations participate in copigmentation and $Ca^{2+}$ coordination, producing a more flexible and stabilized network. At high pH, quinonoid bases interact synergistically with $Ca^{2+}$, maintaining enhanced network flexibility and stability across environments. Legend: Structural states of chitosan (protonated vs deprotonated), $Ca^{2+}$ hydration shell (simplified to one $H_2O$ for clarity), and chloride counter-ions are illustrated.

### 4.3.4 Ionic Strength-Tunable Colorimetric Sensing for $NH_3$ Detection

Colorimetric sensing offers a rapid, intuitive, and equipment-free strategy for preliminary $NH_3$ screening as a marker of food spoilage. By allowing both consumers and industry stakeholders to visually assess quality degradation through direct observation or smartphone imaging, this approach eliminates invasive sampling and complex instrumentation. When integrated into packaging, smart LIG sensors can provide continuous monitoring across the cold-chain (from packaging to storage and refrigerated transport), supporting traceable, point-of-decision screening and reducing risks of fraud or improper handling **(Figure 4.7a)**.

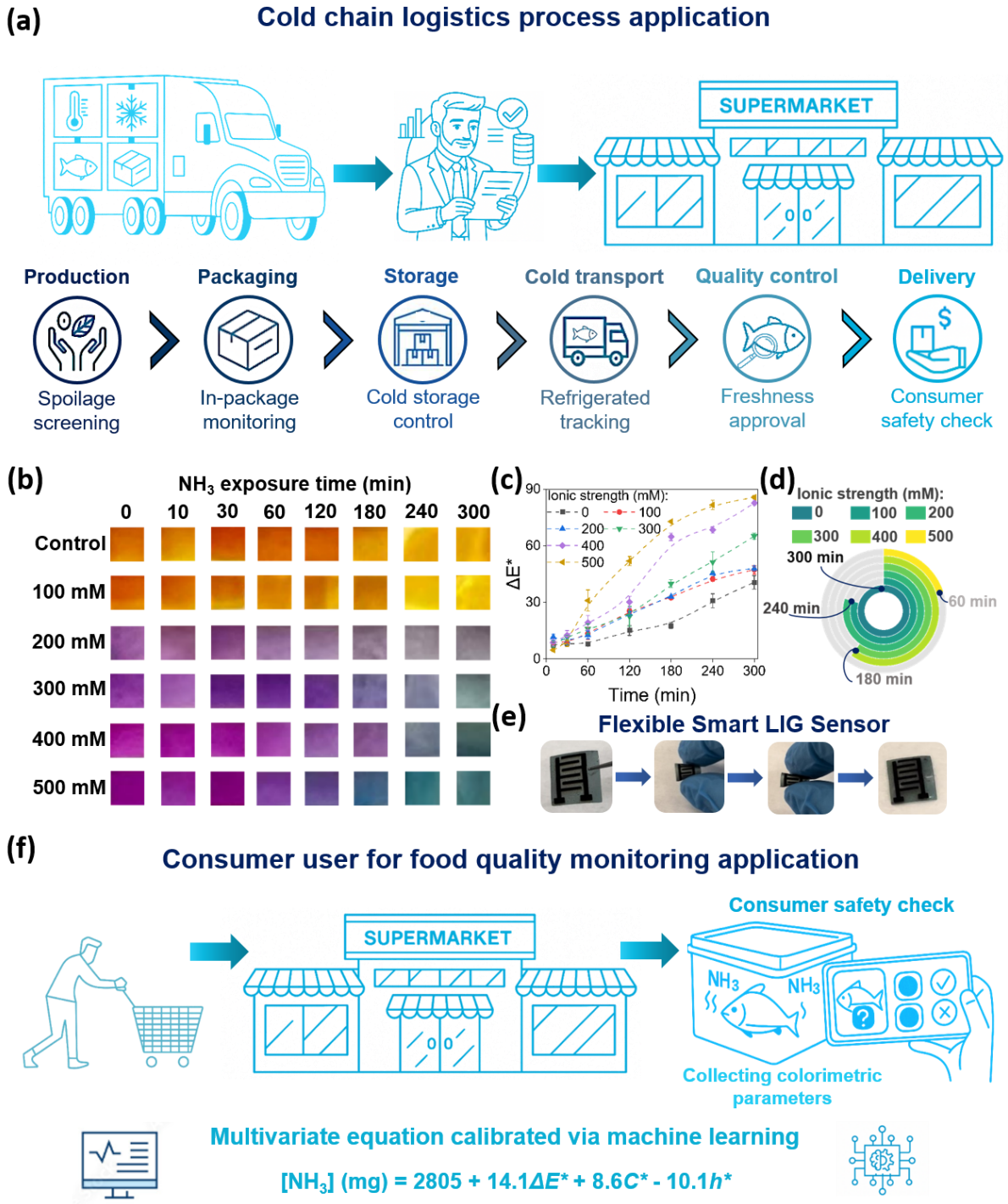


**Figure 4.7.** Illustration of smart LIG sensors for $NH_3$ detection applied to food quality monitoring. (a) Illustration of integration points in cold chain logistics: production (spoilage screening), packaging (in-package monitoring), storage (cold storage control), cold transport (refrigerated tracking), quality control (freshness approval), and delivery (consumer safety check). (b) Time-dependent colorimetric responses under varying ionic strengths (IS) upon $NH_3$ exposure, with digital images of the sensor at IS of 0 (control), 100, 200, 300, 400, and 500 mM across exposure times of 0-300 min. (c) Total color difference (ΔE*) as a function of IS (0-500 mM) and exposure time (0-300 min). (d) Perceptible response times for untrained users with increasing IS. (e) Digital photographs of the flexible smart

LIG sensor. (f) Illustration of a consumer-level application for *in-situ* food quality monitoring and safety verification prior to purchase.

This approach enables both consumers and industry stakeholders to visually assess potential quality degradation simply by capturing a photograph, eliminating the need for invasive sampling or complex instrumentation. When combined with calibrated colorimetric models correlating chromatic parameters (e.g., CIELAB, L*, a*, b*) to [$NH_3$] levels, users can quantify gas concentrations through smartphone imaging, enabling fast, non-destructive assessment of food freshness. This real-time, *in-situ* monitoring is especially critical at the consumer level, where smart LIG labels provide safety verification at the point of purchase by detecting early stages of protein degradation in packaged meat and seafood **(Figure 4.7f)**. This simple, reagent-free readout delivers actionable information to non-experts, reducing risks of foodborne illness and lowering associated public health costs.

Although numerous colorimetric indicators have been reported for $NH_3$ detection, many exhibit poor alignment with actual food spoilage timelines, triggering color changes either prematurely or after critical thresholds are exceeded. To address this, our previous work demonstrated a strategy to fine-tune $NH_3$ sensitivity by modulating the IS of the polymer matrix, enabling precise control over response behavior.[248] This approach enables customizable sensor performance based on specific food types, packaging volumes, storage conditions, and regulatory safety thresholds, offering a rational design pathway for colorimetric freshness indicators aligned with real-world needs.

However, practical deployment demands sensors with rapid response and sensitivity tailored to the specific $NH_3$ thresholds relevant to spoilage progression. Leveraging IS-tuned $NH_3$ sensitivity, we investigated the sensor's time- and IS-dependent color transitions **(Figure 4.7b)** to identify rapid visual responses and construct a predictive model correlating chromatic shifts with $NH_3$ concentration. In IS-free sensors (control), color gradually shifted from orange to bright yellow over 300 min of $NH_3$ exposure, with noticeable hue changes emerging only after ca. 240 min, suggesting delayed proton abstraction from anthocyanins. In contrast, sensors with ≥200 mM IS exhibited accelerated and intensified colour transitions, shifting from magenta/violet to blue-grey hues. At 500 mM IS, distinct chromatic changes appeared within the first 60 min, reaching greenish-blue tones by 300 min. This behavior indicates rapid deprotonation through salt-enhanced hydration and copigmentation. Furthermore, visual contrast quantified by total color difference ($\Delta E^*$) **(Figure 4.7c)** revealed a sharply accelerated chromatic evolution at 500 mM IS, with values rising nearly threefold faster than the control. This

wider chromatic response arises from copigmentation, as illustrated in **Figure 4.8**, whereas the rapid color change results from deprotonation facilitated by salt-enhanced hydration and subsequent hydrolysis, confirming enhanced $NH_3$ sensitivity.

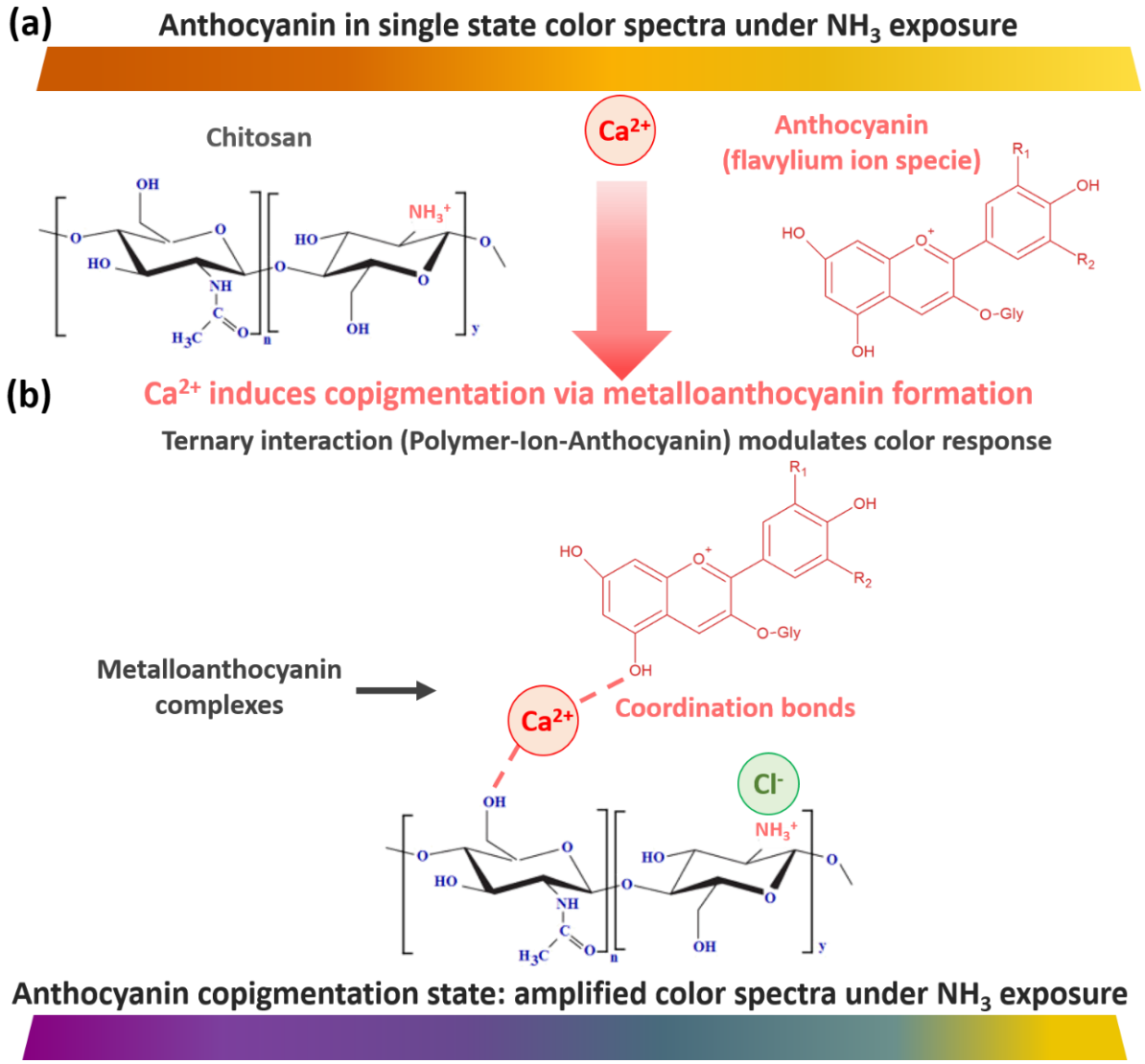


**Figure 4.8.** Mechanistic role of anthocyanins copigmentation in $NH_3$ colorimetric sensing. (a) In the absence of $Ca^{2+}$, anthocyanins (flavylium species) show limited spectral stability under $NH_3$ exposure. (b) $Ca^{2+}$ coordinates anthocyanins and chitosan to form metalloanthocyanin complexes, establishing a ternary polymer-ion-anthocyanin network that amplifies and stabilizes the color response.

As shown in **Figure 4.7d**, sensors formulated with 500 mM IS reached perceptible color changes ($\Delta E^* > 30$) within ~60 min, whereas IS-free sensors (control) required ~300 min. This marked acceleration demonstrates that IS tuning enables real-time spoilage recognition, crucial for logistics decisions. Beyond IS-tuned $NH_3$ sensitivity, we demonstrate that salt-enhanced hydration plasticizes the polymer matrix, conferring flexibility to the LIG electrodes

and preserving stable electrical performance under repeated twisting and bending **(Figure 4.7e)**. This mechanical resilience is essential for packaging integration, in contrast to brittle, rigid sensors that suffer conductive network disruption and functional degradation during handling and transport, thereby compromising $NH_3$ sensing.

The colorimetric response of the anthocyanin-based sensor to $NH_3$ was evaluated by tracking CIELAB coordinates as a function of exposure time and IS. The a* values, indicating red-green shifts, declined steadily under all IS conditions, reflecting flavylium cation ($AH^+$) depletion and conversion to chalcone or quinonoid species **(Figure 4.9a)**. This shift was most pronounced at ≥300 mM IS, where a* values turned negative, confirming accelerated chromatic transitions driven by salt-enhanced hydration and subsequent hydrolysis.

The b* heatmap **(Figure 4.9b)** illustrates blue-yellow transitions, with minimal yellowing over time at low IS levels (0-100 mM). In contrast, sensors with ≥300 mM IS showed an early drop in b*, stabilizing in the negative range, consistent with a shift toward blue-green hues due to chalcone formation. The h° evolution further reinforced this trend **(Figure 4.9c)**. Low-IS sensors remained within the orange-yellow range (h° ca. 40-80°), while high-IS formulations exhibited a continuous decrease in h° (from ca. 350° to ca. 180-240°), reaching greenish-blue tones after 300 min of $NH_3$ exposure, consistent with anthocyanin structural transitions under alkaline conditions. This IS-induced enhancement in sensitivity and response speed is attributed to water-mediated plasticization of the chitosan matrix by hygroscopic $Ca^{2+}$ ions, which facilitates flavylium hydration, proton transfer, and $NH_3$ diffusion. These findings demonstrate that sensor responsiveness can be systematically tuned by modulating IS, enabling sensitivity and dynamic range optimizations for real-time detection of alkaline volatiles in food spoilage.

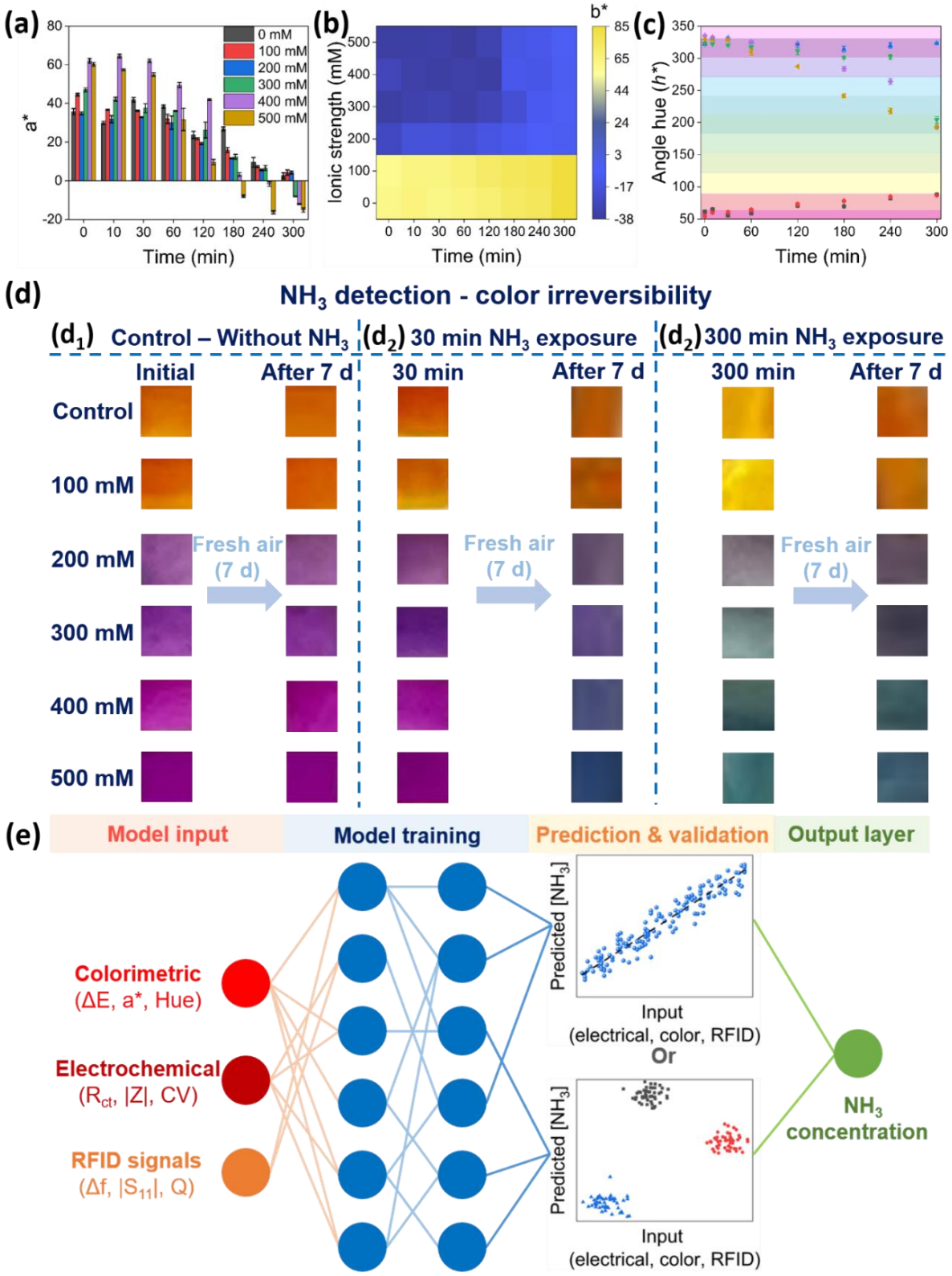


**Figure 4.9.** Colorimetric response and irreversibility of the smart LIG sensor under varying ionic strengths (IS) during $NH_3$ exposure and its integration with machine learning for concentration prediction. (a) Time-dependent changes in the a* coordinate for samples with IS from 0 to 500 mM. (b) Heatmap of the b* coordinate as a function of IS (0-500 mM) and exposure time (0-300 min). (c) Hue angle (h°) as a function of exposure time (0-300 min) and IS (0-500 mM). (d) Digital images of the sensors: ($d_1$) at the beginning and after 7 d of storage under light in an $NH_3$-

free environment; ($d_2$) after 30 min exposure to $NH_3$ followed by 7 d storage under light in an $NH_3$-free environment; and ($d_3$) after 300 min exposure to $NH_3$ followed by 7 d storage under light in an $NH_3$-free environment, showing the most significant irreversible color change for high IS (≥400 mM) after $NH_3$ detection. (e) Machine learning-assisted multimodal sensing workflow. Model input: colorimetric (ΔE*, a*, h°), electrochemical ($R_{ct}$, |Z|, CV), and RFID-derived (Δf, $|S_{11}|$, Q) features. Model training: an artificial neural network extracts nonlinear correlations between multimodal inputs and $NH_3$ exposure. Prediction & validation: regression and classification schemes yield accurate concentration estimates. Output layer: unified optical, electrical, and wireless readouts provide quantitative $NH_3$ concentration for real-time food quality monitoring. Color coding in (a) also applies to (c).

The reversibility of the halochromic response was evaluated by storing samples in $NH_3$-free environments post-exposure **(Figure 4.9d)**. Control and low-IS (0-100 mM) sensors exhibited substantial color recovery after 7 d, reverting to their original orange tones regardless of short (30 min) **(Figure 4.9$_{d1}$)** or prolonged $NH_3$ exposure (300 min) **(Figure 4.9$_{d2}$)**. In contrast, sensors with ≥300 mM IS displayed largely irreversible transitions, particularly after 300 min of $NH_3$ exposure **(Figure 4.9$_{d3}$)**, retaining grayish or bluish hues. This behavior suggests a permanent structural rearrangement of anthocyanin, likely due to the formation of stable chalcone via aromatic ring opening, facilitated by salt-induced matrix plasticization and hydrolytic attack. Collectively, these results demonstrate that IS not only modulates the rate and extent of $NH_3$-triggered color change, but also governs reversibility, enabling tunable design for reversible or permanent sensing depending on application needs. To exemplify, irreversibility may prevent fraud, whereas reversibility enables real-time tracking.

To advance the accuracy of intelligent packaging for $NH_3$ detection, we developed a machine learning-assisted prediction framework that integrates multimodal outputs from smart LIG sensors. By combining complementary colorimetric inputs (ΔE*, a*, b*, C*, h°), the model captures subtle correlations that cannot be resolved using single-signal approaches **(Figure 4.9e)**. During machine learning-driven training, the regression framework learns to recognize fine variations encoding spoilage dynamics, thereby translating optical features into accurate $NH_3$ concentrations. To minimize redundancy and multicollinearity, only statistically significant parameters ($p < 0.05$) were retained through forward stepwise selection, with h° identified as the dominant predictor ($p < 0.001$).[525,526]

The resulting multivariate model demonstrates excellent predictive accuracy ($R^2 = 0.988$, $R^2_{adj} = 0.987$, $R^2_{pred} = 0.984$) **(Table 4.3)**, confirming robust agreement between predicted and experimental concentrations with minimal overfitting. The multivariate regression model was optimized through a machine learning-assisted, forward stepwise selection procedure, which

demonstrated strong predictive power for $NH_3$ quantification. All available colorimetric descriptors (L*, a*, b*, ΔE*, C*, h*) were initially screened, but only statistically significant predictors were retained to maximize model performance while avoiding redundancy. Stepwise selection is a critical process in multivariate analysis, as it reduces the inclusion of collinear or irrelevant variables, thereby improving generalizability and preventing model overfitting. In this case, ΔE*, C*, and h° were identified as the most relevant parameters for predicting $NH_3$ concentrations, yielding high coefficients of determination ($R^2$ = 0.988, $R^2_{adj}$ = 0.987, $R^2_{pred}$ = 0.984) and confirming excellent agreement between predicted and experimental data.

**Table 4.3.** Machine learning–assisted multivariate regression model for $NH_3$ quantification using colorimetric parameters of the optimized sensor (11% RCE – 500 mM IS).

| Multivariate model[a] | p-valor* | | | | $R^2$ | $R_{aj}^2$ | $R_{pred}^2$ |
|---|---|---|---|---|---|---|---|
| | $\beta_{\Delta E^*}$ | $\beta_{C^*}$ | $\beta_{h^*}$ | Model | | | |
| $NH_3$ (mg) = 2805 + 14.1$\Delta E^*$ + 8.6$C^*$ - 10.1$h°$ | 0.08 | 0.142 | <0.001 | <0.001 | 0.988 | 0.987 | 0.984 |

[a]The values obtained for the model construction are means of four repetitions.

Statistical evaluation of the regression coefficients revealed that h° was the most significant variable ($p < 0.001$), consistent with its sensitivity to hue shifts induced by $NH_3$ release. By contrast, ΔE* ($p = 0.08$) and C* ($p = 0.142$) contributed less strongly, though their inclusion improved overall predictive accuracy. These results demonstrate that while general color intensity changes are relevant, the hue angle remains the most critical descriptor for detecting spoilage-related chemical transformations.

The diagnostic plots in **Figure 4.10** further confirm the adequacy of the regression model. The normal probability plot **(Figure 4.10a)** shows that residuals follow a normal distribution, while the residuals versus order plot **(Figure 4.10b)** indicates random scatter, supporting the absence of systematic bias. Model significance testing **(Figure 4.10c)** confirmed a highly significant regression ($p < 0.001$), and the explained variance plot **(Figure 4.10d)** shows that 98.7% of the variability in $NH_3$ concentration is captured by the model. Finally, scatterplots of $NH_3$ concentration against individual predictors **(Figure 4.10e)** reveal strong linear trends for ΔE*, C*, and h°, consistent with their inclusion in the regression.

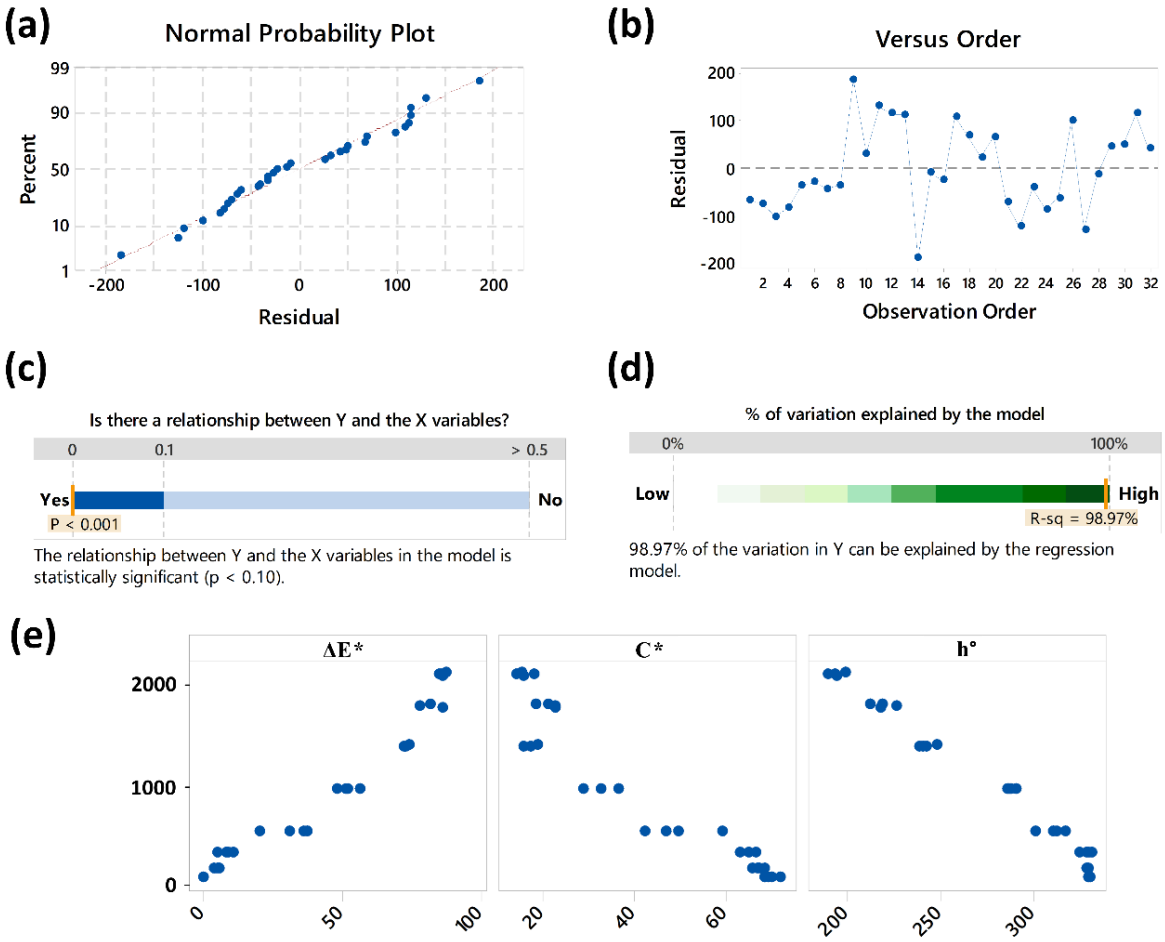


**Figure 4.10.** Statistic evaluation and predictor analysis of the machine learning–assisted multivariate regression model for $NH_3$ prediction: (a) normal probability plot of residuals; (b) residuals versus observation order; (c) model significance test; (d) explained variation; and (e) relationships of $NH_3$ concentration with ΔE, C*, and h° parameters.

Based on the validation of the regression statistical parameters, we reveal that among the descriptors, hue angle (h°) is the dominant factor ($p < 0.001$), while ΔE* ($p = 0.08$) and C* ($p = 0.142$) contribute less significantly. This indicates that chromatic shifts are the primary markers of $NH_3$-induced color changes. The optimized, data-calibrated learning model is expressed in Equation 4.9.

$$NH_3\ (mg) = 2805 + 14.1\Delta E^* + 8.6C^* - 10.1h° \quad (4.9)$$

This equation represents a machine learning-assisted, data-calibrated learning approach that bridges colorimetric outputs, readily acquired through simple photographs, with quantitative $NH_3$ determination for non-invasive and real-time monitoring. Together, these results validate the machine learning–assisted regression framework as a robust and reproducible method for converting colorimetric responses into quantitative $NH_3$ concentrations, thereby

enabling non-invasive, real-time food quality monitoring and highlighting the critical role of variable selection in predictive multivariate models.

Nevertheless, this prediction can be further refined by incorporating independent and uncorrelated variables such as electrochemical ($R_{ct}$, |Z|, CV) and RFID-derived (Δf, $|S_{11}|$, Q) features. This multimodal integration reduces false positives from individual modalities and refines the predictive models through complementary information, thereby enabling more accurate $NH_3$ detection. The following sections provide a detailed characterization of these outputs, laying the groundwork for their integration into the predictive framework.

### 4.3.5 Electrochemical and impedance response of $NH_3$-responsive LIG sensors

To push the boundaries of smart packaging, we report for the first flexible tri-modal LIG-based sensors delivering $NH_3$ detection via anthocyanin-enabled electrochemical transduction. The $NH_3$-responsiveness LIG electrode arises from strategic coordination crosslinking between the redox-active anthocyanins and chitosan using $Ca^{2+}$, as illustrated in **Figure 4.6**. This ternary interaction, commonly referred to as copigmentation,[197,248,514] facilitates the formation of a highly sensitive, conductive LIG network after laser scribing, wherein anthocyanins serve both as molecular dopants that promote high-quality graphene-like synthesis and as reactive sites for $NH_3$ detection.

While individual hydroxyl-$Ca^{2+}$ interactions are relatively weak, their cumulative effect reaches stable coordination through cooperative binding, enhancing charge transport across the graphene-polymer matrix interface. Additionally, the hygroscopic nature of $Ca^{2+}$ generates a hydration shell (6-8 water molecules), which plasticizes the chitosan matrix, thereby improving mechanical flexibility and fracture toughness. $Ca^{2+}$ thus plays a critical dual role, mechanically stabilizing the LIG structure and physically anchoring anthocyanins, both of which are essential for robust $NH_3$ responsiveness. In the absence of $Ca^{2+}$ (e.g., T1 formulation), the electrodes displayed evident delamination, brittleness, and compromised electrical integrity, resulting in reduced $NH_3$ sensitivity and functional performance.

To assess the electrochemical performance of the $NH_3$-responsive smart LIG sensors, cyclic voltammetry (CV) was conducted using long- (L-IDE, 1 mm) and short-gap (S-IDE, 0.5 mm) interdigitated electrodes **(Figure 4.11a,b)**. CV curves showed increasing current with prolonged $NH_3$ exposure, attributed to the progressive conversion of anthocyanins into more electroactive species, such as chalcones. Scan rate-dependent CV **(Figure 4.11c)** revealed that

the current response scales sub-linearly with the scan rate, after short-term $NH_3$ exposure (30 min), with a fitted power-law exponent b = 0.32. This behavior indicates that the charge storage is predominantly diffusion-controlled rather than surface-capacitive, reflecting the slow kinetics and transport limitations associated with anthocyanin transformation and electron transfer within the LIG matrix.

To elucidate the electroactive contribution of anthocyanins to $NH_3$ sensing, CV was performed after 300 min of $NH_3$ exposure using sensors with and without RCE (11% vs 0%) in both L-IDE and S-IDE configurations **(Figure 4.11d)**. Among these, the S-IDE sensor with 11% RCE exhibited the highest oxidation current and a well-defined oxidation peak, attributed to anthocyanin redox transitions under applied potential. This oxidation feature emerged sharply after 180 min in the S-IDE, whereas it appeared later and less prominently (at 240 min) in the L-IDE. The improved response is attributed to the shorter electrode spacing in the S-IDE, which amplifies the local electric field and facilitates more efficient charge carrier mobility. The enhanced $NH_3$ sensitivity of the S-IDE is further corroborated by its greater transferred charge (Q) over time **(Figure 4.11f)**, confirming superior electrochemical responsiveness.

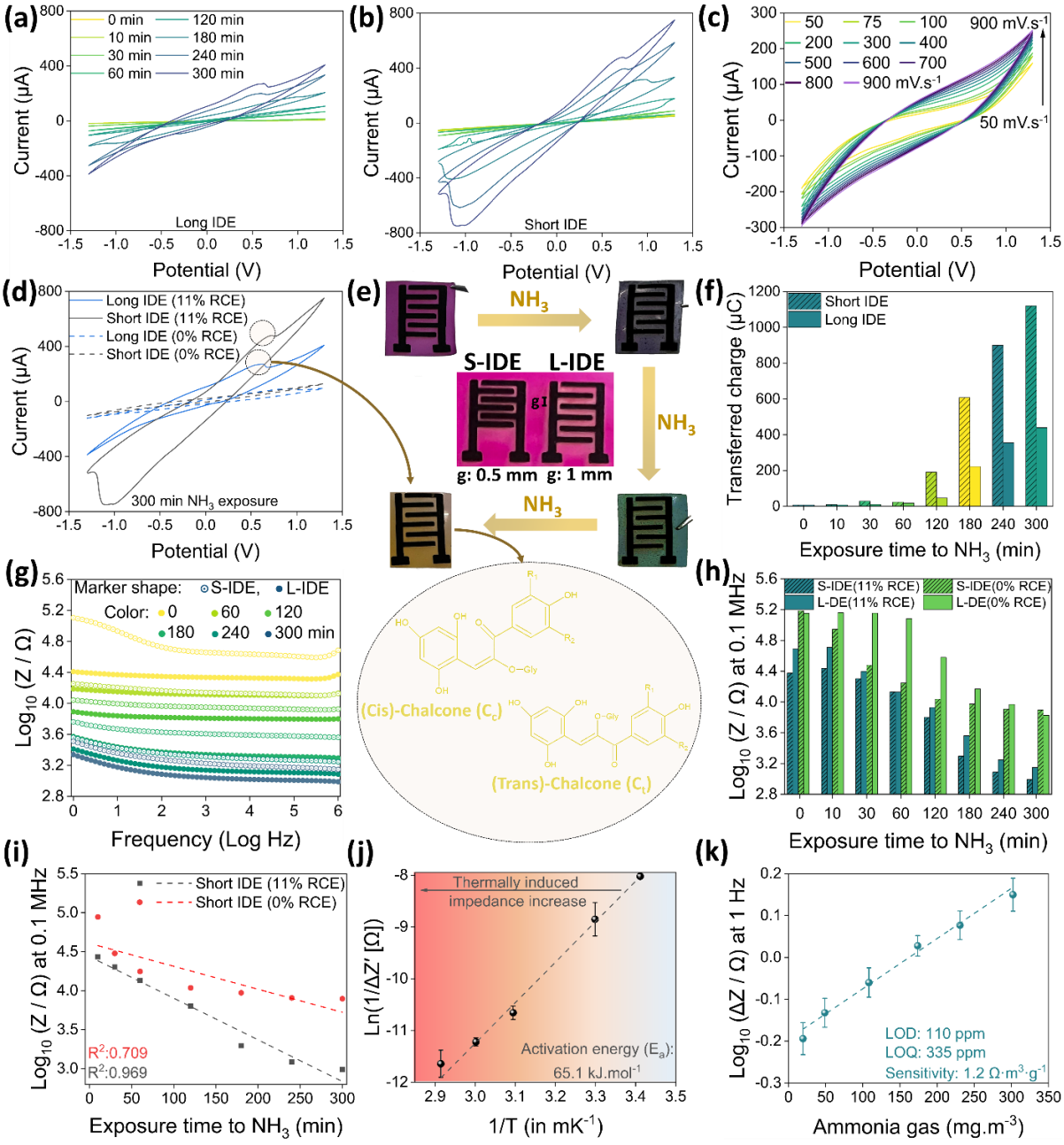


**Figure 4.11.** Electrochemical and impedance characterization of sensors with laser-induced graphene (LIG) interdigitated electrodes (IDEs) under $NH_3$ exposure. (a,b) Cyclic voltammetry (CV) responses of sensors with long- (L-IDE, g = 1 mm) and short-gap IDE (S-IDE, g = 0.5 mm), respectively, at different $NH_3$ exposure times (0-300 min). (c) CV curves at varying scan rates (50-900 $mV \cdot s^{-1}$) for the sensor with 11% red cabbage extract (RCE) and short-gap IDE after 30 min $NH_3$ exposure. (d) Comparative CV responses after 300 min $NH_3$ exposure for sensors with short and long-gap IDEs and with 0% and 11% RCE content, with the oxidation peak highlighted. (e) Schematic illustration of S-IDE and L-IDE designs and associated color change after $NH_3$ exposure, indicating chalcone species formation following the equilibrium shift to an irreversible state under prolonged $NH_3$ exposure. (f) Transferred charge (Q) as a function of $NH_3$ exposure time for short- and long-gap IDEs (11% RCE-500 mM IS). (g) Bode plot impedance spectra showing |Z| over a frequency range (0.1 Hz to 1 MHz) at various $NH_3$ exposure times for sensors with short and long-gap IDEs (11% RCE-500 mM IS). (h) Logarithmic impedance response at 0.1 MHz as a

function of $NH_3$ exposure time for sensors with short- and long-gap IDEs (11% RCE-500 mM IS). (i) Impedance magnitude at 0.1 MHz *versus* $NH_3$ exposure time for S-IDEs with 11% and 0% RCE, both at 500 mM IS. (j) Arrhenius plot of impedance response for ΔZ (initial Z - final Z) for the sensor with S-IDE (11% RCE-500 mM IS), showing thermally induced impedance increase and activation energy ($E_a$ = 65.1 kJ·mol$^{-1}$) when exposure to $NH_3$ for 300 min. (k) Calibration curve of impedance response for ΔZ (initial Z - final Z) at 1 Hz across $NH_3$ concentrations (15 min exposure) sensor with S-IDE (11% RCE-500 mM IS), showing limit of detection (LOD = 110 ppm), limit of quantification (LOQ = 335 ppm), and sensitivity (1.2 Ω·m$^3$·mg$^{-1}$). Color coding in (a) also applies to (b).

The role of anthocyanins in enabling $NH_3$-responsive electroactivity is confirmed by three key features observed in RCE-containing sensors compared to the RCE-free control: (i) increased current response, (ii) expanded CV area, and (iii) the emergence of oxidation peaks, together indicating enhanced charge transfer and redox activity. These effects stem from proton-coupled electron transfer and the pH-induced transformation of anthocyanin species into electroactive chalcone under alkaline $NH_3$ exposure **(Figure 4.11e)**, which correlates with the characteristic pink-to-yellow color transition. $NH_3$ responsiveness is markedly amplified by RCE incorporation, with transferred charge increasing by 22,000% compared to RCE-free controls, underscoring the central role of electroactive anthocyanin-mediated redox pathways of the smart LIG sensor **(Figure 4.12a,b)**.

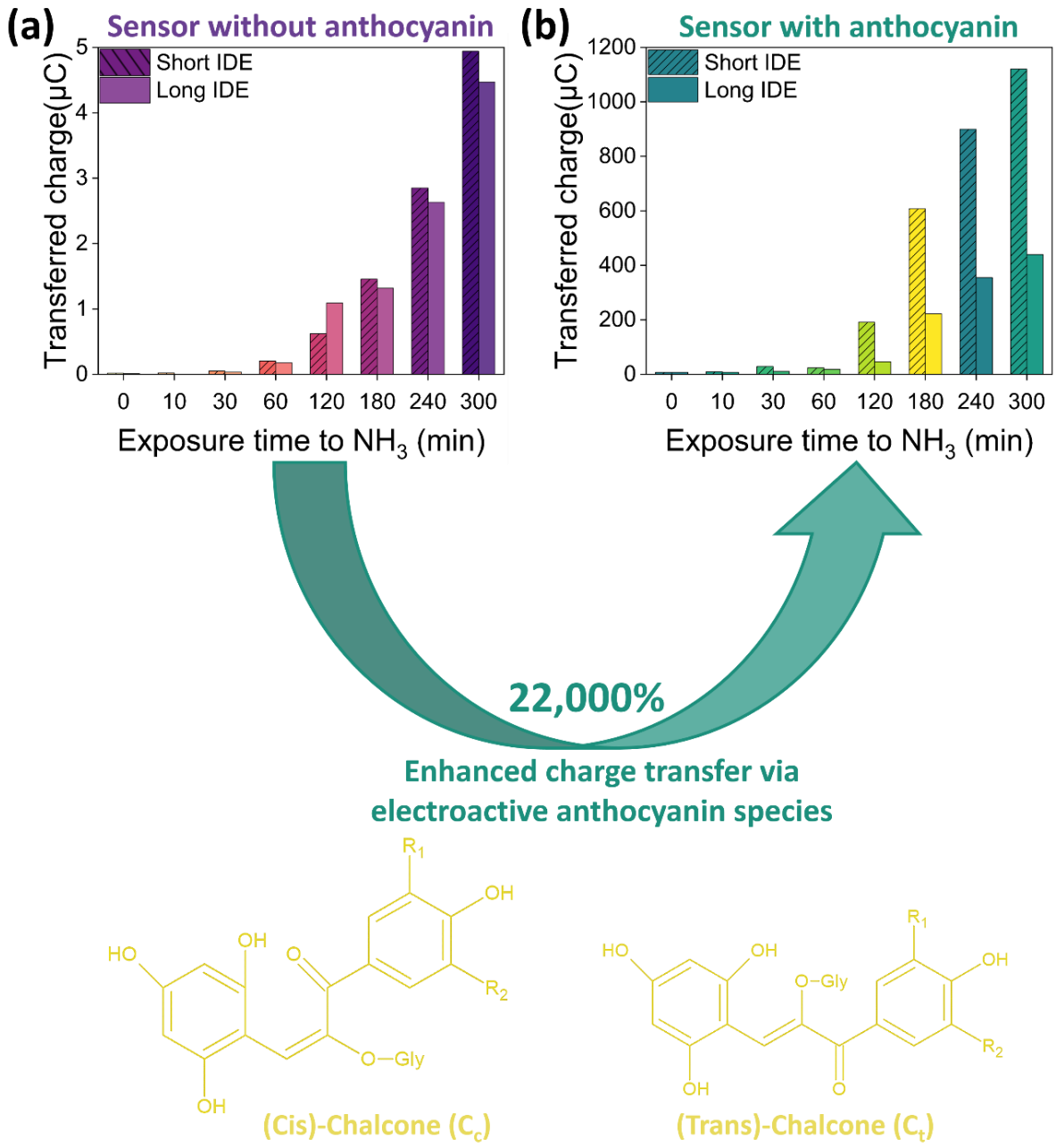


**Figure 4.12.** Charge transfer in $NH_3$-responsive LIG sensors (a) without and (b) with anthocyanins. Incorporation of anthocyanins leads to a 22,000% enhancement in transferred charge, attributed to electroactive chalcone species (cis- and trans-isomers).

This charge-transfer enhancement upon anthocyanin incorporation is attributed to the $NH_3$-induced deprotonation and tautomerization of anthocyanins into cis/trans chalcone forms, which act as redox-active species within the LIG–chitosan framework. These chalcones

facilitate proton-coupled electron transfer, thereby reducing interfacial resistance and enabling diffusion-limited faradaic processes, consistent with the power-law relationship between current and scan rate. Both short- and long-gap IDEs exhibit this behavior, with the short-gap (S-IDE) generating higher charge densities due to stronger electric field intensity, confirming that electroactive anthocyanin-derived species dominate the response and effectively transform the LIG into a highly sensitive smart sensor.

Unlike CV, impedance spectroscopy detects subtle shifts in the sensor's electrochemical environment (e.g., proton mobility), offering frequency-resolved insights into bulk resistance, interfacial charge transfer, and capacitance. These properties are especially relevant for passive RFID applications, where dielectric and interfacial behavior directly impact antenna performance. As shown in **Figure 4.11g**, impedance magnitude (|Z|) consistently decreased across the frequency spectrum with longer $NH_3$ exposure, with S-IDE devices displaying greater sensitivity than L-IDE. The most pronounced reduction occurred at 0.1 MHz, where the S-IDE with 11% RCE exhibited a marked |Z| drop **(Figure 4.11h)**, indicating enhanced ionic conductivity and charge mobility under $NH_3$-rich conditions. This mid-frequency regime is especially responsive to dielectric and interfacial changes, as it is less influenced by slower diffusion effects while still capturing ion transport and polarization dynamics. These findings suggest that $NH_3$ exposure alters the local electrochemical environment, e.g., by increasing matrix hydration and modifying the dielectric constant. Together with chalcone formation, this promotes faster ion transport and contributes to reduced impedance at mid-to-high frequencies.

Based on the superior electrochemical performance of the S-IDE configuration, the figure of merit analysis focused on this optimized design. RCE-containing sensors exhibited a broader impedance response range ($Log_{10}$ 4.5 to $Log_{10}$ 3.0 Ω) and higher linearity ($R^2$= 0.97 *vs* 0.70) under $NH_3$ exposure compared to the control ($Log_{10}$ 5.0 to $Log_{10}$ 4.2 Ω), as shown in **Figure 4.11i**. To gain further insight into the underlying charge transport mechanism, an Arrhenius analysis was performed to distinguish thermally activated ionic conduction from non-thermally driven processes such as interfacial capacitance or diffusion-limited behavior **(Figure 4.11j)**. For example, purely capacitive mechanisms are generally temperature-independent, as they rely on interfacial charge storage rather than ion mobility and thus do not display Arrhenius-type activation. The smart $NH_3$-responsive LIG displayed an activation dependence consistent with ion- and diffusion-mediated processes. These findings indicate a two-stage sensing mechanism modulated by $NH_3$ concentration: at early stages of $NH_3$ exposure

(low uptake), the electrochemical response is dominated by transport and diffusion within the LIG matrix, consistent with the diffusion-controlled scaling observed in the scan-rate study. As [$NH_3$] increases, the mechanism progressively shifts toward redox-active behavior involving proton transfer and structural reorganization of anthocyanins into chalcones under alkaline conditions, as shown in **Figure 4.11a,b**.

To assess the sensor's quantitative performance, the impedance response to varying $NH_3$ concentrations was evaluated by plotting log(ΔZ) - defined as the difference between initial and final impedance after 15 min exposure - at 1 Hz *versus* $NH_3$ concentrations **(Figure 4.11k)**. A clear logarithmic relationship was observed across the 0-300 $mg \cdot m^{-3}$ range, with increasing $NH_3$ leading to progressively lower final impedance values. The sensor exhibited a limit of detection (LOD) of 110 ppm, a limit of quantification (LOQ) of 335 ppm, and a sensitivity of 1.2 $\Omega \cdot m^3 \cdot mg^{-1}$. This quantifiable impedance change supports not only direct electrochemical monitoring but also suggests potential for wireless sensing via passive RFID systems, where impedance and dielectric changes strongly affect return loss (RL) and signal transduction.

### 4.3.6 RFID-based wireless $NH_3$ sensing and self-powered bar code

As a proof-of-concept for wireless ammonia sensing, the $NH_3$-responsive smart LIG electrodes were integrated into a passive RFID resonant circuit based on a toroidal antenna configuration. As shown in **Figure 4.13a**, the sensor operates through magnetic coupling between an external antenna and the RFID tag, where variations in the dielectric environment of the sensing material modulate the resonant frequency and RL of the circuit. Thus, the equivalent circuit model, i.e., mutual inductance (M), resistance ($R_s$), and variable capacitance ($C_s$, $C_t$), captures the sensor's sensitivity to physicochemical changes induced by $NH_3$ exposure.

RFID tags were fabricated in two configurations - thinner (D = 1 mm) and thicker (D = 2 mm) - and exposed to $NH_3$ for 300 min, revealing redox-driven optical transitions **(Figure 4.13b)**. The corresponding RL spectra exhibited consistent leftward and upward shifts in resonant frequency after 300 min of $NH_3$ exposure for both designs **(Figure 4.13c,d)**. Similar shifts and increases in RL values have been reported previously and attributed to enhanced charge carrier mobility in the sensing layer upon $NH_3$ exposure,[527,528] consistent with the expected anthocyanin behavior in this system. Notably, the thin RFID tag showed a more pronounced frequency shift (from ~76 to 70 MHz) than the thicker variant (~77 to 75 MHz), sug-

gesting greater sensitivity to $NH_3$-induced dielectric changes, likely due to improved electromagnetic coupling in the thinner design **(Figure 4.13f,g)**. Together with the colorimetric and electrochemical modalities, and to the best of our knowledge, these findings establish the first tri-modal $NH_3$ sensing platform based on LIG.

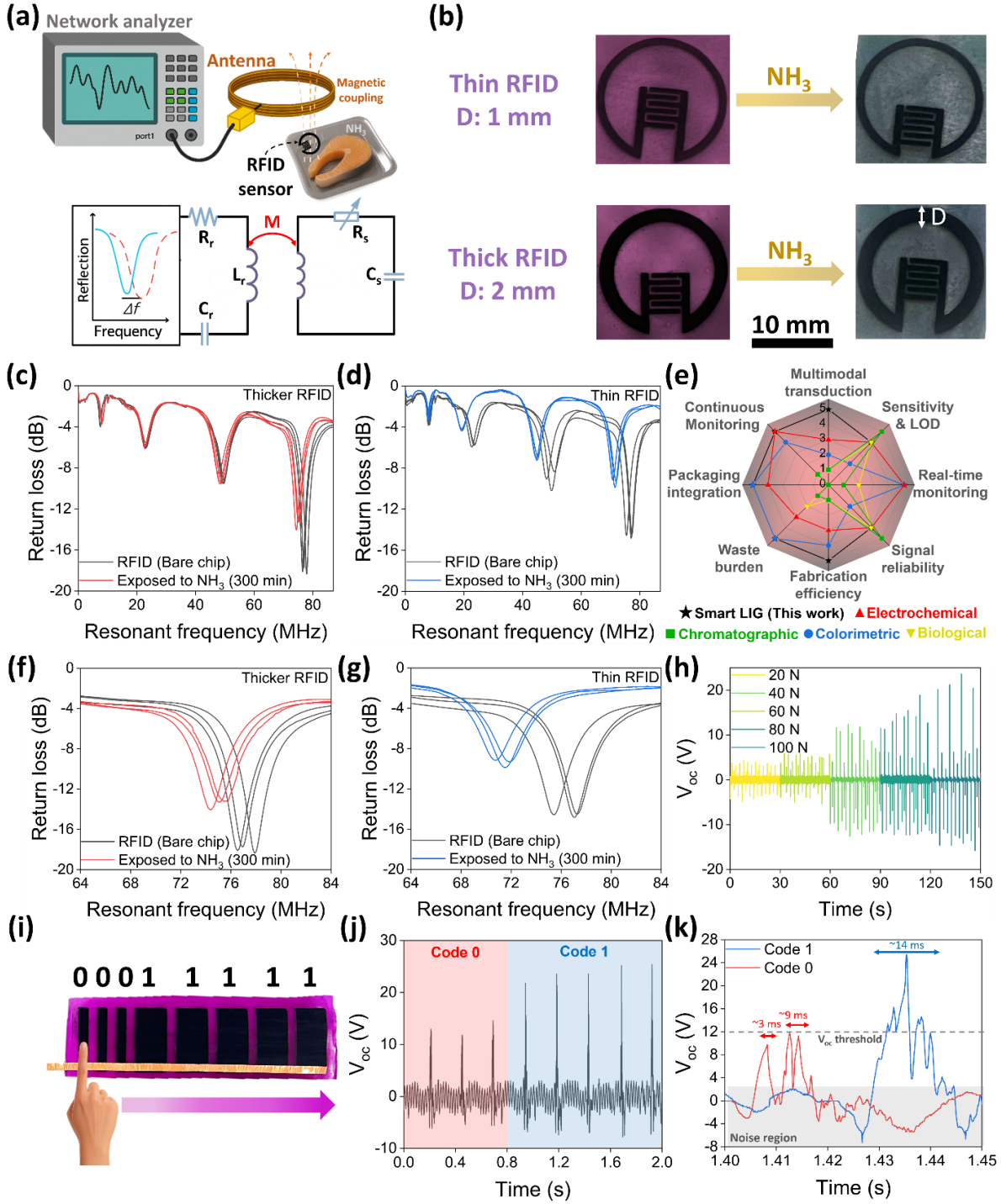


**Figure 4.13.** Wireless RFID sensor response to $NH_3$ and self-powered barcode TENG characterization. (a) Schematic of the passive RFID sensing system showing magnetic coupling between an external antenna and the RFID tag, modeled using an equivalent resonant circuit. (b) Digital photographs of thin (D = 1 mm) and thick (D = 2 mm)

RFID tags before and after 300 min of $NH_3$ exposure. Return loss (RL) spectra of RFID tags (c) thin and (d) thicker designs before and after 300 min $NH_3$ exposure. (e) Radar plot comparing $NH_3$ sensing strategies: chromatographic, biological, electrochemical, colorimetric, and the smart LIG sensor (this work) across eight key performance metrics: multimodality, sensitivity & LOD, response time, reliability, fabrication efficiency, waste burden, packaging integration, and continuous monitoring. (f,g) Zoomed-in high-frequency regions from c,d, respectively. (h) Open-circuit voltage ($V_{oc}$) peaks of smart LIG triboelectric nanogenerator (TENG) under increasing mechanical forces (20-100 N). (i) Self-powered RFID barcode array activated by finger swipe, encoding a binary pattern through differential $V_{oc}$ intensity and duration. (j) Time-domain $V_{oc}$ signals generated from barcode codes ("Code 0" and "Code 1"). (k) Time-domain $V_{oc}$ responses with distinct peak durations for "Code 0" (≤ 10 ms) and "Code 1" (> 10 ms), allowing time-based binary code identification through threshold discrimination.

We further extended the smart LIG electrodes to self-powered operation through TENGs. Under applied forces ranging from 20-100 N, the devices generated open-circuit voltages ($V_{oc}$) up to ~23 V **(Figure 4.13h)**, with amplitude scaling proportionally with load. This enhancement arises from improved interfacial contact at higher applied forces, which increases the effective contact area between the LIG electrode and the polymer surface. The enlarged contact area promotes greater charge separation and transfer, thereby amplifying triboelectric output. These observations align with established triboelectric principles,[43,421,529] with the underlying mechanism illustrated in **Figure 4.14a**.

To emulate a food-packaging scenario, high-density polyethylene (HDPE) was selected as the triboelectric active layer, paired with a smart $NH_3$-responsive LIG electrode supported on an anthocyanin-chitosan film **(Figure 4.14a)**. In the initial state (i), no potential difference exists between the triboelectric layers. Upon contact (ii), interfacial charge separation occurs due to differences in triboelectric affinities: HDPE, with stronger electron affinity, becomes negatively charged, while the wood counterpart acquires a positive charge, forming an oppositely charged interface.

During separation (iii), the increasing gap between layers induces an electrostatic potential difference, driving electron flow through the external circuit and generating a transient current. Upon recontact (iv), the layers are brought back together, leading to electron backflow in the opposite direction to neutralize charge imbalance. This periodic contact-separation cycle yields a continuous alternating current (AC) output, underpinning the self-powered operation of the Smart LIG-TENG.

The output voltage scales with applied mechanical force, as shown by the violin plots of $V_{oc}$ **(Figure 4.14b)**, where median values increase steadily from ~6 V at 20 N to ~20 V at 100 N, confirming force-dependent charge generation. Correspondingly, the short-circuit current ($I_{sc}$)

exhibits sharp oscillations under identical loading **(Figure 4.14c)**, demonstrating stable and reproducible current output. The robustness of the device is highlighted by long-term cycling stability, where $V_{oc}$ remains consistent over 10,000 cycles at 80 N **(Figure 4.14d)**, with only a slight decline in the average trend, underscoring durability under repeated mechanical stress.

Energy harvesting capability was further validated through capacitor charging measurements **(Figure 4.14e)**. The TENG effectively charged 0.1 and 1 μF capacitors to peak voltages within seconds, with charging times of 4.5 and 8.2 s, respectively, followed by predictable discharge behavior. These results confirm efficient conversion of mechanical energy into storable electrical output, directly supporting its integration into self-powered sensing and intelligent packaging systems.

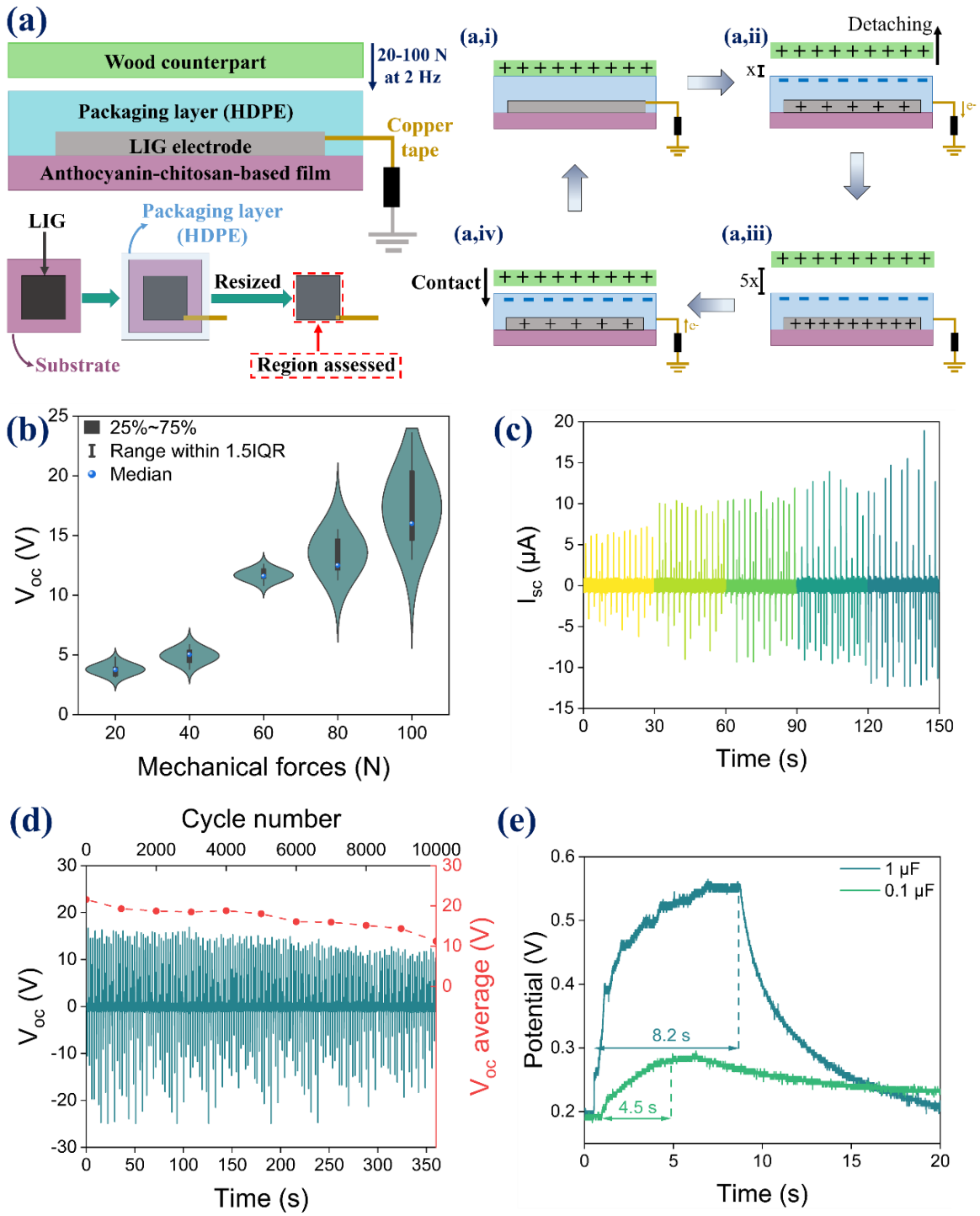


**Figure 4.14.** Working mechanism and mechano-electrical performance of a self-powered smart LIG-based triboelectric nanogenerator (TENG). (a) Schematic illustration of the smart LIG-TENG structure and working mechanism. The device comprises a layered assembly of HDPE packaging, LIG electrode, and an anthocyanin–chitosan-based film, operating in vertical contact-separation mode under cyclic mechanical loading (20-100 N at 2 Hz). (a.i) Initial contact between triboelectric layers induces charge separation via contact electrification. (a.ii) Vertical separation generates a potential difference between electrodes as opposite charges accumulate. (a.iii) The resulting potential drives electron flow through the external circuit, producing measurable current. (a.iv) Recontact neutralizes the

charge imbalance, resetting the system for the next cycle. The active region for electrical output measurement corresponds to the LIG electrode area marked in red. (b) Violin plots of open-circuit voltage ($V_{oc}$) under increasing mechanical forces (20-100 N), boxes represent the interquartile range (25-75%), whiskers indicate the range within 1.5× IQR, and dots mark the median values. (c) Short-circuit current ($I_{sc}$) peaks under identical loading, confirming force-dependent electrical output. (d) Stability of $V_{oc}$ over 10,000 cycles at 80 N and 2 Hz. Left axis: real-time $V_{oc}$; right axis: corresponding average trend. (e) Charge–discharge profiles at 80 N and 2 Hz using 0.1 μF and 1 μF capacitors, showing voltage accumulation and decay rates; inset highlights charging durations.

Building on this force-dependent energy harvesting, the $NH_3$-responsive LIG electrodes were further configured into a self-powered barcode architecture **(Figure 4.13i)**. Upon finger swiping, the barcode generated time-resolved $V_{oc}$ signals, enabling binary code discrimination ("Code 0" vs "Code 1") based on signal intensity and duration, correlated with electrode dimensions **(Figure 4.13j)**. As shown in **Figure 4.13k**, "Code 1" produced sharp, high-amplitude voltage spikes (~14 ms), while "Code 0" yielded sub-threshold responses characterized by lower intensity and shorter duration (≤9 ms, 12 V), allowing for time-based binary differentiation. Together, these findings demonstrate that smart LIG sensors can be transduced not only into wireless electromagnetic outputs, but also into energy-harvesting systems, extending their utility from electrochemical $NH_3$ sensing to passive RFID and self-powered barcoding.

The comparative radar chart **(Figure 4.13e)** underscores the distinct advantages of the smart LIG sensor over conventional $NH_3$ sensing platforms. While chromatographic and biological assays remain benchmarks in terms of sensitivity, they are limited by their invasive nature, labor-intensive protocols, and incompatibility with real-time, in-package monitoring. Electrochemical and colorimetric sensors, though more accessible and rapid, typically lack multimodal capability, food-contact compatibility, and robust signal fidelity, particularly for colorimetric systems with intermediate detection limits and lower reliability.

In contrast, the smart LIG sensor demonstrates well-balanced performance across all eight criteria. Its multimodal transduction, combining colorimetric, electrochemical, and wireless outputs, and packaging compatibility stem from the integration of anthocyanins and flexible chitosan substrates, enabling eco-friendly, food-safe deployment. IS modulation further enhances $NH_3$ sensitivity and enables tunable reversibility, bridging the gap between traditional irreversible colorimetric indicators and quantitative electrochemical detection. While sensitivity and detection limits are marginally lower than laboratory-grade techniques, e.g., chromatography and bioassays, they remain well within the thresholds required for practical food monitoring. Our proposed *in-situ* smart LIG functionalization, achieved via direct laser writing and anthocyanin copigmentation, provides a scalable, solvent-free fabrication route

with minimal material waste, yielding $NH_3$ sensors that circumvent the drawbacks of conventional analytical methods.

Overall, while conventional sensing platforms excel in isolated metrics, the *in-situ* functionalization of LIG electrodes with $NH_3$-responsiveness unlocks a unique combination of multifunctionality, flexibility, and continuous, real-time, non-invasive monitoring. The smart LIG sensor integrates colorimetric detection with electrochemical transduction, passive RFID readout, and self-powered barcoding, within a single eco-friendly platform. This strategy represents a scalable and reagent-free solution for next-generation food quality monitoring in smart packaging. We envision that this fabrication concept could serve as a blueprint for the development of smart LIG sensors and the next generation of intelligent packaging technologies.

## 4.4 Conclusion

In this work, we demonstrated the first tri-modal $NH_3$-responsive smart LIG sensors, integrating chromatic, electrochemical, and wireless detection, fabricated via *in-situ* functionalization with anthocyanin-rich red cabbage extract. Anthocyanins acted as a dual agent, both catalyzing high-quality graphene-like domain formation during laser scribing and conferring intrinsic $NH_3$ redox-responsiveness for smart detection. This dual role produced graphene with $I_D/I_G$ ratios as low as 0.87 and sheet resistances of 48 $\Omega \cdot sq^{-1}$, confirming efficient photothermal graphitization and conductive $sp^2$-carbon network formation. Ionic strength modulation in chitosan matrices through metalloanthocyanin copigmentation provided a powerful lever to accelerate response kinetics, enhance sensitivity, and tune reversibility from recoverable to permanent chromatic transitions, enabling application-specific sensor design.

We reveal that the $\pi$-conjugated anthocyanin rings act as molecular scaffolds, lowering the energy barrier for carbon rearrangement and driving growth through energy-saving localized photothermal conversion. This aromatic effect stabilizes graphene-like nuclei while preserving redox-active centers, thereby coupling structural conductivity with chemical responsiveness, an unprecedented dual function in LIG synthesis. As a result, the smart LIG sensors exhibited multifunctional $NH_3$ detection, combining tunable chromatic responses, impedance-based electrochemical detection (LOD: 110 ppm; sensitivity: 1.2 $\Omega \cdot m^3 \cdot mg^{-1}$), and wireless transduction via passive RFID. Beyond colorimetric and electrochemical outputs, proof-of-concept

demonstrations achieve wireless RFID $NH_3$ readouts and self-powered barcoding via triboelectric nanogenerators (TENGs), delivering up to 28 V from a single finger slide. Our proposed *in-situ* smart LIG functionalization via direct laser writing and anthocyanin copigmentation for $NH_3$ detection provides a scalable, reagent-free technologies that bridge advanced materials innovation with real-world intelligent packaging applications.

Altogether, this study expands the functional boundaries of laser-induced graphene by showing that sustainable electroactive molecular precursors can both engineer graphene microstructures and encode chemical reactivity for sensing. The resulting multifunctional smart LIG sensors open opportunities for real-time, non-invasive, and continuous food-quality monitoring and point toward broader applications in wireless sensing, intelligent packaging, and next-generation self-powered electronics.

# 5

# HIERARCHICALLY STRUCTURED TRANSPARENT ELECTRONIC SKIN FOR SELF-CLEANING AND SELF-POWERED PRESSURE SENSING VIA TRIBOELECTRIC NANOGENERATORS FOR SOFT ROBOTICS

## 5.1 **Introduction**

With the rapid expansion of the Internet of Things (IoT), a new generation of smart electronic systems - e.g., wearables, electronic skins, and intelligent robotics - has been increasingly integrated into healthcare, manufacturing, and human-machine interfaces to enhance safety, precision, and quality of life. Among these technological frontiers, soft robotics,[530–532] prosthetic interfaces,[533–535] and tactile human-machine communication systems[536–538] are emerging as versatile functional platforms for pressure sensing, delicate object manipulation, motion recognition, and rehabilitation monitoring. For instance, automated and robot-assisted surgery represents one of the most recent and transformative applications, offering unprecedented precision and dexterity in minimally invasive procedures.[539,540] These advances are particularly advantageous, as they enable surgeons to operate remotely, thereby reducing travel demands and time constraints during high-risk procedures, while in some cases achieving greater precision than conventional manual techniques.[540] However, such remarkable technological progress also introduces new challenges, including long-term stability, facile sterilization or self-cleaning capability, and minimal energy consumption.[541,542]

As the energy demands of these interconnected devices continue to grow, reports predict that the number of smart systems will reach approximately 125 billion by 2030,[543] underscoring the urgent need for sustainable and reliable power sources to support this vast network while reducing dependence on fossil fuels. In this context, triboelectric nanogenerators (TENGs) have emerged as a green, self-powered energy-harvesting technology that couples triboelectrification and electrostatic induction.[5,529] TENGs offer a self-powered means of converting mechanical stimuli, e.g., pressure, vibration, or motion, into electrical signals that can be analyzed to extract information on the input magnitude and frequency.[119,168,420] Moreover, TENGs can be smartly engineered to function as highly sensitive pressure sensors that operate without external power supply, charging, or maintenance, offering excellent long-term stability.[420,544] This feature is particularly beneficial for prosthetic interfaces and robot-assisted surgical systems, where uninterrupted sensing, lightweight design, and autonomous operation are essential for real-time feedback and precision control.[533]

Despite these advantages, the practical deployment of TENG-based electronic skins remains hindered by persistent surface contamination and environmental degradation, which severely reduce energy-harvesting efficiency and pressure-sensing accuracy.[529] Particulates, debris, and pathogenic microorganisms can accumulate on device surfaces, impairing mechanical contact, altering triboelectric charge density, and even posing infection risks in biomedical applications.[175,529] Considering these challenges and the rapid progress of robot-assisted surgery, developing electronic skins that combine self-cleaning, energy-harvesting, and high-sensitivity pressure-sensing functionalities through TENGs offers a promising route for next-generation biomedical and robotic applications. By preventing contamination and microbial adhesion, such soft multifunctional skins ensure reliable, continuous, and bio-safe operation for next-generation robotic and prosthetic systems.[545–547]

To achieve efficient self-cleaning, nature offers valuable inspiration, most notably the lotus leaf, whose hierarchical micro/nanostructures maintain a clean and functional surface under diverse environmental conditions.[548] By integrating structural features across multiple length scales, artificial surfaces with three-dimensional hierarchical architectures can achieve multifunctionality and offer an effective strategy for enhancing smart surface performance.[549] For instance, microstructures can modulate the effective contact area to improve energy harvesting and pressure sensitivity in TENGs, whereas nanoscale roughness further promotes self-cleaning by amplifying surface hydrophobicity.[209,550] Beyond physical texturing, chemical

functionalization (e.g., fluorination) enhances surface potential, chemical inertness, and hydrophobic durability, thereby strengthening both self-cleaning and triboelectric performance.[551,552] Silva et al. (2025) provided a comprehensive overview of chemical, physical, physicochemical, and biological strategies for TENG surface engineering, highlighting their potential to enable multifunctional capabilities such as pressure sensing, antibacterial activity, wear resistance, and localized sterilization, thereby advancing the development of active TENG-based electronic skins.[529]

Beyond advances in physicochemical surface engineering, robotics and biomedical applications also demand materials with biocompatibility, flexibility, non-toxicity, and long-term chemical stability, key attributes of polydimethylsiloxane (PDMS).[553] PDMS is well known for its chemical inertness, as it does not provoke immune responses or degrade upon skin contact, making it suitable for medical-grade use.[554] Its optical transparency allows integration with optical sensors for pressure mapping through light transmission or waveguiding. The material's intrinsic softness provides mechanical compliance that absorbs impacts during movement, improving comfort and reducing the risk of skin irritation or injury. This same compliance enables robotic systems to manipulate fragile objects, such as glassware, tissues, or organs, without mechanical damage. Moreover, PDMS can be readily surface-engineered to create hierarchical micro/nanostructures that increase effective contact area and enhance triboelectric performance, leading to robust, self-powered, and self-cleaning pressure sensors.[555,556] Thus, we identify PDMS as an ideal soft material for electronic skins, where advanced surface-engineering strategies can further enhance its performance in next-generation soft robotics and prosthetic interfaces.

Guided by this motivation, we introduce a straightforward three-step plasma-engineering strategy to fabricate fluorine-functionalized hierarchical micro/nanostructured TENG-based electronic skins, enabling enhanced self-cleaning, pressure sensing, and energy harvesting. By developing distinct microstructures with nanoscale roughness and fluorination via colloidal lithography, we systematically evaluate their self-cleaning performance under air- and liquid-assisted modes to optimize surface-cleaning efficiency. Our results reveal distinct mechanisms governing each mode: surface chemistry predominantly dictates the self-cleaning and electrical performance of TENGs under air-assisted cleaning and low-pressure triggering, in contrast, microstructures geometry and high-pressure triggering better contribute to liquid-assisted cleaning efficiency and energy-harvesting enhancement.

As a proof of concept, the TENG-based electronic skin exhibits multiple smart functionalities, including powering small electronic devices, operating as a self-powered door lock, and serving as a pressure sensor capable of distinguishing low, medium, and high pressure levels for precise object manipulation. Furthermore, we report for the first time that the open-circuit voltage ($V_{oc}$) of TENGs can be exploited to estimate the superficial contact area, enabling structural health monitoring (e.g., assessing post-impact or post-seismic deformation) and allowing rapid localization of compromised regions without external power dependence. We believe that, by integrating these smart functionalities with self-cleaning capability and energy-harvesting performance, this TENG-based transparent electronic skin constitutes a versatile platform for next-generation robotic and self-powered systems.

## 5.2 Experimental section

### 5.2.1 Materials

Polystyrene (PS) colloidal spheres (1.3 μm diameter) were purchased from Microparticles GmbH and Micromod Partikeltechnologie GmbH. Ethanol (96%) was obtained from LabChem (Zelienople, PA, USA). Sylgard® 184 silicone elastomer kit was purchased from Dow Corning®. Indium zinc oxide (IZO) ceramic targets ($In_2O_3$/ZnO, 89.3/10.7 wt%, 3 in.) were purchased by SCM Inc. Copper tape was supplied by 3M™. Diacetone alcohol and methylene blue (82%) were obtained from Sigma-Aldrich, while toluene (99.8%, anhydrous) was purchased from Fisher Scientific.

### 5.2.2 Fabrication of PDMS-Based Electronic Skin

PDMS films were prepared by mixing silicone elastomer and curing agent (Sylgard 184, Dow Corning) in a 10:1 weight ratio. The mixture was thoroughly stirred and vacuum degassed for 1 h to remove trapped air bubbles, then spin-coated onto clean glass substrates at a constant acceleration of 200 rpm·$s^{-1}$, reaching a final speed of 200 rpm for 60 s. The coated films were cured at 110 °C for 1 h to obtain uniform PDMS layers. After curing, carbon tape was attached to the PDMS surface to serve as both the conductive electrode and the adhesive interface for electronic skin attachment. For smart and transparent TENG applications, IZO electrodes (~100 nm) were deposited following the procedure described in our previous

work.[557] The deposition was carried out in a custom-built radio-frequency magnetron sputtering system at room temperature under a mixed argon/oxygen atmosphere (20/0.4 sccm) at a working pressure of $1.2 \times 10^{-1}$ Pa. The RF power density was maintained at 5 $W \cdot cm^{-2}$, with a target–substrate distance of 10 cm. After deposition, copper tape was applied to extend the conductive path and establish electrical connections to the measurement system.

### 5.2.3 Deposition of polystyrene (PS) particles

PS monolayers were deposited according with Boane et al. (2021).[558] Monodisperse PS spheres (1.3 μm in diameter) were dispersed in water to 2.5 wt%. Diacetone was added at a 1:3 volume ratio to promote uniform spreading. This mixture was then employed to form a close-packed hexagonal monolayer of PS microspheres using the Langmuir-Blodgett deposition technique (Biolin Scientific KSV NIMA, Finland). A total of 800 mL of the suspension was carefully spread at the air-water interface of the Langmuir-Blodgett **(Figure 5.1a)**. The barriers were subsequently compressed at 10 $mm \cdot min^{-1}$, inducing the floating PS spheres to self-assemble into a highly ordered hexagonal monolayer **(Figure 5.1b)**. The resulting PS film was transferred onto PDMS-coated glass substrates by vertical withdrawal of the substrate from the subphase at 2 $mm \cdot min^{-1}$, yielding a uniform, hexagonally packed colloidal template.

### 5.2.4 Hierarchical micro/nanostructures engineering of PDMS surfaces

To fabricate hierarchical micro/nanostructured PDMS surfaces and investigate the influence of multiscale roughness on wettability and surface functionality, we employed a three-step RIE (Trion Minilock Phantom III) process encompassing physical microstructuring, surface activation, and fluorine functionalization. In the 1st-step, physical microstructuring was achieved by exposing PS-masked PDMS substrates to $SF_6$ plasma (0-4800 s) under a radio-frequency (RF) power of 45 W, chamber pressure of 50 mTorr, and plasma flow rate of 50 sccm. This treatment induced plasma-assisted etching, producing ordered microstructure arrays whose geometry was controlled by plasma exposure time. After an optimized 70 min $SF_6$ exposure, the residual PS spheres were completely removed via toluene-assisted ultrasonic cleaning (20 min), followed by acetone rinsing and compressed-air drying.

To optimize surface hydrophobization and achieve durable fluorine incorporation, a design of experiments (DoE) based on the Box-Behnken methodology was implemented after the physical modification step **(Table 5.3)**. The 2nd-step, surface activation, was performed using

$O_2$ plasma (0-900 s) to introduce polar silanol (Si–OH) and siloxane (Si–O–Si) groups, thereby increasing surface energy and generating reactive sites for subsequent fluorination. In the 3rd-step, $SF_6$ plasma treatment (0-900 s) was applied to form covalently bonded Si–F and C–F terminations, yielding a chemically durable, low-surface-energy interface that imparts long-term hydrophobicity and enhanced triboelectric performance.

**Table 5.3.** Experimental conditions for hierarchical micro/nanostructure optimization on PDMS surfaces via reactive ion etching (RIE) following the 1st-step $SF_6$ physical modification.

| Sample | $O_2$ plasma (s) | $SF_6$ plasma (s) | RIW power (W) | Gas pressure (mTorr) | Plasma flow (sccm) |
|---|---|---|---|---|---|
| $T_1$ | 132 | 132 | | | |
| $T_2$ | 768 | 132 | | | |
| $T_3$ | 132 | 768 | | | |
| $T_4$ | 768 | 768 | | | |
| $T_5$ | 0 | 450 | 45 | 50 | 50 |
| $T_6$ | 900 | 450 | | | |
| $T_7$ | 450 | 0 | | | |
| $T_8$ | 450 | 900 | | | |
| $T_9$ | 450 | 450 | | | |

RIW: radio-frequency power. RIE: reactive ion etching.

During the optimization, the RIE parameters were systematically varied while maintaining constant baseline conditions (RIW: 45 W; pressure: 50 mTorr; gas flow: 50 sccm). The experimental matrix was designed to induce nanoscale roughness atop the microstructured architecture and to evaluate the synergistic effects of $O_2$ plasma activation time, $SF_6$ plasma fluorination duration, and etching sequence order on surface wettability and chemical stability. This approach enabled a statistically robust determination of the optimal plasma combination for maximizing hydrophobicity, ensuring long-term durability, and enhancing triboelectric energy-harvesting performance.

### 5.2.5 Surface characterization

Surface morphology was analyzed using AFM (Asylum Research MFP-3D, Oxford Instruments) operated in tapping mode with a silicon probe (Olympus AC160TS, spring constant

K = 26 N·m$^{-1}$, resonance frequency ca. 300 kHz) under ambient laboratory conditions. Complementary topographical and structural examinations were carried out using field-emission scanning electron microscopy (FESEM; Hitachi Regulus 8220). The $R_q$ was calculated using Equation 5.1.

$$R_q = \sqrt{\frac{1}{n}\sum_{i=1}^{n}(z_i)^2} \quad (5.1)$$

where $Z_i$ represents the surface height value at a given point as a function of distance across the scanned region.

### 5.2.6 Chemical characterization

Chemical composition and bonding states were analyzed using Raman spectroscopy and X-ray photoelectron spectroscopy (XPS). Raman spectra were acquired with a Renishaw® inVia™ Qontor® confocal Raman microscope (Gloucestershire, UK) equipped with a Renishaw Centrus 2957T3 detector, primarily to verify the complete removal of the PS mask after optimization of the colloidal lift-off process. Spectra were collected in extended mode over the 500-3200 cm$^{-1}$ range using a 532 nm excitation laser (1800 l·mm$^{-1}$ grating) operated at 5% laser power, with an exposure time of 10 s, three accumulations, and one acquisition per point. Each dataset represents the average of at least three independent measurements.

XPS was performed using a Kratos Axis Supra system (Thermo Scientific, UK) equipped with monochromated Al K$\alpha$ radiation (1486.6 eV) to verify fluorine functionalization and evaluate the surface elemental composition and chemical states of the hierarchical micro/nanostructured PDMS obtained through Box-Behnken optimization treatments. High-resolution spectra of C 1s, F 1s, O 1s, and Si *2p* were analyzed to identify specific bonding environments. Peak fitting and deconvolution were performed using CasaXPS software.

### 5.2.7 Wetting characterization and functional stability

Static water contact angles (CAs) were measured using a DataPhysics OCA 15 Plus goniometer via the sessile drop method, employing 1 μL ultrapure water droplets at room temperature. Images were analyzed with SCA 20 software using the Laplace-Young approximation model, and the reported values represent the average of at least 10 independent measurements per sample. To evaluate the functional stability of surface wettability, static water contact angles were measured after sequential washing cycles with Milli-Q water, followed by air-pressure drying, repeated up to three consecutive sequences.

### 5.2.8 Surface energy

The surface critical energy ($\gamma_c$) of the samples was determined using the Zisman method,[559] based on contact angle goniometry. Sessile drop contact angles were recorded at room temperature using the same DataPhysics OCA 15 Plus system. Four probe liquids with well-defined surface tensions were used: distilled water (72.8 $mN \cdot m^{-1}$), ethylene glycol (47.7 $mN \cdot m^{-1}$), N,N-dimethylformamide (37.1 $mN \cdot m^{-1}$), and glycerol (63.4 $mN \cdot m^{-1}$). These liquids cover a broad range of polarities and surface tensions, enabling reliable extrapolation. For each liquid, ~1 μL droplets were gently deposited on the solid surface using a microsyringe, and the static contact angle ($\theta$) was recorded. Each reported value corresponds to the mean of 10 measurements taken at distinct surface locations. The Zisman approach involves plotting cos $\theta$ as a function of the liquid surface tension ($\gamma_L$), typically expressed in $mN \cdot m^{-1}$. The resulting data were fitted using a linear regression model, and the extrapolated value at $\cos \theta = 1$ (complete wetting, $\theta = 0°$) was taken as the $\gamma_c$ of the solid surface. This parameter serves as an effective indicator of the solid's surface energy and its relative hydrophobicity.

### 5.2.9 Electrical characterization of TENG-based electronic skin

The $V_{oc}$ output of the TENG-based electronic skin was evaluated using the Thévenin equivalent circuit model.[516] Electrical outputs from devices fabricated with increasing $SF_6$ plasma exposure times (0-70 min, 1st physical modification) were measured under a normal force of 100 N at 2 Hz, using wood as the counter material in a custom-built mechanical drive setup. The TENGs were connected to an external circuit, and the resulting signals were recorded using a Tektronix TBS1000C oscilloscope.

To assess the influence of surface chemistry and micro/nanostructuring on electrical performance, HMN-TENGs corresponding to treatments $T_1$-$T_9$ were evaluated at 20 kPa and 100 kPa, representing low and high mechanical contact pressures, respectively. The low-pressure regime (20 kPa) emphasizes the effect of surface chemistry, while the high-pressure regime (100 kPa) captures the contribution of deformation-induced contact area enhancement.

For pressure-sensing calibration, $V_{oc}$ was recorded over a range of applied pressures (10-90 kPa, in 10 kPa increments) for three device configurations: flat PDMS-TENG, 1st-step $SF_6$-modified surface, and hierarchically optimized surface ($T_9$). The long-term mechanical stabil-

ity of the HMN-TENG was examined by monitoring $V_{oc}$ over 10,000 continuous operation cycles under 100 N at 2 Hz to evaluate plastic deformation. The instantaneous power density output (P) was calculated using the relation $P = V^2R^{-1}$, based on voltage measurements across a range of external load resistances (0.1-300 MΩ) at 100 N and 2 Hz.

The functional stability of the TENG-based electronic skin was evaluated by comparing the flat PDMS-TENG (control), the 70 min $SF_6$-modified surface, and the optimized hierarchical surface ($T_9$). Each sample was deliberately contaminated with 0.1 g of MB and tested under a low mechanical load of 30 N, to minimize the permanent attachment of contaminants to the surface, at a frequency of 2 Hz, both before and after air-assisted self-cleaning. The self-cleaning process was performed using a 120 mm cooling fan (2.52 W) positioned 10 cm from the sample surface for 30 s.

To evaluate environmental durability, both flat and hierarchical ($T_9$) devices were exposed to natural outdoor conditions in Caparica, Portugal (GPS: 38°39′36″ N, 9°12′11″ W). The $V_{oc}$ outputs were monitored under a low mechanical load of 30 N, to avoid complete adhesion of naturally accumulated contaminants, and a frequency of 2 Hz over a 70-d period, with measurements taken every 14 d. This long-term assessment enabled analysis of functional stability and contamination resistance under realistic environmental exposure.

### 5.2.10 **Smart TENG-based electronic skin applications**

As a proof of concept, HMN-TENG-based electronic skin was demonstrated as a self-powered pressure sensor. The device was used to detect three levels of mechanical stimuli-light, medium, and high pressure applied by manually squeezing a wash bottle (pipette squeeze test). The corresponding $V_{oc}$ were translated into the illumination of one, two, or three LEDs, respectively, according to predefined $V_{oc}$ thresholds programmed via an Arduino platform **(details and code in Appendix A)**. The sensitivity was determined from the linear regression slope of the $V_{oc}$-pressure curve, while the response and recovery times ($T_{90}$%) were defined as the duration required for the signal to rise or decay from 10 to 90% of its peak intensity. The LOD was calculated using the standard signal-to-noise approach, where $LOD = 3.3\ \sigma \cdot S^{-1}$, with σ representing the standard deviation of the blank signal and S the slope of the calibration curve.

The intelligent lock control system was implemented by gently sliding or tapping the surface of the optimized HMN-TENG ($T_9$), where the generated $V_{oc}$ signals were processed as

unique input codes for unlocking operations. The device further demonstrated effective energy harvesting by directly powering supercapacitors (0.1–1 μF), LED arrays, and a digital calculator via manual tapping, without external power sources.

For the surface-area estimation methodology, we characterized the microstructured PDMS-based TENGs fabricated via 70-min $SF_6$ RIE using a voltage-based calibration approach derived from the linear correlation between the $V_{oc}$ and the contact area (A). As a control, flat PDMS-TENGs with known planar areas were characterized under identical mechanical loading conditions (100 N, 2 Hz) using a standard wood counter-surface, serving as the baseline for statistical area-voltage correlation. The contact area was systematically varied from 0.25 to 6 $cm^2$, and the corresponding $V_{oc}$ was recorded with a digital oscilloscope.

Linear regression analysis was performed to establish the relationship between open-circuit voltage ($V_{oc}$) and effective contact area for both flat and micro/nanostructured PDMS surfaces. Statistical outliers were identified and excluded using Studentized residual analysis ($|t_i| > 3.0$) performed in Minitab 17. The resulting fits exhibited high coefficients of determination ($R^2 > 0.98$), confirming excellent linearity and reliability of the calibration model. This calibration enabled quantitative determination of unknown effective contact areas ($A_{eff}$) from $V_{oc}$ using the inverse relation (Equation 5.2).

$$A_{eff} = \frac{V_{oc} - b}{m} \tag{5.2}$$

where $m$ and $b$ correspond to the slope and intercept of the calibration curve. Repeated measurements (n = 10) were used to estimate the mean and standard deviation.

### 5.2.11 Evaluation of water- and air-assisted self-cleaning performance

To assess the self-cleaning performance of the plasma-engineered PDMS surfaces under both liquid and gaseous environments, MB was selected as a model contaminant due to its well-defined optical signature for residue quantification. For the water-assisted self-cleaning test, the PDMS-based electronic skin was inclined at 45°, and 1 mL of Milli-Q water was released from a height of 5 cm onto the surface. The residual MB on the PDMS was then rinsed with Milli-Q water, and the collected solution was analyzed by UV–Vis spectroscopy to determine the residual contaminant concentration. For the air-assisted self-cleaning test, the MB-contaminated surface was exposed to airflow from a 120 mm cooling fan (2.52 W) positioned 10 cm away for 30 s. In both experiments, ca. 0.1 g of MB powder was uniformly spread over the surface before testing. The self-cleaning efficiency (η) was calculated using Equation 5.3.

$$\eta = \left(1 - \frac{A}{A_0}\right) \times 100\% \quad (5.3)$$

where $A_0$ and $A$ represent the absorbance of the MB solution before and after the cleaning process, respectively.

### 5.2.12 Quantification of self-cleaning efficiency via UV-Vis spectroscopy

Quantitative analysis of self-cleaning efficiency was performed using UV-Vis absorption spectroscopy by monitoring the MB absorbance at its characteristic wavelength of 665 nm. Calibration curves were established with 10 concentration points ranging from 0.25 to 3.75 $\mu g \cdot L^{-1}$, each measured in triplicate to ensure reproducibility. The resulting linear calibration ($R^2 > 0.99$) enabled accurate quantification of residual dye concentration, thereby allowing precise evaluation of the removal efficiency for each plasma-treated PDMS surface.

### 5.2.13 Fine elemental analysis

Finite element simulations were performed using COMSOL® Multiphysics to validate the experimental triboelectric output and elucidate the influence of surface microstructuring on the $V_{oc}$ relative to flat PDMS-TENG controls. The simulation model incorporated the experimentally measured device dimensions, material properties, and boundary conditions to faithfully reproduce the coupled electro-mechanical behaviour observed experimentally.

### 5.2.14 Statistical analyses

All data are reported as mean ± standard error ($n \geq 10$) from independent measurements. Statistical analyses were conducted using OriginPro 8.5 and Minitab 17. Surface-response modeling and optimization of the plasma treatment parameters were performed in Statistica 7 using the Box-Behnken design framework. The Box-Behnken matrix evaluated two independent factors: $O_2$ plasma duration, and $SF_6$ plasma duration. A 2nd-order polynomial regression model was fitted to the experimental data to correlate the effects of these variables on the contact angle, surface energy, and $V_{oc}$. Model adequacy was validated through analysis of variance (ANOVA), lack-of-fit testing, and coefficient of determination ($R^2$), ensuring predictive reliability of the optimized plasma conditions. Quantitative comparisons were further analyzed using one-way ANOVA, followed by Tukey's post hoc test. Statistical significance was established at $p < 0.05$.

## 5.3 Results and discussion

### 5.3.1 Designing hierarchical PDMS surfaces via colloidal lithography

Developing hierarchical micro/nanostructured interfaces that couple self-powered pressure sensing with efficient self-cleaning remains a major challenge for robotic and biomedical skins, where reliable signal generation must coexist with contamination resistance and long-term stability. Such surface engineering is particularly relevant for healthcare and surgical applications, where accurate, self-powered pressure sensing and efficient self-cleaning are essential for reliable object handling and sterile operation. Implementing these micro/nanostructures on PDMS is especially advantageous owing to its inherent biocompatibility, low permeability, human-like softness and elasticity, durability, and excellent chemical and thermal stability, which allow easy sterilization and long-term operation.

To achieve high pressure-sensing accuracy combined with self-cleaning functionality, hierarchical micro/nanostructures PDMS was fabricated via a colloidal lithography route coupled with plasma-assisted surface engineering. Polystyrene (PS) microspheres were first dispersed **(Figure 5.1a$_1$)** and self-assembled into an ordered hexagonal monolayer **(Figure 5.1a$_2$)**, forming a sacrificial template that defines the surface topography with high periodicity on the PDMS substrate **(Figure 5.1a$_3$)**. During the Langmuir-Blodgett assembly **(Figure 5.1b$_1$-b$_3$)**, PS particles were progressively compressed by movable barriers, transitioning from gaseous to liquid and finally to solid or crystalline phases. This evolution, reflected in the surface pressure-area isotherm, enables precise control over particle packing density and monolayer uniformity.

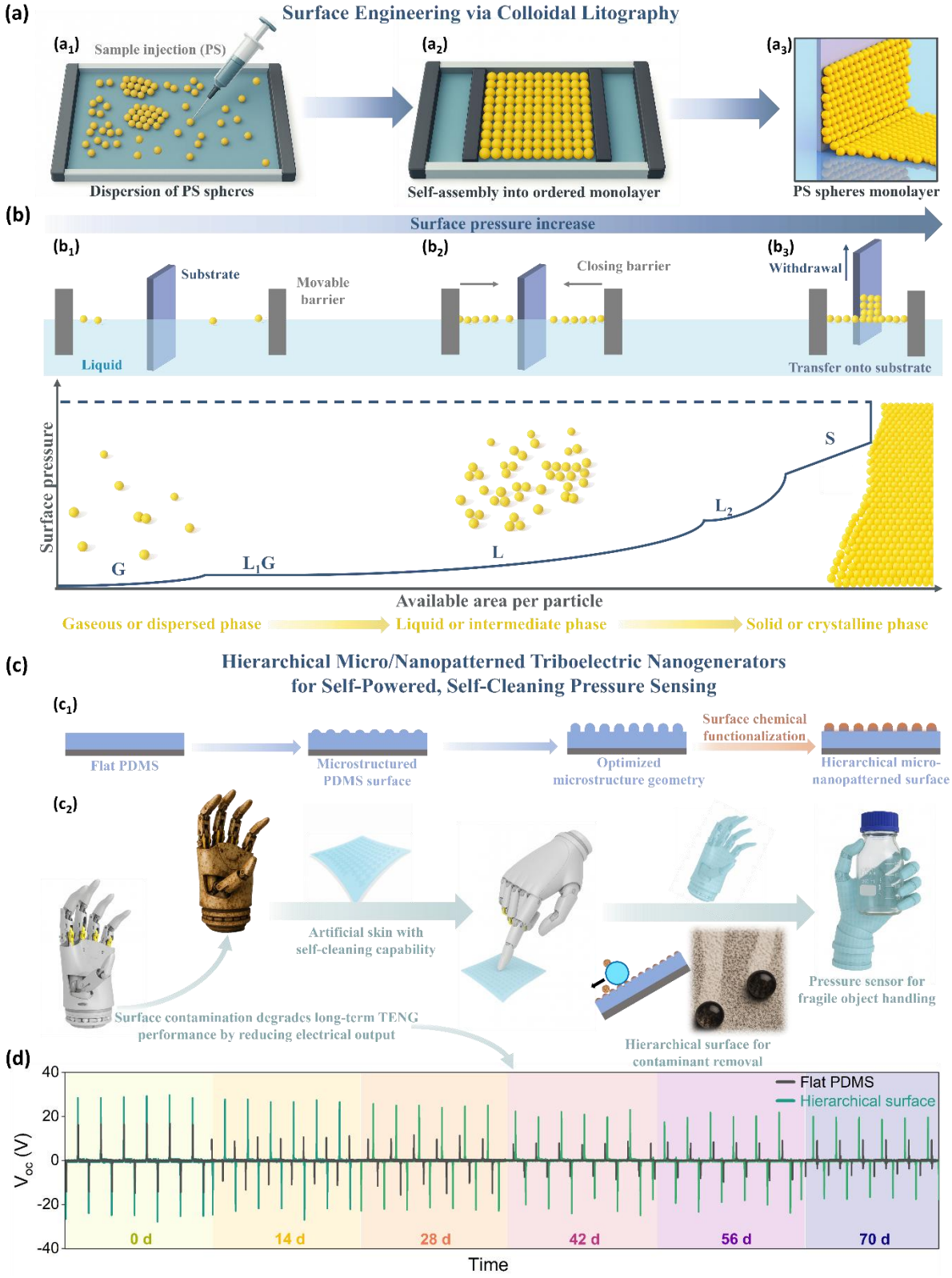


**Figure 5.1.** Surface engineering of hierarchical micro/nanostructures PDMS for self-cleaning and triboelectric energy harvesting. (a) Deposition of ordered PS monolayers by colloidal lithography: ($a_1$) dispersion of PS spheres, ($a_2$) self-assembly into an ordered monolayer, and ($a_3$) formation of a close-packed PS array. (b) Langmuir-Blodgett process: ($b_1$) dispersion of PS particles on the liquid surface, ($b_2$) compression with movable barriers to increase

surface pressure, and ($b_3$) transfer of the monolayer onto a PDMS substrate; and the corresponding surface pressure-area isotherm illustrating gaseous, liquid, and solid states of PS particle packing. (c) Hierarchical micro/nanostructured triboelectric nanogenerators (HMN-TENGs): ($c_1$) stepwise progression from flat PDMS to microstructured PDMS, surface chemical functionalization, and hierarchical surfaces combining topography and chemistry for enhanced self-cleaning and electrical output performance; ($c_2$) potential application of electronic skin as self-powered pressure sensors for fragile object handling with extended lifetime through self-cleaning. (d) Long-term stability of open-circuit voltage ($V_{oc}$) in flat *vs* hierarchical micro/nanostructured PDMS under environmental exposure over 70 d.

Following transfer onto PDMS, reactive ion etching (RIE) was applied for micro/nanostructuring. Template-guided $SF_6$ plasma etching generated the microstructured backbone for hierarchical structuring. Subsequent $O_2$ plasma oxidation introduced polar functionalities, e.g., –OH and Si–O, enhancing surface reactivity, while a final $SF_6$ plasma step produced fluorinated terminations (Si–F, C–F) and nanoscale roughness, reducing surface energy and conferring long-term hydrophobicity. The resulting hierarchical micro/nanostructured electronic skin serves as the active layer for TENGs and self-powered pressure sensors, maintaining stable performance even under contamination **(Figure 5.1c$_2$)**. Inspired by natural self-cleaning surfaces, e.g., lotus leaf,[548] the engineered topography minimizes dirt adhesion while simultaneously increasing the effective contact area for enhanced energy-harvesting efficiency. When integrated into robotic systems, this hierarchical architecture enables precise pressure sensing and safe manipulation of delicate objects, while ensuring long-term functional durability.

To demonstrate long-term functional stability, the $V_{oc}$ was monitored under environmental exposure **(Figure 5.1d)**. The hierarchical micro/nanostructured triboelectric nanogenerators (HMN-TENGs) maintained nearly constant $V_{oc}$ over 70 d, in contrast to the rapid degradation observed to the flat PDMS-TENG, attributed to surface contamination. These results highlight how synergistic control of geometry and chemistry in plasma-engineered hierarchical surfaces enables self-cleaning, and electrical stability in energy-harvesting platforms for next-generation smart electronic skins, particularly suited for healthcare and surgical robotics.

### 5.3.2 Mechanistic insight into $O_2/SF_6$ plasma-driven PDMS surface modification

Elucidating the individual effects of $O_2$ and $SF_6$ plasma treatments on PDMS, covering oxidation, etching, and roughness evolution, is a crucial step toward the rational design of hierarchical micro/nanostructures with controlled wettability and surface reactivity. To this end, sequential $O_2$ and $SF_6$ plasma exposures (0-900 s) were applied to flat PDMS surfaces to decouple their respective physical and chemical contributions.

Atomic force microscopy (AFM) **(Figure 5.2a$_1$-a$_5$)** revealed distinct plasma-specific surface evolutions. Short $O_2$ exposures (~90 s) produced smoother surfaces than $SF_6$, as oxidation-driven activation outweighed physical etching. Prolonged $O_2$ treatment (900 s) further diminished surface irregularities, consistent with isotropic ion-assisted etching that levels out micro-asperities, coupled with the gradual formation of a $SiO_x$-like layer that suppresses roughness growth and yields a more uniform topography **(Figure 5.2a$_2$-a$_3$)**.[560] In contrast, $SF_6$ plasma generated pronounced roughness at short exposure times (~90 s), consistent with the high fluorocarbon-assisted physical etching rate in PDMS and PS, followed by partial smoothing after extended treatment (900 s). This trend is confirmed by the evolution of root-mean-square roughness ($R_q$), which increases up to ~90 s and decreases at longer exposure durations, suggesting a transition from ion-driven etching to a regime dominated by fluorocarbon film redeposition **(Figure 5.2g)**.

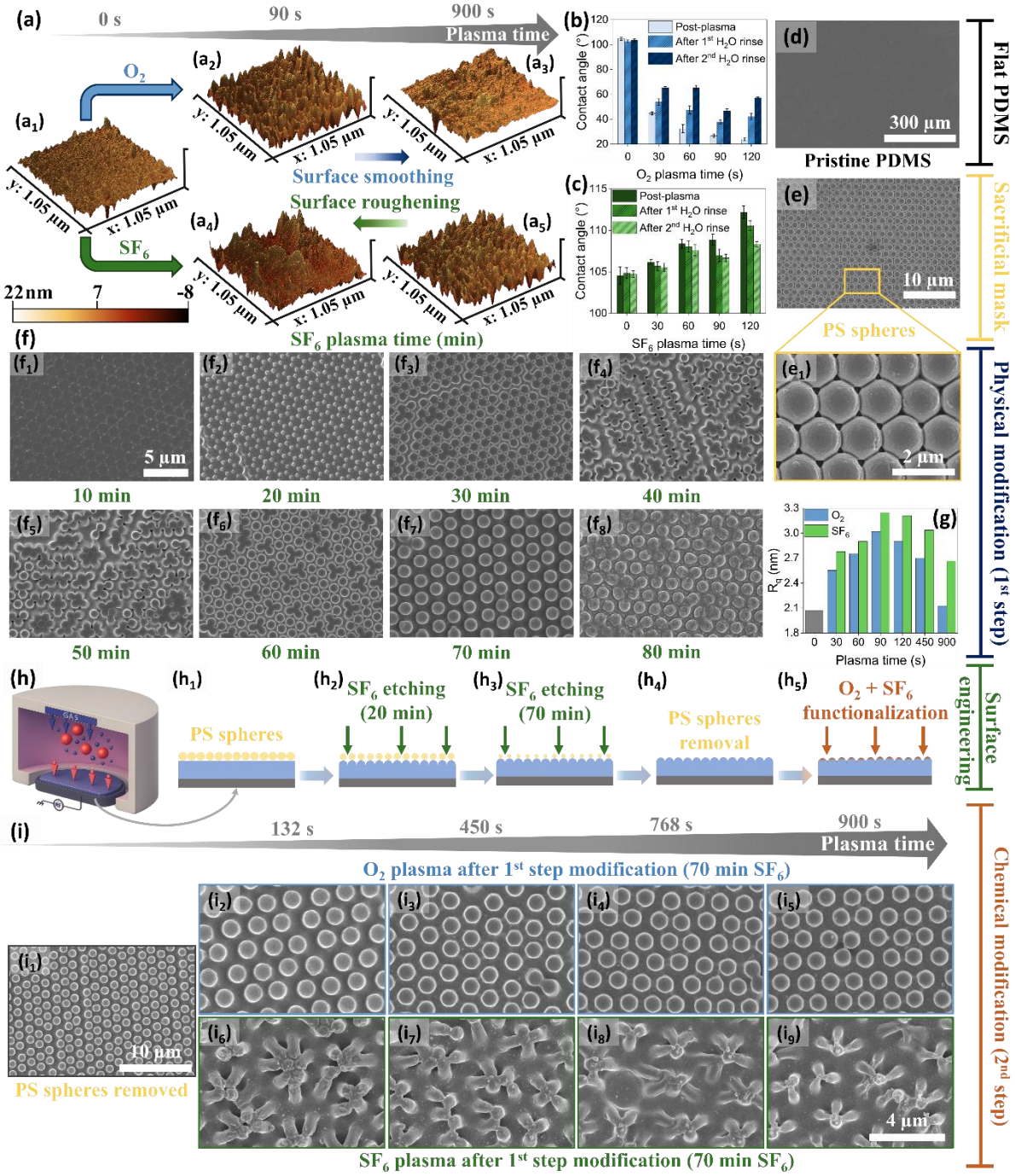


**Figure 5.2.** Stepwise $O_2/SF_6$ plasma processing for hierarchical micro/nanostructuring of PDMS. (a) AFM images of ($a_1$) pristine PDMS, ($a_2$) after 90 s, and ($a_3$) after 900 s $O_2$ plasma showing surface smoothing after short exposure, and ($a_4$-$a_5$) after 90 and 900 s $SF_6$ plasma showing progressive roughening, most pronounced at ~90 s. Water contact angle stability as a function of $O_2$ (b) and $SF_6$ (c) plasma time (0-120 s), including successive water rinsing cycles, demonstrating chemical stability. (d) SEM image of flat pristine PDMS (130×, scale bar = 300 µm). (e) SEM images of colloidal polystyrene (PS) spheres used as a sacrificial mask (4 k×, scale bar = 10 µm); ($e_1$) high-magnification image showing a close-packed hexagonal array (22 k×, scale bar = 2 µm). (f) SEM images of PDMS surfaces etched by $SF_6$ plasma for 10-80 min ($f_1$-$f_8$), revealing the evolution of ordered microstructures (13 k×, scale bars: 5 µm). (g)

Root-mean-square roughness ($R_q$) of flat PDMS as a function of $O_2$ or $SF_6$ plasma time. (h) Schematic illustration of the fabrication sequence for micro/nanostructured PDMS via reactive ion etching: ($h_1$) deposition of PS spheres by Langmuir-Blodgett assembly, ($h_2$,$h_3$) $SF_6$ plasma etching at different times (0-80 min) reducing PS size and generating microstructures, ($h_4$) PS removal by ultrasonic bath in toluene, and ($h_5$) subsequent surface activation by $O_2$ plasma oxidation followed by fluorination with $SF_6$ plasma (0-900 s). (i) SEM images of PDMS after the 1$^{st}$-step modification (70 min $SF_6$), ($i_1$) after PS removal (4 k×, scale bars: 10 μm), followed by ($i_2$-$i_5$) $O_2$ plasma (132, 450, 768, 900 s) and ($i_6$-$i_9$) $SF_6$ plasma (132, 450, 768, 900 s) (13 k×, scale bars: 4 μm).

The interplay between surface morphology and chemistry in governing wettability stability is summarized in **Figure 5.2b-c**. $O_2$ plasma markedly reduced the water contact angle from ~103° to ~24°, reflecting oxidation-driven incorporation of polar oxygenated groups, whereas $SF_6$ plasma enhanced hydrophobicity through the combined effects of surface roughening and fluorination, increasing the contact angle to ~112°. Successive water rinsing cycles led to a partial recovery of hydrophobicity (~238% increase in contact angle) for $O_2$-treated samples, likely due to the removal of physically adsorbed oxygenated fragments. This partial recovery of hydrophobicity after rinsing confirms the removal of non-covalently bound oxygenated species, evidencing that oxidation was primarily superficial rather than forming stable covalent linkages.

Moreover, the non-monotonic evolution of the contact angle with increasing $O_2$ plasma duration is consistent with the Wenzel model, which predicts that increasing surface roughness enhances hydrophilicity on intrinsically hydrophilic surfaces and amplifies hydrophobicity on hydrophobic ones.[561] Consequently, at short treatment times (~90 s), the maximal roughness yields the lowest contact angle by amplifying the interfacial free-energy reduction that promotes spreading on intrinsically hydrophilic substrates. In contrast, prolonged exposure (≥120 s) induces partial surface smoothing, thereby diminishing the roughness-driven wetting enhancement.

Conversely, $SF_6$-treated surfaces exhibited a sustained increase in hydrophobicity that partially reverted toward the pristine state (~103°) after water rinsing, indicating the removal of non-covalently deposited ultrathin fluorocarbon layers. The most pronounced contact-angle recovery occurred after prolonged plasma exposure (~120 s) for both gases, suggesting the formation of weakly adhered ultrathin surface layers susceptible to aqueous removal. Collectively, these results reveal that $O_2$ plasma predominantly induces surface oxidation rather than etching, whereas $SF_6$ plasma drives etching accompanied by chemical modification. However, in both cases, the resulting surface chemistry is unstable and susceptible to aqueous removal. To mitigate this instability, we propose a sequential treatment strategy: an initial $O_2$ plasma

step to activate the surface, followed by $SF_6$ plasma fluorination to stabilize the surface termination. With this sequential plasma strategy, we establish a route to durable, chemically stable surfaces with improved self-cleaning and triboelectric performance.

Inspired by natural self-cleaning surfaces such as lotus leaves,[548] a hierarchical micro/nanostructured PDMS surface was subsequently designed to amplify these effects. A three-step optimization process was implemented **(Table 5.3)**: (1) microstructuring of PDMS via $SF_6$ plasma to generate the physical backbone, (2) surface activation using $O_2$ plasma, and (3) chemical fluorination with $SF_6$ plasma to achieve hydrophobic and nanorough terminations. The schematic in **Figure 5.2h** outlines the fabrication workflow. PS spheres were first deposited by Langmuir-Blodgett assembly **(Figure 5.2h$_1$)**, followed by $SF_6$ plasma etching at controlled durations **(Figure 5.2h$_2$-h$_3$)** to produce microstructured PDMS and correlate topography with electrical performance. The PS template was subsequently removed in toluene **(Figure 5.2h$_4$)**, after which two consecutive plasma treatments were applied: $O_2$ plasma introduced reactive hydroxyl groups, while $SF_6$ plasma fluorination reinforced the hydrophobic functionality by conferring nanoscale roughness and lowering surface energy **(Figure 5.2h$_5$)**.

Initially, the PDMS surface is flat and featureless **(Figure 5.2d)**. After deposition of monodisperse PS spheres **(Figure 5.2e,e$_1$)** in a close-packed hexagonal array, the template serves as a sacrificial mask for reactive ion etching. During $SF_6$ plasma exposure (0-80 min), a progressive evolution of microstructured architectures is observed, transitioning from shallow pits to well-defined cylindrical micropillars **(Figure 5.2f$_1$-f$_8$)**. Optimal fabrication of smooth, single micropillars is achieved after 70 min of $SF_6$ etching, yielding ~1 μm-high structures. While, further $SF_6$ exposure results in overetching and the loss of well-organized, uniform patterns **(Figure 5.2f$_8$)**.

Before proceeding with the 2$^{nd}$ and 3$^{rd}$-step optimization, a key prerequisite is the effective removal of the PS spheres after the 1$^{st}$ step. As shown in **Figure 5.2i$_1$**, complete removal of the PS sacrificial mask using toluene is essential to obtain well-defined micropillar arrays. When PS removal is adequate, subsequent $O_2$ plasma exposures (132-900 s) - which are known to have limited etching capability on PDMS - result in negligible roughness evolution but induce the expected chemical activation **(Figure 5.2i$_2$-i$_5$)**. This behavior is consistent with the oxidation effects previously observed for flat PDMS surfaces.

In contrast, incomplete removal of PS spheres leads to residual polymer adhering to the tops of the micropillars **(Figure 5.2i$_6$-i$_9$)**. These residues act as a "glue," coupling adjacent pil-

lars and preventing the formation of discrete, well-defined microstructures, even under prolonged $SF_6$ plasma etching, e.g., 900 s **(Figure 5.2i$_9$)**. Therefore, we optimized the PS removal process through a wet toluene lift-off method by tuning the immersion time, rinsing cycles, and ultrasonic bath conditions. This optimization was crucial for achieving high-fidelity pattern transfer and preserving the structural integrity of the hierarchical micro/nanostructures on the PDMS surface.

### 5.3.3 Micro/nanostructures-chemical interplay for hydrophobic surface optimization

The efficiency of the removal procedure was further confirmed by Raman spectroscopy **(Figure 5.3a)**, which shows the complete disappearance of PS vibrational signatures after the optimized toluene-assisted ultrasonic cleaning process, confirming complete removal of PS spheres. PDMS coated with PS spheres exhibited characteristic aromatic ring vibrations at ~1001, 1031, and 1602 $cm^{-1}$, with 1001 $cm^{-1}$ band being the most distinctive PS peak attributed to the ring-bending mode[562]. The 3054 $cm^{-1}$ peak corresponds to C–H stretching in the phenyl ring,[563] both of which vanish completely after the toluene-based removal step, confirming full elimination of the sacrificial mask. In contrast, pristine PDMS exhibits distinct bands at 490 $cm^{-1}$ (Si–O–Si bending), 710 $cm^{-1}$ (Si–C symmetric stretching), and 2905 $cm^{-1}$ (C–H stretching of $Si–CH_3$),[564,565] all preserved after plasma treatment, indicating that the 1$^{st}$-step surface modification occurs without degrading the siloxane backbone.

The wettability is strongly influenced by the 1$^{st}$-step $SF_6$ plasma modification, which governs the evolution of micropillar height and surface morphology **(Figure 5.3b)**. Pristine PDMS surfaces exhibit a water contact angle of ~103°, showing a progressive increase in hydrophobicity with longer $SF_6$ exposure, reaching ca. 136° after 70 min. This enhancement correlates with the well-defined structural patterning observed in the SEM images **(Figure 5.2f$_1$-f$_7$)**. However, at 80 min of $SF_6$ exposure, the contact angle decreases slightly to ~130°, which coincides with the loss of structural uniformity and overetched features **(Figure 5.2f$_8$)**. Based on these results, we selected the 70 min $SF_6$ treatment as the optimal 1$^{st}$-step condition for microstructuring, providing a robust foundation for the subsequent 2$^{nd}$ and 3$^{rd}$-step optimization.

After this 1$^{st}$-step physical modification, the effects of $O_2$ and $SF_6$ plasma exposures were analyzed to elucidate the individual competing contributions of surface roughness and chemistry on wettability evolution **(Figure 5.3c)**. $O_2$ plasma treatment significantly reduced the contact angle from ~136 to ~119° due to the oxidation-induced incorporation of polar oxygenated

groups, whereas $SF_6$ plasma increased the contact angle to ~144° through enhanced nanoscale roughening and fluorination. The corresponding water contact-angle images **(Figure 5.3e)** illustrate this tunable transition between hydrophilic and hydrophobic regimes, highlighting the complementary roles of oxidation and fluorination in modulating surface energy.

To achieve higher hydrophobicity with efficient self-cleaning capability and enhanced energy-harvesting performance, a series of sequential $O_2/SF_6$ plasma treatments ($T_1$-$T_9$) were designed to optimize surface fluorination **(Table 5.3)**. Rather than merely depositing an ultrathin fluorocarbon layer, this strategy incorporates a controlled oxidation step for surface activation followed by fluorination to achieve stable covalent functionalization. SEM analysis **(Figure 5.3h$_1$-h$_9$)** reveals the progressive morphological evolution of PDMS under these sequential plasma conditions. The transition from smooth to hierarchically textured surfaces produces an array of micro/nano protrusions capable of trapping air beneath impinging droplets, thereby reducing the real solid–liquid contact fraction ($f_s$), and interfacial adhesion ($\gamma_{sl}$). In our subsequent experiments, we observed that this configuration effectively facilitates contaminant removal, consistent with a Cassie–Baxter wetting regime **(Figure 5.3o)**.

In contrast, a Wenzel wetting state dominates on surfaces with low-aspect-ratio micropillars (i.e., pillar height comparable to or smaller than their radius) and hydrophilic or weakly hydrophobic surface chemistry. Under such conditions, the liquid readily penetrates the surface texture, displacing trapped air and increasing the true contact area, which enhances adhesion and hinders self-cleaning.[561] In this context, we suggest that the optimized surface obtained after 70 min of $SF_6$ etching exhibits a stable Cassie-Baxter wetting state with persistent air entrapment, as increasing the pillar aspect ratio, by extending the height beyond the lateral dimension (e.g., height > radius ≈ 0.5 μm), surpasses the critical threshold required to prevent liquid impalement.[566,567]

To further advance the surface functionality of the electronic skin for diverse robotic and smart applications based on TENGs, we optimized the hierarchical structuring through a 2$^{nd}$ and 3$^{rd}$- plasma-engineering step, balancing topographical geometry and fluorination synergy to enhance self-cleaning and energy-harvesting efficiency. This step is essential, as the low surface energy of fluorinated PDMS suppresses charge recombination by reducing water adsorption and impurity trapping, while the hierarchical architecture increases the effective contact area under deformation, thereby boosting charge density and $V_{oc}$. Accordingly, we analyzed the combined influence of $O_2$ and $SF_6$ plasma-durations optimization on hierarchical

surface morphology through SEM analysis **(Figure 5.3h)** to correlate structural evolution with wettability, self-cleaning, and triboelectric performance.

Short $SF_6$ plasma treatments (e.g., 132 s) preserved the previously formed micropillar structures **(Figure 5.3h$_{1,2}$)**, whereas prolonged exposure (e.g., 768 s, $T_3$ and $T_4$) led to their structural collapse **(Figure 5.3h$_4$)**. Interestingly, combining moderate $SF_6$ plasma exposure (~450 s) with prior $O_2$ plasma activation preserved the micropillar geometry, inducing only minor nanoscale roughening **(Figure 5.3h$_{6,8,9}$)**. In contrast, the absence of an $O_2$ activation step led to partial degradation of the surface features even under mild $SF_6$ exposure (450 s) **(Figure 5.3h$_5$)**. This finding suggests that $O_2$ plasma pretreatment enhances the structural stability of the micropillars by generating oxidative active sites that promote more effective fluorination and structural robustness. Following the 3$^{rd}$-step treatment, all samples except those with minimal or no ($T_2$ and $T_7$, respectively) exhibited pronounced nanoscale textures across the micropillar array, confirming the formation of hierarchical micro/nanostructures. Furthermore, considering the similar micropillar morphologies among the $T_6$-$T_9$ samples, the observed variation in contact angles (from 96 to 152°) can be primarily attributed to differences in surface chemistry.

Because self-cleaning efficiency is maximized under extreme wetting regimes, either superhydrophilic or superhydrophobic,[568,569] low-surface-energy fluorinated terminations are particularly advantageous for high electrical performance in TENGs.[529,570] Such fluorinated surfaces exhibit increased electron affinity upon contact with common counter materials, thereby facilitating efficient charge transfer during contact electrification.[43,529] Moreover, the chemical inertness and hydrophobicity of these surfaces suppress charge recombination and leakage by minimizing interactions with adsorbed water and contaminants. As a result, these surfaces can retain high surface charge densities over extended periods, even under environmental exposure, where surface contamination is well known to degrade electrical output by perturbing the potential wells.[529] When employed as the negative triboelectric layer, such properties contribute to both higher output performance and improved long-term stability of TENGs. Therefore, to elucidate the effects of RIE optimization and identify the most efficient surface treatments exhibiting these characteristics, we evaluated the contact angle and surface energy for each optimization condition.

The 3D surface-response plots **(Figure 5.3f,g)** illustrate the interplay between physical and chemical effects governing surface wettability. We find that contact-angle evolution is primarily driven by physical modification - i.e., micro/nanostructuring - as the most pronounced

increase, from 103° for flat PDMS to 139° after the 1st-step $SF_6$ treatment, arises from topographical restructuring rather than chemistry alone. For comparison, chemical modification alone yielded only ~10° enhancement for both flat and microstructured surfaces **(Figures 5.2c and 5.3c, respectively)**. When both effects were combined after the 3rd-step optimization, the contact angle reached 152.2°, indicating the optimal condition achieved by sequential $O_2$ (450 s) and $SF_6$ (450 s) plasma treatment **(Figure 5.3f)**. Conversely, the reduction in surface critical energy is mainly dictated by chemical modification under $SF_6$ plasma, particularly at longer plasma durations, which promotes the formation of an ultrathin fluorinated layer that effectively lowers the surface energy to values as low as 17 $mN \cdot m^{-1}$ **(Figure 5.3g)**. The convergence of these two effects identifies the $T_9$ condition ($O_2/SF_6$: 450/450 s) as the optimal RIE processing window, yielding surfaces with maximized hydrophobicity, minimized surface energy, and, consequently, the most efficient balance of self-cleaning and energy-harvesting performance.

To confirm the effectiveness of the fluorination functionalization, XPS analysis was performed to elucidate the chemical transformations induced by each plasma condition **(Figure 5.3d)**. After $O_2$ plasma treatment ($T_7$), the survey spectrum revealed a pronounced increase in the O *1s* intensity (~532 eV) accompanied by a corresponding decrease in the C *1s* signal (~285 eV), indicating oxidation-induced depletion of surface –Si–$CH_3$ groups and formation of –Si–O– and –Si–OH functionalities. In contrast, $SF_6$-treated samples ($T_5$ and $T_9$) displayed a F *1s* peak at ~689 eV, consistent with the presence of Si–F bonds,[571] confirming successful fluorination of silicon sites. These compositional transitions from polar oxygenated to non-polar fluorinated chemistries directly account for the observed decrease in surface energy and enhancement in hydrophobicity, establishing RIE treatment as a straightforward route to modulate surface physicochemical properties for self-cleaning and energy harvesting.

To further elucidate the chemical nature of the surface terminations, high-resolution XPS spectra were analyzed under the optimized plasma conditions **(Figure 5.3i-n)**. In pristine PDMS, the F *1s* signal was absent **(Figure 5.3i)**, confirming the lack of fluorine incorporation. In contrast, the optimized $O_2/SF_6$ plasma-treated surface ($T_9$) exhibited a pronounced F *1s* peak centered at 689.5 eV **(Figure 5.3l)**, which was deconvoluted into components at 686.2 eV (Si–F), 687.5 eV (CF–Si interfacial species), and 689.5 eV (C–$F_2$/C–$F_3$), reflecting the coexistence of inorganic and organic fluorinated bonds.[572–574] The presence of the higher-binding-energy component (C–$F_2$/C–$F_3$) evidences the formation of a covalently bound fluorocarbon layer on the oxidized PDMS surface. In contrast, the sample treated without the oxidation step ($T_5$) displayed a narrower single peak at 689.5 eV **(Figure 5.3i)**, indicating predominantly Si–F

bonding and limited chemical coupling between fluorine and carbon or oxygen. This distinction confirms that the $O_2$ pre-activation step introduces oxygenated reactive sites that promote covalent fluorocarbon formation, leading to enhanced chemical stability and surface hydrophobicity.

Further insight into the surface chemical evolution was obtained from the high-resolution Si *2p* and C *1s* spectra **(Figure 5.3j-n)**, supporting the fluorination and oxidation mechanisms inferred from the F *1s* analysis. For pristine PDMS, the Si *2p* spectrum **(Figure 5.3j)** exhibits a single symmetric component at ca. 102.4 eV,[575] characteristic of the Si–O–Si network in the siloxane backbone. After the optimized $O_2/SF_6$ plasma treatment ($T_9$), the Si *2p* envelope broadens and can be deconvoluted into two components: 102.4 eV, assigned to Si–O–Si, and ~103.8 eV, attributed to Si–F/Si–O–F species **(Figure 5.3m)**.[573,575] The shift toward higher binding energy originates from the stronger electronegativity of fluorine, which withdraws electron density from silicon, increasing its effective positive charge and consequently the Si *2p* binding energy. These features confirm the formation of fluorosilane-like bonds ($Si–F_x$) and the partial substitution of surface methyl groups by fluorinated and oxygenated species, consistent with the enhanced chemical stability of fluorinated surfaces shown in **Figure 5.4f**.

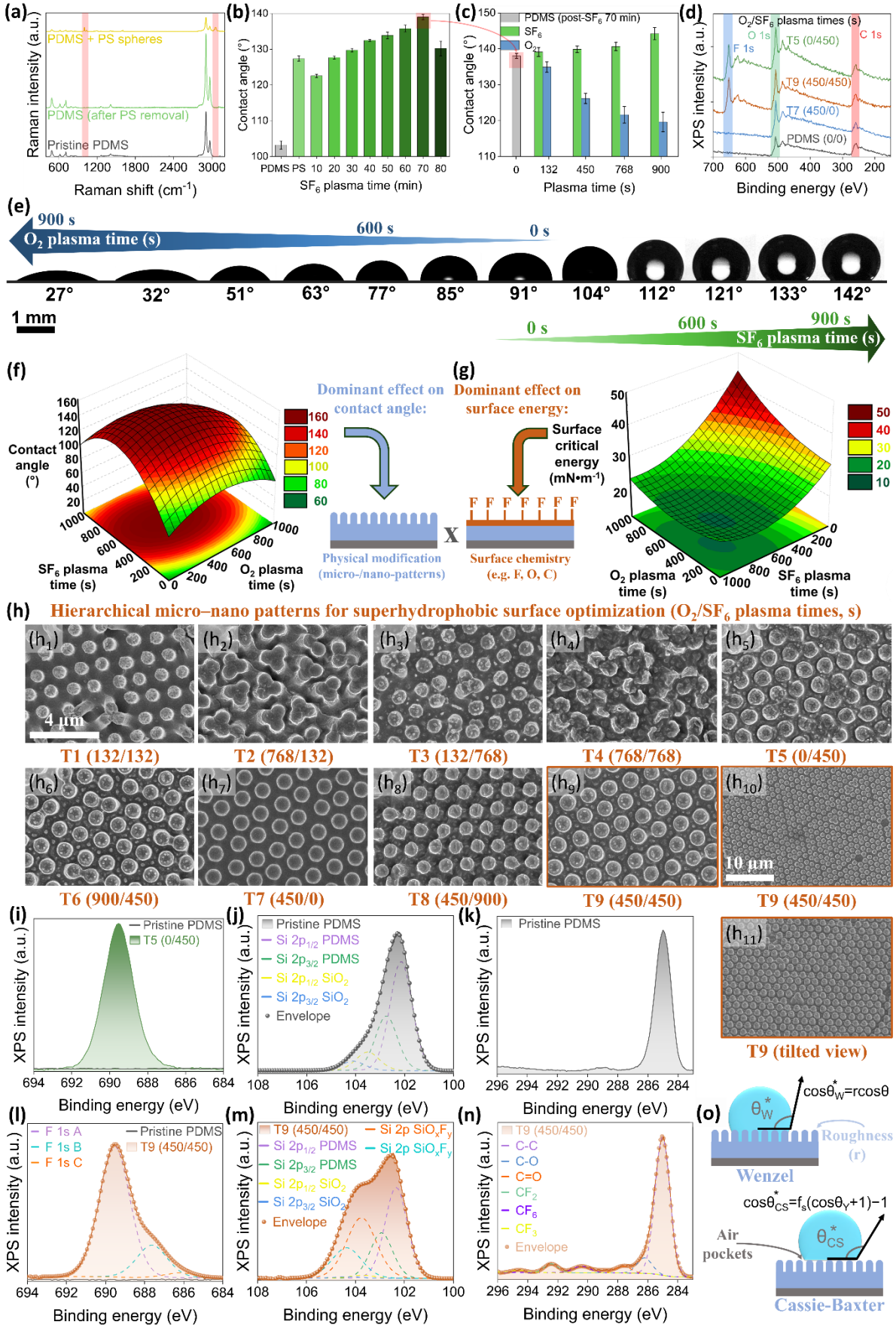
(a)
Raman intensity (a.u.)
PDMS + PS spheres
PDMS (after PS removal)
Pristine PDMS
Raman shift (cm-1)
(b)
Contact angle (°)
PDMS PS 10 20 30 40 50 60 70 80
SF6 plasma time (min)
(c)
PDMS (post-SF6 70 min)
SF6
O2
Contact angle (°)
Plasma time (s)
(d)
O2/SF6 plasma times (s)
O 1s
F 1s
C 1s
T5 (0/450)
T9 (450/450)
T7 (450/0)
PDMS (0/0)
XPS intensity (a.u.)
Binding energy (eV)
(e)
900 s
O2 plasma time (s)
600 s
0 s
27° 32° 51° 63° 77° 85° 91° 104° 112° 121° 133° 142°
1 mm
0 s
600 s
900 s
SF6 plasma time (s)
(f)
Contact angle (°)
SF6 plasma time (s)
O2 plasma time (s)
Dominant effect on contact angle:
Physical modification (micro-/nano-patterns)
(g)
Dominant effect on surface energy:
Surface critical energy (mN•m-1)
Surface chemistry (e.g. F, O, C)
O2 plasma time (s)
SF6 plasma time (s)
(h)
Hierarchical micro–nano patterns for superhydrophobic surface optimization (O2/SF6 plasma times, s)
4 μm
T1 (132/132)
T2 (768/132)
T3 (132/768)
T4 (768/768)
T5 (0/450)
T6 (900/450)
T7 (450/0)
T8 (450/900)
T9 (450/450)
T9 (450/450)
10 μm
T9 (tilted view)
(i)
Pristine PDMS
T5 (0/450)
XPS intensity (a.u.)
Binding energy (eV)
(j)
Pristine PDMS
Si 2p1/2 PDMS
Si 2p3/2 PDMS
Si 2p1/2 SiO2
Si 2p3/2 SiO2
Envelope
(k)
Pristine PDMS
(l)
F 1s A
F 1s B
F 1s C
Pristine PDMS
T9 (450/450)
(m)
T9 (450/450)
Si 2p SiOxFy
Si 2p1/2 PDMS
Si 2p3/2 PDMS
Si 2p1/2 SiO2
Si 2p3/2 SiO2
Envelope
(n)
T9 (450/450)
C-C
C-O
C=O
CF2
CF6
CF3
Envelope
(o)
cosθ*W=rcosθ
θ*W
Roughness (r)
Wenzel
cosθ*CS=fs(cosθY+1)−1
θ*CS
Air pockets
Cassie-Baxter

**Figure 5.3.** Hierarchical micro/nanostructuring surface-chemistry optimization of PDMS via $O_2/SF_6$ plasma treatment. (a) Raman spectra of pristine PDMS, PDMS coated with colloidal polystyrene (PS) spheres, and PDMS after PS sphere removal. (b) Water contact angle as a function of the 1st-step $SF_6$ plasma treatment (0-80 min) applied to PDMS coated with colloidal PS spheres. (c) Water contact angle evolution of microstructured PDMS surfaces subjected to $O_2$ or $SF_6$ plasma treatments (0-900 s) following the initial 70-min $SF_6$ microstructuring step. (d) XPS survey spectra of pristine PDMS (black), $SF_6$-only plasma ($T_5$, green), $O_2$-only plasma ($T_7$, blue), and the optimized $O_2/SF_6$ condition ($T_9$, orange). (e) Digital images of water contact angles on PDMS surfaces after $O_2$ or $SF_6$ plasma treatments with increasing exposure time (0-900 s). (f) Response surface of water contact angle *vs* $O_2$ and $SF_6$ plasma times, highlighting the dominant effect of physical modification (micro/nanostructuring). (g) Response surface of critical surface energy *vs* $O_2$ and $SF_6$ plasma times, highlighting the dominant contribution of chemical modification (oxidation/fluorination). (h) SEM images of micro/nanostructures produced under plasma conditions $T_1$-$T_9$ (12 k×, scale bar = 4 μm); ($h_{10}$) larger-area view of the $T_9$ optimized surface (3.5 k×, scale bar = 10 μm), and ($h_{11}$) tilted view. (i-n) High-resolution XPS spectra with peak deconvolution/envelope: F *1s* for (i) pristine PDMS and $O_2$-only plasma $T_5$, and (l) optimized $T_9$; O *1s* for (j) pristine PDMS, and (m) optimized $T_9$; and C *1s* for (k) pristine PDMS, and (n) optimized $T_9$. (o) Schematics of Wenzel and Cassie-Baxter wetting regimes and their dependence on surface roughness and trapped air, used to infer the intrinsic contact angle from the respective models.

Complementary changes are observed in the C *1s* spectra, where the pristine PDMS surface **(Figure 5.3k)** exhibits a dominant C–Si/C–C peak at ~284.5 eV and a weak C–O contribution near 286 eV,[576,577] characteristic of native surface oxidation. In contrast, the optimized fluorinated surface, i.e., $T_9$ (Figure 5.3n), displays multiple new components in the C *1s* spectrum, assigned to C–O (286.3 eV) and C=O (287.7 eV) species arising from the 450 s $O_2$ activation, together with high-binding-energy fluorocarbon peaks corresponding to $CF_2$ (~290.5 eV) and $CF_3$ (~292.3 eV) formed during the 3rd-step fluorine functionalization.[578–581] The coexistence of oxygenated and fluorinated species demonstrates the synergistic coupling between $O_2$ activation and $SF_6$ fluorination: the oxygen plasma generates surface hydroxyl and silanol groups that serve as reactive anchoring sites for covalent fluorination, while the subsequent $SF_6$ plasma contributes both physical etching and chemical passivation through the formation of stable Si–F and C–$F_x$ moieties. XPS thus confirms that sequential $O_2/SF_6$ plasma processing transforms the initially methyl-terminated PDMS surface into a mixed fluorosiloxane/fluorocarbon interface.

To further corroborate the effectiveness of this fluorination process, the long-term chemical stability of the optimized surfaces was evaluated by monitoring the water contact angle immediately after plasma functionalization and after three sequential $H_2O$ rinsing cycles **(Figure 5.3f)**. The results reveal minimal variation in contact angle for samples subjected to combined oxidation and fluorination ($T_4$, $T_6$, $T_8$, and $T_9$), indicating superior chemical stability and

robust covalent fluorine incorporation, consistent with the XPS findings. In contrast, single-step plasma treatments ($O_2$-only or $SF_6$-only) exhibited the largest contact angle variations, of ca. 14 and 10%, respectively, demonstrating poor functional retention upon aqueous rinsing. Moreover, short $O_2$ activation times (e.g., $T_3$, 132 s) also resulted in significant variation (~12%), suggesting insufficient surface activation and incomplete fluorine grafting. These results collectively confirm that the sequential $O_2/SF_6$ treatment is essential for achieving stable, covalently anchored surface terminations capable of preserving low surface energy and functional durability under humid conditions.

### 5.3.4 Self-cleaning mechanisms of hierarchical $O_2/SF_6$-engineered PDMS surfaces

Before evaluating self-cleaning efficiency and chemical stability, we analyzed how sequential RIE steps modify the PDMS surface, as this understanding underpins the interpretation of the subsequent results. **Figure 5.4d** summarizes the surface evolution during micro/nanostructuring and chemical functionalization designed to enhance self-cleaning and energy harvesting. The chemical inertness of pristine PDMS originates from its outermost methyl groups (–Si–$CH_3$), which shield the siloxane backbone and confer hydrophobicity. Direct $SF_6$ plasma exposure primarily induces fluorine-driven etching with minor formation of a thin fluorinated residue, depending on exposure time and plasma parameters, but without establishing stable covalent fluorination. Although such layers yield transient hydrophobicity, they readily degrade under environmental stress. To overcome this limitation, an $O_2$ plasma pre-activation step was introduced to enable efficient fluorination. $O_2$ plasma oxidizes surface methyl groups, producing silanol (Si–OH) and siloxane (Si–O–Si) functionalities that increase surface energy and create reactive sites. Subsequent $SF_6$ plasma then substitutes these groups with stable Si–F and C–F bonds. This two-step process yields an architecture that contains covalently bonded fluorinated moieties, ensuring a robust and tunable route for durable surface fluorination.

Building upon this mechanistic understanding, we next correlate the surface chemistry with macroscopic by evaluating the self-cleaning capability of the hierarchical micro/nanostructured PDMS surfaces under both water- and air-assisted conditions. This assessment elucidates the interplay between micro/nanostructure, surface chemistry, wettability, and long-term functional stability **(Figure 5.4)**. To ensure quantitative and reproducible as-

sessment of cleaning performance, methylene blue (MB) was employed as a model contaminant owing to its well-defined UV-Vis absorbance characteristics. The calibration curve of MB at $\lambda$ = 665 nm **(Figure 5.4a)** enabled direct quantification of residual surface contamination after self-cleaning, allowing comparison of cleaning efficiencies among treatments. The UV-Vis spectra **(Figure 5.4b)** display the characteristic MB absorbance and confirm that the optimized $O_2/SF_6$ plasma-treated surface ($T_9$) shows the lowest residual signal, corresponding to 83 and 91% contaminant removal efficiency under water and air-assisted cleaning, significantly higher than pristine PDMS (12, and 26%, respectively). We attribute this enhanced self-cleaning performance to the synergistic effects of hierarchical micro/nanostructuring and fluorination, which together produce a low-surface-energy interface that minimizes contaminant adhesion. Furthermore, the optimized hierarchical surface ($T_9$) demonstrates the outstanding water repellence by resisting adhesion even under applied force, a hallmark of superhydrophobicity, which in turn enables facile contaminant removal and efficient self-cleaning performance.[582]

The radar plot **(Figure 5.4c)** quantitatively compares self-cleaning performance across all optimized plasma conditions, highlighting the superior efficiency of sequential $O_2/SF_6$ treatments. For water-assisted self-cleaning, both surface extremes characteristic (hydrophilic and hydrophobic) exhibit high cleaning efficiency due to distinct mechanisms: water infiltration with capillary lifting on hydrophilic surfaces (e.g., $T_7$), and rolling droplet removal on hydrophobic surfaces (e.g., $T_9$). This indicates that surface chemistry dominates over microstructuring in water-assisted cleaning. Conversely, in air-assisted self-cleaning, the best performance was achieved for micro/nanostructured surfaces ($T_8$, $T_9$, and $SF_6$ 70 min), suggesting a structural-driven mechanism. To isolate the chemical effect, flat PDMS samples were selectively hydrophilized by $O_2$ plasma or hydrophobized by $SF_6$ plasma. The optical images **(Figure 5.4e)** reveal progressive contaminant removal with increasing plasma exposure, with both surfaces exhibiting cleaning behavior, most pronounced at the lowest critical surface energy achieved, i.e., after extended $SF_6$ plasma.

Based on these collective results, we propose four distinct self-cleaning mechanisms that depend on the cleaning medium (water *vs* air) and the surface state (hydrophilic *vs* hydrophobic, flat *vs* structured), as summarized in **Figure 5.4g**. Water-assisted cleaning operates through (i) capillary-induced particle lifting on hydrophilic surfaces and (ii) rolling-induced detachment on hydrophobic surfaces, both enhanced by hierarchical roughness. In contrast, for air-assisted cleaning, we identify two distinct behaviors: (iii) drag-induced detachment on

hydrophobic structured surfaces due to reduced adhesion and (iv) particulate retention on hydrophilic surfaces, where high surface energy promotes strong particle adhesion. These complementary mechanisms collectively demonstrate how the synergistic control of surface chemistry and topology governs the balance between contaminant adhesion, detachment, and durability, thereby underpinning the exceptional self-cleaning behavior of the optimized hierarchical micro/nanostructured PDMS surface ($T_9$).

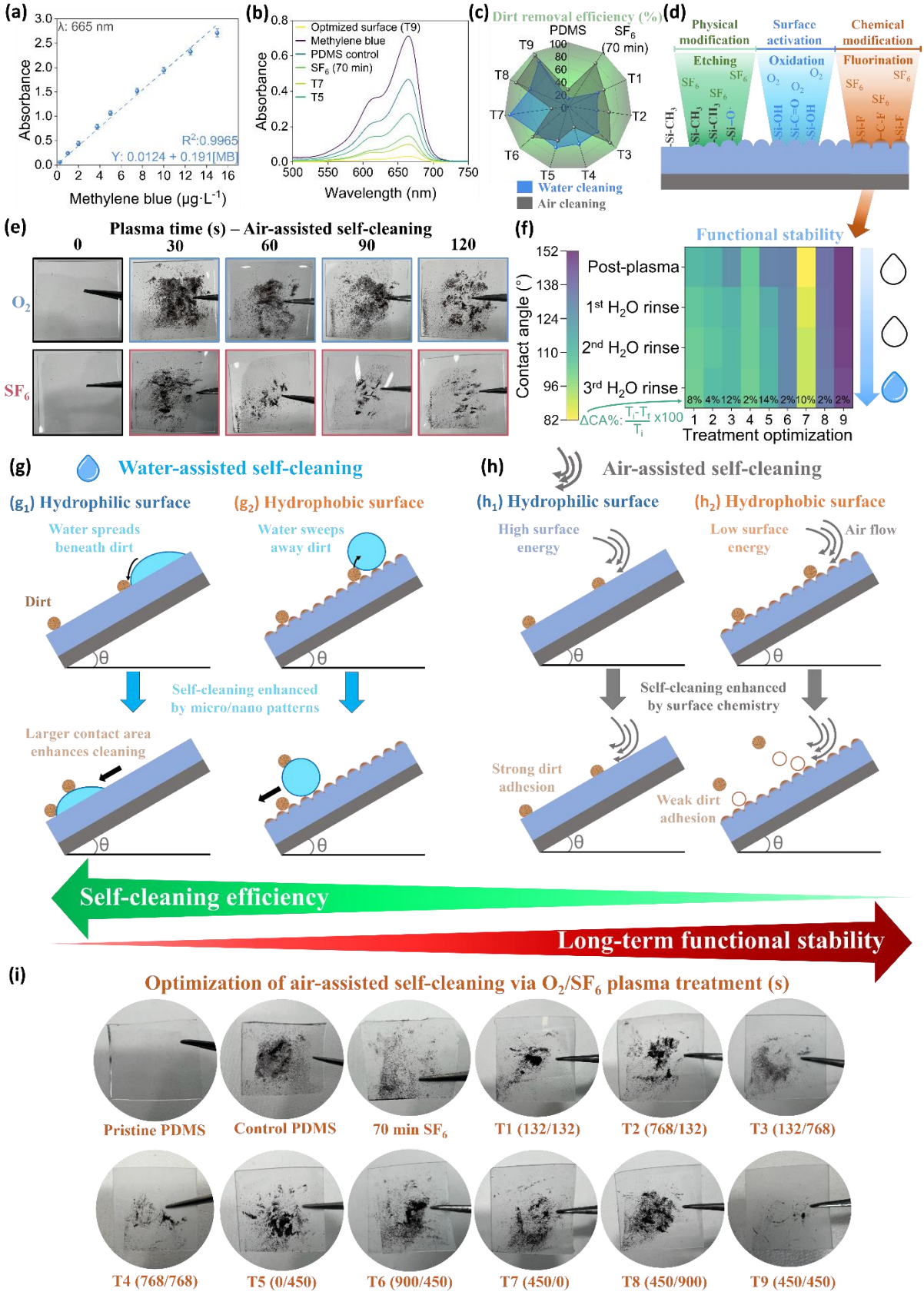


**Figure 5.4.** Surface modification and optimization of PDMS via $O_2/SF_6$ plasma treatment for self-cleaning. (a) Calibration curve of methylene blue (MB) absorbance ($\lambda$ = 665 nm) for quantification of contaminant removal. (b) UV-

Vis spectra comparing pristine PDMS, $SF_6$-only plasma (70 min, $T_5$), $O_2$-only plasma ($T_7$), optimized $O_2/SF_6$ plasma ($T_9$), and MB-contaminated PDMS. (c) Radar plot of dirt removal efficiency for air- and water-assisted cleaning. (d) Schematic illustration of the sequential PDMS modification pathway: $SF_6$ plasma etching removes surface –Si–$CH_3$ groups, oxygen plasma introduces polar groups functionalities (-Si-OH, -Si-O-Si, C=O) that increase reactivity, and subsequent $SF_6$ plasma treatment yields stable fluorinated terminations (Si-F, C-F), lowering surface energy. (e) Digital photographs of PDMS surfaces treated with $O_2/SF_6$ plasma for 0-120 s before and after air-assisted cleaning. (f) Functional stability of surface chemistry by contact angle evaluation after successive $H_2O$ rinsing steps ($1^{st}$-$3^{rd}$ cycles). Schematic illustration of (g) water- and (h) air-assisted self-cleaning mechanisms. In water-assisted cleaning, both hydrophilic ($g_1$) and hydrophobic ($g_2$) surfaces enable efficient contaminant removal: on hydrophilic surfaces, water spreads beneath particles and lifts them away, while on hydrophobic surfaces rolling droplets sweep contaminants off. In air-assisted cleaning, performance mainly depends on surface energy: hydrophilic surfaces ($h_1$) retain dirt due to strong adhesion, whereas hydrophobic surfaces ($h_2$) promote weak adhesion and facile removal under airflow. Arrows indicate that water-assisted cleaning is effective at both extremes of surface wettability but offers limited long-term stability, as water can alter surface chemistry and increase surface energy. In contrast, air-assisted self-cleaning is most efficient on low-surface-energy (hydrophobic) surfaces and, by avoiding water exposure, preserves chemical terminations and ensures greater long-term durability. (i) Digital photographs showing residual contaminants on optimized PDMS surfaces ($T_1$-$T_9$) after air-assisted self-cleaning.

Thus, we propose that air-assisted self-cleaning operates primarily through surface energy and adhesion modulation. Hydrophilic surfaces, characterized by high surface energy, promote strong contaminant adhesion, whereas fluorinated hydrophobic surfaces minimize interfacial forces, facilitating particle detachment under airflow. As illustrated in **Figure 5.4h**, these low-surface-energy fluorinated micro/nanostructures enable efficient dirt removal by reducing, e.g., van der Waals and electrostatic interactions. Furthermore, since $H_2O$ rinsing tends to remove residual $O_2$- and $SF_6$-derived ultrathin films (as evidenced in **Figures 5.2b-c, and 5.4f**), the absence of liquid in air-assisted cleaning ensures that the surface chemistry remains minimally altered, thereby preserving its chemical terminations and ensuring superior long-term functional stability compared to water-assisted cleaning.

**Figure 5.4i** presents the final residual contaminants on surface states after air-assisted self-cleaning, corresponding to the efficiencies summarized in **Figure 5.4c**. exhibits the highest contaminant removal, significantly outperforming all other treatments. Collectively, these results demonstrate that the enhanced self-cleaning performance arises from the synergistic coupling of hierarchical structuring and chemical fluorination, which together reduce surface energy and contamination adhesion while maintaining excellent functional stability. Beyond this, our goal is to translate these surface-engineered PDMS architectures into sustainable, self-

powered pressure sensors for precise and reliable manipulation in soft robotic or surgical applications. Therefore, in *Section 5.3.5*, we investigate how the optimized PDMS surface functions as a TENG-based electronic skin, elucidating its effects on energy harvesting, pressure sensitivity, long-term operational durability, and smart integration.

### 5.3.5 Enhanced energy harvesting and stability via hierarchical surface design

The triboelectric response of the surface-engineered PDMS architectures was evaluated using a single-electrode TENG configuration, in which the structured PDMS layer served as the active triboelectric component and carbon as the counter electrode. The operating principle of the HMN-TENG is schematically illustrated in **Figure 5.5a**. In the initial state (i), no electrostatic potential difference exists between the triboelectric layers. Upon contact **(Figure 5.5a$_1$)**, interfacial charge transfer is triggered by the difference in triboelectric affinities: the hierarchically structured PDMS layer, possessing a higher electron affinity, acquires negative charges, whereas the wood counterpart becomes positively charged, establishing an oppositely charged interface. During separation **(Figure 5.5a$_2$-a$_3$)**, the increasing interlayer gap induces an electrostatic potential difference that drives electron flow through the external circuit. Upon recontact **(Figure 5.5a$_4$)**, electron backflow neutralizes the charge imbalance, and repeated contact-separation generates a continuous AC output that underpins the device's self-powered operation.

Systematic evaluation of $SF_6$ plasma exposure (0-70 min) during the 1$^{st}$-step optimization **(Figure 5.5c)** shows a steady increase in $V_{oc}$ with plasma duration ($V_{oc} = 12.87 + 0.14t_s f_6$; $R^2 = 0.984$), confirming that progressive microstructuring enhances the effective contact area and, consequently, charge generation. The highly ordered surface patterning observed in the tilted SEM image **(Figure 5.5i)** yields a 191% increase in $V_{oc}$, from 12.1 to 23.3 V, demonstrating that the microstructuring substantially improves both energy-harvesting and self-cleaning performance.

To elucidate the origin of this enhancement, COMSOL® simulations were performed using identical device dimensions and material parameters. The results reveal a 469% increase in electric field intensity for the HMN-TENG ($\Delta V$ ~6.1 V·cm$^{-1}$) compared to the flat configuration ($\Delta V$ ~1.3 V·cm$^{-1}$), primarily due to localized field concentration at the micro/nano asperities. We assume that the deviation between simulated and experimental $V_{oc}$ values likely arises from interfacial impedance mismatch and parasitic charge dissipation. Nevertheless, these

findings confirm that the enhanced electrical output originates from the increased real contact area and charge density induced by hierarchical structuring.

The experimental $V_{oc}$ output reveals a distinct transition from a surface-chemistry-dominated regime to a morphology-dominated one as the applied pressure increases. At low pressures (e.g., 20 kPa), the output is primarily governed by surface chemistry, where extended SF6 plasma exposures promote ultrathin surface film formation and higher surface electronegativity, thereby enhancing charge transfer. In contrast, at high pressures (e.g., 100 kPa), deformation of the hierarchical micro/nanostructures becomes the dominant factor, facilitating full interfacial contact and efficient charge transfer.

Accordingly, we propose that at low pressure (20 kPa), $V_{oc}$ is dominated by the triboelectric surface potential difference with counterpart material, thus governed by surface chemistry **(Figure 5.5h)**, while at high pressure (100 kPa), the output is amplified by surface patterning effects, as mechanical compression increases both the effective contact area and charge density **(Figure 5.5j)**. The hierarchical micro/nano architecture thus functions as a mechanical-electrical amplifier, translating subtle mechanical deformations into pronounced electrical signals, thereby enabling high sensitivity self-powered dynamic pressure sensing.

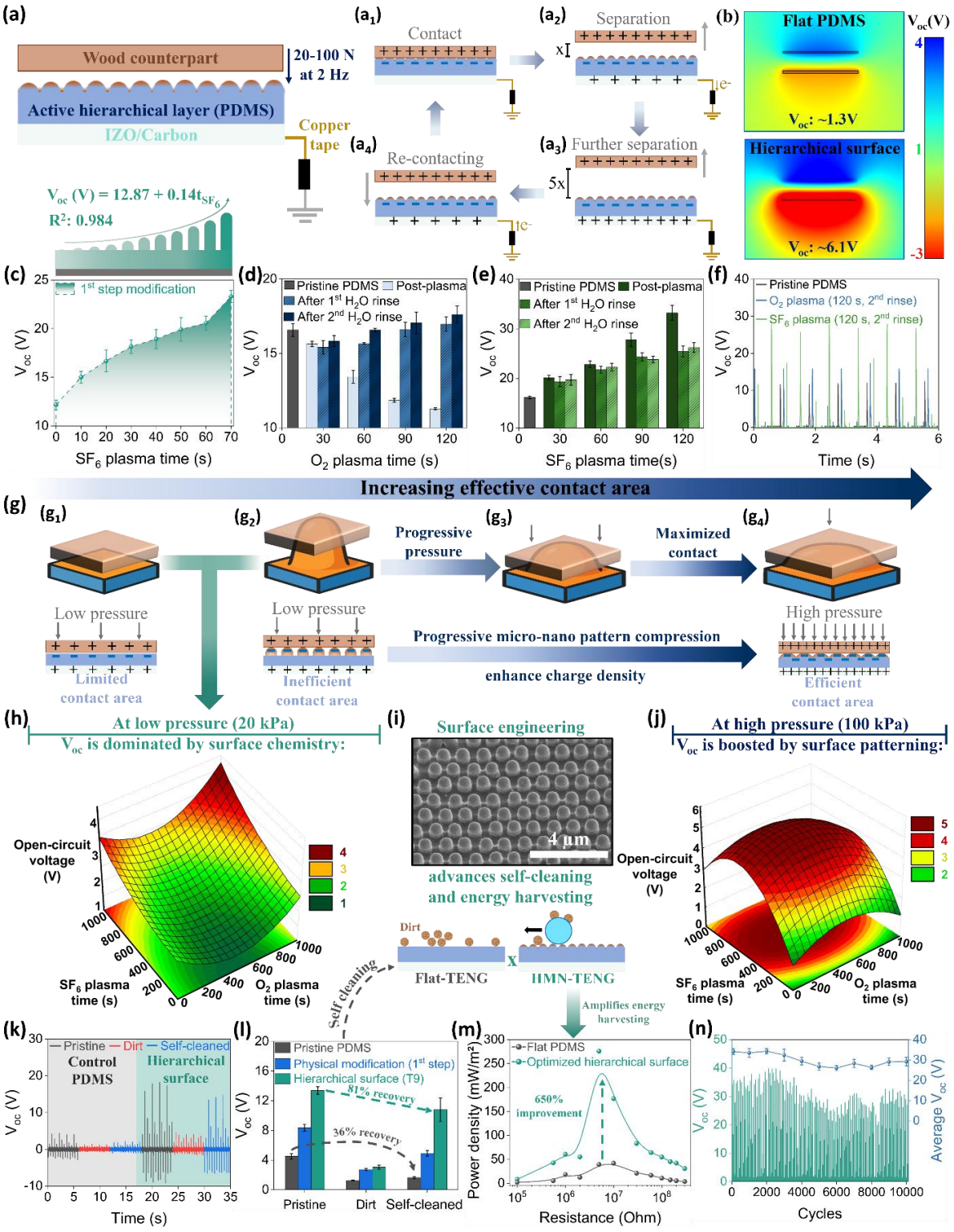


**Figure 5.5.** Hierarchical surface engineering of PDMS for self-cleaning and triboelectric energy harvesting. (a) Architecture of the single-electrode TENG with hierarchical PDMS active layer. ($a_1$-$a_4$) Working cycle illustrating contact, initial separation, extended separation, and maximum separation with charge transfer. (b) COMSOL® simulation of potential distribution on flat *vs* hierarchical PDMS. (c) $V_{oc}$ as a function of $SF_6$ plasma time during 1st-step modification. (d,e) Functional stability of $O_2$ and $SF_6$ plasma treatments evaluated by $V_{oc}$ after successive rinsing cycles, and (f) comparison of $V_{oc}$ peaks for pristine PDMS and plasma-treated PDMS (120 s, 2nd water rinse). (g)

Schematic illustration of contact area evolution: ($g_1$) flat PDMS showing limited contact at low pressure (~20 kPa); ($g_2$) hierarchical PDMS with ineffective contact without deformation; ($g_3$) progressive micro/nanostructures compression increasing contact fraction with pressure; and ($g_4$) efficient full contact at high pressure (~100 kPa), leading to increased charge density. (h-j) Pressure-dependent output mechanisms: $V_{oc}$ dominated by surface chemistry at low pressure (20 kPa, h) and by surface structuring at high pressure (100 kPa, j); (i) SEM of hierarchical PDMS highlighting surface engineering for self-cleaning and energy harvesting. (k) $V_{oc}$ peaks of flat and hierarchical PDMS surfaces under pristine, dirt-contaminated, and self-cleaned conditions. (l) Self-cleaning efficiency comparing flat PDMS and optimized hierarchical PDMS across pristine, dirt-contaminated, and self-cleaned states. (m) Power density *vs* resistance for flat and optimized hierarchical PDMS, with 650% improvement in energy harvesting. (n) Long-term stability of $V_{oc}$ over 10,000 continuous cycles.

To elucidate the origin of the enhanced sensitivity, **Figure 5.5g** illustrates the evolution of the effective contact area with applied pressure. The flat PDMS-TENG ($g_1$) exhibits limited interfacial contact, reaching its maximum contact area rapidly at low pressure. In contrast, the HMN-TENG ($g_2$-$g_4$) progressively deforms under compression, allowing the micro/nanostructures to collapse and maximize the effective contact area ($f_a$). This mechanical adaptability dynamically modulates the interfacial contact state, thereby enhancing charge-transfer efficiency and accounting for the superior pressure sensitivity of the HMN-TENG.

The functional stability of the plasma-engineered PDMS surfaces was evaluated by monitoring the $V_{oc}$ output after repeated water-rinsing cycles following $O_2$ and $SF_6$ plasma treatments **(Figure 5.5d,e)**. For $O_2$ plasma-treated samples, $V_{oc}$ decreased steadily from 16 V (pristine flat-PDMS) to 11 V after 120 s of exposure, indicating that the surface potential approached that of the counterpart material (wood), thereby reducing charge transfer efficiency. Upon successive water rinsing, $V_{oc}$ partially recovered to values close to pristine PDMS, indicating the removal of the loosely bound oxidized surface layer. A slight increase in $V_{oc}$ observed at short $O_2$ plasma durations can be attributed to mild surface roughening **(Figure 5.2g)**, which enhances the effective contact area.

In contrast, $SF_6$ plasma treatment induced a continuous increase in $V_{oc}$ from 16 to 33 V with increasing prolonged plasma exposure, confirming that fluorination and roughening act synergistically to enhance energy harvesting. However, after the 2$^{nd}$ water-rinsing cycle, $V_{oc}$ partially returned toward the pristine PDMS value, suggesting that part of the fluorinated layer was weakly physisorbed and removed upon rinsing, consistent with the contact-angle behavior in **Figure 5.2c**. Nevertheless, even after water-rinsing, the $SF_6$-treated surface retained a 62% higher $V_{oc}$ than pristine PDMS, indicating partial preservation of covalently bonded fluorine functionalities together with topography-induced roughness effects.

The comparison of $V_{oc}$ peaks after the 2nd rinse **(Figure 5.5f)** further supports this observation: while both $O_2$- and $SF_6$-modified PDMS surfaces exhibit similar partial recovery trends, the fluorinated surface retains substantially higher electrical output. These results are consistent with the contact angle and XPS analyses, confirming that both plasma treatments produce ultrathin oxidized or fluorinated surface layers that are partially removed upon aqueous rinsing. This chemical instability reinforces our conclusion that sequential surface activation by oxidation, followed by optimized fluorination, is essential to achieve durable functional stability for self-cleaning and energy-harvesting applications.

To further validate the self-cleaning efficiency and functional applicability of the engineered surfaces, we compared the $V_{oc}$ output of pristine flat PDMS-TENG (control) and the HMN-TENG under contaminated and after air-assisted self-cleaning **(Figure 5.5k)**. The results confirm that surface structuring enhances both dirt removal and electrical recovery: the hierarchical surface restored 81% of its initial output after self-cleaning, compared to only 42% for flat PDMS-TENG **(Figure 5.5l)**. In addition, the optimized hierarchical micro/nanostructures significantly increased the power density from 45 to ~270 $mW \cdot m^{-2}$, corresponding to a 650% improvement relative to pristine flat PDMS-TENG.

To ensure long-term $V_{oc}$ stability for reliable use as electronic skin in robotics **(Figure 5.5n)** we demonstrated excellent operational durability, with only a slight decrease in $V_{oc}$ after ~5,000 continuous cycles. This minor reduction is attributed to mechanical fatigue induced by repeated high-pressure loading within the plastic deformation regime of PDMS, which can locally alter the microstructure geometry. To mitigate this effect, we suggest operating the electronic skin within the elastic deformation range to maintain stable electrical performance during prolonged use.

Overall, these results demonstrate that hierarchical micro/nanostructuring combined with chemical fluorination synergistically enhances both self-cleaning efficiency and triboelectric performance while maintaining functional stability under realistic environmental conditions. This integrated design not only enables sustainable energy harvesting but also extends the functionality of the HMN-TENG toward advanced electronic skin applications, such as self-powered pressure sensing and rapid estimation of contact area, as detailed in *Section 5.3.6*.

### 5.3.6 Smart applications of hierarchical micro/nanostructured (HMN-TENG)

To evaluate the multifunctional potential of the hierarchically micro/nanostructured electronic skin, we demonstrated its implementation in HMN-TENG-based platforms for self-powered sensing, surface-area estimation, intelligent locking, and robotic actuation **(Figure 5.6)**. The self-powered pressure-sensing behavior was assessed by monitoring $V_{oc}$ as a function of applied pressure, comparing the optimized HMN-TENG with a flat PDMS-TENG reference **(Figure 5.6a)**. increased sharply and linearly with pressure, governed by surface-chemistry effects and gradual expansion of the contact fraction; in Region II (medium-high pressure), the flat control exhibited a markedly reduced sensitivity (0.03 $V \cdot kPa^{-1}$), as the contact area saturated, leading to negligible additional charge transfer **(Table 5.4)**.

**Table 5.4.** Figures of merit for structure-dependent PDMS-based TENG pressure sensors.

| Device structure | Pressure region | Detection range (kPa) | Sensitivity ($V \cdot kPa^{-1}$) | LOD ($kPa^{-1}$) | Response time $T_{90}$ (ms) | Recovery time $T_{90}$ (ms) |
|---|---|---|---|---|---|---|
| **Flat PDMS-TENG** | Light-to-medium | 11-55 | 0.13 | 4.6 | 15.3 | 14.7 |
| | Medium-to-high | 55-100 | 0.03 | 30.0 | 10.5 | 9.4 |
| **HMN-TENG** | Light-to-medium | 11-55 | 0.34 | 2.6 | 24.6 | 18.0 |
| | Medium-to-high | 55-100 | 0.06 | 10.0 | 15.8 | 14.1 |

In contrast, the HMN-TENG maintained an expanding effective contact area even under higher pressures, enabling clear pressure differentiation and achieving twice the sensitivity of the control (0.06 $V \cdot kPa^{-1}$ at 100 kPa). The HMN-TENG-based electronic skin exhibited higher sensitivity in the high-pressure regime (0.13 $V \cdot kPa^{-1}$), a low detection limit (LOD) of 2.6 $kPa^{-1}$, and rapid response and recovery times ($T_{90\%}$) of 24.6 and 18 ms, respectively, which is highly advantageous for delicate object handling and medical-surgical applications. The practical capability of the HMN-TENG as a self-powered pressure sensor was demonstrated by its ability to distinguish between light, medium, and high pressures during object manipulation (e.g.,

grasping a pipette), illuminating one, two, or three LEDs accordingly **(Figure 5.6b)**. With these results, we confirm that our hierarchical micro/nanostructures electronic skin enables fully self-powered pressure sensing without reliance on external energy sources, highlighting its potential for integration into intelligent robotic systems.

In addition to direct power generation, the HMN-TENG efficiently charged capacitors ranging from 0.1 to 1.0 μF within 30 s **(Figure 5.6d)**, exhibiting stable charging behavior suitable for wearable sensors applications. Furthermore, the HMN-TENG directly powered small electronic components (e.g., LED arrays and a digital calculator) without the aid of any external storage element. This was achieved solely by tapping an active surface area of ~30 $cm^2$ **(Figure 5.6j,k)**, underscoring its high instantaneous electrical output. These demonstrations confirm that hierarchical micro/nanostructuring markedly enhances energy-harvesting efficiency while maintaining self-cleaning performance and functional stability, establishing the HMN-TENG as a robust platform for next-generation intelligent technologies.

To underscore the exceptional performance and multifunctionality of the fabricated HMN-TENG, **Table 5.5** summarizes key figures of merit for high-performance self-powered triboelectric pressure sensors. Compared with previously reported PDMS-based and hybrid TENG architectures, our HMN-TENG stands out not only for its high sensitivity and broad dynamic range but also for its unique integration of transparency, flexibility, self-cleaning ability, and triboelectric voltage-based surface-area estimation, features rarely achieved concurrently in this field. This combination of electrical sensitivity, mechanical robustness, and multifunctionality positions the HMN-TENG among the most versatile and reliable PDMS-derived electronic skins reported to date, offering a solid foundation for next-generation intelligent and self-powered systems.

**Table 5.5.** Figures of merit comparison table for PDMS-based TENGs pressure sensors with diverse micro/nanostructured architectures.

| Materials (device structure) | Sensitivity ($V \cdot kPa^{-1}$) | Response time (s) | Linear detection range (kPa) | Functional features and smart application | Refs. |
|---|---|---|---|---|---|
| PDMS, BTO (microfrustum array) | 0.3 | 0.008 | 0-200 | - | [583] |
| PDMS, ITO, PET (pyramid arrays) | 0.002 | 0.040 | 0.3-428 | - | [584] |
| PDMS, Nylon, Kapton, $BaTiO_3$, Cu (cuboid-array-structure) | 0.01 | 40 | 0-1100 | - | [585] |
| PDMS, CNT (micro-structure) | 0.51 | 0.45 | 5-450 | - | [586] |
| PDMS, Cu, BC-CS (fiber structure) | 0.24 | - | 10-96 | - | [587] |
| PDMS, P(VDF-TrFE), Ag (flat structure) | 0.03 | - | 0-19.8 | - | [588] |
| PDMS, P(VDF-TrFE), Ag (50 μm ridge hierarchical nanoporous) | 0.37 | | | | |
| PDMS, P(VDF-TrFE), Ag (25 μm ridge hierarchical nanoporous) | 0.55 | | | | |
| PDMS (flat) | 0.009 | - | 5-50 | - | [589] |
| PDMS | 0.025 | | | | |

| | | | | | |
|---|---|---|---|---|---|
| (microstructure) | | | | | |
| PDMS, PTFE<br>(burrs microstructure) | 0.127 | | | | |
| PDMS, CNT, AgNWs, SPX<br>(coaxial structure fiber) | 0.39 | - | 4-18 | Smart glove | [590] |
| PDMS, Cotton, Silicone rubber, Cu<br>(microtilted bilayer sandwich) | 0.24 | 0.026 | 0-75 kPa | Motion recognition | [591] |
| PDMS, ITO<br>(micropyramid) | 0.29 | <0.1 | 0.4-7 | Touch pad | [592] |
| PDMS, CIP, NdFeB<br>(microciliaarray) | <0.001 | 0.2 | 0-1000 | Command controller | [593] |
| PDMS, PVA, Ag NWs<br>(hierarchical micro/nanostructure) | 0.071<br>0.010 | 0.025 | 0-75<br>75-250 | Tactile sensing | [594] |
| **PDMS, IZO, Carbon<br>(flat)** | **0.13<br>0.03** | **0.015<br>0.010** | **11-55<br>55-100** | **Flexible, transparent, and electronic skin** | **This work** |
| **PDMS, IZO, Carbon<br>(Hierarchical micro/nanostructure)** | **0.34<br>0.06** | **0.024<br>0.015** | **11-55<br>55-100** | **Flexible, transparent, electronic skin, self-cleaning, and superficial area estimation** | **This work** |

Footnote: Bacterial cellulose/chitosan (BC/CS); Barium titanate (BTO); Carbon nanotube (CNT); Carbonyl iron powder (CIP); Copper (Cu); Indium tin oxide (ITO); Indium zinc oxide (IZO); Neodymium-iron-boron (NdFeB); Nylon (PA); Poly(dimethylsiloxane) (PDMS); Poly(ethylene terephthalate) (PET); Poly(vinylidene fluoride-co-trifluoroethylene) [P(VDF-TrFE)]; Silver (Ag); Silver nanowires (Ag NWs); Spandex (SPX).

Beyond powering small electronics, the HMN-TENG was further employed as a self-powered electronic lock system **(Figure 5.6c)**, eliminating the need for external power sources and ensuring uninterrupted operation during electrical outages, thus preventing system failure or access interruptions. As a demonstration, real-time $V_{oc}$ signals were recorded during a coded input sequence ("1-3-5-9-Enter"), generated simply by touching the corresponding input electrodes **(Figure 5.6f)**. The resulting color map reveals distinct voltage intensities associated with each keypress, confirming that the generated electrical signals can reliably identify the correct password and unlock the system even in the absence of external power **(Figure 5.6h)**. This result highlights the capability of the HMN-TENG as a smart, self-powered interface for secure electronic access and autonomous IoT applications.

Rapid and self-powered surface-area estimation is a valuable functionality for adaptive soft-robotic and tactile systems, where real-time feedback on contact evolution enables precise manipulation and structural health assessment. Building on this need, we introduce a triboelectric voltage-based approach that estimates superficial area directly from the $V_{oc}$ output of the TENG without requiring external power or circuitry. Because $V_{oc}$ scales proportionally with the effective contact area, we demonstrate, for the first time, a triboelectric voltage-based methodology for real-time superficial-area estimation **(Figure 5.6g)**. The $V_{oc}$ exhibited a strong linear dependence on the planar contact area ($R^2 > 0.98$), with the microstructured surface showing markedly higher sensitivity than the flat PDMS-TENG **(Figure 5.6e)**. To ensure reliable measurement, we emphasize that the applied mechanical trigger must deform the active layer sufficiently to increase the effective contact fraction, thereby amplifying the $V_{oc}$ signal. Accordingly, the relationship between the applied mechanical tension and $V_{oc}$ should be analyzed to identify the plateau region, which indicates the pressure at which the effective contact area becomes saturated. Furthermore, calibration must be performed under identical material configurations and controlled test conditions (frequency, applied force, and temperature) to minimize variations in $V_{oc}$ arising from external parameters.

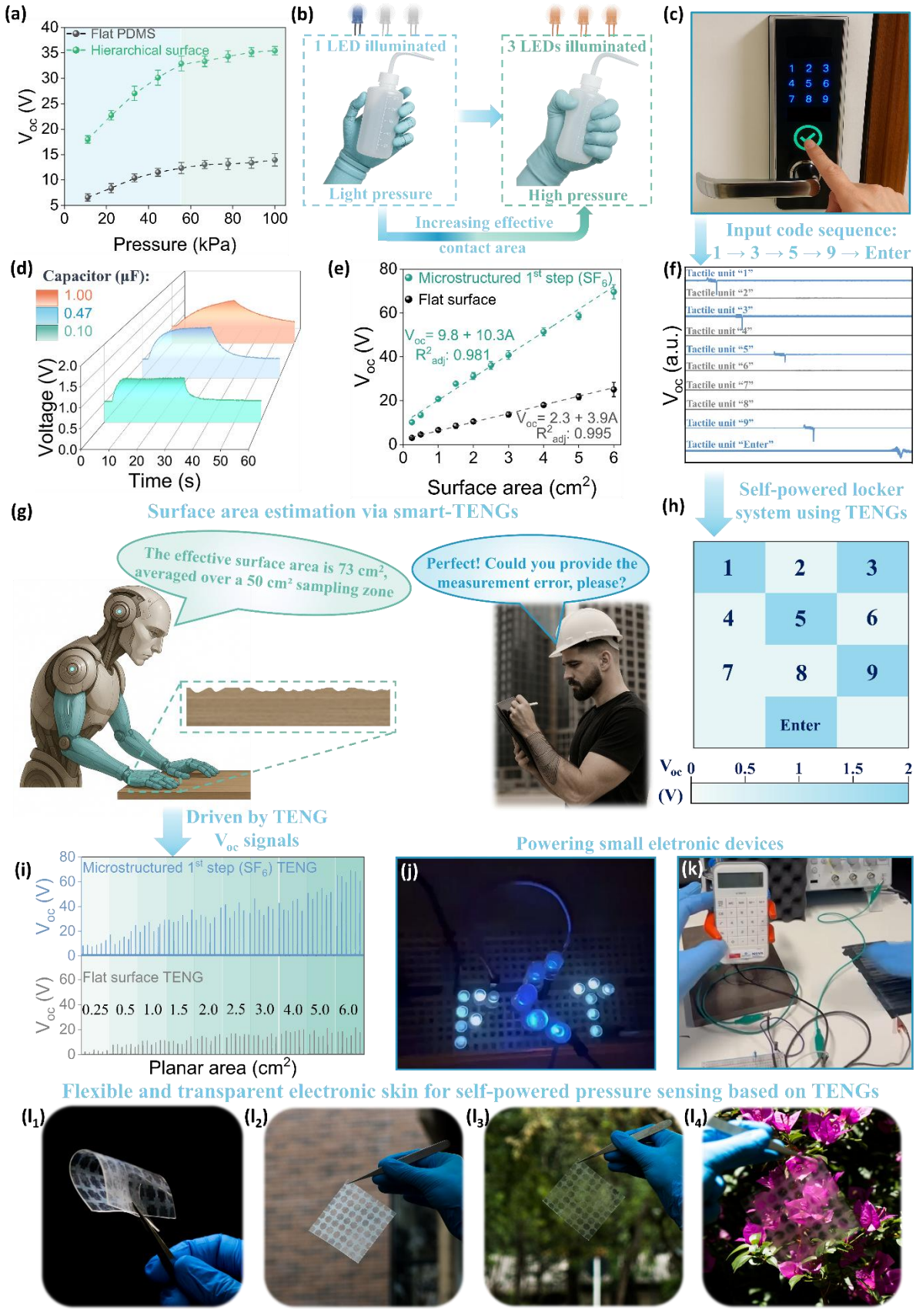


**Figure 5.6.** Smart applications of hierarchical micro/nanostructured triboelectric nanogenerators (HMN-TENGs). (a) Open-circuit voltage ($V_{oc}$) as a function of applied pressure for flat and HMN-TENGs, highlighting two distinct

response regions according to linear regression fits: Region I, light-to-medium pressure, and Region II, medium-to-high pressure regimes. (b) Schematic illustration of one-to-three LED sequential illumination corresponding to the $V_{oc}$ response under varying pressures. (c) Schematic illustration of a self-powered smart locker system operated by the HMN-TENG-based pressure sensor. (d) Charging profiles of capacitors (0.1-1.0 μF) powered by the HMN-TENG. (e) $V_{oc}$ output of flat-TENG and 1st-step ($SF_6$,70 min) TENG used for superficial-area estimation, demonstrating a linear relationship between $V_{oc}$ and contact area. (f) Real-time $V_{oc}$ signal corresponding to a coded input sequence ("1-3-5-9-Enter") in the self-powered smart-locker application. (g) Conceptual illustration of a robotic system utilizing TENG-derived $V_{oc}$ signals for superficial-area estimation, enabling rapid tactile feedback. (h) Color map of $V_{oc}$ response from the HMN-TENG-based keypad in smart-locker application, illustrating signal mapping for individual keypresses. (i) Comparison of $V_{oc}$ output for flat PDMS-TENG and HMN-TENG across planar areas from 0.25 to 6 $cm^2$, confirming the dependence of $V_{oc}$ output on effective contact area. Demonstrations of the HMN-TENG powering small electronic devices, including (j) blue LED arrays and (k) a digital calculator. Digital photographs of the flexible transparent electronic skin for self-powered pressure sensing via TENGs, showing ($I_1$) mechanical flexibility and optical transparency, and transparency retained under ($I_2$) brick, ($I_3$) foliage, and ($I_4$) flower backgrounds.

As shown in **Figure 5.6i**, the microstructured surface generated substantially higher $V_{oc}$ peaks than flat PDMS-TENG, confirming that surface structuring amplifies both the effective contact area. The observed linear correlation arises from the proportional increase in triboelectric charge with contact area. Once a calibration curve and regression model are established, unknown contact areas can be accurately estimated by measuring the corresponding $V_{oc}$ response under identical conditions. We further propose that this methodology can be refined through machine-learning algorithms, e.g. outlier detection and regression optimization, to enhance signal fidelity and predictive reliability.[10,302]

With this proof-of-concept, we highlight that our triboelectric voltage-driven strategy can extend beyond tactile sensing and robotic manipulation to monitor contact quality, deformation, or crack propagation by tracking surface-area variations in real time. Moreover, we envision that portable HMN-TENG patches could be deployed for structural health monitoring, e.g., assessing post-impact or post-seismic deformation, enabling rapid localization of compromised regions without external power depedence. Combined with its self-cleaning capability and energy-harvesting functionality, we believe this triboelectric-voltage-based surface-area estimation strategy, along with its associated smart applications, represents a versatile and valuable approach for next-generation robotic and self-powered systems.

## 5.4 Conclusion

Using colloidal lithography and $O_2/SF_6$ plasma-engineering strategy, we have fabricated a hierarchical micro/nanostructured electronic skin that integrates self-cleaning, energy-harvesting, and pressure-sensing functionalities via TENG. By coupling micropillar geometry with fluorinated nanoroughness, the electronic skin achieves concurrent optimization of surface energy, wettability, self-cleaning, and charge-transfer efficiency for triboelectric energy harvesting. To achieve this, we show that oxidation-induced surface activation enables covalent fluorination, forming stable Si–F and C–F terminations that yield chemically durable, low-surface-energy interfaces resistant to contamination and environmental degradation. The resulting HMN-TENG exhibits hydrophobicity (~152°) with self-cleaning efficiencies up to 91% and a 650% enhancement in power density (~270 $mW \cdot m^{-2}$) compared to flat PDMS-TENG, maintaining >80% electrical-output retention after 10,000 cycles and repeated contamination tests.

Furthermore, the smart HMN-TENG functions as a self-powered pressure sensor with dual-regime sensitivity (0.34 $V \cdot kPa^{-1}$ at low pressure; 0.06 $V \cdot kPa^{-1}$ at high pressure) and LOD: 2.6 $kPa^{-1}$, enabling real-time tactile mapping, smart lock control, and autonomous robotic operation. For the first time, we demonstrate that $V_{oc}$ output from TENGs can be harnessed for real-time superficial-area estimation, extending the multifunctionality and robustness of smart TENG-based electronic skins. Finally, we developed a flexible, transparent electronic skin that can enables real-time optical feedback for robotic sensing and wearable integration, providing a robust platform for next-generation soft-electronic systems. Altogether, this study establishes a comprehensive material–process–function correlation that unites surface physics, plasma chemistry, and triboelectric engineering into a single, tunable architecture.

# 6

# LIQUID FLOW ENERGY HARVESTING: A COMPREHENSIVE INSIGHTS ON THE ROLE OF LIQUID DYNAMICS FROM A WATER DROPLET TO A STREAMLINES

## 6.1 Introduction

Electrical double layers (EDLs) lie at the heart of interfacial electrostatics, governing how charges accumulate, redistribute, and interact across liquid-solid (L-S) boundaries. Its influence spans a broad range of technologies - from capacitive and chemical sensing,[595,596] electrostatic precipitators,[597] and electrospinning to field-effect electronic devices,[598,599] MEMS actuators,[600] and surface-potential imaging[601] - underscoring its central role in modern materials science and electrochemical energy systems. More recently, with the global transition toward sustainable energy technologies, efforts to exploit interfacial phenomena for renewable energy harvesting have intensified.[529,602] Among these, triboelectric nanogenerators (TENGs) have emerged not only as efficient platforms for energy harvesting but also as experimental probes for charge-transfer processes at L-S interfaces.[109,603] They can harvest energy from ubiquitous, low-grade sources, e.g., fluid motion from raindrops, ocean waves, and domestic water streams, which remains one of the most abundant yet least efficiently utilized forms of renewable energy.[529]

Although numerous liquid-solid triboelectric nanogenerators (L-S TENGs) have demonstrated impressive electrical output performance,[15-17] e.g., achieving up to 50.1 $W \cdot m^{-2}$ per wa-

ter droplet,[607] the fundamental origins of charge transfer - arising from electron and ion contributions in liquid flows - remain controversial.[19-22] These mechanisms become even more complex when electrolyte-mediated EDL formation is involved, particularly through ionic interactions and strength coupled with fluid motion. As water transitions from droplet impact to continuous streamline flow, variations in shape, interfacial shear stress, and contact persistence modulate both charge separation and ion redistribution,[611,612] thereby altering the electrical output of L-S TENGs.[102,111] Yet many studies do not isolate the mechanical impact of the liquid or properly ground the system, obscuring the distinction between genuine L-S electrification, residual electrostatic effects, and flow-induced electrostatic induction. Establishing a comprehensive physical framework that decouples interfacial charge transfer from these hydrodynamic and electrostatic complexities is therefore essential for improving energy-conversion efficiency and advancing intelligent sensing applications.[102,111]

Recent advances have begun to address these intertwined L-S electrification phenomena. Wang et al.[87,110] proposed a "two-step" model for EDL formation in which electron transfer plays a dominant role in L-S contact electrification (CE). Their analysis indicates that CE between hydrophilic surfaces and aqueous solutions is governed primarily by ion transfer, whereas that between hydrophobic surfaces and aqueous solutions is dominated by electron transfer. The model further suggests that solutes such as Na+ and Cl- suppress electron transfer across the interface, thereby reducing electrical output. However, this conclusion contrasts with several experimental studies reporting enhanced charge transfer and, consequently, higher energy harvesting at low electrolyte concentrations,[3,128,613–621] underscoring the need for systematic investigations to reconcile these discrepancies and clarify the governing mechanisms.

Comprehending charge transfer in L-S electrification extends beyond the pursuit of new energy-harvesting mechanisms; it also enables devices that function as self-powered sensors, capable of providing electrical energy and environmental information from the same physical event. Because liquids inherently carry ionic species, flow-induced charge transfer is sensitive to chemical composition, serving as a fingerprint for real-time sensing of liquid,[622] heavy metals,[623] and ionic content.[620] This coupling transforms each droplet or streamline from a passive carrier of mass into a generator of both information and power. Establishing these relationships not only provides a mechanistic understanding of interfacial L-S electrification but also lays the groundwork for engineering devices that self-power and self-sense, opening pathways beyond energy conversion toward multifunctional and intelligent technologies.

To bridge this knowledge gap, we propose a unified framework for L-S electrification and dynamic EDL formation during liquid flow, advancing the understanding of interfacial charge transfer under diverse electrolytic conditions. We systematically isolate key factors often overlooked in L-S electrification, e.g., liquid impact, flow regime, dielectric shielding, and flow-induced potentials linked to ionic strength and electrolyte type. By studying L-S electrification across 18 different electrolytes, we decouple the respective roles of EDL dynamics and ionic effects in governing the electrical output of L-S TENGs. We further demonstrate that TENGs can operate as wireless antennas for energy harvesting from flowing liquids via flow-induced electrokinetic potentials, enabling non-contact energy conversion and self-powered sensing such as non-invasive potentiometric detection. Finally, we illustrate their potential in smart applications by activating electrochromic transitions in windows through L-S electrification, simulating raindrop-driven energy for autonomous color modulation in automotive systems.

These findings advance the fundamental understanding of L-S electrification and dynamic EDL behavior, fostering the development of EDL-governed technologies, e.g., supercapacitors, electrocatalysis, electrochemical sensing, and energy harvesting, and opening new avenues toward self-powered, multifunctional, and intelligent applications.

## 6.2 Experimental section

### 6.2.1 Materials

Ethanol (96%) was obtained from LabChem (Zelienople, PA, USA). Sylgard® 184 silicone elastomer kit was purchased from Dow Corning®. Copper tape was supplied by 3M™. sodium sulfate, sodium bromide, magnesium sulfate, potassium chloride, sodium chloride, zinc acetate, sodium carbonate, sodium bicarbonate, potassium iodide, potassium bromide, lithium bromide, sodium hydroxide, lithium hydroxide, and magnesium hydroxide, and titanium dioxide (22 nm), were obtained from Sigma-Aldrich. PS colloidal spheres (1.3 μm diameter) were purchased from Microparticles GmbH and Micromod Partikeltechnologie GmbH. Toluene (99.8%, anhydrous), calcium chloride, lithium chloride, magnesium acetate, and calcium acetate, were purchased from Fisher Scientific.

### 6.2.2 Fabrication of L-S TENG Devices

PDMS films were prepared by mixing Sylgard 184 silicone elastomer and curing agent in a 10:1 weight ratio. The mixture was thoroughly stirred, degassed under vacuum for 1 h, and then spin-coated onto pre-electroded glass substrates at controlled speeds and durations to achieve films of precise thicknesses **(Table 6.1)**. A uniform acceleration rate of 200 rpm·s$^{-1}$ was maintained during spin coating, followed by curing at 110 °C for 1 h. Gold (Au), aluminum (Al), and copper (Cu) electrodes were deposited on glass substrates via electron-beam evaporation using a custom-built setup, with polyamide tape used as a physical mask to define electrode geometry. MXene and PET/ITO electrodes were mechanically laminated onto the PDMS layer to ensure consistent electrical contact. Copper tapes were employed to extend the conductive paths for connection to the measurement circuit.

**Table 6.1.** Spin-coating parameters for precise PDMS film thickness control.

| Thickness (μm) | Time (s) | Velocity (rpm) | Acceleration rate (rpm·s$^{-1}$) |
|---|---|---|---|
| 30 (0.8) | 120 | 800 | 200 |
| 40 (1.2) | 90 | 800 | |
| 80 (1.4) | 120 | 500 | |
| 225 (1.5) | 60 | 200 | |
| 507 (1.3) | 30 | 100 | |
| 803 (3.7) | 15 | 200 | |

Footnote: The average thickness values shown in parentheses were obtained from measurements at 10 different points.

### 6.2.3 Wettability characterization

Static water contact angles were measured using a DataPhysics OCA 15 Plus goniometer (sessile drop method, 1 μL ultrapure water) at room temperature. Contact angles were averaged over at least ten measurements using SCA 20 software with the Laplace-Young fitting model.

### 6.2.4 Surface morphology and structural characterization

The morphology and micropatterning of PDMS surfaces were analyzed by field-emission scanning electron microscopy (FE-SEM; Hitachi Regulus 8220) operated at 5 kV with a secondary electron detector.

### 6.2.5 Electrical characterization of liquid-solid electrification

L-S electrification was evaluated by monitoring the open-circuit voltage ($V_{oc}$ generated across the electrodes of the L-S TENG. This electrical signal serves as a direct indicator of interfacial charge separation and electrostatic potential buildup at the liquid-dielectric interface. Measurements were performed using a Thévenin equivalent circuit model, which enables quantitative assessment of the L-S electrification process under dynamic flow conditions.

All experiments were conducted under controlled environmental conditions of 20 ± 1 °C and 60 ± 5 % relative humidity to minimize environmental artefacts, unless stated otherwise (e.g., temperature-dependence experiments). $V_{oc}$ signals were acquired using a Tektronix TBS 2022 oscilloscope, with data recorded at 625 samples·$s^{-1}$ using a Tektronix TBS1000C. Prior to each test, PDMS surfaces were cleaned with ethanol and dried using compressed air. Each dataset represents the average response over at least five complete release cycles (10 mL of water each), comprising a minimum of 15 independent L-S contact electrification events to extract representative $V_{oc}$ peaks.

### 6.2.6 Probing Liquid-Solid Electrification

To systematically investigate the dynamics of L-S electrification, we examined a broad range of physical, chemical, and physicochemical parameters. To ensure consistency and comparability across measurements, each parameter group (e.g., dielectric thickness or flow-rate dependence) was tested under identical conditions on the same day, with at least 30 repetitions of L-S contact using Milli-Q water.

### 6.2.7 Decoupling Flow-Induced and Impact-Induced Electrification

The effect of liquid release height (0.5-20 cm) was examined at inclination angles of 15 and 75°, using PDMS layers of 30 μm and 800 μm thickness, a flow rate of 215 μL·$min^{-1}$, release frequency of 1 Hz, electrode width of 3 cm, and electrode spacing of 3.5 cm at 24 °C (pH ~ 6.9).

### 6.2.8 **Influence of sliding distance on L-S electrification**

The influence of sliding distance was evaluated under identical conditions, except that the release height was fixed at <0.5 cm. Measurements were performed for both grounded and ungrounded configurations by positioning a single electrode 0.1-7.5 cm from the release point.

### 6.2.9 **Device geometry parameters**

The effects of electrode width (0.2-3.5 cm) and spacing (0.4-4.0 cm) were investigated at inclination angles between 15 and 75°, using 800 μm PDMS layers, under grounded condition, with flow rate of 215 $\mu L \cdot min^{-1}$, a release height of <0.5 cm, and ambient conditions (24 °C, pH ~ 6.9).

### 6.2.10 **Device materials parameters**

To examine the influence of electrode conductivity and work function on L-S electrification, aluminum (Al), copper (Cu), and gold (Au) electrodes were deposited via electron-beam evaporation. MXene and PET/ITO films were physically laminated onto the PDMS surface to compare electrodes with different interfacial coupling strengths to the dielectric active layer. All measurements were conducted using 225 μm PDMS films, a flow rate of 215 $\mu L \cdot min^{-1}$, 1 Hz release frequency, and <0.5 cm release height. Dielectric thickness effects (30-800 μm) were evaluated under identical flow and geometric conditions, both with and without system grounding.

### 6.2.11 **Temperature dependence**

Temperature effects (5-95 °C for both liquid and device) were assessed at a 75° inclination under ungrounded conditions. Water frequency and flow-rate dependencies were studied at 15-75° inclinations using 225 μm PDMS layers, 215 $\mu L \cdot min^{-1}$ flow rate, and <0.5 cm release height.

### 6.2.12 **Influence of liquid dynamics**

After identifying material and geometric parameters yielding the highest electrical output, these were fixed for subsequent tests to ensure comparability of $V_{oc}$ results. Unless other-

wise stated, the optimized configuration used: 3 cm electrode width, 4 cm spacing, Al electrodes, 215 μL·min$^{-1}$ flow rate, <0.5 cm release height, 24 °C, pH ~ 6.9, PDMS thicknesses of 800 μm and 30 μm, and inclination angles of 15° (droplet regime) and 75° (streamline regime).

### 6.2.13 Electrolyte influence on L-S electrification

The influence of pH (1-14, in one-unit increments) was assessed using 800 μm PDMS layers under streamline flow (75° inclination). Under the same conditions, the effects of common electrolytes (KCl, NaCl, HCl, NaOH, and KOH) were systematically evaluated over concentrations of 0-2 M, maintaining all other parameters at their optimized values.

### 6.2.14 Decoupling ionic and electronic effects in EDL-mediated L-S electrification

To further clarify the respective roles of ions and electrons in L-S electrification and to elucidate dynamic EDL effects on $V_{oc}$, we examined a wider set of electrolytes (0.01 and 0.1 M) using both 30 μm and 800 μm dielectric thicknesses under grounded and ungrounded conditions. The following salts and hydroxides were studied: sodium sulfate, sodium bromide, magnesium sulfate, potassium chloride, sodium chloride, calcium chloride, lithium chloride, magnesium acetate, calcium acetate, zinc acetate, sodium carbonate, sodium bicarbonate, potassium iodide, potassium bromide, lithium bromide, sodium hydroxide, lithium hydroxide, and magnesium hydroxide.

As some salts are hygroscopic, all samples were dried for 48 h at 55 °C before use to remove bound water. To account for exothermic or endothermic dissolution effects, electrolyte solutions were prepared one day prior to testing and equilibrated to the controlled laboratory temperature (24 °C) before measurement. Comprehensive details of the physical, chemical, and physicochemical parameters for all L-S electrification experiments are summarized in **Table 6.2**.

**Table 6.2.** Physical, chemical, and physicochemical parameters explored in liquid-solid electrification.

| Parameters | Experimental range and variables |
|---|---|
| Inclination angle (°) | 15, 30, 45, 60, and 75 |
| Flow velocity (cm·s$^{-1}$) | 12, 28, 33, 44, 56 |
| Release height (cm) | <0.5; 2; 4; 6; 8; 10; 15; 20 |

| | |
|---|---|
| Sliding distance (cm) | 0.1; 1.5; 3.0; 4.5; 6.0; 7.5 |
| Electrode width (cm) | 0.2; 1.0; 1.5; 2.0; 3.0 |
| Electrode spacing (cm) | 0.5; 1.5; 2.5; 3.5; 4.5 |
| Water flow rate ($\mu L \cdot min^{-1}$) | 27; 36; 54; 72; 108; 143; 215 |
| Release frequency (Hz) | 0.18; 0.25; 0.50; 0.66; 0.71; 0.77; 0.83; 0.9; 1.0 |
| PDMS thickness (μm) | 30; 40; 80; 225; 500; 800 |
| Device temperature (°C) | 5; 10; 20; 30; 40; 60; 80; 95 |
| Water temperature (°C) | 5; 10; 20; 30; 40; 60; 80; 95 |
| pH | 1-14 (step: 1) |
| Electrolyte concentration (M) | HCl, NaOH, KOH: 0.125; 0.250; 0.500; 1.0; 2.0; 3.0 |
| $O_2$ plasma etching (s) | 0; 5; 10; 15; 20 |
| $SF_6$ plasma etching (s) | 0; 60; 120; 180; 240 |
| $TiO_2$ loading (wt%) | 0; 2.5; 5.0; 10; 20; 30; 40 |

### 6.2.15 Enhancing L-S electrification via surface and dielectric engineering

#### 6.2.15.1 Deposition of polystyrene colloidal monolayer

Close-packed PS colloidal monolayers were fabricated following the procedure detailed previously (*Methods in Chapter 5*). Monodisperse PS spheres (1.3 μm diameter) were dispersed at 2.5 wt% in water and mixed with diacetone alcohol (1:3 $v \cdot v^{-1}$) to improve spreading. The mixture (~800 mL) was gently deposited onto the air-water interface of a Langmuir-Blodgett trough (KSV NIMA, Biolin Scientific), and the barriers were compressed at 10 $mm \cdot min^{-1}$ to induce self-assembly into a hexagonally packed monolayer. The film was then transferred onto PDMS-coated glass substrates by vertical withdrawal at 2 $mm \cdot min^{-1}$, yielding a uniform colloidal mask.

#### 6.2.15.2 Fabrication of micropatterned PDMS surfaces

Micropatterned PDMS surfaces were fabricated via reactive ion etching (RIE; Trion Minilock Phantom III). Physical microstructuring of PS-masked PDMS was achieved using $SF_6$

plasma at 45 W RF power, 50 mTorr chamber pressure, and 50 sccm gas flow for 70 min. Residual PS spheres were removed by ultrasonic cleaning in toluene for 20 min, followed by acetone rinsing and compressed-air drying.

#### 6.2.15.3 **Dielectric constant modulation**

To modulate the dielectric constant, titanium dioxide ($TiO_2$) nanoparticles were incorporated into PDMS at loadings of 2.5, 5, 10, 20, 30, and 40 wt% relative to the polymer matrix. The composite films were fabricated following the same procedure used for the 800-μm-thick PDMS active layer. All other device and liquid-flow conditions were maintained as in the optimized configuration described above. The L-S electrification performance was evaluated under both droplet and continuous streamline flow regimes. Instantaneous power (P) was calculated using $P=V^2 \cdot R^{-1}$, where R is the external load resistance. Power density was determined by normalizing P to the liquid active contact area.

### 6.2.16 **Statistical analysis**

All measurements are presented as mean ± standard error ($n \geq 10$) from independent trials. Statistical analyses were performed using OriginPro 8.5 and Minitab 17. Model adequacy was confirmed through ANOVA, lack-of-fit tests, and coefficient of determination ($R^2$). Pairwise comparisons were evaluated using one-way ANOVA followed by Tukey's post hoc test, with significance set at $p < 0.05$.

## 6.3 **Results and Discussion**

### 6.3.1 **From droplet impact to steady-state liquid–solid electrification**

A critical prerequisite for studying L-S electrification is ensuring that the observed signals originate from sustained liquid-dielectric interactions rather than from collision-induced charge transfer. Therefore, precise control of liquid dynamics, particularly the transition from droplet impact to continuous streamline flow, is essential for accurately evaluating charge transfer governed by L-S electrification. **Figure 6.1** highlights the critical role of controlling liquid release height to achieve consistent flow dynamics in L-S electrification. When droplets impact the PDMS surface from different heights, the open-circuit voltage ($V_{oc}$) scales with release height, reflecting the increase in gravitational potential energy and impact momentum.

Despite the more energetic impacts at 20 cm, the resulting $V_{oc}$ is comparable to that produced when water flows smoothly across the surface **(Figure 6.1a$_3$)**, indicating a more efficient L-S electrification process, with even higher $V_{oc}$ than that observed at 6 cm. Nevertheless, at high release heights (≥6 cm), droplet breakup leads to multiple transient $V_{oc}$ peaks, likely associated with successive mechanical impact and contact-separation events arising from splashing and fragmentation **(Figure 6.1a$_1$-a$_2$)**. The zoomed-in waveforms confirm that these multiple peaks gradually merge into a single broad signal as the release height decreases, characteristic of steady interfacial charge transfer under continuous water flow without mechanical interruption.

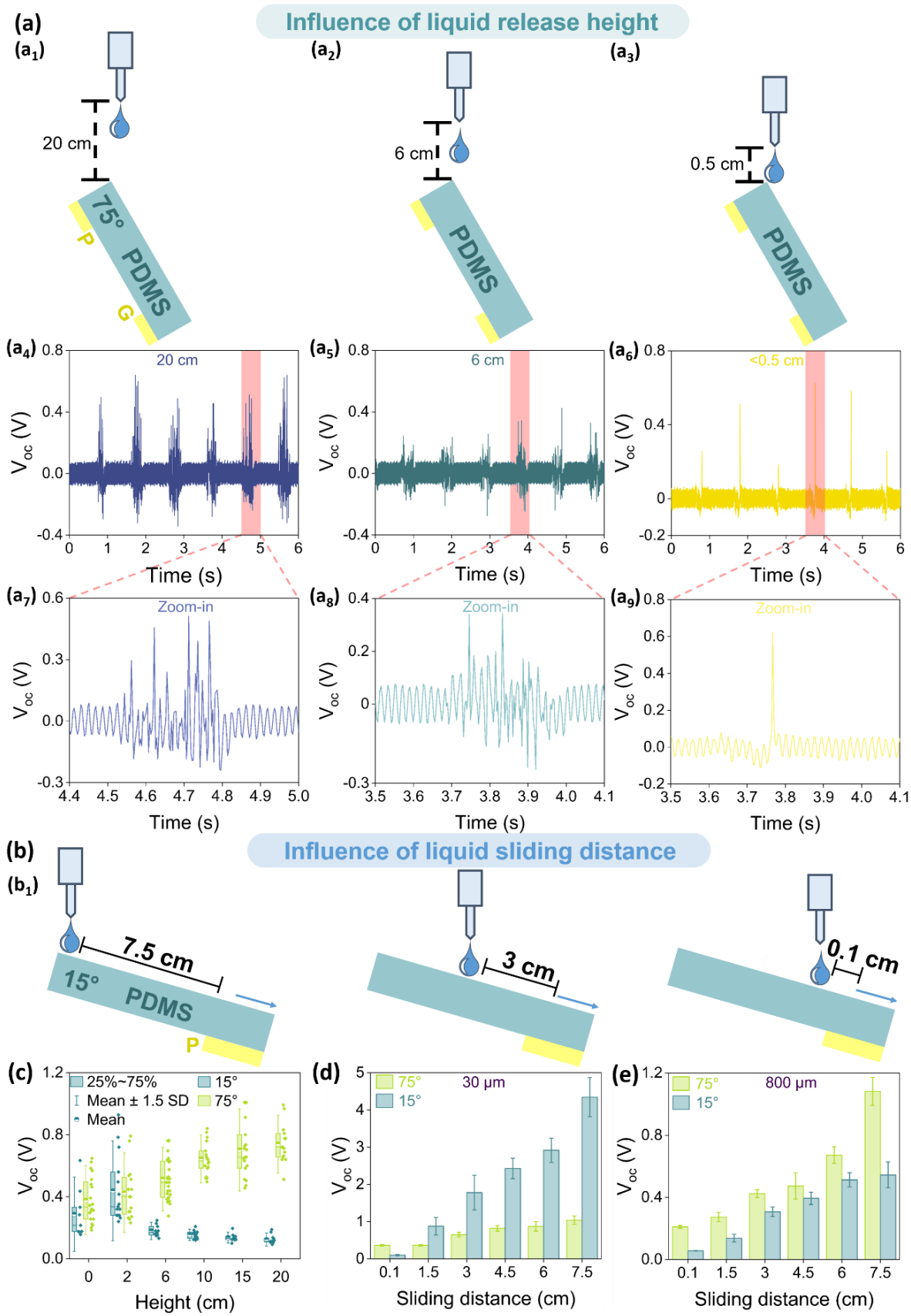


**Figure 6.1**. Influence of liquid release height and sliding distance on electrical output of L-S TENGs. (a) Influence of liquid release height on the open-circuit voltage ($V_{oc}$) generated during water impact on PDMS surfaces (30 μm)

tilted at 75°. ($a_1$-$a_3$) Schematics illustration for water release heights of 20, 6, and <0.5 cm., with ($a_4$-$a_6$) $V_{oc}$ waveforms at the respective release heights, and zoomed-in views ($a_7$-$a_9$) highlighting the transition from multiple peaks, originating from droplet splitting upon impact at higher release heights (>6 cm), to a single peak as the liquid flows continuously without breakup. (b) Schematic illustration of the effect of liquid sliding distance on PDMS surfaces inclined at 15°. ($b_1$) Representative water sliding distances of 7.5, 3, and 0.1 cm before reaching the probing electrode. (c) Distribution of $V_{oc}$ output as a function of water impact height (0-20 cm). Dependence of $V_{oc}$ on sliding distance (0.1-7.5 cm) for PDMS layers with thicknesses of (d) 30 μm and (e) 800 μm.

To further verify the contribution of mechanical impact, we compared $V_{oc}$ responses for TENG devices tilted at 15 and 75° **(Figure 6.1c)**. For the 75° configuration, $V_{oc}$ increases nearly linearly with release height, suggesting that gravitational potential energy adds constructively to the steady-state L-S electrification process. In contrast, at 15°, $V_{oc}$ drops sharply above the flow threshold identified in **Figure 6.1a$_6$**, indicating that excessive impact disrupts efficient charge transfer. The difference in $V_{oc}$ between the two inclinations above 6 cm suggests that the 15° output primarily originates from mechanical collisions, whereas at 75°, it reflects genuine L-S electrification driven by electron and ion transfer along the continuous liquid front. This transition marks a shift from impact-dominated to shear-dominated electrification, where charge transfer arises from interfacial sliding rather than impulsive contact. Consequently, all subsequent experiments were conducted at low release heights to ensure that measured signals correspond to true L-S electrification rather than mechanically induced artifacts.

To further elucidate the effects of sliding distance and dielectric thickness, we evaluated $V_{oc}$ generated as water slid distances ranging from 0.1 to 7.5 cm before reaching the probing electrode **(Figure 6.1b$_1$)**. In both PDMS thicknesses (30 and 800 μm), $V_{oc}$ increases steadily with sliding distance due to enhanced effective contact area and interfacial persistence. However, a distinct dual behavior emerges: for thin PDMS (30 μm), slower water sliding at 15° produces higher $V_{oc}$ than faster sliding at 75° **(Figure 6.1d)**, whereas for thick PDMS (~800 μm), the trend reverses, yielding higher $V_{oc}$ under faster sliding **(Figure 6.1e)**. Furthermore, the overall $V_{oc}$ generated with the thin dielectric layer is approximately five times higher than that of the thicker PDMS. This behavior can be attributed to the stronger dielectric shielding of thicker PDMS, which weakens electrostatic induction at the electrode and consequently reduces $V_{oc}$. Due to this pronounced dependence, the effects of dielectric thickness and liquid-sliding velocity were systematically examined in the following section.

Together, these observations demonstrate that both release height and sliding distance critically influence liquid-flow-to-electric transduction and charge generation efficiency. They

reveal, for the first time, the importance of precisely controlling flow conditions to isolate genuine L-S electrification from spurious mechanical or electrostatic artifacts. Building on these findings, we next investigated how liquid dynamics govern charge transfer in L-S electrification. Understanding this hydrodynamic interaction is a prerequisite for elucidating how electrolyte composition and interfacial electrostatics subsequently influence the overall electrification behaviour.

### 6.3.2 Hydrodynamic and device geometry influence on electrical output

**Figure 6.2** elucidates the coupled influence of liquid dynamics and device geometry on interfacial charge generation in L-S electrification. As shown in **Figure 6.2a**$_1$, the liquid flow regime strongly depends on the surface inclination, transitioning from a discrete droplet mode at 15° to a continuous streamline regime at 30-75°. Because the inclination angle directly influences the liquid velocity, video-derived mean velocities were 12, 28, 33, 44, and 56 cm·s$^{-1}$ for θ = 15, 30, 45, 60, and 75°, respectively. This intrinsic coupling between inclination and flow velocity defines the hydrodynamic transition from droplet impact to streamline flow and thus serves as a key parameter for probing L-S contact electrification, ion transport, and charge redistribution that collectively determine the observed $V_{oc}$.

**Figure 6.2a**$_2$ further confirms that $V_{oc}$ is highly sensitive to the flow regime, increasing from low-efficiency L-S electrification ($V_{oc}$ <0.3 V) in the droplet regime (15°) to approximately 5.5 V under continuous streamline flow at 75°. We propose this $V_{oc}$ enhancement with increasing angle (and corresponding velocity) to two coupled effects. First, at low inclination the surface retains a thin residual water film between cycles due to reduced gravitational drainage. The remaining liquid partially screens the interfacial electric field and mitigates charge transfer in subsequent releases, thereby lowering the overall potential difference. Second, higher inclination angles prevent water accumulation and promote faster flow, which expands the effective wetted area, enhancing interfacial shear. Together, we attribute the reduction of residual-film screening and the increase in shear-assisted charge transfer with angle account for the sharp rise in $V_{oc}$.

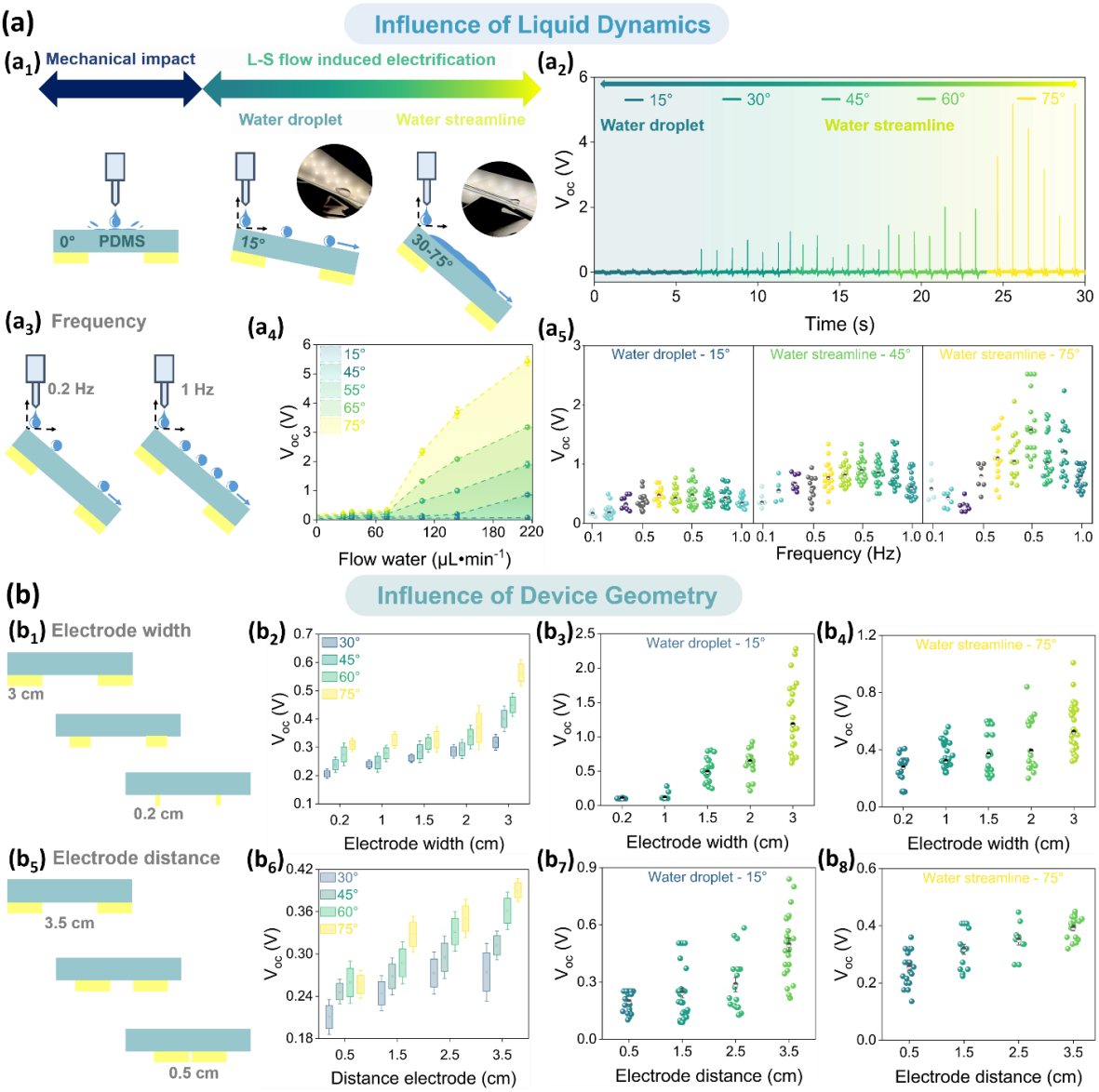


**Figure 6.2.** Influence of liquid dynamics and device geometry on electrical output of L-S TENGs. ($a_1$) Schematic illustration of the transition from mechanical impact to flow-induced L-S electrification with increasing inclination angle, showing a discrete droplet shape at low inclination (15°) and a continuous streamline flow at 30-75°. ($a_2$) $V_{oc}$ waveforms for droplet and streamline regimes at different inclination angles (15-75°), recorded for an 800-μm-thick PDMS layer at 1 Hz droplet release and 215 μL·min$^{-1}$ flow rate. ($a_3$) Schematic illustration of the droplet-release frequency range (0.2-1 Hz). ($a_4$) Dependence of $V_{oc}$ on flow rate (0-215 μL·min$^{-1}$) under inclination angles of 15-75°. ($a_5$) Frequency-dependent $V_{oc}$ distributions comparing the water-droplet regime (15°) with the streamline regime (60-75°). (b) Effect of device geometry. ($b_1$) Schematic representation of electrode-width variation (0.2-3 cm), with a fixed inter-electrode distance of 4 cm. ($b_2$) $V_{oc}$ box plots for L-S electrification in the streamline regime (30-75°) showing the influence of electrode width. ($b_3$-$b_4$) $V_{oc}$ scatter distributions for the water-droplet and streamline regimes, respectively. ($b_5$) Schematic illustration of electrode-separation distances (0.5-3.5 cm) with a standardized electrode width of 3 cm. ($b_6$) $V_{oc}$ box plots showing the effect of electrode spacing in the streamline regime (30-75°). ($b_7$-$b_8$) $V_{oc}$ scatter distributions for the droplet (15°) and streamline (75°) regimes with varying electrode spacing.

We further evaluated how the frequency of water release influences L-S electrification efficiency **(Figure 6.2a$_3$)**. The $V_{oc}$ output exhibits a clear frequency-dependent behavior, reaching an optimal value at intermediate frequencies (~0.5 Hz) regardless of the flow regime (droplet or streamline) **(Figure 6.2a$_4$)**. We propose this trend to the interplay between surface wetting and charge-relaxation dynamics. At high release frequencies, residual water remaining on the PDMS surface between successive impacts limits charge transfer by partially screening the surface potential, as also observed at angle device effect. Conversely, at very low frequencies, the longer intervals between releases likely allow electrostatic charge dissipation through environmental leakage or surface recombination, reducing the effective charge transfer. Thus, the combined influence of residual-water screening and interfacial charge relaxation suggests the intermediate frequency (~0.5 Hz) as the most efficient regime for L-S electrification under these experimental conditions.

When examining the effect of increasing flow rate (from 0.26 to 215 $\mu L \cdot min^{-1}$), a steady rise in $V_{oc}$ is observed, with the strongest enhancement occurring at higher liquid velocities (75°), consistent with the findings of Yun et al.[624] At low flow rates (<60 $\mu L \cdot min^{-1}$), the signal remains weak due to insufficient shear and limited effective contact area interaction, resulting in negligible L-S electrification. Above this threshold (>60 $\mu L \cdot min^{-1}$), $V_{oc}$ increases sharply (particularly at 75°), reaching up to sixfold higher efficiency compared to the streamline regime at lower velocity (30°) for the same liquid volume. In contrast, under same conditions (215 $\mu L \cdot min^{-1}$), however in droplet-like flow at low inclination, $V_{oc}$ remains minimal (~0.07 V). These results demonstrate that L-S electrification is not governed solely by liquid volume, as commonly assumed, but is also dictated by the liquid-flow regime and velocity.

To further elucidate the influence of device geometry on the $V_{oc}$ output of L-S TENGs, we systematically evaluated the electrode configuration **(Figure 6.2b)** in terms of electrode width and inter-electrode distance **(Figure 6.2b$_1$ and 6.2b$_5$, respectively)**. Increasing the electrode width from 0.2 cm to 3 cm steadily amplifies $V_{oc}$, owing to the enlarged effective electrostatic induction area during liquid sliding, which directly enhances charge transfer **(Figure 6.2b$_2$)**. This trend is reproducible regardless of the liquid-flow regime or velocity, confirming that a larger electrode area facilitates greater charge accumulation. Interestingly, the relative increase in $V_{oc}$ is more pronounced in the droplet regime (~420%) than in the streamline regime (~169%) when the electrode width increases from 0.2 to 3 cm **(Figure 6.2b$_3$-b$_4$)**.

We further demonstrate that electrode separation distance plays a decisive role in governing the $V_{oc}$ during L-S electrification. The results show that increasing the spacing between

the grounded and positive electrodes enhances the potential difference across the device, independent of flow regime or velocity **(Figure 6.2b$_6$-b$_8$)**. Because the negative electrode is positioned at the upper section of the L-S TENG, a larger sliding distance between electrodes allows greater cumulative charge transfer during liquid motion, thereby increasing $V_{oc}$. Conversely, short interelectrode spacing limits the active sliding path and yields lower electrical output. This behavior parallels the trend observed for liquid sliding distance **(Figure 6.1d-e)**, with the key distinction that, in this configuration, two electrodes are used, with the first being grounded. Grounding mitigates residual charge induction from previous liquid releases, isolating the contribution of charge transfer generated primarily during water sliding. This interpretation is supported by the substantially lower $V_{oc}$ obtained for the two-electrode configuration compared with the single-electrode mode **(Figure 6.1d)**, indicating that electrostatic charges accumulated during the initial liquid release elevate the potential at the grounded probe and thus reduce the potential difference with the subsequent positive electrode. Furthermore, comparison between the droplet (15°) and streamline (75°) regimes **(Figure 6.2b$_7$-b$_8$)** further confirms that droplet flow establishes a higher potential difference, consistent with the enhanced L-S electrification efficiency, at 30 μm dielectric layers, observed in **Figure 6.1d**.

Together, these findings highlight the critical role of electrode geometry in dictating the electrical performance of L-S TENGs and provide valuable insight into how device architecture can be optimized for more efficient energy harvesting and a deeper understanding of the L-S electrification process.

### 6.3.3 Dielectric shielding and grounding effects on electrostatic induction

**Figure 6.3** elucidates how dielectric shielding and grounding conditions modulate the $V_{oc}$ of L-S TENGs. Under ungrounded conditions, increasing the dielectric-layer thickness markedly enhances $V_{oc}$, rising from approximately 0.4 to 3.6 V at 800 μm under 75° inclination **(Figure 6.3d)**. To isolate the contribution of residual electrostatic charge, grounding experiments were performed **(Figure 6.3f)**. When the liquid was electrically grounded, $V_{oc}$ decreased by up to 97%, confirming that pre-existing electrostatic charges in the water play a dominant role in the apparent output **(Figure 6.3g)**. Once these charges were neutralized, the remaining voltage reflected the intrinsic charge transfer generated solely during each L-S contact event.

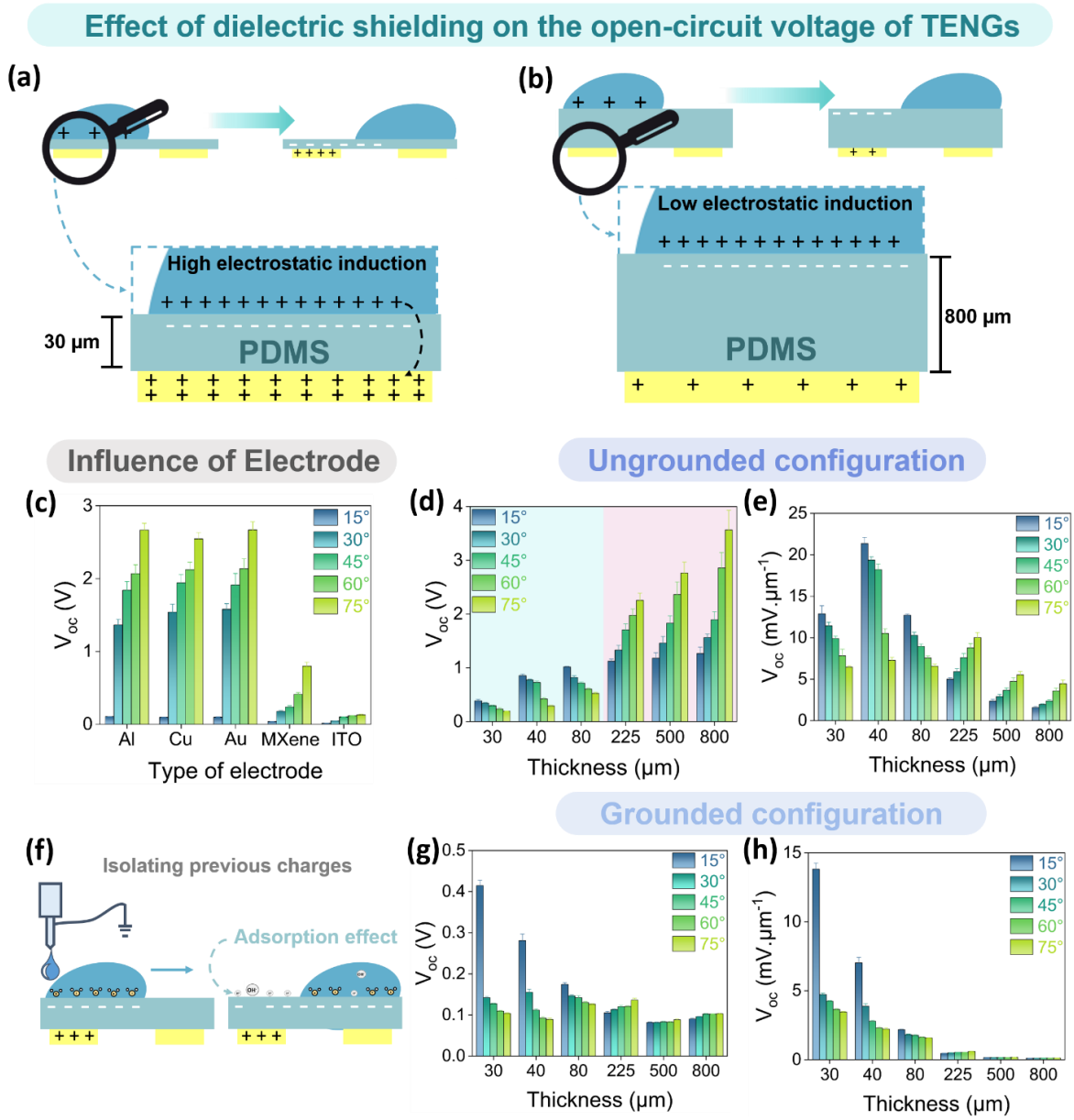


**Figure 6.3.** Effect of dielectric shielding and water grounding on the open-circuit voltage ($V_{oc}$) of L-S TENGs. Schematic illustration of electrostatic induction in PDMS layers with different dielectric thicknesses: (a) a thin dielectric layer (30 μm) reduces dielectric shielding, allowing strong electrostatic induction, whereas (b) a thick dielectric layer (800 μm) increases shielding and weakens charge induction. (c) Influence of electrode material (Al, Cu, Au, MXene, and ITO) on the $V_{oc}$ under inclination angles of 15-75°. (d) $V_{oc}$ as a function of PDMS thickness and (e) $V_{oc}$ normalized by dielectric thickness ($mV \cdot \mu m^{-1}$) in the ungrounded configuration. (f) Schematic of the grounded configuration, where the water is electrically grounded to remove residual electrostatic charges. (g) $V_{oc}$ as a function of PDMS thickness and (h) $V_{oc}$ normalized by dielectric thickness in the grounded configuration.

Furthermore, when $V_{oc}$ is normalized by the dielectric thickness, thinner PDMS layers yield higher normalized output than thicker ones, independent of whether the system is grounded **(Figure 6.3e,h)**. This inversion arises from a trade-off between capacitive charge

storage and electrostatic field attenuation within the dielectric. For thin PDMS layers, the higher capacitance enables greater charge accumulation at the interface, leading to stronger electrostatic induction. As the dielectric thickness increases, the capacitance decreases and the field coupling between the surface and the electrode becomes progressively shielded by the dielectric bulk. Furthermore, the greater separation between interfacial charges and the underlying electrode, compounded by enhanced dielectric shielding, attenuates the electric field reaching the electrode and consequently lowers.

Under ungrounded conditions **(Figure 6.3d)**, $V_{oc}$ increases almost linearly with PDMS thickness, reaching ~3.6 V at 800 μm. We attribute this monotonic rise to two coupled effects. First, thicker PDMS films exhibit lower capacitance per unit area, so for a given stored charge the resulting potential scales approximately with thickness ($V \sim Q/C \propto$ thickness). Second, thicker dielectrics suppress charge leakage to the electrode and thus retain residual charge from previous L-S contacts. Because the system is not grounded, this stored interfacial charge accumulates cycle by cycle and adds to the instantaneous triboelectric contribution. The combination of improved charge retention and higher voltage per unit charge produces an apparent near-linear increase of $V_{oc}$ with thickness, even though thicker dielectrics also introduce stronger electrostatic shielding.

Overall, these findings demonstrate that dielectric thickness governs the extent of electrostatic induction through a balance between charge-storage capacity and electric field shielding. While grounding configuration dictates whether $V_{oc}$ arises primarily from pre-existing electrostatic charges or purely from L-S charge transfer. Together, these results establish a framework for understanding L-S electrification mechanisms, essential not only for optimizing dielectric-layer design in L-S TENGs, but also for clarifying the origin of electrical output in more complex liquid systems, such as electrolytes, explored in the following sections.

To further understand the influence of electrode materials on $V_{oc}$ after L-S electrification, several metallic electrodes with different work functions (Al, Au, and Cu) were evaluated. These electrodes were continuously and uniformly deposited onto glass substrates via e-beam evaporation, after which PDMS was poured and cured. This fabrication process maximized the interfacial contact between the electrode and the dielectric layer by preventing air entrapment and ensuring uniform adhesion. The $V_{oc}$ results show no significant variation among the three metallic electrodes, indicating that differences in work function or electrical conductivity do not substantially affect the energy-harvesting performance in this configuration.

In contrast, devices employing physically attached MXene or ITO electrodes exhibited markedly lower $V_{oc}$ values. We attribute this reduction to imperfect physical contact at the dielectric-electrode interface, where the intrinsic micro/nanoroughness of the PDMS surface and the trapping of air bubbles during attachment likely decrease the effective interfacial area and introduce additional dielectric shielding. These observations confirm that the electrode-dielectric contact quality, rather than the intrinsic work function or conductivity of the electrode, governs the charge-induction efficiency and overall electrical output in this L-S TENG system.

### 6.3.4 **Mechanistic model of liquid–solid charge transfer**

The schematic in **Figure 6.4** illustrates the proposed working mechanism of L-S electrification in the sliding-droplet regime. When a droplet first contacts the PDMS surface, interfacial charge transfer occurs at the liquid-dielectric boundary **(Figure 6.4a$_1$)**. This charging process may arise from electron exchange and ion adsorption within the EDL, or from a combination of both, leaving the PDMS surface locally polarized while the liquid acquires the complementary charge. Upon wetting, the ionization of PDMS surface groups generates negative surface sites (e.g., -Si-O-), which attract counterions (e.g., $H^+$ or solvated cations) in the adjacent liquid,[625] forming an EDL composed of a compact Stern layer and a diffuse counterion layer to preserve electrostatic neutrality.

As the droplet slides along the inclined surface, the charged liquid is carried downstream while the PDMS retains the opposite interfacial charge at the previous contact region **(Figure 6.4a$_2$)**. The longer the droplet remains in motion and in contact with the surface, the greater the cumulative L-S charge transfer, progressively increasing the electrostatic potential difference established between the electrodes **(Figure 6.4a$_3$)**. This evolving potential is recorded as the $V_{oc}$ between the grounded downstream electrode and the upstream positive electrode. The rise of $V_{oc}$ corresponds to the onset of electrostatic induction at the upstream electrode, reaching a maximum when the induced charge density is highest directly above it. As the droplet continues sliding toward the grounded electrode, the potential difference gradually decreases, producing the characteristic $V_{oc}$ peak waveform. When a load is connected, this potential difference drives a transient current through the external circuit during charge equilibration **(Figure 6.4a$_4$)**. Finally, once the liquid leaves the surface, two complementary processes restore electrostatic equilibrium: grounding neutralizes residual charge stored in the electrodes, while environmental recombination dissipates remaining charges on the PDMS

surface. Together, these processes reset the interface to its initial state, ready for the next L–S electrification cycle.

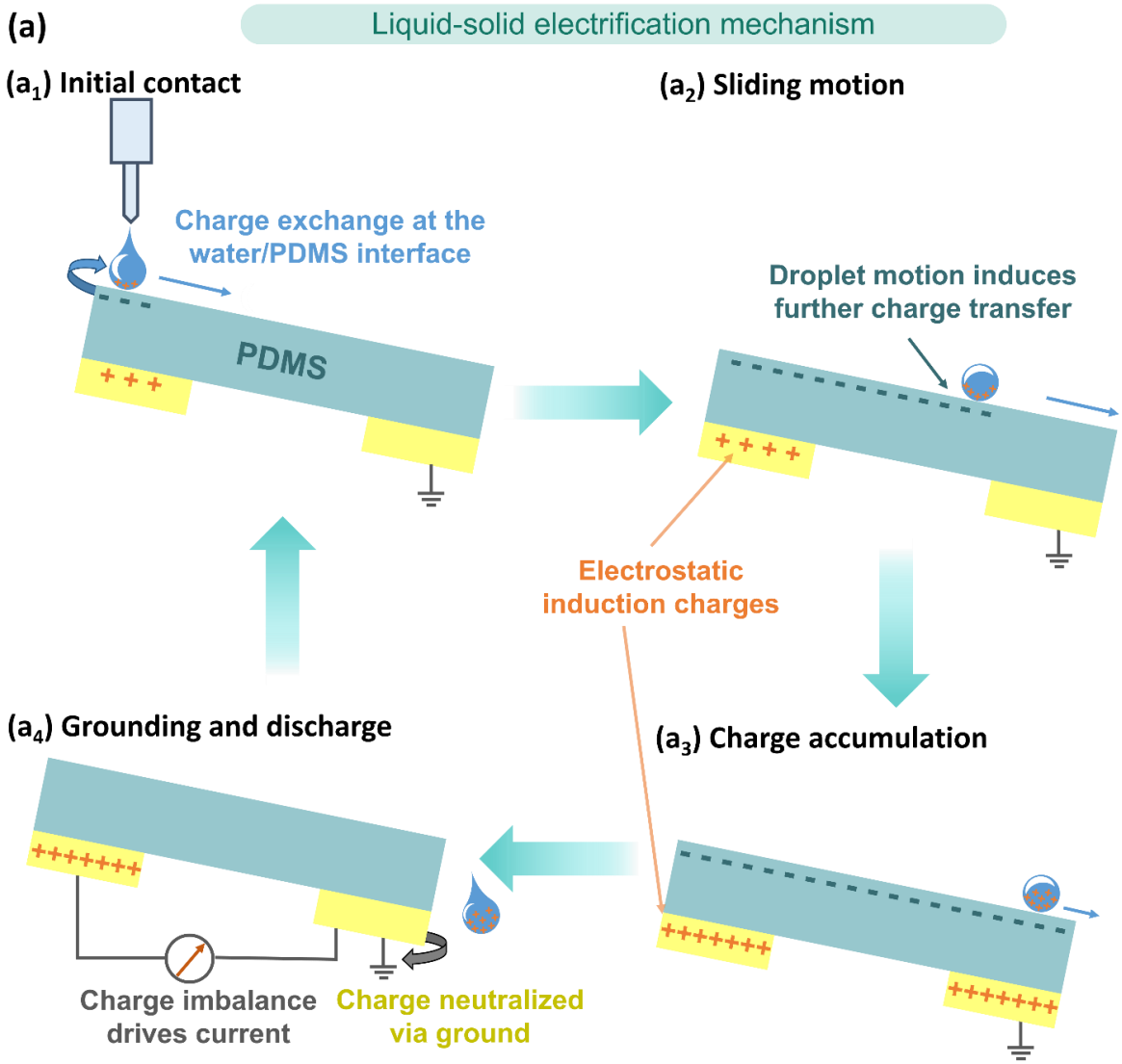


**Figure 6.4.** Liquid-solid electrification mechanism in a water sliding on TENG. A water droplet is released onto an inclined PDMS surface and electrically connected device. Upon initial contact ($a_1$), charge exchange occurs at the water/PDMS interface, producing net interfacial charge on the dielectric. As the droplet slides downstream ($a_2$), this interfacial charge is carried with the liquid, while uncompensated charge remains on the PDMS, generating a spatially separated charge distribution. Continued sliding ($a_3$) increases the axial separation between these charges, strengthening the electrostatic potential difference between the upstream grounded electrode and the downstream sensing electrode. When the droplet reaches the lower electrode ($a_4$), this potential difference drives electron flow through the external circuit. Grounding then discharges residual charge in the liquid, resetting the system for the next cycle.

Beyond interfacial charge transfer via L-S electrification, we demonstrate for the first time that liquid flow itself exerts a decisive influence on the $V_{oc}$ output. This hydrodynamic

contribution has been largely overlooked in previous studies of L-S TENGs, yet we show that distinct flow regimes can generate voltage peaks as high as 38 V from a single water release (30 mL). This enhancement arises because fluid motion - especially in ionic or polar liquids - induces an electrokinetic potential at the interface. When liquid flows over a dielectric surface, shear at the interface advects the mobile ions within the diffuse layer of the electric double layer (EDL), while the compact Stern layer remains bound to the solid. This relative displacement of charge between the stationary and convected layers generates a streaming current and establishes a potential gradient along the flow direction, the classical streaming or electrokinetic potential. The electric field associated with this charge separation superimposes on the triboelectric field at the L-S interface, enhancing electrostatic induction within the TENG electrodes and transiently increasing the measured $V_{oc}$.

Furthermore, we consider that the magnitude of flow-induced $V_{oc}$ is strongly influenced by the nature of the ionic species, which modulate the structure and dynamics of the EDL and consequently alter the streaming potential. Electrolytes with high ionic strength or multivalent ions compress the EDL and intensify local interfacial fields, producing stronger electrokinetic potentials and higher induced voltages, as observed for $CaCl_2$ and $MgCl_2$ **(Figure 6.9j,l)**. Conversely, weakly hydrated or surface-reactive ions, e.g., $I^-$, and $OH^-$, exhibit lower charge mobility and enhanced charge screening, leading to less efficient electrostatic induction and a reduced $V_{oc}$.

Even in deionized water, where the ionic strength is negligible, a measurable field can still emerge from hydrogen-bond asymmetry and the orientation of interfacial water dipoles under shear, producing a weak yet finite streaming potential. In contrast, non-polar liquids such as acetone cannot sustain this effect due to the absence of a structured EDL, confirming that flow-induced polarization is intrinsic to aqueous systems and inseparable contribution in $V_{oc}$ output of L-S electrification.

In this mechanistic framework, L-S electrification is governed by three coupled processes: (i) interfacial charge transfer at the moment of L-S contact and sliding, (ii) hydrodynamic transport of ions and dipoles within the EDL, generating a flow-induced electric field, and (iii) electrostatic induction of the electrodes, resulting in a measurable potential difference. This interplay couples wettability, EDL dynamics, and flow kinematics to the electrical response of the device, providing a unified understanding of voltage generation in L-S TENGs. Together, these mechanistic insights establish a more comprehensive understanding of the energy-harvesting behavior of L-S TENGs, one that extends beyond classical L-S electrification

to include, for the first time, the coupled influence of electrolyte properties and EDL formation on the electrical output via liquid-flow-induced streaming potentials.

### 6.3.5 Physicochemical modulation: role of liquid type and temperature

**Figure 6.5** illustrates how the physicochemical properties of liquids and environmental factors collectively influence L-S contact electrification, as reflected in $V_{oc}$ generation. We compared the L-S electrification of water, acetonitrile, ethanol, DMSO, acetone, and IPA **(Figure 6.5b)**, showing the corresponding $V_{oc}$ waveforms during the first **(Figure 6.5a)** and second **(Figure 6.5c)** contact events. During the first contact, high-polarity solvents such as acetonitrile, ethanol, and DMSO yield the highest $V_{oc}$ peaks, whereas lower-polarity solvents like acetone and IPA generate markedly smaller signals, reflecting reduced charge-transfer efficiency. Upon repeated contact, all liquids exhibit diminished peak amplitudes, indicative of partial charge screening by residual liquid films on the PDMS surface, which suppresses further charge transfer. Wang et al. (2016) demonstrated the positive co-affected of the contact angle and polarity of the liquid on the $V_{oc}$ output of nanogenerators. For instance, ethanol, which shares comparative polarity with IPA, exhibited superior output performance due to its higher contact angle value [626]. On the other hand, despite their similar contact angles, ethanol demonstrates a lower $V_{oc}$ compared to acetone due to its weaker polarity [626].

Notably, acetonitrile maintains the most reproducible signal across cycles, similar to water under streamline flow **(Figure 6.5e)**, suggesting minimal residue accumulation and efficient charge renewal between contacts. In contrast, less-polar solvents (acetone and IPA) show strong signal attenuation, likely due to greater surface spreading that promotes charge screening and rapid signal decay during successive L-S contacts (<10 s). Water, however, exhibits nearly identical $V_{oc}$ amplitudes across the first four contacts **(Figure 6.5d)**, confirming that interfacial charge transfer during L-S electrification is highly reversible, without cumulative charge saturation effects often reported.

Because each liquid exhibits a distinct L-S electrification behavior, **Figure 6.5f** demonstrates that L-S TENGs can discriminate liquid type based on statistical $V_{oc}$ metrics such as peak amplitude, cumulative sum, or maximum voltage. With advanced surface engineering, through controlled hydrophobicity or micro/nanopatterning, such devices could produce unique voltage "fingerprints" for specific liquids, enabling real-time liquid identification via principal component analysis or similar data-driven approaches.

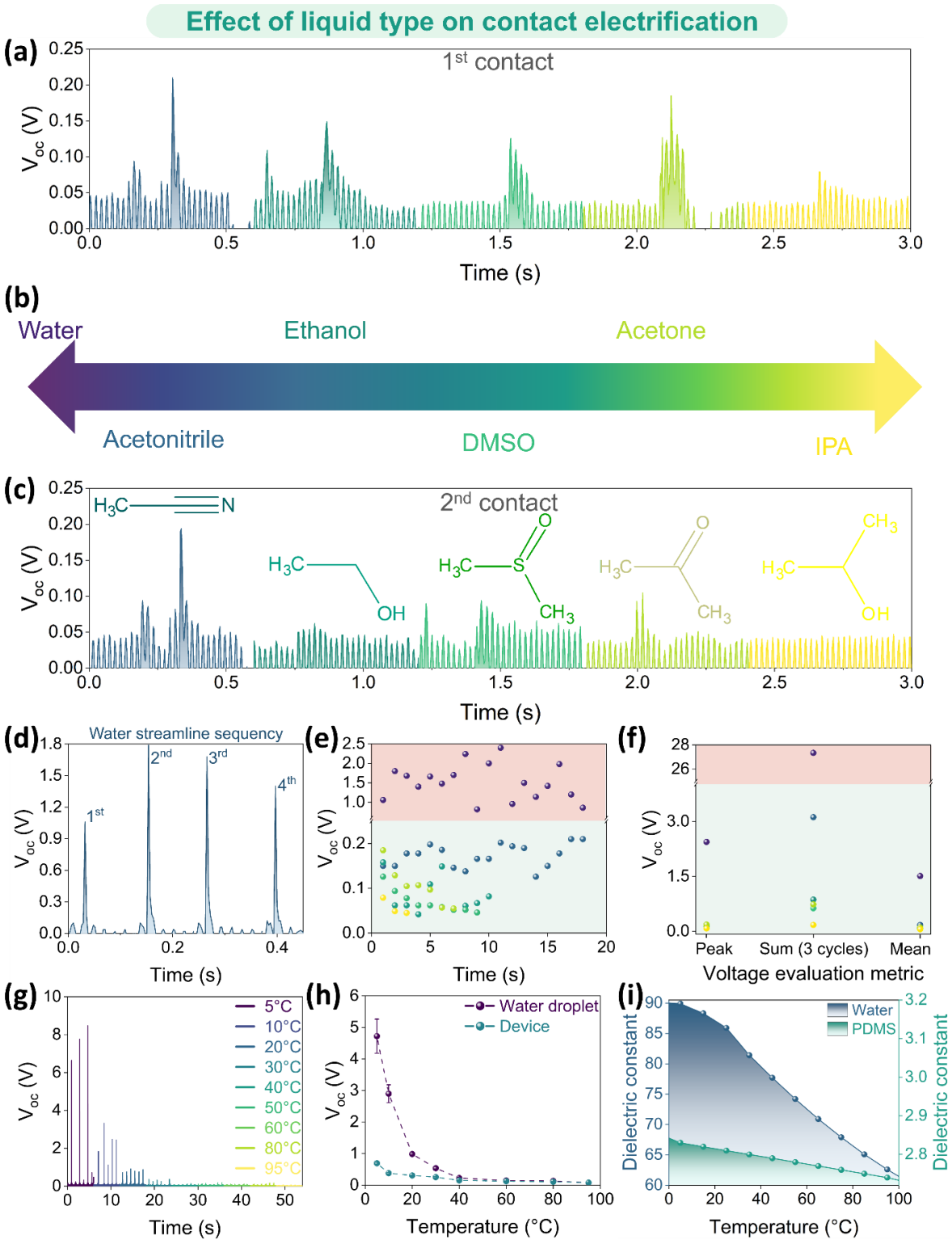


**Figure 6.5.** Effect of liquid type, contact sequence, and temperature on electrical output of L-S TENG. (a) $V_{oc}$ waveforms recorded during the first contact electrification of various liquids with the PDMS surface. (b) Classification of the tested liquids, water, ethanol, acetone, isopropanol (IPA), dimethyl sulfoxide (DMSO), and acetonitrile, ordered by energy-harvesting efficiency based on the $V_{oc}$ output generated over 20 s of contact electrification. (c) $V_{oc}$ responses for the second contact electrification, showing reduced charge transfer compared to the first contact for all liquids except water. (d) $V_{oc}$ waveforms from sequential water streamline flow (75°), confirming stable output

after multiple successive contact events. (e) Temporal evolution of $V_{oc}$ during sequential L-S electrification of different liquids on PDMS surfaces. (f) Statistical comparison of $V_{oc}$ metrics, maximum value, integrated sum (three cycles), and mean, highlighting the potential for liquid discrimination through principal component analysis (PCA). (g) $V_{oc}$ waveforms of L-S electrification in the water streamline regime at different temperatures (5-95 °C) and the corresponding (h) average $V_{oc}$ as a function of temperature. (i) Dielectric constants of water and PDMS as a function of temperature, confirming the correlation between decreasing permittivity and diminished $V_{oc}$. All experiments were performed under a standardized flow rate of 215 $\mu L \cdot min^{-1}$, a 75° streamline configuration, and a 1 Hz droplet-release frequency to ensure quantifiable and comparable signals.

To further highlight the role of thermal effects, we examined the temperature dependence of L-S electrification **(Figure 6.5g-i)**. The $V_{oc}$ decreases sharply when water temperature exceeds 25 °C and approaches zero above 70 °C. A similar, though less pronounced, decline occurs when heating the PDMS device, consistent with thermally induced reductions in both dielectric constant and surface potential. The concurrent decrease in the dielectric constants of water and PDMS **(Figure 6.5i)** corroborates this trend, indicating that elevated temperatures weaken interfacial polarization and hinder charge separation across the EDL.

This behaviour arises primarily from the steep temperature-dependent decline in water's dielectric constant **(Figure 6.5i)**, which directly reduces interfacial capacitance and the ability to sustain separated charges. Additionally, higher temperatures enhance ionic mobility and accelerate charge recombination and leakage, further diminishing $V_{oc}$. Collectively, these findings emphasize the importance of maintaining controlled and consistent liquid and device temperatures to ensure reliable and comparable L-S electrification measurements across different experimental conditions.

### 6.3.6 Electrolyte effects on EDL structure on electrical output

**Figure 6.6** demonstrates that the $V_{oc}$ in L-S triboelectrification is not determined solely by macroscopic hydrodynamics, but is strongly governed by electrolyte-specific modulation of the interfacial EDL. Because all liquids contained the same 0.01 M electrolyte concentration and were tested under identical streamline-flow and device configurations, the observed variations in $V_{oc}$ directly reflect how different ionic species build, sustain, and reorganize interfacial charge within the EDL, and how this interplay affects charge separation and the resulting voltage output.

Among the numerous electrolytes compared, the most pronounced differences in $V_{oc}$ arise from multivalent ions such as $Mg^{2+}$, $Ca^{2+}$, $SO_4^{2-}$, and $CO_3^{2}$. These species are known to produce compact, highly charged EDLs owing to their greater charge density. We propose that such multivalent ions compress the EDL and locally enhance the interfacial electric field by anchoring countercharges closer to the PDMS surface. This tighter ion packing increases the effective potential gradient across the interface and consequently amplifies $V_{oc}$. In this regime, the flow-induced spatial separation of these tightly bound charges generates a potential difference between upstream and downstream regions, analogous to a streaming potential, manifested as the measured $V_{oc}$. This hypothesis is further validated in subsequent sections, where we show that electrolyte addition also enhances energy harvesting under non-contact configurations, confirming that interfacial field transmission is boosted by ion-mediated coupling.

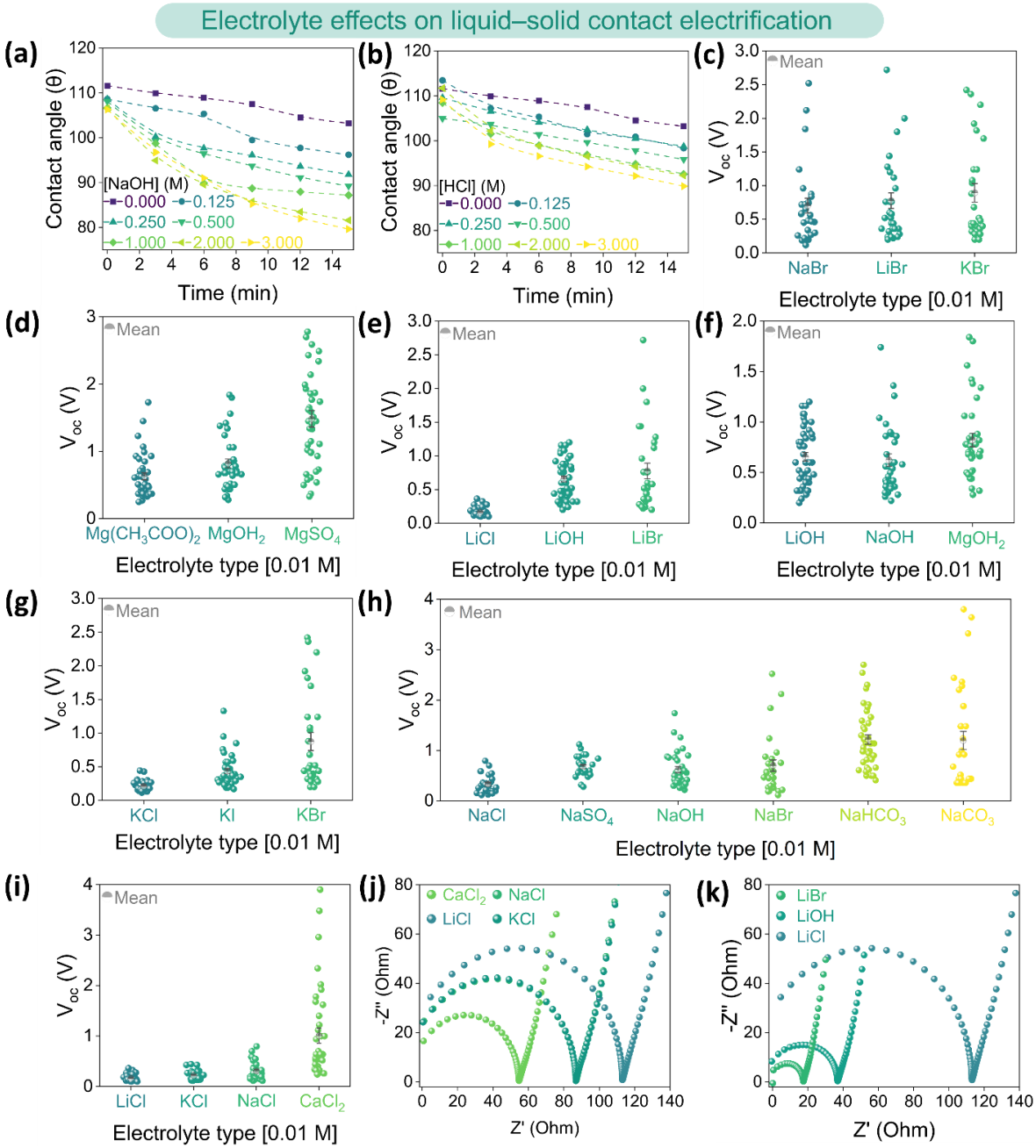


**Figure 6.6.** Influence of electrolytes on $V_{oc}$ output in L-S electrification. (a,b) Contact-angle evolution of PDMS surfaces over 15 min in aqueous NaOH and HCl electrolytes with varying concentrations (0-3 M), showing increased wetability with increasing ionic strength. (c-i) Open-circuit voltage ($V_{oc}$) distributions for L-S electrification using different 0.01 M electrolytes, isolating the effects of specific ionic species: (c) halide series (NaBr, LiBr, KBr) for anion comparison; (d) divalent $Mg^{2+}$ cations ($Mg(CH_3COO)_2$, $Mg(OH)_2$, $MgSO_4$); (e) monovalent $Li^+$ cations (LiCl, LiOH, LiBr); (f) hydroxide anions (LiOH, NaOH, $Mg(OH)_2$); (g) potassium cations (KCl, KI, KBr) to assess the influence of cationic radius; (h) sodium cations paired with various anions (NaCl, $Na_2SO_4$, NaOH, NaBr, $NaHCO_3$, $Na_2CO_3$); (i) chloride anions paired with different cations (LiCl, NaCl, KCl, $CaCl_2$), where $CaCl_2$ introduces two chloride anions per molecule, enabling comparison of charge density effects. (j,k) Nyquist plots from electrochemical impedance spectroscopy of 0.01 M electrolytes: (j) $CaCl_2$, NaCl, LiCl, and KCl; (k) LiBr, LiOH, and LiCl.

A second notable trend emerges from the halide series (KCl, KBr, KI) **(Figure 6.6g)**, which reveals how anion identity reshapes the EDL at the PDMS-liquid interface. Although these anions carry identical charge, their hydration energies and polarizabilities determine how closely they approach the hydrophobic PDMS surface and how effectively they modify the interfacial electric field. The strongly hydrated $Cl^-$ ion remains largely in the diffuse layer, producing weak field coupling and the lowest $V_{oc}$. $Br^-$, with intermediate hydration and higher polarizability, accumulates closer to the interface, forming a more compact and asymmetric EDL that strengthens the interfacial potential and yields the highest $V_{oc}$. The larger, more polarizable $I^-$ can overscreen surface charges, partially neutralizing the local field and producing an intermediate $V_{oc}$. These results demonstrate that the spatial distribution of ions within the EDL, and their ability to asymmetrically screen the dielectric surface, critically determine the efficiency of L-S charge transfer.

Electrochemical impedance spectroscopy **(Figure 6.6j,k)** further links these voltage trends to interfacial charge dynamics. Distinct semicircle sizes and low-frequency tails in the Nyquist plots indicate that electrolytes producing higher $V_{oc}$ also exhibit lower interfacial resistance and more facile polarization. This relationship implies that an effective electrolyte for L-S electrification is not only one that forms a dense, high-charge EDL but also one that allows rapid charge redistribution during liquid flow. In other words, efficient L-S electrification requires both high interfacial charge density and low ionic mobility barriers for dynamic EDL reconfiguration.

Overall, these findings establish that electrolyte chemistry actively influences L-S triboelectrification through the coupled processes of EDL formation, structural compaction, and flow-induced reorganization. The voltage output of an L-S TENG therefore represents not a purely triboelectric response, but an electrochemical fingerprint of the interfacial ion architecture and its dynamic evolution under shear.

Considering the liquid streamline regime, **Figure 6.7** illustrates how electrolyte concentration and pH influence charge transfer during L-S electrification. When NaOH and KOH solutions of increasing concentration flow across the PDMS surface, the $V_{oc}$ decreases markedly with ionic strength **(Figure 6.7a,b)**. This effect is stronger for NaOH than for KOH, the latter still generating up to 0.5 V at low concentrations (~ 0.016 M).

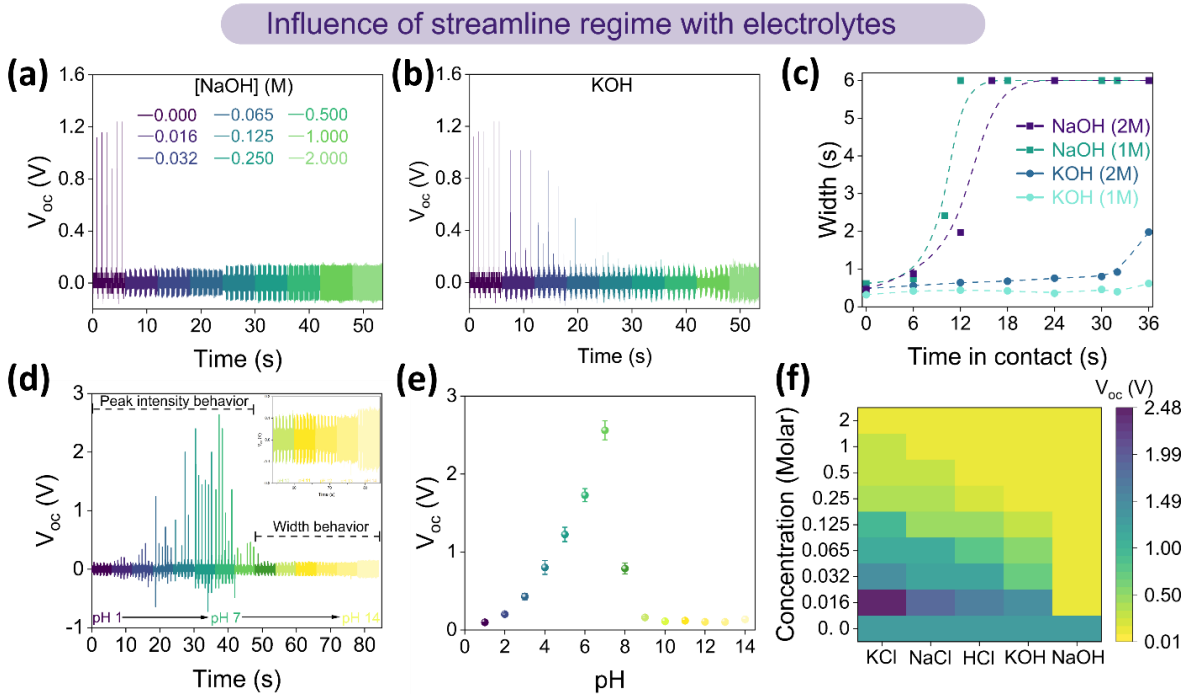


**Figure 6.7.** Influence of electrolyte concentration and pH on liquid-solid electrification under streamline flow (75°). Open-circuit voltage ($V_{oc}$) waveforms generated as (a) NaOH and (b) KOH solutions of varying concentration (0-2 M) flow across the PDMS surface in the streamline regime. (c) Evolution of the temporal width of broadened low-amplitude (~0.1 V) $V_{oc}$ peaks as a function of continuous flow time for concentrated NaOH (1-2 M) and KOH (1-2 M). Rather than producing higher single-peak voltages, high-concentration electrolytes broaden and prolong low-$V_{oc}$ activity, indicating persistent interfacial charge screening by residual liquid films. (d) Representative $V_{oc}$ waveforms recorded for pH values ranging from 1 to 14 (stepwise 1), showing two distinct pH-dependent behaviors: increasing $V_{oc}$ peak intensity from pH 1-8, followed by a transition to extended low-amplitude, broadened signals above pH 8. (e) Mean $V_{oc}$ amplitude corresponding to each pH value, derived from (d). (f) Heat map of $V_{oc}$ as a function of electrolyte concentration (0-2 M, vertical axis) and electrolyte type (horizontal axis: KCl, NaCl, HCl, KOH, and NaOH).

Interestingly, rather than producing higher-intensity voltage peaks, higher ionic concentrations broaden the temporal width of low-amplitude (0.1V) signals, increasing their frequency within a given time window **(Figure 6.7c)**. For NaOH, this expansion reaches a maximum width of ~6 s within just 10 s of continuous flow, whereas KOH shows a smaller broadening (~2 s) even after 36 s of liquid release. This difference likely arises from the greater wettability and surface persistence of NaOH on PDMS, which we further examine through contact-angle analysis.

**Figures 6.6a-b** show the evolution of water contact angle on PDMS over 15 min in NaOH and HCl solutions at various concentrations. Increasing ionic strength progressively decreases the contact angle, indicating enhanced wetting and persistent liquid-residues. This suggests

that electrolytes promote spreading either by screening surface charges on PDMS or by reducing interfacial tension. Although improved wetting increases the effective contact area, it also inhibits successive liquid release and charge renewal, as the residual film screens the PDMS surface and reduces the potential difference, explaining the lower $V_{oc}$ intensities observed in **Figure 6.7d,f**. Wang (2023) demonstrates that acid solutions contacting PTFE induce simultaneous electrons transfer and hydrogen ions adsorption. However, with a high concentration of hydrogen ions adsorbed on the polymer surface, electron transfer between water molecules and PTFE is suppressed.[43] Therefore, the efficacy of electron transfer is influenced by the adsorption of ions, becoming nearly null beyond pH 9 and below pH 2 **(Figure 6.7e)**. This observation also underscores that larger ions more effectively obstruct the surface, impeding electron transfer to a greater degree.

### 6.3.7 Engineering dielectric and surface properties for enhanced energy harvesting

**Figure 6.8** illustrates how engineering both the dielectric layer and surface morphology can substantially enhance charge transfer in L-S TENGs, ultimately enabling smart applications such as electrochromic modulation. Incorporating $TiO_2$ nanoparticles into the PDMS matrix markedly increases the dielectric constant of the active layer, thereby strengthening charge-retention capacity, amplifying the interfacial electric field, and consequently enhancing the $V_{oc}$ output. As shown in **Figure 6.8a**, $V_{oc}$ increases with $TiO_2$ content up to 5-10 wt%, beyond which it declines. This behavior arises from a trade-off: while a higher dielectric constant enhances charge-storage ability, excessive filler loading introduces field shielding and local dielectric inhomogeneity, reducing effective electrostatic induction. This optimum $TiO_2$ range aligns with trends reported in other dielectric-tuning studies. Notably, the optimized composite yields nearly a sixfold increase in $V_{oc}$ under droplet (15°) and a threefold enhancement under streamline (75°) conditions compared to pristine PDMS (0 wt% $TiO_2$). The enhanced energy harvesting achieved through $TiO_2$ incorporation (5 wt%) is reproducible across all inclination angles and also exhibits an increase in $V_{oc}$ with flow velocity in the streamline regime **(Figure 6.8b)**.

To further assess the role of surface morphology, we fabricated microstructured PDMS using colloidal lithography **(Figure 6.8c, inset)**. The resulting micropatterned surface generated significantly higher $V_{oc}$ than flat PDMS **(Figure 6.8c)**, particularly under streamline flow

(75°), owing to the enlarged effective contact area and localized field intensification, as schematically illustrated in **Figure 6.8f**. This morphological engineering establishes an efficient route for optimizing L-S charge transfer through purely geometric enhancement.

Additionally, surface chemistry modification profoundly influences interfacial potential difference and charge transport. Oxidation by $O_2$ plasma, despite improving wettability and contact area, drastically reduces the potential difference between PDMS and water (~99% decrease), severely diminishing $V_{oc}$. In contrast, $SF_6$ plasma treatment enhances $V_{oc}$ by over 250%, primarily by introducing fluorine-rich groups that increase surface potential, promote charge retention, and improve roughness-induced field concentration.

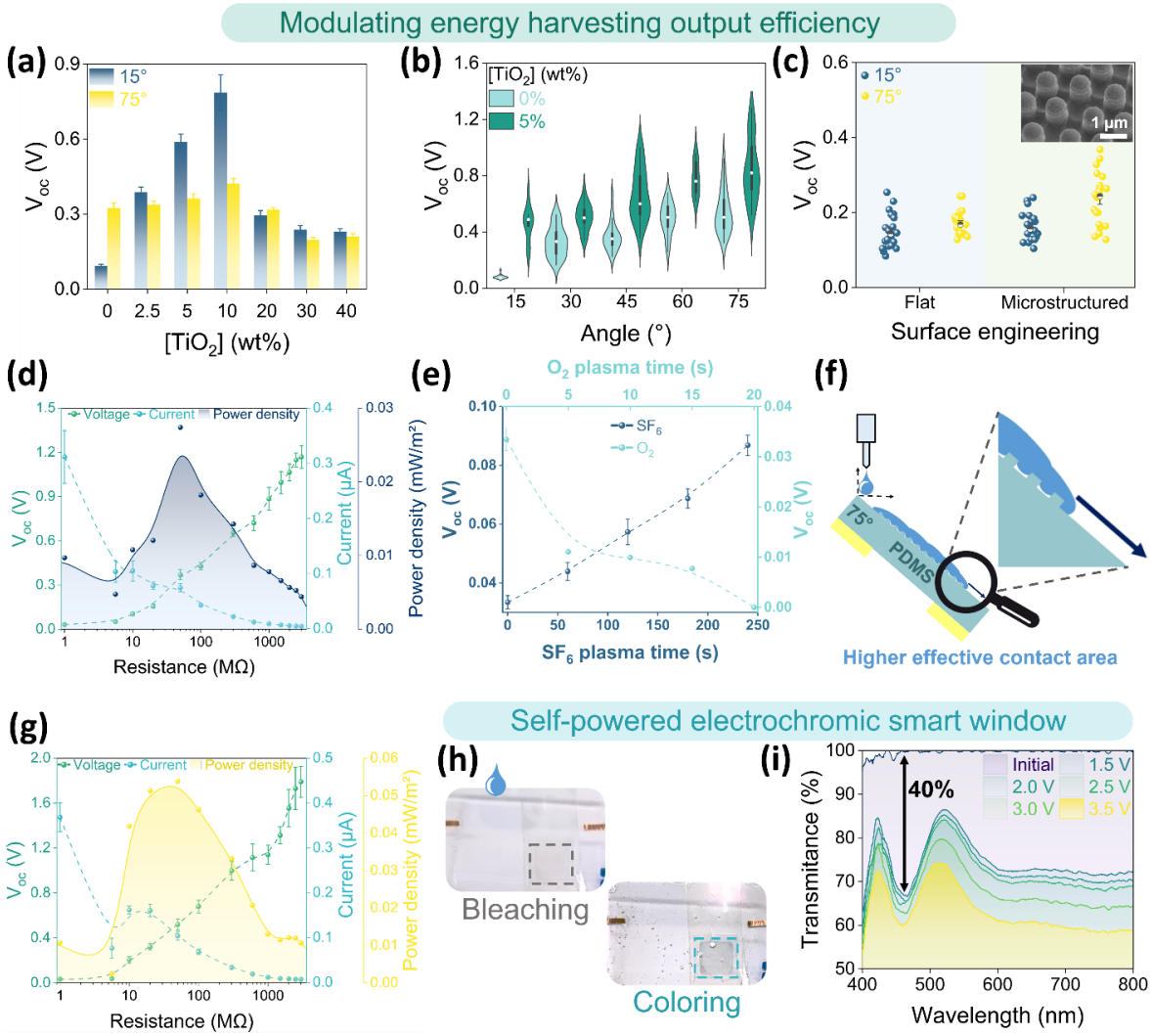


**Figure 6.8.** Engineering dielectric and interfacial properties to enhance energy-harvesting efficiency and demonstrate the L-S TENG as a self-powered electrochromic window. (a) Open-circuit voltage ($V_{oc}$) as a function of $TiO_2$ loading (0-40 wt%) incorporated into PDMS, measured under droplet (15°) and streamline (75°) flow regimes. (b) Dependence of $V_{oc}$ on inclination angle (15, 30, 45, and 75°) for pristine PDMS and 5 wt% $TiO_2$-PDMS composites. (c) Effect of surface microstructuring on $V_{oc}$, comparing flat PDMS with micropatterned PDMS fabricated using PS

colloidal templates (inset: SEM image, scale bar 1 μm). (d) Power density of the L-S TENG as a function of load resistance, showing a maximum of 0.027 mW $m^{-2}$ near 80 MΩ. (e) Influence of plasma-induced chemical surface modification on $V_{oc}$ under streamline flow conditions. (f) Schematic illustration of the L-S interaction at 75°, highlighting that micropatterning enhances effective contact area and charge transfer efficiency. (g) Power density of the optimized L-S TENG based on 10 wt% $TiO_2$-PDMS, showing a peak of 0.053 mW $m^{-2}$ near 100 MΩ. (h) Photographs of the $WO_3$ electrochromic window in bleached and colored states, directly powered by the L-S TENG output. (i) UV-Vis transmittance spectra of the $WO_3$ film under increasing applied voltage, exhibiting up to 40% modulation near 490 nm, confirming the feasibility of a self-powered electrochromic system.

To further evaluate the energy-harvesting performance of the L-S TENGs, we analyzed the power density for the control PDMS device **(Figure 6.8d)** and for the $TiO_2$-enhanced dielectric configuration **(Figure 6.8g**). The pristine PDMS TENG exhibited a peak power density of 0.025 mW·$m^{-2}$ at a load resistance of approximately 80 MΩ, whereas the optimized $TiO_2$-PDMS device achieved 0.055 mW·$m^{-2}$ near 100 MΩ, confirming the enhancement in energy-harvesting efficiency achieved through dielectric constant modulation.

To demonstrate the broader potential of this system for smart applications, we employed the L-S TENG to drive the electrochromic transition of $WO_3$, simulating raindrop or water-flow activation for self-powered smart windows. As shown in **Figure 6.8h**, the device switches between bleached and colored states under liquid-flow-induced electrical excitation. The corresponding UV-Vis spectra **(Figure 6.8i)** reveal up to 40% modulation in optical transmittance near 490 nm upon activation. These results demonstrate the practical viability of L-S TENGs not only for efficient energy harvesting but also for enabling self-powered, adaptive, and responsive technologies such as smart windows.

### 6.3.8 Engineering dielectric and surface properties for enhanced energy harvesting

To validate our hypothesis regarding the impact of flow-induced electrostatic induction on $V_{oc}$ and energy harvesting, **Figure 6.9** demonstrates the ability of the L-S TENG to harvest energy wirelessly, i.e., in a non-contact configuration, from flowing liquids through flow-mediated electric fields. Unlike conventional triboelectrification that relies on direct L-S contact, the system here operates purely by electrostatic coupling: the potential difference (streaming potential) generated within the flowing liquid produces an external electric field that induces mirror charges in the TENG electrodes, establishing a measurable $V_{oc}$ and enabling wireless energy harvesting.

When liquid flows near a dielectric surface, velocity gradients within the liquid induce charge separation along the solid-liquid boundary, even in the absence of direct contact. This phenomenon, described by the Helmholtz-Smoluchowski framework (and conceptually related to the electrostatic induction mechanism of the Kelvin water-dropper), arises because the EDL formed at the interface experiences differential motion: the bound Stern layer remains fixed to the surface, while the mobile diffuse layer is convected downstream. The relative motion between these oppositely charged regions generates a streaming current and an associated potential gradient along the flow direction. We propose that this flow-induced electric field extends into the surrounding medium and capacitively couples to the L-S TENG electrodes, inducing mirror charges and giving rise to the measured $V_{oc}$. Thus, the open-circuit voltage originates from the electrokinetic potential within the flowing liquid and its electrostatic coupling with the electrodes.

The transmission of this field - and hence its coupling efficiency to the electrodes - is strongly dependent on the spatial configuration. As shown in **Figure 6.9d**, the $V_{oc}$ amplitude decreases with increasing lateral distance (x-axis) between the liquid flow and the TENG electrodes **(Figure 6.9a)**, which act as antennas. However, within the evaluated range (up to 8 cm), the vertical separation (y-axis) between the liquid release height and the collector shows negligible influence **(Figure 6.9b,c)**, indicating that field coupling is predominantly lateral rather than vertical.

Interestingly, thinner dielectric layers exhibit higher induced voltages than thicker ones **(Figure 6.9e)**, consistent with reduced dielectric shielding and enhanced capacitive coupling. Moreover, positioning the positive probe at the bottom electrode yields higher $V_{oc}$, which we attribute to stronger field alignment and larger effective separation between the bound Stern layer and the mobile diffuse layer.

To further confirm the electrokinetic origin of this non-contact induction, we examined $V_{oc}$ as a function of liquid type **(Figure 6.9f)**. Deionized water produced the highest output, while partially polar ethanol-water mixtures (20 and 90%) and nonpolar acetone generated progressively lower voltages. This hierarchy reflects the liquid's ability to form an EDL and sustain interfacial polarization. Acetone, being an aprotic and weakly polar solvent with negligible ionic dissociation and poor dielectric screening, cannot sustain a stable EDL; thus, it fails to produce the flow-induced electric field necessary for induction. These results confirm that the formation and mobility of the EDL are prerequisites for flow-mediated field generation and wireless $V_{oc}$ in L-S TENGs.

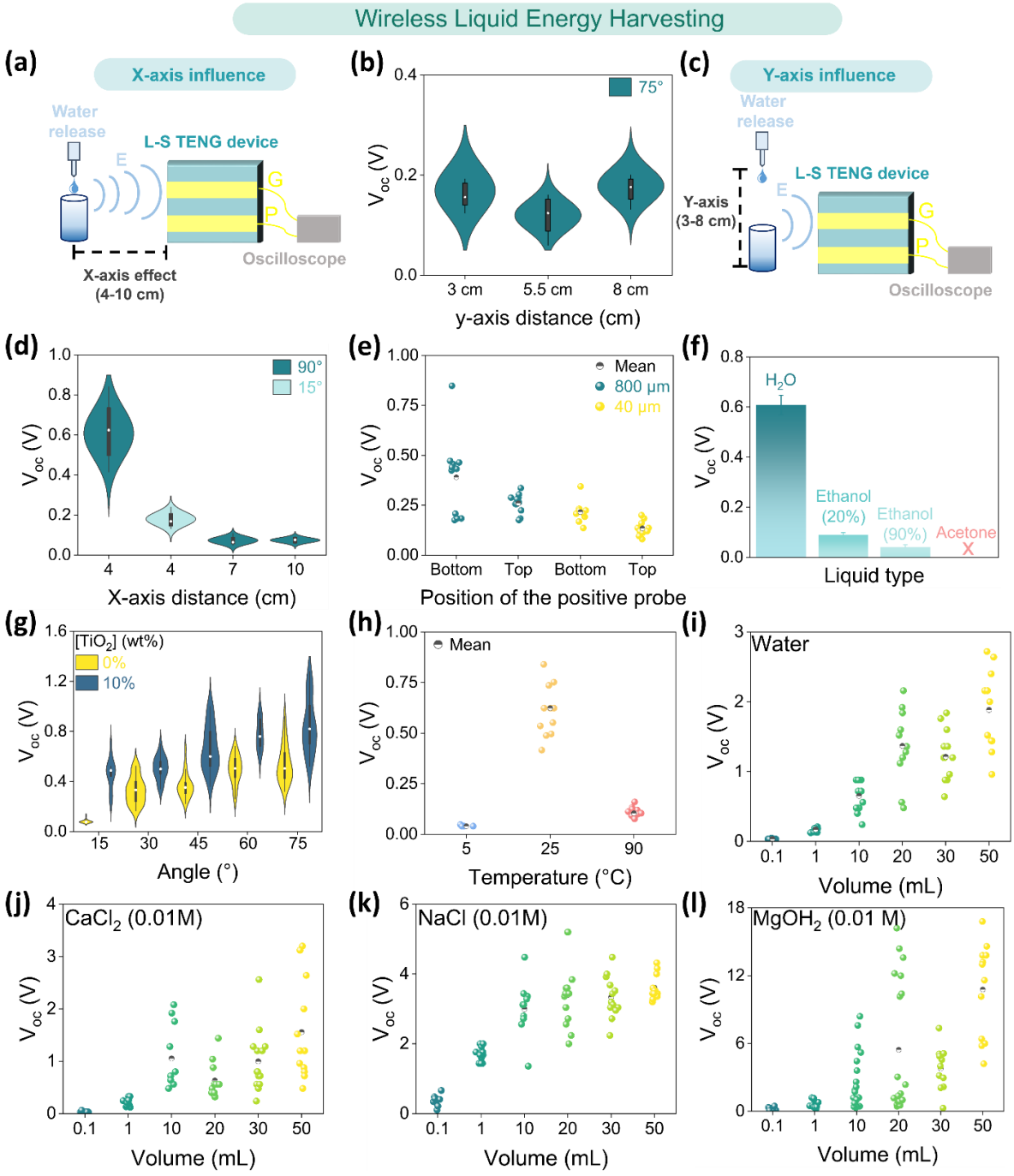


**Figure 6.9.** Wireless energy harvesting via non-contact L-S TENGs, generating open-circuit voltage ($V_{oc}$) induced by flow-mediated electric fields through streaming potential. Schematics illustrate the experimental configurations for wireless $V_{oc}$ measurements, showing (a) x-axis influence (lateral distance, 4-10 cm) between the liquid release point and the L-S TENG position, and (c) y-axis influence (vertical distance, 3-8 cm) between the release height and the collector base. (b) Dependence of $V_{oc}$ on y-axis distance, and (d) variation of $V_{oc}$ with x-axis distance from the collector center to the device. (e) Effect of probe position (bottom vs. top) and dielectric thickness (40-800 μm PDMS) on induced $V_{oc}$. (f) Comparison of flow-induced $V_{oc}$ generated by different liquids, water, ethanol (20 and 90 %),

and acetone, showing the dominant polarization and ionic conductivity of water. (g) Dependence of $V_{oc}$ on inclination angle for pristine PDMS and $TiO_2$-modified (10 wt%) PDMS active layers. (h) Temperature dependence of flow-induced $V_{oc}$, highlighting thermal suppression due to reduced dielectric permittivity and enhanced recombination. (i-l) $V_{oc}$ as a function of flow volume (0.1-50 mL) for representative 0.01 M electrolytes: (i) water, (j) $CaCl_2$, (k) NaCl, and (l) $Mg(OH)_2$. All measurements were performed at 25 °C and 75° inclination, using 3 cm-wide electrodes separated by 4 cm, with the grounding probe positioned at the upper electrode unless otherwise stated.

Analyzing the temperature dependence **(Figure 6.9h)**, we observe that increasing temperature suppresses $V_{oc}$. We attribute this effect to the combined influence of intensified Brownian motion and the reduction in dielectric permittivity at elevated temperatures, both of which weaken charge separation within the EDL and accelerate charge recombination. At low temperatures, a similar reduction in $V_{oc}$ can also occur because decreased ionic mobility limits the convective transport of the diffuse-layer charges, thereby diminishing the streaming potential.

Examining the influence of dielectric properties and device inclination, we find that increasing the dielectric constant significantly enhances $V_{oc}$ across all inclination angles compared with the pristine PDMS control **(Figure 6.9g)**. A higher dielectric constant facilitates stronger capacitive coupling between the flow-induced field and the electrodes. Simultaneously, increasing the inclination angle further amplifies the signal, likely due to improved alignment and coupling of the field lines with the downstream positive probe.

To further verify our mechanistic interpretation of EDL formation and electrolyte effects on L-S TENG performance, we evaluated the non-contact flow-induced potential for 0.01 M aqueous solutions of $CaCl_2$, $Mg(OH)_2$, and NaCl over a range of liquid volumes (0.1-50 mL). A similar trend to that observed in contact-mode L-S electrification **(Figure 6.6d,f)** was reproduced in non-contact mode **(Figure 6.9i-l)**. Multivalent electrolytes such as $Mg(OH)_2$ produce markedly larger $V_{oc}$ values than monovalent salts like NaCl, consistent with their greater charge density and stronger EDL compaction, which intensify the local electric field and electrostatic induction.

These non-contact electrostatic induction results align the L-S electrification behavior established in **Figure 6.6**, confirming that flow-induced mechanisms contribute substantially to the overall $V_{oc}$. For instance, under identical conditions (20 mL flow volume), deionized water generates only ~2.3 V, whereas 0.01 M $Mg(OH)_2$ yields ~18 V, underscoring the dominant role of EDL charge separation in enhancing the final output. Moreover, the magnitude of

the induced potential increases with liquid volume **(Figure 6.9i-l)**, indicating that stronger hydrodynamic motion enhances both the streaming potential within the liquid and its capacitive coupling to the TENG electrodes.

Taken together, these observations confirm our proposed advance in the L-S TENG energy-harvesting mechanism: a previously unreported, yet significant, contribution from flow-induced electrostatic induction driven by dynamic charge separation within the EDL. We demonstrate that all L-S nanogenerators inevitably exhibit this electrokinetic contribution, where the EDL and associated streaming potential establish an external electric field that amplifies the electrode potential difference. Consequently, the measured $V_{oc}$ reflects not only direct L-S contact electrification but also this flow-mediated electrostatic coupling.

This coupling bridges triboelectricity and electrokinetics: whereas conventional L-S TENGs rely on charge transfer through direct contact, here the same interfacial physics operates remotely, with the flowing EDL acting as a wireless charge generator. These findings define a new operational regime for TENGs, flow-mediated, field-coupled energy conversion, that enables non-contact energy harvesting and remote sensing of liquid dynamics. Furthermore, this concept deepens the understanding of EDL formation and relaxation under hydrodynamic flow and opens pathways for self-powered technologies such as potentiometric and pH sensors, advancing the frontier of intelligent, flow-responsive energy systems.

### 6.3.9 **Mechanisms governing electrostatic induction in falling electrolyte droplets**

To advance the understanding of L-S electrification for smart energy-harvesting applications, and to explain the enhanced electrical output observed experimentally, we propose the mechanistic origins that modulate the electrostatic induction signal beyond simple L-S contact electrification contribution. As shown in **Figure 6.9**, the $V_{oc}$ generated by falling electrolyte droplets exhibits a pronounced dependence on electrolyte identity, reflecting variations in the Coulomb field carried by the droplet. We propose that the net surface charge sensed by the electrodes arises not from a single process but from the combined action of four coupled mechanisms: (i) charge transfer at the nozzle, (ii) ion-specific organization at the air–water interface, (iii) electrostatic screening by the EDL, and (iv) the dynamic loss of charge through internal ionic conduction **(Figure 6.10)**. To disentangle this interplay, we discuss how different electrolytes modulate the intrinsic surface charge ($\sigma_0$), the effective surface charge ($\sigma_{eff}$), and ultimately the $V_{oc}$ output.

#### 6.3.9.1 **Contact electrification at the nozzle (L-S interface)**

As the electrolyte flows through the nozzle, charge transfer occurs at the L-S interface through contact electrification **(Figure 6.10a)**. Depending on the surface chemistry of the nozzle and the hydration structure of interfacial ions, the exiting liquid acquires a net surface charge density $\sigma_0$. When the liquid filament necks and detaches, this interfacial charge partitions between the forming droplet and the nozzle wall, leaving the droplet with a finite net $Q=\int\sigma_0\, dA$. This mechanism defines the droplet's initial electrostatic identity prior to free fall. Once released, the charged droplet generates a long-range Coulomb field that polarizes the two floating electrodes, inducing opposite charge accumulation on their surfaces. This polarization occurs purely by electrostatic induction, thus no current flows between electrodes, and the $V_{oc}$ reflects the electrostatic potential difference generated by the droplet's field at the $V^+$ and $V^-$ electrodes.

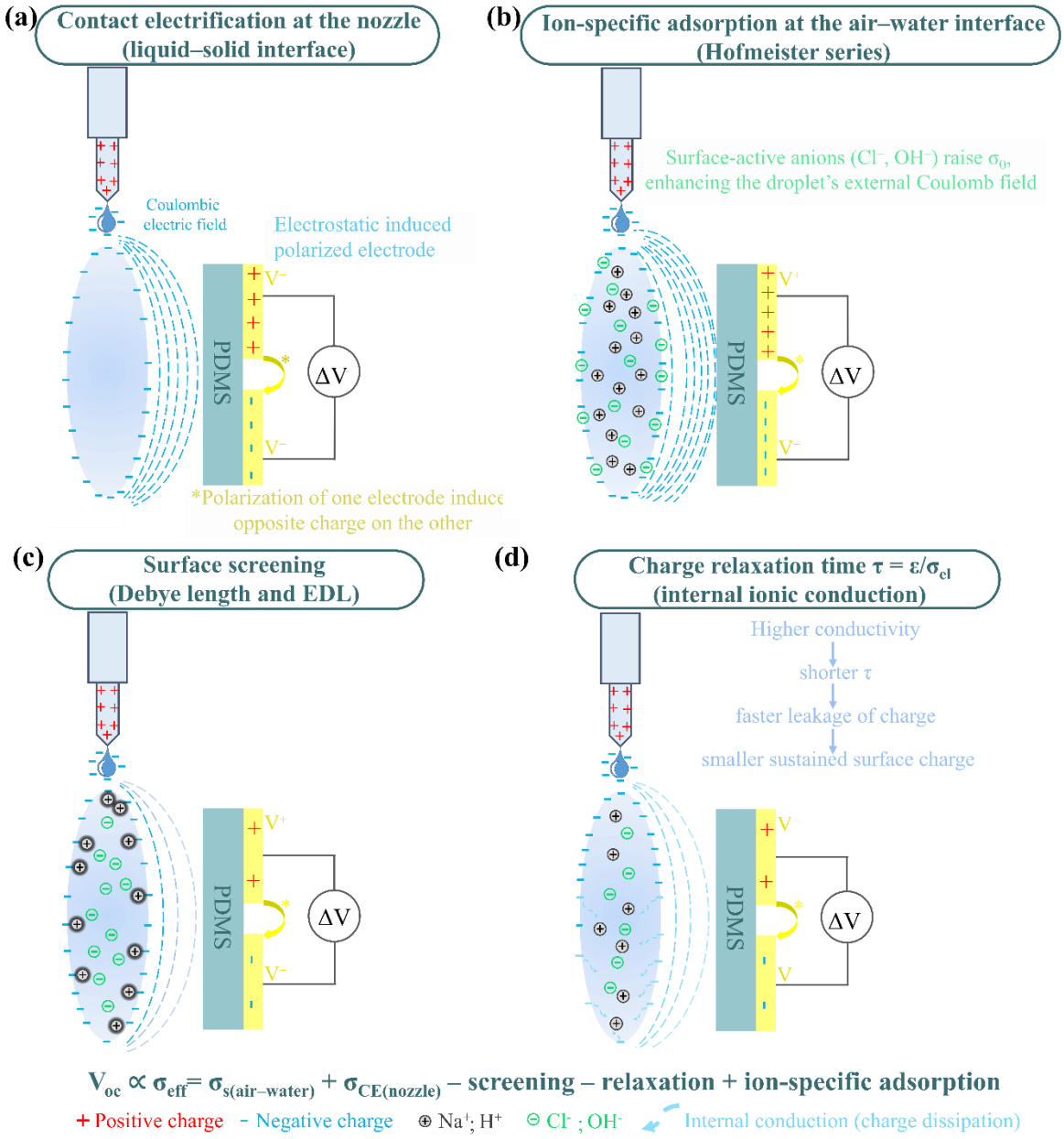


**Figure 6.10.** Mechanisms governing electrolyte-dependent electrostatic induction from falling water. (a) Contact electrification at the nozzle (liquid–solid interface), where charge transfer during detachment sets the droplet's initial surface charge ($\sigma_0$) and net charge (Q), generating the long-range Coulomb field that polarizes the nearby floating electrodes and induces the measured open-circuit voltage ($V_{oc}$). (b) Ion-specific adsorption at the air-water interface (Hofmeister series), where surface-active anions (e.g., $OH^-$, $Cl^-$) accumulate at the droplet surface and increase $\sigma_0$, strengthening the external electric field and enhancing the induced potential difference, which yields a higher $V_{oc}$. (c) Surface screening (Debye length and EDL), where dissolved ions compress the diffuse layer and screen field lines near the interface, reducing the Coulomb field, weakening the induced electrode polarization, and thus lowering $V_{oc}$. (d) Charge relaxation time $\tau=\varepsilon/\sigma_{el}$ (internal ionic conduction), where interfacial charge decays during free fall in high-conductivity droplets, reducing the surviving effective charge $\sigma_{eff}$ at the electrode plane and thereby lowering $V_{oc}$.

#### 6.3.9.2 **Ion-specific adsorption at the air–water interface (Hofmeister series)**

Beyond nozzle charging, the intrinsic surface charge of falling droplets is further modulated by ion-specific interactions at the air–water interface. Although the bulk remains electroneutral, larger and more polarizable anions exhibit measurable surface activity, positioning themselves near the interfacial layer, generating local electric fields that modify the $V_{oc}$ output **(Figure 6.10b)**.[627] This surface stratification, reflected in the Hofmeister series, alters the chemical surface charge density by changing the population of ions that preferentially adsorb at the interface.[628,629] For example, moderately surface-active halides such as $Cl^-$ display interfacial enrichment driven by differences in hydration strength, reaching concentrations up to ~1.8-fold higher at the interface than in the bulk.[630] Moreover, simulations and spectroscopy indicate that a significant fraction of $OH^-$ resides within ~3.5 Å of the air-water interface,[627] further enhancing the electric field and, consequently, the induced electrostatic response at the electrodes. By contrast, strongly hydrated cations (e.g., $Ca^{2+}$, $Na^+$) remain depleted from the interface because their high hydration energy and strong water binding energetically disfavor exposure to the low-dielectric, weakly coordinated interfacial region.

Ion-specific adsorption therefore tunes $\sigma_0$ prior to any electrostatic screening. Surface-active anions increase the net negative interfacial charge, strengthening the droplet's external Coulomb field and enhancing the induced potential contrast between $V^+$ and $V^-$, thereby elevating $V_{oc}$. Conversely, cations are repelled from the air-water interface by image-charge interactions and accumulate in a subsurface layer, where they partially neutralize or even overcompensate the interfacial charge.[627,631] This subsurface cation enrichment suppresses $\sigma_0$ and, together with subsequent EDL formation, attenuates the induction response, an effect addressed in detail in the following section.

#### 6.3.9.3 **Surface screening (Debye length and EDL)**

As discussed previously, the air-water interface carries an intrinsic negative surface charge, and anions with higher surface propensity preferentially occupy the outer interfacial region. Consequently, cations are energetically excluded from the immediate interface and instead populate a subsurface region, where they participate in forming the EDL **(Figure 6.10c)**. Within the Gouy-Chapman-Stern framework, these counter-ions accumulate at the liquid side of the interface, and increasing ionic strength compresses the diffuse layer (shorter $\lambda_D$),[632,633] driving counter-ions close enough to the interface to suppress a substantial fraction

of the field lines originating from $\sigma_0$. Although $\sigma_0$ itself remains largely unchanged, the externally Coulomb field intensity decreases because the field is closer confined within nanometers of the interface.

Since electrostatic induction relies on the long-range Coulomb field extending into air, EDL-mediated screening directly reduces $V_{oc}$. At low ionic strength, field lines propagate freely toward the electrodes, producing strong polarization. At higher ionic strength, most field lines screen within the compact EDL, yielding a diminished potential landscape and lower $V_{oc}$, as observed in **Figure 6.9m,n**. Notably, multivalent cations such as $Ca^{2+}$ compress the EDL far more effectively than monovalent ions such as $Na^{+}$. Owing to their higher charge and stronger electrostatic coupling, $Ca^{2+}$ ions bind more strongly within the interfacial region, dramatically shortening $\lambda_D$. This enhanced EDL compaction traps a greater fraction of field lines arising from $\sigma_0$, thereby reducing Coulomb field, and suppressing $V_{oc}$ more strongly than monovalent salts at the same concentration. In agreement with this, Trefalt et al. showed that the degree of counter-ion accumulation, and thus the extent of screening, scales strongly with counter-ion valence.[377] Together, these effects explain the complex dependence of $V_{oc}$ on electrolyte type and ionic strength: multivalent ions intensify EDL compaction and more strongly attenuate the external Coulomb field, thereby reducing the electrostatic induction that contributes to the measured $V_{oc}$.

#### 6.3.9.4 **Charge relaxation time and internal ionic conduction)**

Surface charge generated at the nozzle does not necessarily persist during free fall. Its stability is governed by the charge relaxation time $\tau=\varepsilon/\sigma_{el}$, which sets the rate at which internal ionic conduction dissipates interfacial charge **(Figure 6.10d)**. In low-conductivity liquids (long $\tau$), internal conduction currents can be negligible on the millisecond flight timescale, and the droplet retains nearly all of its initial charge. The resulting Coulomb field thus remains strong at the electrode plane, producing a pronounced $V_{oc}$. While, in high-conductivity electrolytes (short $\tau$), internal ionic currents rapidly redistribute charge toward the interface, reducing $\sigma_0$ and collapsing the potential gradient established. As a result, the droplet discharges during descent: the externally observable charge $\sigma_{eff}$ decreases even though the initial surface charge $\sigma_0$ was unchanged.

This conductivity-dependent acceleration of charge relaxation is consistent with the low-frequency double-layer relaxation reported by Płowaś et al.,[634] who showed that increasing electrolyte concentration enhances the mobility and response rate of counter-ions at the inter-

face, thereby strengthening EDL screening and accelerating interfacial charge dissipation. Furthermore, because ionic conductivity increases with temperature through enhanced ion mobility, heating the solution shortens $\tau$,[634,635] promotes faster decay of surface charge, leading to the reduction in $V_{oc}$, such as observed in **Figure 6.9h**. Thus, as conductivity increases, the EDL becomes more compact and screens a larger fraction of the field lines near the interface, weakening the long-range Coulomb field, reducing the induced potential difference. In this regime, the charge relaxation time becomes shorter than the droplet's flight time, causing the interfacial charge to dissipate before the droplet reaches the electrodes position level. When $\tau \ll$ flight time, surface charge cannot be sustained and the electrostatic induction signal is suppressed.

Overall, the unified framework developed here clarifies how four interrelated surface-charge mechanisms, i.e., nozzle contact electrification, ion-specific adsorption, EDL screening, and charge relaxation, collectively govern the electrolyte-dependent variation of $V_{oc}$ in L-S TENGs. By explicitly incorporating the often overlooked contribution of long-range electrostatic induction, our work provides a more complete physical picture of energy harvesting in flowing liquids. These insights not only inform the design of more efficient L-S TENGs, but also open opportunities for non-invasive charge-sensing and smart electrochemical instrumentation, including contact-free potentiostatic systems.

## 6.4 Conclusion

This work establishes a comprehensive physical framework for liquid–solid (L–S) electrification, elucidating how interfacial electrostatics, hydrodynamic flow, and dielectric architecture cooperatively govern charge generation at aqueous interfaces. By decoupling mechanical impacts from liquid flow, we demonstrate that hydromechanical-to-electrical transduction emerges from the coupled dynamics of EDL formation, flow-induced electrostatic induction, and hydrodynamic regimes. The resulting mechanism unifies triboelectric and electrokinetic theories under a single dynamic framework, revealing that the observed $V_{oc}$ reflects not merely L-S contact electrification, but a flow-mediated electrostatic coupling between the moving EDL and the solid surface.

We identify that the magnitude and polarity of L-S charge transfer depend nonlinearly on flow velocity, dielectric thickness, and ionic composition. Multivalent electrolytes and

high-permittivity dielectrics (e.g., $TiO_2$–PDMS composite) intensify interfacial fields through EDL compaction, achieving up to 0.055 $mW \cdot m^{-2}$ power density. Furthermore, by demonstrating non-contact (wireless) energy harvesting via flow-induced electrostatic induction, we reveal that the EDL itself can function as a field-coupled charge generator, enabling remote energy transduction without direct interface contact.

We further demonstrate the device's ability to recognize water sliding and to activate electrochromic transitions in $WO_3$, highlighting its potential as a self-powered platform for responsive and adaptive electronics. Beyond energy harvesting, the sensitivity of the flow-induced potential to ionic species further expands the applicability of L-S TENGs as self-powered potentiometric sensors, capable of transducing EDL flow-induced electrostatic induction into measurable electrical signals. This dual functionality bridges energy conversion and chemical sensing, paving the way for intelligent, self-sustained systems capable of operating in a fully non-contact mode.

Overall, we refined the understanding of L-S energy harvesting through TENGs by incorporating the crucial contribution of flow-induced electrostatic potentials. This advance deepens the fundamental understanding of interfacial charge transport and paves the way for scalable, multifunctional devices that integrate energy harvesting, environmental sensing, and adaptive optoelectronic control. The proposed framework extends beyond conventional triboelectric nanogenerators to the broader design of EDL-governed materials and devices, encompassing next-generation sensors, actuators, and flow-responsive systems in micro- and nanofluidic platforms.

# 7

# FINAL CONCLUSIONS

## 7.1 **Conclusions**

With the recent emergence of TENG, first reported in 2012,[5] as disruptive technology for energy harvesting and smart sensing, this thesis contributes to advancing Brazil's role in the rapidly evolving fields of materials science and nanotechnology. It provides model frameworks and practical examples of how fundamental materials science can be translated into applied innovations addressing national priorities such as energy harvesting for sustainable development, environmental monitoring, health diagnostics, agricultural automation, and next-generation IoT devices, as well as smart sensing platforms for autonomous and intelligent systems.

Guided by the principles of the UN SDGs, this thesis advances the frontier of energy harvesting and nanotechnology to develop self-powered, sustainable, and intelligent systems that directly support human health, environmental stewardship, and technological innovation. The research and educational outcomes achieved through this work have been strengthened by international collaborations with institutions in Portugal, Ireland, Italy, England, and Sweden, aligning with CAPES strategic goals of promoting global cooperation, interdisciplinary research, and technological advancement to drive Brazil toward a sustainable, innovation-driven, and knowledge-based economy.

This doctoral thesis explores the convergence of functional materials – e.g., piezoelectric compounds ($NaNbO_3$), $WO_3$, anthocyanins, and LIG – with applied nanotechnology for the development of sustainable, self-powered, and intelligent systems. By integrating chemical, structural, and functional innovations across triboelectric and piezoelectric nanogenerators, the research has established fundamental insights into interfacial charge transfer, material–

structure–function correlations, and energy-conversion mechanisms across multiple scales. These advances have contributed not only to a deeper scientific understanding of energy-harvesting phenomena but also to the design of practical devices capable of operating autonomously in complex environments.

Collectively, the outcomes presented throughout this thesis demonstrate that intelligent material design, hierarchical structuring, and multifunctional integration are key enablers for the next generation of self-sustaining technologies. From bioactive piezoelectric scaffolds to triboelectric-based environmental sensors and L-S energy harvesters, the findings underscore the transformative potential of nanogenerators to bridge fundamental science with real-world applications. To reach these results, each chapter was dedicated to advancing the knowledge of energy harvesting via TENGs and PENGs and their integration into smart sensing systems, highlighting their collective impact on the advancement of materials science and nanotechnology, while outlining future perspectives for continued innovation in this rapidly evolving field.

To reach these results, each chapter was dedicated to advancing the understanding of energy harvesting through TENGs and PENGs and their integration into smart sensing systems, emphasizing their collective contribution to the progress of materials science and nanotechnology. The following sections summarize the main conclusions and highlight their overall significance within this context.

In **Chapter II**, this thesis established the theoretical and conceptual foundation of energy harvesting by elucidating the fundamental mechanisms governing TENGs for environmental applications. The study clarified how ubiquitous ambient mechanical stimuli, e.g., wind, raindrops, and vibrations, can be effectively converted into electrical energy through triboelectrification, forming the basis for self-powered environmental monitoring systems. A central contribution was the introduction of the potential-well model to describe charge-transfer efficiency in TENGs exposed to environmental contamination. This model demonstrated, for the first time, how contamination effects distort potential wells and alter electron, ion, and nanomaterial transfer processes. Additionally, the study established a comprehensive understanding of stiffness compatibility, revealing how the mechanical matching between triboelectric layers influences charge separation and overall energy-conversion efficiency. These insights clarified how interfacial and environmental factors directly affect output stability and performance under real-world conditions.

Beyond theoretical advances, Chapter II proposed multiple strategies to mitigate contamination-induced charge loss by employing functional materials and tailored surface engineering approaches, including hierarchical micro/nanostructuring, chemical modification, and biological immobilization. These strategies not only improved charge retention but also expanded the functionality of TENGs, extending their use beyond conventional energy harvesting toward intelligent and adaptive applications. Overall, this chapter expanded the frontiers of triboelectric science by coupling materials design and surface functionalization to address environmental challenges, thereby advancing TENG technology toward intelligent, self-powered, and sustainable systems.

In **Chapter III**, this thesis advanced the field of energy harvesting through PENGs by introducing stimuli-responsive gyroid scaffolds that redefine bone-regeneration strategies. Using a sacrificial-template methodology, hierarchical $NaNbO_3$@PDMS scaffolds with tunable porosity were fabricated to replicate the cancellous bone microarchitecture and its anisotropic mechanical behavior. The work established clear relationships among porosity, mechanical strength, damping capacity, and electric-field distribution, revealing that higher porosity enhances charge trapping and electric-field intensity through reduced dielectric shielding, whereas lower porosity improves viscoelastic and load-bearing performance. The combination of corona-poled piezoelectric scaffolds and ultrasound stimulation unveiled an efficient mechano-electrical coupling pathway capable of promoting osteogenic activity and tissue mineralization.

Biologically, the study demonstrated that controlled electromechanical stimulation synergistically enhances metabolic activity, calcium deposition, and gene expression of osteogenic markers, with calcium mineralization increasing by over 1200 % compared to non-stimulated controls. Importantly, the aligned electric field within zero-curvature gyroid geometries directed cell organization, achieving up to 10 % improvement in alignment and evidencing the role of electric-field orientation in bone anisotropy. Collectively, these findings establish electrically active gyroid scaffolds as a new class of bioelectric biomaterials that couple mechanical compliance with controlled electrical responsiveness. The overall significance of this chapter lies in bridging piezoelectric energy harvesting and bone-tissue engineering, providing a blueprint for the design of stimuli-responsive scaffolds that advance regenerative medicine, reduce recovery times, and lower healthcare costs through self-powered physiotherapeutic systems.

In **Chapter IV**, this thesis advanced the frontier of self-powered sustainable sensor technologies by demonstrating, for the first time, the *in-situ* functionalization of laser-induced graphene for volatile-ammonia detection in intelligent food-packaging systems. The study established that naturally derived anthocyanins can act simultaneously as graphitization promoters and redox-active transducers, enabling the fabrication of flexible, eco-friendly sensors that integrate colorimetric, electrochemical, and wireless modalities within a single platform. Through anthocyanin-assisted laser writing, a porous graphene-like network with high electrical conductivity ($I_D/I_G$ = 0.87; sheet resistance = 48 $\Omega \cdot sq^{-1}$) was obtained, revealing that π-conjugated flavonoid rings catalyze carbon rearrangement while preserving reactive centers for ammonia redox interactions. Ionic-strength modulation via $Ca^{+2}$-mediated copigmentation further allowed tunable sensitivity and response reversibility, achieving a detection limit of 110 ppm and a sensitivity of 1.2 $\Omega \cdot m^3 \cdot mg^{-1}$.

Beyond material and process innovations, the chapter demonstrated a tri-modal sensing strategy combining chromatic, impedance-based, and RFID wireless readouts, all powered without external energy sources. The integration of TENGs enabled self-powered barcoding, transforming mechanical motion into encoded electrical signals for data transmission. Collectively, these findings establish a sustainable route for the scalable fabrication of multifunctional, food-safe graphene sensors and illustrate how molecularly engineered precursors can embed chemical intelligence into carbon architectures. The overall significance of this work lies in expanding the functionality of LIG beyond conductivity to multifunctional sensing and energy harvesting, bridging materials chemistry, photothermal processing, and device engineering toward real-time, non-invasive food-quality monitoring and next-generation intelligent packaging.

**Chapter V** focused on overcoming key limitations in soft robotics and human–machine interfaces, *i.e.*, durability, contamination, and sustainable energy supply. To overcome these limitations, a transparent, self-cleaning, and self-powered electronic skin (e-skin) was developed, based on hierarchical micro/nanostructured triboelectric nanogenerators (HMN-TENGs). Through a plasma-assisted colloidal-lithography approach, a sequential $O_2/SF_6$ treatment was optimized to decouple oxidation-driven activation and fluorination-driven passivation, yielding chemically stable Si–F and C–F terminations that provide high hydrophobicity (~152° contact angle) and 91% self-cleaning efficiency. The resulting hierarchical PDMS surfaces achieved a 650% increase in power density (≈270 $mW \cdot m^{-2}$) and maintained over 80% of their output after 10 000 mechanical cycles, demonstrating long-term operational stability.

These findings established a clear materials–process–function correlation linking surface chemistry, topology, and triboelectric performance.

Beyond energy harvesting, the HMN-TENGs operated as highly sensitive, self-powered pressure sensors with dual-regime sensitivity (0.34 $V \cdot kPa^{-1}$ at low pressure and 0.06 $V \cdot kPa^{-1}$ at high pressure) and a detection limit of 2.6 $kPa^{-1}$, enabling real-time tactile mapping, smart-lock operation, and autonomous robotic control. Notably, the $V_{oc}$ was exploited for the first time as a direct estimator of superficial contact area, introducing a novel triboelectric voltage-based method for surface-area estimation applicable to structural health monitoring and adaptive robotic feedback. Collectively, this chapter demonstrates that coupling hierarchical surface engineering with fluorinated plasma chemistry can simultaneously enhance self-cleaning, pressure sensor sensitivity, and energy-harvesting efficiency. The overall significance lies in advancing self-powered pressure-sensing technology through transparent, flexible, and contamination-resistant electronic skins, bridging surface physics, plasma chemistry, and triboelectric engineering toward the next generation of sustainable and intelligent soft-robotic systems.

In **Chapter VI**, this thesis established a comprehensive framework for understanding L–S electrification, unifying triboelectric and electrokinetic mechanisms under a single dynamic model. By decoupling mechanical impact from fluid motion, the study demonstrated that charge generation in L–S TENGs arises not only from the commonly reported L–S contact electrification but also from a significant contribution of flow-induced electrostatic induction governed by the dynamics of EDL formation and liquid flow behavior. Systematic experiments across eighteen electrolytes and controlled physicochemical parameters revealed how flow dynamics and ionic conditions jointly enhance electrostatic induction. These findings clarified the respective roles of EDL dynamics and ionic strength in determining the magnitude, polarity, and stability of the electrical output, providing fundamental insights into how electrolyte identity and concentration influence energy conversion at L–S interfaces.

Beyond mechanistic elucidation, Chapter VI introduced the concept of wireless energy harvesting via flow-induced electrostatic coupling, further explaining the additional potential difference established in the open-circuit voltage. It demonstrated that the EDL itself can act as a field-coupled charge generator, resulting from the differential motion between the fixed Stern layer and the mobile diffuse layer, thus enabling non-contact energy transduction from liquid flow. To further demonstrate the applicability of L–S energy harvesting, transparent smart TENG devices were fabricated, capable of activating the electrochromic transition of WO3 films for color modulation in smart windows. Collectively, these findings redefine L–S

electrification as a hybrid triboelectric–electrokinetic process and advance fundamental design principles for EDL-governed materials and devices. The overall significance lies in establishing, for the first time, that energy harvesting in L–S systems extends beyond conventional contact electrification by incorporating EDL formation and differential interfacial motion into the charge-generation mechanism, thus enhancing energy-harvesting efficiency and enabling new routes for intelligent environmental sensing.

Through the combined investigation of triboelectric and piezoelectric nanogenerators, this thesis demonstrated how nanotechnology, materials science, and device engineering can be strategically integrated to convert ambient mechanical energy into usable electrical power and functional signals. The principles of energy harvesting, involving interfacial phenomena at the nanoscale, and their translation into diverse smart, self-powered applications were comprehensively explored throughout this work. By advancing the theoretical understanding of the triboelectric effect and coupling its fundamental mechanisms with materials-engineering strategies, this research bridges the gap between theoretical comprehension and practical implementation of nanogenerators for the development of next-generation, self-powered intelligent systems. These contributions align with and support multiple SDGs, e.g., 3, 4, 7, 9, 12, and 13, further emphasizing the relevance of this work in advancing human well-being and sustainable technological progress.

The knowledge generated in this work is expected to serve as a scientific foundation and guiding framework for future research in this rapidly expanding field. Collectively, these contributions reinforce the impact of this research on the advancement of materials science and nanotechnology, while laying a solid groundwork for continued innovation toward the next generation of sustainable, smart, and self-powered technologies.

## 7.1 Outlook and future directions

The advances achieved in this thesis mark only the beginning of a rapidly evolving technological and scientific frontier in energy-harvesting nanotechnology, a field that has expanded significantly since the first discovery of TENGs in 2012. Given the high sensitivity of TENGs and PENGs to external stimuli, engineering the active surfaces of these devices with functional or stimuli-responsive materials represents a promising direction for advancing smart applications that address a wide range of technological, societal, and sustainability-related challenges.

Future studies should focus on enhancing the specificity and controllability of external stimuli, enabling nanogenerator-based devices to operate reliably under real-world conditions, where environmental factors often introduce noise and complex interference. This approach will be crucial for realizing robust, self-powered smart devices that are free from false inputs and signal artifacts.

From a scientific standpoint, increasing the fundamental understanding of interfacial charge transfer, and electrostatic coupling phenomena, as stablished in this work, but focusing to boost electrical current will be essential to reach an efficient energy harvesting for high power demand electronics. For example, the development of inteligente technologies and data-driven approaches, e.g., machine-learning, can accelerate the discovery of novel materials or even smartly engineer them to synestically boost the electrical current, which concomitantly can also be used for others self-powered smart applications such as material recognition, surface area mapping, and chemical detection.

Thus, because the output power of TENGs, except when enhanced through large-area configurations, remains a key limitation for high-power electronic applications, future research should also explore sensing and signal-processing systems, where low-power operation is sufficient, as exemplified by the smart technologies developed in this thesis. At the same time, materials engineering and device design strategies, including electromagnetic coupling, structural optimization, and multi-mode hybridization, should be further investigated to harvest diverse energy sources and enhance current generation and energy-conversion efficiency.

Building on the demonstration of wireless liquid energy harvesting modulated by EDL formation presented in this work, further exploration of device architectures for fluidic and streaming-potential-based energy harvesting offers significant potential to enhance the efficiency of collecting ubiquitous mechanical energy from liquid flows. In this context, scaling device dimensions could help reduce carbon footprints and dependence on fossil fuels by providing distributed power for autonomous electronic systems. Moreover, based on our findings regarding the dependence of electrical output on electrolyte composition, EDL formation, and ionic strength under wireless energy harvesting, a non-contact potentiometric device could be developed for applications where only minimal material is available or physical contact is undesirable, thereby preserving chemical purity and preventing contamination.

From a technological perspective, the electrical, mechanical, and functional compatibility of nanogenerators with established, commercially available electronic devices and systems

remains largely underexplored. The convergence of energy harvesting, biosensing, and wireless communication holds great promise for the realization of fully self-sustaining devices with applications in smart agriculture, environmental surveillance, and healthcare monitoring. To achieve this, we envision that future studies must prioritize system-level integration and field validation over the mere fabrication of isolated devices, as is often overemphasized. For this purpose, long-term electrical, mechanical, and functional stability, as well as device lifetime and reliability, should be evaluated under real-world operating conditions rather than laboratory-only settings. Thus, future research should focus on advancing TENG Technology Readiness Level (TRL) to accelerate commercialization and global deployment.

Additionally, the use of eco-friendly and biodegradable materials, as demonstrated in Chapter IV, provides a blueprint for developing sustainable electronic devices aligned with circular-economy principles. The incorporation of biowaste-derived or renewable materials can further minimize environmental impact and advance global sustainability goals. Future technological progress can also draw inspiration from nature - as explored in Chapter V of this thesis - the most sophisticated engineer, refined over billions of years - where hierarchical structures, such as those found in trees, combine resilience and functionality while ensuring complete reintegration into the environment at the end of life. Moreover, the exploration of bio-based precursors for functional materials, e.g., the anthocyanin-assisted catalytic synthesis of graphene demonstrated in this thesis, should be further pursued, as it can reduce the carbon footprint and enable the design of materials intrinsically aligned with the SDGs.

Ultimately, by combining expertise in materials science, engineering, and applied physics, and fostering collaboration between academia, industry, and international research initiatives, this field can speed up the shift from conceptual discovery to real-world implementation of next-generation, self-powered technologies. The perspectives presented here reaffirm that the true potential of nanogenerators lies not only in energy harvesting but also in driving societal progress, turning widespread environmental energy into sustainable development.

# REFERENCES


[1] Y. Gui, Y. Wang, S. He, J. Yang, *Energy Convers. Manag.* **2022**, *269*, 116098.
[2] Y. Luo, X. Cao, Z. L. Wang, *Nano Energy* **2023**, *107*, 108097.
[3] A. Gao, Q. Zhou, Z. Cao, W. Xu, K. Zhou, B. Wang, J. Pan, C. Pan, F. Xia, *Adv. Sci.* **2024**, *2309824*.
[4] C. Men, X. Liu, Y. Chen, S. Liu, S. Wang, S. Gao, *Nano Energy* **2022**, *101*, 107578.
[5] F. R. Fan, Z. Q. Tian, Z. Lin Wang, *Nano Energy* **2012**, *1*, 328.
[6] Z. L. Wang, *Mater. Today* **2017**, *20*, 74.
[7] G. Xu, X. Li, J. Fu, Y. Zhou, X. Xia, Y. Zi, *Energy Environ. Sci.* **2023**, 2112.
[8] S. Dai, X. Li, C. Jiang, J. Ping, Y. Ying, *InfoMat* **2023**, *5*, 1.
[9] S. Panda, S. Hajra, Y. Oh, W. Oh, J. Lee, H. Shin, V. Vivekananthan, Y. Yang, Y. K. Mishra, H. J. Kim, *Small* **2023**, *19*, 1.
[10] S. Divya, S. Panda, S. Hajra, R. Jeyaraj, A. Paul, S. H. Park, H. J. Kim, T. H. Oh, *Nano Energy* **2023**, *106*, 108084.
[11] C. Jiang, Q. Zhang, C. He, C. Zhang, X. Feng, X. Li, Q. Zhao, Y. Ying, J. Ping, *Fundam. Res.* **2022**, *2*, 974.
[12] X. Li, J. Luo, K. Han, X. Shi, Z. Ren, Y. Xi, Y. Ying, J. Ping, Z. L. Wang, *Nat. Food* **2022**, *3*, 133.
[13] Q. Li, W. Liu, H. Yang, W. He, L. Long, M. Wu, X. Zhang, Y. Xi, C. Hu, Z. L. Wang, *Nano Energy* **2021**, *90*.
[14] F. Dong, Z. Pang, Q. Lin, D. Wang, X. Ma, S. Song, S. Nie, *Nano Energy* **2022**, *100*, 107515.
[15] C. Zhang, Z. Zhou, X. Wang, J. Liu, J. Sun, L. Wang, W. Ye, C. Pan, A. Medical, C. Zhang, **2022**, 1.
[16] J. Tian, H. Feng, L. Yan, M. Yu, H. Ouyang, H. Li, W. Jiang, Y. Jin, G. Zhu, Z. Li, Z. L. Wang, *Nano Energy* **2017**, *36*, 241.
[17] S. Cho, Z. Hanif, Y. Yun, Z. A. Khan, S. Jang, Y. Ra, Z. H. Lin, M. La, S. J. Park, D. Choi, *Nano Energy* **2021**, *88*, 106228.
[18] C. L. Li, W. Z. Song, D. J. Sun, M. Zhang, J. Zhang, Y. Q. Chen, S. Ramakrishna, Y. Z. Long, *Chem. Eng. J.* **2023**, *452*, 139428.
[19] C. Cai, J. Mo, Y. Lu, N. Zhang, Z. Wu, S. Wang, S. Nie, *Nano Energy* **2021**, *83*, 105833.
[20] H. Guo, J. Chen, L. Wang, A. C. Wang, Y. Li, C. An, J. H. He, C. Hu, V. K. S. Hsiao, Z. L. Wang, *Nat. Sustain.* **2021**, *4*, 147.
[21] R. Lei, Y. Shi, X. Wang, X. Tao, H. Zhai, X. Chen, *Nano Energy* **2021**, *88*, 106230.

[22] X. Xu, Y. Wang, P. Li, W. Xu, L. Wei, Z. Wang, Z. Yang, *Nano Energy* **2021**, *90*, 106573.
[23] Q. Zeng, Y. Luo, X. Zhang, L. Tan, A. Chen, Q. Tang, H. Yang, X. Wang, *Small* **2023**, *19*, 1.
[24] Y. Liu, N. Sun, J. Liu, Z. Wen, X. Sun, S. T. Lee, B. Sun, *ACS Nano* **2018**, *12*, 2893.
[25] B. Zhang, J. Chen, L. Jin, W. Deng, L. Zhang, H. Zhang, M. Zhu, W. Yang, Z. L. Wang, *ACS Nano* **2016**, *10*, 6241.
[26] Y. Wu, X. Zhong, X. Wang, Y. Yang, Z. L. Wang, *Nano Res.* **2014**, *7*, 1631.
[27] H. Jo, D. Park, M. Joo, D. Choi, J. Kang, J. M. Ha, K. H. Kim, K. H. Kim, S. An, *EcoMat* **2023**, *5*, 1.
[28] H. Wu, Z. Chen, G. Xu, J. Xu, Z. Wang, Y. Zi, *ACS Appl. Mater. Interfaces* **2020**, *12*, 56060.
[29] J. Zhang, S. Hu, Z. Shi, Y. Wang, Y. Lei, J. Han, Y. Xiong, J. Sun, L. Zheng, Q. Sun, G. Yang, Z. L. Wang, *Nano Energy* **2021**, *89*, 106354.
[30] L. M. Gorghiu, S. Jipa, T. Zaharescu, R. Setnescu, I. Mihalcea, *Polym. Degrad. Stab.* **2004**, *84*, 7.
[31] K. V. Khopade, S. H. Chikkali, N. Barsu, *Cell Reports Phys. Sci.* **2023**, *4*, 101341.
[32] L. A. Fakhri, B. Ghanbarzadeh, J. Dehghannya, M. Hosseini, S. Dadashi, *Chemosphere* **2021**, *283*, 130972.
[33] Y. Wang, G. Zhang, L. Wang, *J. Agric. Food Chem.* **2015**, *63*, 75.
[34] D. Kim, M. Zarei, S. Lee, H. Lee, G. Lee, S. G. Lee, *Adv. Sci.* **2025**, 12, 16, *2414748*.
[35] Y. Yang, B. Mu, M. Wang, M. A. Nikitina, U. Zafari, X. Xiao, *Mater. Today Sustain.* **2022**, *19*.
[36] Y. Xie, S. Wang, S. Niu, L. Lin, Q. Jing, J. Yang, Z. Wu, Z. L. Wang, *Adv. Mater.* **2014**, *26*, 6599.
[37] Z. L. Wang, J. Chen, L. Lin, *Energy Environ. Sci.* **2015**, *8*, 2250.
[38] C. Hu, Y. Yang, Z. L. Wang, *Nano Energy* **2022**, *103*.
[39] S. K. Karan, S. Maiti, A. K. Agrawal, A. K. Das, A. Maitra, S. Paria, A. Bera, R. Bera, L. Halder, A. K. Mishra, J. K. Kim, B. B. Khatua, *Nano Energy* **2019**, *59*, 169.
[40] Z. Liu, J. Yang, H. Wang, J. Zhang, H. Bai, B. Peng, W. Ai, H. Du, L. Li, P. Chen, *J. Electroanal. Chem.* **2023**, *950*, 117881.
[41] B. Ryu, J. Chung, M. Kumagai, T. Mato, Y. Ando, S. Gunji, A. Tanaka, D. Yana, M. Fujimoto, Y. Imai, Y. Katsura, S. D. Park, *iScience* **2023**, *26*, 106494.
[42] S. N. Alam, A. Ghosh, P. Shrivastava, U. Shukla, K. Garg, A. C. Edara, N. Sahoo, *Nano-Structures and Nano-Objects* **2023**, *34*, 100980.
[43] Z. L. Wang, *Handbook of Triboelectric Nanogenerators*, **2023**.
[44] D. Tainoff, A. Proudhom, C. Tur, T. Crozes, S. Dufresnes, S. Dumont, D. Bourgault, O. Bourgeois, *Nano Energy* **2019**, *57*, 804.
[45] Y. Yang, Z. L. Wang, *Nano Energy* **2014**, *14*, 245.
[46] B. J. Hansen, Y. Liu, R. Yang, Z. L. Wang, *ACS Nano* **2010**, *4*, 3647.
[47] D. Zhang, Y. Wang, Y. Yang, *Small* **2019**, *15*, 1.
[48] F. Hu, Q. Cai, F. Liao, M. Shao, S. T. Lee, *Small* **2015**, *11*, 5611.
[49] M. Acosta, N. Novak, V. Rojas, S. Patel, R. Vaish, J. Koruza, G. A. Rossetti, J. Rödel, *Appl. Phys. Rev.* **2017**, *4*.
[50] N. Sezer, M. Koç, *Nano Energy* **2021**, *80*, 105567.
[51] S. P. Collins, A. Storrow, D. Liu, C. A. Jenkins, K. F. Miller, C. Kampe, J. Butler, **2021**, *1*, 264.

[52] P. K. Panda, *J. Mater. Sci.* **2009**, *44*, 5049.
[53] V. E. Ogbonna, A. P. I. Popoola, O. M. Popoola, *Front. Energy Res.* **2022**, *10*, 1.
[54] X. Li, C. Jiang, F. Zhao, Y. Shao, Y. Ying, J. Ping, *Nano Energy* **2020**, *73*, 104738.
[55] P. Ma, H. Zhu, H. Lu, Y. Zeng, N. Zheng, Z. L. Wang, X. Cao, *Nano Energy* **2021**, *86*, 106032.
[56] X. Hu, Z. Ding, L. Fei, Y. Xiang, Y. lin, *J. Mater. Sci.* **2019**, *54*, 6401.
[57] L. Jin, S. Ma, W. Deng, C. Yan, T. Yang, X. Chu, G. Tian, D. Xiong, J. Lu, W. Yang, *Nano Energy* **2018**, *50*, 632.
[58] Q. Zhang, Q. Liang, Z. Zhang, Z. Kang, Q. Liao, Y. Ding, M. Ma, F. Gao, X. Zhao, Y. Zhang, *Adv. Funct. Mater.* **2018**, *28*, 1.
[59] P. Wang, R. Liu, W. Ding, P. Zhang, L. Pan, G. Dai, H. Zou, K. Dong, C. Xu, Z. L. Wang, *Adv. Funct. Mater.* **2018**, *28*, 1.
[60] G. De Gioannis, A. Dell'Era, A. Muntoni, M. Pasquali, A. Polettini, R. Pomi, A. Rossi, T. Zonfa, *Clean Technol. Environ. Policy* **2023**, *25*, 269.
[61] P. Mullai, S. Vishali, S. M. Sambavi, K. Dharmalingam, M. K. Yogeswari, V. C. Vadivel Raja, B. Bharathiraja, B. Bayar, H. N. Abubackar, M. A. Al Noman, E. R. Rene, *Chemosphere* **2023**, *342*.
[62] H. Wang, F. Qian, Y. Li, *Nano Energy* **2014**, *8*, 264.
[63] S. Rubenwolf, S. Kerzenmacher, R. Zengerle, F. Von Stetten, *Appl. Microbiol. Biotechnol.* **2011**, *89*, 1315.
[64] R. Binner, V. Menath, H. Huber, M. Thomm, F. Bischof, D. Schmack, M. Reuter, *Biomass Convers. Biorefinery* **2011**, *1*, 1.
[65] S. M. S. Rana, M. T. Rahman, M. Salauddin, S. Sharma, P. Maharjan, T. Bhatta, H. Cho, C. Park, J. Y. Park, *ACS Appl. Mater. Interfaces* **2021**, *13*, 4955.
[66] M. Salauddin, S. M. S. Rana, M. T. Rahman, M. Sharifuzzaman, P. Maharjan, T. Bhatta, H. Cho, S. H. Lee, C. Park, K. Shrestha, S. Sharma, J. Y. Park, *Adv. Funct. Mater.* **2022**, *32*, 1.
[67] Y. Tian, Y. An, B. Xu, *Nano Energy* **2022**, *101*.
[68] S. Ghorbanzadeh, W. Zhang, *Nano Energy* **2024**, *125*, 109558.
[69] F. Paquin, J. Rivnay, A. Salleo, N. Stingelin, C. Silva, *J. Mater. Chem. C* **2015**, *3*, 10715.
[70] F. A. T. Furfari, *IEEE Ind. Appl. Mag.* **2005**, *11*, 10.
[71] P. Iversen, D. J. Lacks, *J. Electrostat.* **2012**, *70*, 309.
[72] A. Wåhlin, *Umeå Univ.* **1973**.
[73] C. C. Gillispie, *Scribner, New York* **1970**, 1970.
[74] B. Dibner, *Electr. Eng.* **2013**, *73*, 396.
[75] G. D. Bishop, *Phys. Educ.* **1977**, *12*, 92.
[76] T. Brundtland, *Notes Rec. R. Soc.* **2012**, *66*, 253.
[77] R. Zhang, M. Hummelgård, J. Örtegren, M. Olsen, H. Andersson, Y. Yang, H. Zheng, H. Olin, *Nano Energy* **2021**, *86*.
[78] A. W. Simon, *Rev. Sci. Instrum.* **1933**, *4*, 75.
[79] H. M. Aguilar, **2014**, *8*, 100.
[80] Z. L. Wang, *Faraday Discuss.* **2014**, *176*, 447.
[81] Z. Wen, M. Yeh, H. Guo, J. Wang, Y. Zi, W. Xu, J. Deng, L. Zhu, X. Wang, C. Hu, L. Zhu, X. Sun, Z. L. Wang, **2016**.
[82] X. Pu, H. Guo, J. Chen, X. Wang, Y. Xi, C. Hu, Z. L. Wang, **2017**, 1.

[83] Y. Zi, L. Lin, J. Wang, S. Wang, J. Chen, X. Fan, P. Yang, F. Yi, Z. L. Wang, **2015**, 1.
[84] Z. L. Wang, *Adv. Energy Mater.* **2020**, *10*, 1.
[85] M. R. James, S. J. Lane, J. S. Gilbert, *J. Geophys. Res. Solid Earth* **2000**, *105*, 16641.
[86] C. Xu, Y. Zi, A. C. Wang, H. Zou, Y. Dai, X. He, P. Wang, Y. C. Wang, P. Feng, D. Li, Z. L. Wang, *Adv. Mater.* **2018**, *30*, 1.
[87] Z. L. Wang, A. C. Wang, *Mater. Today* **2019**, *30*, 34.
[88] Y. Zhou, W. Deng, J. Xu, J. Chen, *Cell Reports Phys. Sci.* **2020**, *1*, 100142.
[89] S. Niu, Y. Liu, S. Wang, L. Lin, Y. S. Zhou, Y. Hu, Z. L. Wang, *Adv. Funct. Mater.* **2014**, *24*, 3332.
[90] S. Wang, Y. Xie, S. Niu, L. Lin, Z. L. Wang, *Adv. Mater.* **2014**, *26*, 2818.
[91] Y. Zi, S. Niu, J. Wang, Z. Wen, W. Tang, Z. L. Wang, *Nat. Commun.* **2015**, *6*, 1.
[92] J. Zhang, S. Ciampi, *ACS Cent. Sci.* **2020**, *6*, 611.
[93] X. Cui, Y. Zhang, G. Hu, L. Zhang, Y. Zhang, *Nano Energy* **2020**, *70*, 104513.
[94] D. J. Lacks, R. Mohan Sankaran, *J. Phys. D. Appl. Phys.* **2011**, *44*.
[95] G. Ferreira, A. Opinião, S. Das, S. Goswami, L. Pereira, S. Nandy, R. Martins, E. Fortunato, *Nano Energy* **2022**, *95*.
[96] Q. Zhou, J. Pan, S. Deng, F. Xia, T. Kim, *Adv. Mater.* **2021**, *33*.
[97] D. J. Lacks, T. Shinbrot, *Nat. Rev. Chem.* **2019**, *3*, 465.
[98] F. P. Bowden, D. Tabor, F. Palmer, *Am. J. Phys.* **1951**, *19*, 428.
[99] C. A. Mizzi, L. D. Marks, *Nano Lett.* **2022**, *22*, 3939.
[100] E. C. Shin, J. H. Ko, H. K. Lyeo, Y. H. Kim, *Phys. Rev. Res.* **2022**, *4*.
[101] S. Lin, L. Xu, C. Xu, X. Chen, A. C. Wang, B. Zhang, P. Lin, Y. Yang, H. Zhao, Z. L. Wang, *Adv. Mater.* **2019**, *31*, 1.
[102] H. Ko, W. Son, M. S. Kang, H. U. Lee, C. Y. Chung, S. Han, C. Choi, S. B. Cho, *J. Mater. Chem. A* **2022**, *11*, 1148.
[103] G. Fatti, A. Ciniero, H. Ko, H. U. Lee, Y. Na, C. K. Jeong, S. G. Lee, D. Kwak, K. Il Park, S. B. Cho, D. Dini, *Adv. Electron. Mater.* **2023**, *9*.
[104] P. C. Sherrell, A. Sutka, N. A. Shepelin, L. Lapcinskis, O. Verners, L. Germane, M. Timusk, R. A. Fenati, K. Malnieks, A. V. Ellis, *ACS Appl. Mater. Interfaces* **2021**, *13*, 44935.
[105] S. I. Li Zhuohan, *Phys. Rev. Lett.* **2021**, *3 [9,11 –*, 11.
[106] D. M. Gooding, G. K. Kaufman, *Encycl. Inorg. Bioinorg. Chem.* **2019**, 1.
[107] A. B. Oskouyi, U. Sundararaj, P. Mertiny, *Materials (Basel).* **2014**, *7*, 2501.
[108] S. Pan, Z. Zhang, *Friction* **2019**, *7*, 2.
[109] S. Lin, X. Chen, Z. L. Wang, *Chem. Rev.* **2022**, *122*, 5209.
[110] S. Lin, L. Xu, A. Chi Wang, Z. L. Wang, *Nat. Commun.* **2020**, *11*, 1.
[111] F. Zhan, A. C. Wang, L. Xu, S. Lin, J. Shao, X. Chen, Z. L. Wang, *ACS Nano* **2020**, *14*, 17565.
[112] M. M. Caruso, D. A. Davis, Q. Shen, S. A. Odom, N. R. Sottos, S. R. White, J. S. Moore, *Chem. Rev.* **2009**, *109*, 5755.
[113] A. Šutka, A. Linarts, K. Malnieks, K. Stiprais, L. Lapčinskis, *Mater. Horizons* **2020**, *7*, 520.
[114] L. Lapčinskis, K. Mālnieks, J. Blūms, M. Knite, S. Oras, T. Käämbre, S. Vlassov, M. Antsov, M. Timusk, A. Šutka, *Macromol. Mater. Eng.* **2020**, *305*, 1.
[115] H. T. Baytekin, A. Z. Patashinski, M. Branicki, B. Baytekin, S. Soh, B. A. Grzybowski, *Science (80-. ).* **2011**, *333*, 308.
[116] V. A. Online, *Energy Environ. Sci.* **2019**, *12*, 2417.

[117] O. Verners, L. Lap, K. Pudzs, A. V Ellis, P. C. Sherrell, A. Sutka, **2022**, *104*.
[118] D. Woo, D. Sol, J. Hun, S. Hyeok, Y. Chieh, Y. Joon, C. Bae, S. Lee, J. Il, J. Choi, G. Lee, M. Lee, J. Jae, K. Soo, J. Young, J. Hoon, *Nano Energy* **2022**, *103*, 107813.
[119] G. Ferreira, S. Das, A. Rego, R. R. A. Silva, D. Gaspar, S. Goswami, R. N. Pereira, E. Fortunato, L. Pereira, R. Martins, S. Nandy, *Chem. Eng. J.* **2024**, *480*, 147995.
[120] S. Goswami, S. Nandy, T. R. Calmeiro, R. Igreja, R. Martins, E. Fortunato, *Sci. Rep.* **2016**, *6*, 1.
[121] L. S. McCarty, G. M. Whitesides, *Angew. Chemie - Int. Ed.* **2008**, *47*, 2188.
[122] H. T. Baytekin, B. Baytekin, S. Soh, B. A. Grzybowski, *Angew. Chemie* **2011**, *123*, 6898.
[123] G. Grosjean, S. Waitukaitis, *Phys. Rev. Lett.* **2023**, *130*, 98202.
[124] S. Lee, H. J. Ko, J. Kim, *Micro Nano Syst. Lett.* **2025**, *13*.
[125] I. Firdous, M. Fahim, W. A. Daoud, *Nano Energy* **2021**, *82*, 105694.
[126] W. G. Kim, D. W. Kim, I. W. Tcho, J. K. Kim, M. S. Kim, Y. K. Choi, *ACS Nano* **2021**, *15*, 258.
[127] P. Taylor, J. Lowell, *Adv. Phys.* **1980**, *29*, 947.
[128] Y. Dong, N. Wang, D. Yang, J. Wang, W. Lu, D. Wang, *Adv. Funct. Mater.* **2023**, *33*, 1.
[129] M. Sun, Q. Lu, Z. L. Wang, B. Huang, *Nat. Commun.* **2021**, *12*.
[130] G. Fatti, H. Kim, C. Sohn, M. Park, Y. Lim, Z. Li, K. Park, I. Szlufarska, H. Ko, C. K. Jeong, S. B. Cho, *Phys. Rev. Lett.* **2023**, *131*, 166201.
[131] S. S. Batsanov, *Inorg. Mater.* **2001**, *37*, 871.
[132] J. O. Löfken, G. Yalovega, T. Möller, M. Riedler, A. Wark, C. Nowak, A. Kolmakov, A. V. Soldatov, A. R. B. de Castro, *Phys. Rev. B - Condens. Matter Mater. Phys.* **2001**, *64*, 1.
[133] S. Kournopoulos, M. S. Santos, S. Ravipati, A. J. Haslam, G. Jackson, I. G. Economou, A. Galindo, *J. Phys. Chem. B* **2022**, *126*, 9821.
[134] V. Aquilanti, D. Cappelletti, F. Pirani, *Chem. Phys.* **1996**, *209*, 299.
[135] Q. Li, W. Liu, H. Yang, W. He, L. Long, M. Wu, X. Zhang, Y. Xi, C. Hu, Z. L. Z. Wang, C. Shan, W. He, H. Wu, S. Fu, Q. Tang, Z. L. Z. Wang, Y. Du, J. Wang, H. Guo, C. Hu, *Adv. Energy Mater.* **2022**, *90*, 1.
[136] X. Cao, M. Zhang, J. Huang, T. Jiang, J. Zou, N. Wang, Z. L. Wang, *Adv. Mater.* **2018**, *30*, 1.
[137] M. Kim, H. Park, M. H. Lee, J. W. Bae, K. Y. Lee, J. H. Lee, J. H. Lee, *Nano Energy* **2023**, *107*, 108159.
[138] X. Li, C. Jiang, F. Zhao, L. Lan, Y. Yao, Y. Yu, J. Ping, Y. Ying, *Nano Energy* **2019**, *61*, 78.
[139] H. Sun, Y. Zhao, C. Wang, K. Zhou, C. Yan, G. Zheng, J. Huang, K. Dai, C. Liu, C. Shen, *Nano Energy* **2020**, *76*.
[140] C. Li, H. Guo, Z. Wu, P. Wang, D. Zhang, Y. Sun, *Adv. Funct. Mater.* **2023**, *33*.
[141] C. Xin, Z. Li, Q. Zhang, Y. Peng, H. Guo, S. Xie, *Nano Energy* **2022**, *100*, 107448.
[142] A. A. Maamoun, A. A. Mahmoud, D. M. Naeim, M. Arafa, A. M. K. Esawi, *Mater. Adv.* **2024**, *5*, 6132.
[143] W. Z. Song, T. T. Zhang, D. S. Zhang, C. L. Li, D. J. Sun, J. Zhang, S. Ramakrishna, Y. Z. Long, *Nano Energy* **2023**, *114*, 108621.
[144] X. Han, D. Jiang, X. Qu, Y. Bai, Y. Cao, R. Luo, Z. Li, *Materials (Basel).* **2021**, *14*, 1.
[145] W. Li, J. Liu, L. Chen, W. Wei, K. Qian, Y. Liu, J. Leng, *Small* **2022**, *18*, 1.
[146] C. Li, J. Yang, W. He, M. Xiong, X. Niu, X. Li, D. G. Yu, *Adv. Mater. Interfaces* **2023**, *10*.
[147] M. M. Hasan, C. L. Johnson, A. C. Dunn, *Langmuir* **2022**, *38*, 9454.

[148] C. Zhang, W. Yu, L. Yin, Q. Zeng, Z. Chen, Y. Shao, *Int. J. Solids Struct.* **2023**, *262–263*, 112042.
[149] K. Barri, Q. Zhang, J. Kline, W. Lu, J. Luo, Z. Sun, B. E. Taylor, S. G. Sachs, L. Khazanovich, Z. L. Wang, A. H. Alavi, *Adv. Mater.* **2023**, *35*, 1.
[150] Z. Wang, C. Xiang, X. Yao, P. Le Floch, J. Mendez, Z. Suo, *Proc. Natl. Acad. Sci. U. S. A.* **2019**, *116*, 5967.
[151] J. Zhang, R. J. Perez, E. J. Lavernia, *J. Mater. Sci.* **1993**, *28*, 2395.
[152] H. Mao, S. Mahadevan, *Compos. Struct.* **2002**, *58*, 405.
[153] S. Li, S. Wang, Y. Zi, Z. Wen, L. Lin, G. Zhang, Z. L. Wang, *ACS Nano* **2015**, *9*, 7479.
[154] S. Utrera-Barrios, R. Verdejo, M. A. López-Manchado, M. Hernández Santana, *Mater. Horizons* **2020**, *7*, 2882.
[155] Z. Wei, J. H. Yang, J. Zhou, F. Xu, M. Zrínyi, P. H. Dussault, Y. Osada, Y. M. Chen, *Chem. Soc. Rev.* **2014**, *43*, 8114.
[156] Y. J. Tan, J. Wu, H. Li, B. C. K. Tee, *ACS Appl. Mater. Interfaces* **2018**, *10*, 15331.
[157] K. X. Hou, X. Dai, S. P. Zhao, L. B. Huang, C. H. Li, *Nano Energy* **2023**, *116*, 108739.
[158] C. Li, P. Wang, D. Zhang, *Nano Energy* **2023**, *109*, 108285.
[159] J. Zhao, Y. Wang, B. Wang, Y. Sun, H. Lv, Z. Wang, W. Zhang, Y. Jiang, *Nanoscale* **2023**, *15*, 6812.
[160] M. He, W. Du, Y. Feng, S. Li, W. Wang, X. Zhang, A. Yu, L. Wan, J. Zhai, *Nano Energy* **2021**, *86*, 106058.
[161] H. Wu, Y. A. Huang, F. Xu, Y. Duan, Z. Yin, *Adv. Mater.* **2016**, *28*, 9881.
[162] R. M. Erb, J. S. Sander, R. Grisch, A. R. Studart, *Nat. Commun.* **2013**, *4*, 1.
[163] A. R. Studart, R. M. Erb, *Soft Matter* **2014**, *10*, 1284.
[164] C. A. M. La Porta, M. C. Lionetti, S. Bonfanti, S. Milan, C. Ferrario, D. Rayneau-Kirkhope, M. Beretta, M. Hanifpour, U. Fascio, M. Ascagni, L. De Paola, Z. Budrikis, M. Schiavoni, E. Falletta, A. Caselli, O. Chepizhko, A. Tuissi, A. Vailati, S. Zapperi, *Proc. Natl. Acad. Sci. U. S. A.* **2019**, *116*, 18777.
[165] G. Yang, H. Li, R. Xing, M. Lv, C. Ma, J. Yan, X. Zhuang, *Adv. Funct. Mater.* **2023**, *33*, 1.
[166] W. Yan, Y. Ding, R. Zhang, X. Luo, P. Sheng, P. Xue, J. He, *Polymer (Guildf).* **2022**, *239*, 124436.
[167] S. S. K. Mallineni, Y. Dong, H. Behlow, A. M. Rao, R. Podila, *Adv. Energy Mater.* **2018**, *8*, 1.
[168] J. Islam, R. R. A. Silva, A. Imbrogno, C. G. Otoni, R. Martins, L. H. C. Mattoso, A. J. Quinn, D. Iacopino, *ACS Appl. Electron. Mater.* **2025**, 7, 11, 4801–4813.
[169] J. A. Bouwstra, A. De Graaff, G. S. Gooris, J. Nijsse, J. W. Wiechers, A. C. Van Aelst, *J. Invest. Dermatol.* **2003**, *120*, 750.
[170] S. Liu, C. Gunawan, N. Barraud, S. A. Rice, E. J. Harry, R. Amal, *Environ. Sci. Technol.* **2016**, *50*, 8954.
[171] G. Levicán, J. A. Ugalde, N. Ehrenfeld, A. Maass, P. Parada, *BMC Genomics* **2008**, *9*, 1.
[172] S. Y. Wong, A. L. Hook, W. Gardner, C. Y. Chang, Y. Mei, M. C. Davies, P. Williams, M. R. Alexander, D. Ballabio, B. W. Muir, D. A. Winkler, P. J. Pigram, *Adv. Mater. Interfaces* **2023**, *10*.
[173] P. G. Bowler, B. I. Duerden, D. G. Armstrong, *Clin. Microbiol. Rev.* **2001**, *14*, 244.
[174] S. M. Imani, L. Ladouceur, T. Marshall, R. Maclachlan, L. Soleymani, T. F. Didar, *ACS Nano* **2020**, *14*, 12341.

[175] X. Peng, K. Dong, C. Ye, Y. Jiang, S. Zhai, R. Cheng, D. Liu, X. Gao, J. Wang, Z. L. Wang, *Sci. Adv.* **2020**, *6*.
[176] X. Liu, Y. Xu, K. Ben, Z. Chen, Y. Wang, Z. Guan, *Appl. Surf. Sci.* **2015**, *339*, 94.
[177] C. Cao, M. Ge, J. Huang, S. Li, S. Deng, S. Zhang, Z. Chen, K. Zhang, S. S. Al-Deyab, Y. Lai, *J. Mater. Chem. A* **2016**, *4*, 12179.
[178] J. Wu, J. He, K. Yin, Z. Zhu, S. Xiao, Z. Wu, J. A. Duan, *Nano Lett.* **2021**, *21*, 4209.
[179] Z. W. Yang, Y. Pang, L. Zhang, C. Lu, J. Chen, T. Zhou, C. Zhang, Z. L. Wang, *ACS Nano* **2016**, *10*, 10912.
[180] R. T. Tung, *Appl. Phys. Rev.* **2014**, *1*, 0.
[181] L. Zhao, H. Li, J. Meng, A. C. Wang, P. Tan, Y. Zou, Z. Yuan, J. Lu, C. Pan, Y. Fan, Y. Zhang, Y. Zhang, Z. L. Wang, Z. Li, *Adv. Funct. Mater.* **2020**, *30*, 1.
[182] E. Llorens, E. Armelin, M. del M. Pérez-Madrigal, L. J. del Valle, C. Alemán, J. Puiggalí, *Nanomembranes and Nanofibers from Biodegradable Conducting Polymers*, **2013**.
[183] A. N. Andriianova, Y. N. Biglova, A. G. Mustafin, *RSC Adv.* **2020**, *10*, 7468.
[184] G. Ciric-Marjanovic, *Synth. Met.* **2013**, *177*, 1.
[185] S. Bhadra, D. Khastgir, N. K. Singha, J. H. Lee, *Prog. Polym. Sci.* **2009**, *34*, 783.
[186] K. M. Molapo, P. M. Ndangili, R. F. Ajayi, G. Mbambisa, S. M. Mailu, N. Njomo, M. Masikini, P. Baker, E. I. Iwuoha, *Int. J. Electrochem. Sci.* **2012**, *7*, 11859.
[187] T. Abbasi, P. Poornima, T. Kannadasan, S. A. Abbasi, *Int. J. Environ. Eng.* **2013**, *5*, 229.
[188] M. Stjerndahl, K. Holmberg, *J. Colloid Interface Sci.* **2005**, *291*, 570.
[189] R. R. A. Silva, C. S. Marques, T. R. Arruda, S. C. Teixeira, T. V. de Oliveira, *Macromol* **2023**, *3*, 371.
[190] M. Stjerndahl, D. Lundberg, V. Chauhan, R. Bordes, K. Holmberg, *J. Surfactants Deterg.* **2019**, *22*, 1139.
[191] K. M. Zohdy, R. M. El-Sherif, A. M. El-Shamy, *J. Bio- Tribo-Corrosion* **2021**, *7*, 1.
[192] K. Zheng, H. Li, L. Wang, X. Wen, Q. Liu, *Environ. Sci. Pollut. Res.* **2017**, *24*, 21710.
[193] H. Gerengi, G. Bereket, M. Kurtay, *J. Taiwan Inst. Chem. Eng.* **2016**, *58*, 509.
[194] Z. Pilić, I. Martinović, *Int. J. Mater. Res.* **2016**, *107*, 925.
[195] A. Nomura, K. Okayasu, K. Ohno, T. Fukuda, Y. Tsujii, *Macromolecules* **2011**, *44*, 5013.
[196] M. Wagman, S. Medalion, Y. Rabin, *Macromolecules* **2012**, *45*, 9517.
[197] R. R. A. Silva, P. A. V. de Freitas, S. C. Teixeira, T. V. de Oliveira, C. S. Marques, P. C. Stringheta, A. C. dos Santos Pires, S. O. Ferreira, N. de Fátima Ferreira Soares, *Food Biophys.* **2022**, *17*, 59.
[198] X. Cheng, B. Meng, X. Chen, M. Han, H. Chen, Z. Su, M. Shi, H. Zhang, *Small* **2016**, *12*, 229.
[199] W. Lu, X. Wang, C. Wang, K. Gong, J. Li, X. Li, P. Wang, *InfoMat* **2024**, *6*, 1.
[200] S. Akram, S. Ou, I. U. Haq, X. Zhu, Z. Fang, M. Tayyab, M. T. Nazir, *Surfaces and Interfaces* **2024**, *52*, 104835.
[201] D. Aben, H. Ahn, T. M. Nguyen, S. H. Ha, Y. Amangeldinova, W. Lee, D. M. Shin, Y. H. Hwang, *J. Electron. Mater.* **2024**.
[202] L. Zhou, D. Liu, Z. Zhao, S. Li, Y. Liu, L. Liu, Y. Gao, Z. L. Wang, J. Wang, *Adv. Energy Mater.* **2020**, *10*, 1.
[203] S. H. Chung, J. Chung, M. Song, S. Kim, D. Shin, Z. H. Lin, B. Koo, D. Kim, J. Hong, S. Lee, *Adv. Energy Mater.* **2021**, *11*, 1.
[204] C. Park, G. Song, S. M. Cho, J. Chung, Y. Lee, E. H. Kim, M. Kim, S. Lee, J. Huh, C. Park,

*Adv. Funct. Mater.* **2017**, *27*, 1.
[205] Y. Su, G. Xie, H. Tai, S. Li, B. Yang, S. Wang, Q. Zhang, H. Du, H. Zhang, X. Du, Y. Jiang, *Nano Energy* **2018**, *47*, 316.
[206] Z. Li, J. Chen, H. Guo, X. Fan, Z. Wen, M. H. Yeh, C. Yu, X. Cao, Z. L. Wang, *Adv. Mater.* **2016**, *28*, 2983.
[207] S. Cui, Y. Zheng, T. Zhang, D. Wang, F. Zhou, W. Liu, *Nano Energy* **2018**, *49*, 31.
[208] F. R. Fan, L. Lin, G. Zhu, W. Wu, R. Zhang, Z. L. Wang, *Nano Lett.* **2012**, *12*, 3109.
[209] J. Ahn, Z. J. Zhao, J. Choi, Y. Jeong, S. Hwang, J. Ko, J. Gu, S. Jeon, J. Park, M. Kang, D. V. Del Orbe, I. Cho, H. Kang, M. Bok, J. H. Jeong, I. Park, *Nano Energy* **2021**, *85*, 105978.
[210] S. A. Khan, M. A. Ahmed, M. M. Baig, M. M. Rehman, Y. Yang, S. G. Lee, J. W. Choi, W. Y. Kim, *Chem. Eng. J.* **2024**, *485*, 149660.
[211] D. Jang, Y. Kim, T. Y. Kim, K. Koh, U. Jeong, J. Cho, *Nano Energy* **2016**, *20*, 283.
[212] S. Chen, N. Wu, S. Lin, J. Duan, Z. Xu, Y. Pan, H. Zhang, Z. Xu, L. Huang, B. Hu, J. Zhou, *Nano Energy* **2020**, *70*, 104460.
[213] G. Liu, J. Nie, C. Han, T. Jiang, Z. Yang, Y. Pang, L. Xu, T. Guo, T. Bu, C. Zhang, Z. L. Wang, *ACS Appl. Mater. Interfaces* **2018**, *10*, 7126.
[214] J. Chen, J. Li, P. Wang, Y. Peng, C. Wang, J. Wang, D. Zhang, *Adv. Sustain. Syst.* **2023**, *7*, 1.
[215] X. Chen, Y. Zhao, F. Wang, D. Tong, L. Gao, D. Li, L. Wu, X. Mu, Y. Yang, *Adv. Sci.* **2022**, *9*, 1.
[216] H. Luo, G. Gu, W. Shang, W. Zhang, T. Wang, P. Cui, B. Zhang, J. Guo, G. Cheng, Z. Du, *Nanotechnology* **2021**, *32*.
[217] D. Heo, J. ho Son, H. Yong, J. Hur, K. Cha, S. Kim, M. Choi, J. Hong, S. Lee, *Nano Energy* **2023**, *116*, 108793.
[218] M. Heo, J. Yang, B. Kim, C. Lee, H. Park, S. K. Kim, J. Lee, S. Son, J. Cheon, J. Choi, W. Seung, S. W. Kim, J. H. Lee, *Nano Energy* **2024**, *121*, 109257.
[219] A. Fernández, A. Francone, L. H. Thamdrup, A. Johansson, B. Bilenberg, T. Nielsen, M. Guttmann, C. M. Sotomayor Torres, N. Kehagias, *J. Micromechanics Microengineering* **2017**, *27*.
[220] N. Kanovsky, T. Iline-Vul, S. Margel, *Results in Surfaces and Interfaces* **2023**, *10*, 100101.
[221] P. Mazumder, Y. Jiang, D. Baker, A. Carrilero, D. Tulli, D. Infante, A. T. Hunt, V. Pruneri, *Nano Lett.* **2014**, *14*, 4677.
[222] M. Psarski, D. Pawlak, J. Grobelny, G. Celichowski, *J. Adhes. Sci. Technol.* **2015**, *29*, 2035.
[223] B. Kim, S. B. Seo, K. Bae, D. Y. Kim, C. H. Baek, H. M. Kim, *Surf. Coatings Technol.* **2013**, *232*, 928.
[224] Y. Li, S. Chen, H. Yan, H. Jiang, J. Luo, C. Zhang, Y. Pang, Y. Tan, *Chem. Eng. J.* **2023**, *468*, 143572.
[225] C. Zhi, S. Shi, S. Meng, H. Wu, Y. Si, K. Zhang, S. Zhang, J. Hu, *Nano Energy* **2023**, *115*, 108734.
[226] D. Wang, J. Zhao, F. Zhang, P. Claesson, J. Pan, Y. Shi, *Nano Energy* **2023**, *112*, 108479.
[227] N. Miljkovic, D. J. Preston, R. Enright, E. N. Wang, *Nat. Commun.* **2013**, *4*, 1.
[228] S. O. Araújo, R. S. Peres, J. Barata, F. Lidon, J. C. Ramalho, *Agronomy* **2021**, *11*, 1.
[229] D. C. Rose, R. Wheeler, M. Winter, M. Lobley, C. A. Chivers, *Land use policy* **2021**, *100*, 104933.
[230] Y. Won, K. Schwartzenberg, K. A. Gray, *Chemosphere* **2018**, *208*, 899.

[231] L. Bergamonti, G. Predieri, Y. Paz, L. Fornasini, P. P. Lottici, F. Bondioli, *Microchem. J.* **2017**, *133*, 1.
[232] A. Rosales, L. Ortiz-Frade, I. E. Medina-Ramirez, L. A. Godínez, K. Esquivel, *Ultrason. Sonochem.* **2021**, *73*, 105483.
[233] P. Han, E. R. Adler, Y. Liu, L. St Marie, A. El Fatimy, S. Melis, E. Van Keuren, P. Barbara, *Nanotechnology* **2019**, *30*, 0.
[234] R. Nur, T. Tsuchiya, K. Toprasertpong, K. Terabe, S. Takagi, M. Takenaka, *Commun. Mater.* **2020**, *1*, 1.
[235] Q. Zheng, D. P. Durkin, J. E. Elenewski, Y. Sun, N. A. Banek, L. Hua, H. Chen, M. J. Wagner, W. Zhang, D. Shuai, *Environ. Sci. Technol.* **2016**, *50*, 12938.
[236] D. Bhanderi, P. Lakhani, C. K. Modi, *RSC Sustain.* **2023**, *2*, 265.
[237] P. P. Kunturu, J. Huskens, *ACS Appl. Energy Mater.* **2019**, *2*, 7850.
[238] T. Iivonen, M. J. Heikkilä, G. Popov, H. E. Nieminen, M. Kaipio, M. Kemell, M. Mattinen, K. Meinander, K. Mizohata, J. Räisänen, M. Ritala, M. Leskelä, *ACS Omega* **2019**, *4*, 11205.
[239] M. H. Miah, M. U. Khandaker, M. B. Rahman, M. Nur-E-Alam, M. A. Islam, *RSC Adv.* **2024**, *14*, 15876.
[240] V. Kumar, A. Kathiravan, M. A. Jhonsi, *Nano Energy* **2024**, *125*, 109523.
[241] C. B. Jacobs, A. B. Maksov, E. S. Muckley, L. Collins, M. Mahjouri-Samani, A. Ievlev, C. M. Rouleau, J. W. Moon, D. E. Graham, B. G. Sumpter, I. N. Ivanov, *Sci. Rep.* **2017**, *7*, 1.
[242] X. Shi, Y. Ye, H. Wang, F. Liu, Z. Wang, *ACS Appl. Mater. Interfaces* **2018**, *10*, 38449.
[243] U. T. Do, Q. T. Nguyen, J. Kim, Q. S. Luu, Y. Park, M. Song, S. Yang, J. Choi, S. Yun, D. K. Kang, Y. Lee, *Int. J. Biol. Macromol.* **2024**, *270*, 132178.
[244] Y. Zou, K. Lu, Y. Lin, Y. Wu, Y. Wang, L. Li, C. Huang, Y. Zhang, J. L. Brash, H. Chen, Q. Yu, *ACS Appl. Mater. Interfaces* **2021**, *13*, 45191.
[245] Z. Shao, X. Cao, H. Luo, P. Jin, *NPG Asia Mater.* **2018**, *10*, 581.
[246] H. Joo, S. Gwak, H. Park, H. J. Yoon, H. Ryu, S. A. Han, J. H. Lee, *Nano Energy* **2024**, *126*, 109706.
[247] G. P. Alcantara, L. E. B. Ribeiro, A. F. Alves, C. M. G. Andrade, F. Fruett, *Microporous Mesoporous Mater.* **2017**, *247*, 38.
[248] R. R. A. Silva, P. A. V. de Freitas, T. V. de Oliveira, S. C. Teixeira, T. C. B. Rigolon, P. C. Stringheta, C. G. Otoni, N. de F. F. Soares, *Int. J. Biol. Macromol.* **2024**, *277*, 134486.
[249] R. R. A. Silva, C. S. Marques, T. R. Arruda, S. C. Teixeira, T. V. de Oliveira, P. C. Stringheta, A. C. dos Santos Pires, N. de Fátima Ferreira Soares, *Polysaccharides* **2022**, *3*, 426.
[250] G. Tang, C. Zhao, X. Zhao, D. Mei, Y. Pan, B. Li, L. Li, Y. Wang, *Sensors Actuators B Chem.* **2023**, *393*.
[251] A. K. M. M. Alam, C. Xiang, *ACS Omega* **2025**, *10*, 12346.
[252] T. C. Pham, S. Lee, D. Kim, O. S. Jung, M. W. Lee, S. Lee, *ACS Omega* **2020**, *5*, 31254.
[253] D. J. Discenza, M. Levine, *New J. Chem.* **2016**, *40*, 789.
[254] N. Serio, J. Roque, A. Badwal, M. Levine, *Analyst* **2015**, *140*, 7503.
[255] Z. Li, J. Chen, J. Yang, Y. Su, X. Fan, Y. Wu, C. Yu, Z. L. Wang, *Energy Environ. Sci.* **2015**, *8*, 887.
[256] D. Zhang, Y. Yang, Z. Xu, D. Wang, C. Du, *J. Mater. Chem. A* **2022**, *10*, 10935.
[257] H. Zhang, D. Zhang, Y. Yang, L. Zhou, Y. Liu, W. Liu, Y. Sun, Y. Guo, Y. Ji, *Nano Energy*

**2024**, *128*, 109978.
[258] N. Zheng, Y. Xu, Q. Zhao, T. Xie, *Chem. Rev.* **2021**, *121*, 1716.
[259] T. M. FitzSimons, E. V. Anslyn, A. M. Rosales, *ACS Polym. Au* **2022**, *2*, 129.
[260] S. Fujii, S. Kameyama, S. P. Armes, D. Dupin, M. Suzaki, Y. Nakamura, *Soft Matter* **2010**, *6*, 635.
[261] J. G. Kennemur, *Macromolecules* **2019**, *52*, 1354.
[262] A. Muralidharan, R. R. McLeod, S. J. Bryant, *Adv. Funct. Mater.* **2022**, *32*, 2106509.
[263] J. Zhang, X. Cai, R. Dou, C. Guo, J. Tang, Y. Hu, H. Chen, J. Chen, *Mol. Ther. Nucleic Acids* **2023**, *32*, 568.
[264] Y. Huang, Y. Cheng, H. Zhang, L. Mai, L. Xu, *Chem. Eng. J.* **2023**, *470*, 144120.
[265] Y. Wan, K. A. M. Creber, B. Peppley, V. T. Bui, *Polymer (Guildf).* **2003**, *44*, 1057.
[266] Q. Yue, Z. Luo, X. Li, L. A. Fielding, *Soft Matter* **2023**, *19*, 6513.
[267] Q. Du, *Mater. Res. Soc.* **2022**, *37*, 239.
[268] A. Yusuf, J. Sánchez del Río, X. Ao, I. A. Olaizola, D. Y. Wang, *Nano Energy* **2022**, *103*.
[269] S. Throat, S. Bhattacharya, *Adv. Polym. Technol.* **2024**, *2024*, 1444990.
[270] F. Y. Pong, M. Lee, J. R. Bell, N. T. Flynn, *Langmuir* **2006**, *22*, 3851.
[271] W. Lee, M. Seo, J. Kim, *Compos. Sci. Technol.* **2022**, *220*, 109282.
[272] A. Veismoradi, M. Ghalambaz, H. Shirivand, A. Hajjar, A. Mohamad, M. Sheremet, A. Chamkha, O. Younis, *Appl. Therm. Eng.* **2021**, *190*, 116793.
[273] F. Luo, J. Sun, Y. Zou, X. Yang, B. Lin, Y. Feng, H. Li, *Chem. Eng. J.* **2025**, *511*, 161905.
[274] P. Wang, L. Yang, B. Dai, Z. Yang, S. Guo, G. Gao, L. Xu, M. Sun, K. Yao, J. Zhu, *Eur. Polym. J.* **2020**, *123*, 109382.
[275] Z. Z. Tangzhe Nie, Peng Zhang, Peng Chen, Haijun Liu, Lili Jiang, Zhongyi Sun, Shuai Yin, Tianyi Wang, Tiecheng Li, *Clim. Smart Agric.* **2025**, 108993.
[276] S. Wang, S. Yan, L. Zhang, H. Zhao, T. Yang, F. Li, H. Li, *Macromol. Mater. Eng.* **2020**, *305*, 1.
[277] B. Ko, T. Badloe, Y. Yang, J. Park, J. Kim, H. Jeong, C. Jung, J. Rho, *Nat. Commun.* **2022**, *13*.
[278] N. Huynh, J. J. Valle-Delgado, W. Fang, S. Arola, M. Österberg, *Carbohydr. Polym.* **2023**, *317*.
[279] J. Zhu, P. Zhu, Y. Zhu, Y. Ye, X. Sun, Y. Zhang, O. J. Rojas, P. Servati, F. Jiang, *Carbohydr. Polym.* **2024**, *335*, 122059.
[280] P. A. V. Freitas, T. V. de Oliveira, R. R. A. Silva, A. R. Fialho e Moraes, A. C. dos S. Pires, R. R. A. Soares, N. S. Junior, N. F. F. Soares, *Food Packag. Shelf Life* **2020**, *26*.
[281] A. R. Cardoso, A. C. Marques, L. Santos, A. F. Carvalho, F. M. Costa, R. Martins, M. G. F. Sales, E. Fortunato, *Biosens. Bioelectron.* **2019**, *124–125*, 167.
[282] P. Kanokpaka, L. Y. Chang, B. C. Wang, T. H. Huang, M. J. Shih, W. S. Hung, J. Y. Lai, K. C. Ho, M. H. Yeh, *Nano Energy* **2022**, *100*, 107464.
[283] I. Banga, A. Paul, S. Muthukumar, S. Prasad, *ACS Appl. Mater. Interfaces* **2021**, *13*, 16155.
[284] L. E. Kreno, K. Leong, O. K. Farha, M. Allendorf, R. P. Van Duyne, J. T. Hupp, *Chem. Rev.* **2012**, *112*, 1105.
[285] Y. Lu, H. Xiang, Y. Jie, X. Cao, Z. L. Wang, *Adv. Mater. Technol.* **2023**, *8*, 1.
[286] Y. Xie, X. Zhang, Y. Wang, C. Liu, Z. Zhang, *Adv. Funct. Mater.* **2025**, *05747*, 1.
[287] S. Nie, H. Guo, Y. Lu, J. Zhuo, J. Mo, Z. L. Wang, *Adv. Mater. Technol.* **2020**, *5*, 1.
[288] E. Dhanumalayan, G. M. Joshi, *Adv. Compos. Hybrid Mater.* **2018**, *1*, 247.

[289] J. X. Xiang-Shuo Meng, Yujiu Zhou, Jianfeng Li, Hu Ye, Fujia Chen, Yuetao Zhao, Qifeng Pan, *Polymers (Basel).* **2023**, *15*.
[290] R. Zhang, Y. Wen, F. Sun, Z. Xie, M. Zhang, Z. An, B. Liu, Y. Sun, F. Wang, Y. Mao, *Cell Reports Phys. Sci.* **2024**, *27*, 101888.
[291] X. Cao, Y. Xiong, J. Sun, X. Xie, Q. Sun, Z. L. Wang, *Multidiscipline Applications of Triboelectric Nanogenerators for the Intelligent Era of Internet of Things*, Springer Nature Singapore, **2023**.
[292] Y. Wen, F. Sun, Z. Xie, M. Zhang, Z. An, B. Liu, Y. Sun, F. Wang, Y. Mao, *iScience* **2024**, *27*, 109615.
[293] Y. Zhou, M. Shen, X. Cui, Y. Shao, L. Li, Y. Zhang, *Nano Energy* **2021**, *84*, 105887.
[294] M. J. Wenzel, A. Mensah-Brown, F. Josse, E. E. Yaz, *IEEE Sens. J.* **2011**, *11*, 225.
[295] D. Melgar, Y. Bock, D. Sanchez, B. W. Crowell, *J. Geophys. Res. Solid Earth* **2013**, *118*, 1177.
[296] M. A. Mneimneh, E. E. Yaz, M. T. Johnson, R. J. Povinelli, *Comput. Cardiol.* **2006**, *33*, 253.
[297] P. Liu, D. Pan, X. Y. Jiao, J. N. Liu, P. H. Du, P. C. Li, M. Z. Xue, Y. C. Jin, C. S. Wang, X. R. Wang, Y. Z. Ding, G. N. Zhu, J. H. Yang, W. Z. Wu, L. F. Liang, X. H. Liu, L. P. Li, *npj Clean Water* **2025**, *8*.
[298] F. Zhu, J. Gao, J. Yang, N. Ye, *Pattern Recognit.* **2022**, *123*, 108422.
[299] N. Garakyaragh, K. Shahtalebi, *AEU - Int. J. Electron. Commun.* **2022**, *149*, 154171.
[300] K. Kim, I. A. Akbar, K. K. Bae, J. S. Um, C. M. Spooner, J. H. Reed, *2007 2nd IEEE Int. Symp. New Front. Dyn. Spectr. Access Networks* **2007**, 212.
[301] L. Cui, J. Zhang, L. Gao, F. Ding, *Proc. 2007 Int. Conf. Wavelet Anal. Pattern Recognition, ICWAPR '07* **2007**, *3*, 1221.
[302] R. Zhang, *Cell Reports Phys. Sci.* **2024**, *5*, 101888.
[303] W. Zhang, L. Deng, L. Yang, P. Yang, D. Diao, P. Wang, Z. L. Wang, *Nano Energy* **2020**, *77*, 105174.
[304] B. Münch, P. Trtik, F. Marone, M. Stampanoni, *EMPA Act.* **2009**, *17*, 34.
[305] M. F. Issa, Z. Juhasz, *Brain Sci.* **2019**, *9*.
[306] T. Goto, M. Kishita, Y. Sun, T. Sako, I. Okajima, *Polymers (Basel).* **2020**, *12*, 1.
[307] T. A. Hottle, M. L. Agüero, M. M. Bilec, A. E. Landis, *Compost Sci. Util.* **2016**, *24*, 159.
[308] J. E. Cooper, E. L. Kendig, S. M. Belcher, *Chemosphere* **2011**, *85*, 943.
[309] J. Wierzbowska, S. Sienkiewicz, S. Krzebietke, T. Bowszys, *Water. Air. Soil Pollut.* **2016**, *227*.
[310] A. Tarafdar, R. Sirohi, P. A. Balakumaran, R. Reshmy, A. Madhavan, R. Sindhu, P. Binod, Y. Kumar, D. Kumar, S. J. Sim, *J. Hazard. Mater.* **2022**, *423*, 127097.
[311] Q. E. A. Sirianni, E. R. Gillies, *Polymer (Guildf).* **2020**, *202*, 122638.
[312] G. Finnveden, M. Z. Hauschild, T. Ekvall, J. Guinée, R. Heijungs, S. Hellweg, A. Koehler, D. Pennington, S. Suh, *J. Environ. Manage.* **2009**, *91*, 1.
[313] A. Balaguera, G. I. Carvajal, J. Albertí, P. Fullana-i-Palmer, *Resour. Conserv. Recycl.* **2018**, *132*, 37.
[314] X. Xiang, N. Liu, L. Xu, Y. Cai, *Ecotoxicol. Environ. Saf.* **2021**, *224*, 112631.
[315] A. L. Quinn, A. Dalu, L. S. Meeker, P. A. Jean, R. G. Meeks, J. W. Crissman, R. H. Gallavan, K. P. Plotzke, *Reprod. Toxicol.* **2007**, *23*, 532.
[316] G. Ferreira, S. Das, A. Rego, R. R. A. Silva, D. Gaspar, S. Goswami, R. N. Pereira, E. Fortunato, L. Pereira, R. Martins, S. Nandy, *Chem. Eng. J.* **2024**, *480*, 147995.
[317] T. Kuang, J. Zhang, G. M. Huang, T. Liu, Z. X. Huang, *Nano Energy* **2024**, *128*, 109877.

[318] A. Guchait, A. Haridas C. P., S. Chattopadhyay, T. Mondal, *Small* **2025**, *2411410*, 1.
[319] L. Lamanna, G. Pace, I. K. Ilic, P. Cataldi, F. Viola, M. Friuli, V. Galli, C. Demitri, M. Caironi, *Nano Energy* **2023**, *108*, 108168.
[320] S. Mitra, A. J. Chakraborty, A. M. Tareq, T. Bin Emran, F. Nainu, A. Khusro, A. M. Idris, M. U. Khandaker, H. Osman, F. A. Alhumaydhi, J. Simal-Gandara, *J. King Saud Univ. - Sci.* **2022**, *34*, 101865.
[321] X. Zhou, X. Zhou, C. Wang, H. Zhou, *Chemosphere* **2023**, *313*, 137489.
[322] C. H. Halios, C. Landeg-Cox, S. D. Lowther, A. Middleton, T. Marczylo, S. Dimitroulopoulou, *Sci. Total Environ.* **2022**, *839*, 156201.
[323] M. S. Hussain, G. Gupta, R. Mishra, N. Patel, S. Gupta, S. I. Alzarea, I. Kazmi, P. Kumbhar, J. Disouza, H. Dureja, N. Kukreti, S. K. Singh, K. Dua, *Pathol. Res. Pract.* **2024**, *255*, 155157.
[324] E. Khalili Sadrabad, S. A. Hashemi, A. Nadjarzadeh, E. Askari, F. Akrami Mohajeri, F. Ramroudi, *Food Sci. Nutr.* **2023**, *11*, 3718.
[325] K. Tumu, K. Vorst, G. Curtzwiler, *Compr. Rev. Food Sci. Food Saf.* **2023**, *22*, 1337.
[326] Y. Liu, Y. Zhao, B. Sun, C. Chen, *Acc. Chem. Res.* **2013**, *46*, 702.
[327] A. Sani, C. Cao, D. Cui, *Biochem. Biophys. Reports* **2021**, *26*, 100991.
[328] S. Shabbir, M. F. e. A. Kulyar, Z. A. Bhutta, P. Boruah, M. Asif, *Bionanoscience* **2021**, *11*, 621.
[329] X. N. Xie, H. J. Chung, C. H. Sow, K. Adamiak, A. T. S. Wee, *J. Am. Chem. Soc.* **2005**, *127*, 15562.
[330] M. T. Sebastian, R. Ubic, H. Jantunen, *Int. Mater. Rev.* **2015**, *60*, 392.
[331] A. R. Mule, B. Dudem, S. A. Graham, J. S. Yu, *Adv. Funct. Mater.* **2019**, *29*, 1.
[332] S. Roberts, *Phys. Rev.* **1947**, *71*, 890.
[333] K. Uchino, S. Nomura, *Ferroelectrics* **1982**, *44*, 55.
[334] I. M. McKinley, L. Pilon, *Appl. Phys. Lett.* **2013**, *102*, 2.
[335] W. D. Callister, D. G. Rethwisch, *Materials Science and Engineering: An Introduction*, Wiley, Hoboken, NJ, **2014**.
[336] H. Li, C. Li, L. Duan, Y. Qiu, *Isr. J. Chem.* **2014**, *54*, 918.
[337] Q. Y. Ren, L. F. Wang, Q. A. Huang, *IEEE SENSORS* **2015**, *1*, *1–4*.
[338] A. Slonopas, B. Kaur, P. Norris, *Appl. Phys. Lett.* **2017**, *110*, 0.
[339] M. T. Ajide, N. J. English, *J. Mol. Liq.* **2023**, *389*, 122675.
[340] P. K. Sharma, J. Y. Chung, *Micromachines* **2023**, *14*, 1.
[341] Z. Ahmad, *Intech* **2016**, *11*, 13.
[342] R. H. Cole, *Mol. Phys.* **1973**, *26*, 969.
[343] B. Cheng, Q. Xu, Y. Ding, S. Bai, X. Jia, Y. Yu, J. Wen, Y. Qin, *Nat. Commun.* **2021**, *12*, 1.
[344] C. X. Lu, C. B. Han, G. Q. Gu, J. Chen, Z. W. Yang, T. Jiang, C. He, Z. L. Wang, *Adv. Eng. Mater.* **2017**, *19*, 1.
[345] B. B. Owen, R. C. Miller, C. E. Milner, H. L. Cogan, *J. Phys. Chem.* **1961**, *65*, 2065.
[346] C. G. Malmberg, A. A. Maryott, *J. Res. Natl. Bur. Stand. (1934).* **1956**, *56*, 1.
[347] D. Liu, L. Zhou, S. Cui, Y. Gao, S. Li, Z. Zhao, Z. Yi, H. Zou, Y. Fan, J. Wang, Z. L. Wang, *Nat. Commun.* **2022**, *13*.
[348] Y. Zi, C. Wu, W. Ding, Z. L. Wang, *Adv. Funct. Mater.* **2017**, *27*, 1.
[349] N. H. Malik, A. H. Qureshi, *IEEE Trans. Electr. Insul.* **1979**, *EI-14*, 1.
[350] Y. Zheng, T. Liu, J. Cui, Z. Zhang, C. Du, X. Gao, C. Chu, C. Xue, *Sensors Actuators A*

*Phys.* **2023**, *362*, 114613.
[351] D. Ghosh, D. Khastgir, *ACS Omega* **2018**, *3*, 11317.
[352] C. F. Gorin, E. S. Beh, M. W. Kanan, *J. Am. Chem. Soc.* **2012**, *134*, 186.
[353] M. Meincken, T. A. Berhane, P. E. Mallon, *Polymer (Guildf).* **2005**, *46*, 203.
[354] J. Fu, G. Xu, C. Li, X. Xia, D. Guan, J. Li, Z. Huang, Y. Zi, *Adv. Sci.* **2020**, *7*, 1.
[355] V. Nguyen, R. Yang, *Nano Energy* **2013**, *2*, 604.
[356] G. Khandelwal, A. Chandrasekhar, N. P. Maria Joseph Raj, S. J. Kim, *Adv. Energy Mater.* **2019**, *9*, 1.
[357] C. Huang, G. Chen, A. Nashalian, J. Chen, *Nanoscale* **2021**, *13*, 2065.
[358] A. W. Decho, in *Riding, R.E., Awramik, S.M. Microb. Sedimentsments*, Springer, Berlin, Heidelberg, **2000**, pp. 9–15.
[359] R. M. Donlan, J. W. Costerton, R. M. Donlan, J. W. Costerton, *Clin. Microbiol. Rev.* **2002**, *15*.
[360] A. W. Decho, *Ecol. Eng.* **2010**, *36*, 137.
[361] M. F. Moradali, B. H. A. Rehm, *Nat. Rev. Microbiol.* **2020**, *18*, 195.
[362] S. Achinas, N. Charalampogiannis, G. J. W. Euverink, *Appl. Siences* **2019**, *9*, 1.
[363] Y. Zi, H. Guo, Z. Wen, M. H. Yeh, C. Hu, Z. L. Wang, *ACS Nano* **2016**, *10*, 4797.
[364] Y. Li, Z. Zhao, L. Liu, L. Zhou, D. Liu, S. Li, S. Chen, Y. Dai, J. Wang, Z. L. Wang, *Adv. Energy Mater.* **2021**, *11*, 1.
[365] B. Zhang, Q. Gao, W. Li, M. Zhu, H. Li, T. Cheng, Z. L. Wang, *Adv. Funct. Mater.* **2023**, *33*, 1.
[366] J. Zhao, G. Zhen, G. Liu, T. Bu, W. Liu, X. Fu, P. Zhang, C. Zhang, Z. L. Wang, *Nano Energy* **2019**, *61*, 111.
[367] Y. Qi, G. Liu, Y. Kuang, L. Wang, J. Zeng, Y. Lin, H. Zhou, M. Zhu, C. Zhang, *Nano Energy* **2022**, *99*, 107427.
[368] X. Liu, T. Ueki, H. Gao, T. L. Woodard, K. P. Nevin, T. Fu, S. Fu, L. Sun, D. R. Lovley, J. Yao, *Nat. Commun.* **2022**, *13*, 1.
[369] J. Moyal, P. H. Dave, M. Wu, S. Karimpour, S. K. Brar, H. Zhong, R. W. M. Kwong, *Rev. Environ. Contam. Toxicol.* **2023**, *261*, 1.
[370] X. Sun, L. Wang, R. Fu, Y. Yang, R. Cheng, J. Li, S. Wang, J. Zhang, *Int. J. Biol. Macromol.* **2020**, *164*, 2641.
[371] W. Wang, L. Yao, C. Y. Cheng, T. Zhang, H. Atsumi, L. Wang, G. Wang, O. Anilionyte, H. Steiner, J. Ou, K. Zhou, C. Wawrousek, K. Petrecca, A. M. Belcher, R. Karnik, X. Zhao, D. I. C. Wang, H. Ishii, *Sci. Adv.* **2017**, *3*, 1.
[372] N. S. Malvankar, M. T. Tuominen, D. R. Lovley, *Energy Environ. Sci.* **2012**, *5*, 5790.
[373] H. Boudarel, J. D. Mathias, B. Blaysat, M. Grédiac, *npj Biofilms Microbiomes* **2018**, *4*.
[374] B. W. Peterson, Y. He, Y. Ren, A. Zerdoum, M. R. Libera, P. K. Sharma, A. J. van Winkelhoff, D. Neut, P. Stoodley, H. C. van der Mei, H. J. Busscher, *FEMS Microbiol. Rev.* **2015**, *39*, 234.
[375] M. Ammam, *RSC Adv.* **2012**, *2*, 7633.
[376] I. Szilagyi, G. Trefalt, A. Tiraferri, P. Maroni, M. Borkovec, *Soft Matter* **2014**, *10*, 2479.
[377] G. Trefalt, S. H. Behrens, M. Borkovec, *Langmuir* **2016**, *32*, 380.
[378] X. Li, Y. Cao, X. Yu, Y. Xu, Y. Yang, S. Liu, T. Cheng, Z. L. Wang, *Appl. Energy* **2022**, *306*, 117977.
[379] M. T. Rahman, S. M. S. Rana, P. Maharjan, M. Salauddin, T. Bhatta, H. Cho, C. Park, J.

Y. Park, *Nano Energy* **2021**, *85*, 105974.
[380] C. Jiang, X. Li, Y. Ying, J. Ping, *Nano Energy* **2020**, *74*, 104863.
[381] Y. Liu, M. Zhu, D. Nan, X. Li, Y. Wang, W. Su, Z. L. Wang, T. Cheng, *Adv. Sustain. Syst.* **2023**, *7*, 1.
[382] G. Gu, G. Gu, W. Shang, Z. Zhang, W. Zhang, C. Wang, D. Fang, G. Cheng, Z. Du, *Nano Energy* **2022**, *102*, 107699.
[383] S. Fu, H. Wu, C. Shan, K. Li, W. He, Q. Li, X. Yu, S. Du, G. Li, C. Hu, *Nano Energy* **2023**, *116*.
[384] X. Li, C. Jiang, Y. Yao, Q. Zhang, S. Dai, Y. Ying, J. Ping, *Small* **2021**, *17*, 1.
[385] S. Dai, X. Li, C. Jiang, Q. Zhang, B. Peng, J. Ping, Y. Ying, *Nano Energy* **2022**, *91*, 106686.
[386] L. Hu, Z. Duan, J. Song, B. Wu, H. Wang, J. He, *Electron.* **2023**, *12*.
[387] Y. Wang, Q. Gao, W. Liu, C. Bao, H. Li, Y. Wang, Z. L. Wang, T. Cheng, *ACS Appl. Mater. Interfaces* **2024**.
[388] C. Zhao, Y. Wu, X. Dai, J. Han, B. Dong, L. B. Huang, *Mater. Des.* **2022**, *221*, 111005.
[389] S. Wang, Y. Liu, K. Zhang, S. Gao, *Nano Energy* **2023**, *112*, 108434.
[390] B. Zhang, S. Zhang, W. Li, Q. Gao, D. Zhao, Z. L. Wang, T. Cheng, *ACS Nano* **2021**, *15*, 20278.
[391] B. Zhang, W. Li, J. Ge, C. Chen, X. Yu, Z. L. Wang, T. Cheng, *Nano Res.* **2023**, *16*, 3149.
[392] H. Dang, Y. Wang, S. Zhang, Q. Gao, X. Li, L. Wan, Z. L. Wang, T. Cheng, *Mater. Today Energy* **2022**, *29*, 101136.
[393] N. Yang, Y. Li, Z. Xu, Y. Zhu, Q. He, Z. Wang, X. Zhang, J. Liu, C. Liu, Y. Wang, M. Zhou, T. Cheng, Z. L. Wang, *ACS Appl. Mater. Interfaces* **2024**, *16*, 33404.
[394] S. Dai, X. Li, C. Jiang, Y. Shao, J. Luo, Y. Ying, J. Ping, *Small* **2022**, *18*, 1.
[395] L. Dong, J. Zhu, H. Li, J. Zhang, D. Zhao, Z. L. Wang, L. Gu, T. Cheng, *Nano Energy* **2024**, *127*.
[396] Q. Zhang, C. Jiang, X. Li, S. Dai, Y. Ying, J. Ping, *ACS Nano* **2021**, *15*, 12314.
[397] Y. Hu, Y. Hu, J. Li, Z. Wang, J. Ma, T. Cheng, J. Wen, *Mech. Syst. Signal Process.* **2023**, *201*, 110649.
[398] Y. T. Huang, C. C. Huang, C. Y. Su, Y. C. Tsai, *Jpn. J. Appl. Phys.* **2024**, *63*.
[399] M.-C. Wong, W. Xu, J. Hao, *Educ. Res.* **2010**, *29*, 1.
[400] X. Wang, D. Zhang, H. Zhang, L. Gong, Y. Yang, W. Zhao, S. Yu, Y. Yin, D. Sun, *Nano Energy* **2021**, *88*, 106242.
[401] X. Ma, T. Zhou, L. Gong, X. Zhang, F. Yao, C. Wang, *Sensors* **2023**, *23*.
[402] C. Jiang, X. Li, Y. Yao, L. Lan, Y. Shao, F. Zhao, Y. Ying, J. Ping, *Nano Energy* **2019**, *66*, 104121.
[403] S. He, Y. Gui, Y. Wang, J. Yang, *Nano Energy* **2023**, *107*, 108132.
[404] K. Wang, D. Sun, S. Li, M. Liu, W. Liu, Z. He, W. Tang, Z. Li, Y. Lu, Z. Wang, Z. Song, Z. Zhu, Z. Li, *Nano Energy* **2023**, *113*, 108538.
[405] W. Wang, Y. Shang, K. Han, X. Shi, T. Jiang, W. Mai, J. Luo, Z. L. Wang, *ACS Appl. Mater. Interfaces* **2024**.
[406] Z. Hou, X. Li, X. Zhang, W. Zhang, Z. L. Wang, H. Zhang, *Nano Res.* **2023**, *16*, 10198.
[407] C. Han, J. Choi, J. Ahn, H. Kim, J. H. Ha, H. Han, S. Cho, Y. Jeong, J. Gu, I. Park, *Adv. Mater. Technol.* **2023**, *8*, 1.
[408] D. T. Mathew, M. Sunil, N. Joseph, H. K. Raj, A. Mayeen, N. Manoj, P. Sagar, H. John, *ACS Appl. Eng. Mater.* **2024**, 2, 7, 1845-1856.

[409] H. H. Hsu, X. Zhang, K. Xu, Y. Wang, Q. Wang, G. Luo, M. Xing, W. Zhong, *Chem. Eng. J.* **2021**, *422*, 129499.
[410] P. Chen, J. An, S. Shu, R. Cheng, J. Nie, T. Jiang, Z. L. Wang, *Adv. Energy Mater.* **2021**, *11*, 1.
[411] H. Wang, M. Zhang, Z. Yang, Z. Wang, X. Liu, Y. Lu, L. Ji, Z. L. Wang, J. Cheng, *Nano Energy* **2021**, *89*, 106328.
[412] Z. Wang, X. Liu, M. Yue, H. Yao, H. Tian, X. Sun, Y. Wu, Z. Huang, D. Ban, H. Zheng, *Nano Energy* **2022**, *102*, 107681.
[413] T. Liu, Y. Zheng, Y. Xu, X. Liu, C. Wang, L. Yu, M. Fahlman, X. Li, P. Murto, J. Chen, X. Xu, *Nano Energy* **2022**, *103*, 107776.
[414] L. Liu, J. Li, Z. Guan, L. Zhao, Z. Tian, S. Jia, H. Hong, Z. He, H. Wen, R. Huang, H. Cui, W. Ou-Yang, X. Yang, *Chem. Eng. J.* **2023**, *472*, 145039.
[415] R. Zhang, R. Xia, X. Cao, N. Wang, *Adv. Mater. Interfaces* **2022**, *9*, 1.
[416] L. Lan, J. Xiong, D. Gao, Y. Li, J. Chen, J. Lv, J. Ping, Y. Ying, P. S. Lee, *ACS Nano* **2021**, *15*, 5307.
[417] G. Min, G. Khandelwal, A. S. Dahiya, S. Mishra, W. Tang, R. Dahiya, *ACS Sustain. Chem. Eng.* **2024**, *12*, 695.
[418] L. Luo, C. Liu, R. Gu, M. Chen, Y. Wang, N. Xu, Y. Xiong, J. Yang, Z. Huo, Y. Liu, L. Wei, Z. L. Wang, Q. Sun, *Int. J. Extrem. Manuf.* **2025**, *7*.
[419] Y. K. Jung, K. N. Kim, J. M. Baik, B. S. Kim, *Nano Energy* **2016**, *30*, 77.
[420] H. Lei, Y. Chen, Z. Gao, Z. Wen, X. Sun, *J. Mater. Chem. A* **2021**, *9*, 20100.
[421] S. Wang, L. Lin, Z. L. Wang, *Nano Energy* **2015**, *11*, 436.
[422] C. Ning, R. Cheng, Y. Jiang, F. Sheng, J. Yi, S. Shen, Y. Zhang, X. Peng, K. Dong, Z. L. Wang, *ACS Nano* **2022**, *16*, 2811.
[423] J. Wu, Y. Zhang, X. T. Zheng, *Sensors and Diagnostics* **2024**, *3*, 698.
[424] Y. Zhang, X. He, C. Xu, *APL Mater.* **2023**, *11*.
[425] S. Chen, C. Gao, W. Tang, H. Zhu, Y. Han, Q. Jiang, T. Li, X. Cao, Z. Wang, *Nano Energy* **2014**, *14*, 217.
[426] J. Shi, Z. Zhao, Y. Gao, W. Yuan, W. Ma, J. Zhang, B. Zhang, D. Liu, J. Wang, *Small* **2024**, *2311930*, 1.
[427] Y. Pang, Z. Huang, Y. Fang, X. Xu, C. Cao, *Nano Energy* **2023**, *114*, 108659.
[428] Y. Li, Y. Wang, B. Wang, Y. Wang, W. Yu, *J. Plant Biol.* **2019**, *62*, 120.
[429] R. K. Aaron, D. M. K. Ciombor, B. J. Simon, *Clin. Orthop. Relat. Res.* **2004**, *419*, 21.
[430] C. T. Brighton, Z. B. Friedenberg, E. I. Mitchell, R. E. Booth, *Clin Orthop Relat Res .* **1977**, *124*, 106.
[431] C. T. Brighton, W. WANG, R. SELDES, G. ZHANG, S. POLLACK, *J. Bone Jt. Surgery. Am. Vol.* **2001**, *83*, 1514.
[432] B. M. Isaacson, R. D. Bloebaum, *J. Biomed. Mater. Res. - Part A* **2010**, *95*, 1270.
[433] M. Levin, *Bioelectromagnetics* **2003**, *24*, 295.
[434] J. Zhang, M. Li, E. T. Kang, K. G. Neoh, *Acta Biomater.* **2016**, *32*, 46.
[435] P. Moroder, M. B. Runge, H. Wang, T. Ruesink, L. Lu, R. J. Spinner, A. J. Windebank, M. J. Yaszemski, *Acta Biomater.* **2011**, *7*, 944.
[436] J. Tian, R. Shi, Z. Liu, H. Ouyang, M. Yu, C. Zhao, Y. Zou, D. Jiang, J. Zhang, Z. Li, *Nano Energy* **2019**, *59*, 705.
[437] M. N. Collins, G. Ren, K. Young, S. Pina, R. L. Reis, J. M. Oliveira, *Adv. Funct. Mater.*

**2021**, *31*.
[438] C. N. Kelly, J. Francovich, S. Julmi, D. Safranski, R. E. Guldberg, H. J. Maier, K. Gall, *Acta Biomater.* **2019**, *94*, 610.
[439] S. B. G. Blanquer, M. Werner, M. Hannula, S. Sharifi, G. P. R. Lajoinie, D. Eglin, J. Hyttinen, A. A. Poot, D. W. Grijpma, *Biofabrication* **2017**, *9*.
[440] H. Montazerian, M. G. A. Mohamed, M. M. Montazeri, S. Kheiri, A. S. Milani, K. Kim, M. Hoorfar, *Acta Biomater.* **2019**, *96*, 149.
[441] S. D. Smith, D. A. Agard, R. J. Spontak, *Adv. Mater.* **2002**, *14*, 1615.
[442] S. J. P. Callens, D. C. Tourolle né Betts, R. Müller, A. A. Zadpoor, *Acta Biomater.* **2021**, *130*, 343.
[443] R. V. Chernozem, M. A. Surmeneva, S. N. Shkarina, K. Loza, M. Epple, M. Ulbricht, A. Cecilia, B. Krause, T. Baumbach, A. A. Abalymov, B. V. Parakhonskiy, A. G. Skirtach, R. A. Surmenev, *ACS Appl. Mater. Interfaces* **2019**, *11*, 19522.
[444] M. T. Arafat, C. X. F. Lam, A. K. Ekaputra, S. Y. Wong, X. Li, I. Gibson, *Acta Biomater.* **2011**, *7*, 809.
[445] K. Zheng, J. Wu, W. Li, D. Dippold, Y. Wan, A. R. Boccaccini, *ACS Biomater. Sci. Eng.* **2018**, *4*, 1546.
[446] S. Afewerki, A. Sheikhi, S. Kannan, S. Ahadian, A. Khademhosseini, *Bioeng. Transl. Med.* **2019**, *4*, 96.
[447] X. Li, J. Xie, X. Yuan, Y. Xia, *Langmuir* **2008**, *24*, 14145.
[448] T. Ibn-Mohammed, S. C. L. Koh, I. M. Reaney, A. Acquaye, D. Wang, S. Taylor, A. Genovese, *Energy Environ. Sci.* **2016**, *9*, 3495.
[449] T. Ibn-Mohammed, S. C. L. Koh, I. M. Reaney, D. C. Sinclair, K. B. Mustapha, A. Acquaye, D. Wang, *MRS Commun.* **2017**, *7*, 1.
[450] A. Sharma, U. Bhardwaj, D. Jain, H. S. Kushwaha, *ACS Omega* **2022**, *7*, 7595.
[451] A. Sharma, U. Bhardwaj, D. Jain, H. S. Kushwaha, *iScience* **2022**, *25*, 104915.
[452] J. H. Jung, M. Lee, J. Il Hong, Y. Ding, C. Y. Chen, L. J. Chou, Z. L. Wang, *ACS Nano* **2011**, *5*, 10041.
[453] G. D'Ambrogio, O. Zahhaf, M. Q. Le, M. Bordet, P. Lermusiaux, N. Della Schiava, R. Liang, P. J. Cottinet, J. F. Capsal, *Mater. Des.* **2022**, *223*, 111195.
[454] A. L. Metze, A. Grimm, P. Nooeaid, J. A. Roether, J. Hum, P. J. Newby, D. W. Schubert, A. R. Boccaccini, *Key Eng. Mater.* **2013**, *541*, 31.
[455] N. Chaiyo, B. Boonchom, N. Vittayakorn, *J. Mater. Sci.* **2010**, *45*, 1443.
[456] M. S. Carvalho, L. Alves, I. Bogalho, J. M. S. Cabral, C. L. da Silva, *Front. Cell Dev. Biol.* **2021**, *9*, 1.
[457] G. Gouget, M. Duttine, E. Durand, A. Villesuzanne, V. Rodriguez, F. Adamietz, T. Le Mercier, M. D. Braida, A. Demourgues, *ACS Appl. Electron. Mater.* **2019**, *1*, 513.
[458] S. Li, Q. Xu, E. Uchaker, X. Cao, G. Cao, *CrystEngComm* **2016**, *18*, 2532.
[459] S. L. Fernandes, L. G. S. Albano, L. J. Affonço, J. H. D. da Silva, E. Longo, C. F. de O. Graeff, *Front. Chem.* **2019**, *7*, 1.
[460] U. Farooq, R. Phul, S. M. Alshehri, J. Ahmed, T. Ahmad, *Sci. Rep.* **2019**, *9*, 1.
[461] M. Boukriba, F. Sediri, N. Gharbi, *Mater. Res. Bull.* **2013**, *48*, 574.
[462] T. Y. Ke, H. A. Chen, H. S. Sheu, J. W. Yeh, H. N. Lin, C. Y. Lee, H. T. Chiu, *J. Phys. Chem. C* **2008**, *112*, 8827.
[463] S. K. Mohanty, B. Behera, B. Pati, P. R. Das, *J. Mater. Sci. Mater. Electron.* **2018**, *29*, 12269.

[464] M. Nyman, A. Tripathi, J. B. Parise, R. S. Maxwell, T. M. Nenoff, **2002**, 0.
[465] M. J. Hossan, M. A. Gafur, M. Kadir, M. M. Karim, *Int. J. Eng. Technol.* **2014**, *14*, 113.
[466] C. Wang, D. Xu, L. Lin, S. Li, W. Hou, Y. He, L. Sheng, C. Yi, X. Zhang, H. Li, Y. Li, W. Zhao, D. Yu, *Mater. Sci. Eng. C* **2021**, *131*.
[467] G. Li, L. Wang, W. Pan, F. Yang, W. Jiang, X. Wu, X. Kong, K. Dai, Y. Hao, *Sci. Rep.* **2016**, *6*, 1.
[468] J. Parthasarathy, B. Starly, S. Raman, A. Christensen, *J. Mech. Behav. Biomed. Mater.* **2010**, *3*, 249.
[469] F. S. L. Bobbert, K. Lietaert, A. A. Eftekhari, B. Pouran, S. M. Ahmadi, H. Weinans, A. A. Zadpoor, *Acta Biomater.* **2017**, *53*, 572.
[470] S. Chen, L. Li, C. Zhao, J. Zheng, *Polymer (Guildf).* **2010**, *51*, 5283.
[471] S. M. Mantila Roosa, J. M. Kemppainen, E. N. Moffitt, P. H. Krebsbach, S. J. Hollister, *J. Biomed. Mater. Res. - Part A* **2010**, *92*, 359.
[472] N. Abbasi, S. Hamlet, R. M. Love, N. T. Nguyen, *J. Sci. Adv. Mater. Devices* **2020**, *5*, 1.
[473] M. Q. Cheng, T. Wahafu, G. F. Jiang, W. Liu, Y. Q. Qiao, X. C. Peng, T. Cheng, X. L. Zhang, G. He, X. Y. Liu, *Sci. Rep.* **2016**, *6*, 1.
[474] D. E. Discher, D. J. Mooney, P. W. Zandstra, *Science (80-. ).* **2009**, *324*, 1673.
[475] S. H. Parekh, K. Chatterjee, S. Lin-Gibson, N. M. Moore, M. T. Cicerone, M. F. Young, C. G. Simon, *Biomaterials* **2011**, *32*, 2256.
[476] L. E. Jansen, N. P. Birch, J. D. Schiffman, A. J. Crosby, S. R. Peyton, *J. Mech. Behav. Biomed. Mater.* **2015**, *50*, 299.
[477] Y. S. Lai, W. C. Chen, C. H. Huang, C. K. Cheng, K. K. Chan, T. K. Chang, *PLoS One* **2015**, *10*.
[478] E. B. W. Giesen, M. Ding, M. Dalstra, T. M. G. J. Van Eijden, *J. Biomech.* **2001**, *34*, 799.
[479] E. F. Morgan, G. U. Unnikrisnan, A. I. Hussein, *Annu. Rev. Biomed. Eng.* **2018**, *20*, 119.
[480] C. Ma, T. Du, X. Niu, Y. Fan, *Bone Res.* **2022**, *10*.
[481] J. A. Stammeier, B. Purgstaller, D. Hippler, V. Mavromatis, M. Dietzel, *MethodsX* **2018**, *5*, 1241.
[482] L. Leppik, K. M. C. Oliveira, M. B. Bhavsar, J. H. Barker, *Eur. J. Trauma Emerg. Surg.* **2020**, *46*, 231.
[483] D. Khare, B. Basu, A. K. Dubey, *Biomaterials* **2020**, *258*, 120280.
[484] B. C. Heng, X. Zhang, D. Aubel, Y. Bai, X. Li, Y. Wei, M. Fussenegger, X. Deng, *Front. Cell Dev. Biol.* **2020**, *8*, 1.
[485] J. K. Virdi, P. Pethe, *Tissue Eng. Regen. Med.* **2021**, *18*, 199.
[486] L. Azzolin, T. Panciera, S. Soligo, E. Enzo, S. Bicciato, S. Dupont, S. Bresolin, C. Frasson, G. Basso, V. Guzzardo, A. Fassina, M. Cordenonsi, S. Piccolo, *Cell* **2014**, *158*, 157.
[487] A. A. Bertrand, S. H. Malapati, D. T. Yamaguchi, J. C. Lee, *Adv. Healthc. Mater.* **2020**, *9*.
[488] K. K. Das, B. Basu, P. Maiti, A. K. Dubey, *Appl. Mater. Today.* **2024**, *39*, 102332.
[489] Y. Wu, J. Wu, X. Huang, X. Zhu, W. Zhi, J. Wang, D. Sun, X. Chen, X. Zhu, X. Zhang, *Mater. Today Bio* **2023**, *23*, 100891.
[490] M. Guillot-Ferriols, C. M. Costa, D. M. Correia, J. C. Rodríguez-Hernández, P. M. Tsimbouri, S. Lanceros-Méndez, M. J. Dalby, J. L. Gómez Ribelles, G. Gallego-Ferrer, *ACS Appl. Polym. Mater.* **2024**, 6, 2, 13710–13722.
[491] U. N. E. P. (UNEP), *Food Waste Index Report 2024: Think Eat Save — Tracking Progress to Halve Global Food Waste*, Nairobi, **2024**.

[492] U. N. E. P. (UNEP), *Food Waste Index Report*, Nairobi, **2021**.
[493] WHO - World Health Organization, *Towards Stronger Food Safety Systems and Global Cooperation*, **2022**.
[494] C. Papuc, G. V. Goran, C. N. Predescu, V. Nicorescu, *Compr. Rev. Food Sci. Food Saf.* **2017**, *16*, 96.
[495] Y. K. Ip, S. F. Chew, *Front. Physiol.* **2010**, *1 OCT*, 1.
[496] S. Zhuang, L. Tian, Y. Liu, L. Wang, H. Hong, Y. Luo, *Food Chem.* **2023**, *399*, 133989.
[497] T. Abekoon, B. L. S. K. Buthpitiya, H. Sajindra, E. R. J. Samarakoon, J. A. D. C. A. Jayakody, K. Kantamaneni, U. Rathnayake, *Discov. Sustain.* **2024**, *5*.
[498] S. N. Marques CS, Silva RRA, Arruda TR, Oliveira TV, *Intelligent Packaging – Indicators. In: Bangar SN, Trif M (Eds) Intelligent Packaging: Current Technologies and Applications*, Academic Press/Elsevier, **2024**.
[499] R. S. Andre, L. A. Mercante, M. H. M. Facure, R. C. Sanfelice, L. Fugikawa-Santos, T. M. Swager, D. S. Correa, *ACS Sensors* **2022**, *7*, 2104.
[500] S. C. Teixeira, T. V. de Oliveira, R. R. Assis Silva, A. R. C. Ribeiro, P. C. Stringheta, T. C. B. Rigolon, M. R. M. R. Pinto, N. de F. F. Soares, *Food Biosci.* **2022**, *48*.
[501] B. Kuswandi, Jayus, A. Restyana, A. Abdullah, L. Y. Heng, M. Ahmad, *Food Control* **2012**, *25*, 184.
[502] S. Aarya, Y. Kumar, R. K. Chahota, *J. Inorg. Organomet. Polym. Mater.* **2020**, *30*, 269.
[503] X. Liu, S. Cheng, H. Liu, S. Hu, D. Zhang, H. Ning, *Sensors (Switzerland)* **2012**, *12*, 9635.
[504] D. Kwak, Y. Lei, R. Maric, *Talanta* **2019**, *204*, 713.
[505] L. Huang, J. Su, Y. Song, R. Ye, *Nano-Micro Lett.* **2020**, *12*.
[506] T. Pinheiro, M. Morais, S. Silvestre, E. Carlos, J. Coelho, H. V. Almeida, P. Barquinha, E. Fortunato, R. Martins, *Adv. Mater.* **2024**, *36*.
[507] J. Lin, Z. Peng, Y. Liu, F. Ruiz-Zepeda, R. Ye, E. L. G. Samuel, M. J. Yacaman, B. I. Yakobson, J. M. Tour, *Nat. Commun.* **2014**, *5*, 5.
[508] J. Zhu, X. Huang, W. Song, *ACS Nano* **2021**, *15*, 18708.
[509] S. Aftab, G. Koyyada, M. Mukhtar, F. Kabir, G. Nazir, S. A. Memon, M. Aslam, M. A. Assiri, J. H. Kim, *ACS Sensors* **2024**, *9*, 4536.
[510] H. T. M. Hoa, K. J. Lee, H. P. Pham, T. A. Doan, H. H. Nguyen, T. Q. Nguyen, Q. T. Tran, T. V. Cuong, *J. Nanomater.* **2020**, *7680508*.
[511] M. Gautam, A. H. Jayatissa, *Solid. State. Electron.* **2012**, *78*, 159.
[512] Y. Mu, J. Islam, R. Murray, C. Larrigy, A. Russo, X. Zhang, A. J. Quinn, D. Iacopino, *Analyst* **2023**, *148*, 3087.
[513] Y. Zhang, N. Li, Y. Xiang, D. Wang, P. Zhang, Y. Wang, S. Lu, R. Xu, J. Zhao, *Carbon N. Y.* **2020**, *156*, 506.
[514] E. Gençdağ, E. E. Özdemir, K. Demirci, A. Görgüç, F. M. Yılmaz, *Curr. Plant Biol.* **2022**, *29*.
[515] P. A. V. Freitas, R. R. A. Silva, T. V. de Oliveira, R. R. A. Soares, N. S. Junior, A. R. F. Moraes, A. C. dos S. Pires, N. F. F. Soares, *LWT* **2020**, *132*.
[516] L. Paralı, *J. Mater. Sci. Mater. Electron.* **2024**, *35*, 1.
[517] S. C. Q. Chen, V. Thomas, *IEEE Int. Symp. Electron. Environ.* **2001**, 82.
[518] A. Castañeda-Ovando, M. de L. Pacheco-Hernández, M. E. Páez-Hernández, J. A. Rodríguez, C. A. Galán-Vidal, *Food Chem.* **2009**, *113*, 859.
[519] S. Roy, J. W. Rhim, *Crit. Rev. Food Sci. Nutr.* **2021**, *61*, 2297.

[520] L. Meng, S. Chirtes, X. Liu, M. Eriksson, W. C. Mak, *Biosens. Bioelectron.* **2022**, *218*, 114742.
[521] H. Zhang, Q. Yan, Y. Peng, Z. Cai, C. Wan, *Adv. Energy Sustain. Res.* **2024**, *5*.
[522] P. Zhao, C. Liang, Y. Zhang, C. Zhang, X. Mao, J. Song, N. Zhao, M. Liu, *J. Anal. Appl. Pyrolysis* **2025**, *186*, 106927.
[523] J. Coelho, R. F. Correia, S. Silvestre, T. Pinheiro, A. C. Marques, M. R. P. Correia, J. V. Pinto, E. Fortunato, R. Martins, *Microchim. Acta* **2023**, *190*, 0.
[524] X. Chen, X. Wang, D. Fang, *Fullerenes Nanotub. Carbon Nanostructures* **2020**, *0*, 1048.
[525] S. Ray, in *Proc. Int. Conf. Mach. Learn. Big Data, Cloud Parallel Comput. Trends, Prespectives Prospect. Com.*, IEEE, **2019**, pp. 35–39.
[526] D. Maulud, A. M. Abdulazeez, *J. Appl. Sci. Technol. Trends* **2020**, *1*, 140.
[527] L. Zhang, Q. Tan, H. Kou, D. Wu, W. Zhang, J. Xiong, *Sci. Rep.* **2019**, *9*, 1.
[528] J. Jun, J. Oh, D. H. Shin, S. G. Kim, J. S. Lee, W. Kim, J. Jang, *ACS Appl. Mater. Interfaces* **2016**, *8*, 33139.
[529] R. R. A. Silva, G. Fatti, E. Carlos, G. Ferreira, S. Goswami, S. Nandy, L. H. C. Mattoso, E. Fortunato, C. G. Otoni, R. Martins, *Adv. Funct. Mater.* **2025**, *36*, 13, e13924.
[530] L. Gao, K. Liu, W. Wang, X. Li, Q. Deng, N. Hu, X. Chen, X. Mu, *Adv. Funct. Mater.* **2025**, *17158*, 1.
[531] M. Zhu, M. Xie, X. Lu, S. Okada, S. Kawamura, *Nano Energy* **2020**, *73*, 104772.
[532] J. Chen, K. Han, J. Luo, L. Xu, W. Tang, Z. L. Wang, *Nano Energy* **2020**, *77*, 105171.
[533] P. Li, H. P. Anwar Ali, W. Cheng, J. Yang, B. C. K. Tee, *Adv. Mater. Technol.* **2020**, *5*, 1.
[534] U. Tanriverdi, G. Senesi, T. Asfour, H. Kurt, S. L. Smith, D. Toderita, J. Shalhoub, L. Burgess, A. M. J. Bull, F. Güder, *Nat. Commun.* **2025**, *16*, 1.
[535] R. Green, M. R. Abidian, *Adv. Mater.* **2015**, *27*, 7620.
[536] W. Sun, B. Li, F. Zhang, C. Fang, Y. Lu, X. Gao, C. Cao, G. Chen, C. Zhang, Z. L. Wang, *Nano Energy* **2021**, *85*.
[537] G. Ferreira, S. Das, G. Coelho, R. R. A. Silva, S. Goswami, R. N. Pereira, L. Pereira, E. Fortunato, R. Martins, S. Nandy, *J. Energy Chem.* **2025**, *102*, 230.
[538] Y. Liu, J. Wang, T. Liu, Z. Wei, B. Luo, M. Chi, S. Zhang, C. Cai, C. Gao, T. Zhao, S. Wang, S. Nie, *Nat. Commun.* **2025**, *16*, 1.
[539] A. Moglia, K. Georgiou, E. Georgiou, R. M. Satava, A. Cuschieri, *Int. J. Surg.* **2021**, *95*, 106151.
[540] P. Fiorini, K. Y. Goldberg, Y. Liu, R. H. Taylor, *Proc. IEEE* **2022**, *110*, 993.
[541] A. Chen, X. Zou, Y. Tan, Y. Chen, X. Ye, S. Hao, *Gland Surg.* **2021**, *10*, 3305.
[542] A. Fuschi, A. L. Pastore, Y. Al Salhi, A. Martoccia, C. De Nunzio, G. Tema, O. A. Rera, F. Carbone, A. D. Asimakopoulos, M. B. Sequi, F. M. Valenzi, P. Pietro Suraci, S. Scalzo, F. Del Giudice, S. Nardecchia, G. Bozzini, A. Corsini, A. Sciarra, A. Carbone, *Prostate Cancer Prostatic Dis.* **2024**, *27*, 272.
[543] S. K. Sharma, X. Wang, *IEEE Commun. Surv. Tutorials* **2020**, *22*, 426.
[544] Y. Cao, Y. Guo, Z. Chen, W. Yang, K. Li, X. He, J. Li, *Nano Energy* **2022**, *92*, 106689.
[545] Q. Tu, Q. Zhang, Y. Wang, Y. Jiao, J. Xiao, T. Peng, J. Wang, *Prog. Org. Coatings* **2019**, *129*, 247.
[546] T. P. Xavier, M. Piraviperumal, *ACS Appl. Mater. Interfaces* **2024**, 16, 33, 44114–44126.
[547] N. Lu, W. Zhang, Y. Weng, X. Chen, Y. Cheng, P. Zhou, *Food Control* **2016**, *68*, 344.
[548] R. Jiang, L. Hao, L. Song, L. Tian, Y. Fan, J. Zhao, C. Liu, W. Ming, L. Ren, *Chem. Eng. J.*

**2020**, *398*, 125609.
[549] W. Yao, L. Li, O. L. Li, Y. W. Cho, M. Y. Jeong, Y. R. Cho, *Chem. Eng. J.* **2018**, *352*, 173.
[550] J. S. Y. Bhaskar Dudem, Yeong Hwan Ko, Jung Woo Leem, Joo Ho Lim, *ACS Appl. Mater. Interfaces* **2016**, *8*, 30165.
[551] H. Wu, X. Liu, W. Li, S. Kang, B. Zhu, L. Yang, R. Liao, Z. An, J. Wang, *Nano Energy* **2024**, *123*, 109441.
[552] E. Cho, K. N. Kim, H. Yong, W. J. Choi, J. S. Park, S. J. Lee, *Nano Energy* **2022**, *103*, 107785.
[553] R. R. A. Silva, F. Barbosa, G. Ferreira, C. Ureña, E. H. Backes, J. M. Inácio, J. A. Belo, R. Igreja, J. C. Silva, L. H. C. Mattoso, E. Fortunato, H. M. V. Almeida, R. Martins, C. G. Otoni, *Mater. Today* **2025**, *88*, 186.
[554] I. Miranda, A. Souza, P. Sousa, J. Ribeiro, E. M. S. Castanheira, R. Lima, G. Minas, *J. Funct. Biomater.* **2022**, *13*.
[555] Y. Li, Z. Song, G. Tian, H. Hu, G. Cheng, X. Feng, J. Ding, *Surf. Coatings Technol.* **2024**, *492*, 131242.
[556] S. J. Lee, D. Z. Segu, C. L. Kim, *RSC Adv.* **2024**, *14*, 37062.
[557] G. Gonçalves, E. Elangovan, P. Barquinha, L. Pereira, R. Martins, E. Fortunato, *Thin Solid Films* **2007**, *515*, 8562.
[558] J. L. N. Boane, P. Centeno, A. Mouquinho, M. Alexandre, T. Calmeiro, E. Fortunato, R. Martins, M. J. Mendes, H. Águas, *Micro* **2021**, *1*, 215.
[559] H. W. Fox, W. A. Zisman, *J. Colloid Sci.* **1950**, *5*, 514.
[560] H. Hillborg, J. F. Ankner, U. W. Gedde, G. D. Smith, H. K. Yasuda, K. Wikström, *Polymer (Guildf).* **2000**, *41*, 6851.
[561] R. N. Wenzel, *Ind. Eng. Chem.* **1936**, *28*, 988.
[562] C. Mayorga, S. M. Athalye, M. Boodaghidizaji, N. Sarathy, M. Hosseini, A. Ardekani, M. S. Verma, *Anal. Chem.* **2025**, *97*, 8908.
[563] B. Taudul, F. Tielens, M. Calatayud, *J. Phys. Chem. B* **2024**, *128*, 4243.
[564] S. E. Kichanov, D. P. Kozlenko, N. M. Belozerova, S. H. Jabarov, R. Z. Mehdiyeva, E. V. Lukin, A. I. Mammadov, H. P. Liermann, W. Morgenroth, L. S. Dubrovinsky, B. N. Savenko, I. P. Raevskii, N. T. Dang, *Ferroelectrics* **2017**, *520*, 22.
[565] H. Y. Jung, R. K. Gupta, E. O. Oh, Y. H. Kim, C. M. Whang, *J. Non. Cryst. Solids* **2005**, *351*, 372.
[566] Q. Sun, Y. N. Chen, Y. Z. Liu, *Materials (Basel).* **2025**, *18*, 1.
[567] C. E. Cansoy, H. Y. Erbil, O. Akar, T. Akin, *Colloids Surfaces A Physicochem. Eng. Asp.* **2011**, *386*, 116.
[568] S. Nundy, A. Ghosh, T. K. Mallick, *ACS Omega* **2020**, *5*, 1033.
[569] Y. Quan, L. Zhang, R. Qi, R. Cai, *Nat. Publ. Gr.* **2016**, 1.
[570] F. Shi, X. Wei, S. Wang, H. Zhang, F. Yan, Y. Li, Y. Tian, T. Lin, *ACS Appl. Mater. Interfaces* **2025**, *17*, 52556.
[571] J. Pereira, L. E. Pichon, R. Dussart, C. Cardinaud, C. Y. Duluard, E. H. Oubensaid, P. Lefaucheux, M. Boufnichel, P. Ranson, *Appl. Phys. Lett.* **2009**, *94*, 2.
[572] H. T. Sahin, *J. Wood Chem. Technol.* **2020**, *40*, 91.
[573] N. Ahmadizadeh, M. Sobhani, A. Habibolahzadeh, *Appl. Surf. Sci.* **2023**, *641*, 158534.
[574] C. Wang, Y. Liu, Y. Li, Y. Tian, C. Wang, T. Suga, *ECS J. Solid State Sci. Technol.* **2017**, *6*, P373.
[575] G. T. Roman, C. T. Culbertson, *Langmuir* **2006**, *22*, 4445.

[576] S. K. Rath, J. G. Chavan, S. Sasane, M. Patri, A. B. Samui, B. C. Chakraborty, *Appl. Surf. Sci.* **2010**, *256*, 2440.
[577] G. G. Martinelli E, Guazzelli E, Glisenti A, *Coatings* **2019**, *9*, 26.
[578] G. Antoun, A. Girard, T. Tillocher, P. Lefaucheux, J. Faguet, K. Maekawa, C. Cardinaud, R. Dussart, *ECS J. Solid State Sci. Technol.* **2022**, *11*, 013013.
[579] M. Kanezashi, M. Murata, H. Nagasawa, T. Tsuru, *ACS Omega* **2018**, *3*, 8612.
[580] D. Ricci, A. Maio, C. Jahns, E. Piacenza, D. F. Chillura Martino, R. Scaffaro, M. Schulze, A. Pace, C. Rizzo, I. Pibiri, *European J. Org. Chem.* **2025**, *28*.
[581] A. P. Dementjev, A. V. Eletskii, K. I. Maslakov, E. G. Rakov, V. F. Sukhoverhov, A. V. Naumkin, *Fullerenes Nanotub. Carbon Nanostructures* **2006**, *14*, 287.
[582] X. Shi, R. Bi, X. Shu, P. Wang, Y. Chun, Z. Chen, C. Zhou, Y. Lu, O. J. Rojas, **2025**, *2504381*, 1.
[583] J. Yu, L. Chen, X. Hou, J. Mu, J. He, W. Geng, X. Qiao, X. Chou, *J. Mater.* **2022**, *8*, 247.
[584] X. Z. Jiang, Y. J. Sun, Z. Fan, T. Y. Zhang, *ACS Nano* **2016**, *10*, 7696.
[585] D. Yang, H. Guo, X. Chen, L. Wang, P. Jiang, W. Zhang, L. Zhang, Z. L. Wang, *J. Mater. Chem. A* **2020**, *8*, 23827.
[586] M. S. Rasel, P. Maharjan, M. Salauddin, M. T. Rahman, H. O. Cho, J. W. Kim, J. Y. Park, *Nano Energy* **2018**, *49*, 603.
[587] J. Huang, Y. Hao, M. Zhao, H. Qiao, F. Huang, D. Li, Q. Wei, *Compos. Part A Appl. Sci. Manuf.* **2021**, *146*, 106412.
[588] M. Ha, S. Lim, S. Cho, Y. Lee, S. Na, C. Baig, H. Ko, *ACS Nano* **2018**, *12*, 3964.
[589] G. Yao, L. Xu, X. Cheng, Y. Li, X. Huang, W. Guo, S. Liu, Z. L. Wang, H. Wu, *Adv. Funct. Mater.* **2020**, *30*, 1.
[590] C. Ning, K. Dong, R. Cheng, J. Yi, C. Ye, X. Peng, F. Sheng, Y. Jiang, Z. L. Wang, *Adv. Funct. Mater.* **2021**, *31*, 1.
[591] R. Xu, F. Luo, Z. Zhu, M. Li, B. Chen, *ACS Appl. Electron. Mater.* **2022**, 4, 8, 4051–4060.
[592] Y. Yang, H. Zhang, Z. H. Lin, Y. S. Zhou, Q. Jing, Y. Su, J. Yang, J. Chen, C. Hu, Z. L. Wang, *ACS Nano* **2013**, *7*, 9213.
[593] B. Ji, Q. Zhou, B. Hu, J. Zhong, J. Zhou, B. Zhou, *Adv. Mater.* **2021**, *33*, 1.
[594] M. Zhu, Y. Wang, M. Lou, J. Yu, Z. Li, B. Ding, *Nano Energy* **2021**, *81*, 105669.
[595] R. Puers, D. Lapadatu, *Sensors Actuators A* **1996**, *56*, 203.
[596] K. Lee, J. O. Lee, S. Choi, J. Yoon, G. Cho, *Biosens. Bioelectron.* **2012**, *31*, 343.
[597] A. Mizuno, *IEEE Trans. Dielectr. Electr. Insul.* **2000**, *7*.
[598] D. Tang, X. Zhuang, C. Zhang, B. Cheng, X. Li, *J. Appl. Polym. Sci.* **2015**, *42326*, 1.
[599] C. Zhang, W. Tang, L. Zhang, C. Han, Z. L. Wang, C. Academy, M. Science, U. States, *ACS Nano* **2014**, *8*, 8702.
[600] T. L. Sounart, T. A. Michalske, K. R. Zavadil, *J. Microelectromech. Syst.* **2005**, *14*, 125.
[601] S. M. Kathmann, I. W. Kuo, C. J. Mundy, G. K. Schenter, *J. Phys. Chem. B* **2011**, *115*, 4369.
[602] J. Chun, B. U. Ye, J. W. Lee, D. Choi, C. Y. Kang, S. W. Kim, Z. L. Wang, J. M. Baik, *Nat. Commun.* **2016**, *7*, 1.
[603] B. Luo, T. Liu, C. Cai, J. Yuan, Y. Liu, C. Gao, X. Meng, J. Wang, S. Zhang, M. Chi, Y. Qin, J. Zhao, X. Zhuang, S. Wang, S. Nie, *Nano Energy* **2023**, *113*, 108532.
[604] Z. H. Lin, G. Cheng, S. Lee, K. C. Pradel, Z. L. Wang, *Adv. Mater.* **2014**, *26*, 4690.
[605] L. Zhao, L. Liu, X. Yang, H. Hong, Q. Yang, J. Wang, Q. Tang, *J. Mater. Chem. A* **2020**, *8*, 7880.

[606] C. Hu, W. Wang, Y. Liu, W. Sun, H. Wang, J. Meng, W. Wang, W. Li, X. Wu, D. Wang, *Nano Energy* **2024**, *130*, 110132.
[607] W. Xu, H. Zheng, Y. Liu, X. Zhou, C. Zhang, Y. Song, X. Deng, M. Leung, Z. Yang, R. X. Xu, Z. L. Wang, X. C. Zeng, Z. Wang, *Nature* **2020**, *578*, 392.
[608] K. R. Kaja, S. Hajra, S. Panda, M. A. Belal, U. Pharino, H. Khanbareh, N. Vittayakorn, V. Vivekananthan, C. Bowen, H. J. Kim, *Nano Energy* **2024**, *131*, 110319.
[609] Z. Yuan, L. Guo, *Sci. Rep.* **2024**, *14*, 1.
[610] J. Fu, G. Xu, H. Wu, C. Li, Y. Zi, *Adv. Energy Sustain. Res.* **2022**, *3*.
[611] D. Wei, Z. L. Wang, *Nat. Commun.* **2024**, 1.
[612] N. M. Vargas-Barbosa, B. Roling, *ChemElectroChem* **2020**, *7*, 367.
[613] J. Park, Y. Yang, S. Kwon, Y. S. Kim, *J. Phys. Chem. Lett.* **2015**, *6*, 745.
[614] L. Zhang, X. Li, Y. Zhang, Y. Feng, F. Zhou, D. Wang, *Nano Energy* **2020**, *78*, 105370.
[615] P. Jiang, L. Zhang, H. Guo, C. Chen, C. Wu, S. Zhang, Z. L. Wang, *Adv. Mater.* **2019**, *31*, 1.
[616] J. Nie, Z. Ren, L. Xu, S. Lin, F. Zhan, X. Chen, Z. L. Wang, *Adv. Mater.* **2020**, *32*, 1.
[617] S. Lin, M. Zheng, J. Luo, Z. L. Wang, *ACS Nano* **2020**, *14*, 10733.
[618] S. Jang, M. La, S. Cho, Y. Yun, J. H. Choi, Y. Ra, S. J. Park, D. Choi, *Nano Energy* **2020**, *70*, 104541.
[619] X. Wu, T. Cai, Q. Wu, J. Meng, W. Wang, W. Li, C. Hu, X. Zhang, D. Wang, *ACS Appl. Mater. Interfaces* **2025**, *17*, 13762.
[620] J. Zhang, X. Wang, L. Zhang, S. Lin, S. Ciampi, Z. L. Wang, *J. Am. Chem. Soc.* **2024**, *146*, 6125.
[621] J. H. Ahn, J. Y. Hwang, C. G. Kim, G. H. Nam, K. K. Ahn, *Nano Energy* **2020**, *67*, 104269.
[622] W. Kim, D. Choi, J. Y. Kwon, D. Choi, *J. Mater. Chem. A* **2018**, *6*, 14069.
[623] Y. T. Huang, A. Khan, A. Ganguly, K. Kaswan, S. Suresh, Y. Y. Cheng, K. M. Lee, J. H. Yu, Z. H. Lin, *Adv. Sci.* **2025**, *12*, 1.
[624] B. Kil Yun, H. Soo Kim, Y. Joon Ko, G. Murillo, J. Hoon Jung, *Nano Energy* **2017**, *36*, 233.
[625] Z. Lin, G. Cheng, L. Lin, S. Lee, Z. L. Wang, *Angew. Chem. Int. Ed.* **2013**, *52*, 12545.
[626] J. Wang, Z. Wu, L. Pan, R. Gao, B. Zhang, L. Yang, H. Guo, R. Liao, Z. L. Wang, *ACS Nano* **2019**, *13*, 2587.
[627] Y. Litman, K. Chiang, T. Seki, Y. Nagata, M. Bonn, *Nat. Chem.* **2024**, *16*, 12.
[628] T. Seki, C. Yu, K. Chiang, A. Greco, X. Yu, F. Matsumura, M. Bonn, Y. Nagata, *J. Am. Chem. Soc. 2023*, **2023**, *145*, 10622.
[629] L. M. Pegram, M. T. Record, *J. Phys. Chem. B* **2007**, *111*, 5411.
[630] L. Piatkowski, Z. Zhang, E. H. G. Backus, H. J. Bakker, M. Bonn, *Nat. Commun.* **2014**, *5:4083*, 1.
[631] Y. Levin, A. P. Santos, A. Diehl, *Phys. Rev. Lett.* **2009**, *257802*, 1.
[632] B. Chu, D. Biriukov, P. Milan, *Faraday Discuss* **2023**, *246*, 407.
[633] N. Goswami, R. Kant, *Adv. Theory Simul.* **2025**, 1.
[634] I. Płowaś, J. Świergiel, J. Jadżyn, *Electrochim. Acta* **2015**, *178*, 511.
[635] A. Lyashchenko, A. Lileev, *J. Chem. Eng. Data* **2016**, *55*, 2008.

# A

# AN APPENDIX

Code for illuminating one, two, or three LEDs according to predefined $V_{oc}$ thresholds of the HMN-TENG:

```
//data_type variable_name = assigned value;
int ledPin1 = 2;
int ledPin2 = 4;
int ledPin3 = 7;

#define TENGvoltage A0

void setup() {
  // put your setup code here, to run once:

  pinMode(ledPin1,OUTPUT);
  pinMode(ledPin2,OUTPUT);
  pinMode(ledPin3,OUTPUT);
  Serial.begin(9600);

}

void loop() {
  // put your main code here, to run repeatedly:
```

```
int voltage = analogRead(TENGvoltage);
Serial.print("TENG voltage: ");
Serial.println(voltage);

if ( 1023 >= voltage && voltage > 650)
{digitalWrite(ledPin1,HIGH);
  digitalWrite(ledPin2,HIGH);
  digitalWrite(ledPin3,HIGH);
  delay(2000);}

else if (650 >= voltage && voltage > 350) {
  digitalWrite(ledPin1,HIGH);
  digitalWrite(ledPin2,HIGH);
  delay (2000);
}

else if ( 350 >= voltage && voltage > 320) {
  digitalWrite(ledPin1,HIGH);
  delay(2000);
}

else {
  digitalWrite(ledPin1,LOW);
  digitalWrite(ledPin2,LOW);
  digitalWrite(ledPin3,LOW);
}
}
```

RAFAEL RESENDE ASSIS SILVA

# NANOTECHNOLOGY FOR ENERGY HARVESTING: FROM FUNDAMENTAL TRIBOELECTRIFICATION TO SELF-POWERED SMART APPLICATIONS VIA TRIBOELECTRIC AND PIEZOELECTRIC NANOGENERATORS

〈2025〉